DOT/FAA/AR-08/13

Air Traffic Organization
Operations Planning
Office of Aviation Research
and Development
Washington, DC 20591

Experimental Study of Supercooled Large Drop Impingement on Ice Shapes

July 2008

Final Report

U.S. Department of Transportation
Federal Aviation Administration

NOTICE

This report is available at the Federal Aviation Administration William J. Hughes Technical Center's Full-Text Technical Reports page: actlibrary.act.faa.gov in Adobe Acrobat portable document format (PDF).

Technical Report Documentation Page

1. Report No.	2. Government Accession No.	3. Recipient's Catalog No.
DOT/FAA/AR-08/13		

4. Title and Subtitle	5. Report Date
EXPERIMENTAL STUDY OF SUPERCOOLED LARGE DROP IMPINGEMENT ON ICE SHAPES	July 2008
	6. Performing Organization Code

7. Author(s)	8. Performing Organization Report No.
Michael Papadakis[1], Arief Rachman[1], See-Cheuk Wong[1], Hsiung-Wei Yeong[1], Kuohsing E. Hung[2], Giao T. Vu[2], and Colin S. Bidwell[3]	

9. Performing Organization Name and Address	10. Work Unit No. (TRAIS)
[1]Wichita State University Department of Aerospace Engineering Wichita, KS 67260 [2]The Boeing Company Wichita, KS 67260 [3]NASA Glenn Research Center Cleveland, OH 44135	
	11. Contract or Grant No.

12. Sponsoring Agency Name and Address	13. Type of Report and Period Covered
U.S. Department of Transportation Federal Aviation Administration Air Traffic Organization Operations Planning Office of Aviation Research and Development Washington, DC 20591	Final Report
	14. Sponsoring Agency Code AIR-100

15. Supplementary Notes

The Federal Aviation Administration Airport and Aircraft Safety R&D Division COTR was James Riley.

16. Abstract

Water drop impingement data were obtained at the National Aeronautics and Space Administration (NASA) Glenn Icing Research Tunnel for a 36-in chord National Advisory Committee for Aeronautics 23012 airfoil and ten simulated ice shapes using a dye-tracer method. The simulated ice shapes were defined with the NASA Glenn LEWICE 2.2 ice accretion code and included one rime, four mixed, and five glaze ice shapes. The impingement experiments were performed with spray clouds having median volumetric diameters (MVD) of 20, 52, 111, 154, and 236 μm. Flow conditions included an angle of attack of 2.5 degrees, total air temperature in the range of 40°-77°F, and airspeed of 175 mph, corresponding to a Reynolds number of approximately 1.6 million per foot. Test repeatability was established by computing the maximum difference of the peak and total impingement efficiencies of individual test results from the average of all repeated tests at a given condition. The maximum variation of the peak impingement efficiency, $\overline{\beta}_{max}$, from the average, was less than 10% for 52 of the 56 cases tested, while the maximum variation of the total impingement efficiency from the average was less than 10% for 55 out of the 56 cases. The experimental data showed that in general, the peak efficiencies and impingement limits for the clean and iced cases increased as the MVD was increased. The impingement curves of the glaze and mixed ice shapes exhibited multiple peaks in the region between the horns. In many cases, peaks in the impingement curves were also observed downstream of the horns. For the large MVD cases, the majority of the ice shapes tested had considerable impingement downstream of the horns along the airfoil upper and lower surfaces.

An analysis of impingement data was performed with a modified version of the NASA Glenn LEWICE 1.6 code (this code can use drop distributions with more than ten drop sizes; a Monte-Carlo method is also available for impingement computations) and was compared to the experimental results. For the 20-μm MVD and the clean airfoil, the LEWICE results and the experimental data were in good agreement. For the iced configurations, however, the predicted impingement efficiency for the 20-μm MVD was higher than that obtained experimentally. For the large MVD cases of 52, 111, 154, and 236 μm, the LEWICE impingement data for the clean and iced configurations exhibited considerably higher local and total impingement efficiencies and larger impingement limits than the experimental results. This discrepancy was attributed to drop splashing experienced by the large drops during impingement.

17. Key Words	18. Distribution Statement
Water drop impingement, Dye-tracer method, LEWICE, Simulated ice shape	This document is available to the U.S. public through the National Technical Information Service (NTIS), Springfield, Virginia 22161.

19. Security Classif. (of this report)	20. Security Classif. (of this page)	21. No. of Pages	22. Price
Unclassified	Unclassified	336	

ACKNOWLEDGEMENTS

Funding for this work was provided by the Federal Aviation Administration (FAA) and the National Aeronautics and Space Administration (NASA) Glenn Research Center. The authors would like to thank the following FAA and NASA senior personnel for their encouragement and support: Manny Rios and Jim Riley, Project Managers, Eugene Hill, National Icing Research Specialist for the FAA, and Tom Bond, Chief of the Icing Branch at the NASA Glenn Research Center. Thanks are also expressed to Robert F. Ide, Dave Sheldon, Tim Bencic, John R. Oldenburg, Charlie Andracchio, and the Icing Research Tunnel personnel of the NASA Glenn Research Center for their extensive support with the impingement tests. Finally, acknowledgement is made for the support provided by The Boeing Company and the extensive contributions to this program by Art Porter, Emily Smythe, Norma Campos, Duc Pham, and Dennis Regnier of the Wichita State University.

TABLE OF CONTENTS

APPENDICES

LIST OF FIGURES

LIST OF TABLES

LIST OF SYMBOLS, ACRONYMS, ABBREVIATIONS, AND DEFINITIONS

α	Angle of attack
A_f	Frontal area of a body projected parallel to freestream velocity direction
A_∞	Area perpendicular to freestream direction, defined by the tangent trajectories
$\overline{\beta}_1$	Absolute maximum local impingement efficiency observed at the leading-edge region of the clean or iced models
$\overline{\beta}_2$	Minimum local impingement efficiency observed between the upper and lower horns of the glaze and mixed ice shapes tested
c	Model chord length
C_D	Drop drag coefficient
C_f	Nozzle flow coefficient
D, d	Drop diameter
D_{max}	Maximum drop diameter in clouds of nonuniform drop size
D_{min}	Minimum drop diameter in clouds of nonuniform drop size
D_{MVD}	Drop diameter based on MVD
$\overline{E}$	Total impingement efficiency in clouds of nonuniform drop size
g	Acceleration due to gravity
K	Drop inertia parameter, $\rho_{droplet} \cdot V_\infty \cdot MVD^2 / (18 \cdot \mu \cdot c)$
K_{IP}	Impact parameter
K_0	Modified drop inertia parameter, $K \cdot \lambda / \lambda_s$
L	Characteristic dimension of a body
M	Mach number of airflow relative to drop
M_∞	Freestream Mach number of airflow
Oh	Ohnesorge number
R_{MAX}	Repeatability based on maximum local impingement efficiency
R_{AREA}	Repeatability based on total impingement efficiency
Re	Reynolds number
Re_c	Reynolds number based on chord length
Re_v	Reynolds number of airflow relative to drop
Re_{MVD}	Reynolds number based on MVD and freestream speed
R_n	Normalized reflectance
S	Surface distance from highlight
S_l	Surface distance from highlight to impingement limit on lower surface
S_u	Surface distance from highlight to impingement limit on upper surface
t	Time; Airfoil thickness
U_i	Initial drop velocity
V	Potential flow velocity dimensionless with V_∞
V_i	Initial potential flow velocity
V_∞	Freestream airspeed
$\dot{w}$	Water flow rate from WSU spray nozzles
We	Weber number
x,y	Cartesian coordinates
x_l	Chordwise distance corresponding to the impingement limit on the lower surface
x_u	Chordwise distance corresponding to the impingement limit on the upper surface

$\bar{\beta}$	Local impingement efficiency
ΔP	P_{water}-P_{air}
δ_{ij}	Kronecker delta
ϕ	Independent impingement parameter, $(\mathrm{Re}_{MVD})^2 / K$
λ	True range of drop as projectile injected into still air
λ_s	Range of drop as projectile following Stokes' law
ρ	Air density
ρ_ω	Density of water
AOA	Angle of attack
CCD	Charge-coupled device
CFR	Code of Federal Regulations
DAQ	Data acquisition
DIO	Digital input output
ESP	Electronically scanned pressure
FAA	Federal Aviation Administration
FSSP	Forward Scattering Spectrometer Probe
IRT	Icing Research Tunnel
JAA	Joint Aviation Authority
LED	Light emitting diode
LWC	Liquid water content
min	Minute
MVD	Median volumetric diameter
NACA	National Advisory Committee for Aeronautics
NASA	National Aeronautics and Space Administration
nm	Nanometers
OAP	Optical array probe
OAP-C	Optical Array Cloud Probe
OAP-P	Optical Array Precipitation Probe
PC	Personal computer
psi	Pounds per square inch
psig	pounds per square inch gauge
SCB	Shielded connector block
SLD	Supercooled large drops
SSR	Solid-state relay
WSU	Wichita State University
Highlight	Reference point on test geometry for measuring impingement efficiency

EXECUTIVE SUMMARY

Aircraft flying through clouds below 26,000 ft at subsonic speeds can experience ice formation on critical aerodynamic surfaces. This situation can lead to the deterioration of aircraft aerodynamic performance and handling qualities. Typically, ice accretion results from small (5-50 μm), supercooled drops (drops cooled below freezing) that can freeze upon impact with the aircraft surface. Recently, however, ice accretions resulting from supercooled large drops have become a safety concern.

Ice accretion and drop trajectory computer codes, such as the National Aeronautics and Space Administration (NASA) Glenn Research Center LEWICE code (LEWICE), can provide cost-effective information for the design and certification of ice protection systems. In addition, these codes are often used to predict ice shapes on critical aerodynamic surfaces for icing conditions within the Appendix C icing envelope found in Title 14 Code of Federal Regulations (CFR). These ice shapes are then examined to select those that have the potential to cause large performance losses for further evaluation and testing.

The computation of ice shapes with ice accretion codes is usually performed incrementally by building small layers of ice until the required ice shape is obtained. During each ice accretion increment, a new flowfield is computed by the ice accretion code. This is followed by drop trajectory and impingement calculations for the new ice shape and an ice accretion analysis. It is important that during each ice accretion step, the impingement characteristics of the iced airfoil are computed accurately, since the prediction of the next layer of ice relies heavily on the computed impingement data.

Current drop trajectory and ice accretion codes were extensively tested for the 14 CFR Appendix C icing conditions and, in general, have demonstrated good agreement with experimental impingement data. Computation of large drop (i.e., drops outside the 14 CFR Appendix C certification envelope) impingement characteristics, however, may require additional improvements to the existing numerical models to include large drop impingement dynamics phenomena, such as drop splashing and breakup, which were observed in recent experimental impingement studies.

The main goal of the research effort described in this report was the development of an extensive impingement database for a range of simulated LEWICE ice shapes to validate ice accretion codes. Impingement experiments were conducted in the NASA Glenn Icing Research Tunnel with an airfoil section representative of general aviation and commuter aircraft, with five glaze, four mixed, and one rime ice shapes. Impingement data were obtained for median volumetric diameters of 20, 52, 111, 154, and 236 μm and an airspeed of 175 mph. Comparison of the experimental impingement data with LEWICE-2D analysis data showed that, in general, agreement between analysis and experiment was good for the 20-μm case. However, for the large drop cases, the impingement efficiencies predicted by LEWICE were considerably greater than the experimental results for both the clean and iced airfoil cases. The observed differences between experiment and analysis for the large drop cases were attributed to drop splashing, differences between the analysis and experimental flowfields (particularly for the 22.5-min and 45-min ice shapes) and, in some cases, to drop breakup downstream of the ice shape horns.

1. INTRODUCTION.

Aircraft flying at subsonic speeds through clouds below 8000 meters (approximately 26,000 ft) can be subject to ice formation on critical aerodynamic surfaces. This situation can lead to the deterioration of aircraft aerodynamic performance and handling qualities. Typically, ice accretion results from small supercooled (cooled below freezing) drops freezing upon impact with the aircraft surface. These drops are usually 5 to 50 microns in diameter. Recently, however, ice accretions resulting from supercooled large drops (SLD) have become a safety concern. The impact of SLD ice accretions on aircraft safety is under evaluation by the Federal Aviation Administration (FAA) and the Joint Aviation Authorities (JAA). FAA/JAA rulemaking is under development to ensure safe flight in SLD icing conditions.

Ice accretion and drop trajectory computer codes, such as the National Aeronautics and Space Administration (NASA) Glenn Research Center LEWICE code (LEWICE), can provide information for the design and certification of ice protection systems. In addition, ice accretion codes are often used by aircraft manufacturers to predict ice shapes on critical aerodynamic surfaces for a range of icing conditions within the Appendix C icing envelope in Title 14 Code of Federal Regulations (CFR) Part 25. These ice shapes are then examined to select those that have the potential of causing considerable losses in performance for further evaluation and testing.

The computation of ice shapes with ice accretion codes is usually performed incrementally by building small layers of ice until the required ice shape is obtained. For example, a 22-minute (min) glaze ice accretion might be constructed using 2-min time increments. During each ice accretion increment, a new flowfield is computed by the ice accretion code. This is followed by drop trajectory and drop impingement calculations for the new ice shape and an ice accretion analysis. It is important that during each ice accretion step, the computer code provides an accurate prediction of the impingement characteristics of the iced airfoil since the prediction of the next layer of ice relies heavily on the computed impingement data.

Current drop trajectory and ice accretion codes were extensively tested for cloud conditions within the 14 CFR Appendix C icing envelope and, in general, have demonstrated good agreement with experimental impingement data. Application of these codes to compute large drop (drops outside the current icing certification envelope) impingement, however, may require additional improvements to the existing numerical models to include physical phenomena related to large drop impingement dynamics, such as drop splashing and breakup [1, 2, and 3], that have been observed in recent experimental impingement studies with large drops [4 and 5]. The impact of these phenomena on the simulation of the impingement characteristics of aerodynamic surfaces can be considerable, as demonstrated in references 6 and 7. Large drop experimental and LEWICE impingement data presented in references 6 and 7 for two-dimensional airfoil sections exhibited considerable differences in the magnitude and extent of the local impingement efficiency. The main reason for the observed discrepancy between experiment and analysis was attributed to large drop splashing effects. More impingement data are needed for clean- and iced-wing geometries and for a range of large median volumetric diameters (MVD) to support the development and validation of trajectory and ice accretion codes.

This report presents experiments conducted to provide the first extensive impingement database on progressively larger glaze, mixed, and rime ice shapes for SLD, as well as 14 CFR Appendix C icing conditions. The ice shapes tested were defined with the LEWICE ice accretion code for a National Advisory Committee for Aeronautics (NACA) 23012 airfoil using 14 CFR Appendix C icing conditions. In the following sections, the experimental and data reduction methods used to generate the impingement data are discussed, and the results are compared to impingement predictions obtained with the LEWICE code.

2. BACKGROUND.

The first extensive water drop impingement database was developed by NACA in the 1950s. A dye-tracer technique was developed for measuring local impingement efficiency on aircraft aerodynamic surfaces [8]. In this technique, water containing a small amount of water-soluble dye was injected into the airstream ahead of the test article in the form of drops through a system of spray nozzles. The surface of the body was covered with blotter material, upon which the dyed water impinged and was absorbed. At the point of impact and drop absorption, a permanent dye deposit (dye trace) was obtained. The impingement limits were obtained directly from the rearmost dye trace on the absorbent material.

Data analysis consisted of removing the dyed blotter strips from the test article and punching out small segments of the blotter material to determine local impingement characteristics. The dye was dissolved out of each segment in a known quantity of water. The weight of the dye in this solution was determined by the amount of light in a proper wavelength that was transmitted through the solution using a calibrated colorimeter, a process known as colorimetric analysis. The weight of water that impinged at any surface location per unit time was determined from the weight of dye collected per unit area and from knowledge of the original concentration of the dye in the water drops.

The liquid water content (LWC) in the cloud was determined using an aspirating device [8 and 9]. This device consisted essentially of a tube that sucked in the approaching air and cloud drops at the freestream velocity (inlet velocity ratio 1) so that both the air streamlines and drops entered the tube along straight-line paths. The dyed drops were deposited on a filter mounted within the tube, leaving a dye trace that could be analyzed using colorimetric analysis. The drop size distribution was determined by comparing experimental local impingement rates on cylinders of different sizes with theoretical predictions of drop trajectories and impingement points using a differential analyzer.

Between 1955 and 1958, NACA personnel developed a water drop impingement database for a wide range of cylinders, airfoils sections, bodies of revolution, and a supersonic inlet [8-12]. For most test configurations, the NACA method was sufficiently accurate. The error in evaluating maximum local impingement efficiency varied from 10 to 25 percent [8 and 9]. The major limitations of the NACA method included reduced spatial resolution and a laborious and time-consuming process for reducing the experimental data. In addition, the uncertainty in measuring the LWC and MVD values of the spray clouds used in the impingement tests was considerable.

In 1984, a research program was initiated to further expand and update the experimental water drop impingement database. This program was sponsored by the NASA Glenn Research Center, Cleveland, Ohio, and the FAA William J. Hughes Technical Center, Atlantic City International Airport, New Jersey. The work was performed by researchers at Wichita State University (WSU) and The Boeing Company. During this research program, an experimental method, similar to the one used in the early 1950s by NACA researchers, was developed for measuring local impingement efficiency [13]. A new method for extracting the impingement data from the blotter strips was also developed. In this method, the amount of dye obtained on a blotter strip in a given time interval was converted into local impingement efficiency distribution using a laser reflectance spectroscopy method. Numerous tests showed the new data reduction method was significantly more efficient than the method of colorimetric analysis used in the 1950s by NACA personnel.

To generate the required spray clouds for the impingement tests, a 12-nozzle spray system was fabricated. This system was designed to have a very fast on/off response because the spray duration had to be very short (approximately 2-4 seconds) to avoid saturation of the blotter paper. To achieve accuracy in using the reflectance method, dye penetration into the blotter paper had to be kept to a minimum.

The first series of impingement tests was conducted in September 1985 for a period of 4 weeks in the NASA Glenn Icing Research Tunnel (IRT). The geometries tested included a 4-inch cylinder, a NACA 65_2-015, an MS(1)-0317 supercritical airfoil, three simulated ice shapes, an axisymmetric engine inlet model, and a Boeing 737-300 engine inlet model. The second, and final, series of impingement tests was performed in the IRT in April 1989 and lasted for approximately 4 weeks. Models tested during this phase of the research included two simulated ice shapes, a Natural Laminar Flow airfoil section NLF(1)-0414F, an infinite span 30 degree swept MS(1)-0317 wing, a finite span 30 degree swept NACA 0012 wing, and a Boeing 737-300 engine inlet model. The experimental impingement data obtained during the 1985 and 1989 impingement tests can be found in references 13 and 14. In summary, the water drop impingement research program conducted between 1984 and 1993 was successful and expanded the impingement database considerably.

A peer review of NASA Glenn Research Center icing research activities, conducted in 1994, indicated that additional water drop impingement data were needed. Large drop impingement data were also requested in response to a recent commuter aircraft icing-related accident that had raised the question of the effect of ice accretion due to SLD on aircraft performance and handling characteristics [15 and 16].

To address the needs of the icing community, the Icing Technology Branch at NASA Glenn Research Center awarded WSU a research grant in 1995 to begin work on modernizing and expanding the water drop impingement database. WSU and NASA conducted an industry survey in November 1995 to identify geometries and conditions to be considered for the next series of water drop impingement tests.

In December 1996, NASA awarded a second grant to WSU to improve the experimental method developed during the 1984 to 1993 research program and to develop a more efficient reflectance

method using a charge-coupled device (CCD) camera to extract the impingement data from the blotter strips. In addition, extensive impingement tests were planned in the NASA Glenn Icing Research Tunnel with a range of two-dimensional airfoils, finite wings, and a turboprop S-duct engine inlet.

The first series of the IRT impingement tests was conducted during the period of July 25 to September 7, 1997. The second series of impingement tests was conducted from January 31 to March 1, 1999. A total of 11 wind tunnel models were tested during these two IRT entries. Test models included six two-dimensional airfoils, a two-dimensional, high-lift system, three swept horizontal tails, and an engine inlet S-duct. Tests were performed for a range of angles of attack (AOA) and for MVDs of 11, 11.5, 21, 92, and 94 microns. The 92- and 94-micron MVD case was selected to provide preliminary SLD impingement data for assessing the performance of trajectory computer codes for large drop conditions. Comparison of the experimental impingement data with analysis data obtained with the NASA Glenn LEWICE-2D and LEWICE-3D computer codes demonstrated good agreement for the 11-, 11.5-, and 21-micron cases. However, for the 92- and 94-micron cases, the analysis produced considerably higher overall impingement than the experiment for 9 of the 11 models tested and for all AOA. Details of the 1997 and 1999 impingement research effort are provided in reference 17. The discrepancy between analysis and experiment for large MVD conditions was attributed to drop splashing and drop breakup effects, which are not currently modeled in the LEWICE code. It was determined that additional experimental work was needed to elucidate SLD impingement physics and to provide a more extensive SLD impingement database for trajectory code development and validation.

Recent developments in aviation rulemaking addressing aircraft operations in SLD conditions, which are outside the current icing certification envelopes, have heightened the need for additional large drop impingement research. Specifically, the impact of SLD ice accretions on aircraft safety is under evaluation by the FAA and the JAA. FAA/JAA rulemaking is under development to ensure safe flight in large supercooled drop icing conditions. In support of the rulemaking, NASA has provided a roadmap describing the technology required for implementing the proposed SLD rulemaking, including atmospheric environment definition and instrumentation, test methods, test facilities, and computer codes required to provide means of compliance with the proposed rule.

Current drop trajectory and ice accretion computer codes are not validated for SLD conditions. To address the need for validated analysis tools for simulating SLD impingement on aircraft surfaces, the FAA awarded a grant to WSU in 2000 to document large drop impingement dynamics using advanced imaging methods, to apply the dye tracer method developed at WSU to obtain large drop impingement data for a range of airfoils, and to investigate the use of this method for measuring impingement on airfoils with simulated ice shapes. To address the program goals, WSU refined the experimental methodology for measuring large drop impingement and made extensive updates to the hardware and software of the laser and CCD reflectometers used for the reduction of the raw impingement data. In June 2001, experiments were conducted with a 21-inch chord NACA 0012 airfoil section in the Goodrich Icing Wind Tunnel facility using advanced flow visualization techniques to document basic large drop impingement splashing for the first time. In September and October 2001, extensive

impingement tests were conducted at the NASA Glenn IRT facility. Impingement data were obtained for a range of airfoil sections including three 36-inch chord airfoils (MS(1)-0317, GLC-305, and NACA 652-415), as well as a 57-inch chord Twin Otter horizontal tail section, and a 22.5- and 45-min LEWICE glaze ice shape for the Twin Otter tail section. Data were obtained for MVDs of 11, 21, 79, 137, and 168 microns. The experimental impingement data were compared to analysis data obtained with the LEWICE-2D computer code. The comparisons demonstrated that for the large drop cases the LEWICE total collection efficiencies were considerably greater than the experimental values for both the clean and iced airfoil cases. Details of the 2000-2002 impingement program are provided in reference 6.

During the 2000-2002 impingement program, it was demonstrated that the improvements and modifications made to the experimental methodology produced highly repeatable experimental impingement data for airfoils with simulated ice shapes. Thereafter, in fall 2002, the FAA awarded a grant to WSU to obtain small and large drop impingement data on a NACA 23012 airfoil with a series of progressively larger LEWICE ice shapes. The impingement data were needed to expand the validation scope and database for the LEWICE code. The computation of ice shapes with LEWICE is usually performed incrementally by building small layers of ice until the required ice shape is obtained. During each ice accretion increment, a new flowfield is computed by the ice accretion code. This is followed by drop trajectory and drop impingement calculations for the new ice shape and an ice accretion analysis. It is important that during each ice accretion step, the computer code provides an accurate prediction of the impingement characteristics of the iced airfoil since the prediction of the next layer of ice relies heavily on the computed impingement data. Impingement tests were performed in March and April 2003 with ten simulated LEWICE ice shapes that included five glaze, four mixed, and one rime cases. The new water drop impingement program from 2002 through 2004 was a collaborative effort between the FAA, NASA, WSU, and Boeing. This report provides details of the methods used and results obtained during this water drop impingement research effort.

3. DROP TRAJECTORY AND IMPINGEMENT PARAMETERS.

In this section, impingement parameters that are commonly used in the presentation of theoretical and experimental data are discussed. They constitute the governing nondimensional form of the drop trajectory equations. Their relevance to conditions with icing clouds of uniform and nonuniform drop size distributions from small to large supercooled drops is also discussed.

3.1 DROP TRAJECTORY.

The forces acting on a small spherical drop moving in the steady flow of air include drop drag, weight, and buoyancy. The predominant force exerted on a drop is the fluid dynamic drag resulting from the relative (slip) velocity of air with respect to the drop. The development of the drop trajectory equations is based on a simplified approach taken by researchers as early as the 1940s. In this approach, the quasi-steady motion of small spherical drops moving in the steady flow of air is considered and it is assumed that the motion of drops does not disturb the airflow. Since the physical phenomena involved in the process of ice accretion are very complex, these assumptions are necessary and are commonly used in analytical tools for modeling ice

accretions. The main assumptions used in the derivation of the small particle trajectory equations are summarized below:

- The Single phase airflow about the body, i.e., flowfield, is not disturbed by the presence of drops.
- Quasi-steady-state approximation: at each instant and position, the steady-state drag and other forces act on the particle.
- The drag coefficient for stationary sphere applies.
- Particles are assumed to be solid and spherical in shape.
- Particles do not rotate and have no lift and no moment.
- All drops that strike the airfoil deposit on the surface. Drops do not splash or breakup during the impingement process.
- Drops do not interact with other drops.
- Compressible or incompressible potential flowfield of the gas phase about the body.
- Viscous flow effects, such as thick boundary layer formation and flow separation, are not considered.

The drop trajectory equation is given below.

$$\frac{dU_i}{dt} = \frac{C_D(\mathrm{Re}_v)\cdot \mathrm{Re}_v \cdot (V_i - U_i)}{24K} - \frac{(1-\sigma)\cdot g \cdot L \cdot \delta_{i2}}{V_\infty^2} \qquad (1)$$

where $K = \rho_p V_\infty d^2 / 18\mu\ L$, inertia parameter of drop

d = Drop diameter
μ = Absolute air viscosity
V_∞ = Freestream speed
t = Time, dimensionless with L/V_∞
σ = ρ/ρ_p, density ratio of air to particle
L = Characteristic dimension of body
Re_v.. = Reynolds number of airflow relative to drop
U_i = i^{th} directional component of particle velocity, dimensionless with V_∞
V_i = i^{th} directional component of air velocity, dimensionless with V_∞

3.2 IMPINGEMENT PARAMETERS.

Spray cloud characteristics and drop impingement parameters for clouds with a range of drop sizes are discussed below.

3.2.1 Liquid Water Content.

Generally expressed in grams of water per cubic meter of cloud, the LWC of a cloud is defined as the amount of water contained in a given volume of cloud. LWC_{max} values for icing clouds according to the 14 CFR Appendix C icing envelopes are presented in reference 18. In icing tunnels, the cloud LWC is controlled by the water and air pressures of the spray system used to create the spray clouds.

3.2.2 Cloud Drop Distribution.

The distribution of drops in a cloud can be expressed in various forms [13]. The following four types of distributions are most commonly used:

- Number density of drops versus drop diameter
- Percent of LWC versus drop diameter
- Percent of LWC versus drop diameter normalized to MVD
- Percent cumulative LWC versus drop diameter normalized to MVD

The Langmuir "D" is a distribution that has been employed in various analytical studies. This and other similar distributions were established by Langmuir [19] from natural-icing cloud measurements made on Mt. Washington. The rate of deposition of ice on slowly rotating cylinders exposed to supercooled clouds blowing over the summit was correlated with theoretical calculations. A dimensionless Langmuir "D" distribution is shown in figure 1.

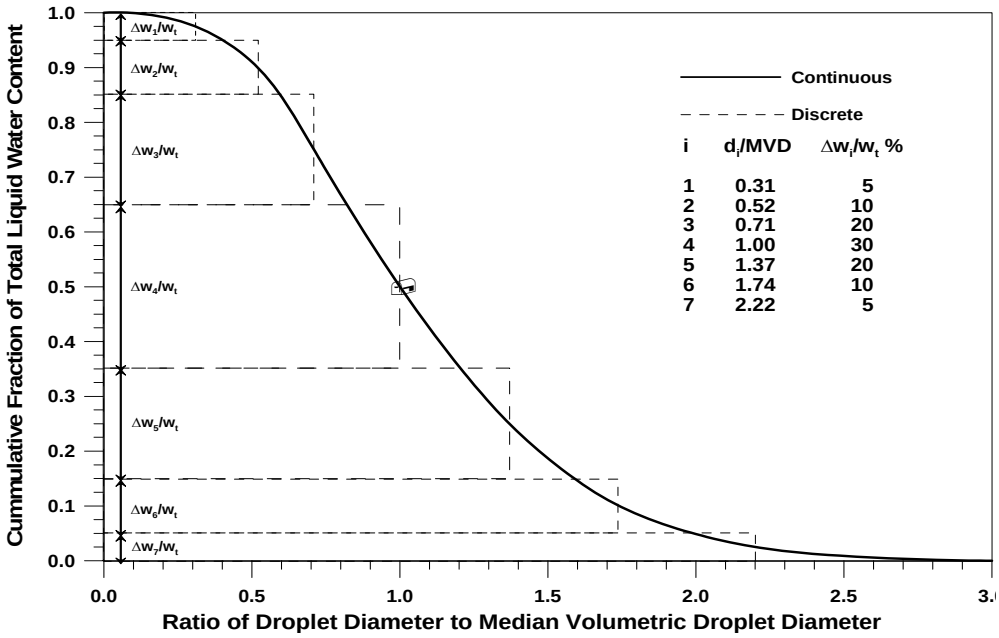

Figure 1. Langmuir "D" Dimensionless Distribution of Drop Sizes

3.2.3 Median Volumetric Diameter.

The MVD of a drop distribution is defined as the drop diameter for which half the total LWC is contained in drops larger than the median and half in drops smaller than the median. Given a drop distribution, the MVD can be calculated as follows:

- For a continuous distribution, if $n(D)$ is the number of particles per unit sampling volume having diameters between D and $D+dD$ (volumes between V and $V+dV$), then D_{MVD} can be calculated from

$$\frac{\frac{\pi}{2}\rho_\omega \int_{D_{\min}}^{D_{MVD}} n(x)\, x^2 dx}{\frac{\pi}{2}\rho_\omega \int_{D_{\min}}^{D_{\max}} n(x) x^2\, dx} = 0.5 \qquad (2)$$

- For a discrete distribution, if the particle number density is given in N, discrete groups such that $n_i(D_i)$ is the number of the particles in group i having diameters between D and $D+dD$, then equation 2 can be written as

$$\frac{\frac{\pi}{6}\rho_\omega \sum_{i=1}^{K} n_i(D_i) D_i^3}{\frac{\pi}{6}\rho_\omega \sum_{i=1}^{N} n_i(D_i) D_i^3} = 0.5 \qquad (3)$$

where

D_K = the diameter of group K, is equal to the MVD (D_{MVD})
ρ_ω = density of water, kg/m^3

3.2.4 Local Impingement Efficiency.

Considering a body in a cloud with uniform drop size distribution, the local impingement efficiency $\overline{\beta}$ for any point on the body surface is defined as the local drop flux rate at the body surface normalized to the freestream flux rate. Referring to figure 2a, β is defined as the ratio of that infinitesimal area dA_∞ to the corresponding impingement area on the body surface dA_s. This definition follows from the continuity of drop mass flow.

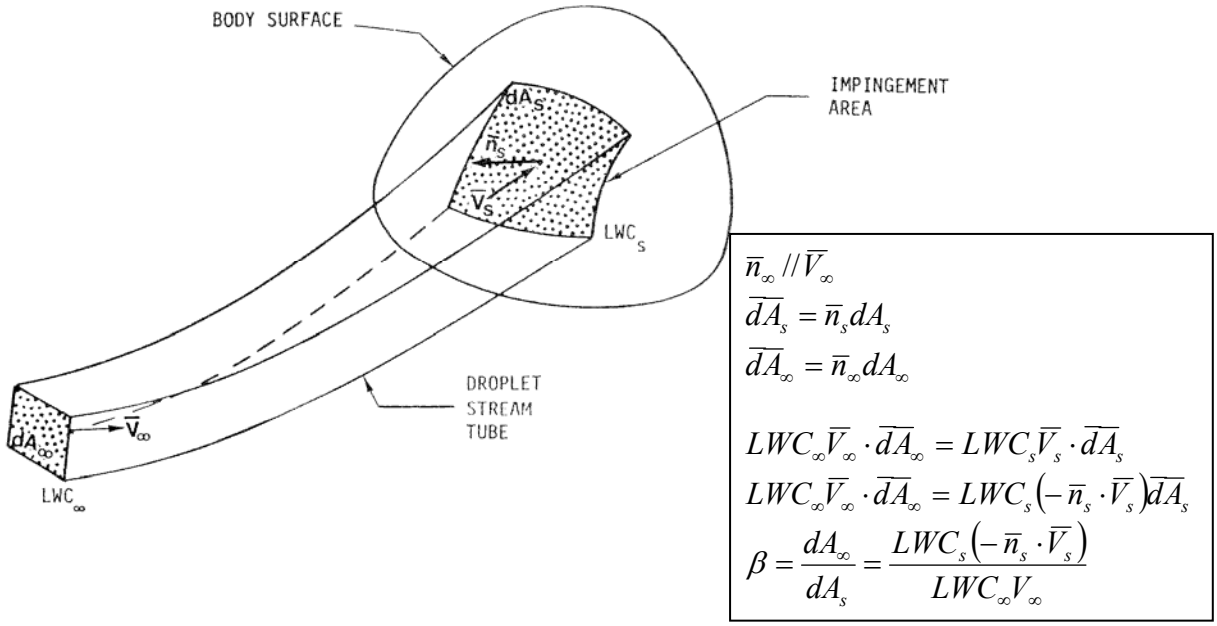

Figure 2a. Definition of Local Impingement Efficiency for a Body in a Cloud of Uniform Drop Size

For a continuous nonuniform cloud distribution, the impingement efficiency is given by the following expression:

$$\bar{\beta} = \frac{1}{\omega_t} \int_0^{\omega_t} \beta \, d\omega \tag{4}$$

where β is a function of drop size and therefore can be expressed as a function of ω, the liquid content for a given drop size.

For a discrete cloud distribution, $\bar{\beta}$ is defined as the weighted average of the local impingement efficiency values due to each drop group in the cloud. Let ω_t be the LWC of the cloud, $\Delta\omega_i$ is the partial LWC in the drops of size (d_i) in the group (i) of the distribution, and N is the total number of discrete size drop groups available. For a body exposed to a cloud with such a drop distribution, the local impingement efficiency due to a single drop group of size d_i is β_i, where β is defined in figure 2a. The local impingement efficiency due to all N groups in the distribution over an infinitesimal area of the body is given by the following expression:

$$\bar{\beta} = \frac{1}{\omega_t} \sum_{i=1}^{N} \beta_i \Delta\omega_i \tag{5}$$

3.2.5 Total Impingement Efficiency.

The total impingement efficiency of a three-dimensional body exposed to a cloud of drop distribution is defined as

$$\overline{E} = \frac{1}{A_f} \int \overline{\beta} \, dA_s \tag{6}$$

where

A_f is the projected frontal area of the body
dA_s is an infinitesimal impingement area on the surface of the body

To integrate equation 6, $\overline{\beta}$ must be known as a function of surface location. Such a function can be defined from experimental or analytical results.

3.2.6 Impingement Limits.

Drops that start out at freestream position (y_∞) (figure 2b), with respect to a reference line that passes through the highlight (the most forward point at $\alpha=0^\circ$) of a body downstream, will impinge at some locations on that body. As these initial freestream drop positions increase in distance from the reference line, they will impinge farther back along the surface of the body until a maximum distance ($y_{\infty,max}$) is obtained. This limiting trajectory is defined as the tangent trajectory to the body at point P shown in figure 2b. Any drops starting at a freestream location farther from the reference line than $y_{\infty,max}$ will miss the body entirely. The distance (S_m) measured along the body surface from the highlight of the body to point P is called the limit of impingement. This distance is usually expressed in dimensionless form by dividing S_m by the characteristic length (L) of the body.

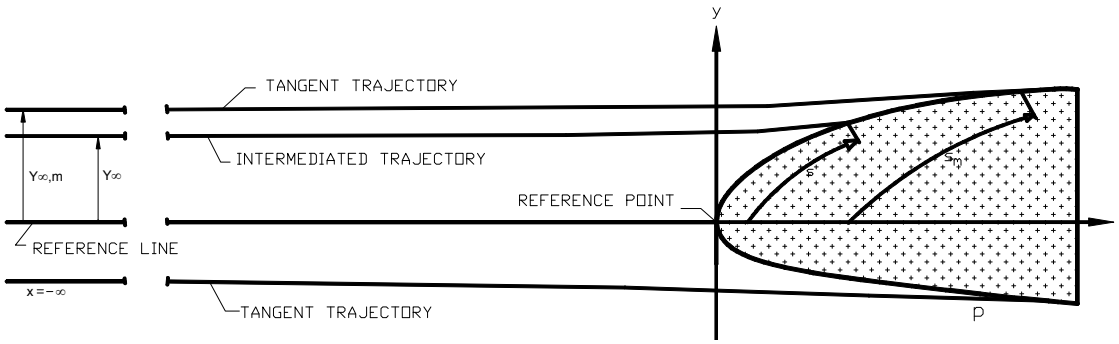

Figure 2b. Two-Dimensional Drop Trajectories for a Body in a Cloud of Uniform Drop Size

For two-dimensional flow, there are two impingement limits, an upper and lower (for external flow, e.g., airfoil section) or an outer and inner (for partly internal flow, e.g., engine inlet). For three-dimensional flow, the limits of impingement may vary spanwise along the surface of a finite wing, or circumferentially along the surface of an engine inlet. For a drop distribution that

varies from D_{min} to D_{max}, the impingement limits can be established for each drop size. The maximum impingement limits are defined by the impingement limits of the largest drop diameter in the distribution.

3.2.7 Summary of Drop Impingement Parameters.

Table 1 provides a list of definitions and expressions for key nondimensional parameters that relate to drop impingement and trajectory. They include drop inertia parameter, K; drop modified inertia parameter, K_0; Reynolds number based on MVD, Re_{MVD}; true drop range, λ; and independent impingement parameter, ϕ, which represents the deviation of the drop drag force from Stokes' law. They are defined in such way that the drop diameter, d, has been eliminated from the formulations. These nondimensional impingement parameters are also useful in linking the impingement data presented in this report with early experimental and numerical studies of airfoil water impingement characteristics [8 and 9]. In some of the early studies, the impingement characteristics of bodies were sometimes presented in terms of nondimensional impingement parameters, such as K and ϕ. Note that the definitions in table 1 are based on the reference length, typically the airfoil chord for two-dimensional sections.

Table 1. List of Drop Trajectory Parameters

Parameter	Definition	Expression
Re_{MVD}	Reynolds number based on drop diameter	$MVD \cdot V_\infty \cdot \frac{\rho_{air}}{\mu}$ where MVD represents MVD, ρ_{air} is the air density and μ is the absolute air viscosity
K	Drop inertia parameter	$\rho_{droplet} \cdot V_\infty \cdot \frac{MVD^2}{18 \cdot \mu \cdot c}$ where ρ_{drop} is the drop (water) density and c is the chord length of the airfoil model
$\frac{\lambda}{\lambda_s}$	Ratio of the true range of drop as projectile injected into still air to the range of drop as projectile following Stokes' law	$-0.022466 \cdot x^4 + 0.20109 \cdot x^3 - 0.59067 \cdot x^2 + 0.36072 \cdot x + 0.74544$ where $x = log(Re_{MVD})$ and $6 < Re_{MVD} < 1000$
K_0	Drop modified inertia parameter	$K \cdot \frac{\lambda}{\lambda_s}$
ϕ	Deviation of the drop drag force from Stokes' law	$\frac{(Re_{MVD})^2}{K}$

3.3 LARGE DROP IMPINGEMENT ISSUES.

The mathematical models for drop trajectory and impingement analysis have shown to be accurate for icing conditions within the intermittent and continuous maximum icing envelopes defined in the 14 CFR Appendix C [6 and 17]. For large drop impingement, however, the current numerical models do not account for large drop impingement phenomena, such as drop splashing and drop breakup [5 and 6]. In addition, large drop distortion, due to pressure gradients, can result in considerably more drag force than that predicted by the current models, which assume spherical drops.

3.3.1 Large Drop Deformation and Breakup.

Drops are held together by surface tension; however, as a drop moves closer to a surface, it is subjected to nonuniform pressure forces, which cause the drop to deform. If the pressure force is large enough, the drop cannot sustain its surface integrity and begins to break up.

The drag change due to drop deformation was studied by Wright and Potapczuk [20]. Wright compared calculations of impingement efficiency using LEWICE with two different drag models. The first model was a standard drag model used in LEWICE. The second model was devised by increasing the drag coefficient by 15% at all Reynolds numbers. Wright concluded that the effect of drop deformation on impingement efficiency is negligible, as long as breakup does not occur. The latter drag model was based on experimental results by Beard and Pruppacher [21], which showed that drag of a deformed or nonspherical drop was at most 15% higher than a sphere.

A variety of independent variables were used to correlate drop breakup properties such as Weber, Bond, and Rabin numbers [4 and 22]. These parameters are defined as follows:

Weber Number $$We = \frac{\rho V_r^2 D}{\sigma_d} \tag{7}$$

Bond Number $$Bo = \frac{\rho_d D^2}{\sigma_d}\left(\frac{dV_r}{dt}\right) \tag{8}$$

Rabin Number $$Ra = \frac{We}{\sqrt{\mathrm{Re}_v}} \tag{9}$$

and

Reynolds Number $$\mathrm{Re}_v = \frac{\rho V_r D}{\mu} \tag{10}$$

Pilch [22] stated that there is a critical Weber number (We_c) below which drop breakup does not occur. The critical Weber number was investigated experimentally for fluids with different surface tension and viscosity values. A useful empirical correlation for the critical Weber number was given by Pilch as:

$$We_c = 12 \cdot \left(1 + 1.077 \cdot Oh^{1.6}\right) \tag{11}$$

where

Ohnesorge number (Oh) is given as:

$$Oh = \frac{\mu_d}{\sqrt{\rho_d D \sigma_d}} \quad (Oh \approx 0.01 \text{ for water [4]}) \tag{12}$$

The critical Weber number was found to be approximately 12 when the Ohnesorge number is small ($Oh < 0.1$).

3.3.2 Large Drop Splashing and Reimpingement.

When water drops impinge on a surface, they may either (1) spread out on the surface without splashing and create a thin film of water, (2) splash on impact and create secondary drops, or (3) bounce off without breakup at very shallow impact angles [3 and 4]. Drop splashing is a function of drop kinetic energy and contact angle [3 and 6], thus it depends heavily on the drop mass and velocity profiles.

A splashing test conducted in 2001 [6] provided insight into the relation between drop mass and velocity with splashing intensity. Splashing images were obtained using a 512- by 512-pixel CCD PI-MAX-intensified camera from Princeton Instruments, which is capable of collecting 16-bit images at a readout rate of 1 million pixels per second with 100-milliwatt red laser sheet illumination. Although these images did not provide quantitative results, the experiments showed that splashing phenomena are indeed related to drop size and the impact velocity. The intensity of drop splashing increased as the spray cloud MVD was increased for fixed airspeed; it also increased as the airspeed was increased for fixed spray cloud MVD.

The impact parameter (K_{IP}) [3] was used to define threshold conditions for incipient splash. The K_{IP} parameter is defined as follows:

$$K_{IP} = Oh \cdot Re^{1.25} \tag{13}$$

Research by Mundo [3] has shown that a value of K_{IP} exceeding 57.7 leads to incipient splashing, whereas K_{IP} less than 57.7 leads to complete deposition of the drop. Tan [4] showed that on a 21-inch chord NACA0012 airfoil with a relative drop-air velocity of 100 m/s and drop diameter of 100 μm, splashing occurred over a significant part of the surface.

When splashing occurred, secondary drops were ejected from the impingement point. Rutkowsky, et al. [23] observed that for drop velocities below a threshold value, these secondary drops reimpinged on the surface. However, when the velocity of the splashed drop exceeded the threshold value, they were carried by the external flow past the trailing edge of an airfoil and did not reimpinge. This threshold velocity was referred to as the escape velocity. Even though splashed drops with velocity below the threshold value were shown to reimpinge on the airfoil surface, locating the point of drop reimpingement was not a simple matter. The numerical study conducted by Rutkowsky, et al., demonstrated that splashed drops did not necessarily reimpinge close to the initial impingement location. As a result, drop splashing and reimpingement can result in redistribution of the impinging water mass in ways not currently accounted for by state-of-the-art ice accretion codes.

4. EXPERIMENTAL SETUP.

4.1 THE WIND TUNNEL FACILITY.

The 2003 water drop impingement tests were conducted in the NASA Glenn IRT. The IRT test section has a 6- by 9-ft cross section and measures 20 ft long and can attain a maximum speed of 390 mph when it is empty. A plan view of the IRT circuit is shown in figure 3. The IRT is a

closed-looped refrigerated facility with a total temperature controllable (from -20° to +33°F) test section. The operational static pressure at the tunnel test section is near or below the atmospheric value. Test models are typically installed on the tunnel turntable using a floor mounting plate as shown in figure 4. A view of the test section is provided in figure 5. Two sets of nozzles (the standard and MOD-1 types) are used in the IRT spray system, which consists of 10 spray bars with 54 nozzle locations per bar. The basic IRT nozzle design is shown in figure 6. Only 251 nozzles are currently being used to generate the required icing clouds. Two mechanical vent doors located upstream of the heat exchanger can be open and shut remotely to allow air to vent in and out of the facility. The IRT spray system is capable of simulating icing clouds with MVDs in the range of 14 to 40 μm, and LWC of 0.3 to 3 g/m^3, as shown in figures 7 and 8. In addition, a limited range of large drop clouds with MVDs in the range 70 to 270 microns can be produced in this facility. Further details regarding the IRT facility are provided in reference 24.

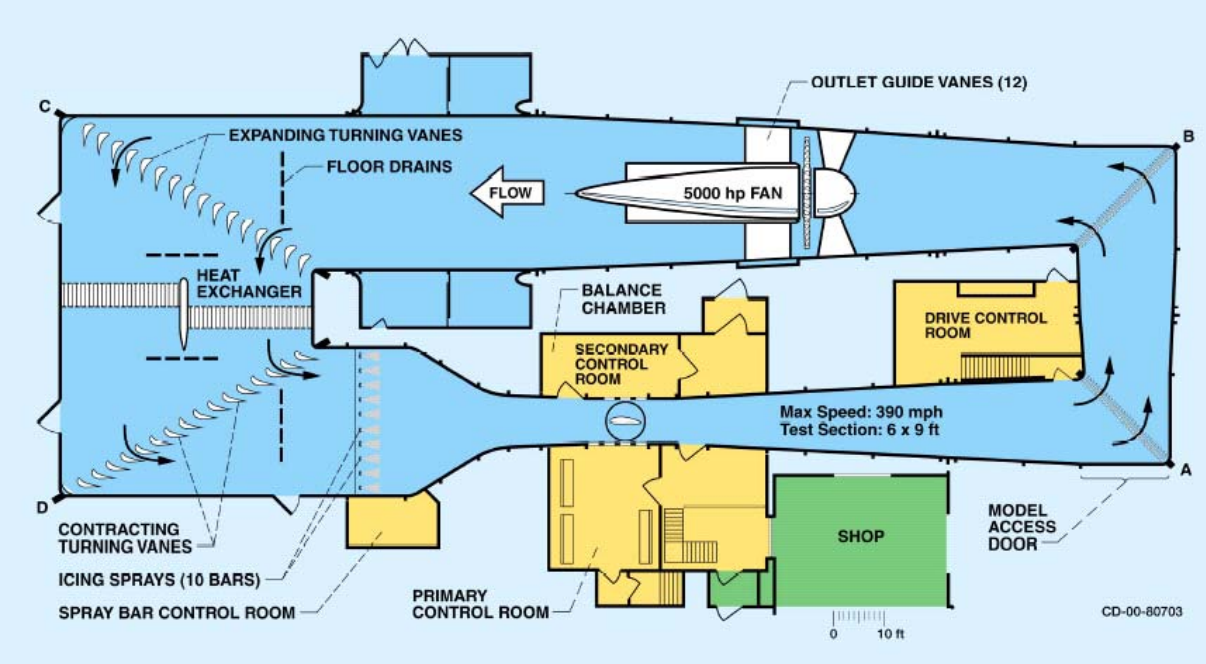

Figure 3. Plan View of NASA Glenn IRT

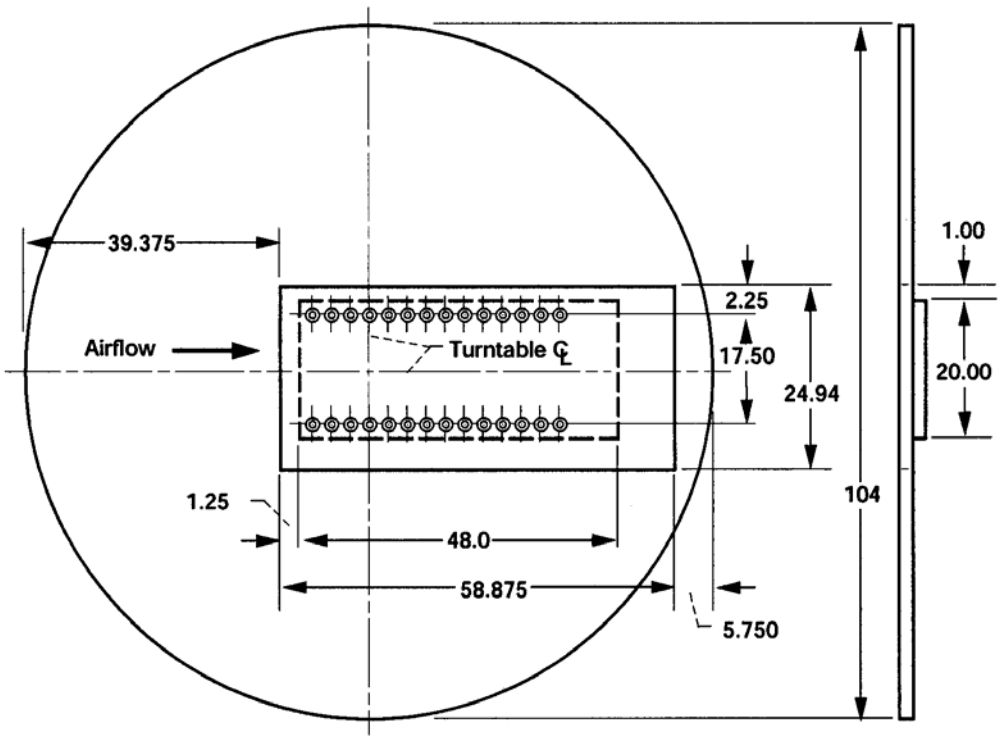

Figure 4. The IRT Turntable and Model Mounting Plate (all dimensions are given in inches)

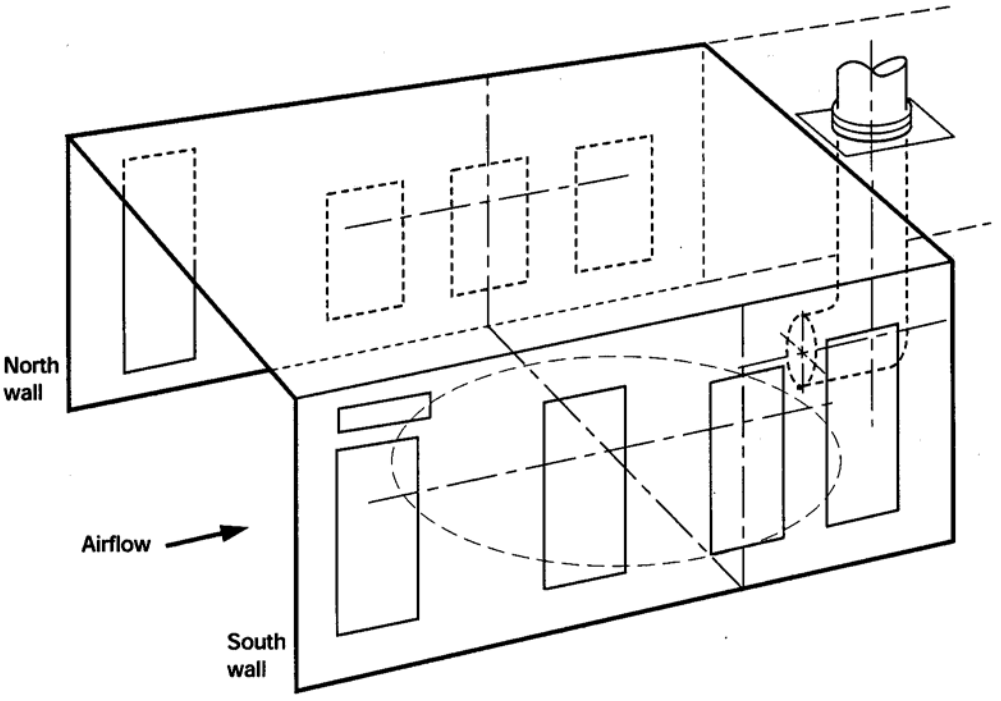

Figure 5. The IRT Test Section's North and South Walls Showing Visual Access Windows, Turntable, and Altitude Exhaust Piping

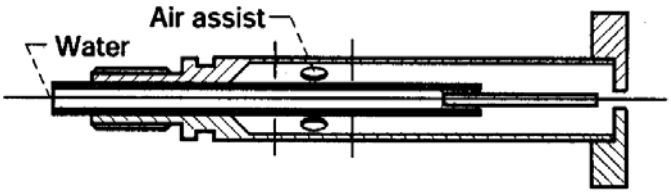

Figure 6. Schematic of an IRT Spray Nozzle

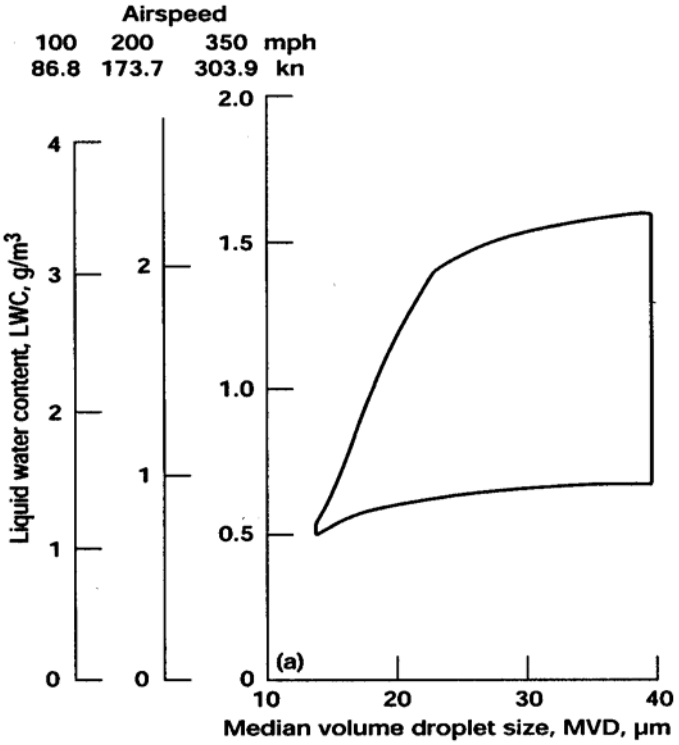

Figure 7. The IRT Icing Cloud Operating Envelopes for Standard Nozzles

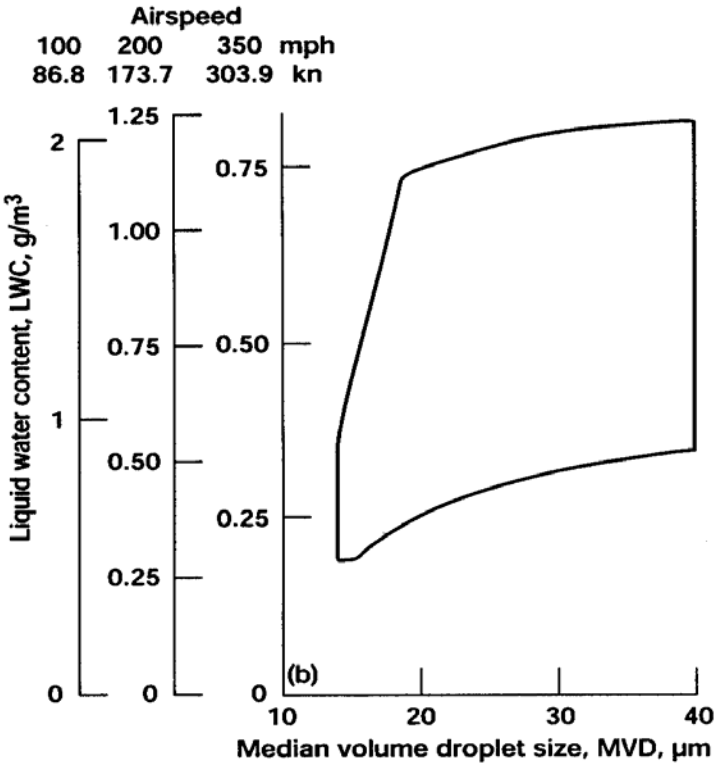

Figure 8. The IRT Icing Cloud Operating Envelopes for MOD-1 Type Nozzles

4.2 TEST MODELS.

Details of the test models used in the 2003 impingement experiments and their related instrumentation are given below.

4.2.1 MS(1)-317 Airfoil.

The MS(1)-317 airfoil is representative of modern medium speed airfoils. It was designed in the mid-1970s for general aviation aircraft [25]. This two-dimensional airfoil was constructed out of fiberglass skin, which was epoxied to an aluminum spar and aluminum ribs. The interior of the airfoil model was filled with foam. An aluminum plate was installed at each end of the model for mounting in the IRT test section. The model had a nominal span of 72 inches and a chord of 36 inches and was mounted vertically in the test section. The maximum thickness for this airfoil was 6.12 inches (t_{max}/c = 0.17) and was located at 37.5% chord. The airfoil's center of rotation was at 42% chord. A total of 47 static pressure taps were available for this airfoil. These taps were distributed in the chordwise direction 35.5 inches above the tunnel floor. The MS(1)-317 airfoil section and model installation details are given in figures 9a-9c. Impingement data for this airfoil were obtained during the 1985, 1997, 1999, and 2001 IRT tests performed by WSU and Boeing. This airfoil was used during the 2003 IRT impingement to verify the repeatability of the experimental setup.

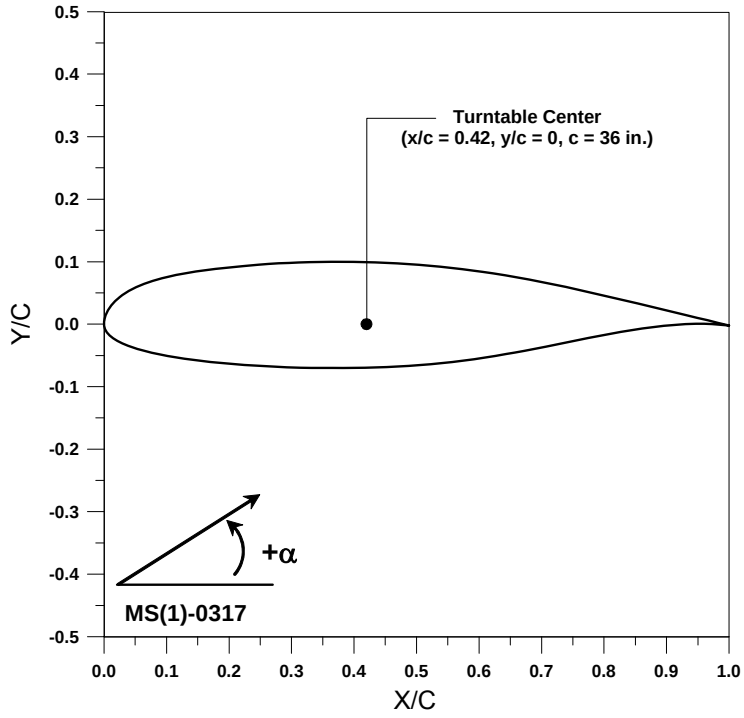

Figure 9a. MS(1)-0317 Airfoil Section

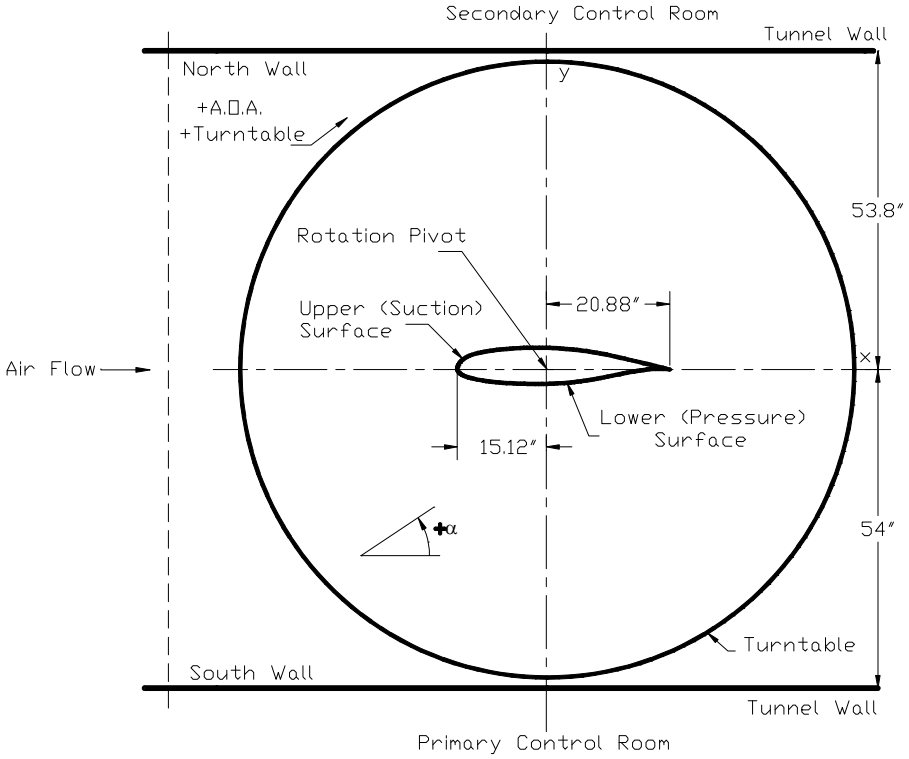

Figure 9b. MS(1)-0317 Airfoil Installation in the IRT Test Section (top view)

Figure 9c. MS(1)-0317 Airfoil Installed in the IRT Test Section

4.2.2 NACA 23012 Airfoil.

The NACA 23012 airfoil is representative of general aviation and commuter aircraft wing sections. The two-dimensional wind tunnel model was designed and fabricated at WSU. It was constructed out of aluminum with a 72-inch span and 36-inch chord. The maximum thickness for this airfoil was 4.32 inches ($t_{max/c}$ = 0.12), and it was located at approximately 30% chord. The airfoil's center of rotation was at 50% chord. The airfoil was instrumented with 65 pressure taps at a spanwise location 30 inches above the tunnel floor—40 taps on the suction surface, 23 on the pressure surface, plus 2 pressure ports located at the leading and trailing edges of the airfoil. The NACA 23012 airfoil section and model installation details are given in figures 10a-10c.

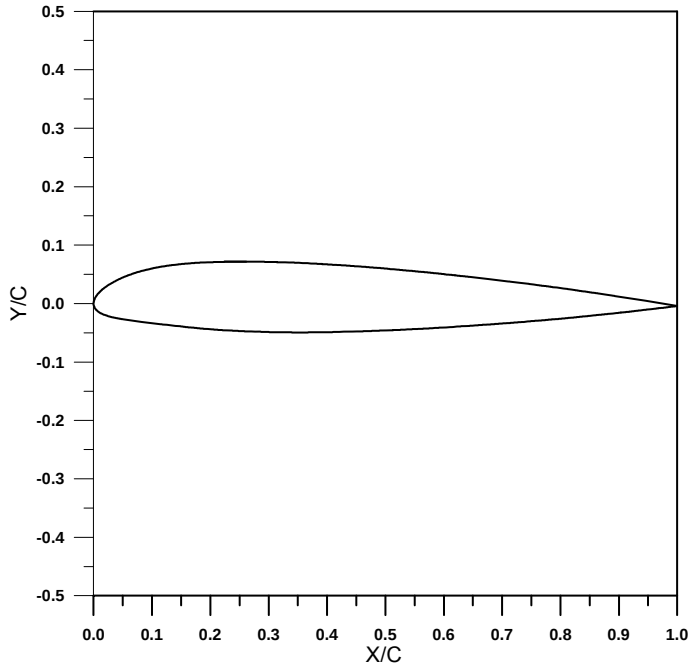

Figure 10a. NACA 23012 Airfoil Section

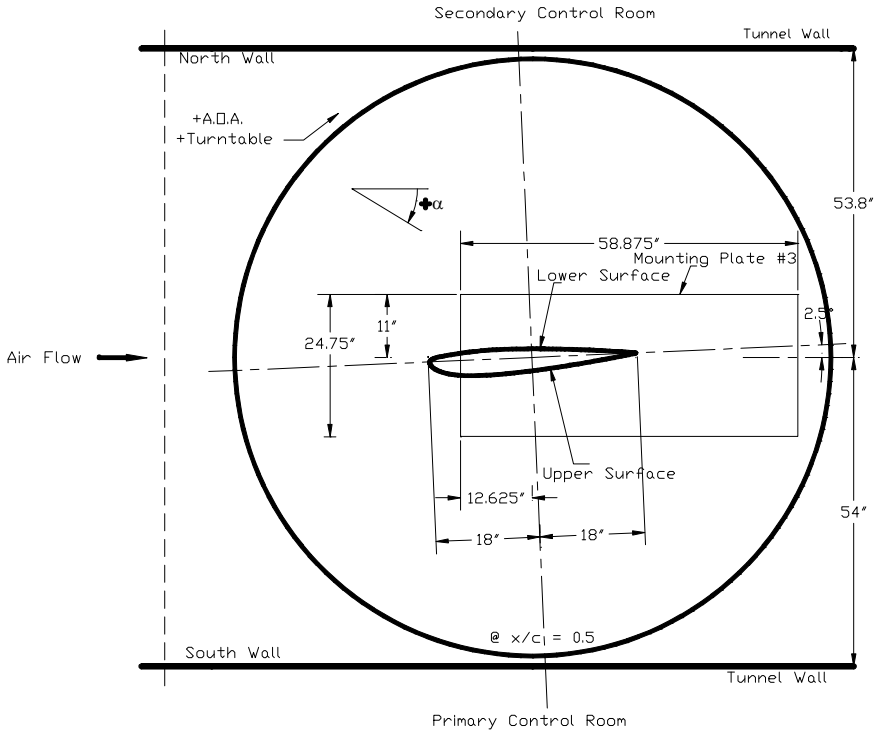

Figure 10b. NACA 23012 Airfoil Installation in the IRT Test Section (top view)

Figure 10c. NACA 23012 Airfoil Installed in the IRT Test Section

4.2.3 LEWICE Ice Shapes for NACA 23012 Airfoil.

The simulated ice shapes for the 36-inch airfoil were determined using the LEWICE 2.2 computer code [26] with the following icing conditions:

- V_∞ = 175 mph
- AOA = 2.5°
- MVD = 20 μm
- LWC = 0.5 g/m^3
- Pressure altitude: 1,800 ft—selected to approximate the static pressure (approximately 13.75 pounds per square inch (psi); 13.75 × 6,895 = 94,806 Pa) in the IRT test section for a test speed of 175 mph. In the actual tests, the freestream static pressure ranged from 13.73 to 13.87 with an average value of 13.80, which is close to 13.75 used in the icing analysis.

The ice shapes tested for the 2003 impingement test are listed below:

- Glaze Icing Conditions
  - 5-min Glaze: 5-min glaze ice accretion, 1.25-min time step, model installation details are given in figures 11a-11c
  - 10-min Glaze: 10-min glaze ice accretion, 1.25-min time step, model installation details are given in figures 12a-12c
  - 15-min Glaze: 15-min glaze ice accretion, 1.25-min time step, model installation details are given in figures 13a-13c
  - 22.5-min Glaze: 22.5-min glaze ice accretion, 1.25-min time step, model installation details are given in figures 14a-14c
  - 45-min Glaze: 45-min glaze ice accretion, 2.5-min time step, model installation details are given in figures 15a-15c
- Mixed Icing Conditions
  - 7.5-min Mixed: 7.5-min mixed ice accretion, 1.25-min time step, model installation details are given in figures 16a-16c
  - 15-min Mixed: 15-min mixed ice accretion, 1.25-min time step, model installation details are given in figures 17a-17c
  - 22.5-min Mixed: 22.5-min mixed ice accretion, 1.25-min time step, model installation details are given in figures 18a-18c
  - 45-min Mixed: 45-min mixed ice accretion, 2.5-min time step, model installation details are given in figures 19a-19c
- Rime Icing Condition
  - 45-min Rime: 45-min rime ice accretion, 2.5-min time step, model installation details are given in figures 20a-20c

All glaze ice shapes were computed by NASA personnel with LEWICE 2.2 using a total temperature of 267.9 K (approximately -5°C). All mixed ice shapes were obtained at 264 K (approximately -9°C), whereas the 45-min rime ice shape was obtained at 252.3 K (approximately -21°C). The LEWICE input files for the above ice shapes are provided in appendix A.

The two airfoil sections, MS-317 and NACA 23012, are shown in figure 21. The glaze, mixed, and rime ice shapes tested are presented in figures 22 and 23.

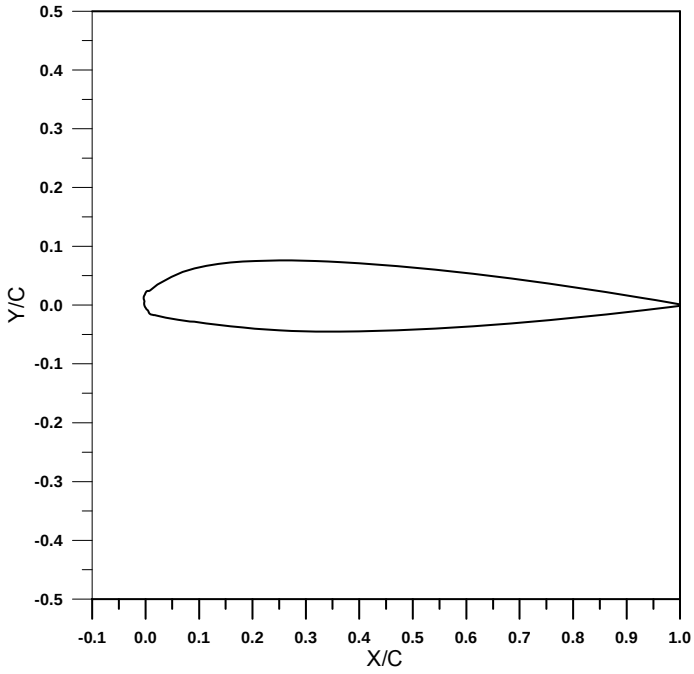

Figure 11a. NACA 23012 With 5-min Glaze Ice Shape

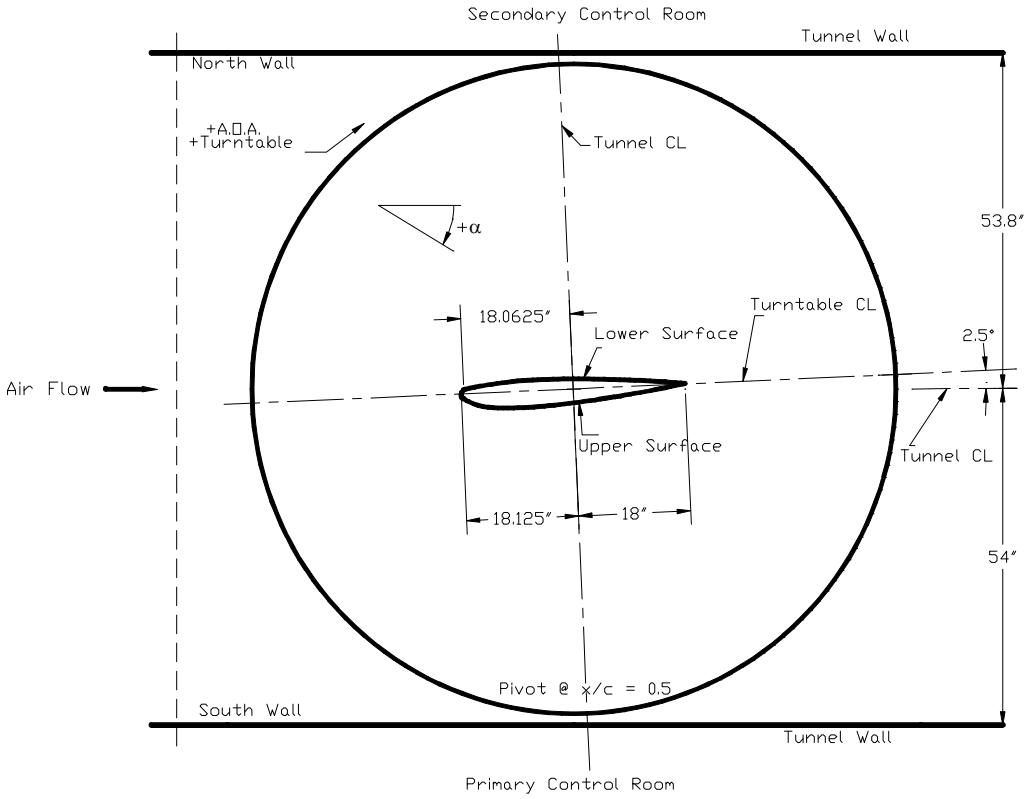

Figure 11b. NACA 23012 With 5-min Glaze Ice Shape Installation in the IRT Test Section (top view)

Figure 11c. Various Views of NACA 23012 With 5-min Glaze Ice Shape Installation in the IRT Test Section and Blotter Strip Installation

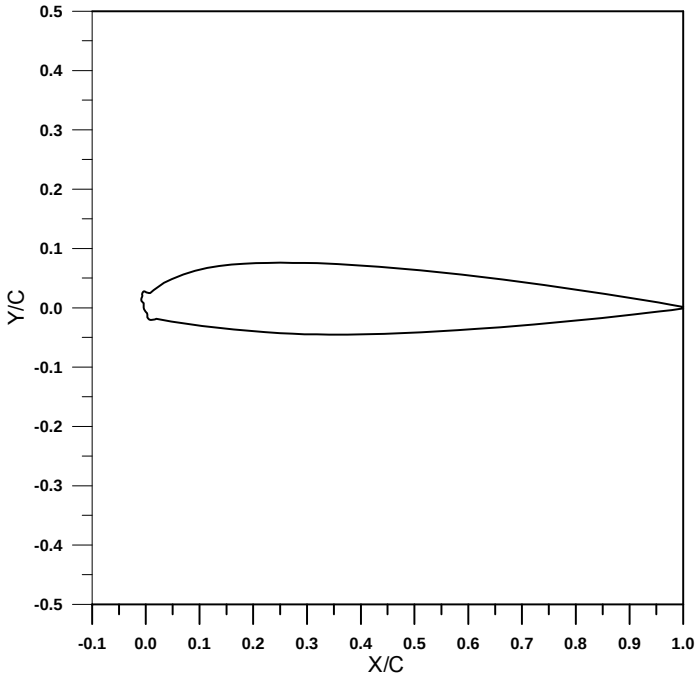

Figure 12a. NACA 23012 With 10-min Glaze Ice Shape

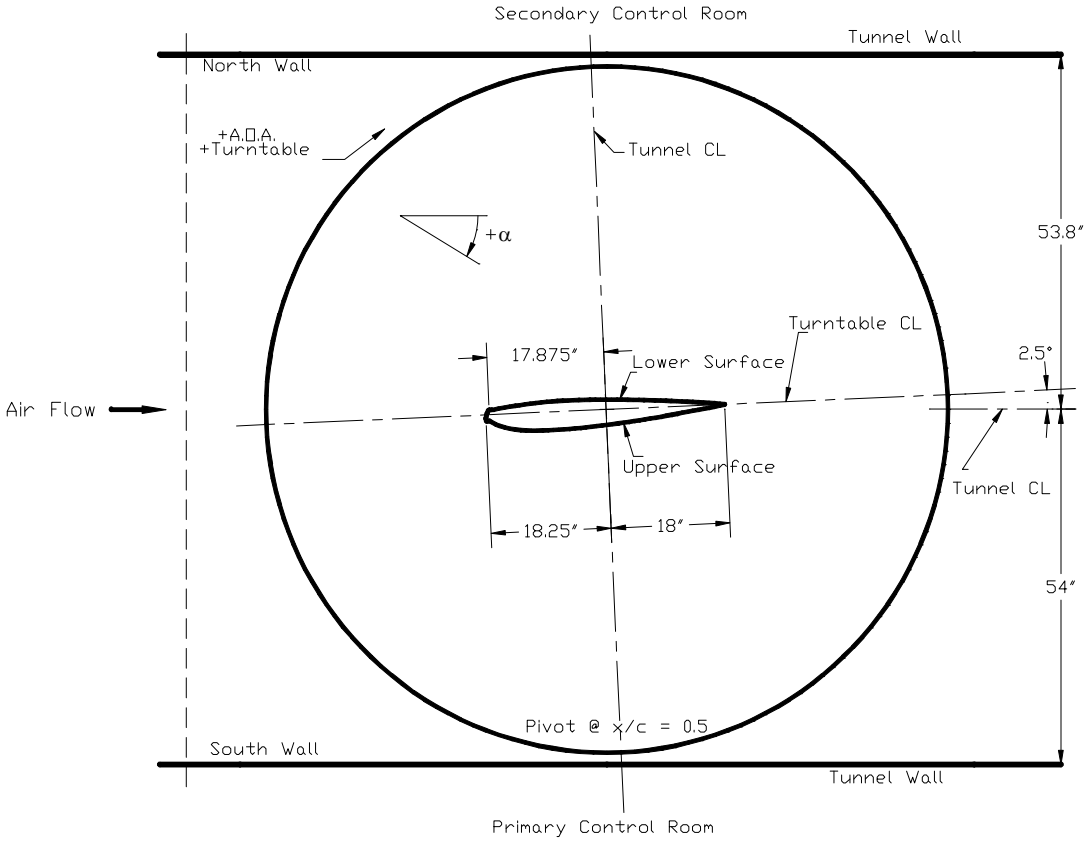

Figure 12b. NACA 23012 With 10-min Glaze Ice Shape Installation in the IRT Test Section (top view)

Figure 12c. Various Views of NACA 23012 With 10-min Glaze Ice Shape Installation in the IRT Test Section and Blotter Strip Installation

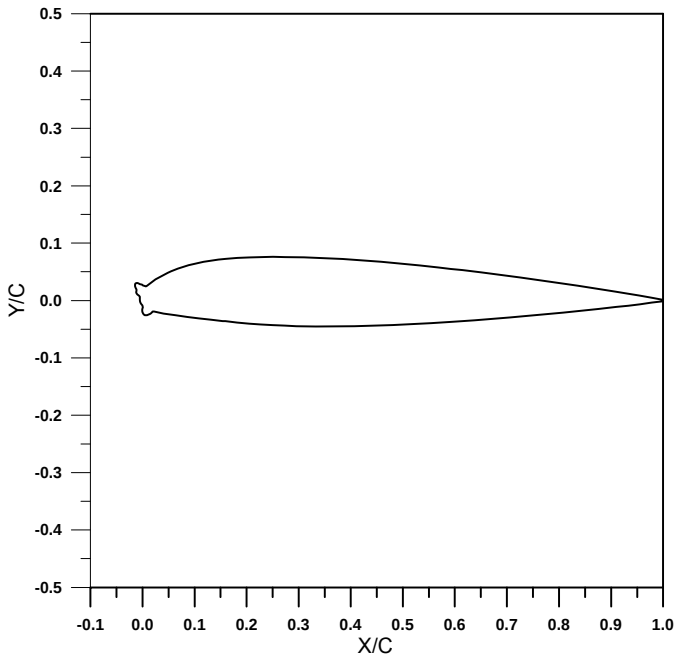

Figure 13a. NACA 23012 With 15-min Glaze Ice Shape

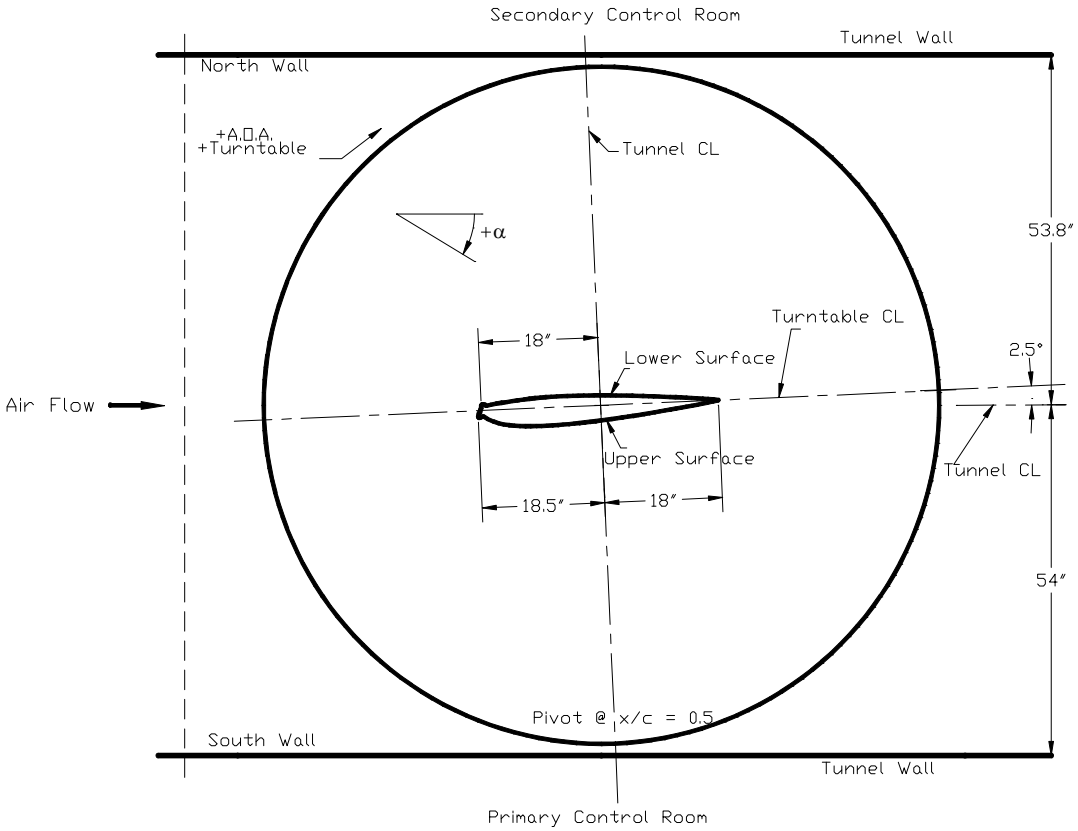

Figure 13b. NACA 23012 With 15-min Glaze Ice Shape Installation in the IRT Test Section (top view)

Figure 13c. Various Views of NACA 23012 With 15-min Glaze Ice Shape Installation in the IRT Test Section ad Blotter Strip Installation

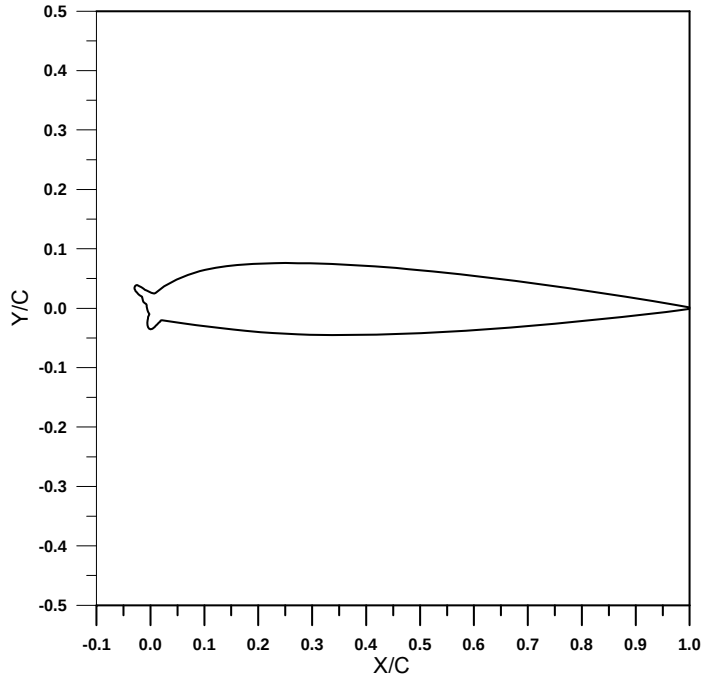

Figure 14a. NACA 23012 With 22.5-min Glaze Ice Shape

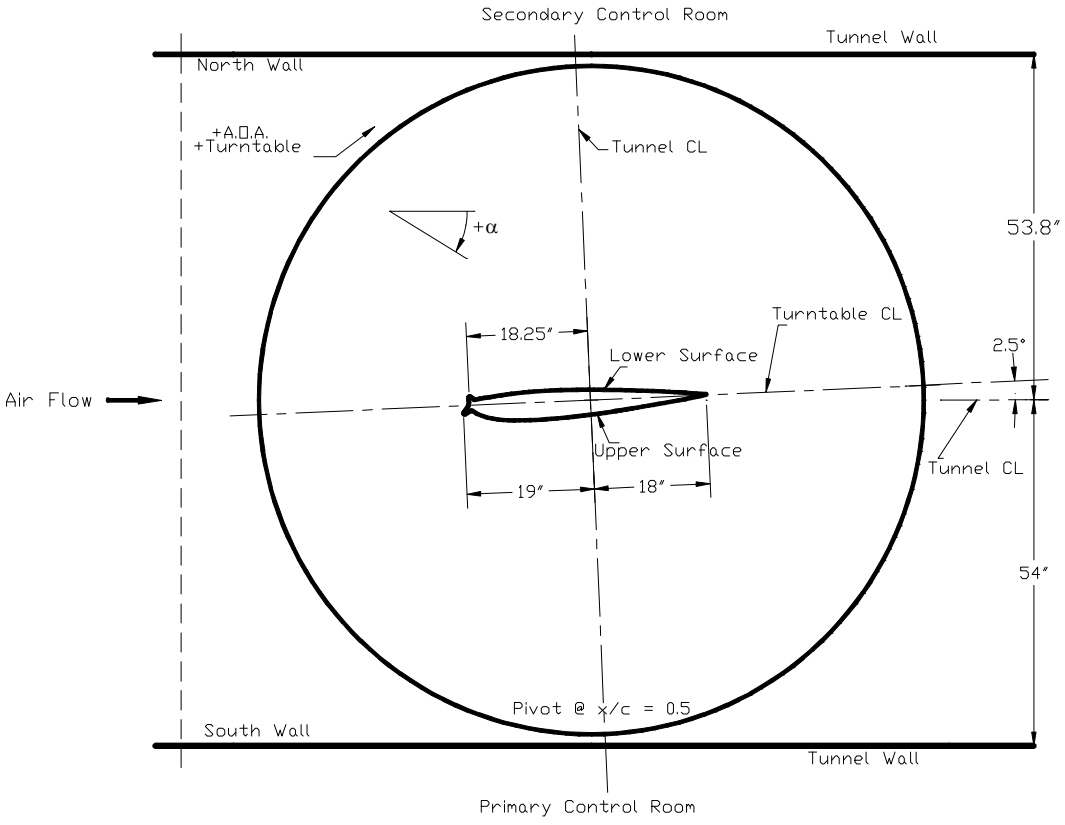

Figure 14b. NACA 23012 With 22.5-min Glaze Ice Shape Installation in the IRT Test Section (top view)

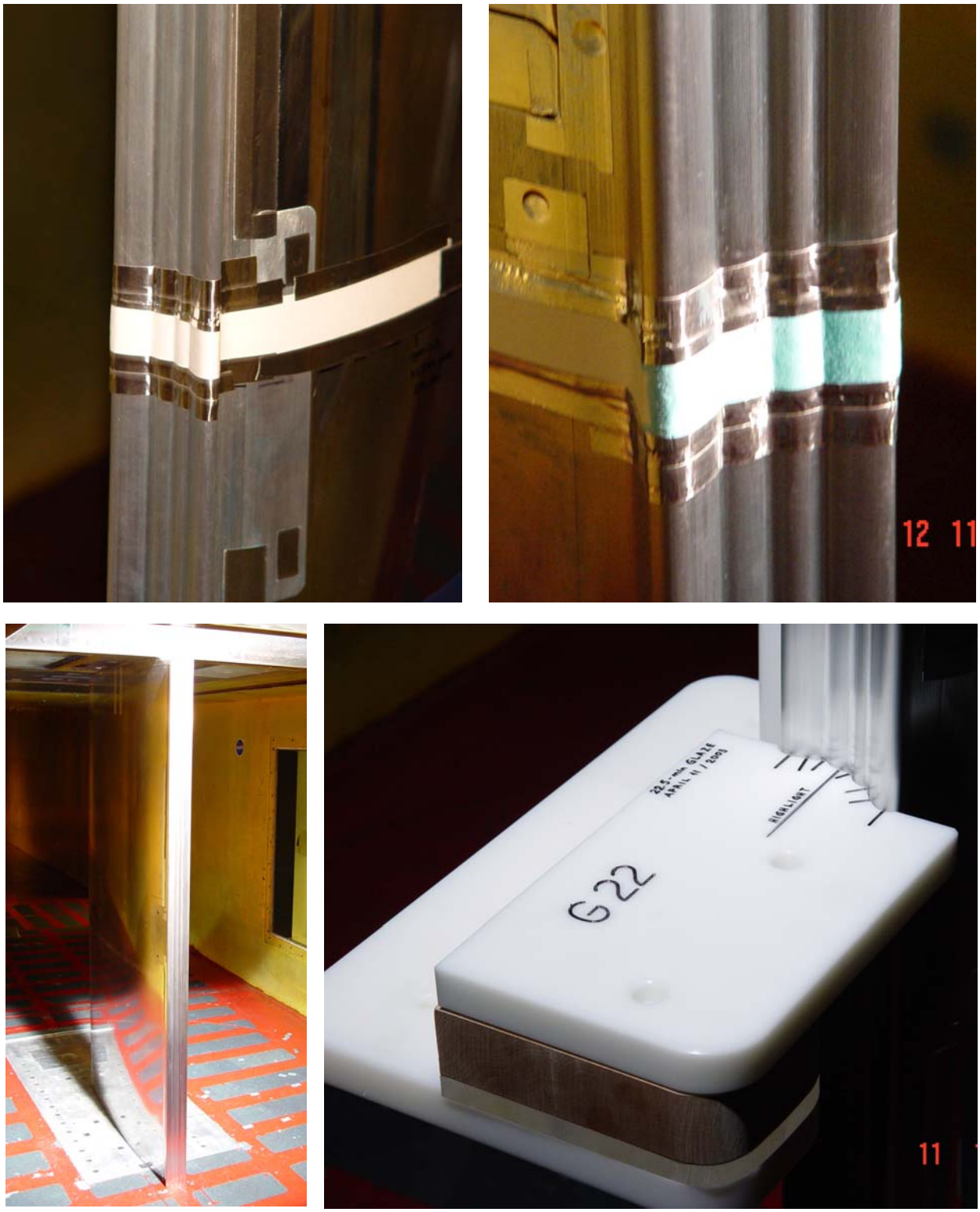

Figure 14c. Various Views of NACA 23012 With 22.5-min Glaze Ice Shape Installation in the IRT Test Section ad Blotter Strip Installation

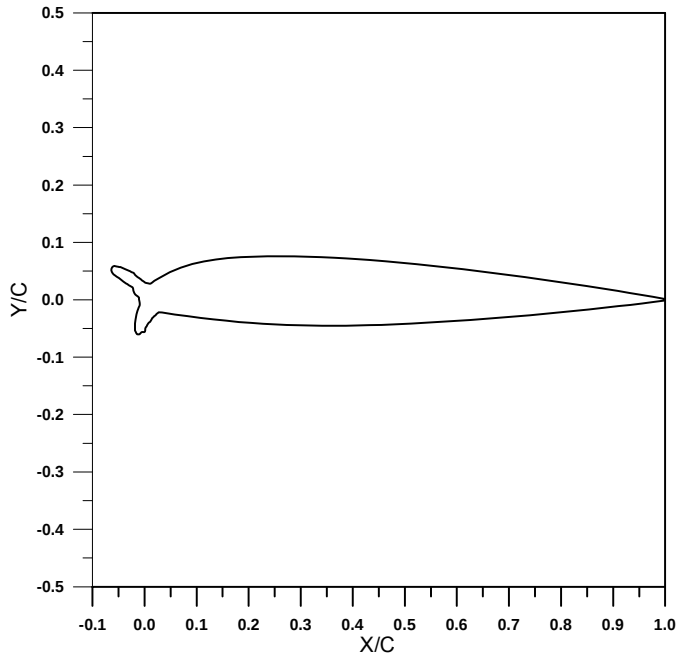

Figure 15a. NACA 23012 With 45-min Glaze Ice Shape

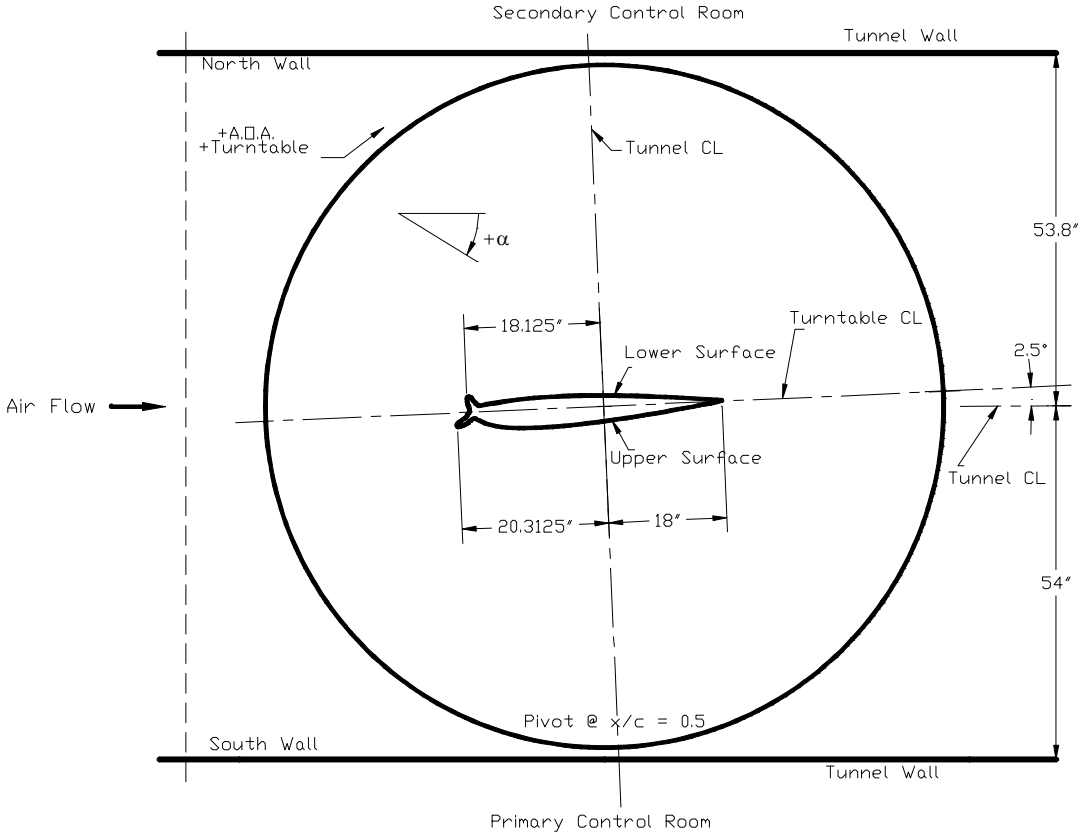

Figure 15b. NACA 23012 With 45-min Glaze Ice Shape Installation in the IRT Test Section (top view)

Figure 15c. Various Views of NACA 23012 With 45-min Glaze Ice Shape Installation in the IRT Test Section and Blotter Strip Installation

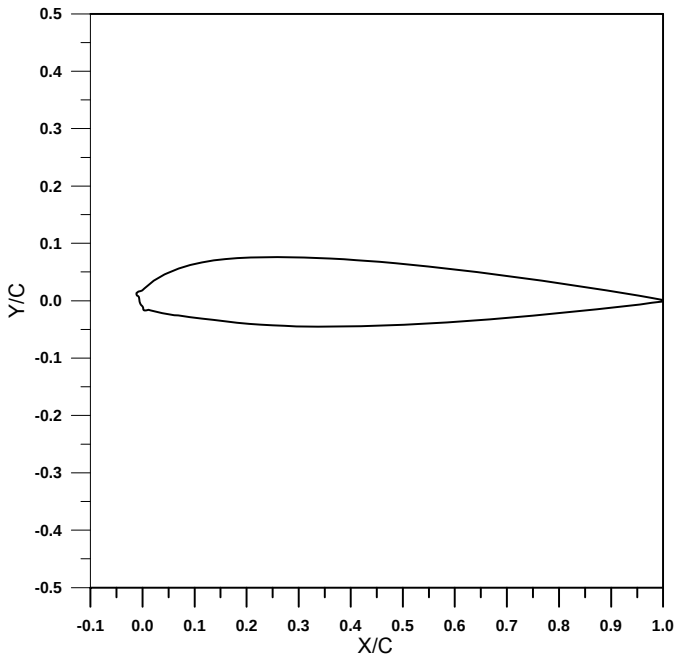

Figure 16a. NACA 23012 With 7.5-min Mixed Ice Shape

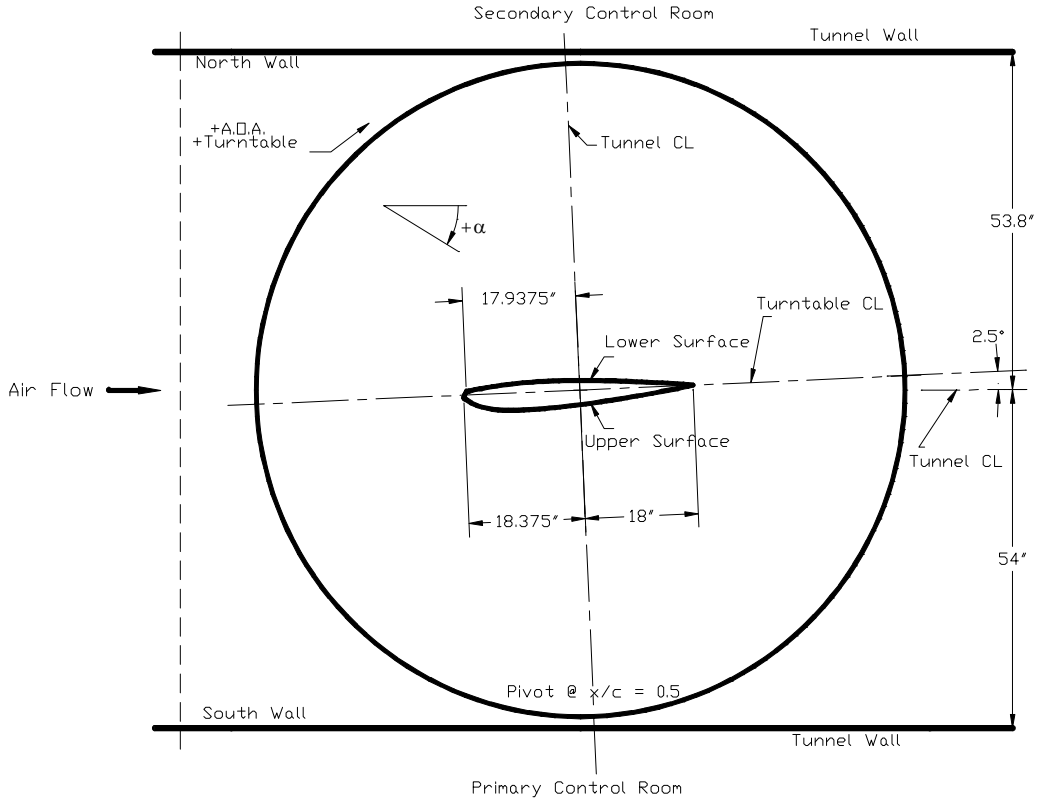

Figure 16b. NACA 23012 With 7.5-min Mixed Ice Shape Installation in the IRT Test Section (top view)

Figure 16c. Various Views of NACA 23012 With 7.5-min Mixed Ice Shape Installation in the IRT Test Section and Blotter Strip Installation

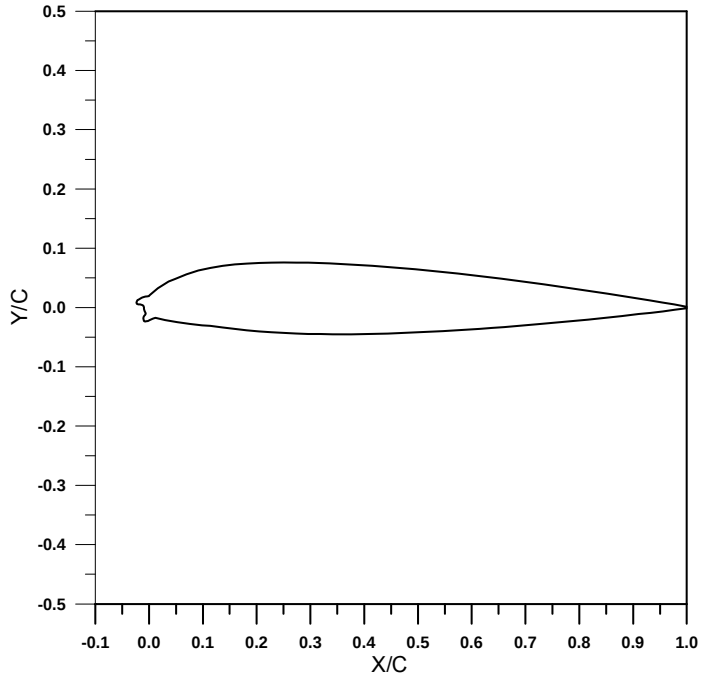

Figure 17a. NACA 23012 With 15-min Mixed Ice Shape

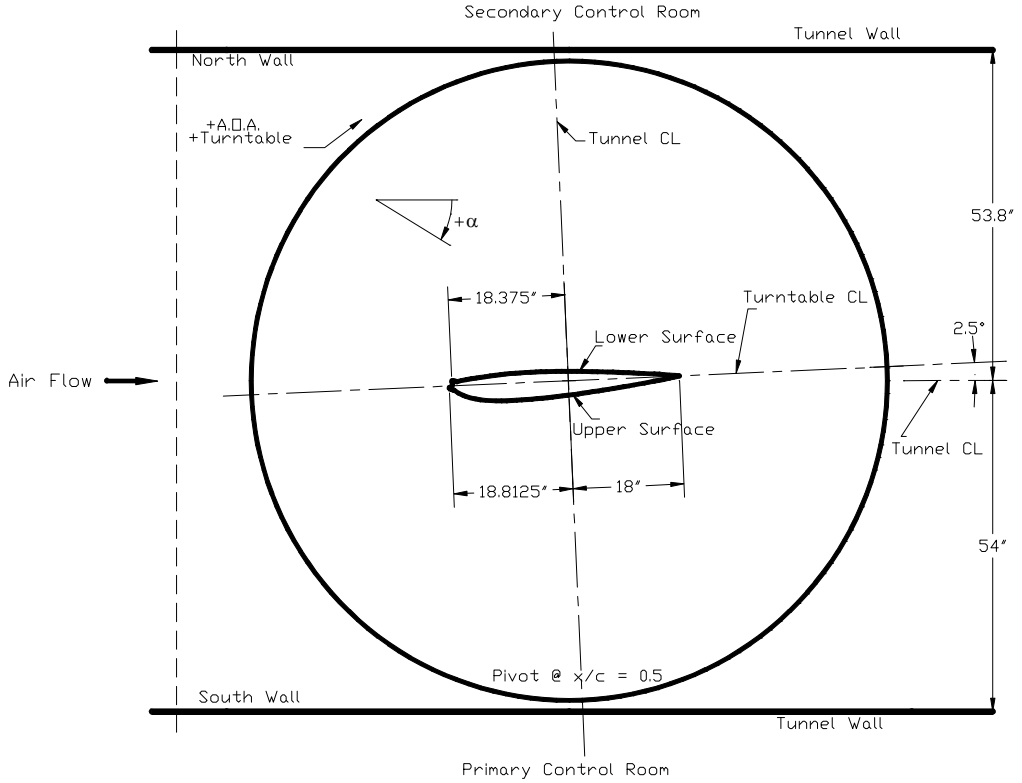

Figure 17b. NACA 23012 With 15-min Mixed Ice Shape Installation in the IRT Test Section (top view)

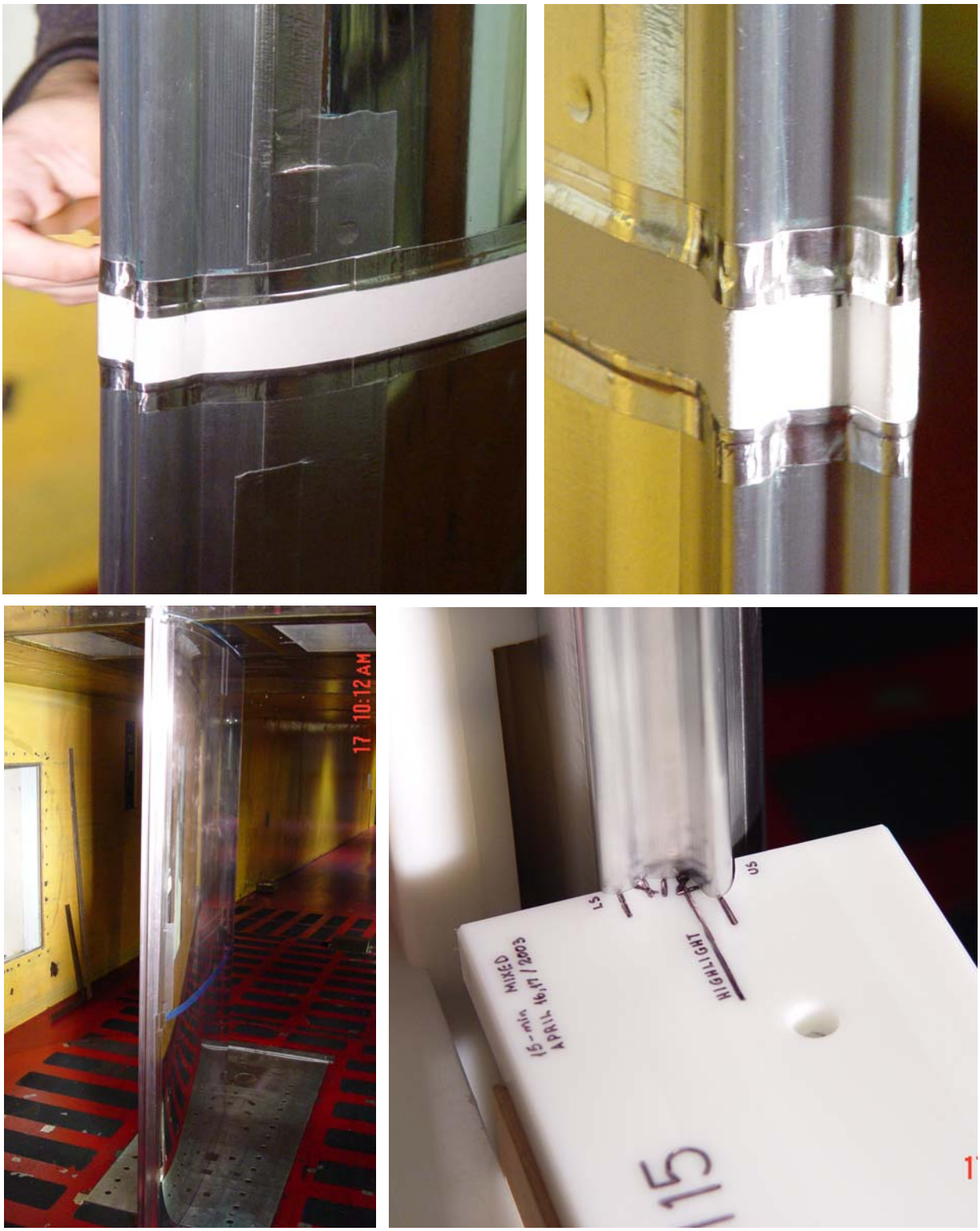

Figure 17c. Various Views of NACA 23012 With 15-min Mixed Ice Shape Installation in the IRT Test Section and Blotter Strip Installation

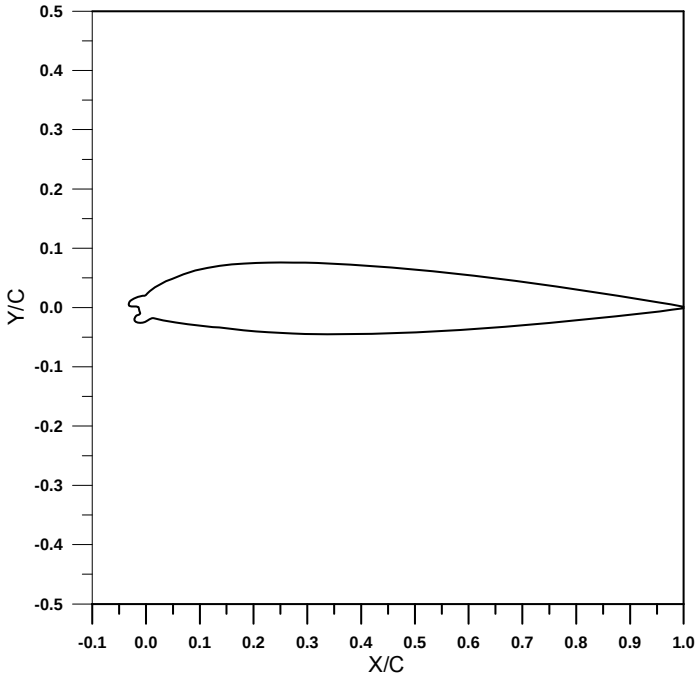

Figure 18a. NACA 23012 With 22.5-min Mixed Ice Shape

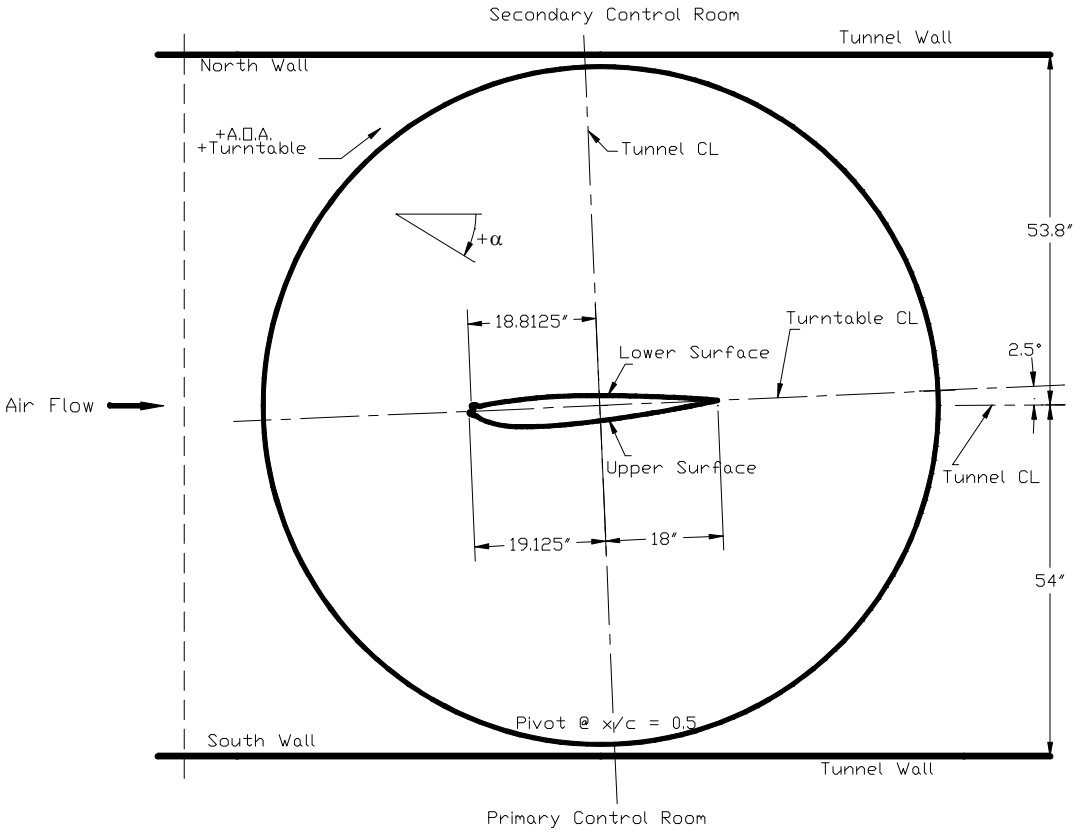

Figure 18b. NACA 23012 With 22.5-min Mixed Ice Shape Installation in the IRT Test Section (top view)

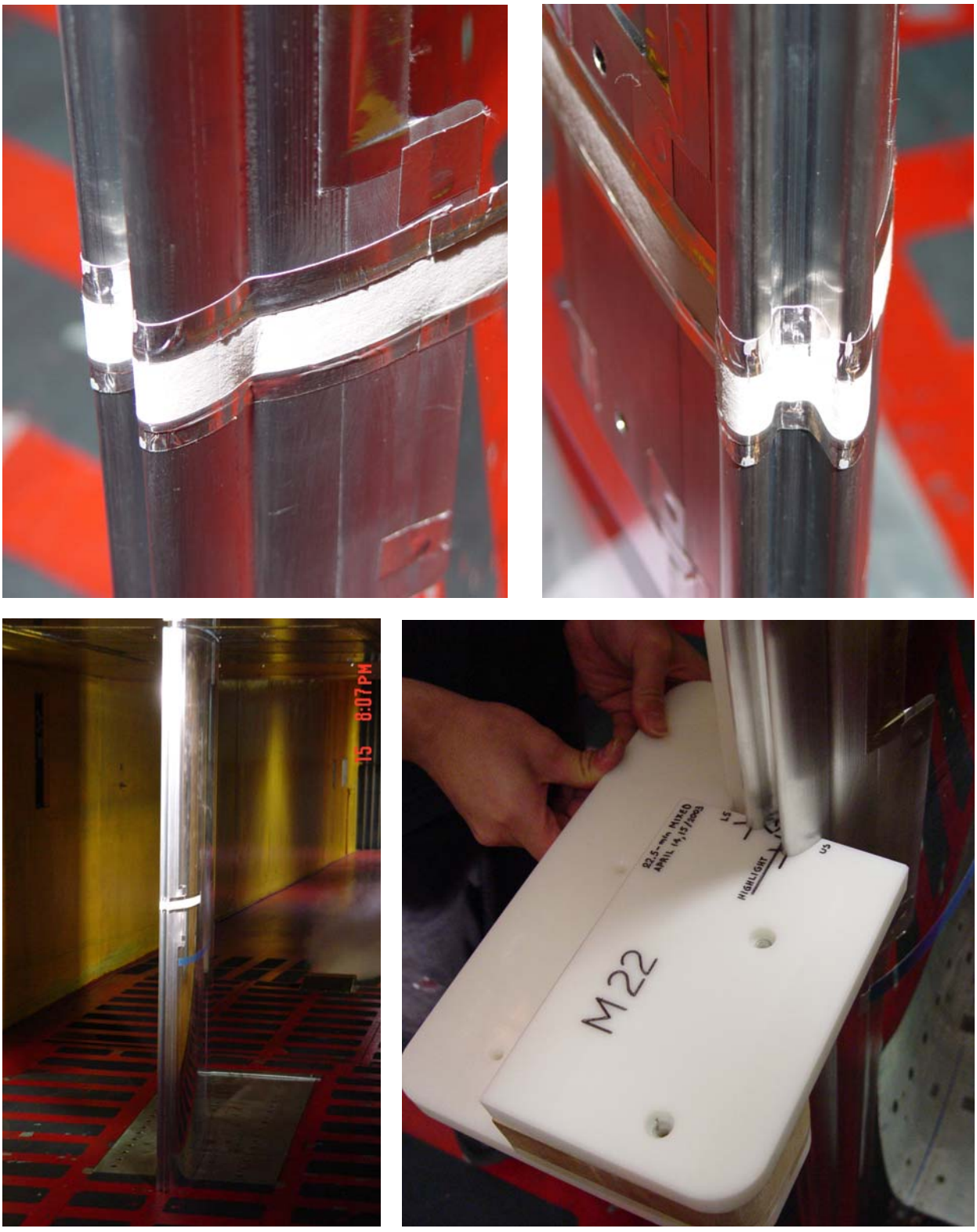

Figure 18c. Various Views of NACA 23012 With 22.5-min Mixed Ice Shape Installation in the IRT Test Section and Blotter Strip Installation

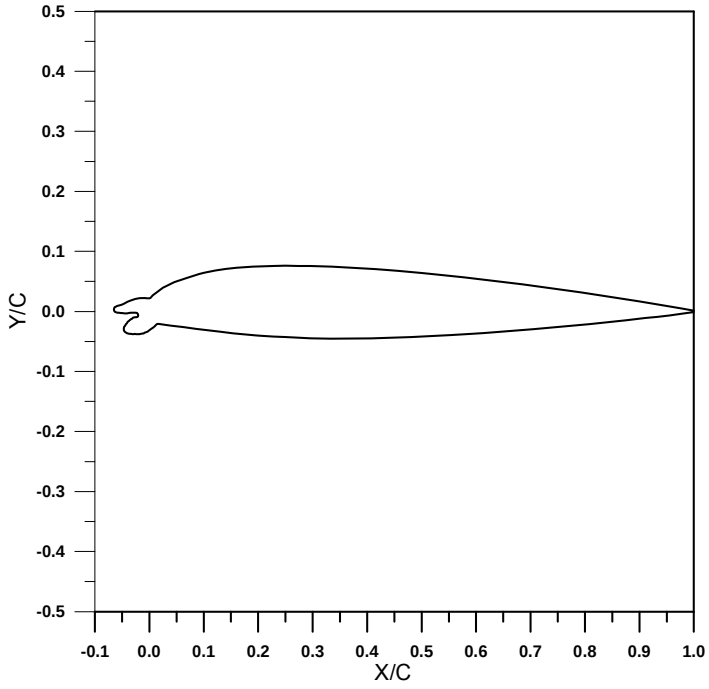

Figure 19a. NACA 23012 With 45-min Mixed Ice Shape

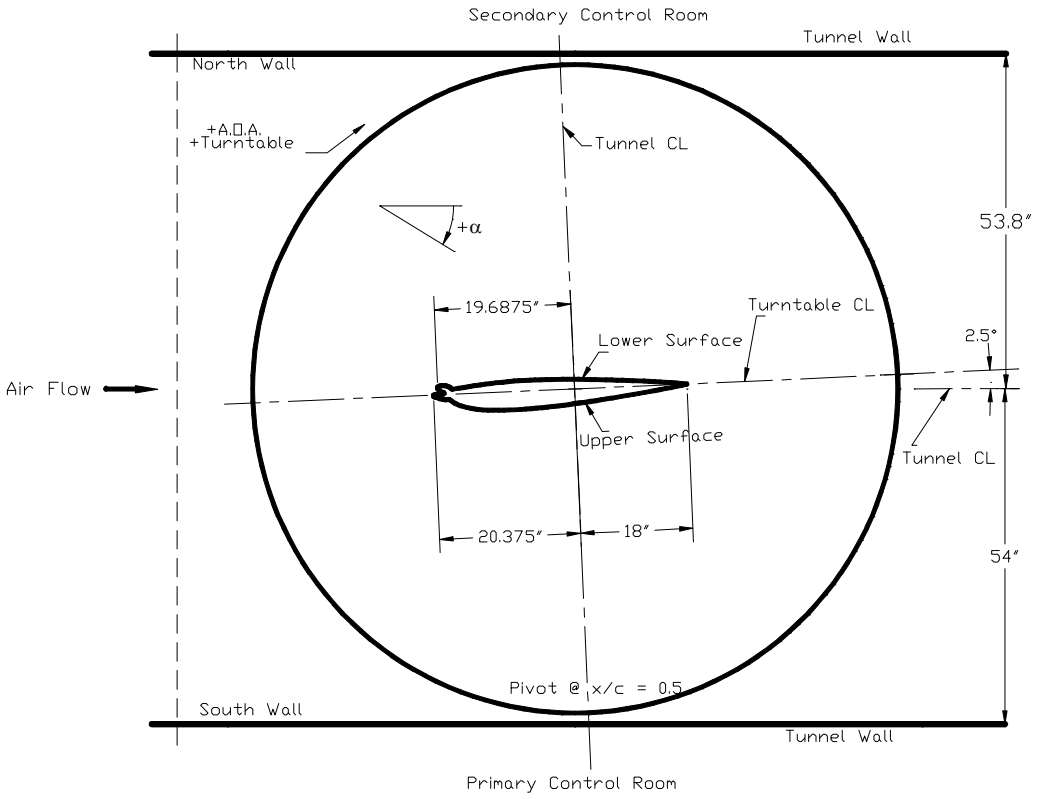

Figure 19b. NACA 23012 With 45-min Mixed Ice Shape Installation in the IRT Test Section (top view)

Figure 19c. Various Views of NACA 23012 With 45-min Mixed Ice Shape Installation in the IRT Test Section and Blotter Strip Installation

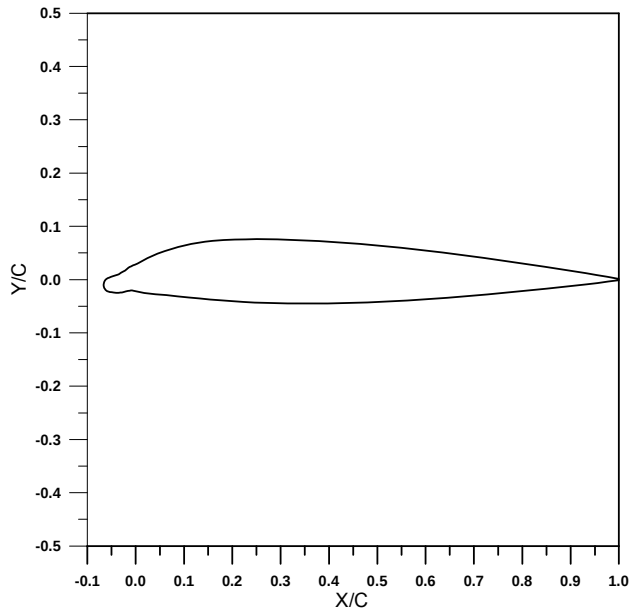

Figure 20a. NACA 23012 With 45-min Rime Ice Shape

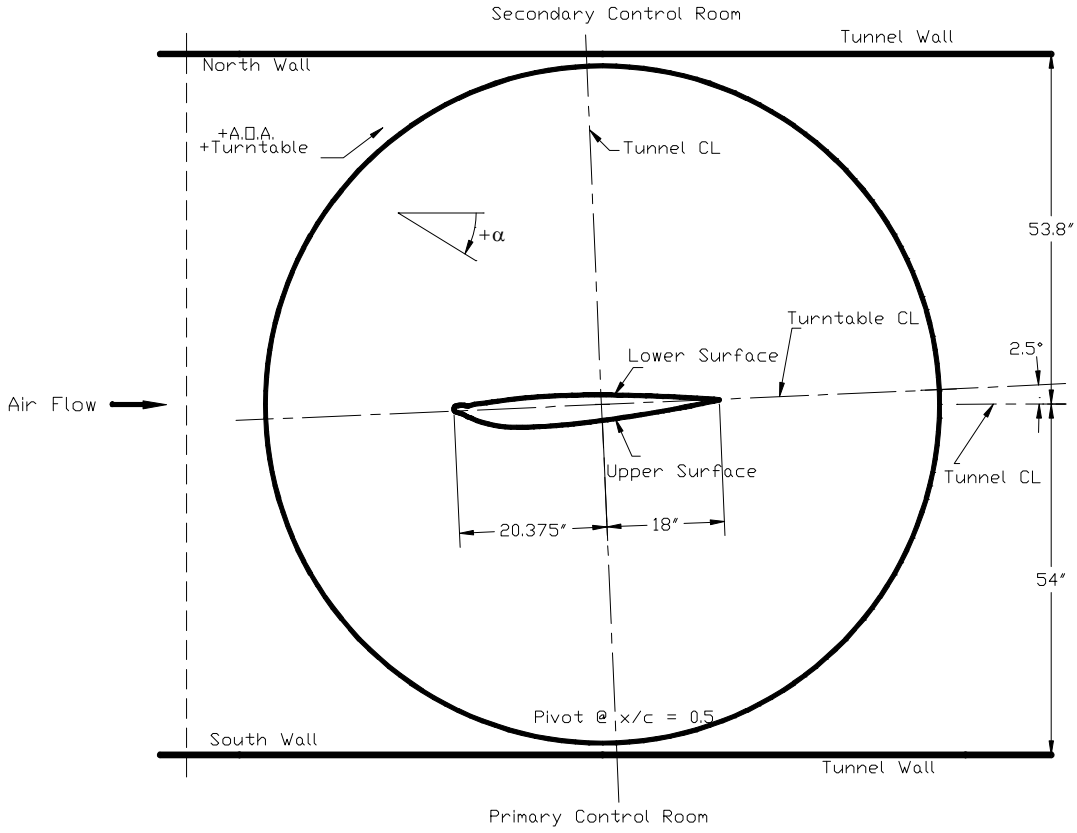

Figure 20b. NACA 23012 With 45-min Rime Ice Shape Installation in the IRT Test Section (top view)

Figure 20c. Various Views of NACA 23012 With 45-min Rime Ice Shape Installation in the IRT Test Section and Blotter Strip Installation

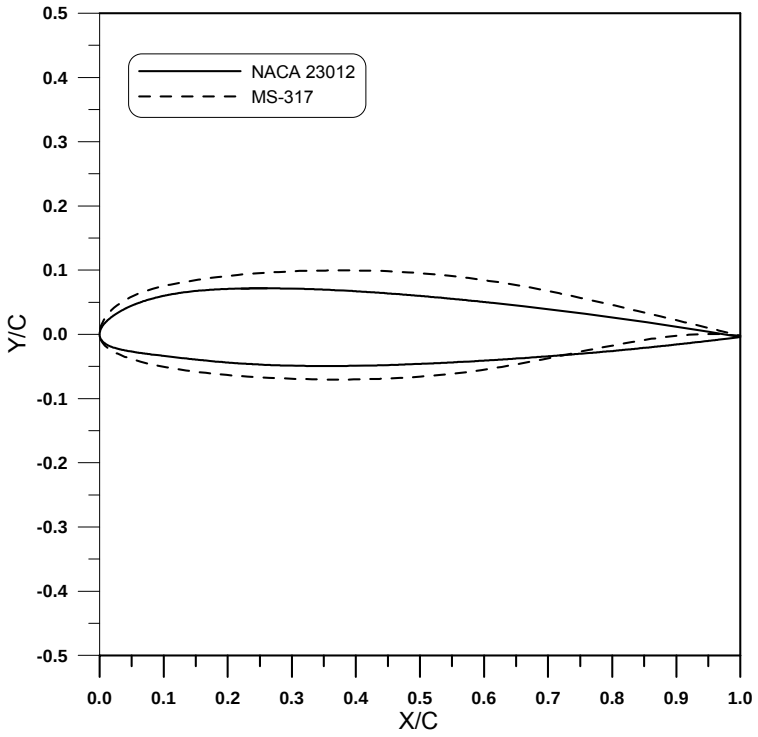

Figure 21. Comparison of Clean Airfoil Sections

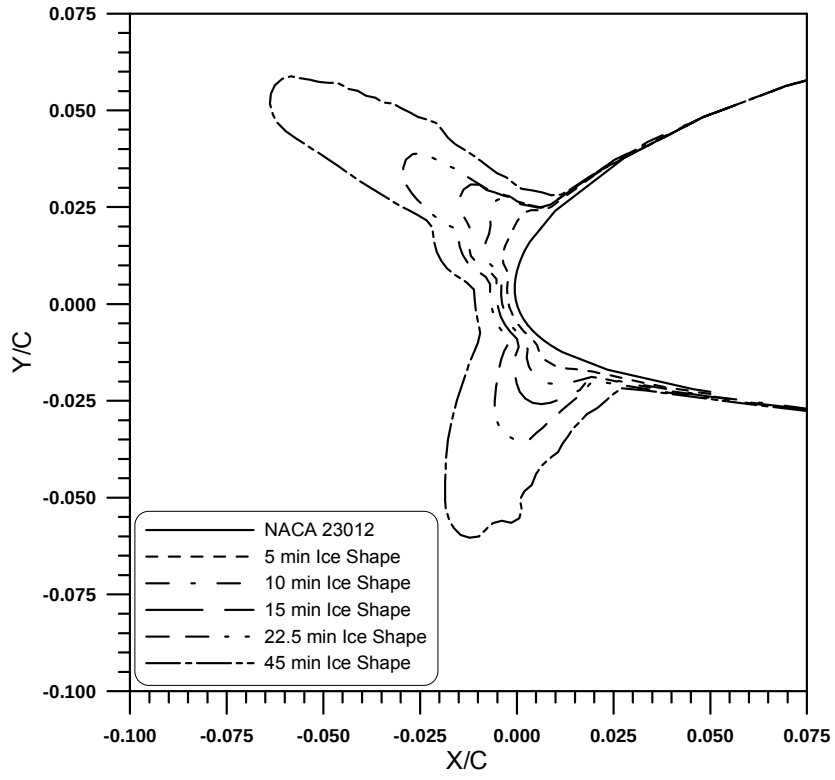

Figure 22a. Comparison of Clean NACA 23012 and Glaze Ice Shape Sections

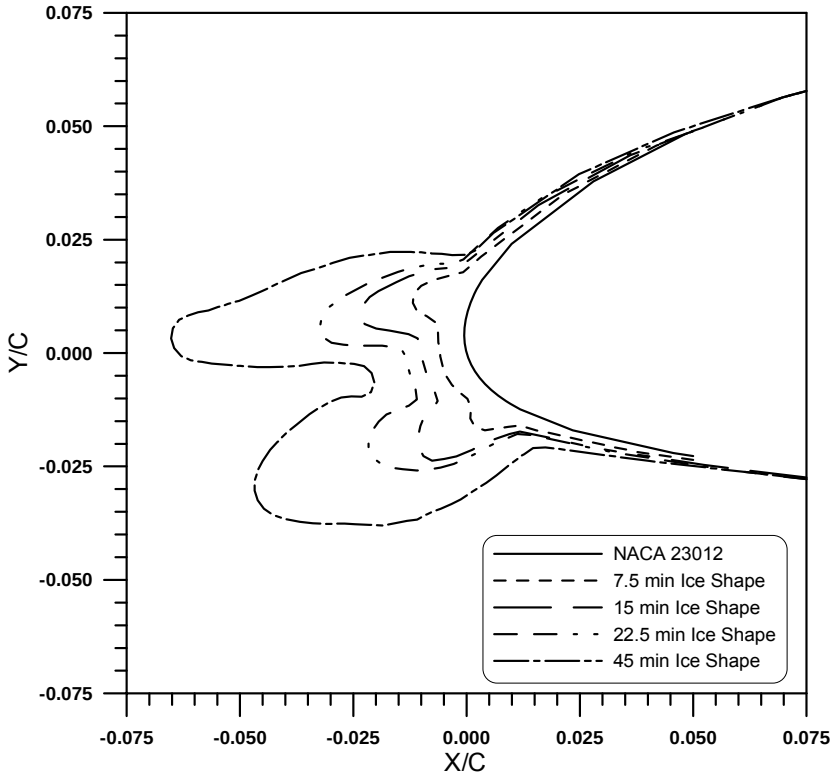

Figure 22b. Comparison of Clean NACA 23012 and Mixed Ice Shape Sections

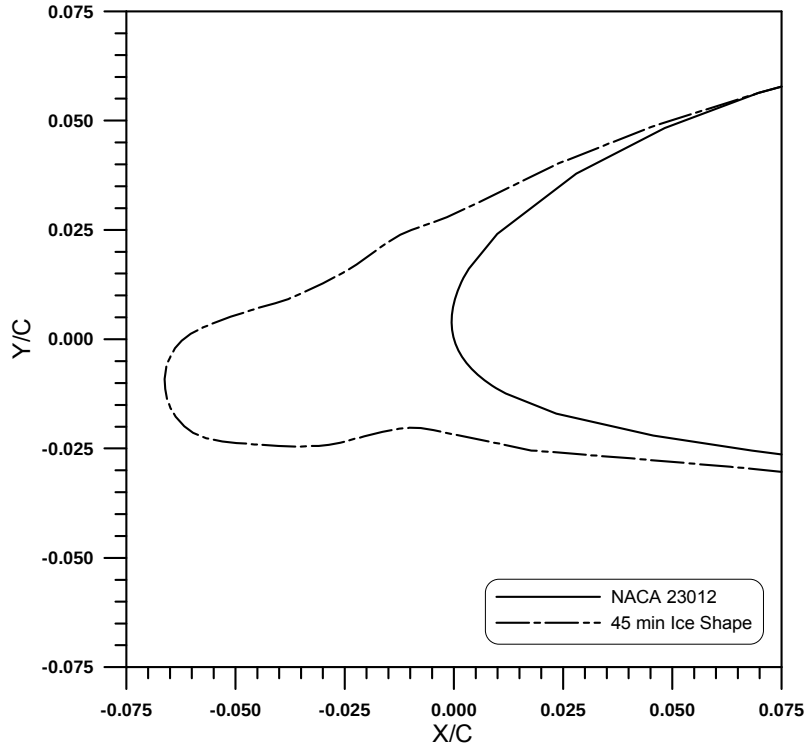

Figure 22c. Comparison of Clean NACA 23012 and Rime Ice Shape Sections

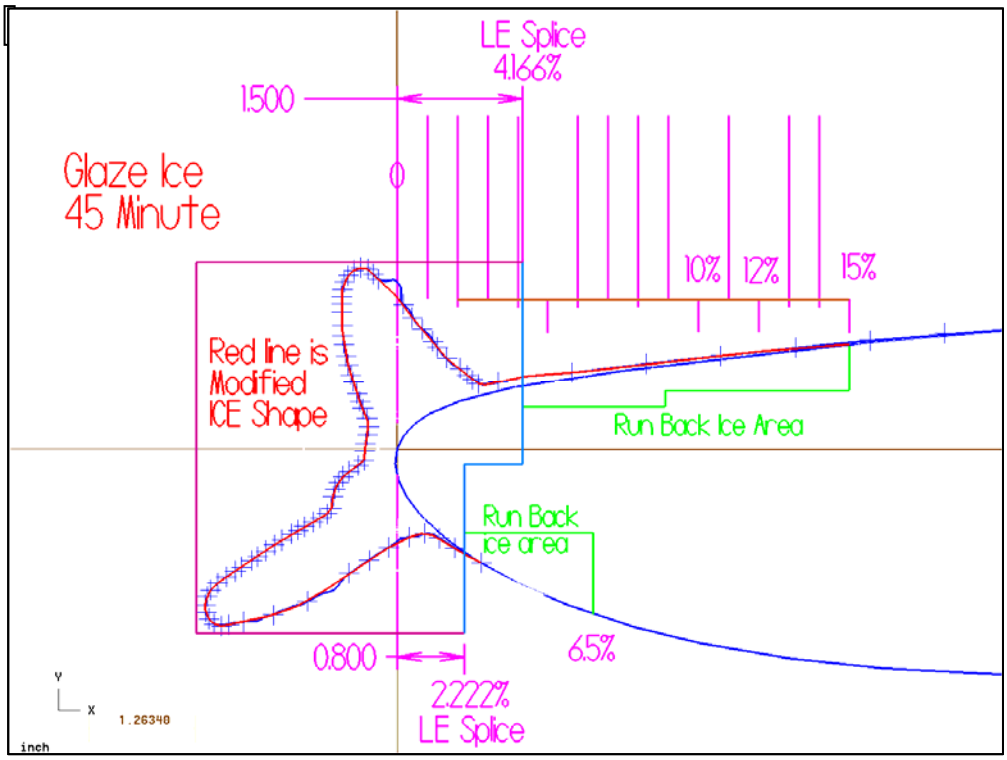

Figure 23a. Removable Wing Leading Edge and 45-min Glaze Ice Shape

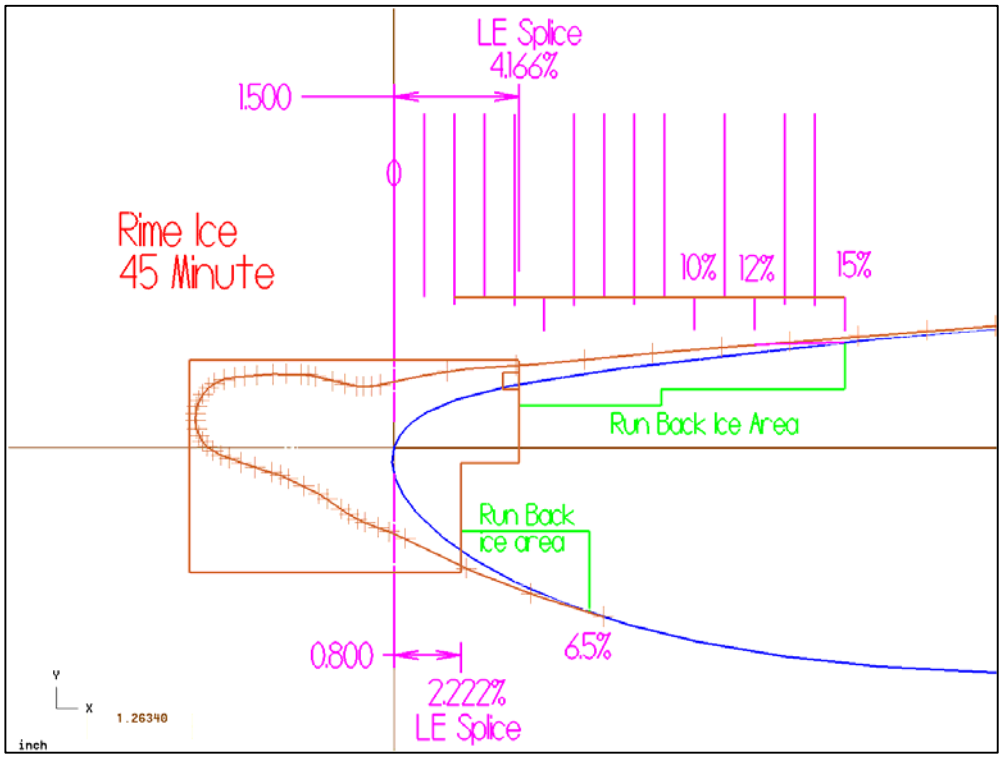

Figure 23b. Removable Wing Leading Edge and 45-min Rime Ice Shape

4.2.4 Installation of LEWICE Ice Shapes on NACA 23012.

To ensure repeatable and precise installation of the LEWICE ice shapes to the wing leading edge, the airfoil was designed with a removable leading edge, as shown in figure 24a. The removable leading edge extended 1.5 inch on the pressure surface (4.167% chord) and 0.8 inch on the suction surface (2.22% chord) over the entire span of the wing model. All the LEWICE ice shapes were constructed out of aluminum and were designed so the removable portion of the wing leading edge was part of each ice shape, as shown in figure 23. For ice shapes with long ice limits, however, this method of ice shape installation resulted in a small step between the wing surface and the ice shape trailing edge as shown in figure 24b. To maintain a smooth transition between the ice shape and the wing surface over the spanwise region where the impingement data were collected, 6-inch span inserts (plugs) were fabricated that extended to the ice limits in the chordwise direction as shown in figure 24b. Each ice shape was designed with two inserts, one for the upper surface and one for the lower surface. On the suction (upper) surface the inserts extended from 2.22% chord to 6.5% chord, while along the lower surface, the inserts extended from 4.167% chord to 15% chord. In the spanwise direction, the inserts extended from 33 inches to 39 inches above the tunnel floor. Photos of the slots on wing surface for the ice shape inserts are provided in figures 24c-24d. Note that all pressure taps on the airfoil were placed 30 inches above the tunnel floor so the installation of the ice shape inserts did not affect the number of active ports. However, when an ice shape was installed, approximately ten pressure ports near the airfoil leading edge were eliminated. Active pressure ports for the clean wing and for each ice shape configuration are provided in appendix A.

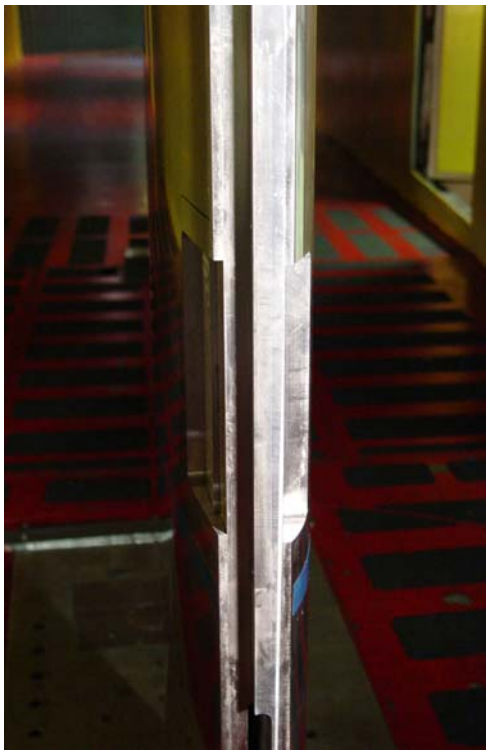

Figure 24a. NACA 23012 Airfoil With the Leading-Edge Section Removed

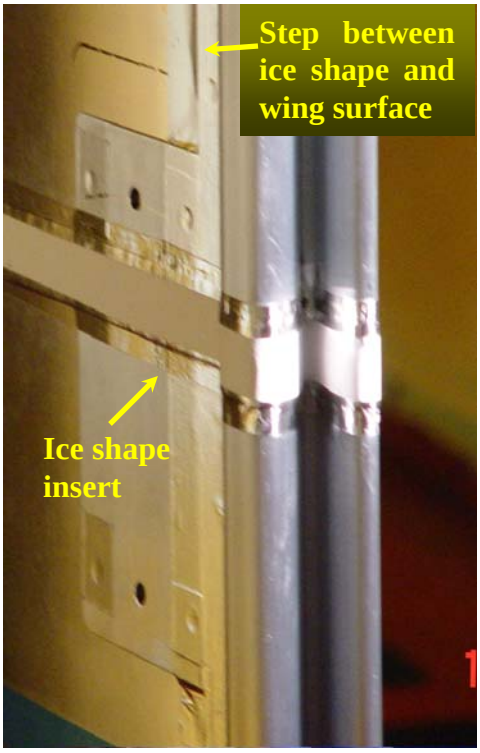

Figure 24b. Ice Shape Insert Installed on the Pressure Surface

Figure 24c. Slot for Ice Shape Insert on the Pressure Surface

Figure 24d. Slot for Ice Shape Insert on the Suction Surface

4.3 DYE TRACER METHOD.

The dye tracer technique was initially developed by NACA [8] and was subsequently modified by Papadakis, et al. [13 and 14]. In the modified method, distilled water containing a known concentration of blue dye (0.3 g of FD&C Blue No. 1 dye per liter of water) is injected into the airstream of the IRT in the form of a drop spray cloud through a specially designed 16-nozzle spray system. The test models are covered with thin strips of blotter paper (James River Paper Company Verigood 100# Blotting Paper) in areas of interest and are exposed to the spray cloud for a certain length of time. The amount of dye mass per unit area of blotter strip obtained in a given time interval is measured using reflectance spectroscopy. The water impingement characteristics of a test model are obtained by converting the dye color density distribution on each strip into water impingement density using specially developed calibration curves.

4.4 SPRAY SYSTEM.

The impingement tests were conducted with an automated 16-nozzle spray system, which was developed by WSU and can produce consistent and repeatable short-duration sprays (as short as 0.75 second). The short spray duration was needed to avoid blotter saturation and dye penetration into the blotter paper. These requirements were dictated by the data extraction method, which relies on accurate reflectance measurements from the surface of the dye-laden blotter strips. The IRT spray system was not capable of providing short-duration sprays and could not be used with the blue dye solution required for the impingement tests. The 16-nozzle system was based on a 12-nozzle system also developed by WSU. Details of the development and testing of the 12-nozzle spray system can be found in references 13 and 17. The expansion

from 12 to 16 nozzles was based on tests conducted by Papadakis, et al. [17], which showed that for large drop clouds, cloud uniformity over the region of interest was considerably reduced and more nozzles were needed to cover the impingement region for the test models selected.

Blue dye solution was stored in a 30-gallon stainless steel supply tank. The dye was transported under pressure to 16 nozzle assemblies using rubber hoses. Each nozzle assembly consisted of an IRT MOD-1 spray nozzle, nozzle housing, a fast action solenoid valve, an oil-filled pressure gage, a SETRA™ 206 pressure transducer to monitor water pressure, an adjustable flow valve, a 0.75-in.-diameter, 3-ft-long stainless steel pipe for the atomizing air supply, a support bracket for attaching the nozzle to the IRT spray bars, and a range of fittings for connecting the nozzle to the spray system air and water supply lines.

Water pressure for the supply tank was obtained from a 125 pounds per square inch gauge (psig) air line, while a separate 100 psig high-volume flow air source (atomizing air manifold) provided air to the nozzle assemblies for atomizing the water. Quick-response pressure regulators were used for setting the water and atomizing air pressures. These regulators were continually adjusted using miniature electropneumatic transducers to maintain the required pressures. The electropneumatic transducers were controlled by feedback loops incorporated into the spray system computer control unit. The activation pressure for the electropneumatic transducers was set to 130 psig and was obtained from a low-volume high-pressure source. This source was independent of the water and atomizing air pressure lines to ensure that fluctuations in the high volume lines did not affect the operation of the electropneumatic transducers.

The pressure of the atomizing air was monitored at the supply-line regulator with a SETRA 204 transducer. In addition, three SETRA 206 transducers were used to monitor atomizing air pressures at selected nozzles. A SETRA 204 pressure transducer was installed in the water tank to monitor the water pressure. Also, two high-precision analog pressure gauges were installed at the water tank and at the regulator of the atomizing air line to confirm the pressure readings from the electronic transducers. Pressure transducers characteristics are summarized in table 2. Before the IRT test entry, the NASA Glenn flow calibration laboratory tested and calibrated all the pressure transducers used in the WSU spray system.

Table 2. Summary of Pressure Transducer Characteristics

Transducer	Usage	Range (psig)	Error	Thermal Zero Shift Error	Thermal Span Shift Error
16 SETRA 206	Water lines	0-125	±0.13% FS	±1.0% FS/100°F	±1.5% FS/100°F
1 SETRA 204	Main air line	0-100	±0.11% FS	±0.4% FS/100°F	±0.3% FS/100°F
1 SETRA 204	Water tank	0-100	±0.11% FS	±0.4% FS/100°F	±0.3% FS/100°F
4 SETRA 206	Nozzle air lines	0-100	±0.13% FS	±1.0% FS/100°F	±1.5% FS/100°F

Note: All transducers were calibrated at a temperature of 50°F.

The NASA Glenn IRT MOD-1 nozzles were selected for the 2003 impingement tests. Details of the specific spray nozzles used can be found in reference 6. These nozzles have a lower flow rate (approximately 1/3) for a given air pressure and delta pressure (P_{water}-P_{air}) than the standard IRT nozzles so that longer spray times could be achieved without saturating the blotter strips.

Longer spray times are desirable because they result in more stable sprays. These nozzles were also capable of producing the large MVD sizes that were needed for the large drop impingement tests.

Although the impingement tests are conducted at warm temperatures, typically 50°F, sometimes during testing the tunnel temperature is lowered to near freezing to control the humidity levels in the airstream. To ensure that nozzle freeze-out did not occur during impingement tests, the water temperature in the spray system was monitored continually with two thermocouples. One thermocouple was placed inside the housing of spray nozzle 9, and the other was placed immediately downstream, of the 30-gallon supply tank. Nozzle 9 was chosen because it was located approximately in the center of the tunnel plenum where the total air temperature was approximately equal to the average of the total freestream temperature. T-Type NPT thermocouples (Omega TC-T-NPT-G-72) were used and were connected to Omega TX-251 transmitters to amplify the voltage difference before connecting to the spray system computer. Two drum heaters were also wrapped around the supply tank to maintain the dye solution at the desired temperature and prevent the water in the spray system from freezing.

A sensitive flow meter was installed in the main water supply line of the spray system to ensure that the spray system was working properly and that the amount of water sprayed was repeatable. This instrument was capable of measuring volume flow rates in the range 0.02 to 1.0 gallon per minute with an accuracy of 0.2% full scale (FS). The flow meter was calibrated by the NASA Glenn flow calibration laboratory prior to the start of the tests.

Fast-acting solenoid valves were used to turn the spray on and off. During testing, the main air supply solenoid was turned on approximately 30 seconds before the spray was initiated to allow the atomizing air pressure to stabilize. Next, the 16 water solenoid valves were activated by the computer system and a spray cloud was produced. The MVD of the spray cloud was set by varying the spray system air-to-water pressure ratio. The duration of the spray was controlled by the computer hardware.

Sixteen brackets were designed and built for mounting the 16-nozzle spray system to the IRT spray bars. The brackets allowed for a more precise installation of the 16 nozzle assemblies. The complete 16-nozzle spray system is shown in figures 25a and 25b. The installation of the spray system and the coordinates of each spray nozzle with respect to the IRT spray bars are shown in figures 26a and 26b.

Figure 25a. The WSU Spray System Installed in the IRT Plenum Chamber

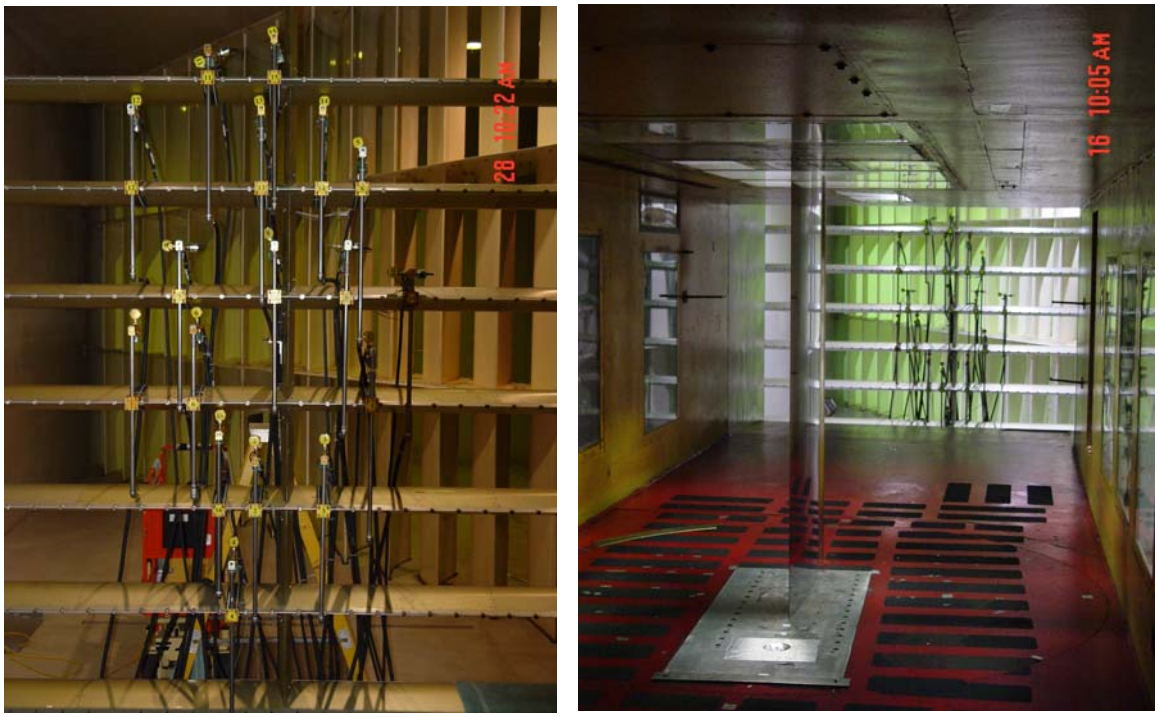

Figure 25b. Views of WSU Spray System Installed From the IRT Test Section

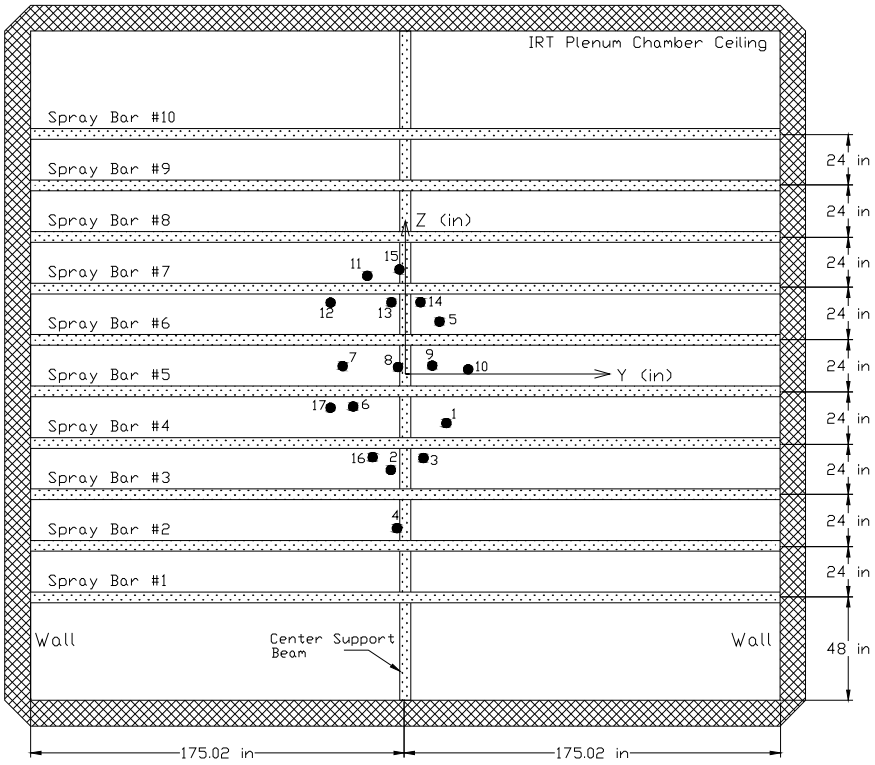

Figure 26a. Schematic Drawing of the 2003 WSU Spray System
(all dimensions in inches)

WSU Nozzle Assembly #	NASA MOD-1 Nozzle #	C_f	Y-Coordinate (in)	Z-Coordinates (in)
1	M277	0.00400	+19.000	+9.000/SP4
2	M264	NA	-7.000	+11.500/SP3
3	M234	0.00399	+8.500	+17.500/SP3
4	M217	0.00398	-3.750	+8.750/SP2
5	M308	0.00401	+16.125	+8.500/SP6
6	M243	0.00401	-24.000	+17.250/SP4
7	M300	NA	-28.875	+11.750/SP5
8	M233	0.00400	-3.500	+11.500/SP5
9	M242	0.00401	+12.750	+12.000/SP5
10	M210	0.00406	+29.500	+10.250/SP5
11	M249	0.00401	-18.000	+6.000/SP7
12	M252	0.00403	-34.750	+17.500/SP6
13	M269	NA	-6.500	+17.500/SP6
14	M291	NA	+7.250	+17.750/SP6
15	M268	NA	-3.000	+9.000/SP7
16	M203	NA	-15.125	+17.250/SP3
17		NA	-34.75	+16.500/SP4

Figure 26b. The WSU Spray System Nozzle Locations With Respect to the IRT Spray Bars
(2003 IRT entry)

A heavy-duty electronic balance was used to monitor the amount of liquid that remained in the supply tank. A Vaisala humidity sensor was also installed at the inlet of the IRT test section, to record the relative humidity and temperature of the airstream. In previous impingement tests [6, 13, and 17], the only available humidity and temperature readings were provided by the IRT humidity sensor, which was located on the IRT spray bar in the plenum chamber.

Various components of the spray system—the stainless steel pressure tank for storing the dye solution, the main air and water pressure lines, and the air and water pressure regulators are shown in figures 27 and 28. A close-up view of one of the WSU nozzle assemblies is provided in figure 29. The schematic of the spray system shown in figure 30 provides a summary of key system components.

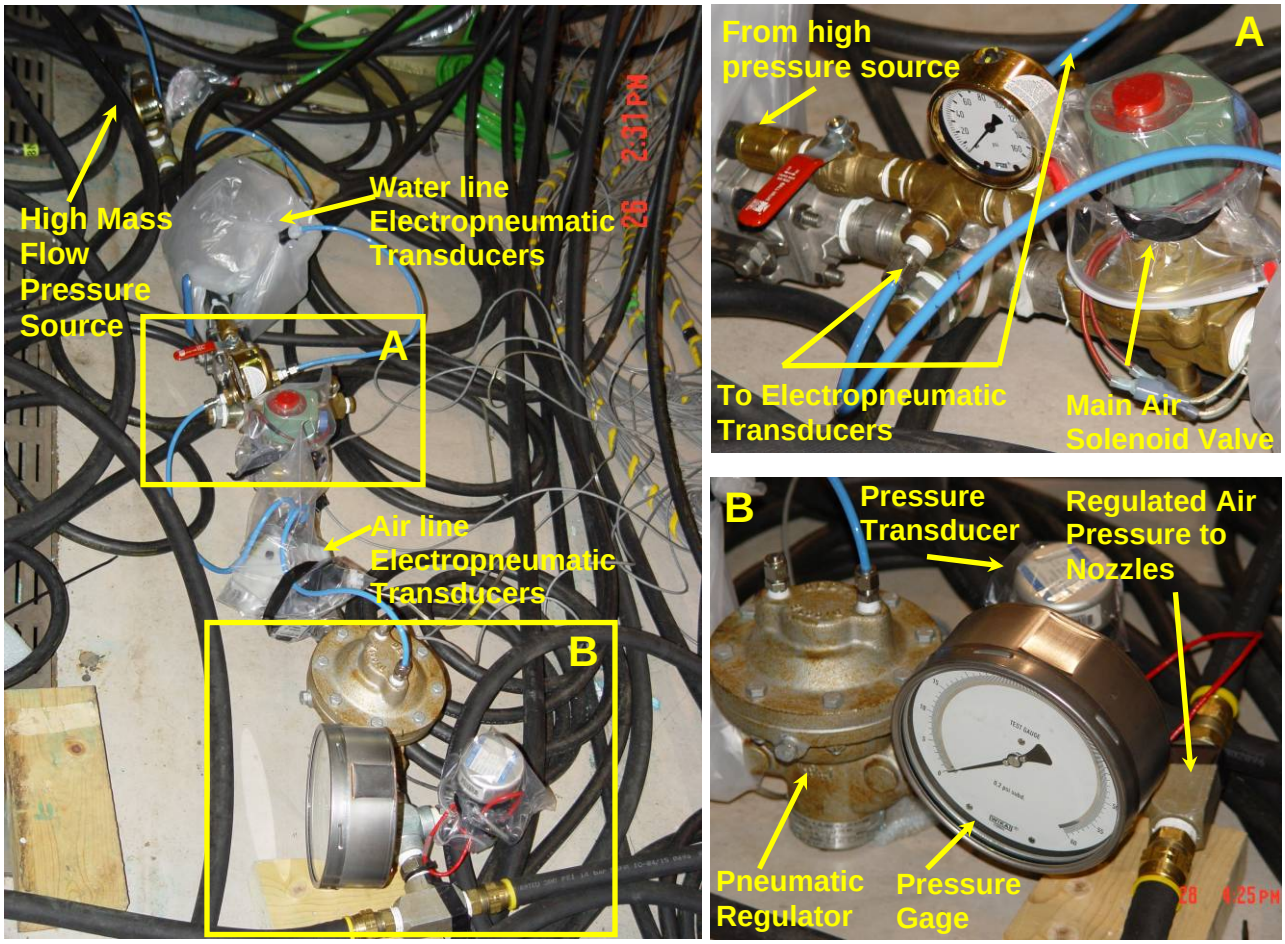

Figure 27. Main Air Supply Control System for WSU Spray Nozzles

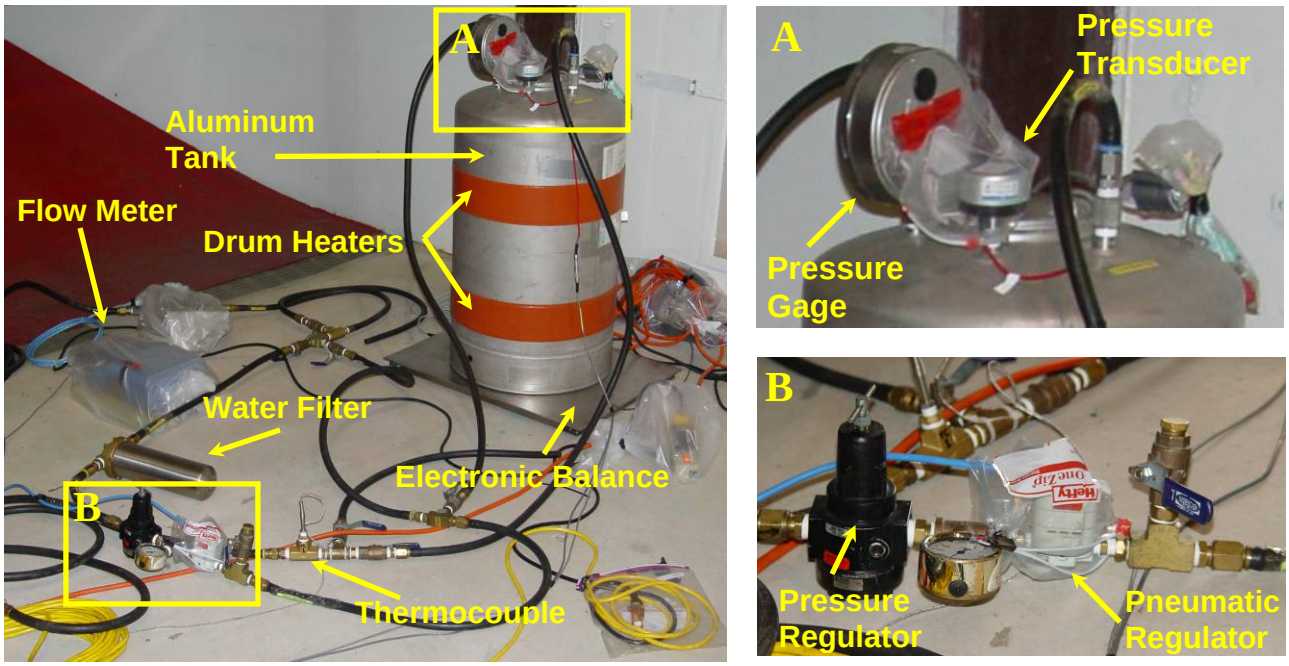

Figure 28. Water Supply Tank and the Water Line System

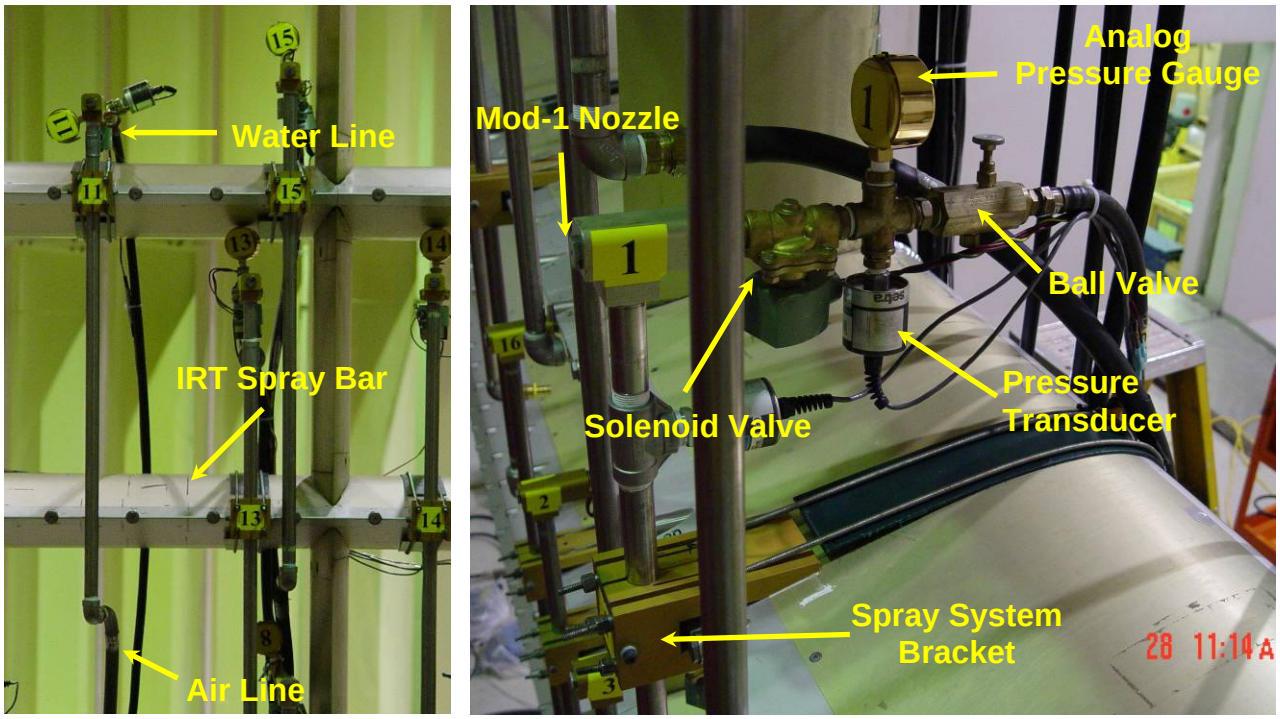

Figure 29. Components of Nozzle Assembly

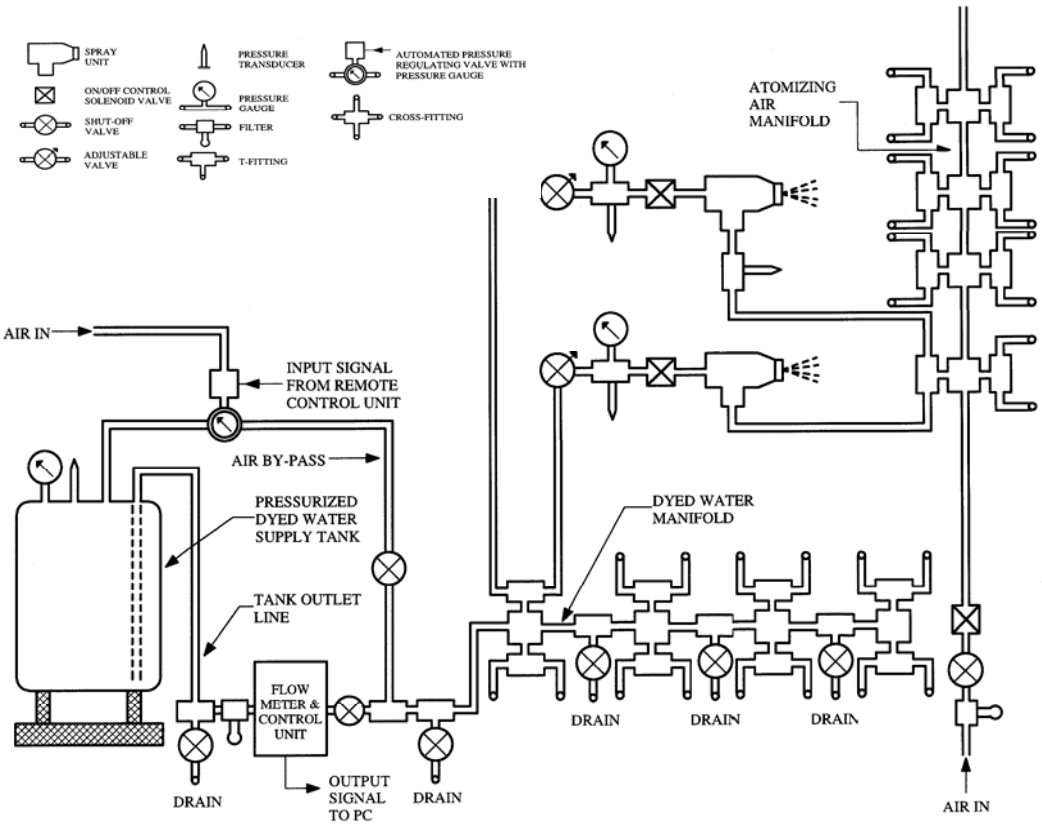

Figure 30. Schematic of the New WSU 16-Nozzle Spray System

The WSU spray system was assembled and tested extensively at WSU before it was transported to NASA Glenn for the water drop impingement tests. During the impingement tests at the NASA Glenn IRT facility, detailed analyses of recorded spray system parameters were performed. The results showed that the system was capable of maintaining air and water pressures to within ±1.5 psi from the required settings, as demonstrated in table 3.

Table 3. Cloud MVD and Corresponding Spray System Parameters From Test Measurements (2003 IRT tests)

MVD Range (μm)	Average Air Supply Pressure at Regulator (psig ±psi)	Average Tank Water Pressure (psig ±psi)	Average Water Pressure at Nozzle (psig ±psi)	Average Air Pressure at Nozzle (psig ±psi)	$\Delta P = P_{water}-P_{air}$ at Nozzle (psi)	Average Volume Flow Rate 16 Nozzles (GPM)	Spray Time (sec)
20 ±0.5	22.1 ±0.3	70.4 ±1.0	66.2 ±1.3	18.2 ±0.5	48.0	0.276	1.5
52 ±2.0	9.9 ±0.5	45.3 ±1.0	41.9 ±1.2	7.6 ±0.3	34.3	0.167	1.5
111 ±5.0	5.8 ±0.3	37.2 ±0.9	34.2 ±1.0	4.3 ±0.3	29.9	0.104	1.5
154 ±5.0	4.8 ±0.3	55.5 ±1.2	52.0 ±1.4	3.5 ±0.2	48.5	0.105	1
236 ±10.0	4.8 ±0.4	70.4 ±1.1	66.4 ±1.3	3.5 ±0.3	62.9	0.091	0.75

(Pressures, flow rates, and errors were calculated from randomly selected tests for each MVD case.)

During the impingement tests, high-pressure air from the IRT spray bars was used to enhance cloud mixing and to improve the uniformity of LWC in the test section. The IRT spray bars were also used periodically to produce very fine sprays to maintain the required relative humidity in the test section. These fine sprays were produced prior to the start of the impingement tests. Another method used to control the humidity was releasing water steam downstream of the test section.

4.5 SPRAY SYSTEM DATA ACQUISITION AND CONTROL.

A 900-MHz Pentium™ III personal computer (PC), equipped with a data acquisition (DAQ) card and a digital input/output (DIO) board was used to monitor and control the performance of the spray system. Data acquisition and system control software was developed to monitor, store, and analyze spray system performance parameters. A schematic of the spray system data acquisition and control is shown in figure 31.

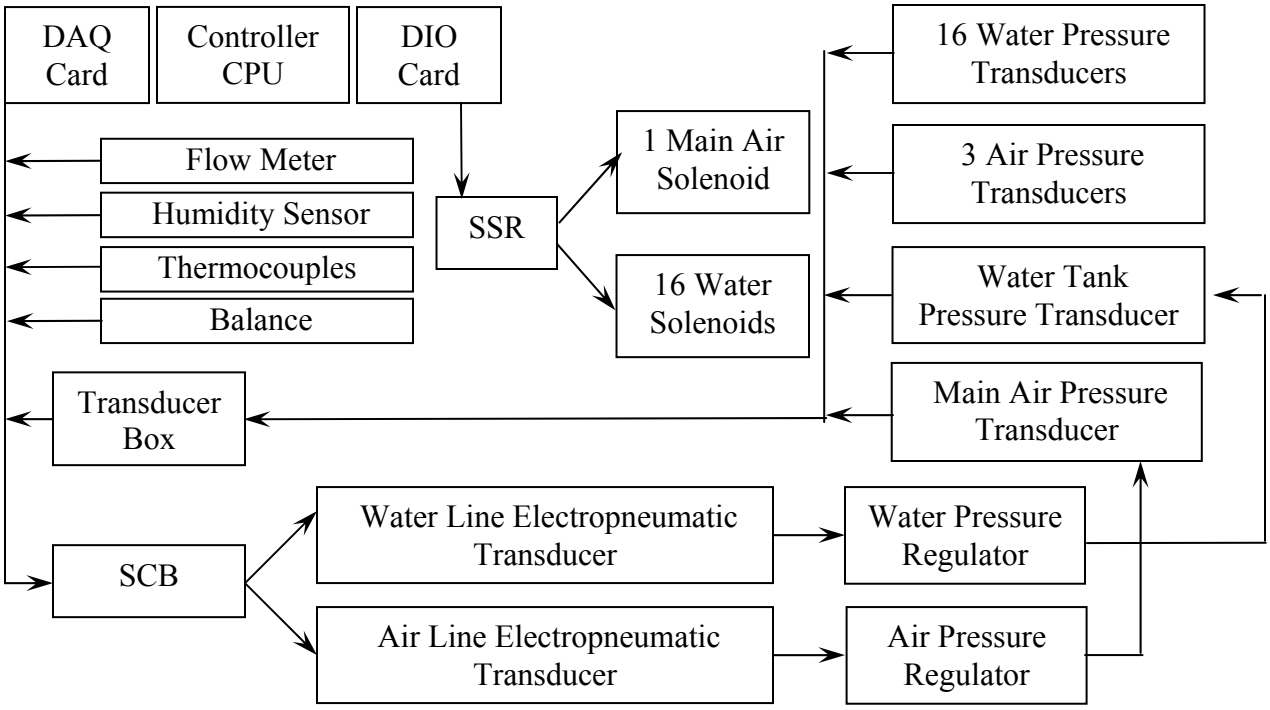

CPU = Computer processing unit
SSR = Solid-state relay

Figure 31. Schematic of the Spray System Data Acquisition and Control

The DAQ card used was a PCI-6071E from National Instruments[sm], with 32 input differential channels and a sampling rate capability of up to 1,200,000 samples per second. The signals from all spray system pressure transducers, thermocouples, the humidity sensor, flow meter, and tank balance were directed to the PCI-6071 board through an I/O shielded connector block (SCB). All signals from the pressure transducers were transferred to the SCB through shielded cables from two control units that provided the excitation voltage for the SETRA transducers. The signals from the electropneumatic transducers used to control the air and water pressures were

processed through a Fairchild™ control box before connecting to the SCB (figure 32). Thermocouple signals were passed through a National Instruments SC-2311 signal-conditioning unit that was modified to provide the required excitation voltages. The humidity sensor and the tank balance were equipped with their own power supplies and signal-conditioning units. Consequently, they were directly connected to the SCB.

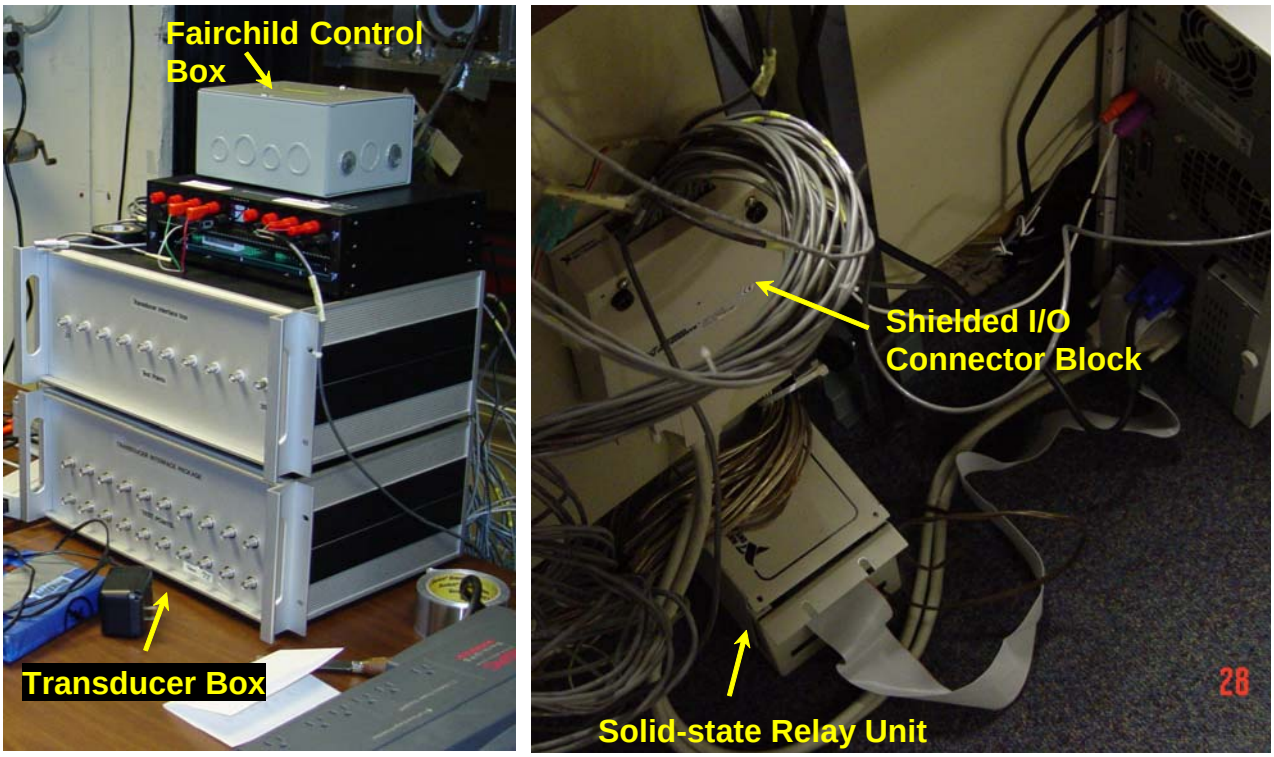

Figure 32. Main Components of the Spray System Data Acquisition and Control

A solenoid valve on the water line of each nozzle assembly enabled the spray to be switched on and off individually from the spray system computer. Another solenoid valve was installed in the main air supply, which provided high-pressure air for atomizing water sprays. Seventeen digital solid-state relay (SSR) modules were installed on three backplane boards to activate and deactivate these solenoid valves. The SSR modules were controlled by a high-speed, 32-bit parallel digital I/O ISA interface DIO card, PCI-DIO-32HS from National Instruments.

The spray system software was developed using LabVIEW™, a graphical programming language for DAQ, analysis, and presentation. The LabVIEW software provided a Windows®-driven menu for controlling and monitoring the performance of the spray system. Any combination of nozzles and transducers could be selected from the window menu. The user could also specify spray time, plot the transducer signals in real time, and store a range of test parameters as well as other information related to each test. Figure 33 shows spray system performance parameters recorded with LabVIEW during a typical spray system test. All test parameters and transducer readings were also written to a Microsoft® Excel® file at the end of each test.

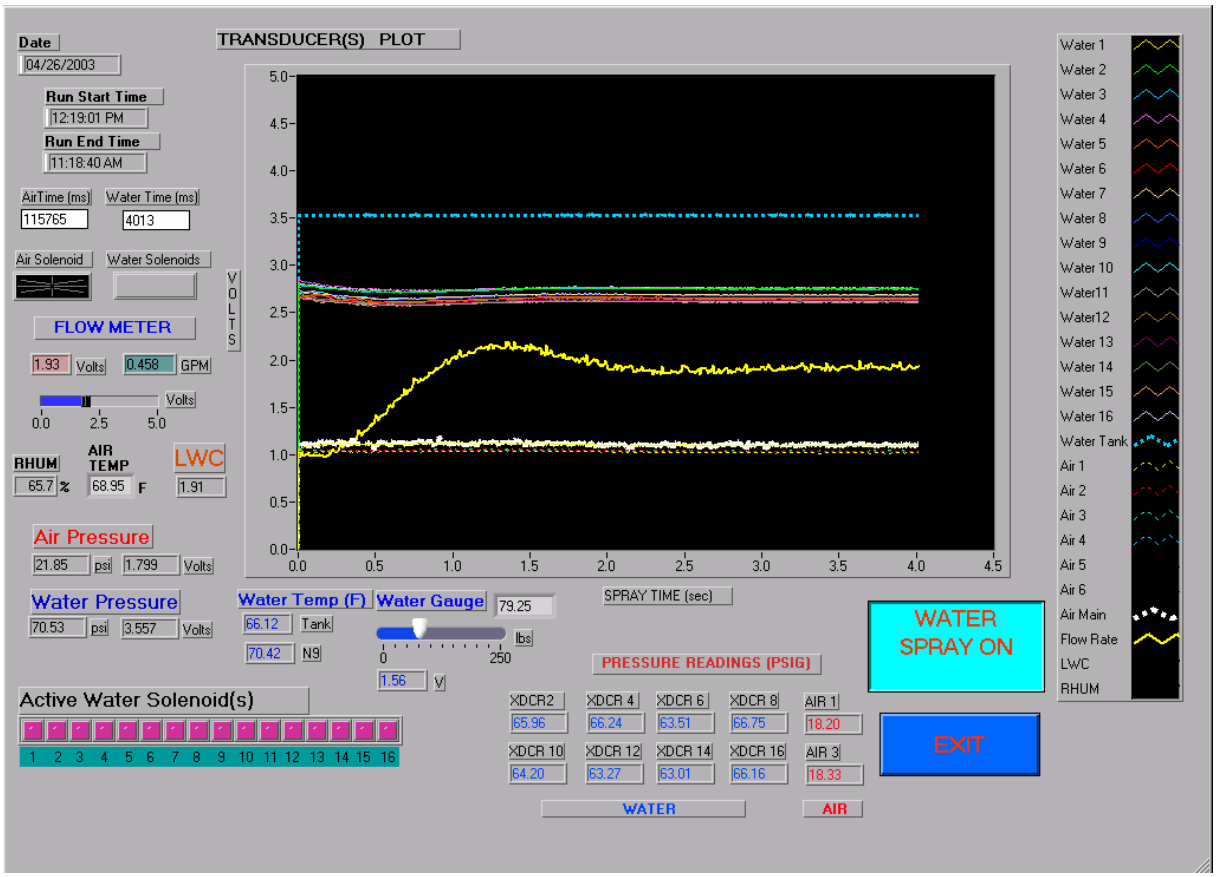

Figure 33. LabVIEW Program Used to Control and Monitor Spray System Performance (Display is not from an actual test run.)

Data from the DAQ board were recorded at regular time intervals for the complete spray duration. The sampling rates were varied based on spray time. For the shortest 0.75-sec spray, the sampling interval was 0.005 sec. For the longer sprays (1-4 sec), a sampling interval of 0.01 sec was used. This was done to keep the size of the output files to a manageable level, while providing sufficient resolution for monitoring the spray system parameters.

4.6 CLOUD UNIFORMITY.

One of the vital aspects of the experimental method is cloud uniformity, since it has a significant effect on test repeatability and accuracy. A spray cloud is characterized by three parameters: drop size, drop distribution, and LWC. Of the three parameters, LWC uniformity is the most difficult to control. Extensive cloud uniformity tests were conducted to set the locations of the 16 nozzles to provide a 1-ft-high by 2-ft-wide uniform cloud region centered in the IRT test section. Cloud uniformity was accomplished when LWC variation within the 1- by 2-ft test area for all spray conditions selected for the impingement tests was within ±20% of the average. Note that for the test models, AOA, and MVD cases used in the 2003 impingement tests, the cloud area corresponding to model impingement region was 0.5 ft high by 1 ft wide. For this smaller cloud region, LWC uniformity was within ±10% of the average.

During the 2003 impingement tests, cloud uniformity was measured using a laser imaging method and a grid and blotter method. In the laser imaging method, a laser sheet was established in the test section with its plane normal to the tunnel axis. Light scattered by the drops crossing the laser sheet was recorded with a CCD camera and was converted through software to LWC intensity. The laser sheet was established with a 5-watt argon-ion laser beam that was transmitted to a collimator through a fiber optic cable. The beam from the collimator was directed to a mirror attached to a rotating galvanometer that reflected the beam to a large (64-cm long) cylindrical lens. As the laser beam scanned the span of the lens, a laser sheet was produced across the tunnel test section. The laser sheet setup is shown in figures 34a through 34e. The location of the laser sheet plane with respect to the IRT test section is shown in figure 35a.

Figure 34a. Argon-Ion Laser Emission

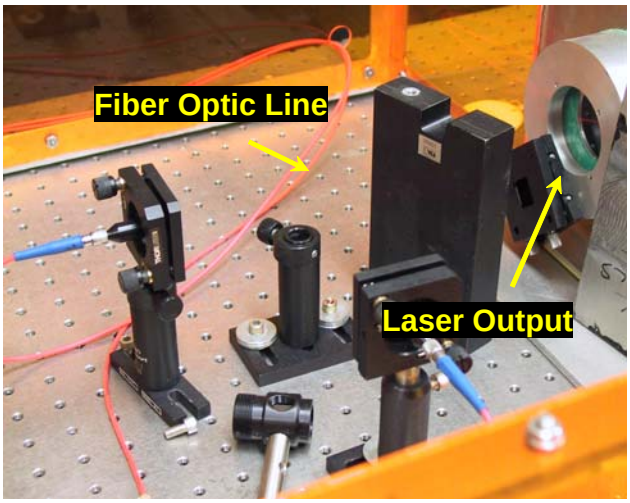

Figure 34b. Close-Up of the Laser Head Setup

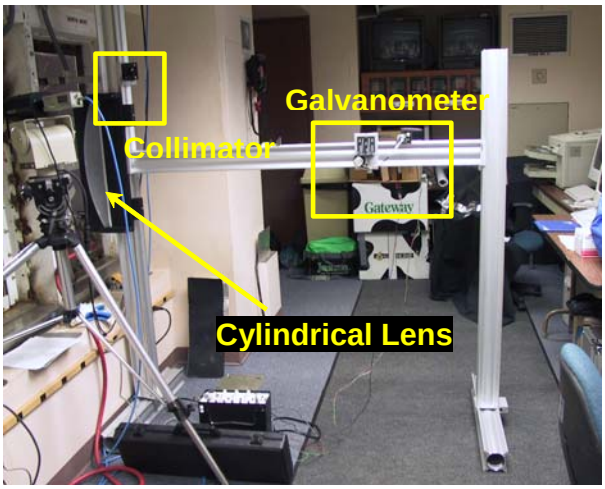

Figure 34c. Laser Sheet Generator Setup

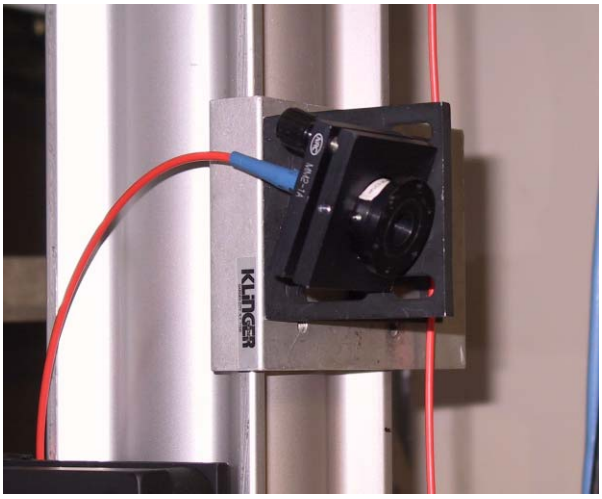

Figure 34d. Close-Up of the Collimator

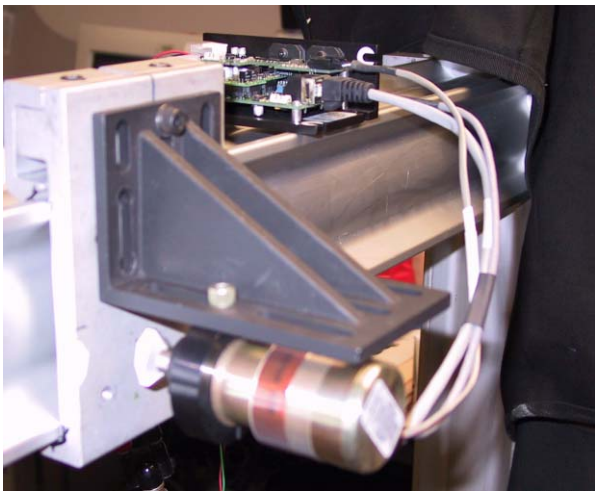

Figure 34e. Close-Up of the Galvanometer

A 14-bit CCD array camera installed outside the tunnel near the second tunnel control room was used to capture the laser sheet images by means of a borescope. The borescope was installed through the tunnel sidewall and was placed downstream of the laser sheet as shown in figures 35a and 35b. Approximately 2 inches of the borescope was extended into the tunnel and was exposed to the flow. The uniformity tests were conducted with all the lights turned off in the test section and in the secondary control room. In addition, the lights in the main control room were dimmed. All light sources other than the laser light sheet had to be eliminated to ensure that the cloud images recorded by the CCD camera were not affected by unwanted light sources and reflections. With the tunnel set to the required airspeed (175 mph), the spray system was activated for approximately 30 to 50 seconds and several CCD images were recorded. In the CCD images, the high light-intensity regions corresponded to high LWC regions and vice versa. Using camera software, the images were analyzed to determine variations in LWC within the desired uniformity region.

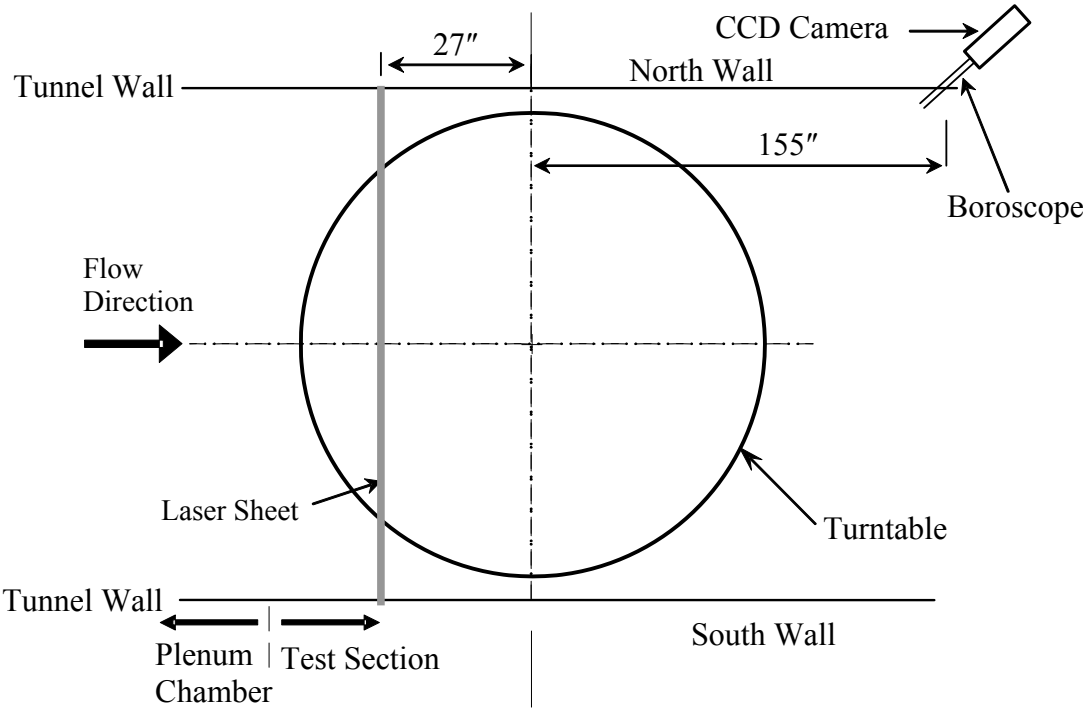

Figure 35a. Laser Sheet and CCD Camera Axial Locations in the IRT Test Section

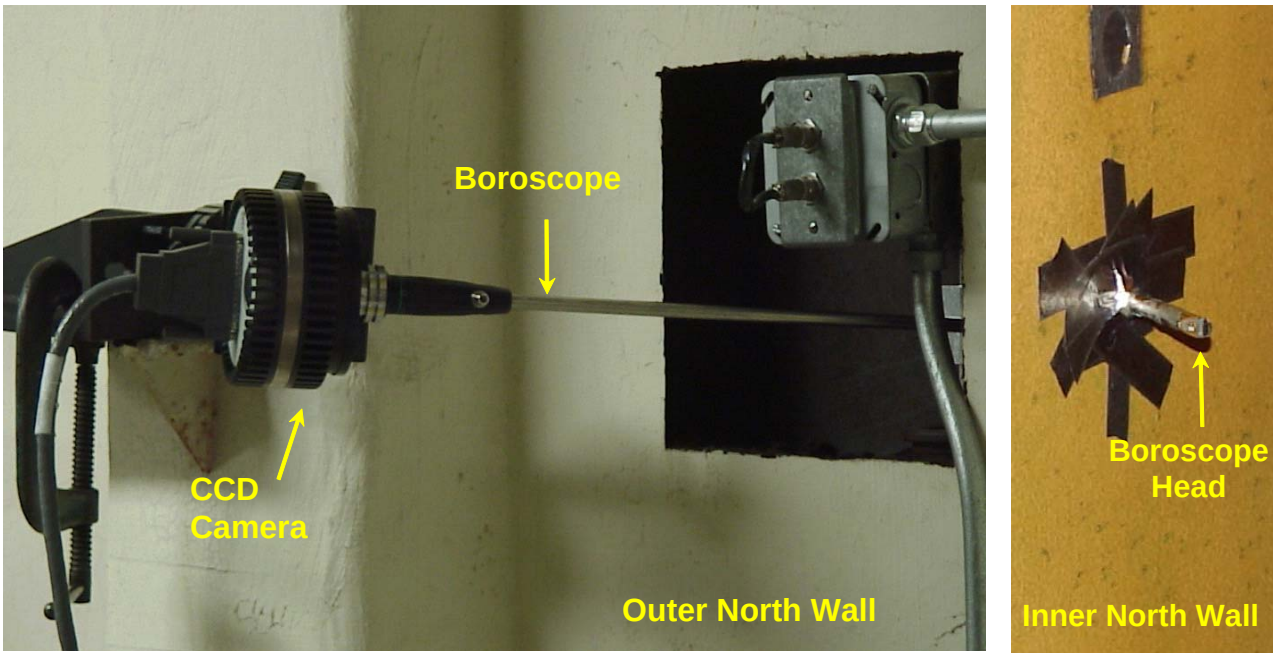

Figure 35b. The CCD Camera Installation in the IRT

In the second method (grid/blotter) for establishing cloud uniformity, a 6- by 6-ft stainless steel grid with horizontal and vertical grid spacing of 6 inches was installed in the test section as shown in figure 36. The plane of the grid was normal to the flow and passed through the center of the turntable. Blotter strips were installed on the grid to cover an area 2 ft high by 2 ft wide, as shown in figure 37. The tunnel was brought up to test speed and the blotters were sprayed. The dye distribution on each blotter was determined using the CCD reflectometer described in section 5. This grid/blotter method was found to be laborious and time-consuming.

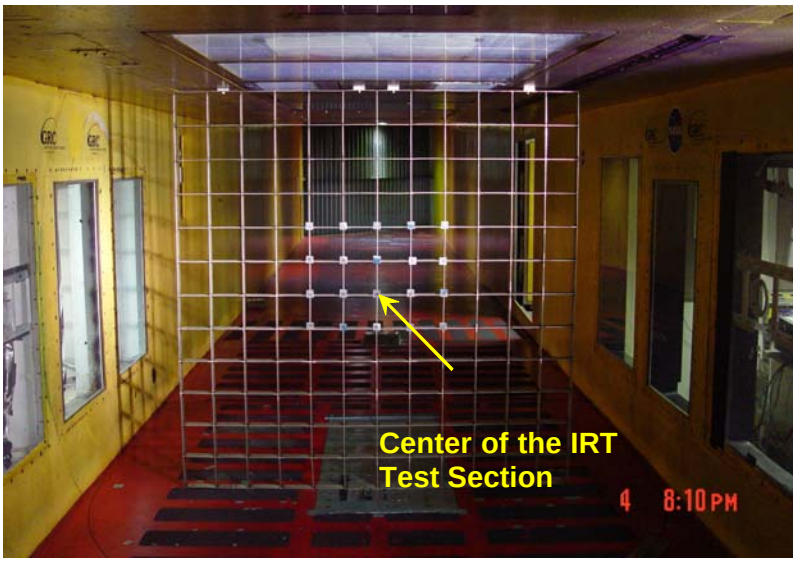

Figure 36. The 6- by 6-ft Grid Installed in the IRT Test Section

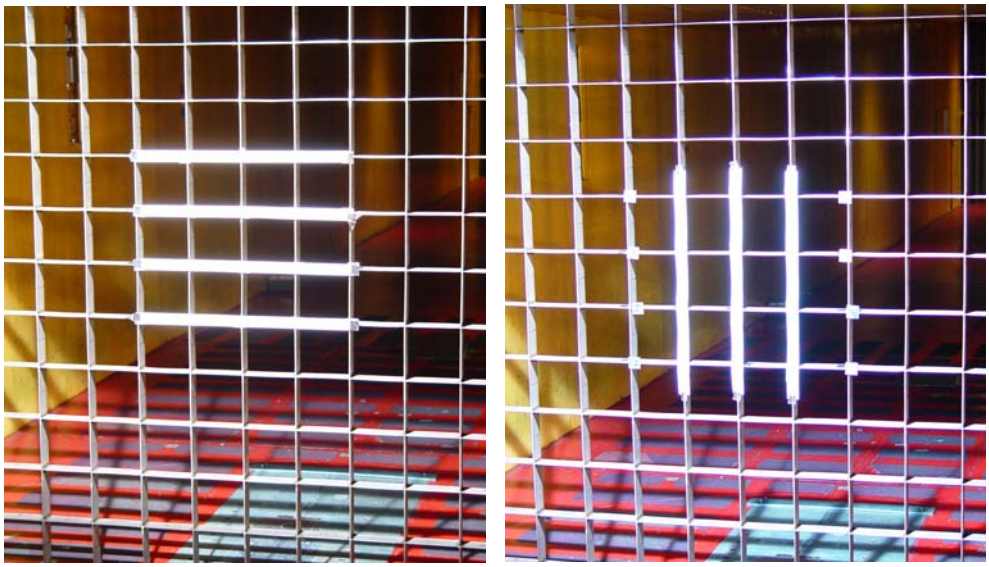

Figure 37. Blotter Strips Attachment on the 6- by 6-ft Grid

The majority of the cloud uniformity tests were conducted with the laser sheet method. The grid/blotter method was used at the end of the uniformity tests to verify the results obtained with the laser sheet method. The final spray nozzles locations are given in figure 26.

4.7 MVD AND LWC MEASUREMENTS.

Drop size and distribution measurements for all spray conditions were determined using the NASA Glenn Forward Scattering Spectrometer Probe (FSSP), the one-dimensional (1D) Optical Array Cloud Probe (OAP-C), and the 1D Optical Array Precipitation Probe (OAP-P). The OAP-P is also known as the OAP-Y probe due to the geometrical arrangement of the two probe arms containing the mirrors that are used to direct the laser beam. Details of the FSSP and OAPs can be found in reference 27. The data from these instruments were combined to obtain a single drop distribution using algorithms customarily employed for this purpose by the IRT drop-sizing specialists. Configuration diagrams and pictures of the installed FSSP and OAP are provided in figures 38a and 38b and 39a through 39c. The LWC measurements were conducted using the NASA Glenn heated wire King Probe Model KLWC-5 described in reference 28. The probe operates on the theory that when a heated wire is maintained at a constant temperature, any excess power consumed by the wire impacted by the water is proportional to the mass of the water. The installation of the King Probe in the IRT test section is shown in figures 40a and 40b.

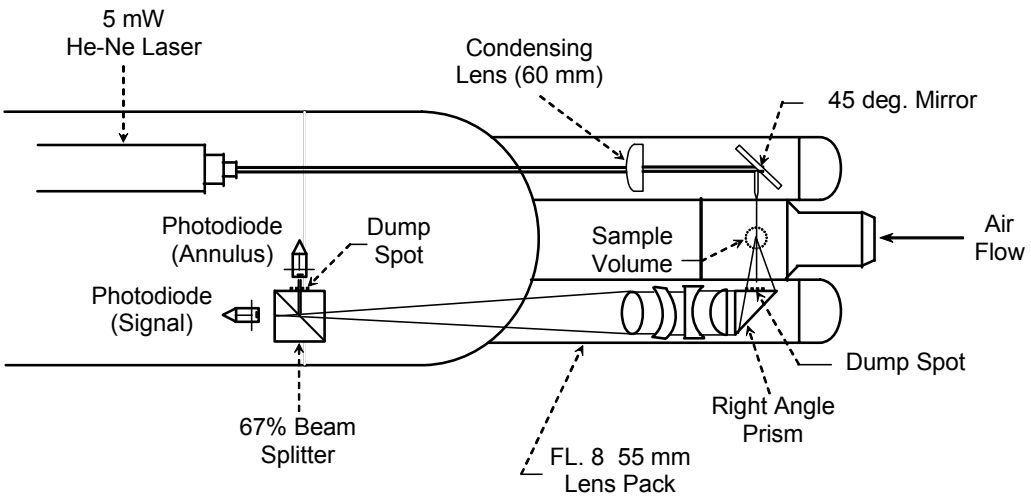

Figure 38a. Forward Scattering Spectroscopy Probe Optical Configuration

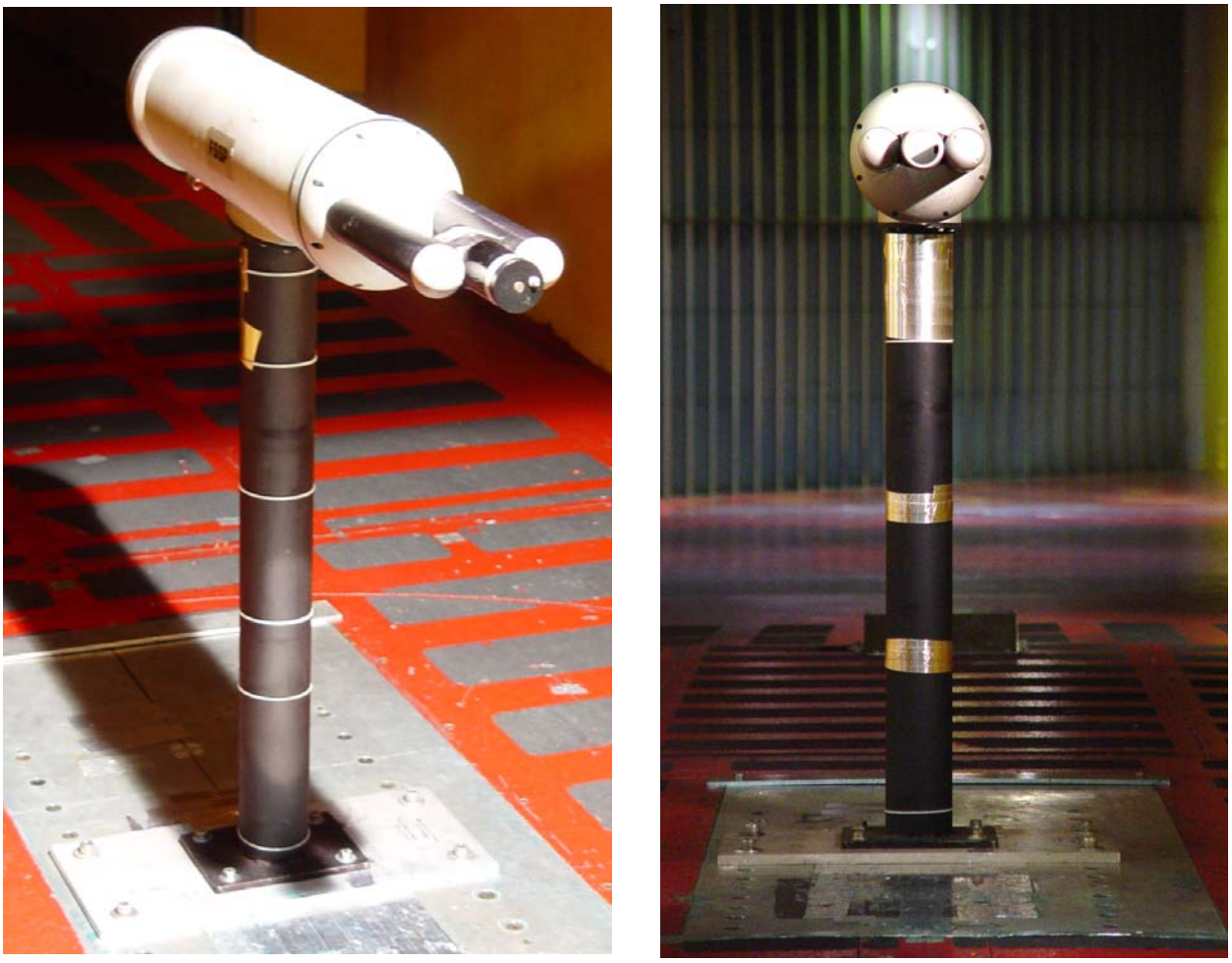

Figure 38b. The FSSP Installed in the IRT Test Section

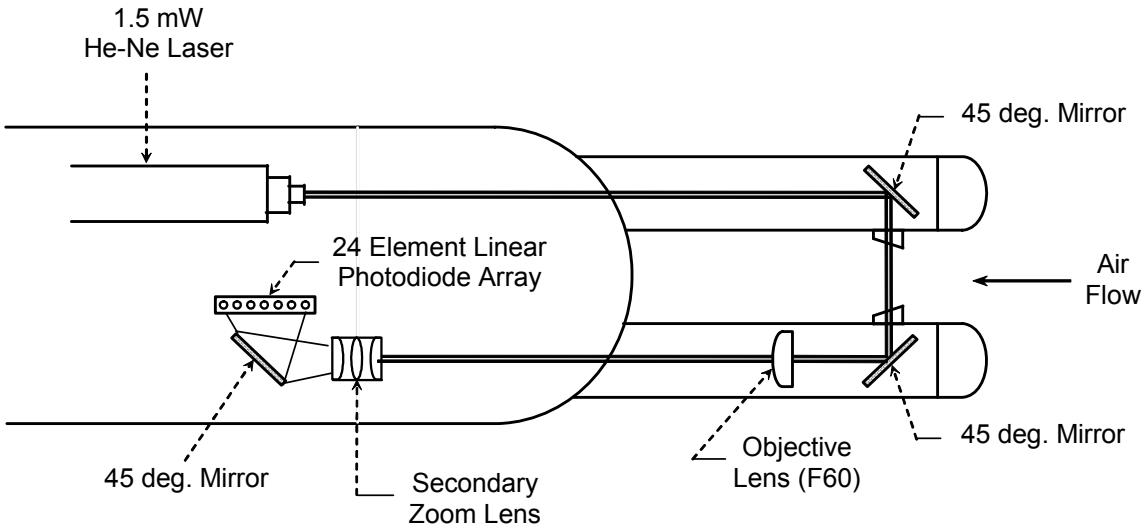

Figure 39a. Optical Array Probe Configuration

Figure 39b. The OAP-C Installed in the IRT Test Section

Figure 39c. The OAP-P Installed in the IRT Test Section

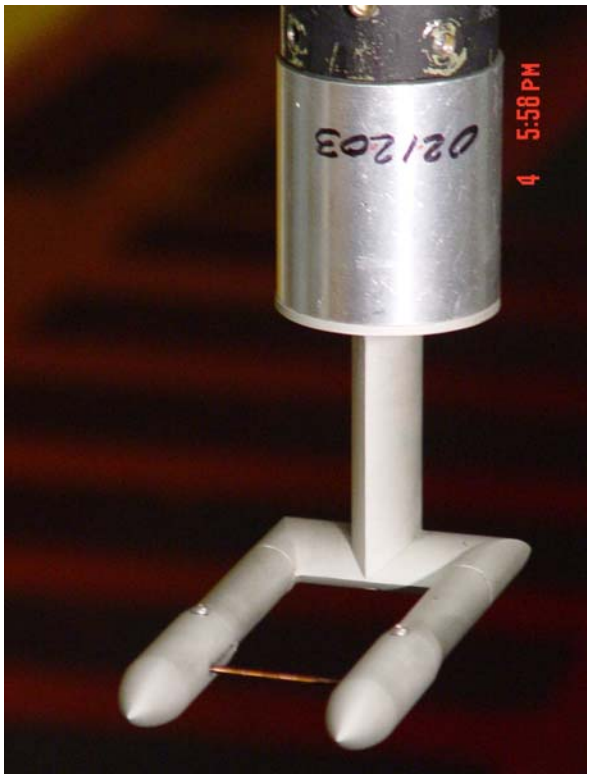

Figure 40a. King Probe Installed in the IRT Test Section

Figure 40b. King Probe (looking downstream)

Two sets of drop and LWC measurements were conducted during the 6-week impingement tests. The first set was performed after the completion of the cloud uniformity tests and the second near the end of the impingement tests. Each series of drop size, drop distribution, and LWC tests consisted of several repeated measurements of the desired spray cloud conditions. Note that the LWC measurements taken with the King Probe were used to evaluate spray cloud characteristics and to compare with local LWC measurements conducted with the collector mechanism. The King probe LWC measurements were not used in the reduction of the experimental impingement data.

To determine the effect of cloud unsteadiness on LWC, short- and long-duration sprays were conducted during the LWC measurements. Traces of LWC as a function of time showed no significant impact of spray duration on the average LWC value. Measured MVD and LWC distributions obtained at the center of the IRT test section are summarized in figures 41 through 45. MVD sizes and corresponding spray system air and water pressure settings are given in table 3.

Relative humidity studies conducted during the 1997 and 1999 impingement tests [17 and 29] showed that the effect of relative humidity on LWC was considerable, particularly for the 11-micron MVD. Based on the findings of these studies, the 2003 impingement tests were conducted at a relative humidity of 70% ±4%.

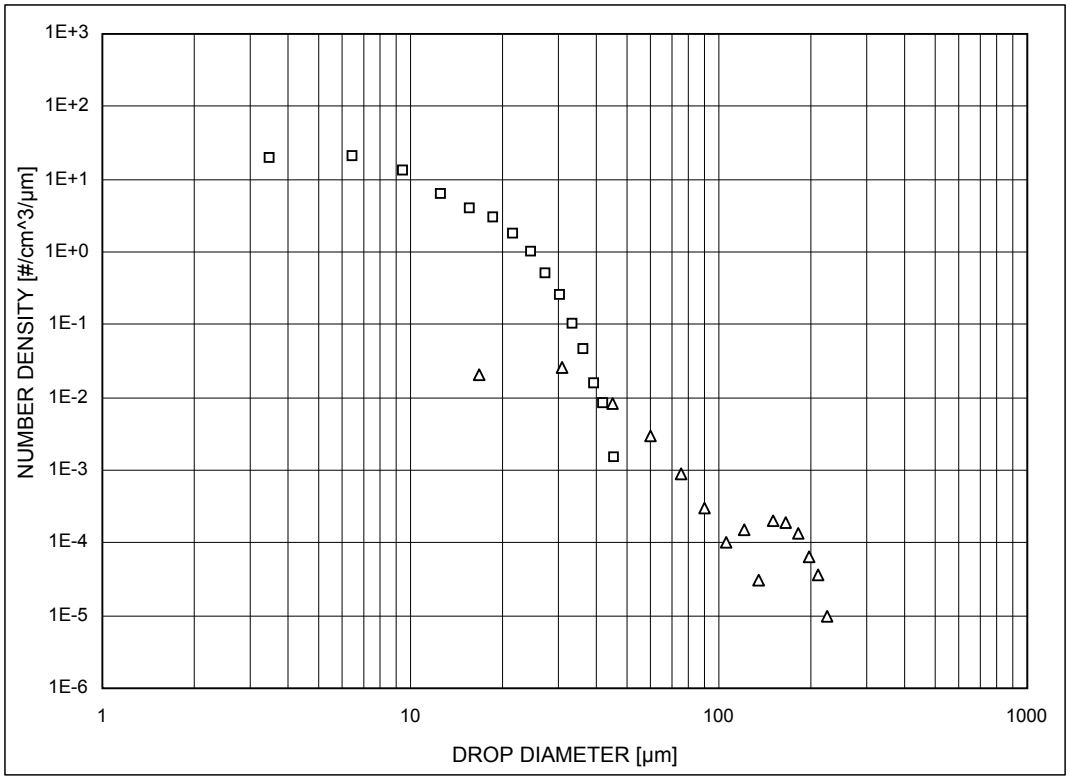

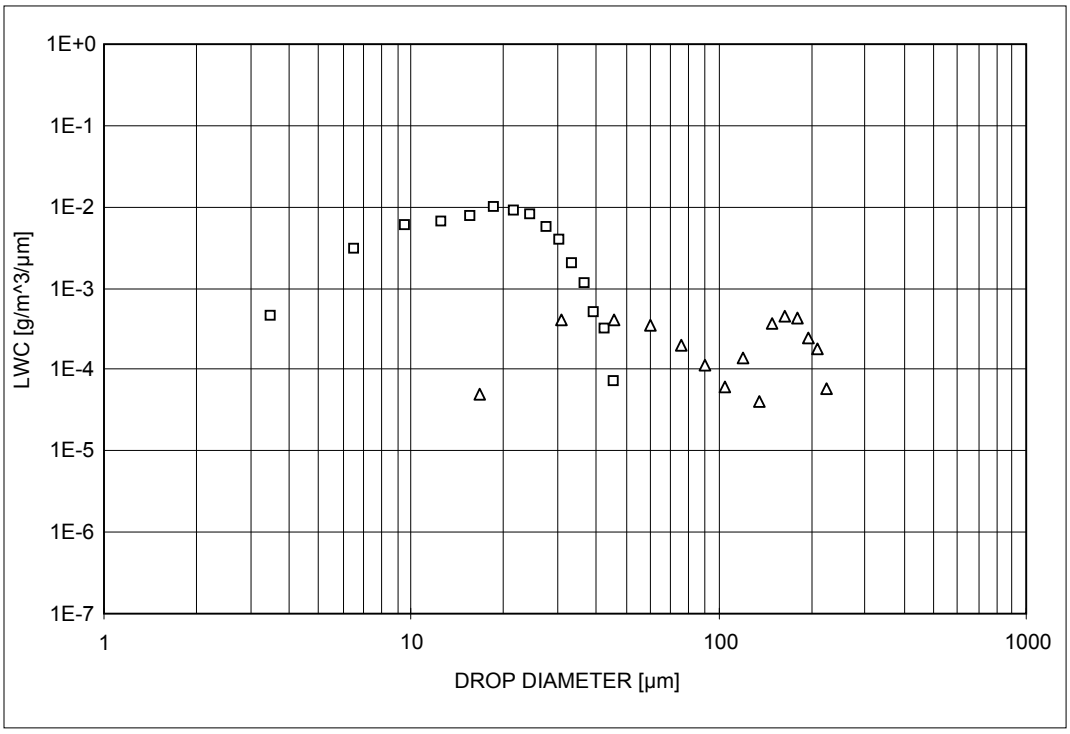

Figure 41. Measured MVD and LWC Distributions for 2003 IRT Tests (MVD = 20 µm)

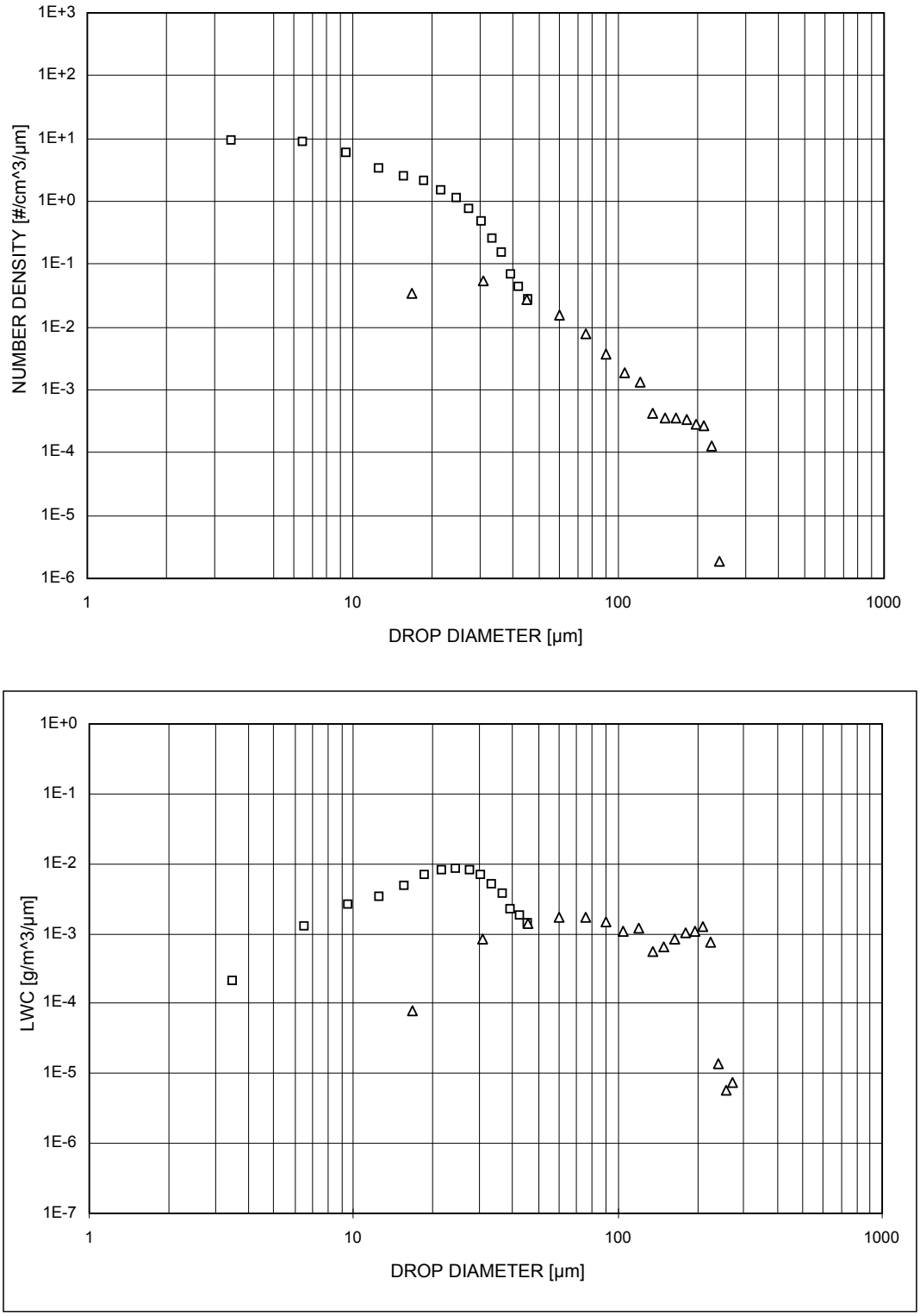

Figure 42. Measured MVD and LWC Distributions for 2003 IRT Tests (MVD = 52 µm)

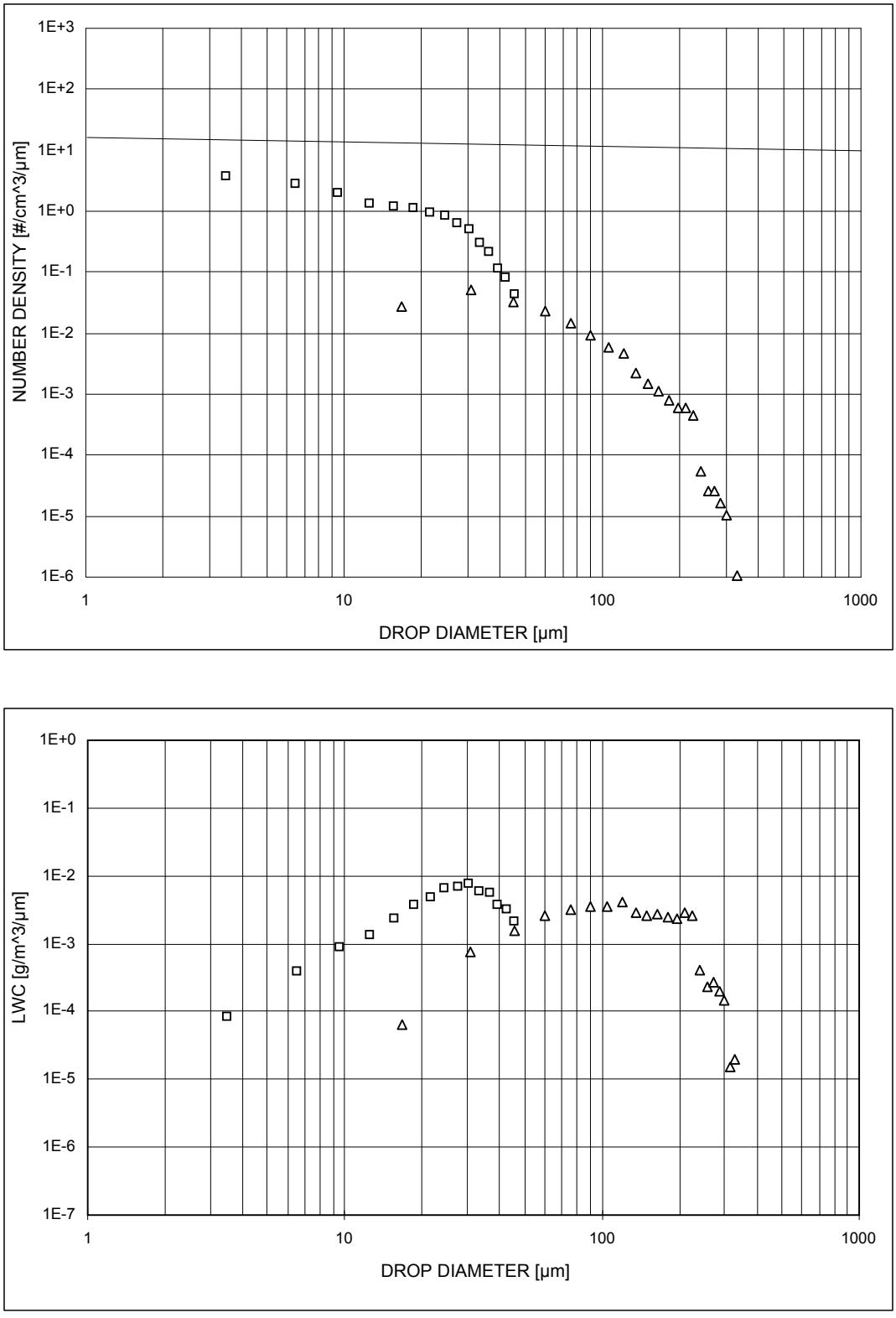

Figure 43. Measured MVD and LWC Distributions for 2003 IRT Tests (MVD = 111 µm)

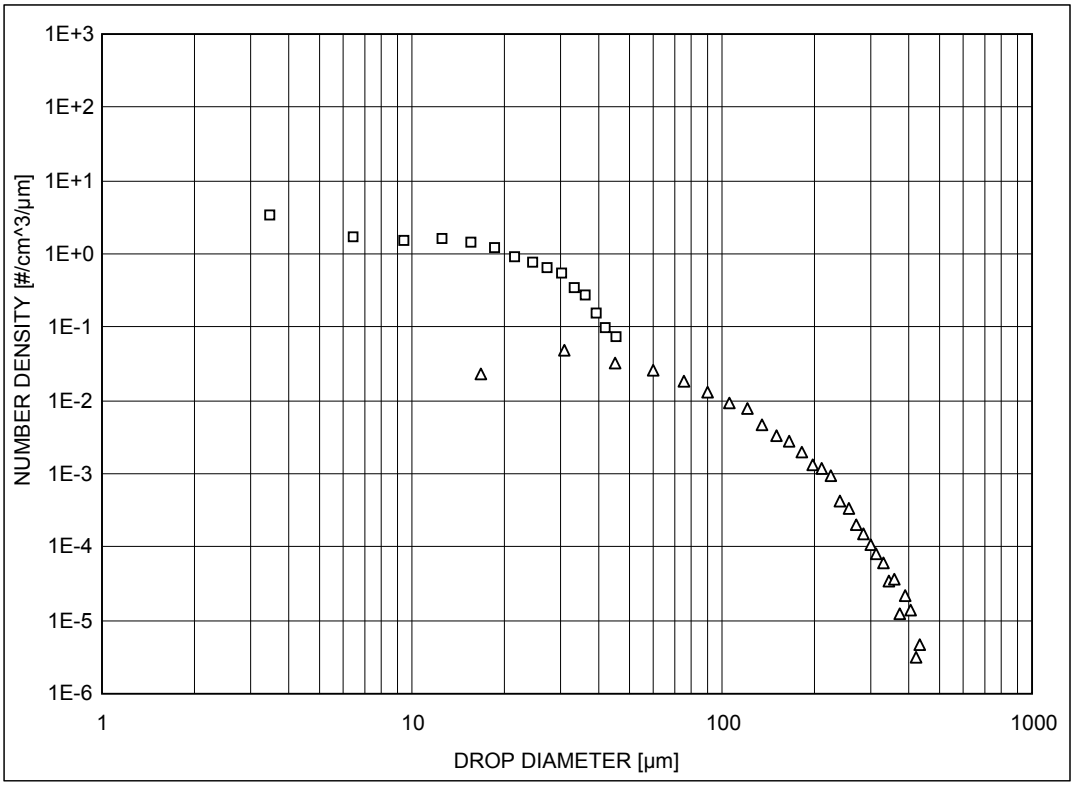

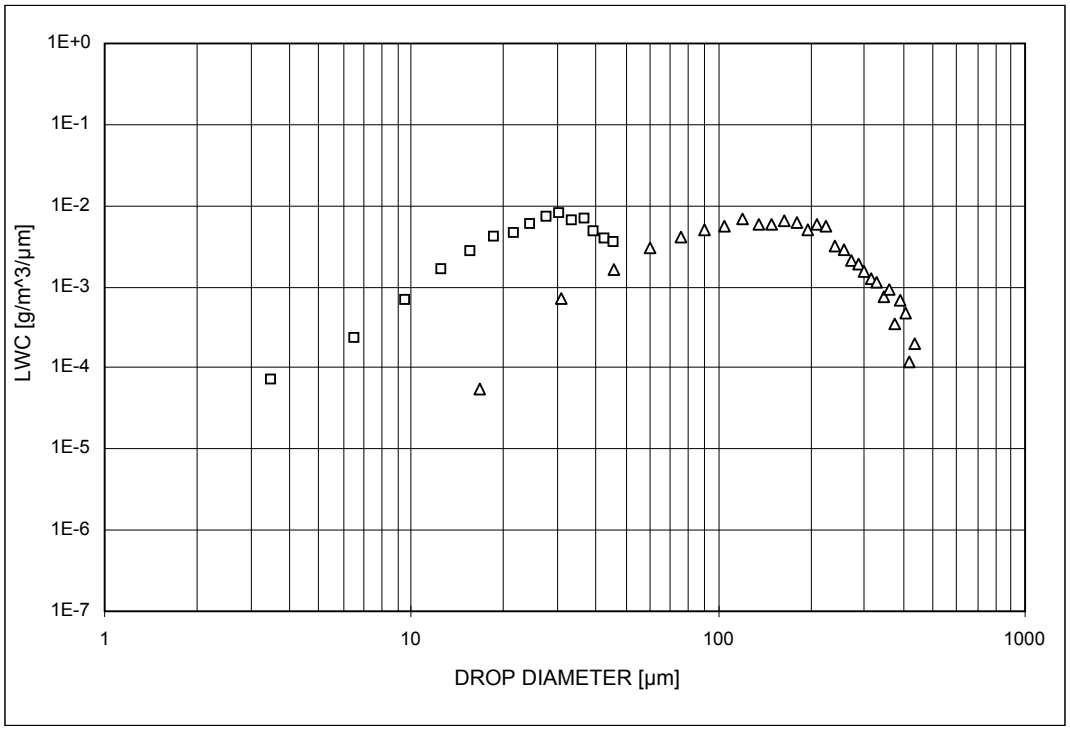

Figure 44. Measured MVD and LWC Distributions for 2003 IRT Tests (MVD = 154 µm)

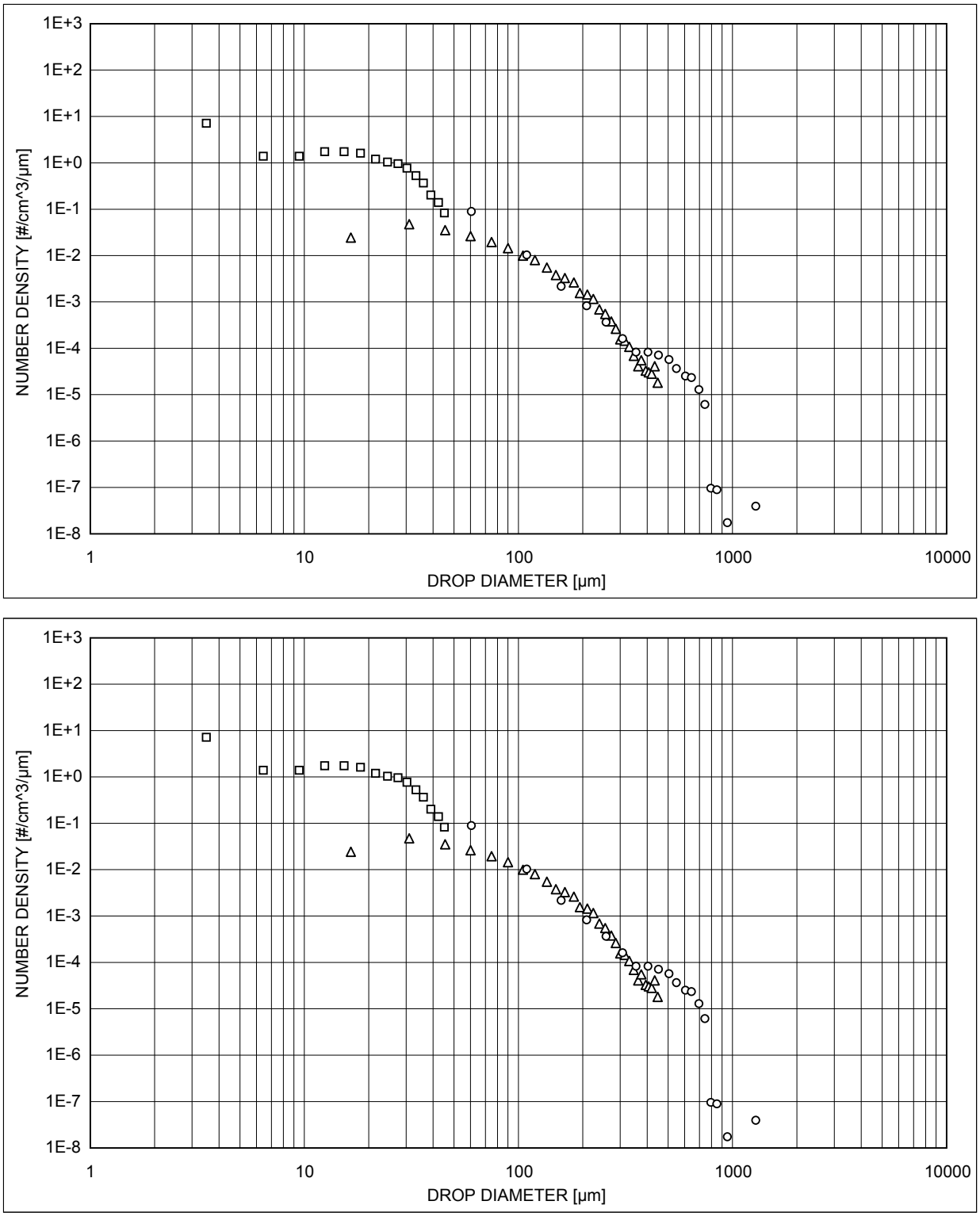

Figure 45. Measured MVD and LWC Distributions for 2003 IRT Tests
(MVD = 236 µm)

4.8 REFERENCE COLLECTOR MECHANISM.

To correct the experimental impingement data for local variations in LWC, a measurement of local LWC was needed at all locations in the IRT test section where the test model blotter strips were positioned. A reference collector device was developed at WSU to address this need. Details of the development of the collector device are provided in reference 13.

The collector device had six short blades and one long blade. Each blade was 0.2 inch wide and 1 inch in chord, as shown in figure 46a. The original cross section of the blade was triangular as discussed in references 6, 13, and 14. For the 2003 impingement tests, computational fluid dynamic analysis was used to redesign the cross section of the collector blade to reduce flow separation and improve local LWC measurements. A rectangular shaped section was found to provide the least disturbance to the flowfield because it minimized vortex shedding downstream of the blade leading edge. The length (span) of the collector blades was 4 inches for the short blades and 9 inches for the long blade.

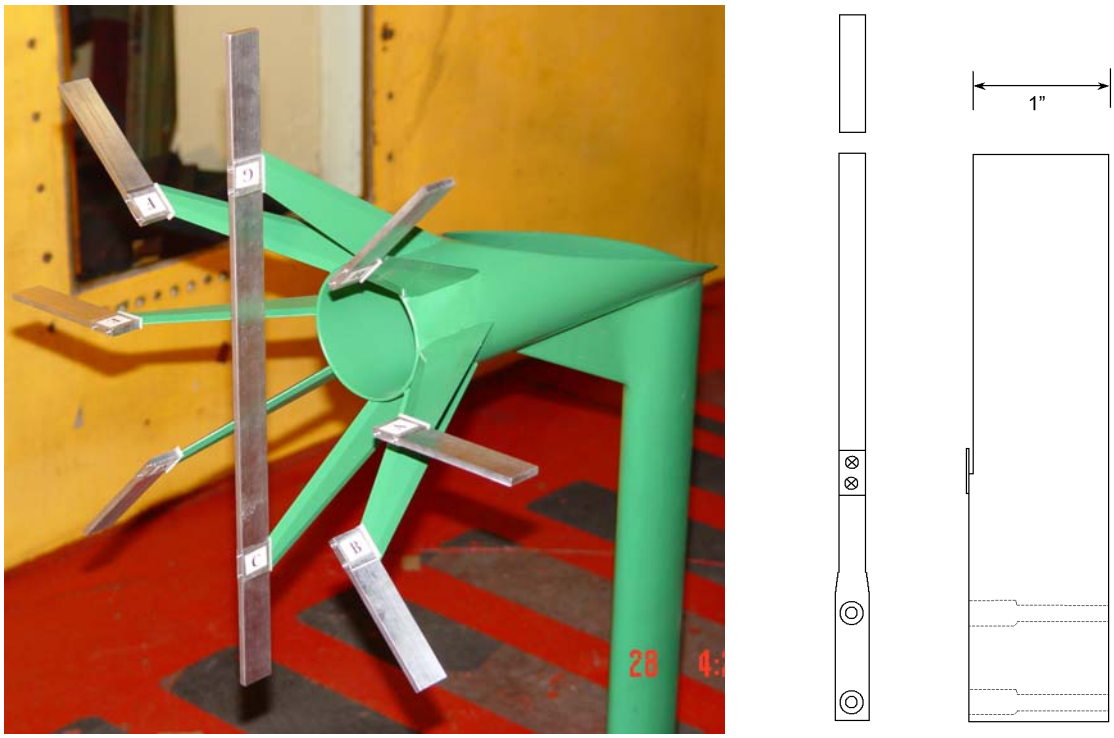

Figure 46a. Reference Collector Mechanism Blades

The collector device was tested in the empty IRT test section, with its long 9-inch blade placed both horizontally and vertically to provide a detailed map of the local LWC in the proximity of model blotter strip locations. The horizontal extent of local LWC measurements was determined by the distance between the upper and lower ice horns of the largest ice shape tested. This distance was approximately 4.7 inches and required data from the reference collector device to be collected at multiple locations in the test section. Collector tests were performed with the

long blade placed vertically at locations A, B, C, and D to provide local LWC values for data reduction. The four locations are shown in figure 46b and described below.

- Location A: the furthest point provided by the lower horn of all ice shapes away from the centerline of the tunnel at the test AOA.
- Location B: the centerline of the tunnel.
- Location C: the projected location of the leading edge of the clean airfoil at the test AOA.
- Location D: the furthest point provided by the upper horn of all ice shapes away from the centerline of the tunnel at the test AOA.

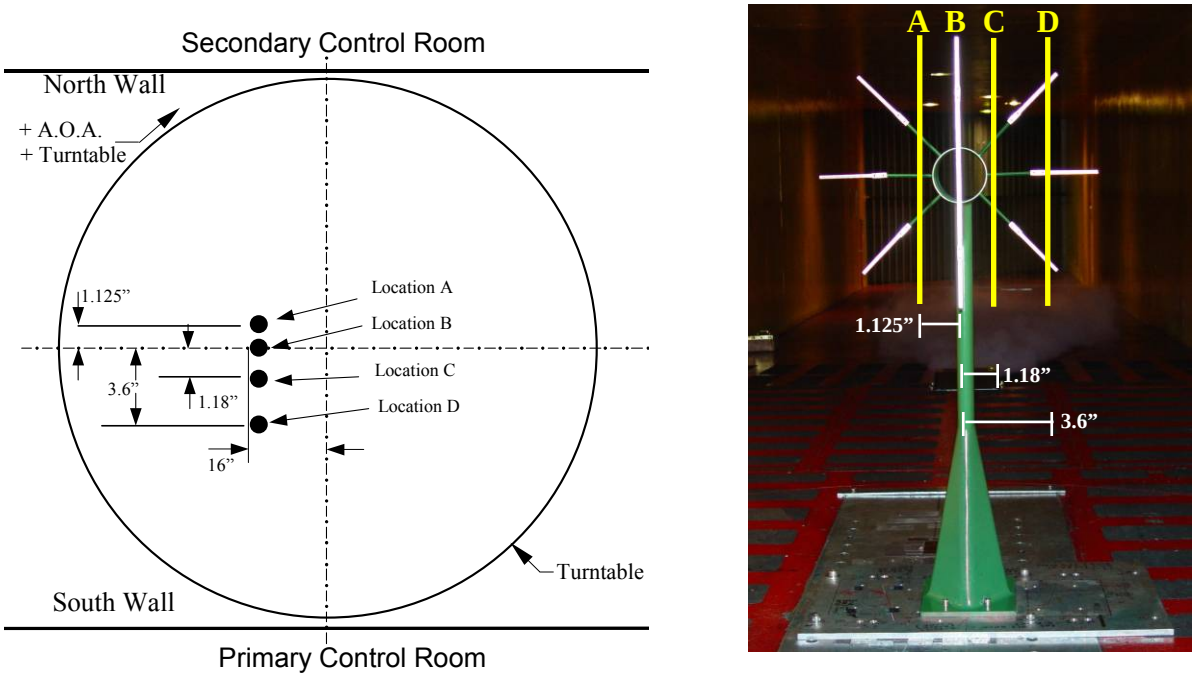

Figure 46b. Collector Vertical Blade Locations in the IRT Test Section

In addition, extensive tests were performed with the collector blade placed horizontally 37.5 inches above the tunnel floor. With the blade horizontal, local LWC data could be collected over the complete horizontal extent of the impingement region of interest. The problem with placing the blade horizontally is that small vertical fluctuations in the spray cloud could impact the accuracy of the local LWC measurements for sprays less than 2 seconds in duration. Local LWC data obtained with the horizontal blade are typically used to provide a more accurate assessment of local LWC variation over the region of impingement compared to the results obtained from uniformity tests. Approximately 168 collector tests were performed to provide the required local LWC measurements for the analysis of the impingement data. On the average, eight repeated tests were performed for each MVD and collector location case.

For the collector tests, 0.2-inch-wide blotter strips were placed on the long collector blade so the plane of each blotter strip was normal to the flow. All collector tests were performed at the same airspeed and cloud conditions as those used for the test models. In addition, the spray duration for the collector tests was identical to that used for the airfoil tests.

The impingement data from the collector strips were analyzed using the data reduction methods described in section 5. The collector dye mass per unit area and its impingement efficiency were used to obtain the LWC in the freestream, which was then used to convert the raw impingement data for each test model into impingement efficiency distributions. Table 4 provides computed impingement efficiencies obtained with the LEWICE code for the collector blades for all spray cloud conditions used in the impingement tests. The table shows that the collector blade had high impingement collection efficiency. This is attributed to the small chord and thickness of the collector blades.

Table 4. Collector Theoretical Efficiency and King Probe LWC Measurements for 2003 Test MVDs

MVD (μm)	Average LWC* (g/m^3)	Collector Efficiency (%)
20	0.19	89
52	0.40	92
111	0.73	95
154	1.44	97
236	1.89	100

*The King Probe LWC data is not used in the data reduction, it is only used to compare with collector trends

For clean, glaze, and mixed ice geometries, the collector dye mass used for normalization of the local impingement data was the average value from locations A, B, C, and D, which were obtained with the long collector blade placed vertically. The collector dye mass selected for the reduction of the rime ice shape data was from location B only. This was done because the horn of this ice shape was very close to location B, and its extent in the direction normal to the airfoil chord (i.e., ice thickness) was considerably smaller than the other ice shapes tested.

4.9 TEST MATRIX.

Models and conditions for the 2003 impingement tests are provided in table 5. All tests were conducted at total air temperature of 40°-77°F and a relative humidity of 70% ±4%.

Table 5. Test Models and Conditions for 2003 Impingement Tests

Test Model	Total Number of Surface Pressure Taps	Number of Active Surface Pressure Taps	Angle of Attack	MVD (μm)	Average Airspeed (mph)	Number of Runs per MVD	Total Number of Runs
MS(1)-0317 (c = 36 in.)	47	34	α = 0°	20, 52, 111, 154, 236	175	1 to 4	15
NACA 23012 (c = 36 in.)	65	61	α = 2.5°	20, 52, 111, 154, 236	175	4	20
NACA 23012 with 5-min glaze ice shape (c = 36 in.)	55	52	α = 2.5°	20, 52, 111, 154, 236	175	2 to 4	14
NACA 23012 with 10-min glaze ice shape (c = 36 in.)	55	52	α = 2.5°	20, 52, 111, 154, 236	175	4 to 5	21
NACA 23012 with 15-min glaze ice shape (c = 36 in.)	55	52	α = 2.5°	20, 52, 111, 154, 236	175	4 to 5	21
NACA 23012 with 22.5-min glaze ice shape (c = 36 in.)	55	52	α = 2.5°	20, 52, 111, 154, 236	175	4 to 5	21
NACA 23012 with 45-min glaze ice shape (c = 36 in.)	55	52	α = 2.5°	20, 52, 111, 154, 236	175	3 to 5	20
NACA 23012 with 7.5-min mixed ice shape (c = 36 in.)	55	52	α = 2.5°	20, 52, 111, 154, 236	175	2 to 4	14
NACA 23012 with 15-min mixed ice shape (c = 36 in.)	55	52	α = 2.5°	20, 52, 111, 154, 236	175	4 to 5	22
NACA 23012 with 22.5-min mixed ice shape (c = 36 in.)	55	52	α = 2.5°	20, 52, 111, 154, 236	175	4	20
NACA 23012 with 45-min mixed ice shape (c = 36 in.)	55	52	α = 2.5°	20, 52, 111, 154, 236	175	4	20
NACA 23012 with 45-min rime ice shape (c = 36 in.)	55	52	α = 2.5°	20, 52, 111, 154, 236	175	2 to 3	12
Collector mechanism	N/A	N/A	N/A	20, 52, 111, 154, 236	175	33 to 36	169
Uniformity 6 x 6 ft grid	N/A	N/A	N/A	20, 52, 111, 154, 236	175	5 to 6	28
MVD LWC measurements	N/A	N/A	N/A	20, 52, 111, 154, 236	175	2	10

N/A = Not applicable

4.10 PRESSURE MEASUREMENTS.

The two airfoil models used in the 2003 impingement test were equipped with surface pressure ports, as discussed in section 4.2. Note that the ten ice shapes tested were not instrumented with pressure taps. However, pressure measurements were made immediately downstream of the ice shapes. The IRT electronically scanned pressure (ESP) system was used to perform the pressure measurements. The ESP system consisted of six 32-port pressure modules with a range of ±5 psi differential. One data port in each module was used for pressure checks. Thus, the total number of ports available for pressure measurements was 186 ports (31 ports per module). The ESP system used a three-point pressure calibration system to all port transducers. The calibration pressures were measured with precision digital quartz transducers. The three-point calibration was performed every 400 cycles (approximately 15 minutes) to ensure that the error in the measurements did not exceed 0.1% of the full-scale [6].

4.11 IMPINGEMENT TEST PROCEDURE.

To obtain water drop impingement data for each test model, the following procedures were followed:

1. The spray system air and dyed water pressures were set to generate the desired MVD. Air and water pressure settings for all MVD sizes used in the impingement tests are given in table 3.

2. Blotter strips were attached to the model at the required spanwise location using aluminum tape. The blotter strips were approximately 1.5 inches wide and had two different lengths (24 and 48 in.). The longer strips were used on selected cases and for long duration sprays to study the extent of the impingement limits. For the 2003 impingement test, blotter strip installation fixtures were designed to ensure that the blotter attachment was precise and consistent between tests. The fixtures consisted of ten 0.75-in.-thick plastic plates (one for each ice shape), which were cut to match the LEWICE ice shape traces, as shown in figure 15. In addition, each plastic plate was undercut to accommodate the thickness of the blotter paper. A table platform was also constructed with brackets for attaching the table platform to the wing. The platform was used to maintain the blotter installation fixtures horizontally while installing the blotter paper. After the blotter strip was fitted and taped down following the contour of the ice shape, pencil marks were used to mark locations of interest on each ice shape, e.g., the peaks and valleys between the horns and the location corresponding to the clean wing leading edge. The marks were inscribed on the blotter installation tools to make certain that the pencil markings were consistent.

3. Once the tunnel was set to the required speed, water steam was injected into the airstream to attain the required level of relative humidity. Once the speed, relative humidity, and the airstream temperature were stable, the spray system was activated for a certain period of time (0.75 to 4.5 seconds, based on the MVD, as shown in table 3) and a dye trace was obtained on the blotter strips attached to the model.

4. After the spray was completed, the tunnel speed was set to idle. Each blotter strip was carefully removed from the model and hung in the control room to dry before storage. The model was then wiped clean with alcohol and a new blotter strip was attached for the next test.

5. Each test condition was repeated two to three times (i.e., three to four tests per MVD and AOA) to establish a measure of test repeatability. Blotter strips from the repeated tests were processed immediately after the strips were dried, using the CCD system (a description of the CCD data reduction system can be found in section 5.2.3) to evaluate test repeatability before model changes. Note that the data reduction conducted in the IRT was preliminary and was only used to evaluate data repeatability.

Prior to the production impingement tests, test sprays for all MVD cases were carried out with model blotter strips and collector strips to assess dye penetration into the blotter and to set the

appropriate spray time duration for each MVD case. Dye penetration into the blotter strips was evaluated by carefully segmenting the strip and viewing the cross section of each strip under a microscope to determine the level of dye penetration. The allowed depth of dye penetration into the blotter strip was limited to less than 30% of the blotter thickness to ensure that reflectance measurements were not adversely affected by dye penetration.

The collector mechanism was tested several times between model tests to provide local LWC measurements for reducing the model impingement results.

5. DATA REDUCTION METHODS.

Two different methods were used to extract the data from the dye-laden blotter strips. The first method, developed by NACA in the 1950s, was based on colorimetric analysis [8]. The second method, which was found to be significantly more efficient and provided higher-resolution impingement data, was based on diffuse reflectance spectroscopy [13 and 17] developed by WSU and Boeing in the 1980s. Descriptions of the data reduction methods and the systems used for analyzing the 2003 raw impingement data from the blotter strips are presented below.

5.1 COLORIMETRIC ANALYSIS.

The principle of colorimetric analysis conforms to Beer's law, which states that the light absorbance of a solute at a particular wavelength is a function of its concentration in the solution. Thus, absorbance measurement can be used to measure concentration. To extract the dye amount from a blotter strip, it was cut into small segments and stored in test tubes. Cutting each blotter segment into smaller pieces helped to speedup the dye-dissolving process. A precise amount of deionized water was then added to each test tube to fully submerge the pieces of each small blotter strip segment.

After sealing the tubes, the diluted blotter strips were refrigerated for 1 to 2 days to allow dye extraction to occur. A highly soluble dye was used in the impingement test so no mechanical agitation was required to extract the dye from the blotter paper. A white blotter strip (i.e., blotter strip with no dye on it) was also diluted to observe if the blotter fiber in suspension could affect the concentration reading and whether any correction was needed. The dye solution concentration was then measured using a spectrophotometer. The device used in this analysis was a GENESYS™ 20 spectrophotometer using a wavelength of 629 nanometers (nm). This wavelength was used since the maximum absorption of the blue dye selected for the impingement tests occurred at 629.5 nm [6]. Figure 47 depicts the equipment used in the colorimetric analysis.

For the colorimetric analysis to work, a relation between absorption and dye concentration must be established. Carefully prepared dye solutions with known concentrations were measured using the spectrophotometer to provide the relation needed. The relation between concentration and absorption readings from the spectrophotometer was found to be linear.

Figure 47. Spectrophotometry Equipments Used for Colorimetric Analysis

After the concentration of the diluted blotter strip was determined, it was multiplied by the volume of the deionized water added in the dilution process to obtain the dye mass. Due to the fact that the colorimetric analysis is laborious and time-consuming, this method was used only with specially prepared dyed blotter strips for the purpose of defining the reflectance calibration curves (described in section 5.2.1). In addition, a few model impingement strips and collector strips were reduced using colorimetric analysis to verify the impingement results obtained from the reflectance measurements.

5.2 REFLECTANCE SPECTROSCOPY.

The principle of the reflectance spectroscopy method is that when a dye-laden blotter strip is illuminated by a light source, the intensity of light scattered from the blotter surface can be used to measure the dye mass per unit area of the blotter strip. Regions on the blotter strip corresponding to high impingement rates are darker in color and reflect less light than those corresponding to low impingement rates. Regions with no dye accumulation are white and scatter the maximum amount of light. The relation between dye concentration and reflectance is not linear and is defined from calibration tests.

To enhance the sensitivity of the reflectance method, the dye must have strong absorption at the wavelength of the light source used for illuminating the blotter strips. For improved accuracy, dye penetration normal to the blotter surface should be kept to a minimum since the data reduction method relies on surface reflectance measurements. Tests to define the calibration curves and the two data reduction systems are described below.

5.2.1 Reflectance Calibration Curve.

The reflectance calibration curve relates normalized reflectance from the dye-laden blotter strip (i.e., reflectance of dye-laden blotter paper divided by reflectance of white blotter paper) to dye

mass and therefore, water impingement on the blotter strip. The curve is a standard against which the reflectance of each blotter strip is compared during the data reduction process.

Blotter strips were placed on a 6- by 6-ft grid installed in the IRT tests section, as described in section 4.6, and were sprayed with same dye solution used for the tests models. By varying the time that the strips were exposed to the spray, blotter strips with a range of uniform color densities were obtained, covering the spectrum from a very light blue to a dark blue color. The strips were measured 24 in. long and 1.5 in. wide.

These blotter strips were stored for analysis at WSU. The calibration strips were scanned using laser and CCD reflectometers. The recorded reflectance measurements were then used to identify uniform color density regions on each sample strip. Disks with a diameter of 1 inch were then punched out from these uniform color areas. The mass of the blue dye on each disk was extracted using colorimetric analysis described in section 5.1. Subsequently, the dye mass from each blotter disk was divided by the disk area to provide the dye mass per unit area. In addition to the calibration disks, selected and tested collector blotter strips were also analyzed using colorimetric analysis and used as calibration points.

The dye mass per unit area and reflectance data obtained from the disks and collector strips were used to define the standard reflectance calibration curves for the laser and the CCD reflectometer systems. The normalized reflectance calibration curve, as shown in figure 48, was produced by plotting the normalized reflectance from all blotter calibration samples against the corresponding dye mass per unit area. The calibration results show that the normalized reflectance of the laser data reduction system is very similar to the CCD system, thus, only one calibration curve was needed. In this curve, a normalized reflectance value of 1.0 corresponds to the white blotter paper and indicates zero dye mass.

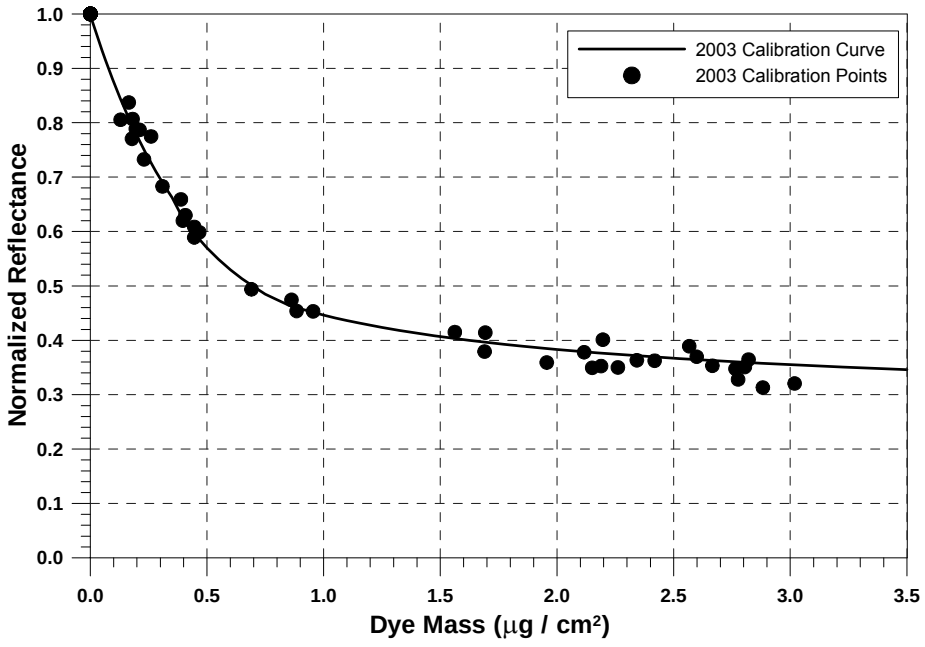

Figure 48. Reflectometer Calibration Curve

5.2.2 Laser Reflectometer.

The first data reduction system used for the analysis of the 2003 impingement data was the laser reflectometer, which was developed and tested extensively during the 1985 and 1993 impingement research programs conducted by WSU and The Boeing Company [13 and 17]. The data reduction system uses a laser beam to illuminate the blotter strip. In brief, the ratio of the intensity of the reflected light from the blotter paper to the light intensity of the laser beam is a measure of impingement efficiency.

The main components of the laser reflectometer are depicted in figures 49a and 49b and include (1) a red helium-neon (He-Ne) laser with a wavelength of 632.8 nm, (2) a rotating drum for mounting the blotter strips, (3) a convergent lens for focusing the reflected light from the blotter strip onto a silicon photo detector, (4) an EG&G silicon photo detector for converting the reflected light collected by the lens into a voltage (V_1), which was stored for further analysis, and (5) a splitter glass plate and another silicon photo detector for monitoring fluctuations in laser light intensity. The voltage (V_2) from the second photo detector was also stored and was used in the data analysis. Note that the maximum absorption of the blue dye selected for the impingement tests occurred at 629.5 nm, which is very close to the wavelength of the laser, thus ensuring that small changes in the dye color density could be resolved by the system.

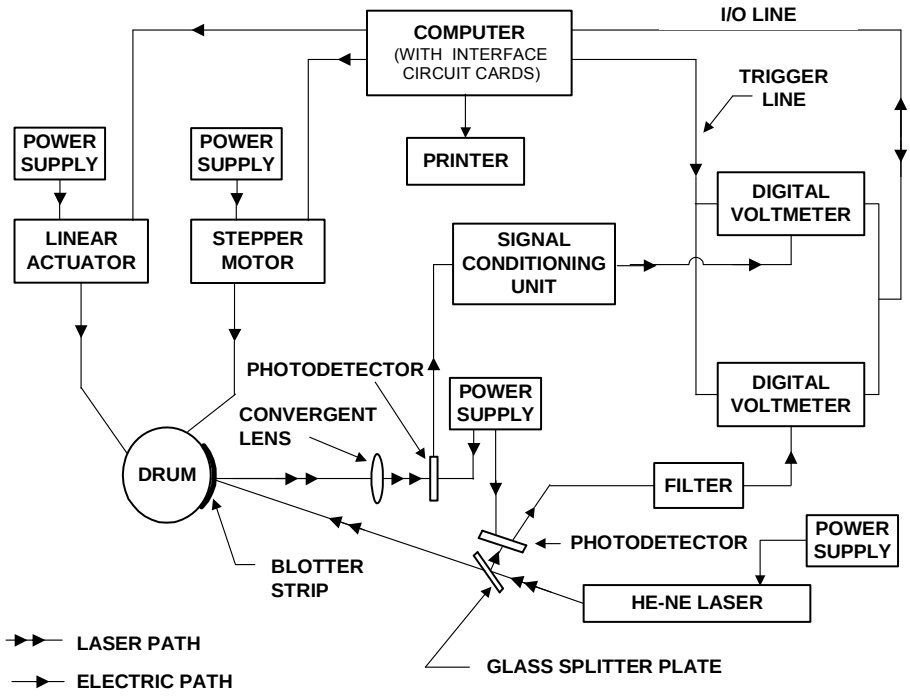

Figure 49a. Schematic of Automated Laser Reflectometer and Digital Data Acquisition System

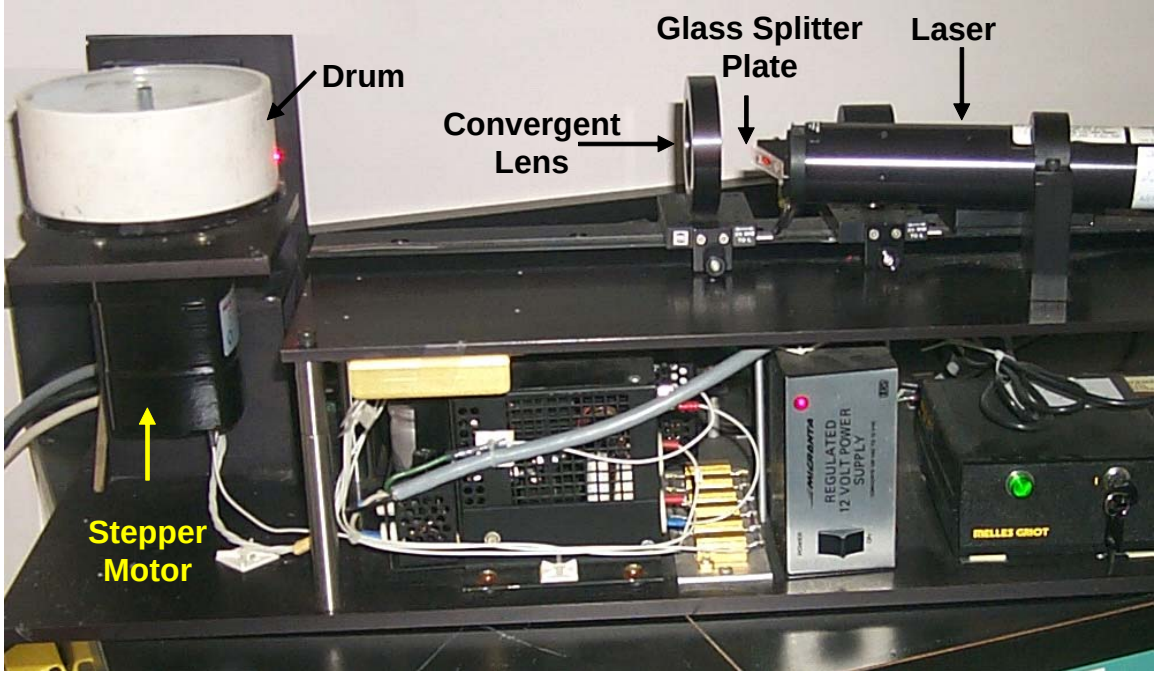

Figure 49b. Laser Reflectometer Data Reduction Setup

Voltages from the photo detectors and the rotating drum were monitored and controlled by a PC by means of a data acquisition board. A LabVIEW program was developed during this research program to control the operation of the reflectometer, but also analyze and plot the reflectance data. Details of the laser reflectometer can be found in reference 17.

Converting raw color-density distribution from a dye-laden blotter strip into impingement efficiency distribution involved a number of steps. First, the raw reflectance versus surface distance data were extracted by mounting each blotter strip on the drum of the laser reflectometer and scanning the strip along its length, as shown in figure 50a. The voltages V_1 and V_2 obtained from the two photo detectors during a scan were stored in computer files and their ratio was used to generate the raw reflectance values, as shown in equation 14. These values were then normalized by the average raw reflectance of a reference white blotter strip, which was scanned before and after each dye-laden blotter strip. The normalization equation is shown in the equation below.

$$R_{raw} = \frac{Laser\ Intensity\ After\ Reflectance}{Laser\ Intensity\ Prior\ to\ Reflectance} = \frac{V_1}{V_2} \tag{14}$$

$$R_{normalized} = \frac{R_{Raw}(Dyed\ blotter\ strip)}{R_{Raw}(White\ blotter\ strip)} \tag{15}$$

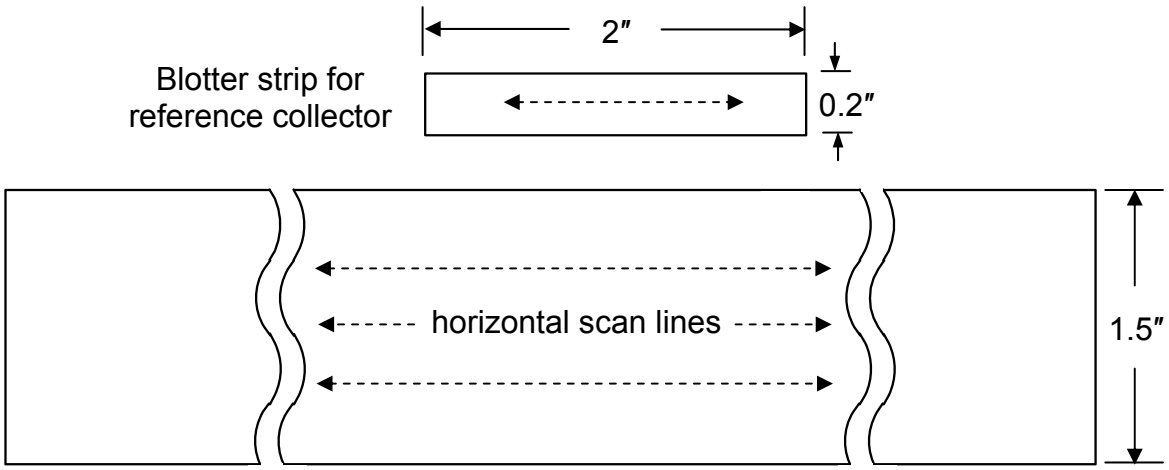

Figure 50a. Scan Locations for Test Model and Reference Collector Strips

Typical normalized reflectance values from a blotter strip are plotted in figure 50b. Note that long blotter strips had to be scanned in segments because the reflectometer could only accommodate rectangular strips with a maximum length of 16.5 inches. The normalized reflectance data from each segment of the blotter were then combined, using a computer program, and stored for further analysis. The spatial resolution of the reflectometer was 47 data points per inch.

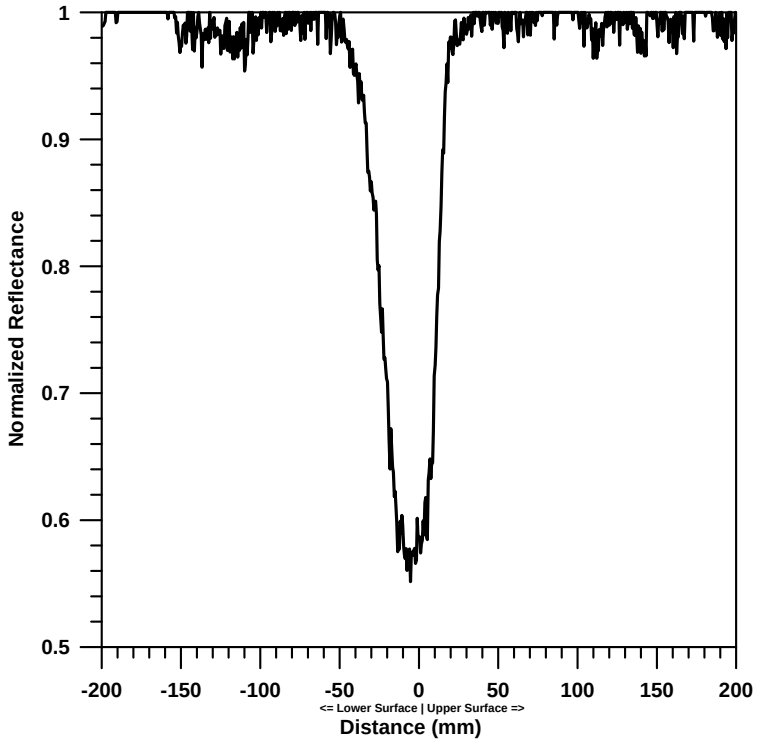

Figure 50b. Typical Normalized Surface Reflectance Distribution for a Dyed Blotter Strip Using the Laser Data Reduction System

5.2.3 Charge-Coupled Device Reflectometer.

The second data reduction system made use of a CCD array camera for digitizing the images of the dyed blotter strips, which were then stored in arrays of reflectance intensities for later analysis. The CCD system developed by WSU is shown in figures 51a and 51b. The system consisted of a Pentium 200-MHz PC, a CCD array camera with 14-bit resolution, a camera electronics unit, a camera PC controller, a 24-mm Nikkor™ lens, 12 red high-flux light emitting diode (LED) lights, a power supply for the LEDs, a camera stand, and a portable dark room for reducing the data.

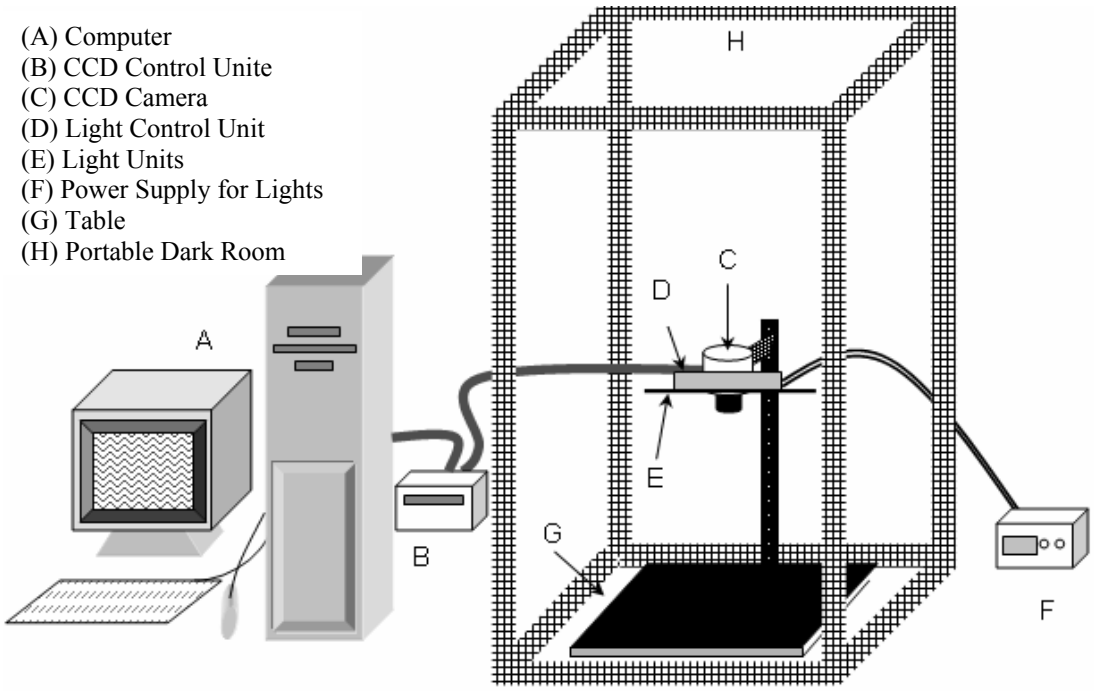

Figure 51a. Schematic Diagram of the CCD Reflectometer

Figure 51b. Charge-Coupled Device Data Reduction System Setup

The lighting system that was developed by WSU personnel in 2001 [6] consisted of 12 red high-flux LED illuminators, as shown in the schematic provided in figure 52a. The LEDs were OptoTechnology High Flux LED Illuminators, Shark Series, OTL-630A-5-10-66-E, with 630 nm wavelength. This wavelength was chosen to match the absorption characteristics of the blue dye so small changes in dye color density could be better resolved by the system. The LEDs were connected in parallel to a single power supply. A 1-kilowatt potentiometer was connected in series to each LED. With its light intensity adjusted individually, uniform illumination covered a large area. The potentiometers were placed on a single circuit board and mounted onto an aluminum frame designed for the 12 LEDs. The aluminum frame consisted of two plates with a wide rectangular slot to house the LEDs and a T-shape bar for structural reinforcement. The rectangular slot allowed adjustment of the LED locations to achieve uniform illumination over the image capture area. Uniform illumination was determined with a sensitive light meter. The aluminum plate holding the LEDs and the potentiometers was mounted on a light steel frame attached to the CCD camera mount, as shown in figure 52b.

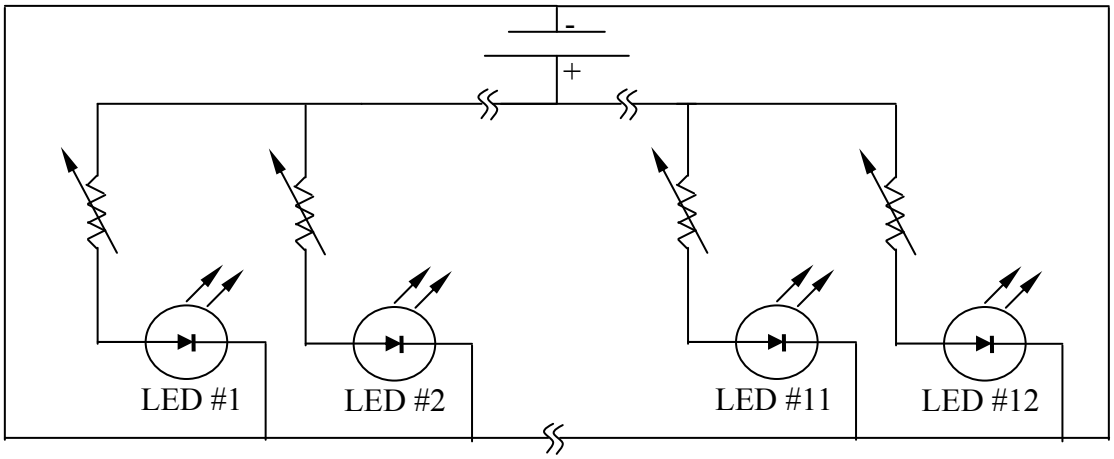

Figure 52a. Schematic Diagram of the CCD Reflectometer Lighting System

The data from each dye-laden blotter strip were extracted as follows. Each strip was placed next to a reference scale on a table inside a specially constructed dark room. The highlight on the blotter strip was aligned with a fixed mark on the reference scale. The LED lights were set to the required intensity level by adjusting the voltage and amperage of the two power supplies. The camera shutter was activated through the PMIS® software, and it was kept open for a specified time period, which was determined during the system calibration. A 512- by 512-pixel array image of the blotter strip was obtained and stored on disk for later analysis. The camera was capable of resolving nearly 14 bits (or approximately 16,000 level) of intensity values of scattered light from the blotter strip. The blue strip was removed and a white reference strip was placed on the table in the same location. The process was repeated and a 512- by 512-pixel image of the white strip was also obtained and stored.

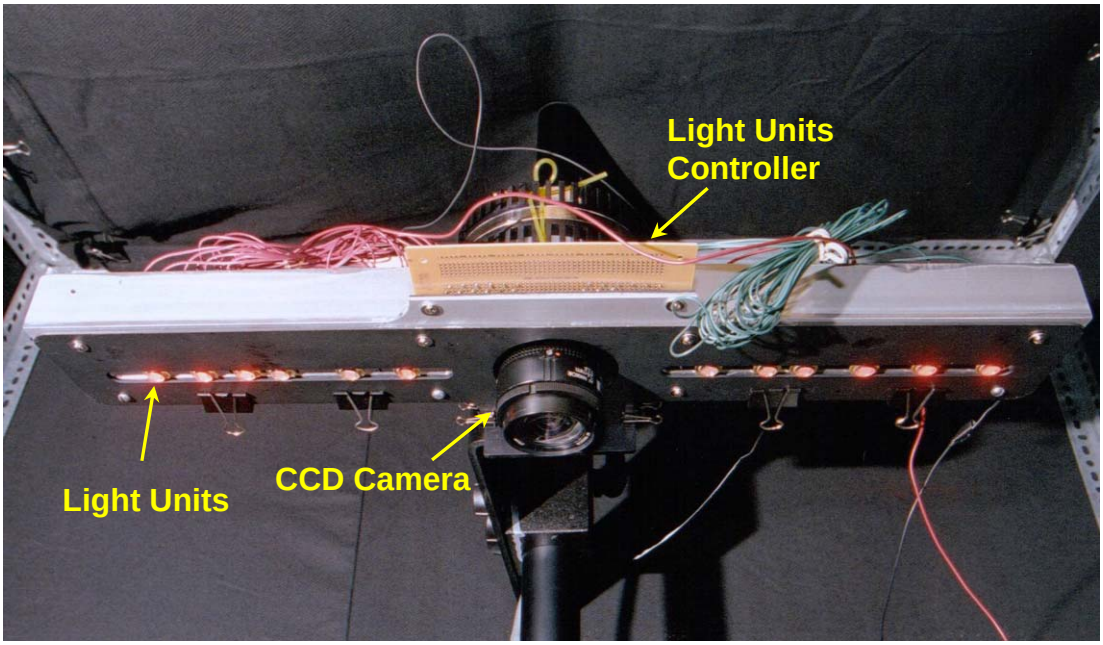

Figure 52b. Charge-Coupled Device Reflectometer Lighting Setup

After the data were extracted, the images were processed through Windows-driven software that was written in PV-WAVE command language. The process for generating the reflectance data from these images involved the following steps:

1. Each dyed strip image and the corresponding white strip image were read using the PV-WAVE software developed at WSU. Both images were corrected using reference images to compensate for camera noise and lens distortions, which were obtained and stored during the calibration of the CCD array camera.

2. The stored images were in arrays of reflectance intensities and pixel locations only, thus, a relation between real distance and pixel location had to be established. The program allowed users to define a length scale by selecting two points on the blotter strip image. The number of pixels in the horizontal direction and the actual distance between the selected points were used to establish the length scale.

3. Using the computer mouse, a rectangular region was selected on the white strip image. This region was processed by the software to provide an average reflectance value for the white paper.

4. For a dye-laden blotter strip, a region that was large enough to cover the complete extent of dye impingement was selected using the computer mouse as shown in figure 53. Using the highlight on the strips (typically the point on the leading edge of the test geometry corresponding to y/c = 0), the location of zero distance can be defined.

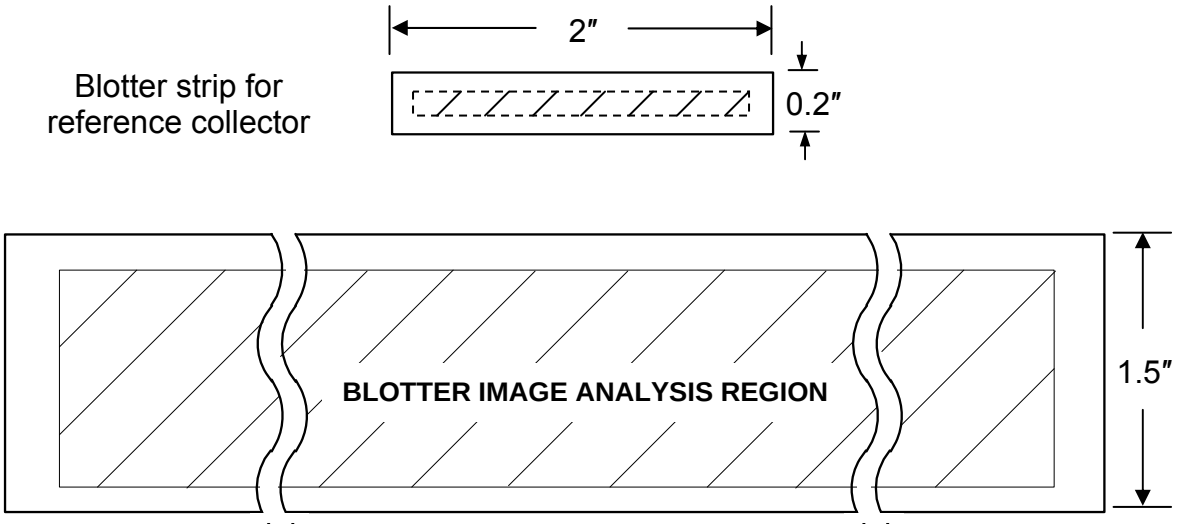

Figure 53. Blotter Strip Image Analysis Region for CCD Data Reduction System

The software produced an array of reflectance versus surface distance for the dyed strip. These values were processed through a 3-point moving average algorithm and the smoothed values were normalized by the average intensity of a white blotter strip using equation 15. An array of normalized intensity values (i.e., 0 to 1) versus surface distance was obtained for each blotter strip, as shown in figure 54, and was stored in a file for further analysis.

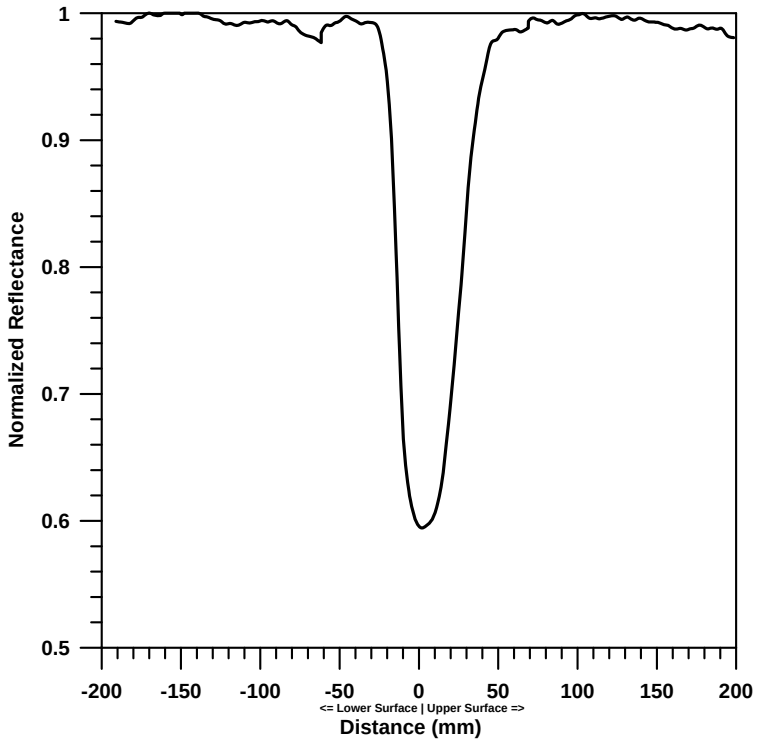

Figure 54. Typical Normalized Surface Reflectance Distribution for a Dyed Blotter Strip Using CCD Data Reduction System

A FORTRAN program was developed to extract the impingement efficiency distribution from the stored normalized reflectance data that were generated from either reflectance measurement method. Because impingement tests were repeated a number of times for each test condition, the program processed the normalized intensity values from several blotter strips into a single array of averaged normalized intensity versus surface distance. This array was then converted into dye mass ($\mu g/cm^2$) versus surface distance using the calibration curve shown in figure 48. The impingement efficiency for each data point recorded was then obtained using the following equation.

$$\overline{\beta} = \frac{\text{Local Dye Mass per Unit Area}}{\text{Average Collector Dye Mass per Unit Area}} \times \overline{\beta}_{collector} \tag{16}$$

Collector strips were reduced prior to the model strips since the collector dye mass was required for normalization in defining the impingement efficiency of each test model. The values of $\overline{\beta}_{collector}$ for all spray cloud conditions used in the impingement tests are given in table 4.

6. LEWICE-2D IMPINGEMENT ANALYSIS METHOD.

Analysis results for all test cases presented in this report were obtained by NASA Glenn personnel using the LEWICE-2D code. This code is a panel-based ice accretion code that applies a time-stepping procedure to calculate an ice shape. The potential flowfield in LEWICE [30] is calculated with the Douglas Hess-Smith 2-D panel code. This potential flowfield is then used to calculate the trajectories of the water drops and the impingement distribution on the body.

Prior to the impingement analyses, the computed flowfield from the LEWICE code was compared to the measured pressured distributions for each model and AOA tested. If the agreement between the experimental and the computed pressure was not favorable, the AOA in the computer code was slightly modified until a good match was obtained. This small adjustment in AOA was necessary because the LEWICE code does not account for wind tunnel wall and flow angularity effects. For the cases involving the large 22.5- and 45-min ice shapes, it was not possible to match the experimental pressure distributions due to flow separation immediately downstream from the ice shape horns. LEWICE uses a potential flow code that cannot simulate regions with extensive flow separation. For such cases, a Navier-Stokes flowfield should be used prior to conducting trajectory analysis with the LEWICE code. This was not attempted in this work.

Next, the impingement characteristics were computed using a 27-point (also referred to as 27-bin) discrete approximations of the experimental drop distributions measured with the FSSP, OAP-C, and OAP-P during the impingement tests (table 6 and figure 55). A 10-bin discrete drop size distribution was also generated for each MVD case for use with the public version of the LEWICE code, which allows up to a maximum of 10 drop sizes per distribution. The 10-bin drop size distributions is shown in table 7 and figure 56.

Table 6. The 27-Bin Drop Distributions

Bin Number	%	Analytical Drop Size (μm)				
		MVD = 20 μm	MVD = 52 μm	MVD = 111 μm	MVD = 154 μm	MVD = 236 μm
1	4.75	3.771785	6.544005	10.86511	13.63081	15.90700
2	4.75	8.424081	15.16583	24.51947	32.00148	45.33918
3	4.75	10.07453	18.61629	29.64239	47.12857	74.84499
4	4.75	11.55813	21.20615	34.95594	67.20577	102.0387
5	4.75	12.97915	23.57229	44.73852	84.29376	122.5518
6	4.75	14.30065	25.88050	58.34341	98.09358	141.6284
7	4.75	15.50242	28.27308	70.67189	110.1533	160.5375
8	4.75	16.65027	30.93579	81.29308	120.7427	178.4472
9	4.75	17.67680	34.45036	91.18996	131.1980	197.6876
10	4.75	18.60940	40.80994	100.9387	142.4821	217.9631
11	4.75	19.54230	51.35849	110.5958	153.9673	240.7987
12	4.75	20.50887	63.07714	119.4937	164.8876	271.0245
13	4.75	21.50879	73.98405	128.8270	175.5589	320.0266
14	4.75	22.50936	85.72330	140.1095	187.0793	393.5336
15	4.75	23.58441	99.79768	152.8340	199.5778	455.5443
16	4.75	24.73329	115.9025	165.8621	211.8856	494.6245
17	4.75	25.98042	138.7903	179.3563	223.9060	534.1075
18	4.75	27.47479	164.9857	193.7323	240.1437	577.9580
19	4.75	29.32443	185.6289	207.1929	263.9714	624.0164
20	4.75	31.84920	202.7462	219.6752	299.4286	670.9214
21	1.00	33.81317	212.4191	227.3925	327.2080	701.1499
22	1.00	34.83165	215.5869	230.1392	341.6878	713.6254
23	1.00	36.21635	219.7380	237.7504	358.1966	728.3444
24	0.50	37.46642	223.6459	250.5209	375.0911	742.1095
25	0.50	38.74237	226.3273	264.2335	389.0540	752.6775
26	0.50	40.66698	229.0086	279.5445	400.9250	763.2454
27	0.50	44.36609	253.9263	312.5888	425.0598	1046.765

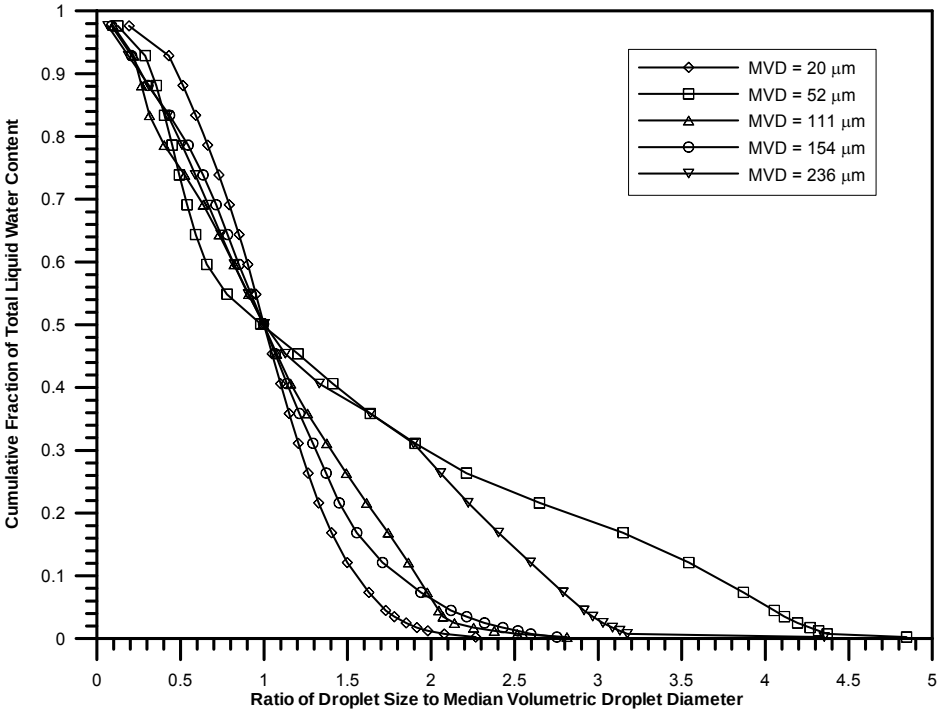

Figure 55. The 27-Bin Drop Distributions

Table 7. The 10-Bin Drop Distributions

Bin Number	%	Analytical Drop Size (μm)				
		MVD = 20 μm	MVD = 52 μm	MVD = 111 μm	MVD = 154 μm	MVD = 236 μm
1	5.00	3.850397	6.693706	11.05374	13.88450	16.25037
2	10.00	9.390637	16.88090	27.48959	44.44510	63.65823
3	20.00	13.80175	25.44875	56.48542	90.28305	135.4827
4	30.00	19.60797	59.17969	111.1060	154.1635	298.5197
5	20.00	25.4820	131.2511	170.8107	218.3283	508.4572
6	10.00	30.73474	192.7506	212.7639	284.4519	645.4684
7	3.00	35.19787	216.5703	235.0038	343.7168	715.8689
8	1.00	38.32569	224.9867	257.7010	380.2672	747.3936
9	0.50	40.66701	229.0087	279.5447	400.9252	763.2455
10	0.50	44.36619	253.9279	312.5901	425.0601	1046.767

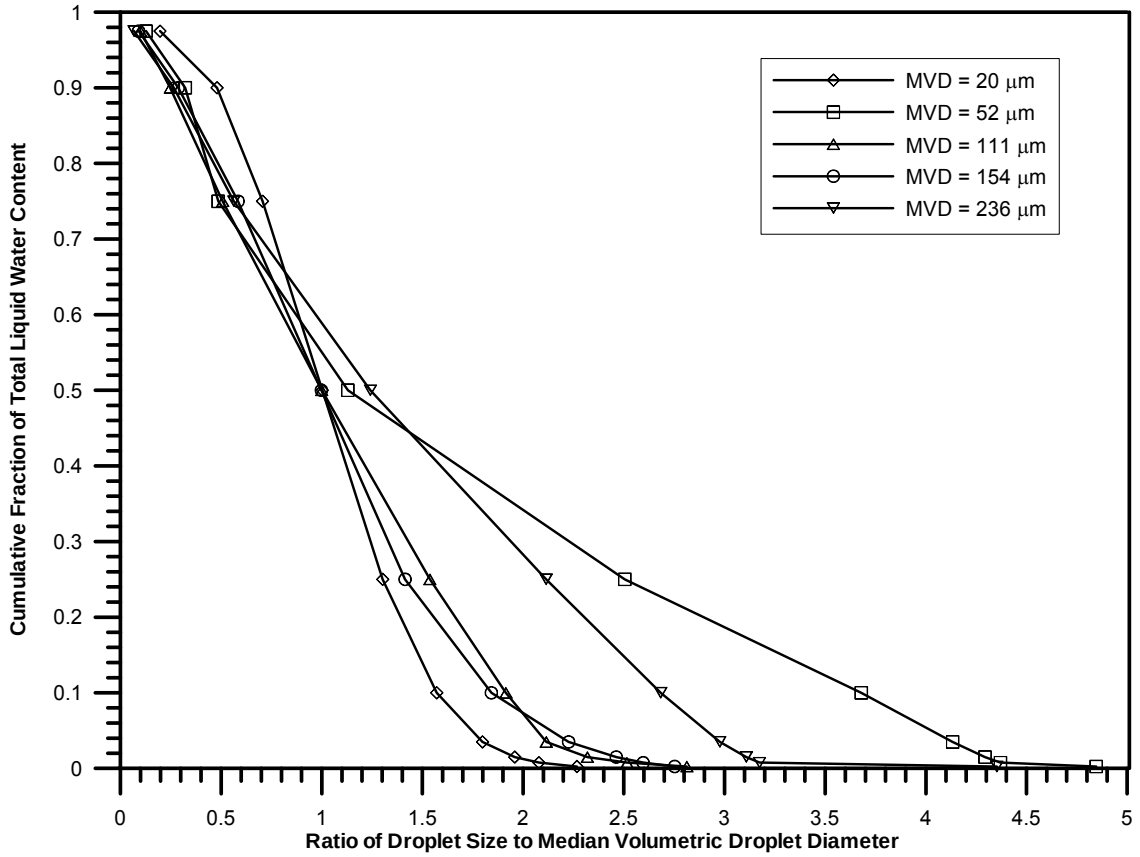

Figure 56. The 10-Bin Drop Distributions

7. RESULTS AND DISCUSSION.

In this section, potential sources of experimental error and the steps taken to minimize or eliminate these errors are discussed. In addition, the experimental water drop impingement data for the two airfoils and the ten ice shapes tested in 2003 are presented and compared to the LEWICE analysis data. All experimental data are averaged data from repeated tests. The impingement analysis data were obtained with the LEWICE computer code using the procedure discussed in section 6.

In most cases, the impingement data are presented in the form of local impingement efficiency ($\overline{\beta}$) plotted versus surface distance(s) in millimeters (mm). Surface distance is measured from the highlight (a reference point where s = 0 mm), which in all cases, corresponds to the location near the leading edge where y/c is zero. For the clean airfoil, the highlight was at the leading edge, while for the ice shapes, the highlight was located between the ice horns. Note that negative surface distance corresponds to the upper surface of the airfoil. Geometric parameters, as well as flow and drop parameters for the airfoils and ice shapes, are summarized in table 8.

Table 8. Summary of Model Geometry and Impingement Parameters

Geometry	Chord (in.)	t_{max} (in.)	x/c at t_{max}	V∞ (mph)	AOA (deg.)	MVD (μm)	Re_c (million)	Re_{MVD}	K	K_0	φ
MS(1)-0317	36 (0.914)	6.12 (0.155)	0.376	175	0	20	4.92	108	0.108	0.037	107,054
						52	4.91	279	0.731	0.170	106,772
						111	4.91	596	3.329	0.542	106,613
						154	4.91	828	6.409	0.873	106,851
						236	4.92	1269	15.053	1.544	106,985
NACA 23012	36 (0.914)	4.32 (0.110)	0.300	175	2.5	20	4.58	100	1.106	0.038	94,271
						52	4.58	260	0.720	0.172	94,243
						111	4.57	554	3.278	0.553	93,795
						154	4.58	772	6.314	0.895	94,346
						236	4.59	1184	14.832	1.602	94,554
NACA 23012 with 5-min glaze ice shape	36 (0.914)	4.32 (0.110)	0.300	175	2.5	20	4.61	101	0.106	0.038	95,313
						52	4.60	261	0.720	0.172	94,988
						111	4.60	558	3.279	0.552	94,936
						154	4.61	776	6.315	0.892	95,413
						236	4.61	1190	14.831	1.596	95,488
NACA 23012 with 10-min glaze ice shape	36 (0.914)	4.32 (0.110)	0.300	175	2.5	20	4.56	100	0.106	0.038	93,612
						52	4.57	260	0.719	0.172	94,043
						111	4.53	550	3.269	0.554	92,569
						154	4.56	768	6.307	0.896	93,635
						236	4.56	1177	14.807	1.607	93,539
NACA 23012 with 15-min glaze ice shape	36 (0.914)	4.32 (0.110)	0.300	175	2.5	20	4.53	99	0.106	0.038	92,286
						52	4.53	258	0.718	0.173	92,569
						111	4.54	551	3.271	0.554	92,703
						154	4.52	762	6.292	0.898	92,274
						236	4.52	1167	14.776	1.613	92,195

All dimensions are in English units (inch and mph); values inside parenthesis are in SI units (meter and m/s)

Table 8. Summary of Model Geometry and Impingement Parameters (Continued)

Geometry	Chord (in.)	t_{max} (in.)	x/c at t_{max}	V∞ (mph)	AOA (deg.)	MVD (μm)	Re_c (million)	Re_{MVD}	K	K_0	φ
NACA 23012 with 22.5-min glaze ice shape	36 (0.914)	4.32 (0.110)	0.300	175	2.5	20	4.54	99	0.106	0.038	92,558
						52	4.56	259	0.720	0.173	93,289
						111	4.54	551	3.278	0.555	92,779
						154	4.55	766	6.310	0.898	93,080
						236	4.55	1174	14.808	1.610	93,075
NACA 23012 with 45-min glaze ice shape	36 (0.914)	4.32 (0.110)	0.300	175	2.5	20	4.56	100	0.106	0.038	93,496
						52	4.56	259	0.719	0.173	93,676
						111	4.56	554	3.275	0.553	93,688
						154	4.57	769	6.301	0.895	93,781
						236	4.57	1179	14.800	1.604	93,871
NACA 23012 with 7.5-min mixed ice shape	36 (0.914)	4.32 (0.110)	0.300	175	2.5	20	4.55	99	0.106	0.038	92,950
						52	4.54	258	0.718	0.173	92,944
						111	4.55	552	3.274	0.554	93,050
						154	4.55	765	6.303	0.897	92,970
						236	4.55	1174	14.803	1.609	93,067
NACA 23012 with 15-min mixed ice shape	36 (0.914)	4.32 (0.110)	0.300	175	2.5	20	4.52	99	0.106	0.038	91,965
						52	4.53	258	0.719	0.173	92,440
						111	4.54	551	3.275	0.555	92,755
						154	4.52	761	6.298	0.900	91,909
						236	4.52	1166	14.790	1.616	91,846
NACA 23012 with 22.5-min mixed ice shape	36 (0.914)	4.32 (0.110)	0.300	175	2.5	20	4.46	98	0.106	0.038	89,894
						52	4.47	254	0.717	0.173	90,247
						111	4.47	543	3.265	0.557	90,287
						154	4.46	752	6.283	0.904	89,913
						236	4.46	1152	14.756	1.626	89,960
NACA 23012 with 45-min mixed ice shape	36 (0.914)	4.32 (0.110)	0.300	175	2.5	20	4.49	98	0.106	0.038	90,951
						52	4.48	255	0.717	0.173	90,419
						111	4.47	543	3.264	0.557	90,214
						154	4.49	756	6.288	0.902	90,799
						236	4.50	1161	14.774	1.619	91,280
NACA 23012 with 45-min rime ice shape	36 (0.914)	4.32 (0.110)	0.300	175	2.5	20	4.55	100	0.106	0.038	93,158
						52	4.55	259	0.719	0.173	93,272
						111	4.56	553	3.277	0.554	93,400
						154	4.55	767	6.306	0.897	93,174
						236	4.55	1175	14.811	1.609	93,184

All dimensions are in English units (inch and mph); values inside parenthesis are in SI units (meter and m/s)

7.1 DISCUSSION OF EXPERIMENTAL ERRORS.

A discussion of potential sources of error affecting the impingement data can be found in reference 17. In general, the experimental errors can be divided into two groups. The first group involves errors in the experimental method used to obtain the raw impingement data, while the second group includes errors related to the data reduction methods. Errors in the experimental method originate from variations in spray system performance, cloud uniformity, cloud unsteadiness, tunnel flow conditions, relative humidity, inaccuracies in measuring local LWC, cloud MVD, and cloud drop distribution. Errors in the data reduction methods arise from variations in blotter paper properties, light illumination intensity, and errors in the normalized

reflectance calibration curves and in the data reduction systems. As discussed in reference 17, several improvements have been made to the experimental and data reduction methods since 1996, and these improvements have significantly enhanced the quality of the experimental.

During the impingement experiments, extreme care is taken to monitor all aspects of the experiment and to perform daily checks of all systems used in the experimental and data reduction methods. Experience gained from 20 years of testing has shown that the best indicator of data quality is test repeatability. During production runs, each test condition is typically repeated three to four times. In addition, during each IRT entry a considerable number of repeats (as many as 10 to 20) are performed with selected configurations to better assess test repeatability. In addition, prior to the start of the production runs, impingement tests are conducted with a calibration model to verify the experimental setup with results from prior IRT entries. During the 2003 impingement tests, processes were developed to ensure consistency in all aspects of the experimental and data reduction methods, as described in sections 7.1.1 and 7.1.2. Samples of the variation in the spray system water flow rates for different geometries are presented in figure 57, whereas the time traces in spray system pressures for different MVD conditions are presented in figure 58.

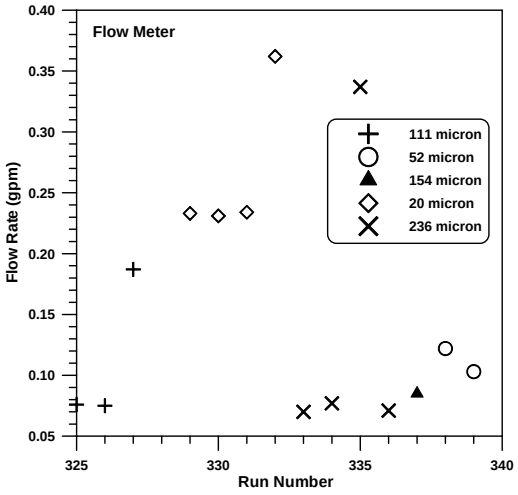

a. MS(1)-0317 Airfoil

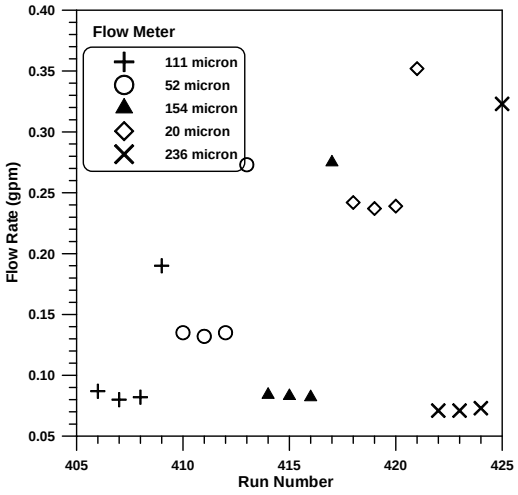

b. NACA 23012 Airfoil

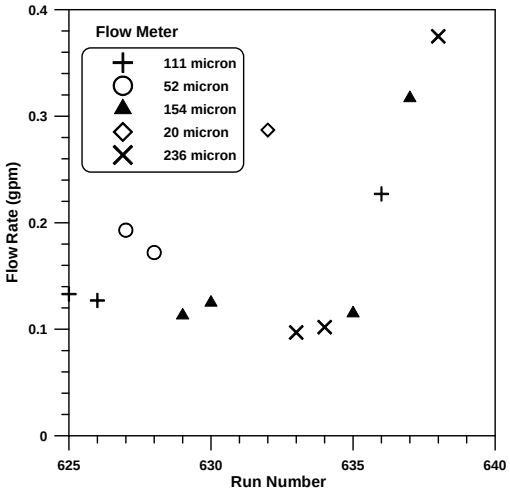

c. NACA 23012 With 5-min. Glaze Ice Shape

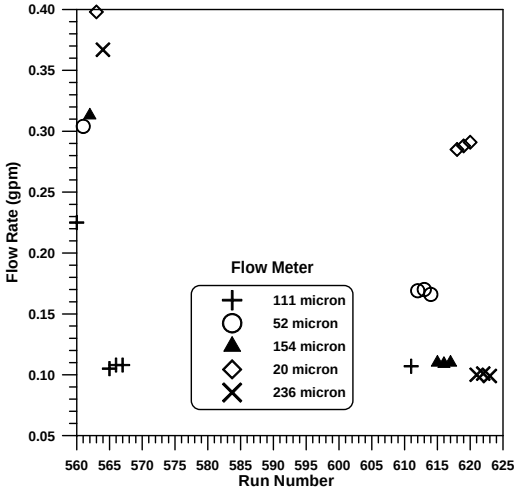

d. NACA 23012 With 10-min Glaze Ice Shape

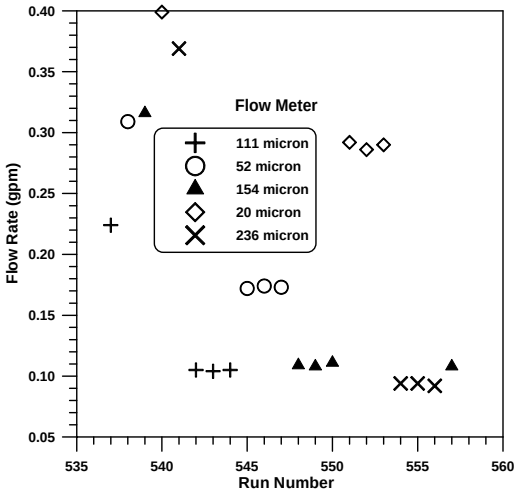

e. NACA 23012 With 15-min Glaze Ice Shape

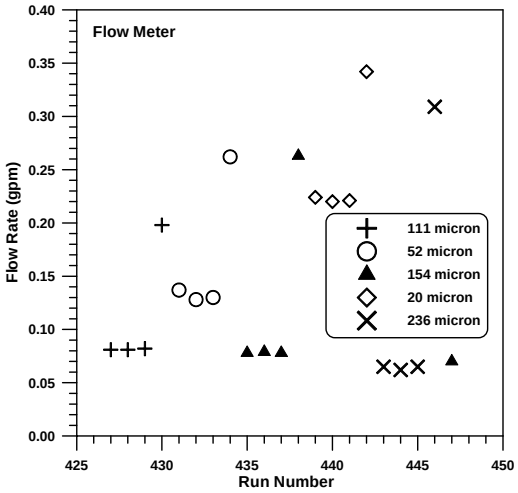

f. NACA 23012 With 22.5-min Glaze Ice Shape

Figure 57. Variation in WSU 16-Nozzle Spray System Water Flow Rates (2003 Tests)

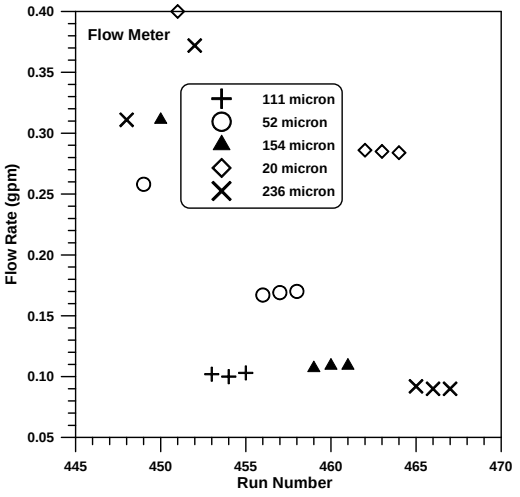

g. NACA 23012 With 45-min Glaze Ice Shape

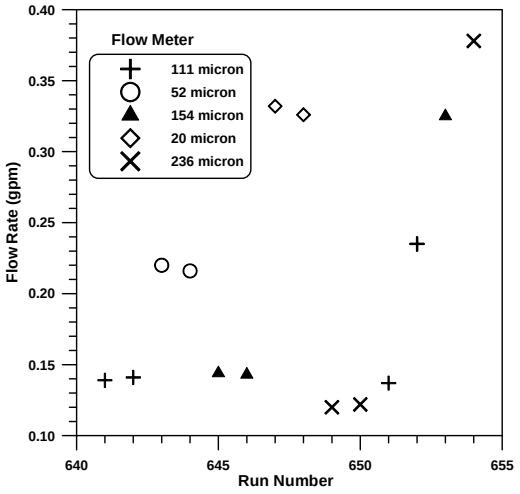

h. NACA 23012 With 7.5-min Mixed Ice Shape

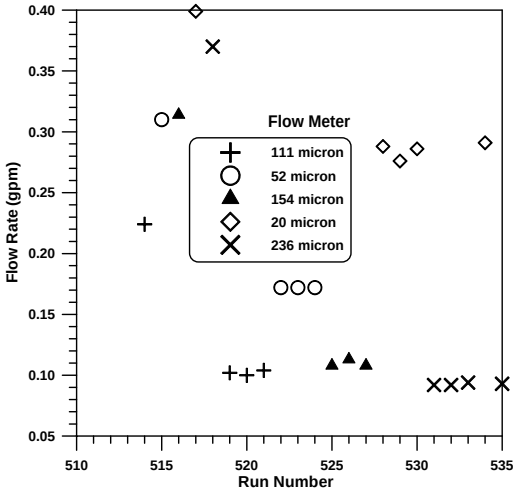

i. NACA 23012 With 15-min Mixed Ice Shape

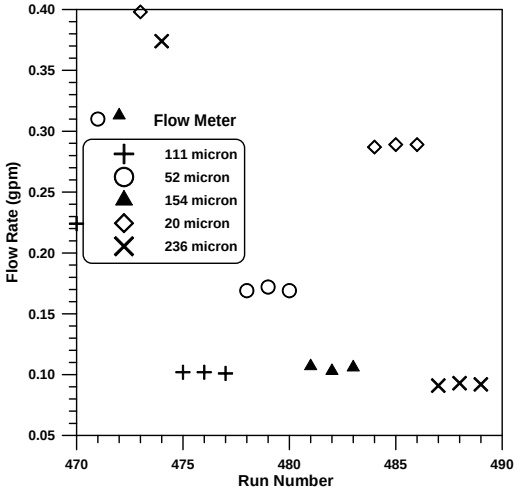

j. NACA 23012 With 22.5-min Mixed Ice Shape

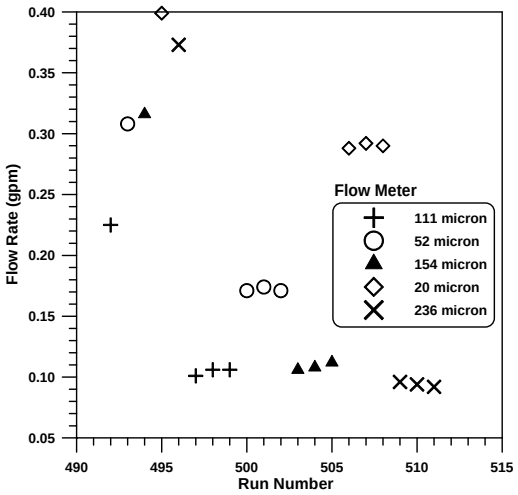

k. NACA 23012 With 45-min Mixed Ice Shape

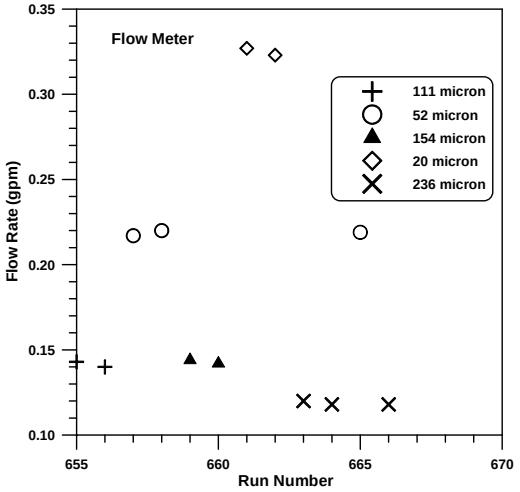

l. NACA 23012 With 45-min Rime Ice Shape

Figure 57. Variation in WSU 16-Nozzle Spray System Water Flow Rates (2003 Tests) (Continued)

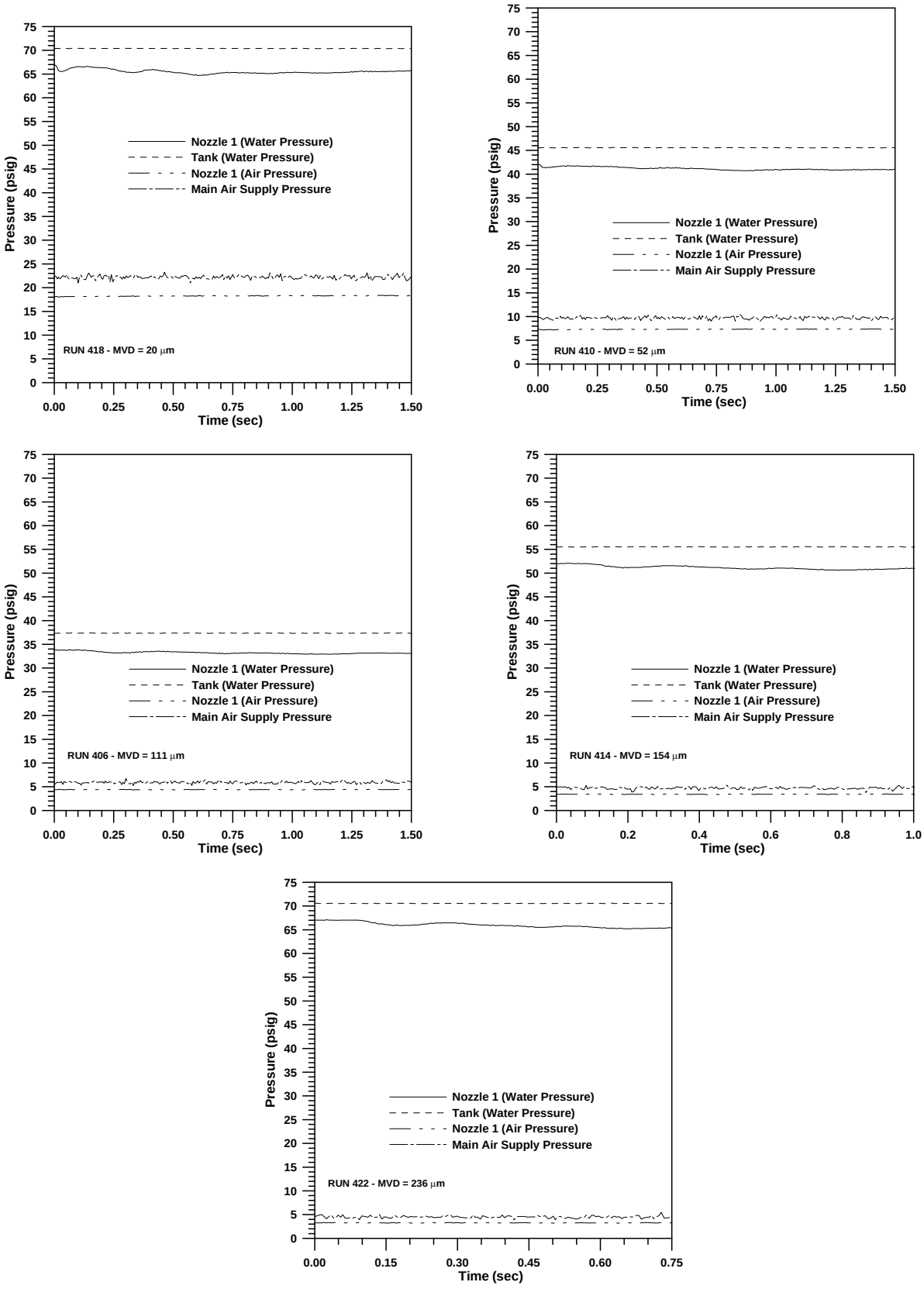

Figure 58. Spray System Pressures Versus Spray Time for all MVD Cases

7.1.1 Experimental Method.

Some important aspects of the experimental method that was used are as follows.

- Extensive tests were performed in a WSU laboratory to calibrate and verify the performance of the spray system two months prior to the impingement tests. During these tests the spray behavior of each of the 16 nozzles was documented and analyzed to determine the on-off response of each nozzle. This was done for all MVD conditions selected for the tests.

- All spray system transducers were calibrated by the NASA Glenn calibration laboratory prior to the IRT entry.

- A process was developed for preparing large quantities (about 30 gallons) of dye solution. Accurate gravimetric balances were used to precisely measure the amount of dye and water to be mixed every time a new batch of dye solution was prepared. Solution samples were checked with a spectrophotometer to ensure consistency in the dye concentration. Furthermore, each time a new batch of solution was added to the tank, samples of the solution were taken from various parts of the spray system, such as the tank, before and after the water filter, and from selected spray nozzles to ensure that the solution was consistent throughout the spray system components.

- Experiments were conducted in a laboratory for the first time to investigate the effect of dye on water surface tension properties, as discussed in reference 17. It was found that the dye had no impact on water surface tension. Surface tension plays a significant role in large drop impingement dynamics, as discussed in reference 2.

- Preliminary spray tests were performed in the IRT with all MVD conditions selected for the impingement tests to determine the spray time required for optimum color density and dye penetration into the blotter paper. Blotter strips from these preliminary tests were segmented and examined under a microscope to determine the level of dye penetration. The spray times selected maintained maximum dye penetration to less than 30% of the blotter paper thickness for most MVD cases.

- The spray system was tested each day prior to the start of the tests by conducting single and combination nozzle sprays. During each test, the volume flow from each nozzle was monitored to ensure consistent nozzle performance. Note that a slightly blocked nozzle can affect cloud uniformity and impact the experimental results. The IRT MOD-1 nozzles installed on the WSU spray system were carefully picked to have very similar flow rates.

- To eliminate potential problems with nozzle freeze-out during the impingement tests, thermocouples were installed at strategic locations of the spray system to monitor the temperature of the dye solution. Water temperature was maintained above 40°F using heaters attached to the dye solution tank of the spray system. Nozzle freeze-out can have a significant impact on LWC uniformity.

- Extensive uniformity tests were performed prior to the start of the production runs to ensure uniform LWC distribution in the test section for all MVD conditions, as described in section 2.4.

- During production runs, test sprays were performed prior to the tunnel start and the spray system performance was assessed by examining the time traces stored by the computer system that was used to control and monitor spray system performance. The test sprays were performed to determine if all nozzles were spraying properly.

- Special tools were developed for installing the blotter strips on the ice shape. Experience with impingement tests showed that data repeatability was considerably affected by how well the blotter conformed to the surface of the geometry. Even if the blotter paper was only slightly raised above the surface of the geometry, the impingement data would be affected. The tools ensured that the paper conformed to the model surface and that the paper installation was identical for each test. A tool was designed for each ice shape using a computer numerically controlled milling machine. Each tool had several reference markings on it for relating the dye trace on the blotter paper to locations on the surface of the airfoil and ice shape.

- Each impingement test was repeated several times and the blotter strips were analyzed with the CCD reflectometer to verify test repeatability. All data obtained from each day were analyzed the following morning. The results were used to determine if additional runs were needed for a specific test condition before installing the next ice shape on the airfoil.

- For each test condition, one long spray was performed and the dye trace on the blotter paper was used to verify the impingement limits obtained from the short sprays. The verification was performed by visual inspection. Blotter strips from the long sprays were saturated with dye and could not be analyzed with the data reduction systems. However, selected strips were analyzed using colorimetric analysis, and the results were used to verify the data from the laser and CCD reflectometers.

- Humidity has been shown to have a significant effect on LWC for small and large drops [11, 14, and 17]. During the 2003 impingement tests, the relative humidity in the IRT test section was maintained at 70% ±4%. Humidity was monitored with humidity sensors installed in the test section and on the IRT spray bars. A process was also developed for setting tunnel humidity for the impingement tests.

- Repeated measurements of spray cloud drop distribution and LWC properties were performed to document the spray clouds and to assess the repeatability of the spray system air and water pressure settings. Measurements were conducted before and after the impingement tests to warrant consistencies within the test period.

- Over 160 local LWC measurements were performed in the IRT test section using the collector device. These measurements were taken over a range of model surface

locations to evaluate local variations in LWC uniformity and to obtain reference LWC values for data analysis (figures 59a and 59b).

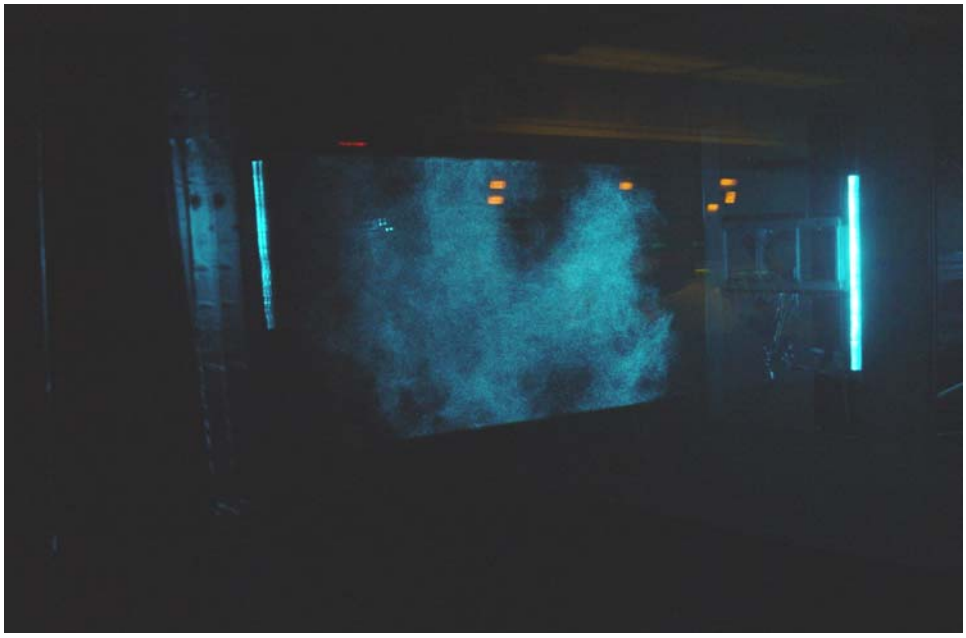

Figure 59a. Typical Laser Sheet Produced in the IRT Test Section

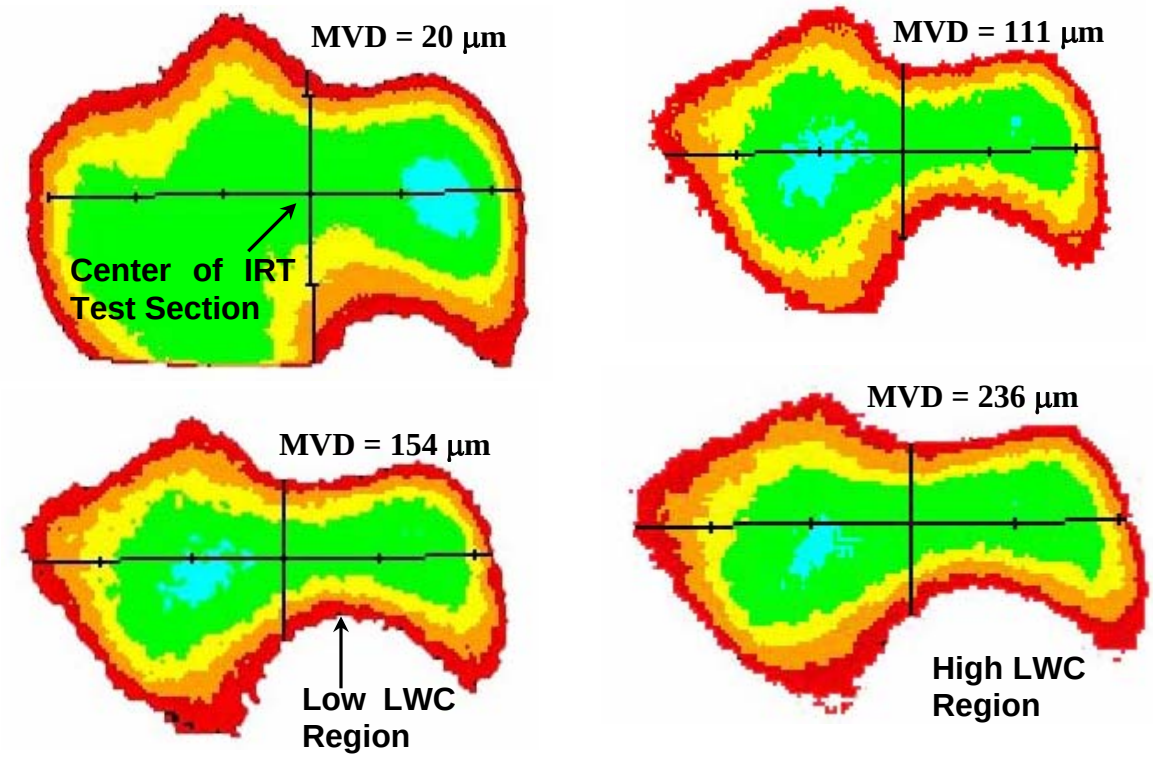

Figure 59b. Sample of Cloud Uniformity Images Obtained Using the Laser Sheet Method

- During production runs, impingement data for the test models and collector device were obtained with the same batch of dye to ensure that potential small changes in dye concentration did not affect the impingement data.

- A concern in impingement testing was dye recirculation in the IRT circuit. Blotter strips were placed at strategic locations upstream of the spray bars and were monitored at regular intervals during the impingement tests. No dye trace was ever found on these blotter strips.

- Pressure data for each test model were obtained at the start and end of the impingement tests to verify flow conditions and evaluate the repeatability of the pressure data.

7.1.2 Data Reduction Method.

Some important aspects of the data reduction method that were used are as follows.

- Blotter paper properties are important to the quality of impingement results, as discussed in reference 11. The complex geometries of the tested ice shapes resulted in crease formation on certain locations of the blotter strips. The effect of creasing on reflectance measurements was evaluated during laboratory tests at WSU with the CCD reflectometer, and it was found that it did not affect the data reduction.

- New calibration curves were prepared for both data reduction systems to develop the relationship between normalized reflectance and dye mass density. The calibration was conducted using dyed blotter strips that were generated in laboratory tests, as well as those generated during the IRT tests.

- The impingement data from the dye-laden blotter strips were extracted using both laser and CCD reflectometers, and the results from the two systems were compared for consistency.

- During the data reduction process, reference strips were used at regular time intervals to verify the repeatability of the data reduction systems.

- Selected blotter strips were reduced repeatedly over a period of several months to evaluate the repeatability of the data reduction process.

- Blotter strip illumination uniformity during data reduction with the CCD reflectometer was monitored at selected locations with an accurate light meter to verify that the light intensity over the blotter strip was consistent throughout the data reduction process.

- Each blotter strip was visually inspected independently by two researchers to verify the impingement curves produced by the data reduction systems.

- Selected collector strips were analyzed, using colorimetric analysis, for comparison with the collector dye mass data obtained with the laser and CCD reflectometers. The results were found to be in good agreement.

7.2 PRESSURE DISTRIBUTIONS.

Experimental pressure data for the MS(1)-0317 at zero AOA were compared to the analysis results obtained with LEWICE, as shown in figure 60, and demonstrated good agreement. Pressure data for the clean and iced NACA 23012 airfoil with an AOA of 2.5° are presented in figures 61 through 71. The pressures provided are for the airfoil surfaces only, since the ice shapes were not instrumented with pressure taps. The LEWICE pressure distributions presented were obtained at an AOA of 2.1°, because this angle resulted in the closest match to the experimental pressure distributions. Note that LEWICE uses a potential flow (panel) method to compute surface pressures that does not model tunnel wall effects and viscous flow effects, such as boundary layers and wakes and regions of flow separation.

Comparison of the experimental and LEWICE pressure distributions were in good agreement for the clean NACA 23012 airfoil and for the 5- and 10-min glaze ice shapes, as shown in figures 61 through 63. For the 15- and 22.5-min glaze ice shapes, LEWICE did not match the experimental data over the forward 10% to 20% chord, as shown in figures 64 and 65. In both cases, flow separation in the form of a long leading-edge bubble is evident in the experimental pressure distributions. For the 45-min ice shape, the leading-edge bubble over the forward 30%-35% chord of the NACA 23012 airfoil downstream of the ice shape upper and lower horns was not predicted by LEWICE, as shown in figure 66.

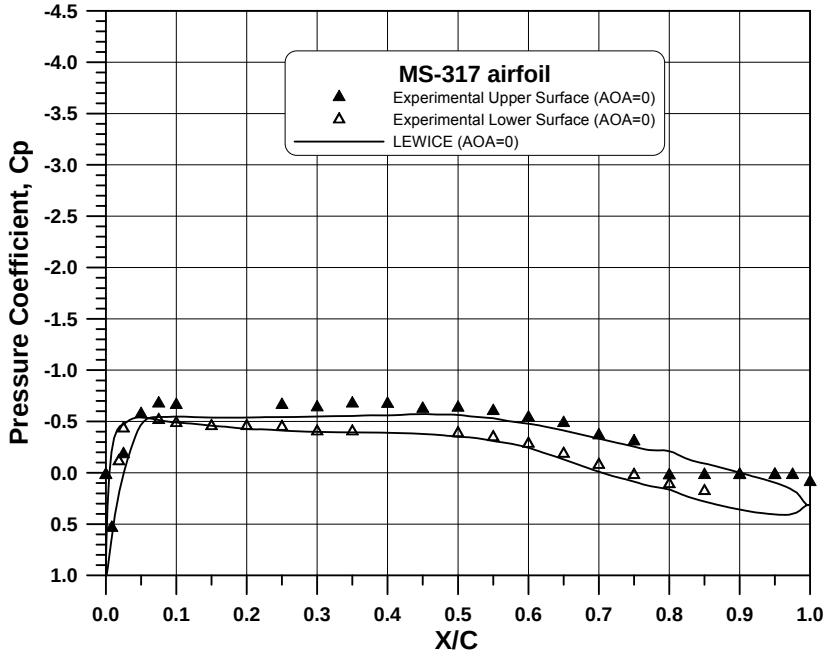

Figure 60. Comparison of Pressure Distribution for MS(1)-317 Airfoil at $\alpha = 0°$

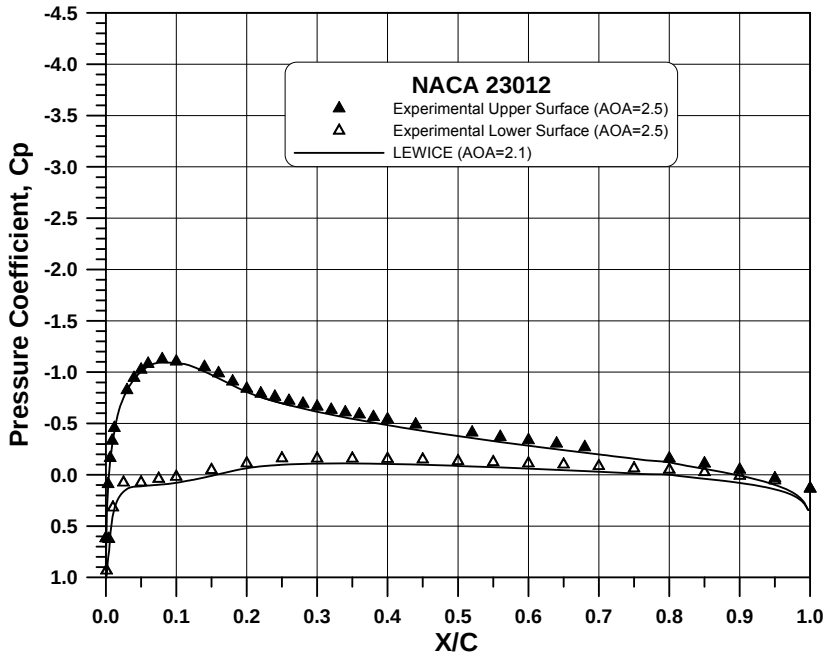

Figure 61. Comparison of Pressure Distribution for NACA 23012 Airfoil at $\alpha = 2.5°$

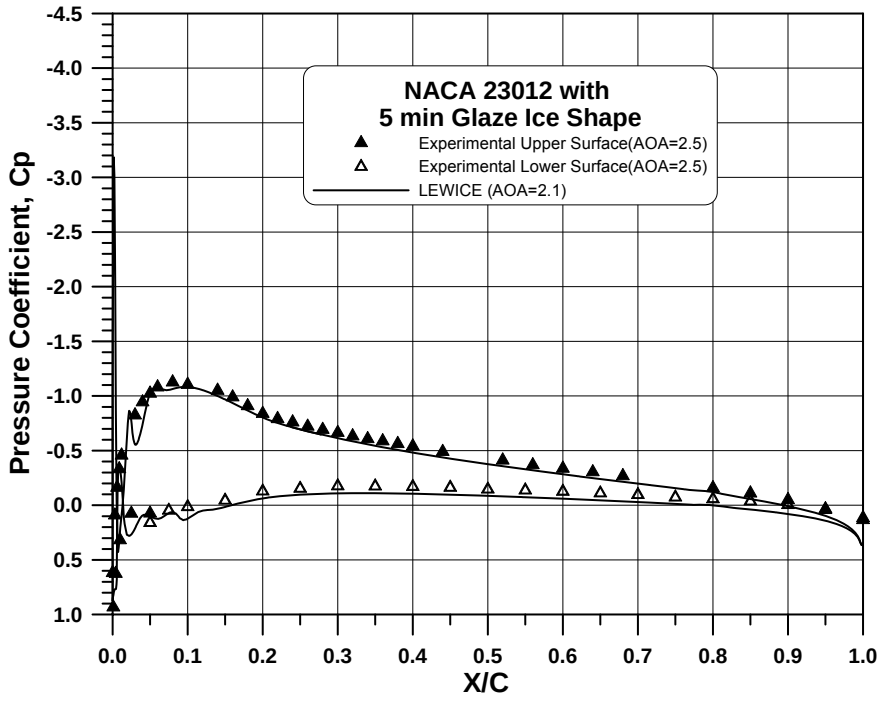

Figure 62. Comparison of Pressure Distribution for NACA 23012 With 5-min Glaze Ice Shape at $\alpha = 2.5°$

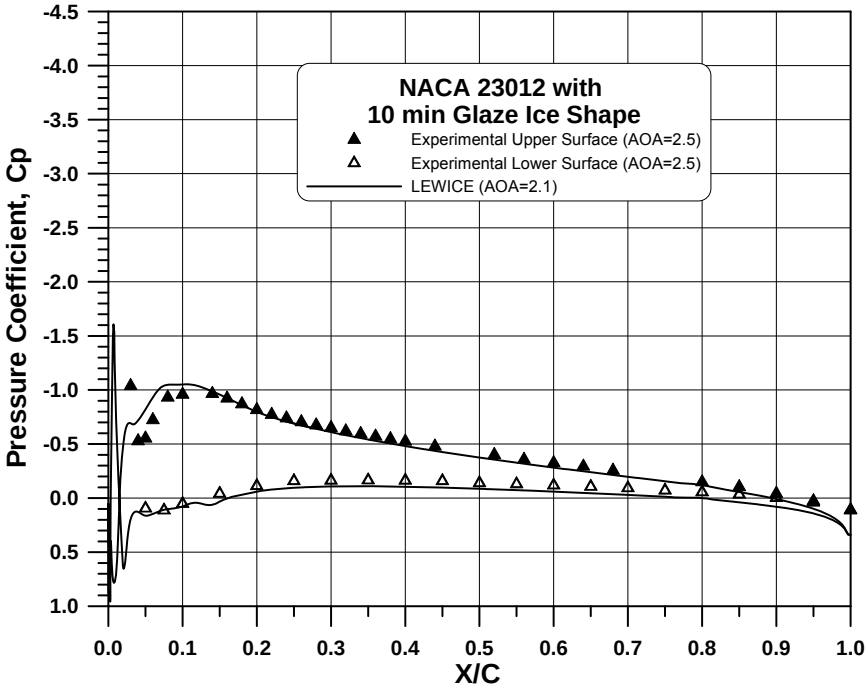

Figure 63. Comparison of Pressure Distribution for NACA 23012 With 10-min Glaze Ice Shape at $\alpha = 2.5°$

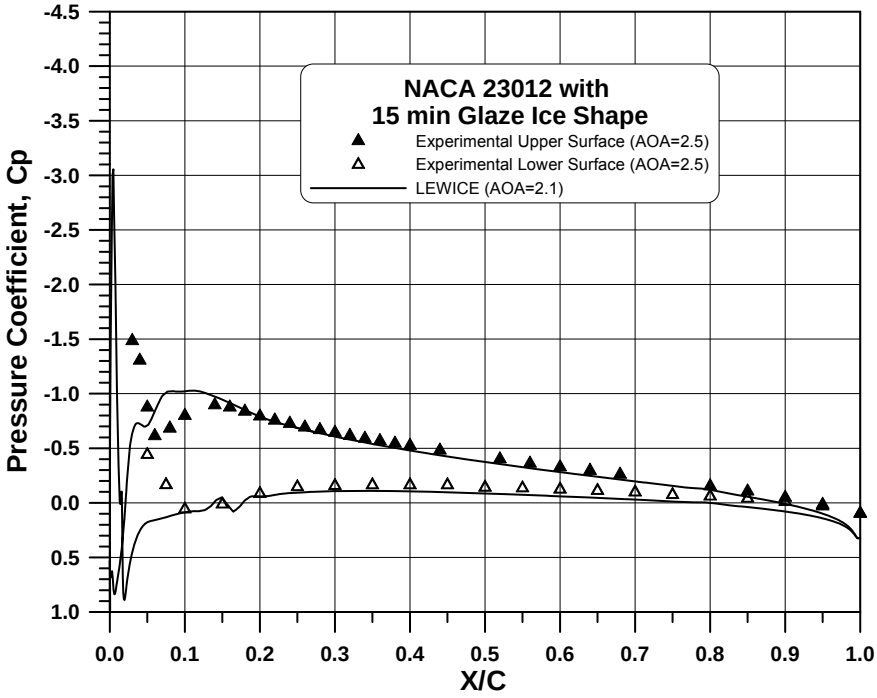

Figure 64. Comparison of Pressure Distribution for NACA 23012 With 15-min Glaze Ice Shape at $\alpha = 2.5°$

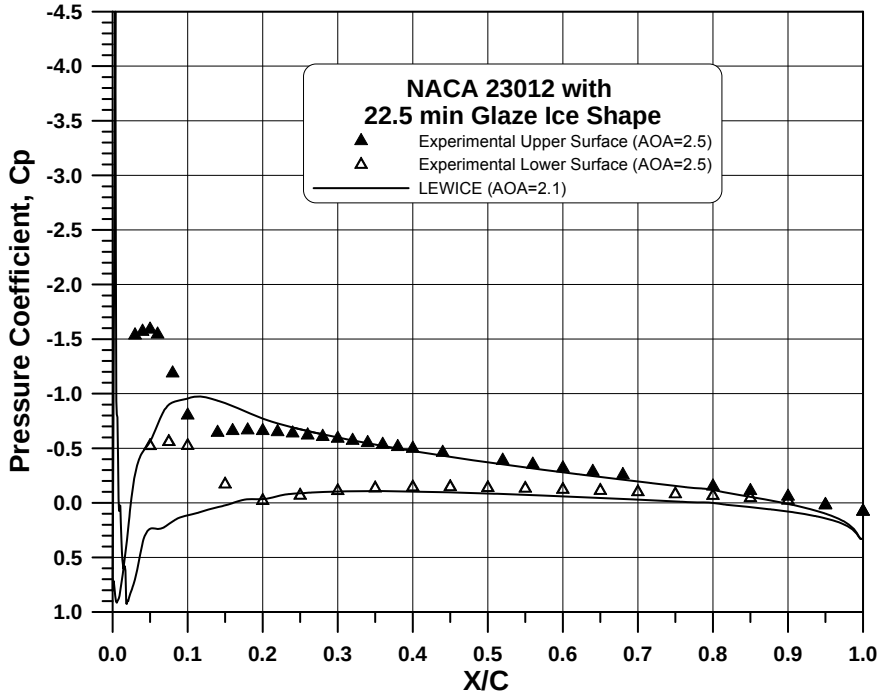

Figure 65. Comparison of Pressure Distribution for NACA 23012 With 22.5-min Glaze Ice Shape at $\alpha = 2.5°$

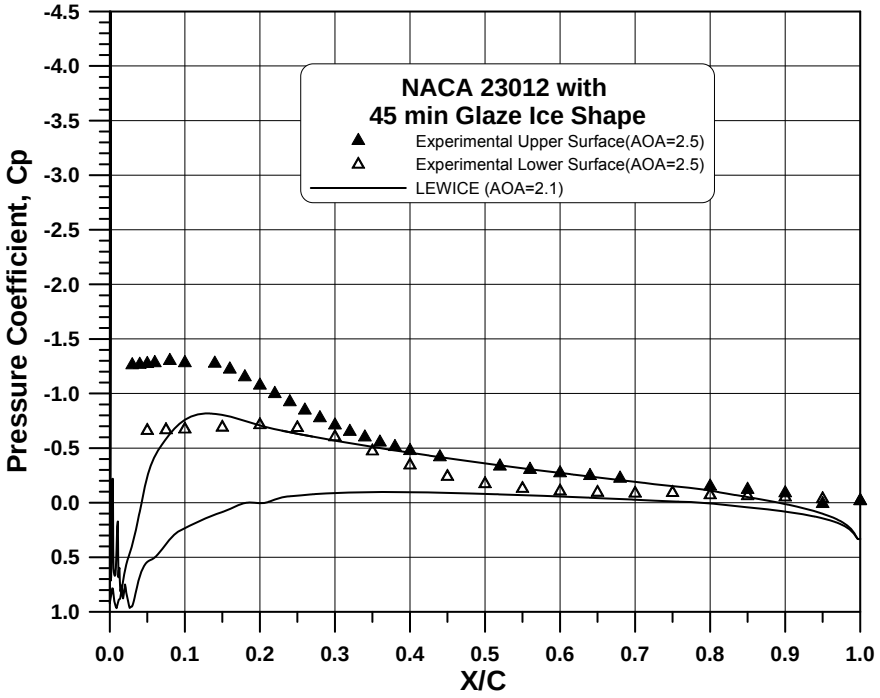

Figure 66. Comparison of Pressure Distribution for NACA 23012 With 45-min Glaze Ice Shape at $\alpha = 2.5°$

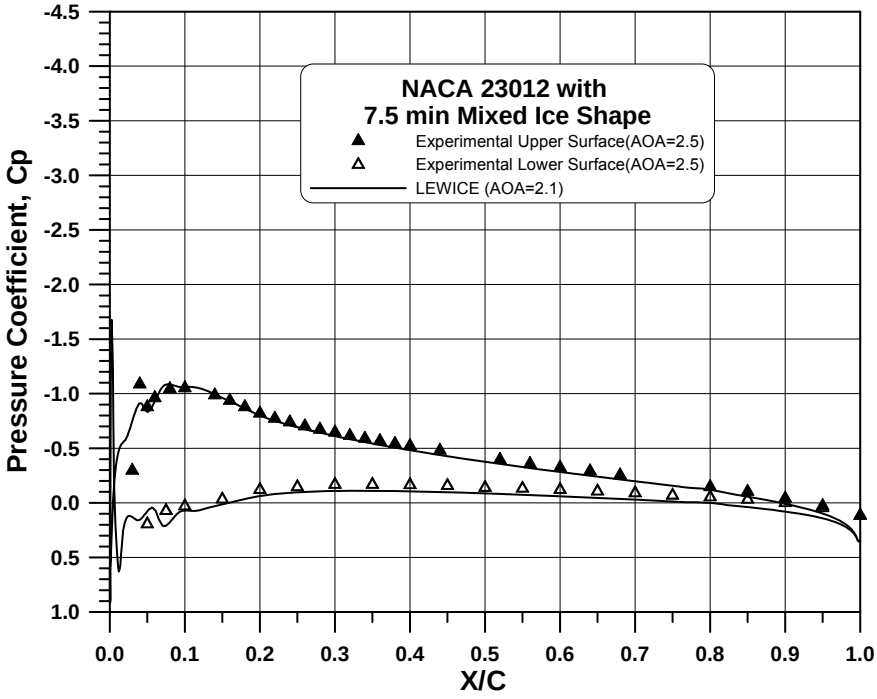

Figure 67. Comparison of Pressure Distribution for NACA 23012 With 7.5-min Mixed Ice Shape at $\alpha = 2.5°$

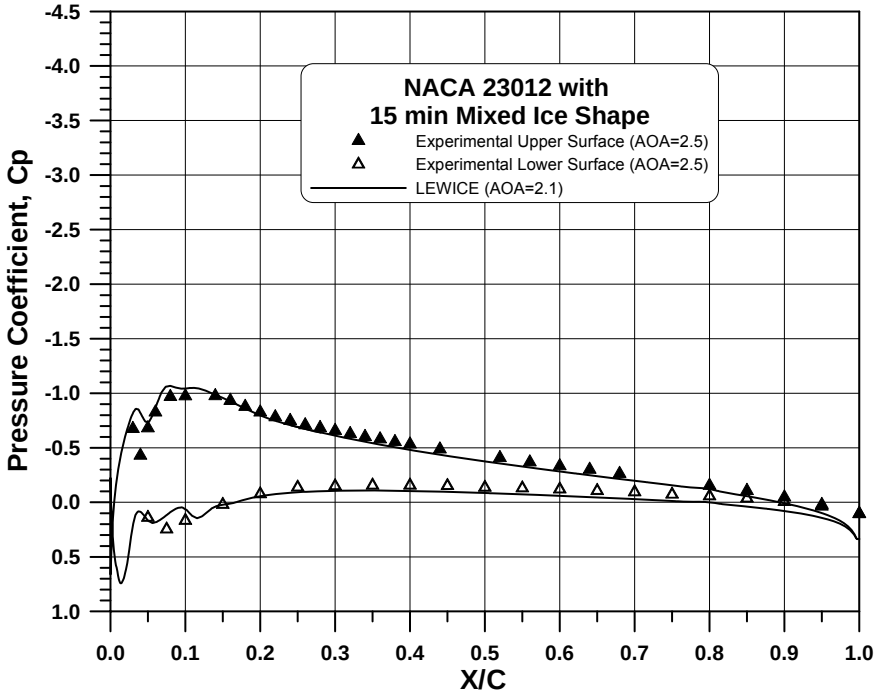

Figure 68. Comparison of Pressure Distribution for NACA 23012 With 15-min Mixed Ice Shape at $\alpha = 2.5°$

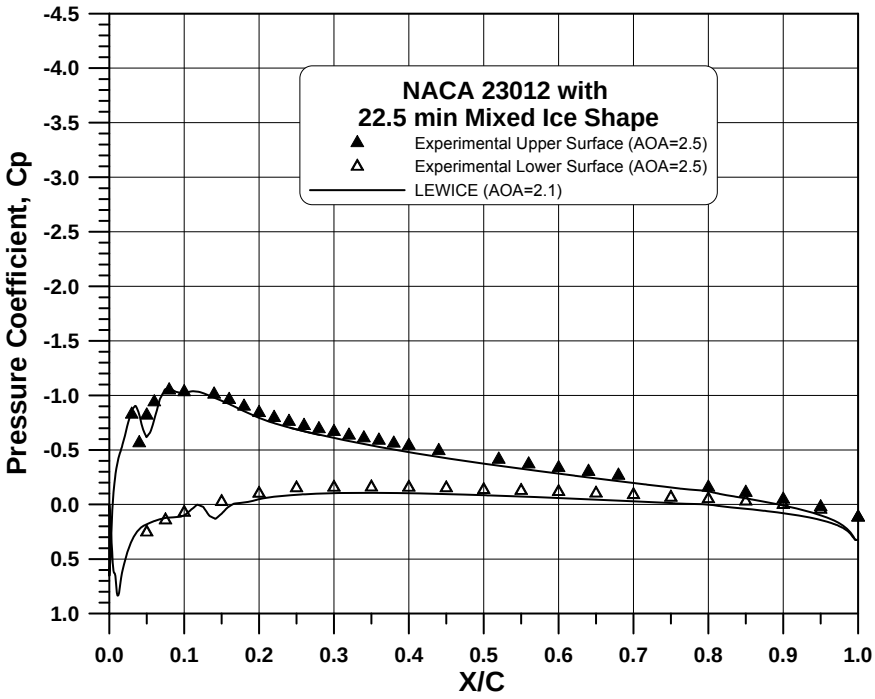

Figure 69. Comparison of Pressure Distribution for NACA 23012 With 22.5-min Mixed Ice Shape at $\alpha = 2.5°$

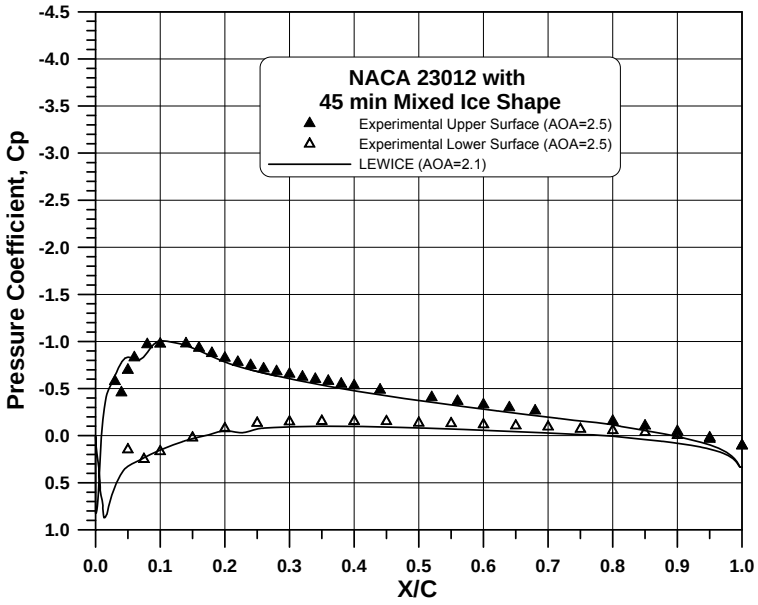

Figure 70. Comparison of Pressure Distribution for NACA 23012 With 45-min Mixed Ice Shape at $\alpha = 2.5°$

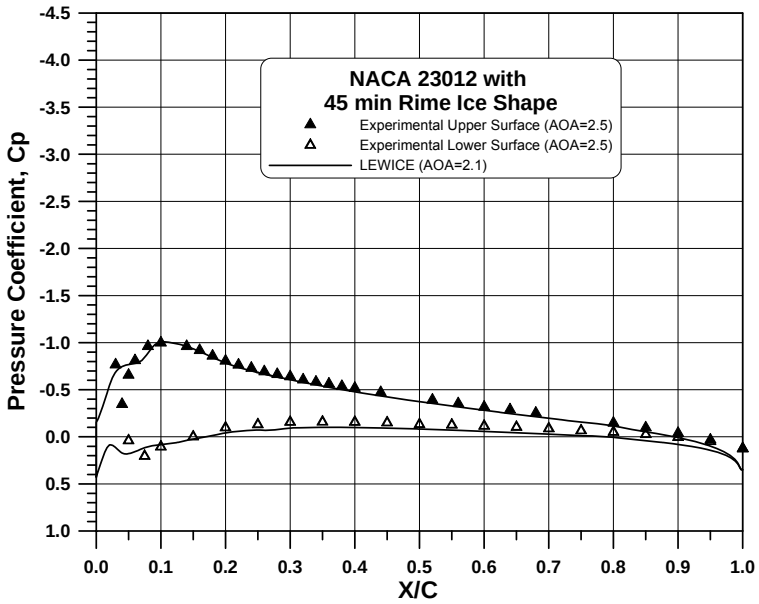

Figure 71. Comparison of Pressure Distribution for NACA 23012 With 45-min Rime Ice Shape at $\alpha = 2.5°$

For the NACA 23012 airfoil tested with the 7.5-, 15-, 22.5-, and 45-min mixed ice shapes, the computational and experimental pressure data were in good agreement, as shown in figures 67 through 70. The reason for the improved correlation between LEWICE and the experimental data in the case of the mixed ice accretion is attributed to the more streamlined shape of the mixed ice shapes.

The experimental and analysis pressure data for the NACA 23012 airfoil with the 45-min rime ice shape exhibited good agreement, as shown in figure 71. This was attributed to the streamlined shape of the rime ice.

7.3 IMPINGEMENT RESULTS.

7.3.1 Test Repeatability.

Test repeatability is an important indicator of the quality of the experimental results. Test repeatability is assessed by computing the maximum percent variation, R_{MAX} of repeated tests from the average. For clean airfoils and wings, the maximum variation in the test data is typically observed at the point of maximum impingement efficiency (i.e., the peak of the impingement curve). However, with the simulated ice shapes tested, multiple sharp impingement peaks were obtained, making it difficult to compute the value of R_{MAX}. The absolute maximum local impingement efficiency observed at the leading-edge region of the clean or iced models is denoted by $\overline{\beta}_1$, whereas the minimum local impingement efficiency observed between the upper and lower horns of the tested glaze and mixed ice shapes is denoted by $\overline{\beta}_2$. The $\overline{\beta}_1$ and $\overline{\beta}_2$ values of the experimental data are shown in table 10. To better define test repeatability for the iced configurations, an additional parameter, R_{AREA}, was computed by

determining the maximum percent difference in the total area under the impingement curve of each repeated test from the average. This difference is representative of the variation in total impingement efficiency.

Table 9. Summary of Test Repeatability Results

Test Case	AOA (deg.)	MVD 20 μm		MVD 52 μm		MVD 111 μm		MVD 154 μm		MVD 236 μm	
		R_{AREA}	R_{MAX}	R_{AREA}	R_{MAX}	R_{AREA}	R_{MAX}	R_{AREA}	R_{MAX}	R_{AREA}	R_{MAX}
MS(1)-0317	0	2.1	1.6	NA	NA	NA	NA	NA	NA	NA	NA
NACA 23012	2.5	5.6	4.9	2.6	1.6	7.6	9.4	2.2	1.3	5.3	4.8
NACA 23012 with 5-min glaze ice shape	2.5	5.1	2.9	1.5	0.2	1.9	0.6	9.1	11.4	1.4	0.4
NACA 23012 with 10-min glaze ice shape	2.5	1.8	1.2	5.1	3.9	6.9	6.4	1.4	7.2	8.6	3.4
NACA 23012 with 15-min glaze ice shape	2.5	1.0	1.4	2.0	2.2	3.4	7.8	2.5	7.5	7.8	8.8
NACA 23012 with 22.5-min glaze ice shape	2.5	1.4	2.5	2.9	2.1	5.3	7.1	3.6	8.2	12.3	12.5
NACA 23012 with 45-min glaze ice shape	2.5	5.3	12.5	2.3	4.1	3.2	4.5	2.7	2.5	0.8	1.3
NACA 23012 with 7.5-min mixed ice shape	2.5	1.2	0.2	0.9	0.4	1.1	4.4	3.8	6.0	2.3	5.0
NACA 23012 with 15-min mixed ice shape	2.5	3.2	2.5	3.2	1.9	5.1	6.9	8.5	12.4	6.6	5.9
NACA 23012 with 22.5-min mixed ice shape	2.5	1.8	2.6	0.6	4.8	1.1	3.7	6.7	7.4	7.3	7.8
NACA 23012 with 45-min mixed ice shape	2.5	3.4	8.4	8.2	8.4	1.8	2.6	3.1	7.8	3.8	7.5
NACA 23012 with 45-min rime ice shape	2.5	3.6	2.1	4.1	5.1	6.8	8.7	3.4	6.5	2.1	2.4

R_{AREA} = % repeatability for the area under the curve
R_{MAX} = % repeatability of the maximum beta
NA = Data not available

Table 10. Summary of Impingement Efficiency Data for 2003 IRT Tests

Model	Test Conditions		β_1	S_1 (mm)	β_2	S_2 (mm)	S_u (mm)	S_l (mm)	X_u/C	Xl/C	$\bar{E}_L$	$\bar{E}_E$	$\frac{\bar{E}_L - \bar{E}_E}{E_E}$ (%)
	AOA (deg.)	MVD (μm)											
MS(1)-0317	0	20	0.46	-3	NA	NA	-98	80	0.0744	0.0696	0.1868	0.1759	6.2
NACA 23012	2.5	20	0.56	3	NA	NA	-64	145	0.0458	0.1505	0.1738	0.1865	-6.8
		52	0.71	3	NA	NA	-84	200	0.0661	0.2104	0.5102	0.3000	70.1
		111	0.85	3	NA	NA	-105	277	0.0882	0.2945	0.6753	0.4150	62.7
		154	0.92	2	NA	NA	-121	340	0.1052	0.3634	0.7643	0.5118	49.3
		236	0.95	2	NA	NA	-131	380	0.1159	0.4072	0.8403	0.5622	49.5
NACA 23012 with 5-min glaze ice shape	2.5	20	0.43	-8	0.35	10	-91	171	0.0679	0.1748	0.1788	0.1805	-0.9
		52	0.53	-9	0.44	11	-100	233	0.0773	0.2424	0.5236	0.2823	85.5
		111	0.68	-8	0.54	11	-110	270	0.0879	0.2829	0.6928	0.3961	74.9
		154	0.73	-9	0.53	9	-130	310	0.1092	0.3266	0.7830	0.4963	57.8
		236	0.73	-8	0.58	9	-140	360	0.1200	0.3813	0.8590	0.5228	64.3
NACA 23012 with 10-min glaze ice shape	2.5	20	0.40	13	0.33	8	-101	205	0.0676	0.2056	0.1902	0.1713	11.0
		52	0.49	14	0.42	9	-122	250	0.0886	0.2547	0.5539	0.2366	134.1
		111	0.60	14	0.48	9	-135	329	0.1035	0.3411	0.7400	0.3251	127.6
		154	0.70	13	0.48	8	-148	357	0.1175	0.3717	0.8320	0.4103	102.8
		236	0.73	14	0.55	9	-165	367	0.1359	0.3827	0.9168	0.4942	85.5
NACA 23012 with 15-min glaze ice shape	2.5	20	0.45	-23	0.33	8	-121	205	0.0754	0.1960	0.2124	0.1862	14.1
		52	0.59	-23	0.43	8	-125	250	0.0796	0.2451	0.6223	0.2857	117.8
		111	0.67	14	0.49	-7	-142	280	0.0976	0.2779	0.8198	0.3423	139.5
		154	0.85	14	0.53	-8	-162	343	0.1191	0.3468	0.9269	0.4351	113.0
		236	0.92	14	0.58	-9	-170	395	0.1277	0.4036	1.0177	0.5277	92.9
NACA 23012 with 22.5-min glaze ice shape	2.5	20	0.47	-35	0.28	-8	-45	38	-0.0268	0.0023	0.2515	0.2319	8.5
		52	0.59	-36	0.39	-8	-45	257	-0.0268	0.2348	0.7069	0.3236	118.4
		111	0.71	14	0.46	-7	-45	271	-0.0268	0.2501	0.9212	0.4015	129.4
		154	0.80	12	0.47	-8	-210	325†	0.1411	0.3091†	1.0874	0.4436	145.1
		236	0.88	13	0.53	-8	-230	325†	0.1628	0.3091†	1.1840	0.4988	137.4

Table 10. Summary of Impingement Efficiency Data for 2003 IRT Tests (Continued)

Model	Test Conditions		β_1	S_1 (mm)	β_2	S_2 (mm)	S_u (mm)	S_l (mm)	X_u/C	X_l/C	$\bar{E}_L$	$\bar{E}_E$	$\frac{\bar{E}_L - \bar{E}_E}{E_E}$ (%)
	AOA (deg.)	MVD (μm)											
NACA 23012 with 45-min glaze ice shape	2.5	20	0.33	-64	0.11	-7	-83	61	-0.0555	-0.0555	0.3227	0.2705	19.3
		52	0.46	-65	0.26	-8	-83	57	-0.0555	-0.0555	0.6360	0.4360	45.9
		111	0.53	-68	0.33	-29	‡	‡	‡	‡	0.7586	0.5239	44.8
		154	0.62	12	0.38	-30	‡	‡	‡	‡	0.8097	0.6072	33.3
		236	0.65	13	0.41	-30	‡	‡	‡	‡	0.8455	0.6362	32.9
NACA 23012 with 7.5-min mixed ice shape	2.5	20	0.47	-9	0.36	9	-85	190	0.0548	0.0548	0.1896	0.1377	37.7
		52	0.60	14	0.47	9	-98	252	0.0681	0.0681	0.5434	0.2411	125.4
		111	0.66	-11	0.50	-4	-130	300	0.1019	0.1019	0.7108	0.3496	103.3
		154	0.79	14	0.59	9	-152	375	0.1256	0.1256	0.8006	0.4600	74.0
		236	0.79	13	0.60	8	-155	380	0.1289	0.1289	0.8751	0.4754	84.1
NACA 23012 with 15-min mixed ice shape	2.5	20	0.45	-14	0.23	-6	-125	310	0.0814	0.0814	0.1921	0.1563	22.9
		52	0.61	-14	0.28	-6	-135	330	0.0919	0.0919	0.5942	0.2963	100.5
		111	0.67	-15	0.29	-8	-145	360	0.1026	0.1026	0.7789	0.3854	102.1
		154	0.77	17	0.30	-8	-170	430	0.1295	0.1295	0.8683	0.5024	72.8
		236	0.77	15	0.29	-8	-175	460	0.1349	0.1349	0.9501	0.5040	88.5
NACA 23012 with 22.5-min mixed ice shape	2.5	20	0.51	-17	0.11	-5	-110	280	0.0534	0.0534	0.1809	0.1579	14.6
		52	0.61	-17	0.13	-6	-140	325	0.0845	0.0845	0.6021	0.2602	131.4
		111	0.68	-18	0.13	-7	-160	330	0.1058	0.1058	0.7939	0.3566	122.6
		154	0.76	24	0.13	-7	-175	425	0.1220	0.1220	0.8892	0.4718	88.5
		236	0.81	23	0.12	-7	-185	440	0.1328	0.1328	0.9671	0.5140	88.2
NACA 23012 with 45-min mixed ice shape	2.5	20	0.55	-1	0.04	27	-140	85	0.0698	0.0698	0.1690	0.1713	-1.3
		52	0.72	-2	0.07	25	-150	90	0.0804	0.0804	0.5424	0.2874	88.7
		111	0.73	-2	0.08	23	-180	420	0.1123	0.1123	0.8819	0.3731	136.4
		154	0.78	73	0.11	22	-200	490	0.1340	0.1340	1.0041	0.4737	112.0
		236	0.87	-1	0.10	22	-205	520	0.1394	0.1394	1.0808	0.5208	107.5
NACA 23012 with 45-min rime ice shape	2.5	20	0.52	0	NA	NA	-125	263	0.0629	0.0629	0.1855	0.1253	48.0
		52	0.68	-4	NA	NA	-144	320	0.0829	0.0829	0.5424	0.2683	102.2
		111	0.74	-2	NA	NA	-174	350	0.1149	0.1149	0.7135	0.3697	93.0
		154	0.83	1	NA	NA	-188	390	0.1300	0.1300	0.8041	0.4491	79.0
		236	0.91	-1	NA	NA	-191	440	0.1333	0.1333	0.8772	0.5670	54.7

NA = Data not available
† = End of blotter strip
‡ = Analysis in progress

The nomenclature for table 10 is as follows:

1. β_1 represents the maximum impingement efficiency.

2. S_1 represents the surface distance from the reference point (the highlight) to the location of the maximum impingement efficiency.

3. β_2 represents the minimum impingement efficiency on the front surface of the simulated ice shapes.

4. S_2 represents the surface distance from the reference point (the highlight) to the location of the minimum impingement efficiency on the front surface of the simulated ice shapes.

5. S_u and S_l represent the surface distances of impingement limits on the upper and lower surfaces. x_u/c and x_l/c represent the stations of the impingement limits on the upper and lower surfaces with respect to the chord.

6. $\overline{E}$ represents the total impingement efficiency, which is defined as $\overline{E} = \frac{A_{\overline{\beta}}}{A_f}$, where A_f represents the projected frontal area of the airfoil (A_f = 2.672″ per unit span). $\overline{E}_L$ is computational total impingement efficiency using LEWICE 1.6 (modified 27-bin version) and $\overline{E}_E$ is the experimental total impingement efficiency. A few $\overline{E}_L$ exceeded 1.0 due to the presence of artificial impingement tails.

Data repeatability for the 2003 impingement tests, conducted with the NACA 23012 airfoil, and the five glaze ice shapes are shown in figures 72 through 82 and in table 9. The maximum variation (R_{max}) in $\overline{\beta}_1$ from the average of repeated runs (3 to 4 per test case) was less than 10% for 52 out of 56 cases tested. In addition, the maximum variation in the area under the impingement curve (R_{AREA}), was less than 10% for 55 out of 56 cases tested. These values indicate very good test repeatability. In only 4 out of the 56 tested cases, R_{MAX} was between 10% and 13%, and in one case, the value of R_{AREA} was between 10% and 13%.

Figure 83 shows the repeatability of the experimental setup by comparing experimental impingement data obtained with the MS(1)-0317 airfoil during five IRT entries spanning the time period from 1985 to 2003 [6, 13, 17, and 29]. The results are for MVDs in the range of 19 to 21 μm and show very good agreement in magnitude and overall trend. LEWICE analysis data for an MVD of 20 μm are also provided for comparison and are in very good agreement with the experimental data.

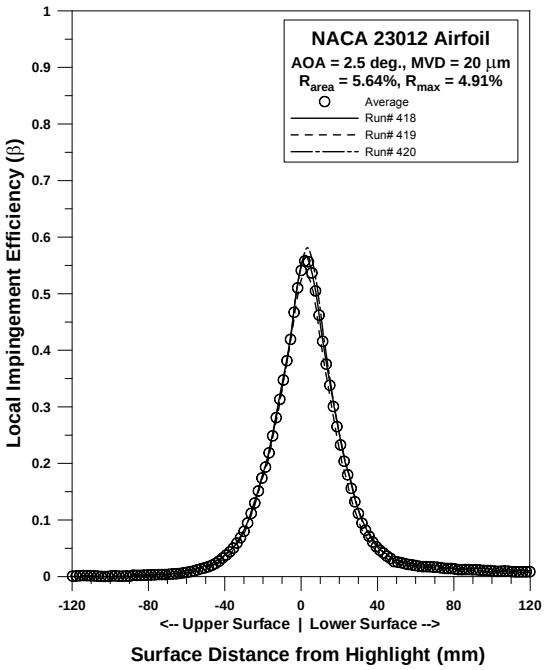

Figure 72a. NACA 23012 Repeatability, MVD = 20 μm

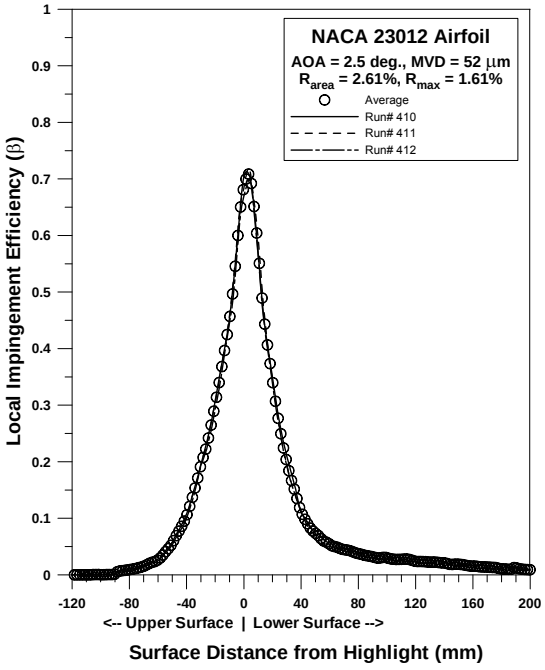

Figure 72b. NACA 23012 Repeatability, MVD = 52 μm

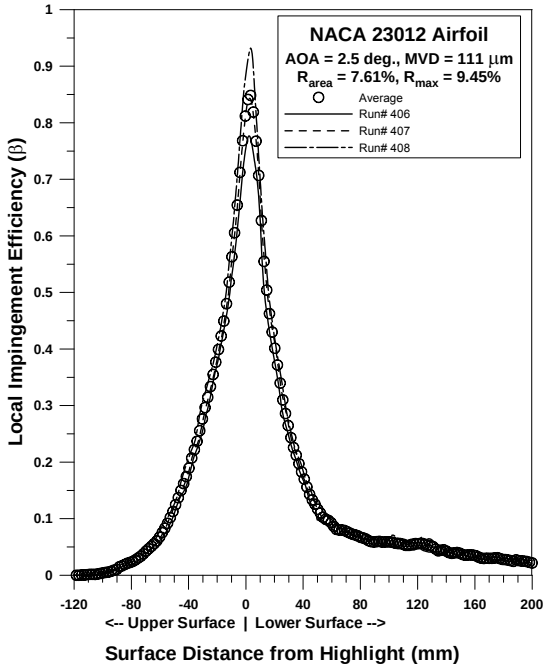

Figure 72c. NACA 23012 Repeatability, MVD = 111 μm

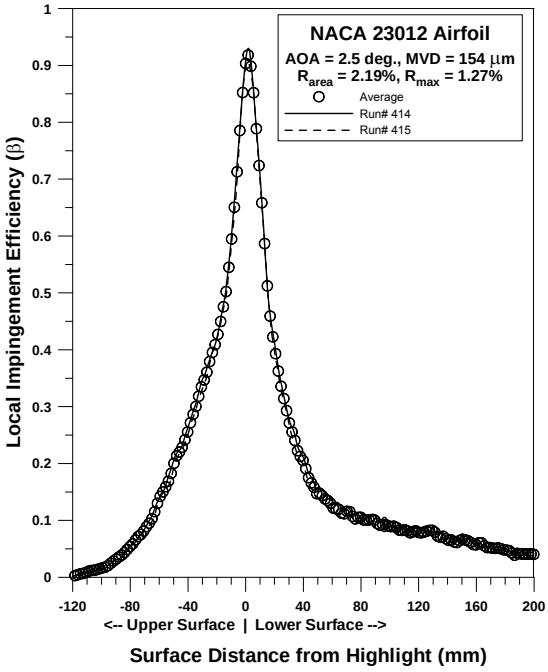

Figure 72d. NACA 23012 Repeatability, MVD = 154 μm

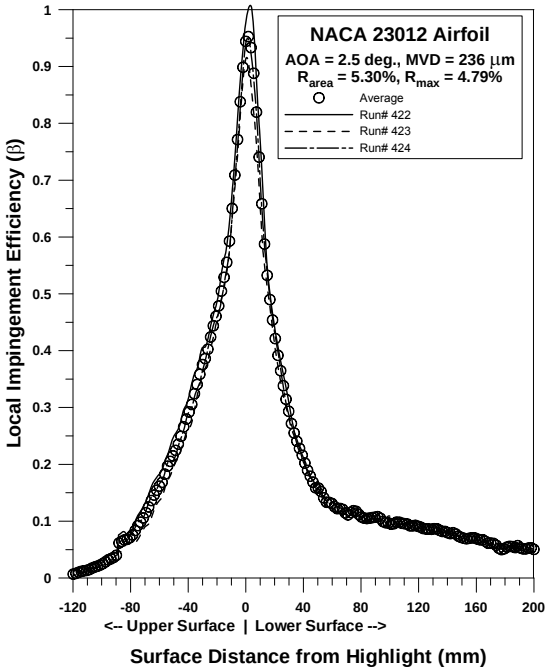

Figure 72e. NACA 23012 Repeatability, MVD = 236 μm

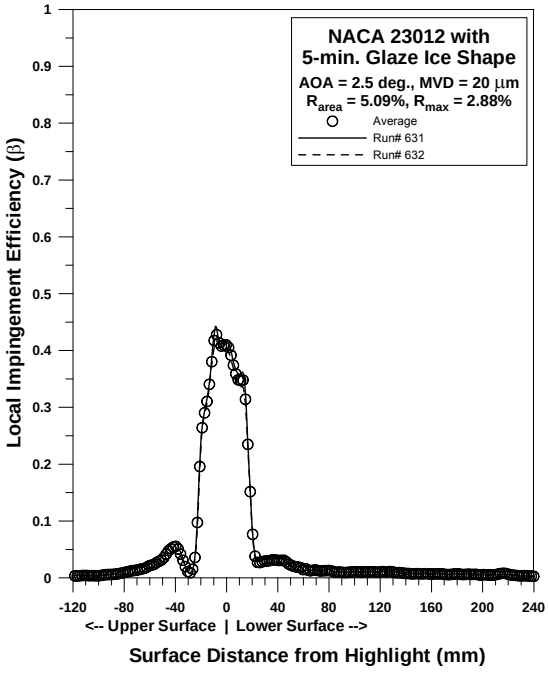

Figure 73a. NACA 23012 With 5-min Glaze Ice Repeatability, MVD = 20 μm

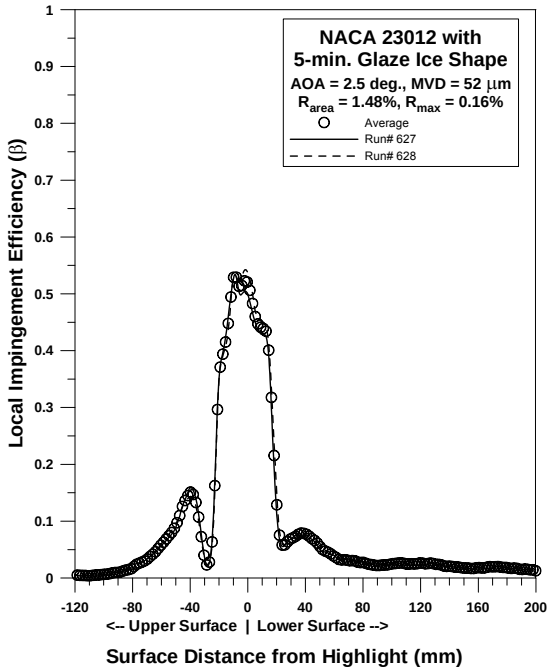

Figure 73b. NACA 23012 With 5-min Glaze Ice Repeatability, MVD = 52 μm

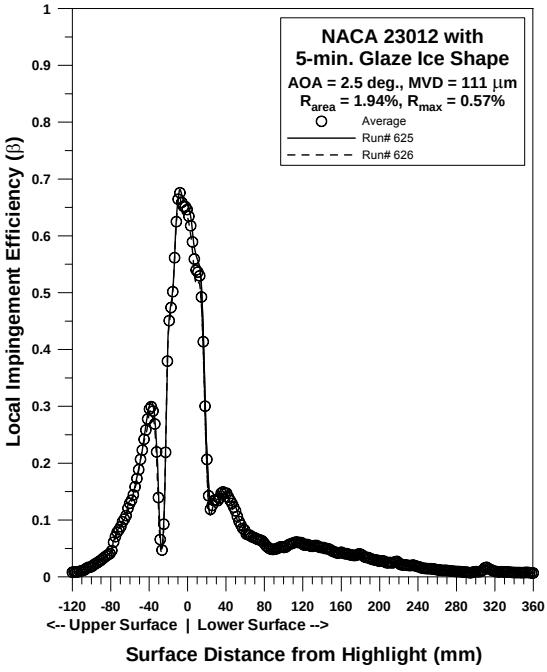

Figure 73c. NACA 23012 With 5-min Glaze Ice Repeatability, MVD = 111 μm

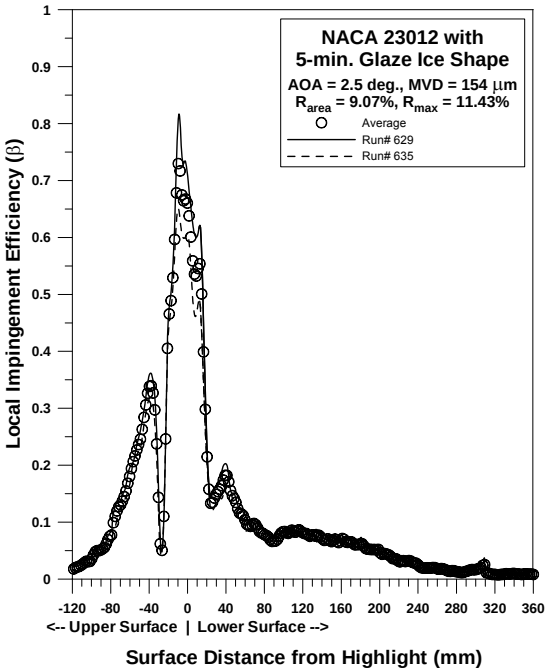

Figure 73d. NACA 23012 With 5-min Glaze Ice Repeatability, MVD = 154 μm

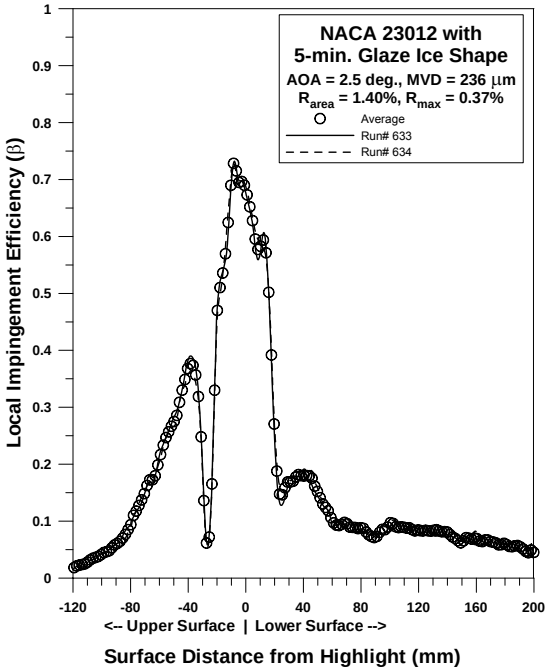

Figure 73e. NACA 23012 With 5-min Glaze Ice Repeatability, MVD = 236 μm

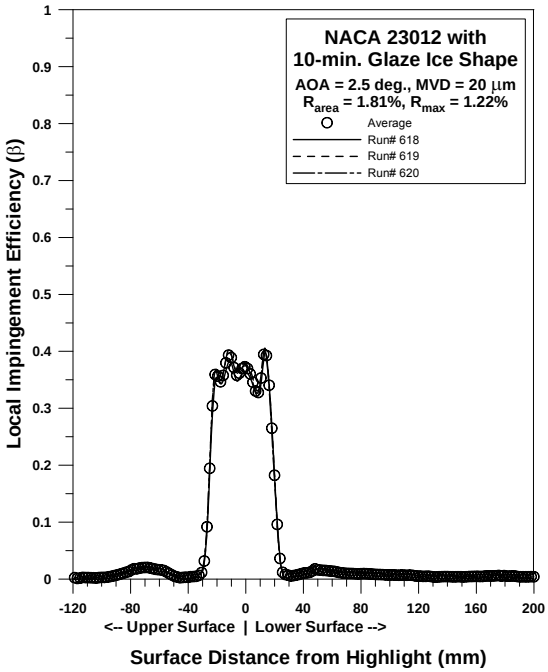

Figure 74a. NACA 23012 With 10-min Glaze Ice Repeatability, MVD = 20 μm

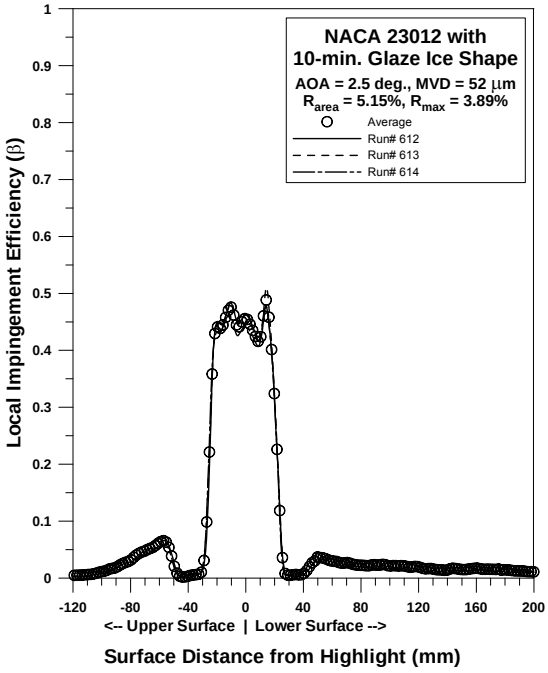

Figure 74b. NACA 23012 With 10-min Glaze Ice Repeatability, MVD = 52 μm

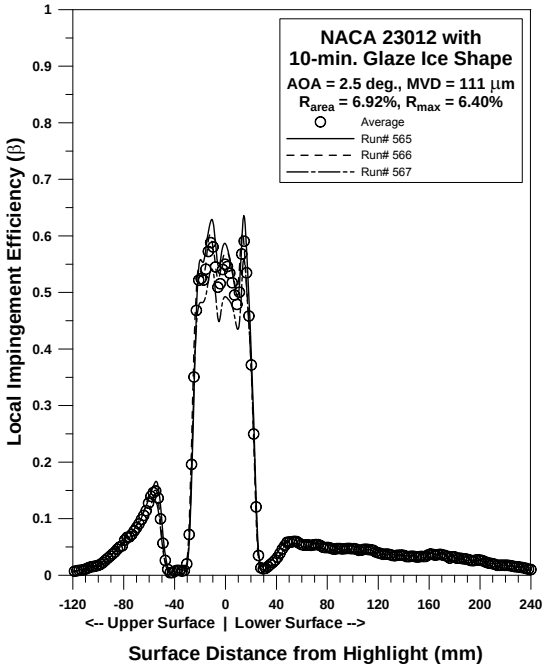

Figure 74c. NACA 23012 With 10-min Glaze Ice Repeatability, MVD = 111 μm

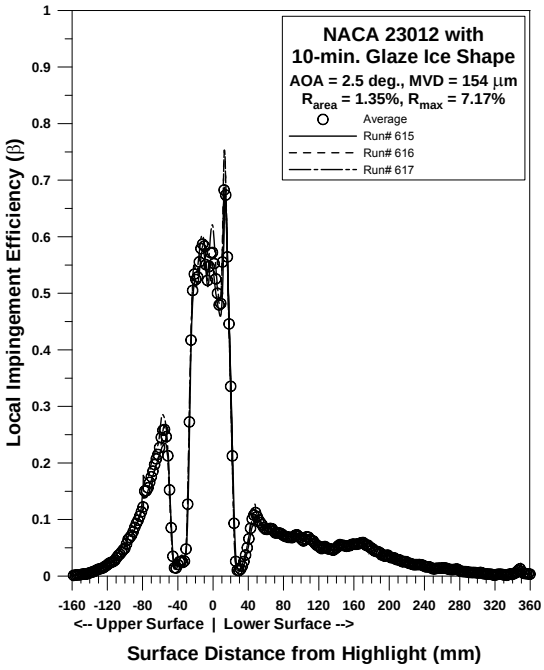

Figure 74d. NACA 23012 With 10-min Glaze Ice Repeatability, MVD = 154 μm

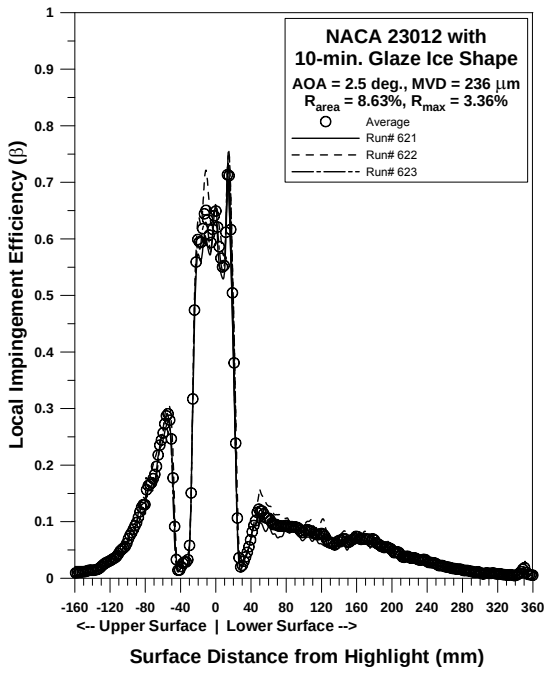

Figure 74e. NACA 23012 With 10-min Glaze Ice Repeatability, MVD = 236 μm

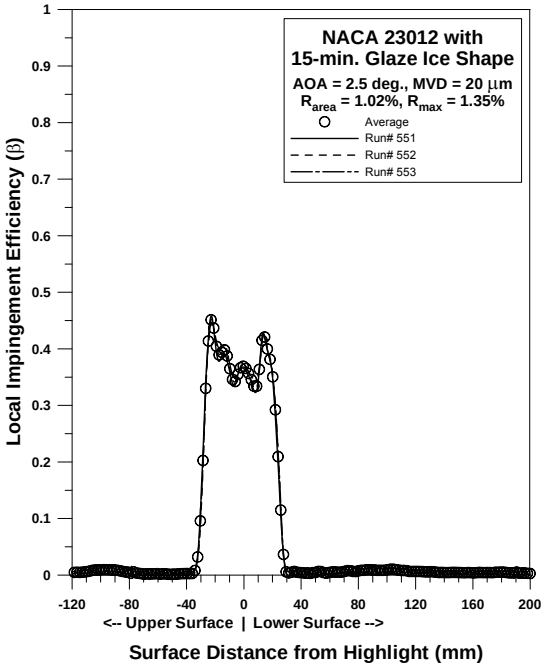

Figure 75a. NACA 23012 With 15-min Glaze Ice Repeatability, MVD = 20 μm

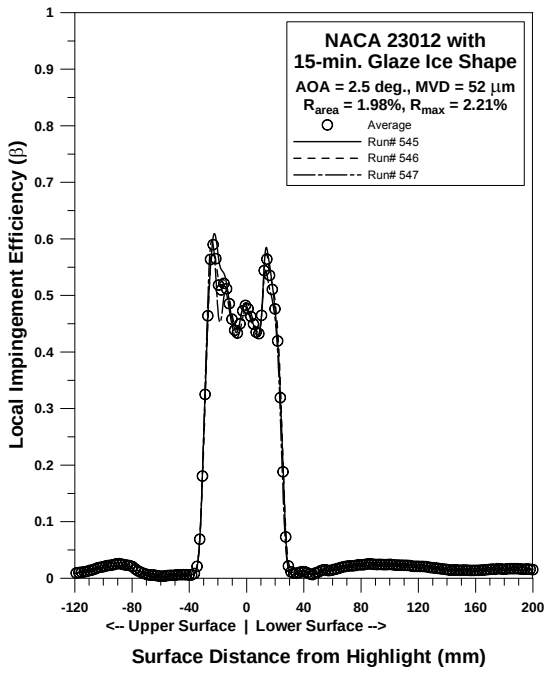

Figure 75b. NACA 23012 With 15-min glaze Ice Repeatability, MVD = 52 μm

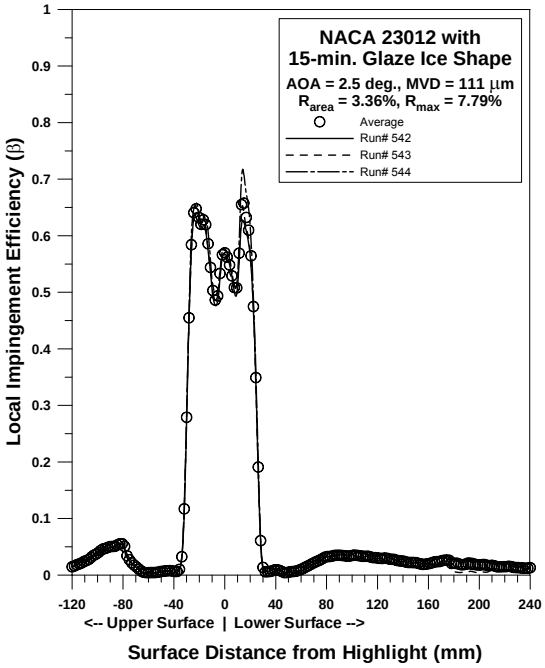

Figure 75c. NACA 23012 With 15-min Glaze Ice Repeatability, MVD = 111 μm

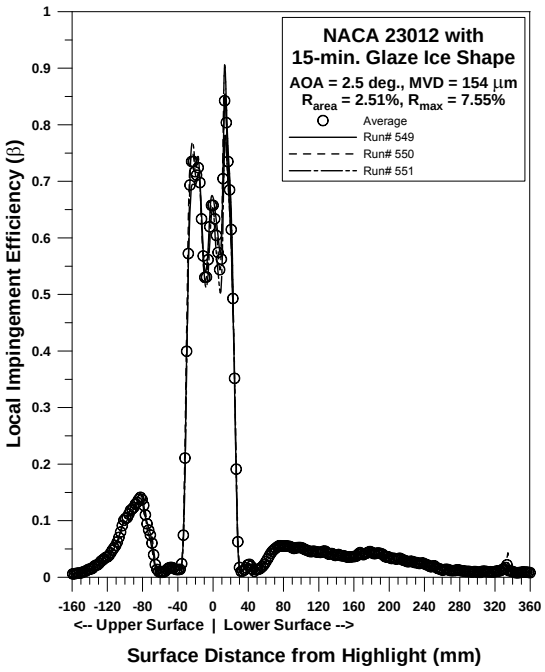

Figure 75d. NACA 23012 With 15-min Glaze Ice Repeatability, MVD = 154 μm

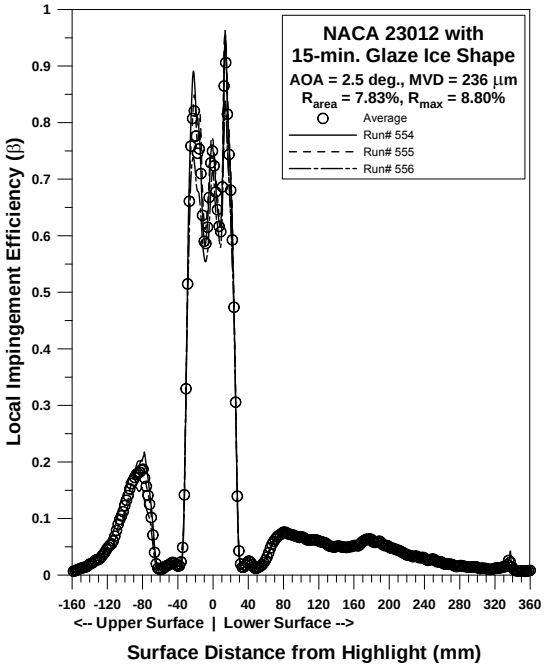

Figure 75e. NACA 23012 With 15-min Glaze Ice Repeatability, MVD = 236 μm

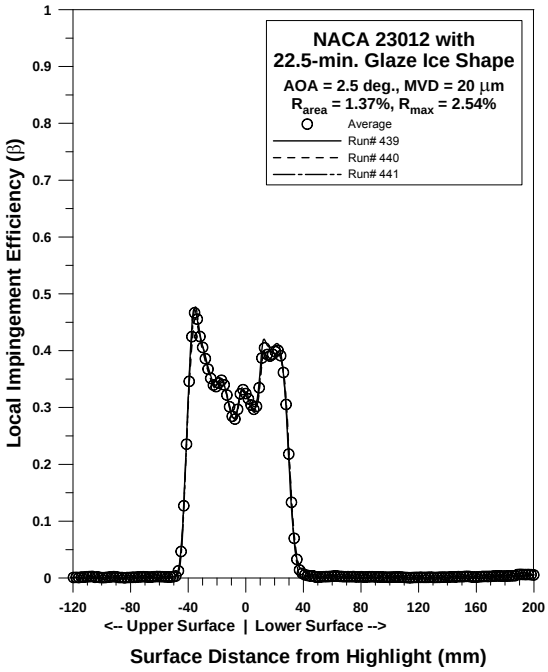

Figure 76a. NACA 23012 With 22.5-min Glaze Ice Repeatability, MVD = 20 μm

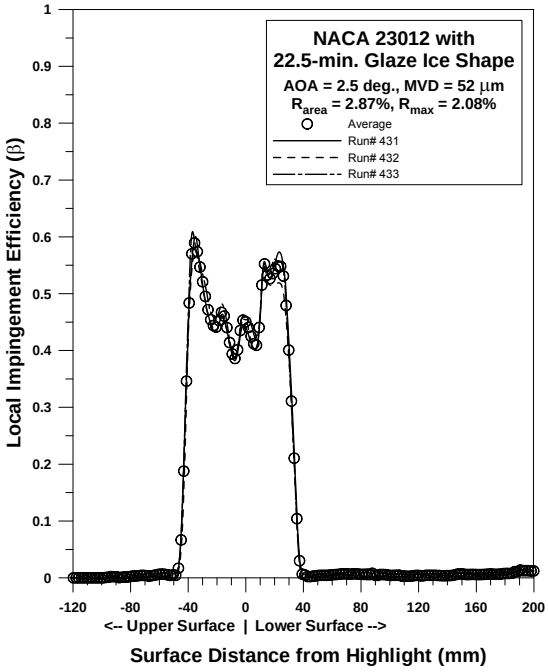

Figure 76b. NACA 23012 With 22.5-min Glaze Ice Repeatability, MVD = 52 μm

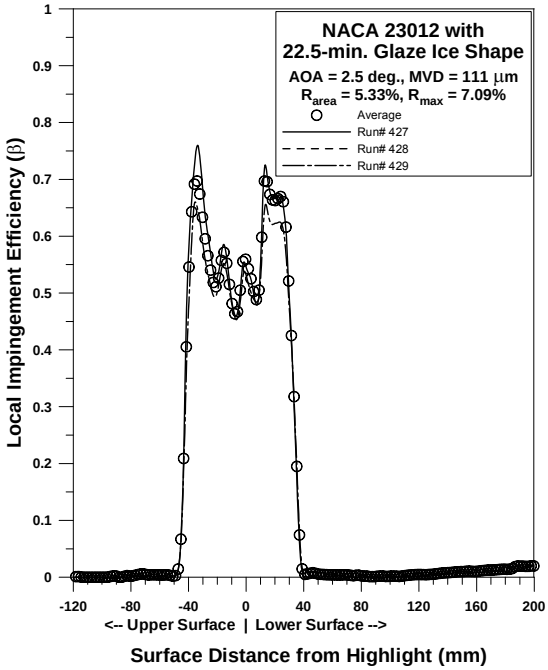

Figure 76c. NACA 23012 With 22.5-min Glaze Ice Repeatability, MVD = 111 μm

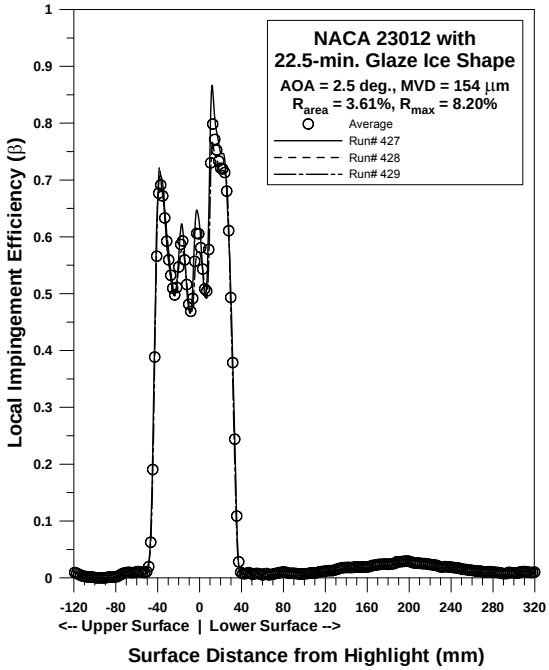

Figure 76d. NACA 23012 With 22.5-min Glaze Ice Repeatability, MVD = 154 μm

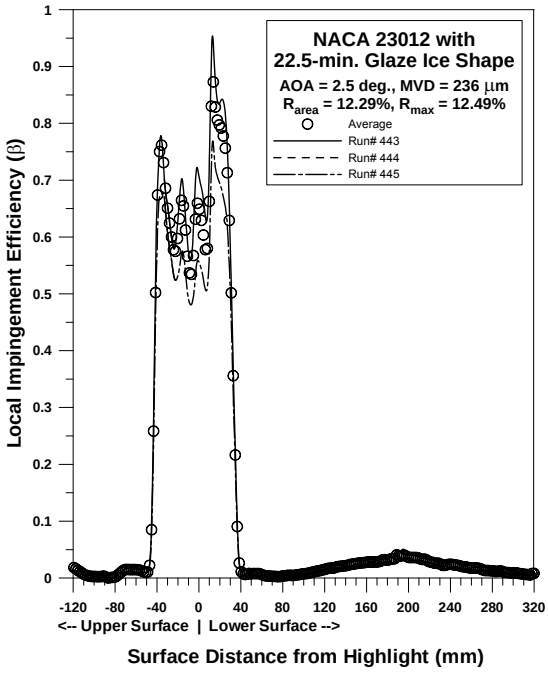

Figure 76e. NACA 23012 With 22.5-min Glaze Ice Repeatability, MVD = 236 μm

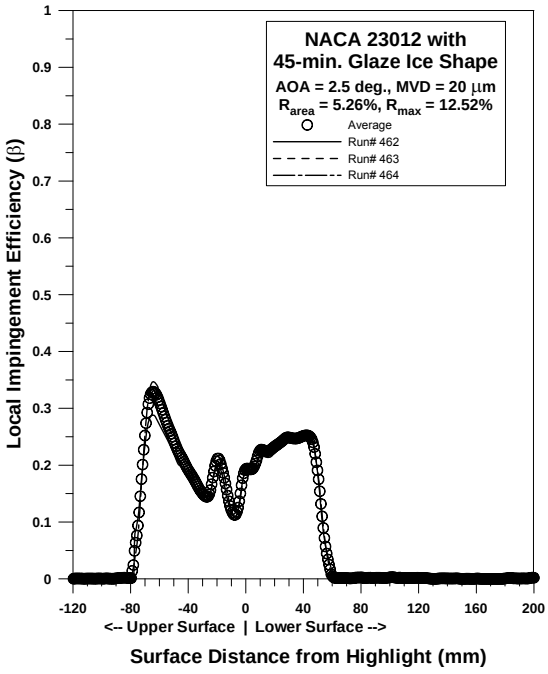

Figure 77a. NACA 23012 With 45-min Glaze Ice Repeatability, MVD = 20 μm

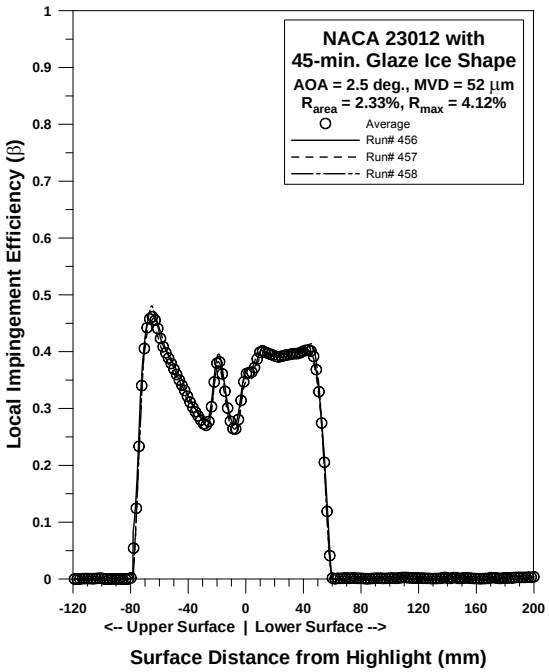

Figure 77b. NACA 23012 With 45-min Glaze Ice Repeatability, MVD = 52 μm

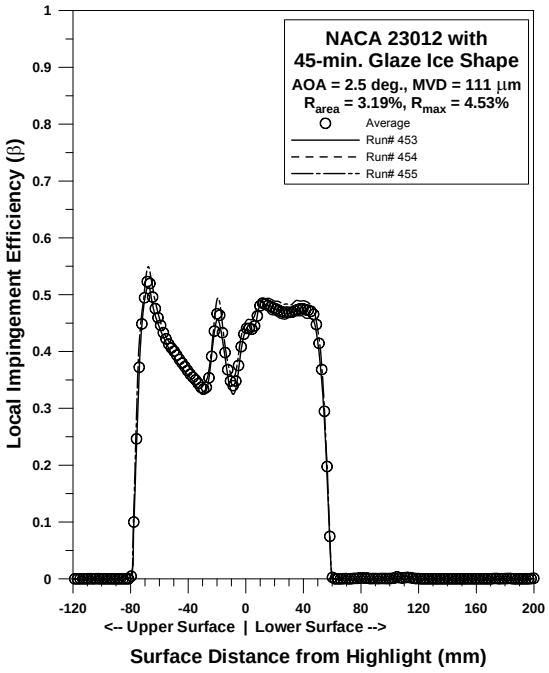

Figure 77c. NACA 23012 With 45-min Glaze Ice Repeatability, MVD = 111 μm

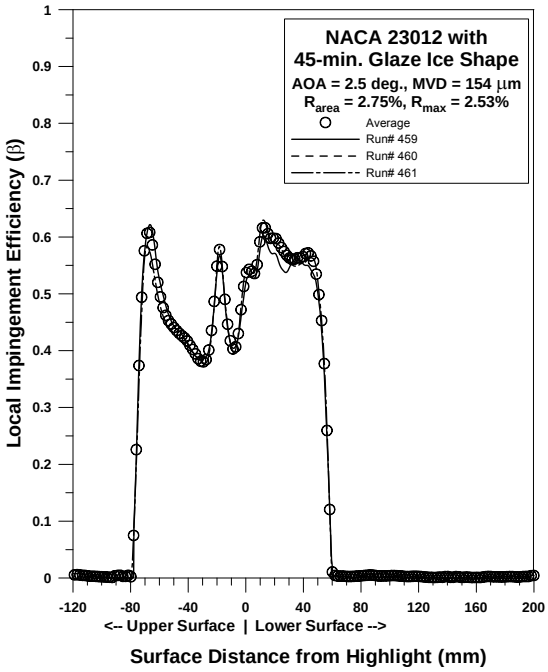

Figure 77d. NACA 23012 With 45-min Glaze Ice Repeatability, MVD = 154 μm

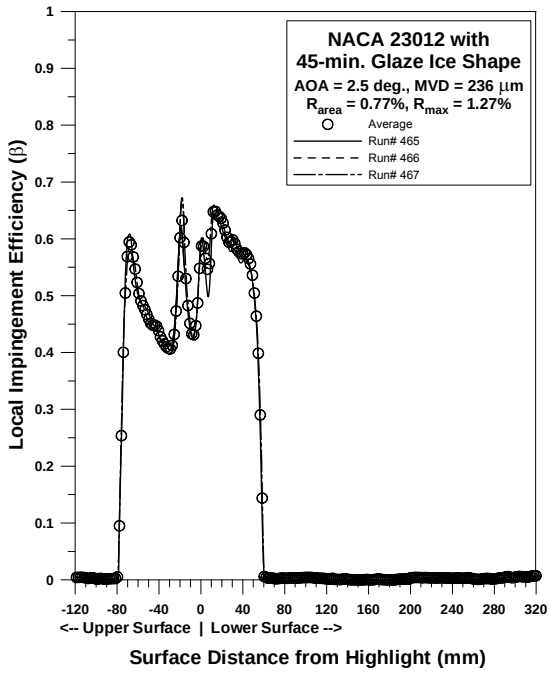

Figure 77e. NACA 23012 With 45-min Glaze Ice Repeatability, MVD = 236 μm

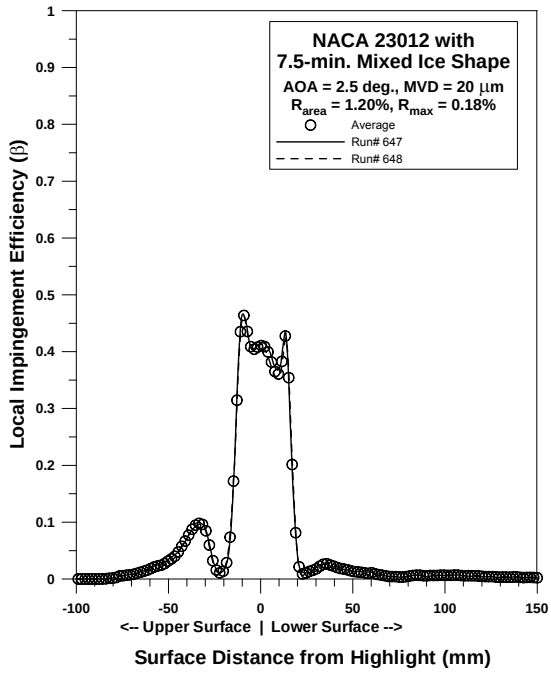

Figure 78a. NACA 23012 With 7.5-min Mixed Ice Repeatability, MVD = 20 μm

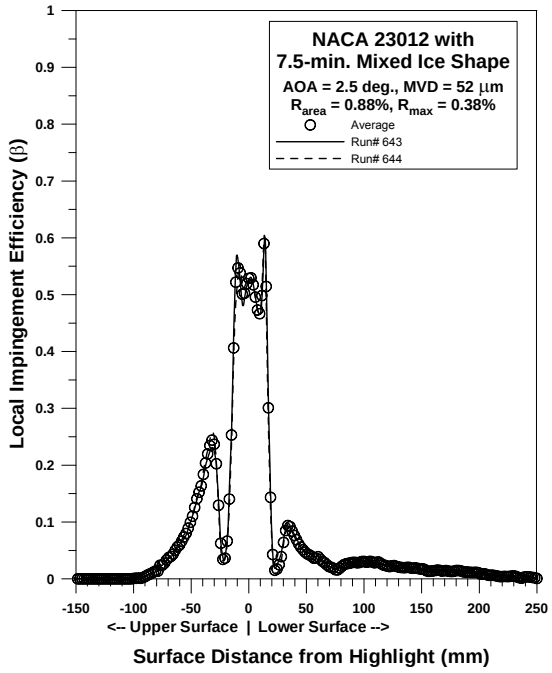

Figure 78b. NACA 23012 With 7.5-min Mixed Ice Repeatability, MVD = 52 μm

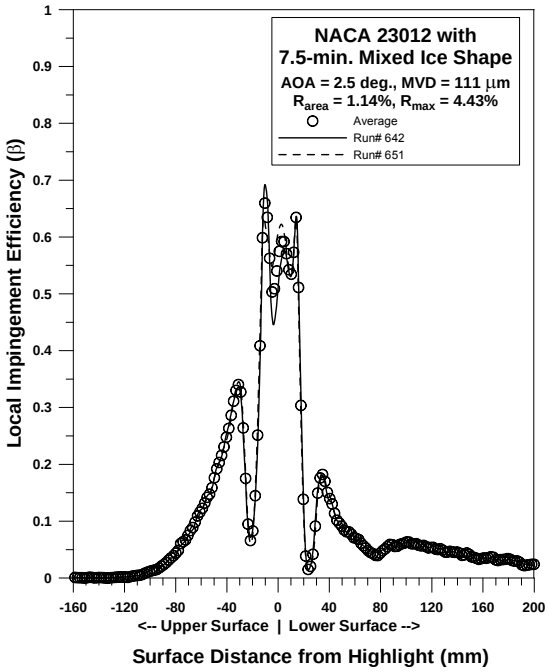

Figure 78c. NACA 23012 With 7.5-min Mixed Ice Repeatability, MVD = 111 μm

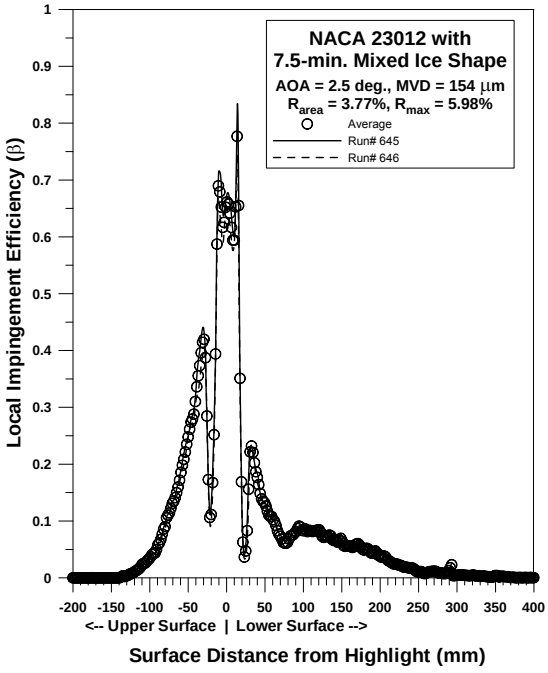

Figure 78d. NACA 23012 With 7.5-min Mixed Ice Repeatability, MVD = 154 μm

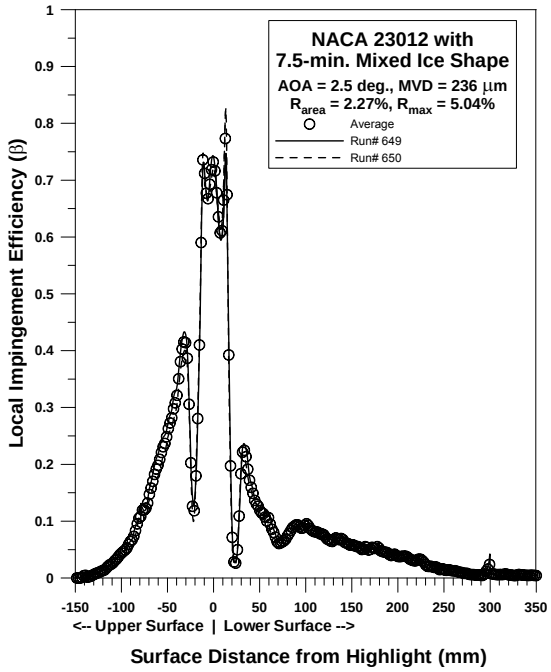

Figure 78e. NACA 23012 With 7.5-min Mixed Ice Repeatability, MVD = 236 μm

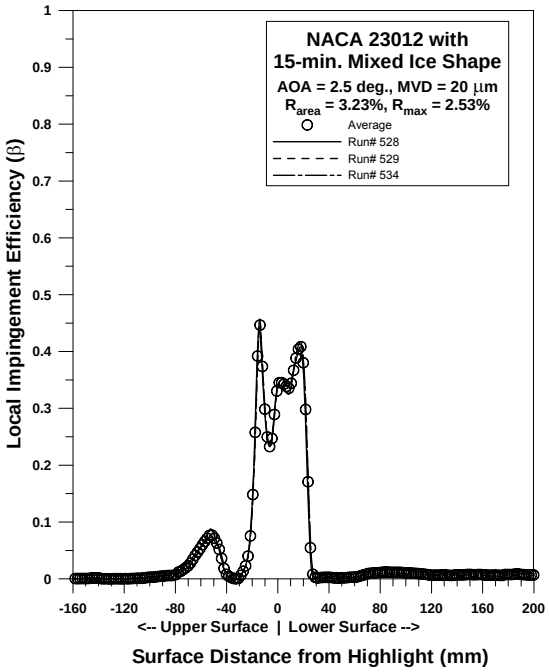

Figure 79a. NACA 23012 With 15-min Mixed Ice Repeatability, MVD = 20 μm

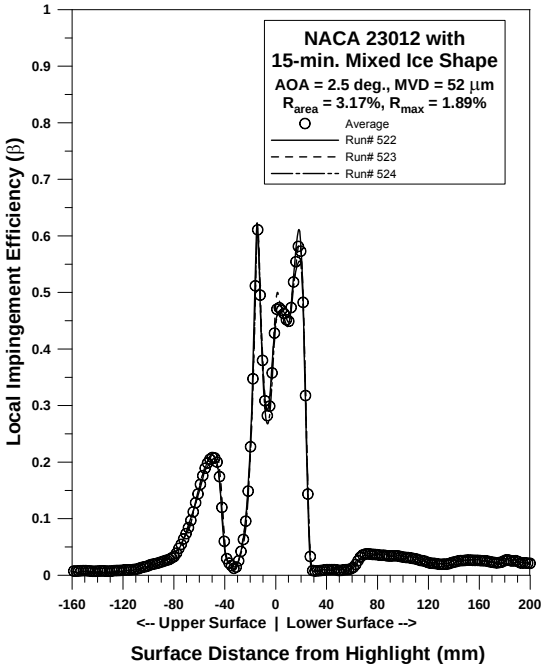

Figure 79b. NACA 23012 With 15-min Mixed Ice Repeatability, MVD = 52 μm

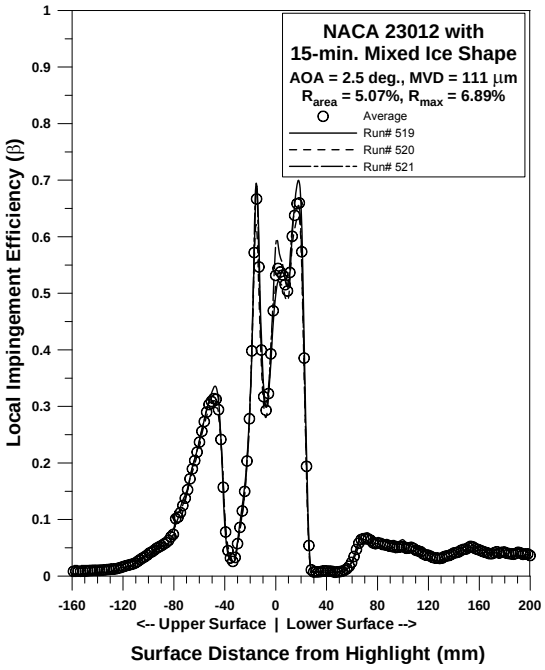

Figure 79c. NACA 23012 With 15-min Mixed Ice Repeatability, MVD = 111 μm

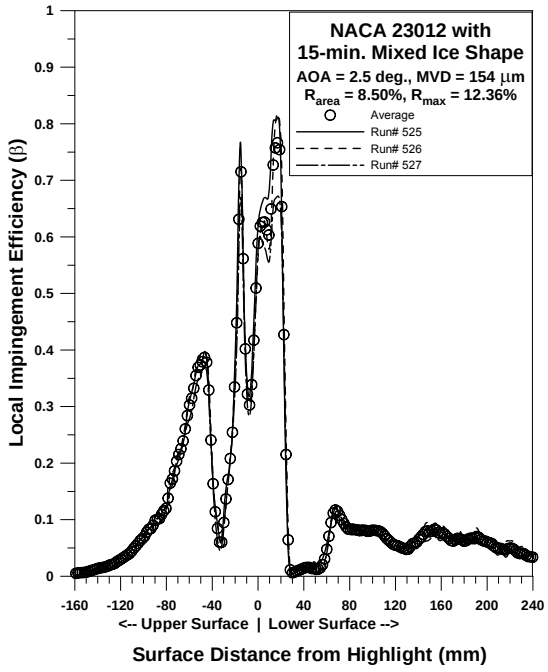

Figure 79d. NACA 23012 With 15-min Mixed Ice Repeatability, MVD = 154 μm

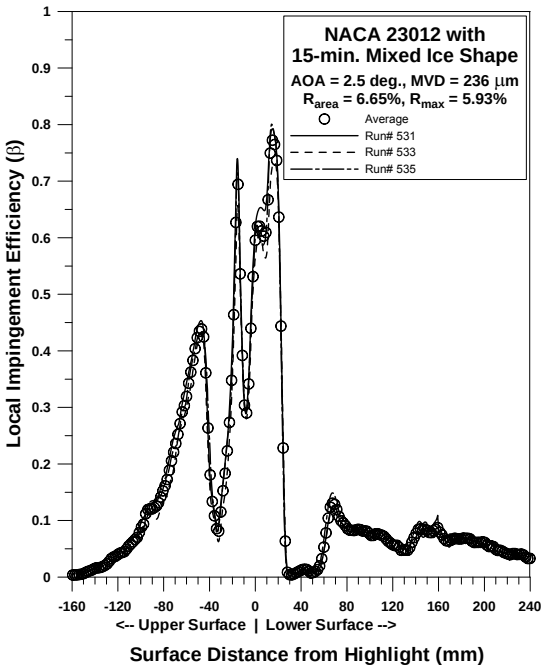

Figure 79e. NACA 23012 With 15-min Mixed Ice Repeatability, MVD = 236 μm

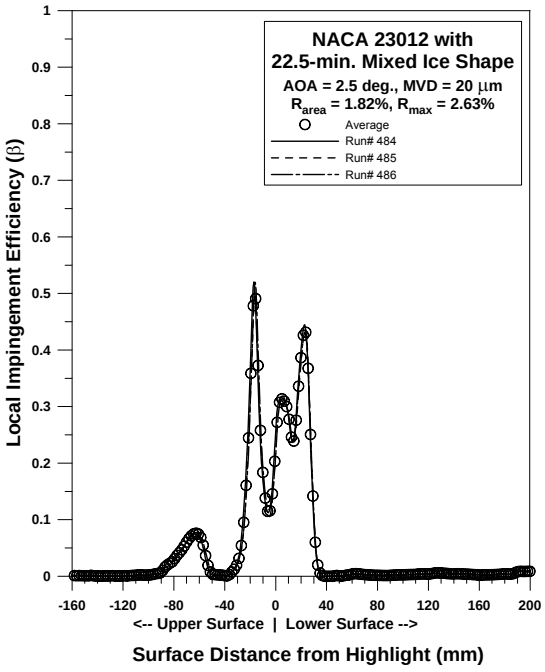

Figure 80a. NACA 23012 With 22.5-min Mixed Ice Repeatability, MVD = 20 μm

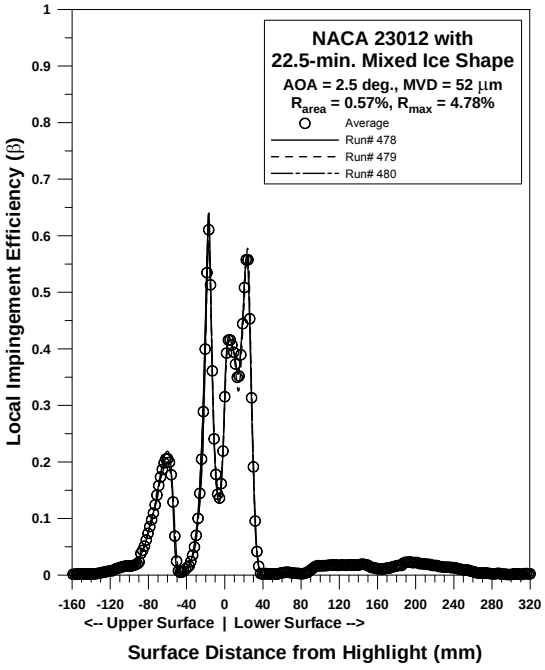

Figure 80b. NACA 23012 With 22.5-min Mixed Ice Repeatability, MVD = 52 μm

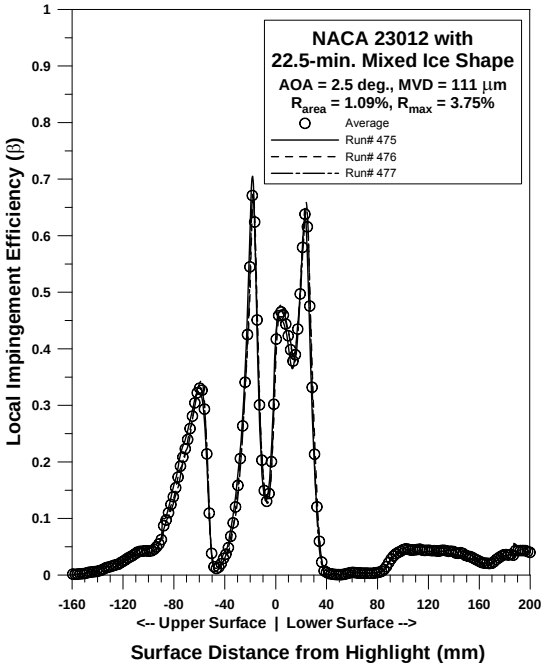

Figure 80c. NACA 23012 With 22.5-min Mixed Ice Repeatability, MVD = 111 μm

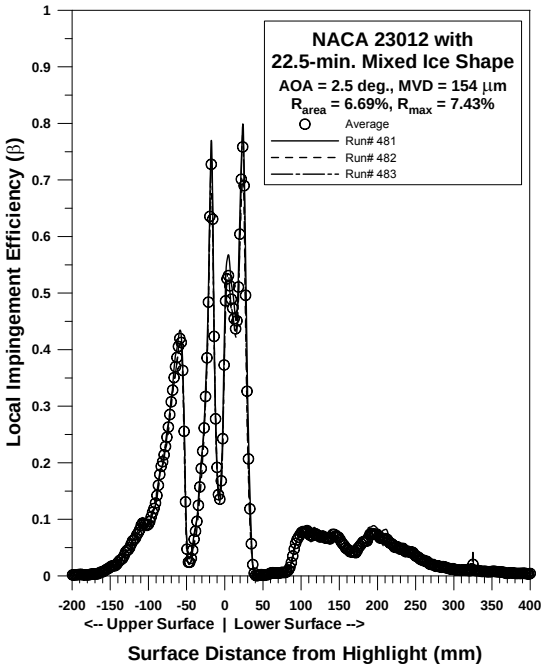

Figure 80d. NACA 23012 With 22.5-min Mixed Ice Repeatability, MVD = 154 μm

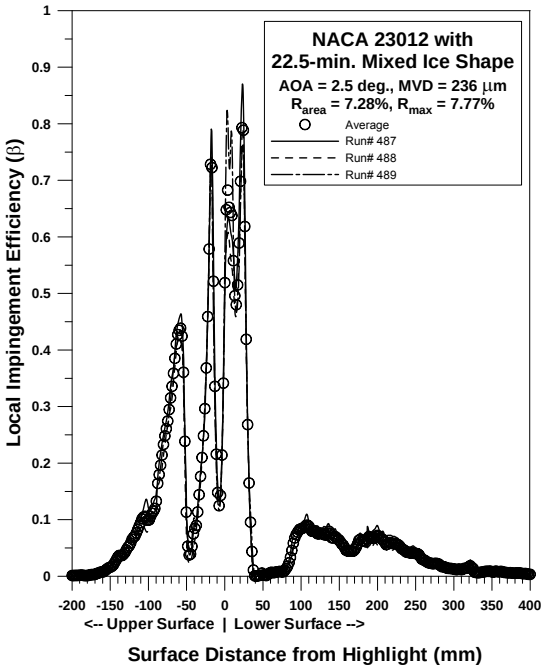

Figure 80e. NACA 23012 With 22.5-min Mixed Ice Repeatability, MVD = 236 μm

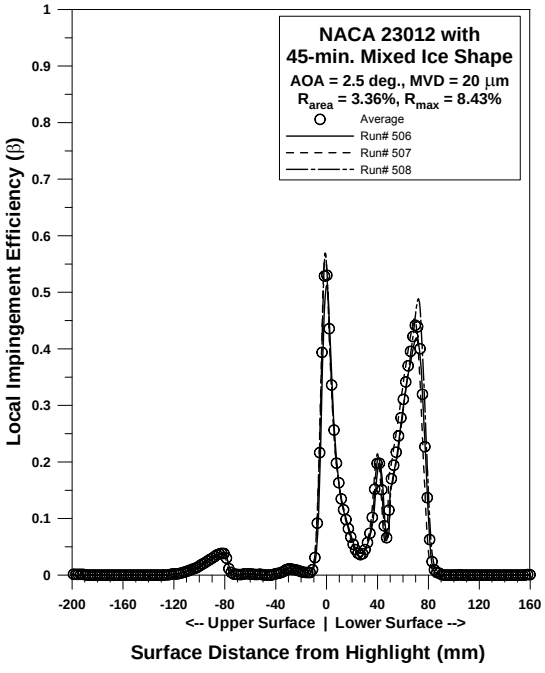

Figure 81a. NACA 23012 With 45-min Mixed Ice Repeatability, MVD = 20 μm

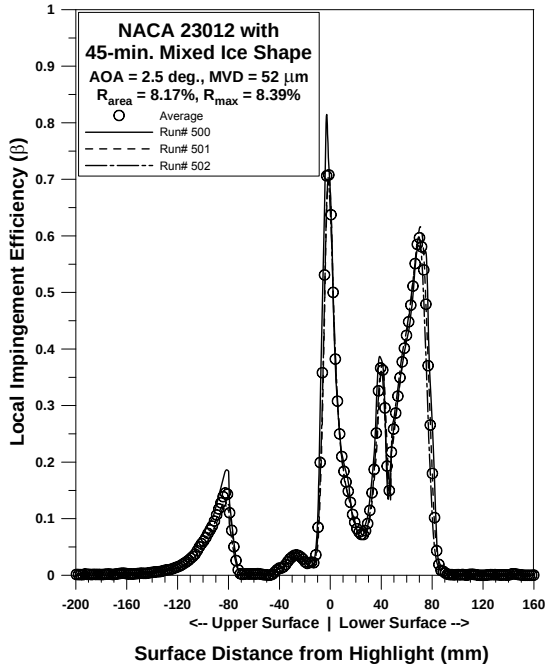

Figure 81b. NACA 23012 With 45-min Mixed Ice Repeatability, MVD = 52 μm

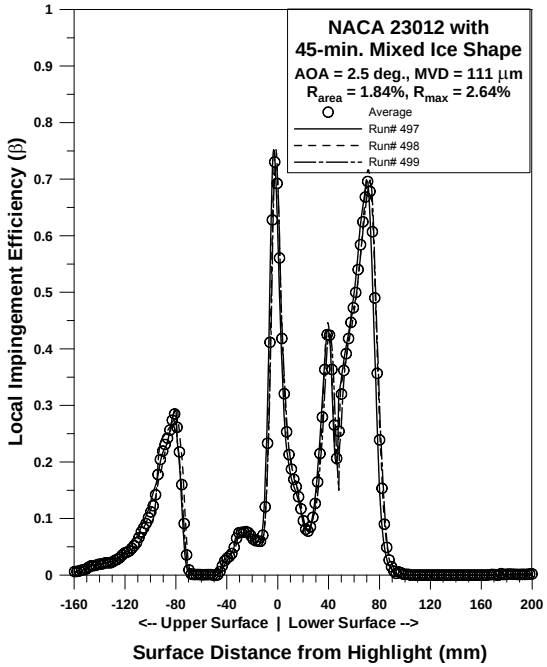

Figure 81c. NACA 23012 With 45-min Mixed Ice Repeatability, MVD = 111 μm

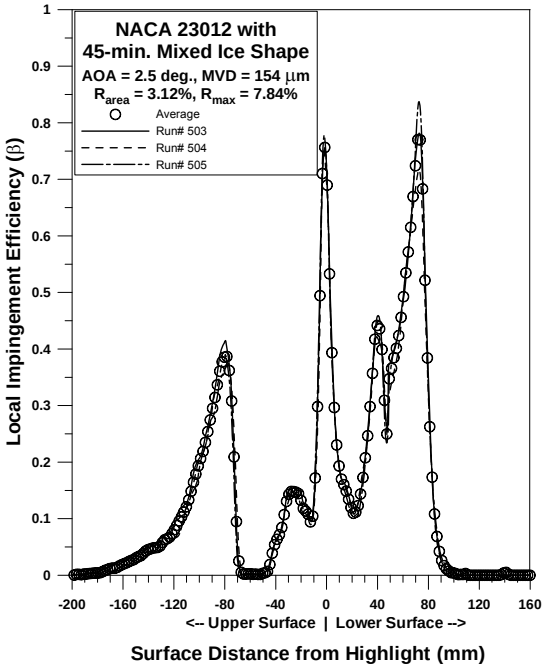

Figure 81d. NACA 23012 With 45-min Mixed Ice Repeatability, MVD = 154 μm

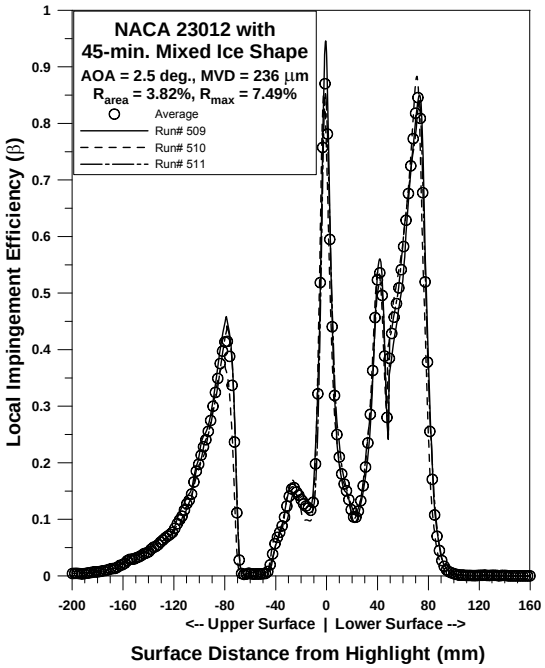

Figure 81e. NACA 23012 With 45-min Mixed Ice Repeatability, MVD = 236 μm

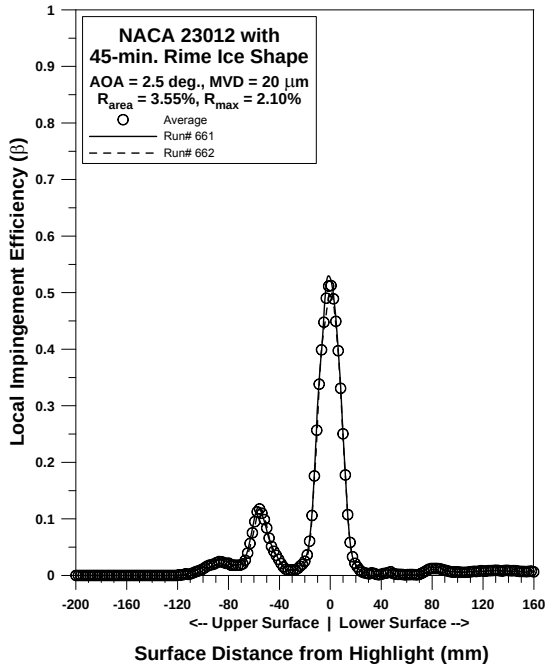

Figure 82a. NACA 23012 With 45-min Rime Ice Repeatability, MVD = 20 μm

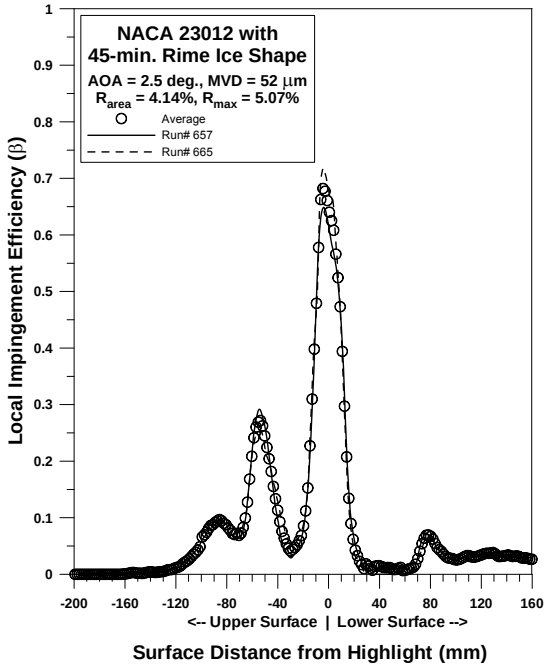

Figure 82b. NACA 23012 With 45-min Rime Ice Repeatability, MVD = 52 μm

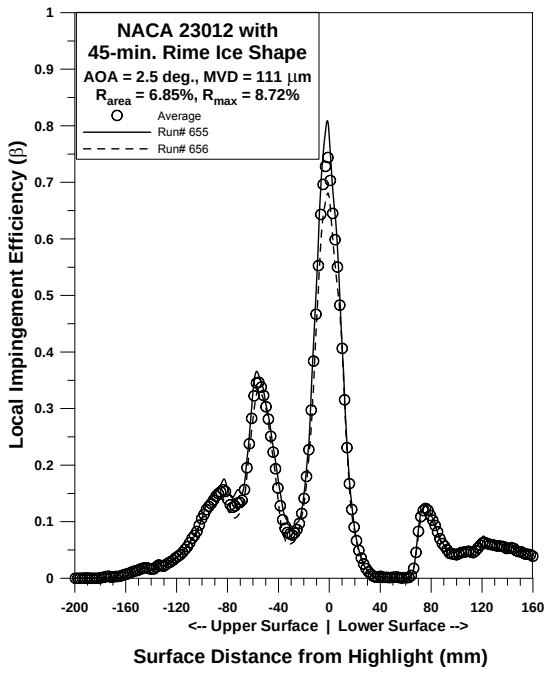

Figure 82c. NACA 23012 With 45-min Rime Ice Repeatability, MVD = 111 μm

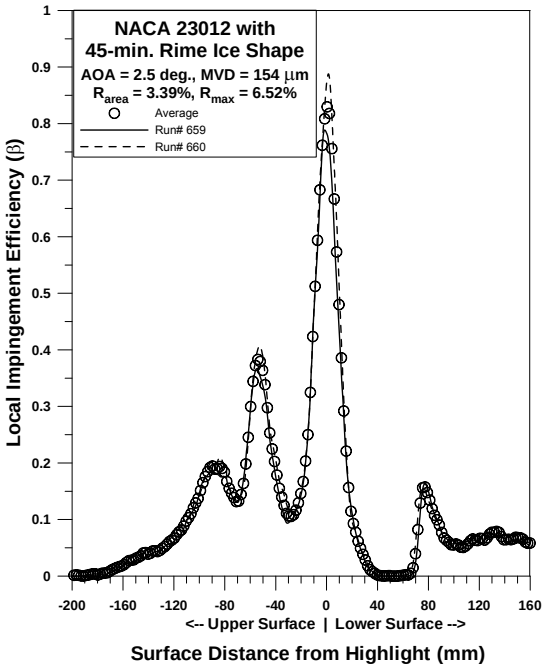

Figure 82d. NACA 23012 With 45-min Rime Ice Repeatability, MVD = 154 μm

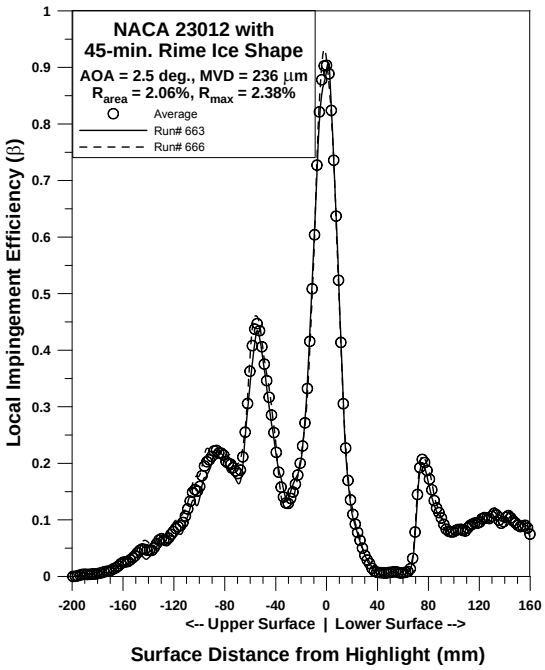

Figure 82e. NACA 23012 With 45-min Rime Ice Repeatability, MVD = 236 μm

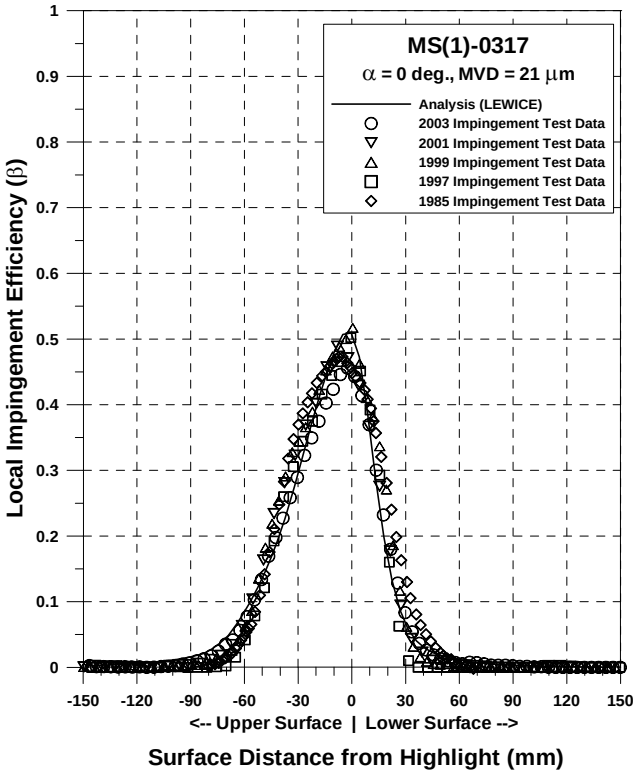

Figure 83. Impingement Efficiency Distribution for MS-317 Airfoil From 1985, 1997, 1999, 2001, and 2003 Entries (c = 36 in., V_∞ = 175 mph, AOA = 0°, MVD = 20-21 μm)

7.3.2 Experimental and LEWICE Impingement Data.

Comparisons of LEWICE and experimental impingement data are provided in figures 84a through 94e for all tested configurations. The experimental data presented were obtained by averaging results from repeated tests conducted for each geometry and test condition. All experimental data presented were reduced with the CCD reflectometer. Impingement data reduced using the laser reflectometer were practically identical to those obtained with the CCD data reduction system. The main difference between the CCD and laser reflectometer data occurred in regions between the ice shape horns where creases were present in the blotter paper. The laser reflectometer, which relies on point reflectance measurements, was more sensitive to the crease formation than the CCD system. Consequently, the impingement curves obtained from the laser reflectometer data reduction were not as smooth in the region between the ice shape horns as those from the CCD system. The LEWICE impingement curves were generated by NASA personnel using LEWICE 1.6. As discussed in section 6, the LEWICE analyses were performed by NASA personnel using 27-bin approximations of the spray cloud drop distributions measured with the FSSP and OAPs during the experimental investigation.

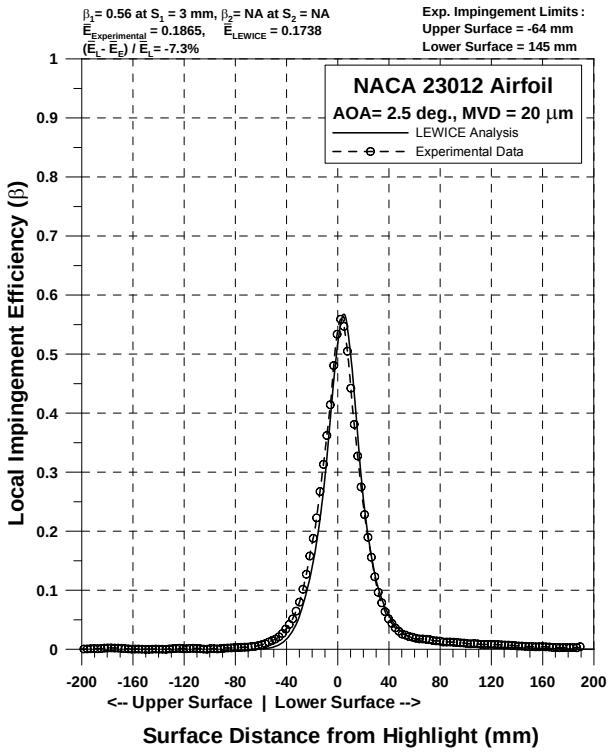

Figure 84a. Impingement Efficiency Distribution for NACA 23012 Airfoil (c = 36 in., V_∞ = 175 mph, AOA = 2.5°, MVD = 20 μm)

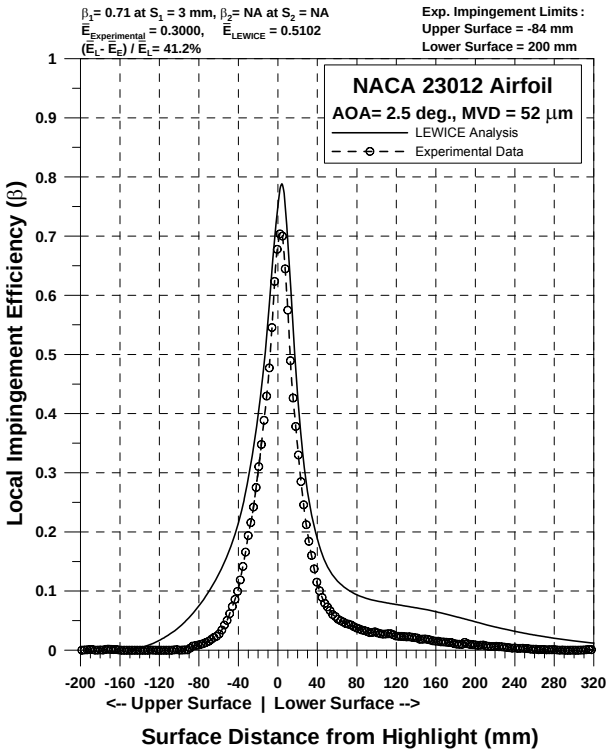

Figure 84b. Impingement Efficiency Distribution for NACA 23012 Airfoil (c = 36 in., V_∞ = 175 mph, AOA = 2.5°, MVD = 52 μm)

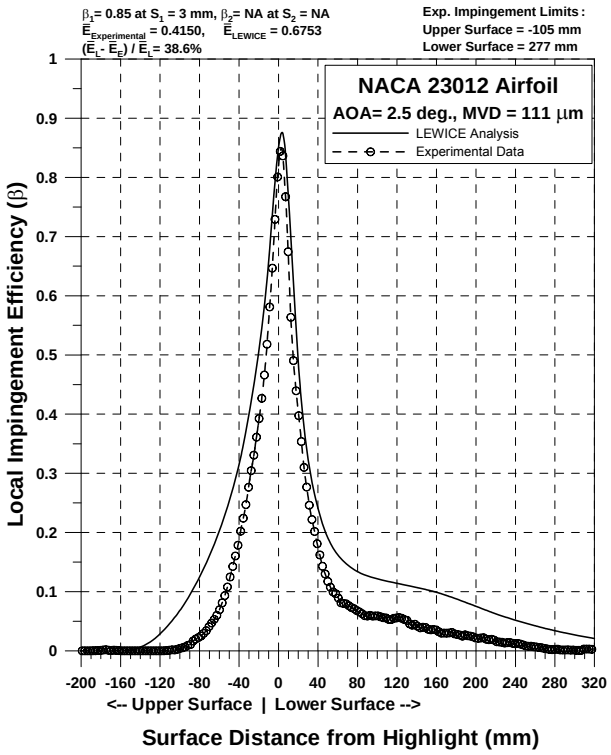

Figure 84c. Impingement Efficiency Distribution for NACA 23012 Airfoil (c = 36 in., V_∞ = 175 mph, AOA = 2.5°, MVD = 111 μm)

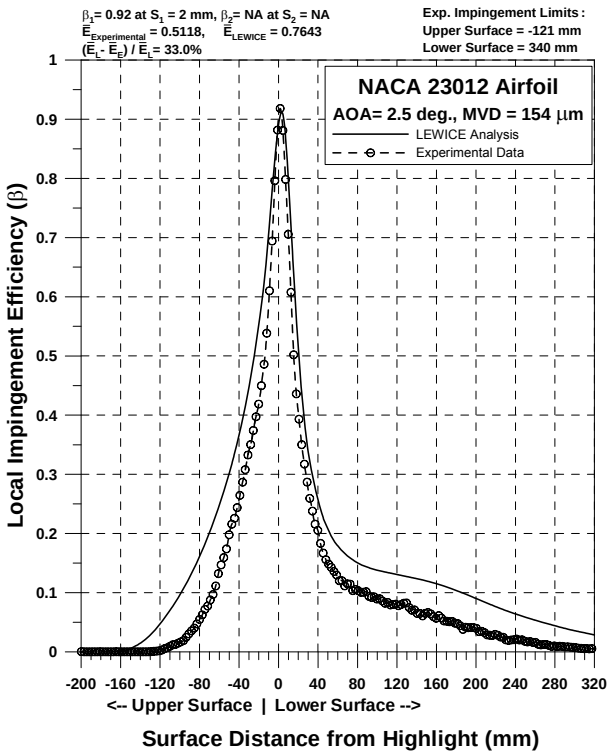

Figure 84d. Impingement Efficiency Distribution for NACA 23012 Airfoil (c = 36 in., V_∞ = 175 mph, AOA = 2.5°, MVD = 154 μm)

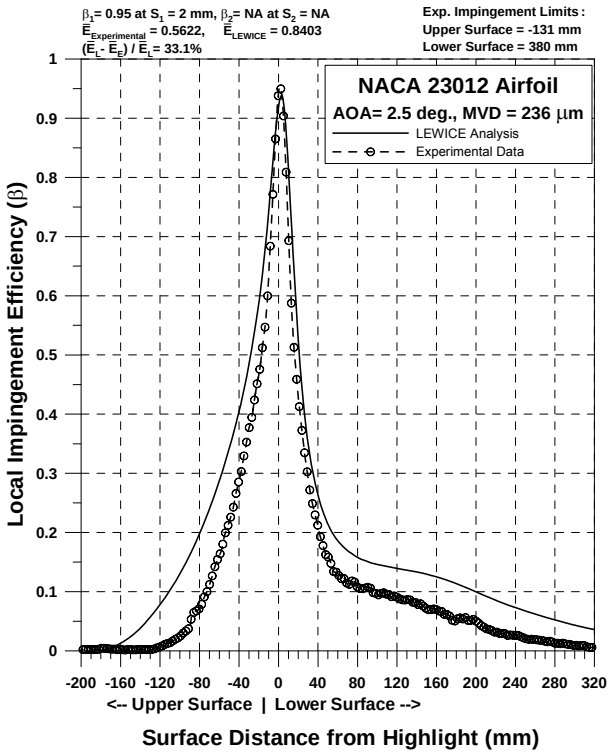

Figure 84e. Impingement Efficiency Distribution for NACA 23012 Airfoil (c = 36 in., V_∞ = 175 mph, AOA = 2.5°, MVD = 236 μm)

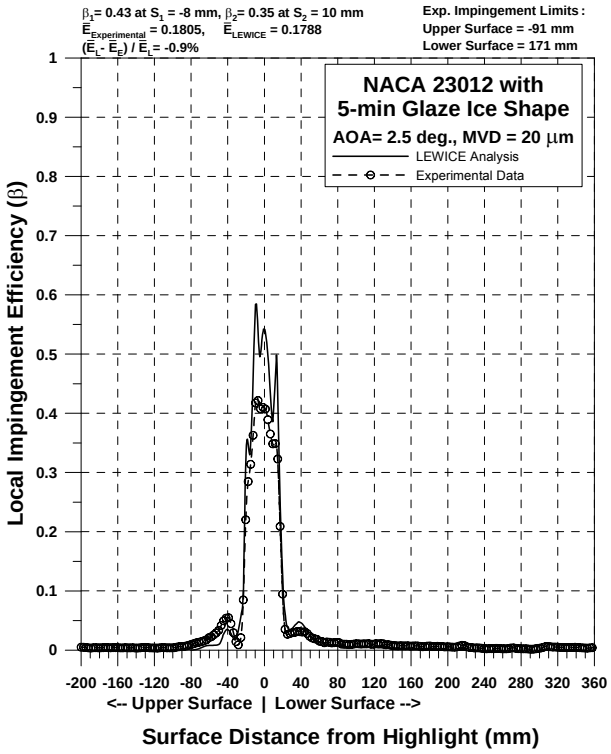

Figure 85a. Impingement Efficiency Distribution for NACA 23012 Airfoil With 5-min Glaze Ice Shape (c = 36 in., V_∞ = 175 mph, AOA = 2.5°, MVD = 20 μm)

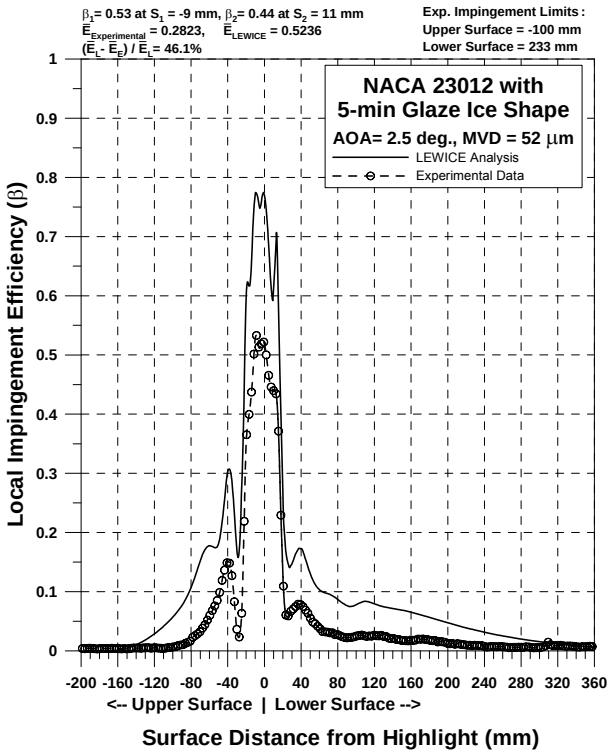

Figure 85b. Impingement Efficiency Distribution for NACA 23012 Airfoil With 5-min Glaze Ice Shape (c = 36 in., V_∞ = 175 mph, AOA = 2.5°, MVD = 52 μm)

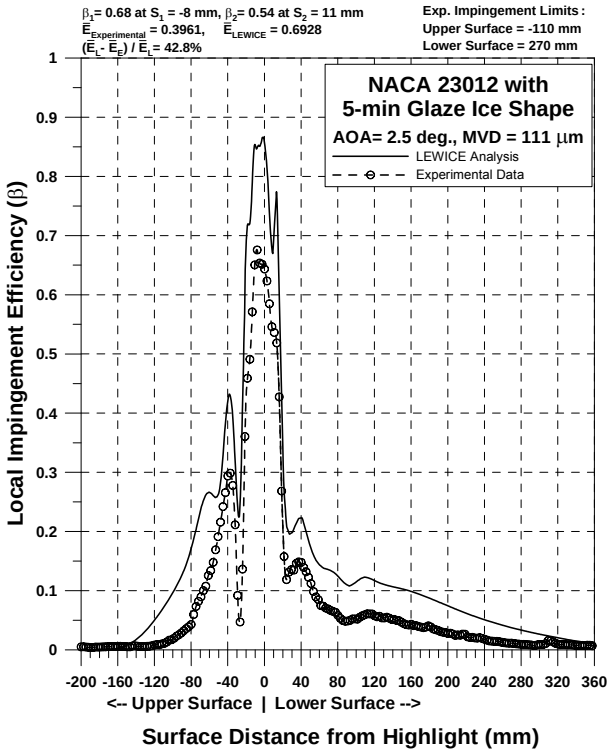

Figure 85c. Impingement Efficiency Distribution for NACA 23012 Airfoil With 5-min Glaze Ice Shape (c = 36 in., V_∞ = 175 mph, AOA = 2.5°, MVD = 111 μm)

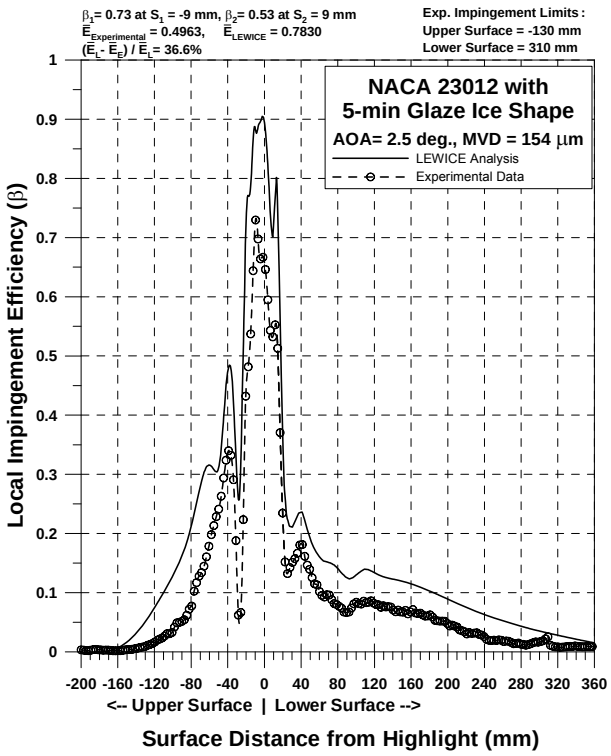

Figure 85d. Impingement Efficiency Distribution for NACA 23012 Airfoil With 5-min Glaze Ice Shape (c = 36 in., V_∞ = 175 mph, AOA = 2.5°, MVD = 154 μm)

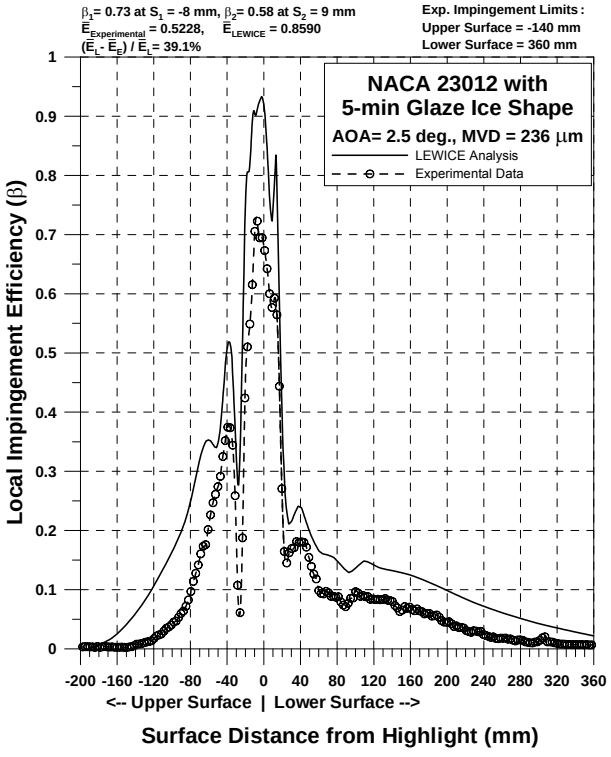

Figure 85e. Impingement Efficiency Distribution for NACA 23012 Airfoil With 5-min Glaze Ice Shape (c = 36 in., V_∞ = 175 mph, AOA = 2.5°, MVD = 236 μm)

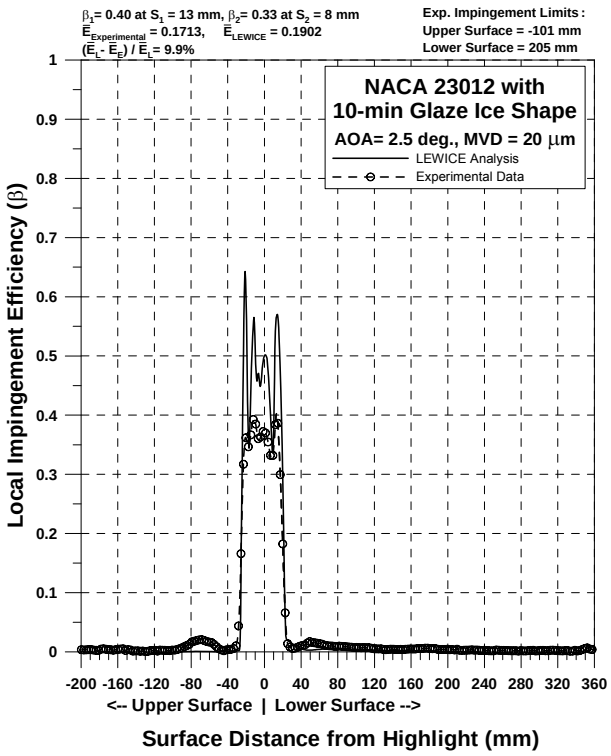

Figure 86a. Impingement Efficiency Distribution for NACA 23012 Airfoil With 10-min Glaze Ice Shape (c = 36 in., V_∞ = 175 mph, AOA = 2.5°, MVD = 20 μm)

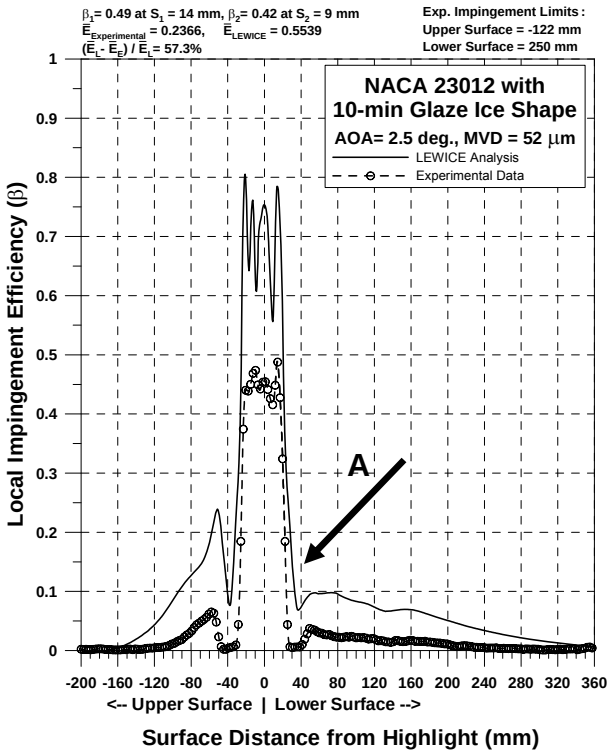

Figure 86b. Impingement Efficiency Distribution for NACA 23012 Airfoil With 10-min Glaze Ice Shape (c = 36 in., V_∞ = 175 mph, AOA = 2.5°, MVD = 52 μm)

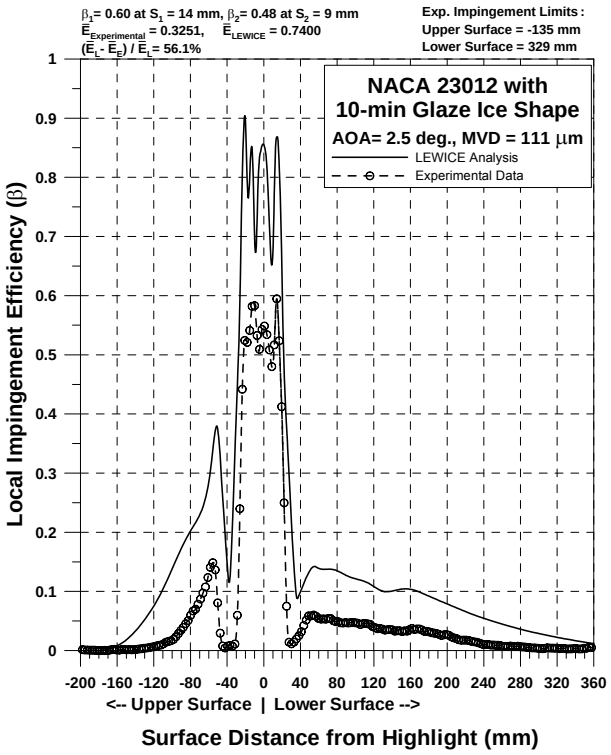

Figure 86c. Impingement Efficiency Distribution for NACA 23012 Airfoil With 10-min Glaze Ice Shape (c = 36 in., V_∞ = 175 mph, AOA = 2.5°, MVD = 111 μm)

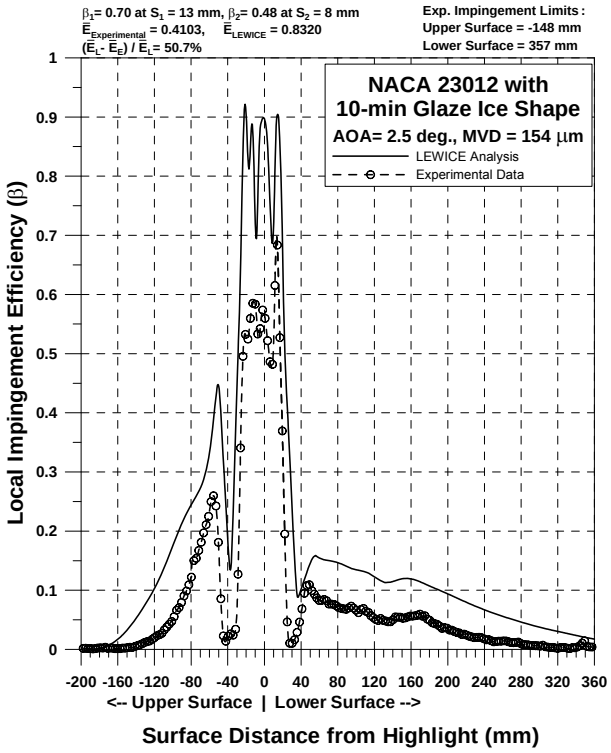

Figure 86d. Impingement Efficiency Distribution for NACA 23012 Airfoil With 10-min Glaze Ice Shape (c = 36 in., V_∞ = 175 mph, AOA = 2.5°, MVD = 154 μm)

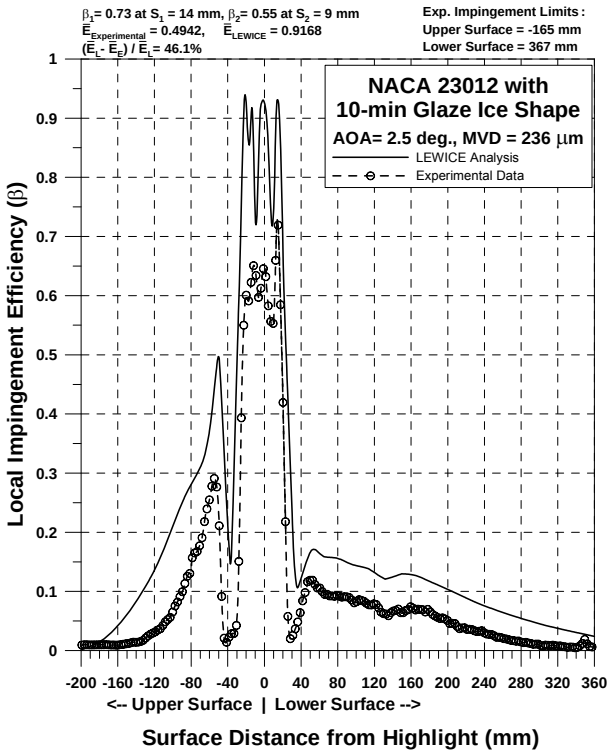

Figure 86e. Impingement Efficiency Distribution for NACA 23012 Airfoil With 10-min Glaze Ice Shape (c = 36 in., V_∞ = 175 mph, AOA = 2.5°, MVD = 236 μm)

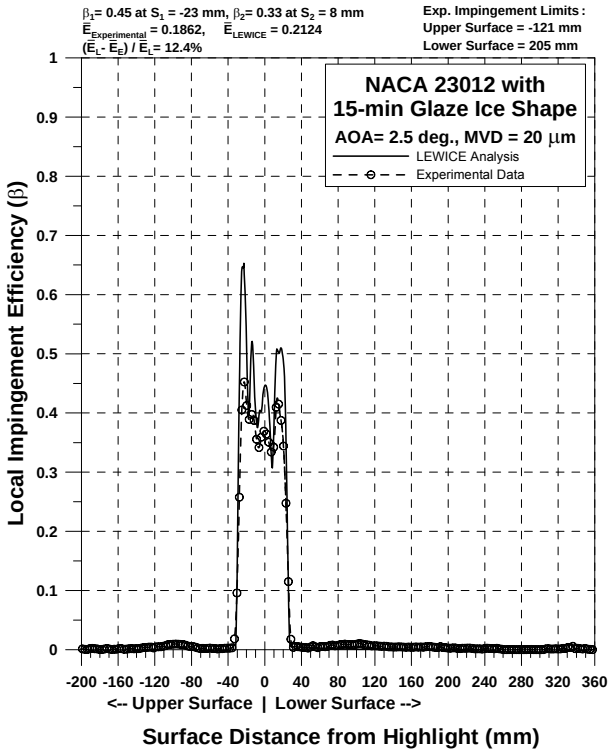

Figure 87a. Impingement Efficiency Distribution for NACA 23012 Airfoil With 15-min Glaze Ice Shape (c = 36 in., V_∞ = 175 mph, AOA = 2.5°, MVD = 20 μm)

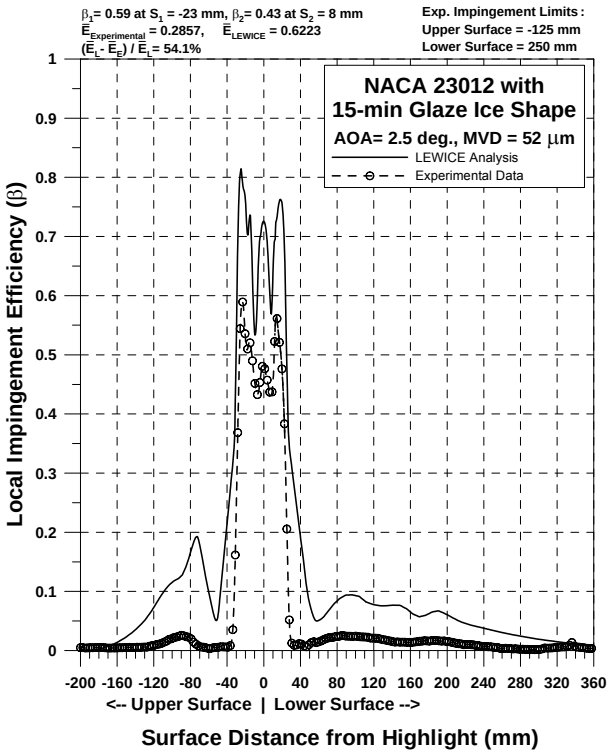

Figure 87b. Impingement Efficiency Distribution for NACA 23012 Airfoil With 15-min Glaze Ice Shape (c = 36 in., V_∞ = 175 mph, AOA = 2.5°, MVD = 52 μm)

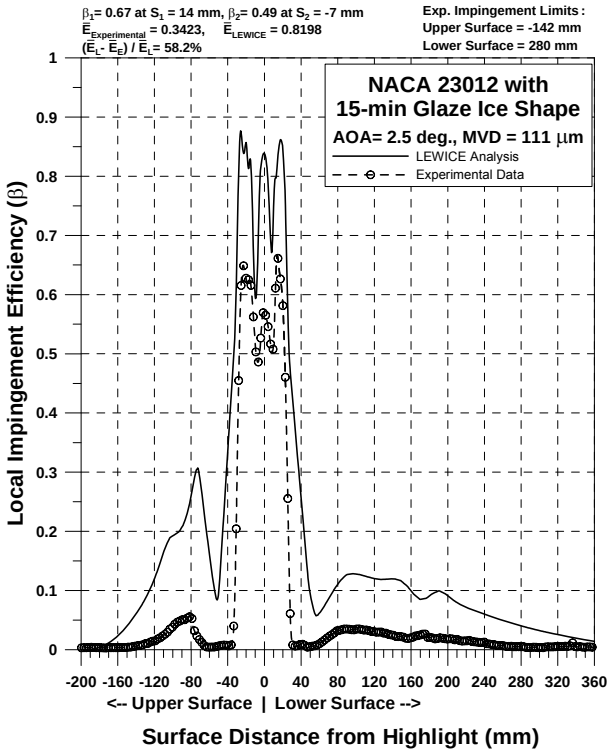

Figure 87c. Impingement Efficiency Distribution for NACA 23012 Airfoil With 15-min Glaze Ice Shape (c = 36 in., V_∞ = 175 mph, AOA = 2.5°, MVD = 111 μm)

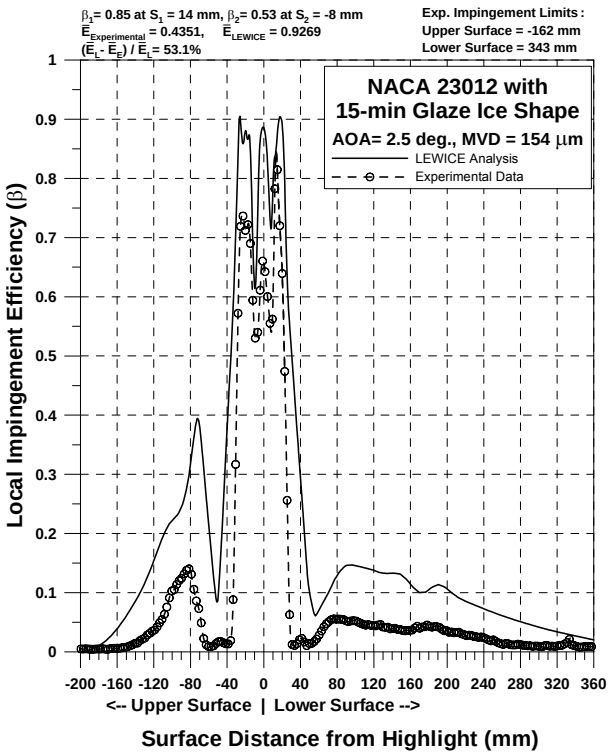

Figure 87d. Impingement Efficiency Distribution for NACA 23012 Airfoil With 15-min Glaze Ice Shape (c = 36 in., V_∞ = 175 mph, AOA = 2.5°, MVD = 154 μm)

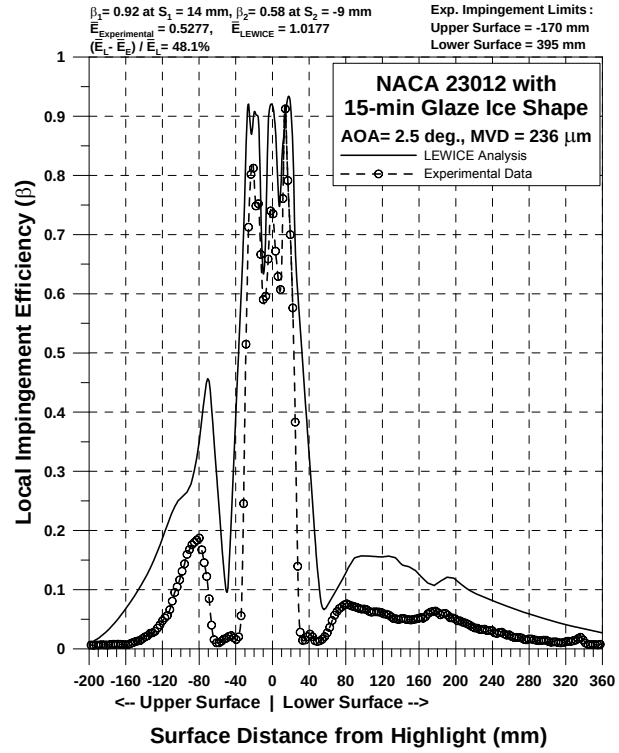

Figure 87e. Impingement Efficiency Distribution for NACA 23012 Airfoil With 15-min Glaze Ice Shape (c = 36 in., V_∞ = 175 mph, AOA = 2.5°, MVD = 236 μm)

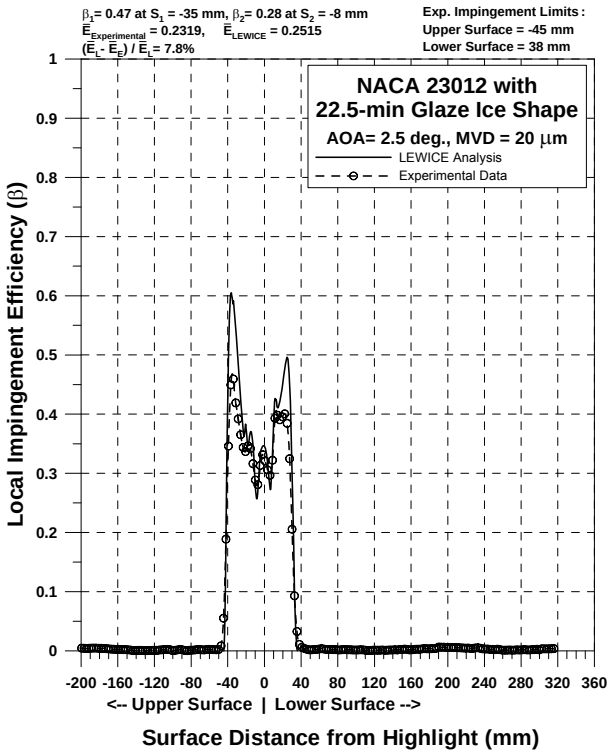

Figure 88a. Impingement Efficiency Distribution for NACA 23012 Airfoil With 22.5-min Glaze Ice Shape (c = 36 in., V_∞ = 175 mph, AOA = 2.5°, MVD = 20 μm)

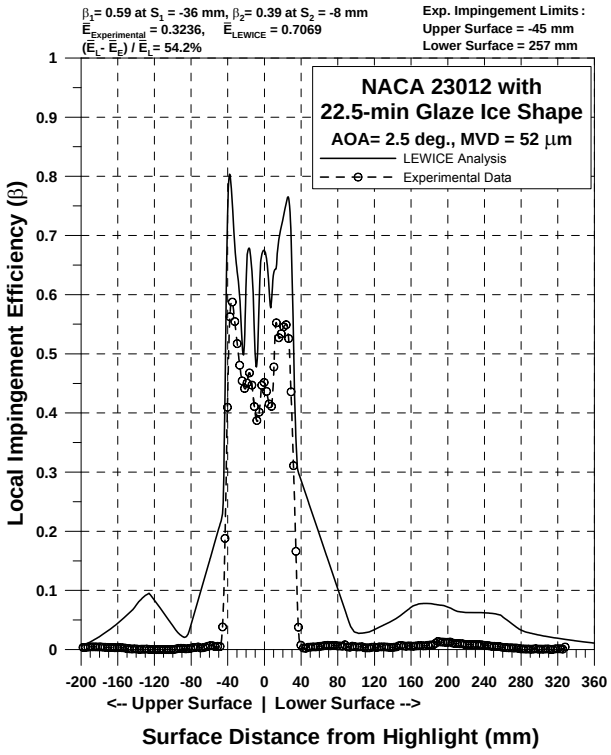

Figure 88b. Impingement Efficiency Distribution for NACA 23012 Airfoil With 22.5-min Glaze Ice Shape (c = 36 in., V_∞ = 175 mph, AOA = 2.5°, MVD = 52 μm)

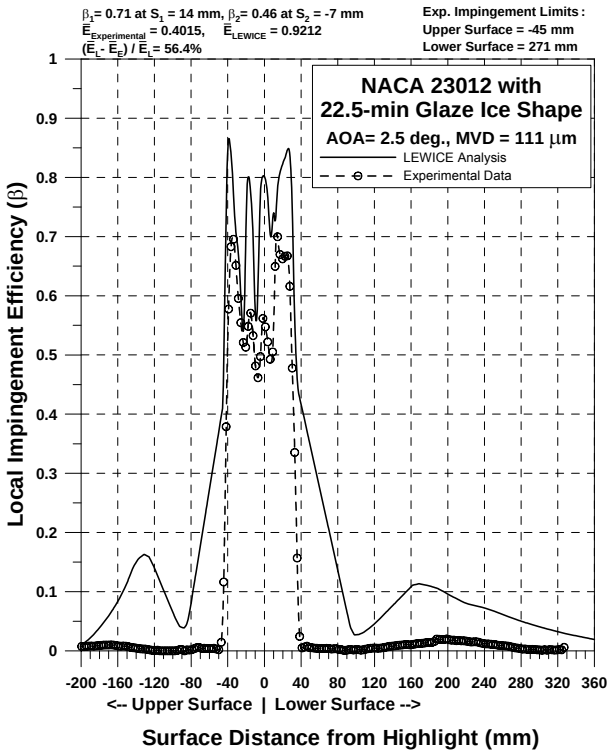

Figure 88c. Impingement Efficiency Distribution for NACA 23012 Airfoil With 22.5-min Glaze Ice Shape (c = 36 in., V_∞ = 175 mph, AOA = 2.5°, MVD = 111 μm)

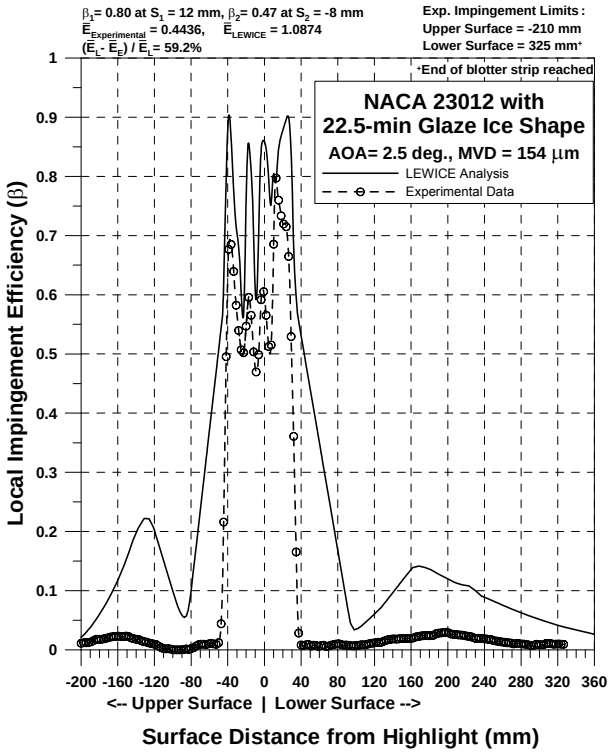

Figure 88d. Impingement Efficiency Distribution for NACA 23012 Airfoil With 22.5-min Glaze Ice Shape (c = 36 in., V_∞ = 175 mph, AOA = 2.5°, MVD = 154 μm)

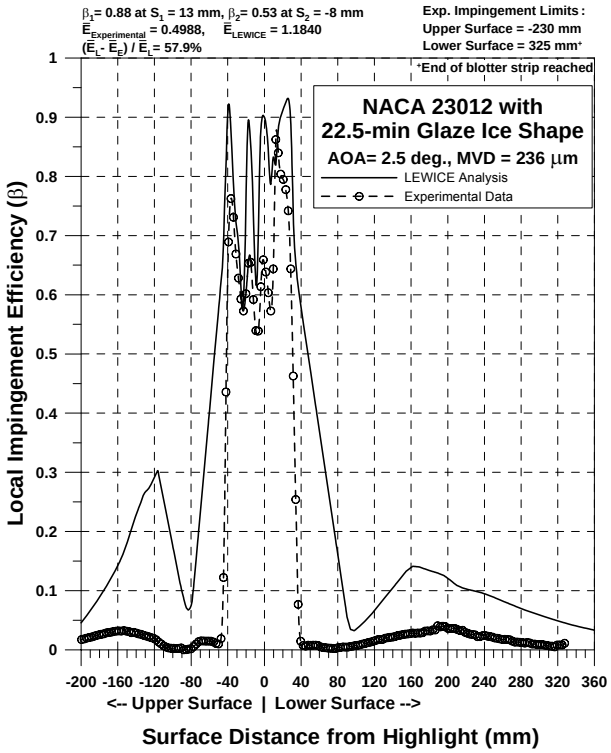

Figure 88e. Impingement Efficiency Distribution for NACA 23012 Airfoil With 22.5-min Glaze Ice Shape (c = 36 in., V_∞ = 175 mph, AOA = 2.5°, MVD = 236 μm)

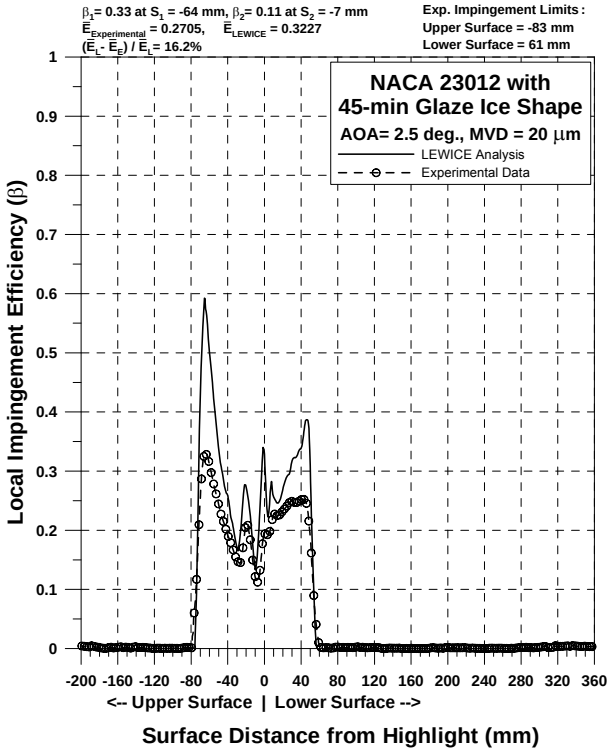

Figure 89a. Impingement Efficiency Distribution for NACA 23012 Airfoil With 45-min Glaze Ice Shape (c = 36 in., V_∞ = 175 mph, AOA = 2.5°, MVD = 20 μm)

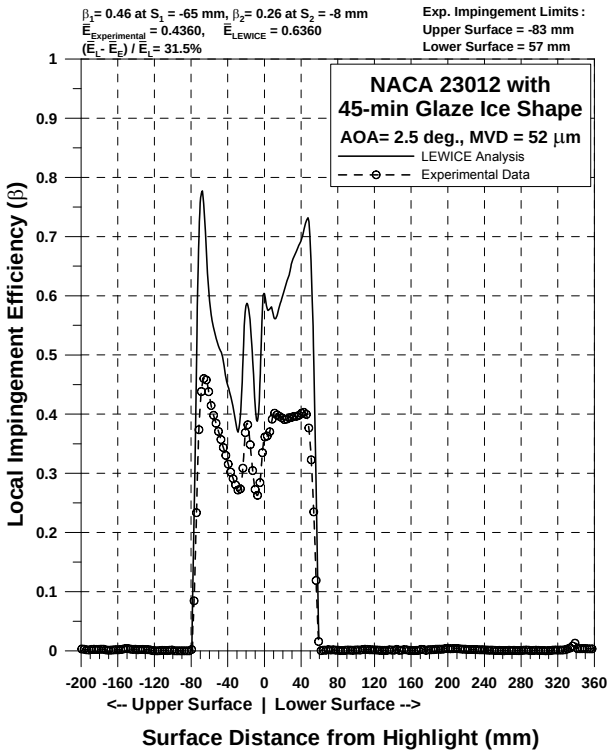

Figure 89b. Impingement Efficiency Distribution for NACA 23012 Airfoil With 45-min Glaze Ice Shape (c = 36 in., V_∞ = 175 mph, AOA = 2.5°, MVD = 52 μm)

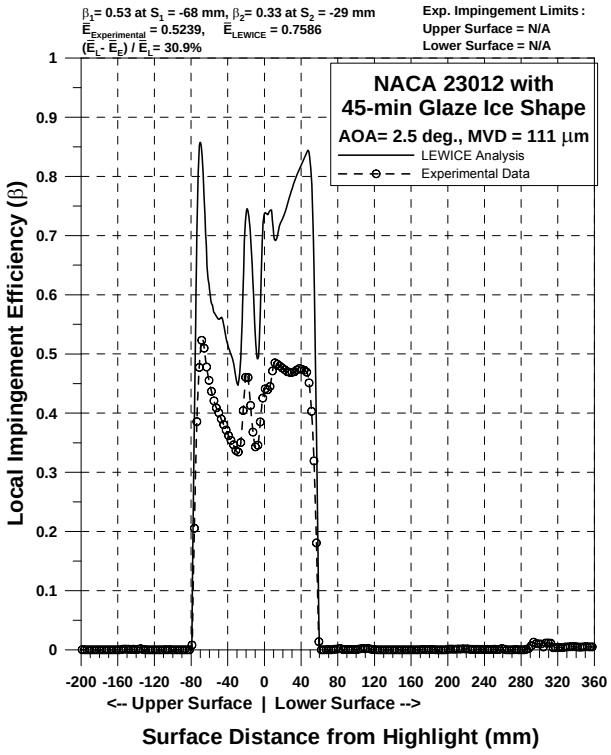

Figure 89c. Impingement Efficiency Distribution for NACA 23012 Airfoil With 45-min Glaze Ice Shape (c = 36 in., V_∞ = 175 mph, AOA = 2.5°, MVD = 111 μm)

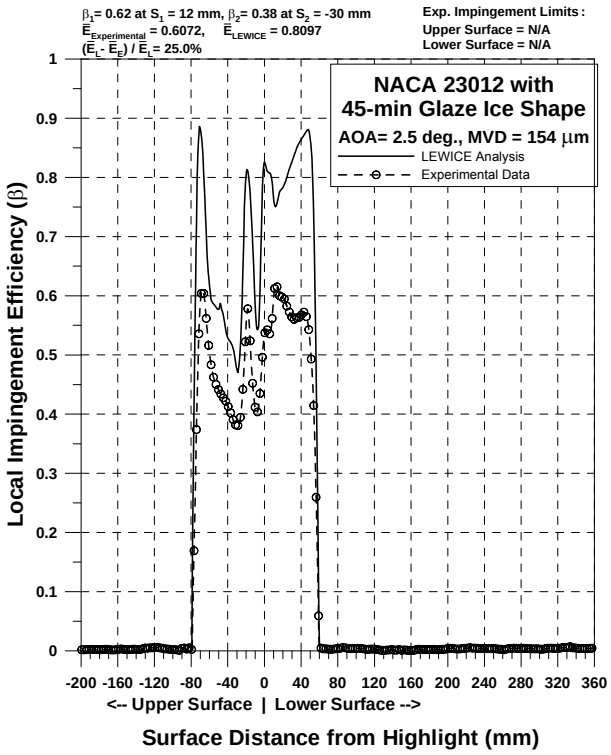

Figure 89d. Impingement Efficiency Distribution for NACA 23012 Airfoil With 45-min Glaze Ice Shape (c = 36 in., V_∞ = 175 mph, AOA = 2.5°, MVD = 154 μm)

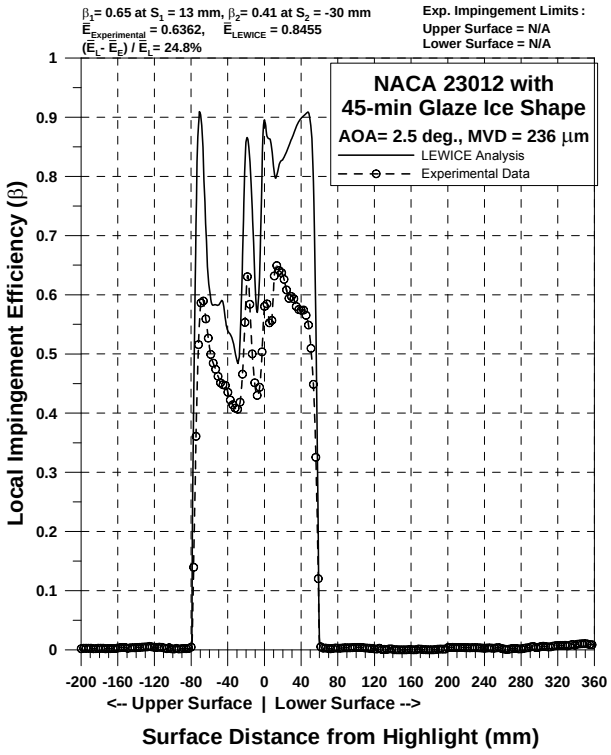

Figure 89e. Impingement Efficiency Distribution for NACA 23012 Airfoil With 45-min Glaze Ice Shape (c = 36 in., V_∞ = 175 mph, AOA = 2.5°, MVD = 236 μm)

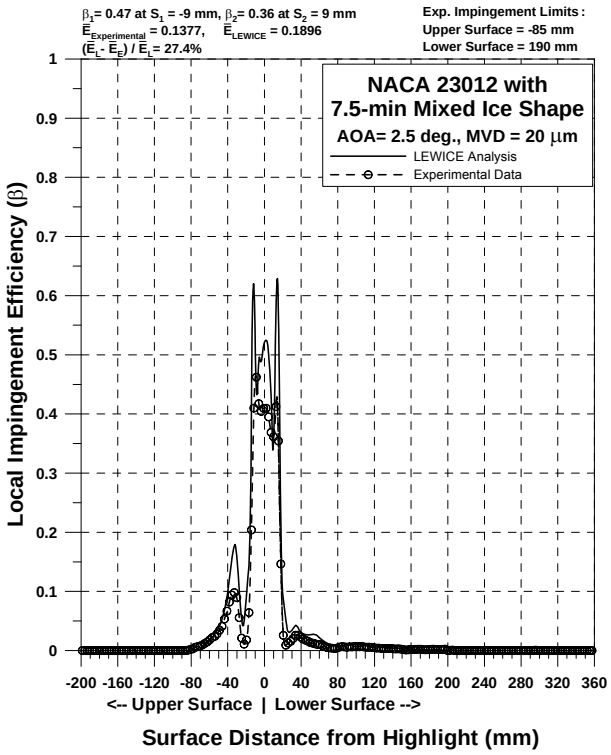

Figure 90a. Impingement Efficiency Distribution for NACA 23012 Airfoil With 7.5-min Mixed Ice Shape (c = 36 in., V_∞ = 175 mph, AOA = 2.5°, MVD = 20 μm)

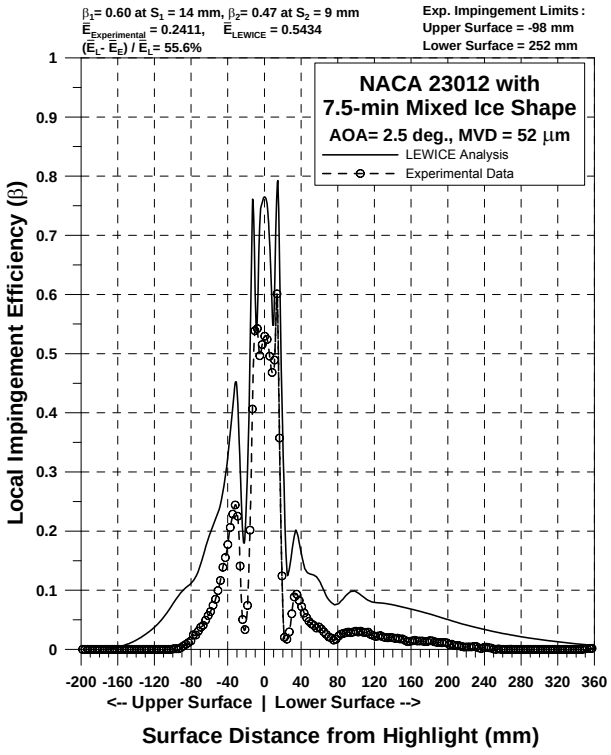

Figure 90b. Impingement Efficiency Distribution for NACA 23012 Airfoil With 7.5-min Mixed Ice Shape (c = 36 in., V_∞ = 175 mph, AOA = 2.5°, MVD = 52 μm)

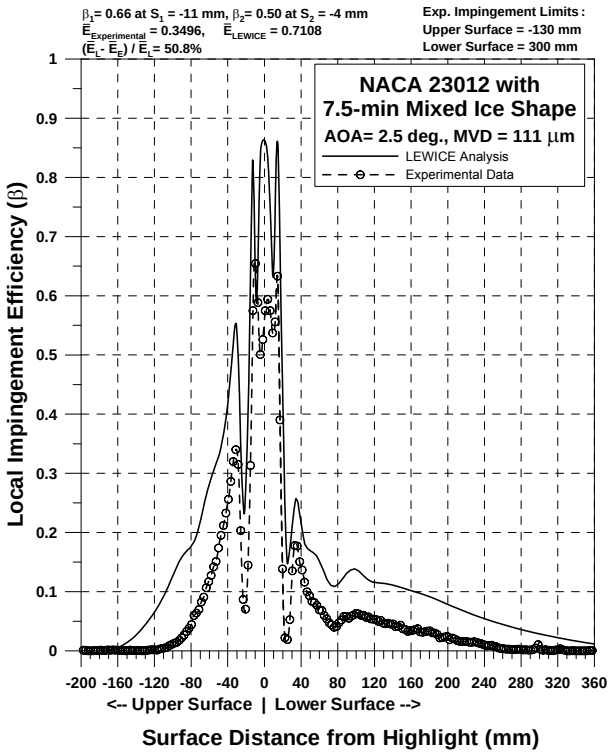

Figure 90c. Impingement Efficiency Distribution for NACA 23012 Airfoil With 7.5-min Mixed Ice Shape (c = 36 in., V_∞ = 175 mph, AOA = 2.5°, MVD = 111 μm)

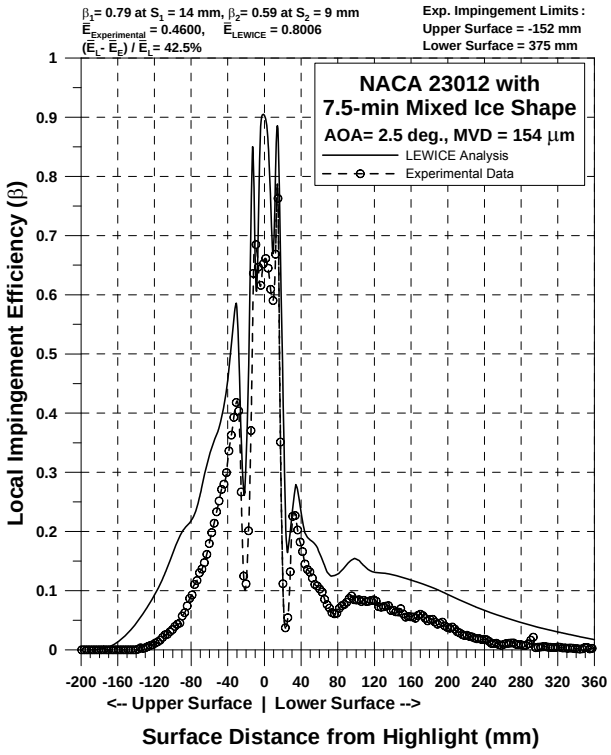

Figure 90d. Impingement Efficiency Distribution for NACA 23012 Airfoil With 7.5-min Mixed Ice Shape (c = 36 in., V_∞ = 175 mph, AOA = 2.5°, MVD = 154 μm)

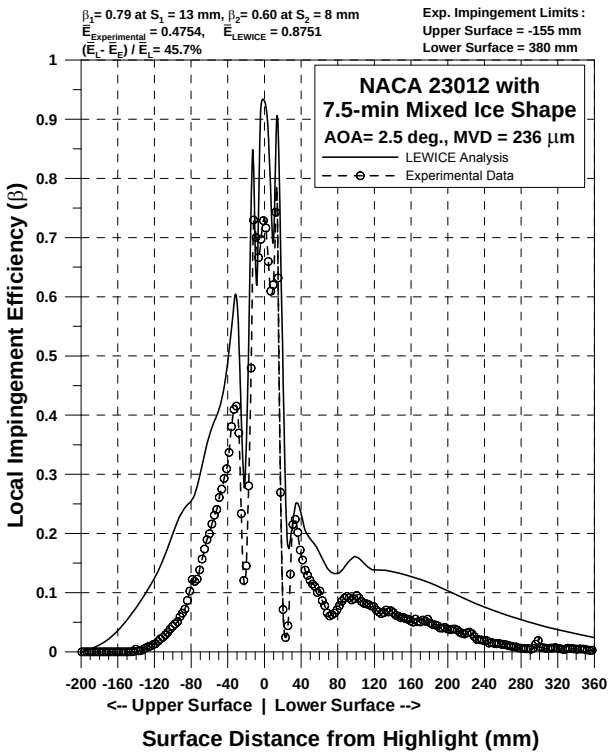

Figure 90e. Impingement Efficiency Distribution for NACA 23012 Airfoil With 7.5-min Mixed Ice Shape (c = 36 in., V_∞ = 175 mph, AOA = 2.5°, MVD = 236 μm)

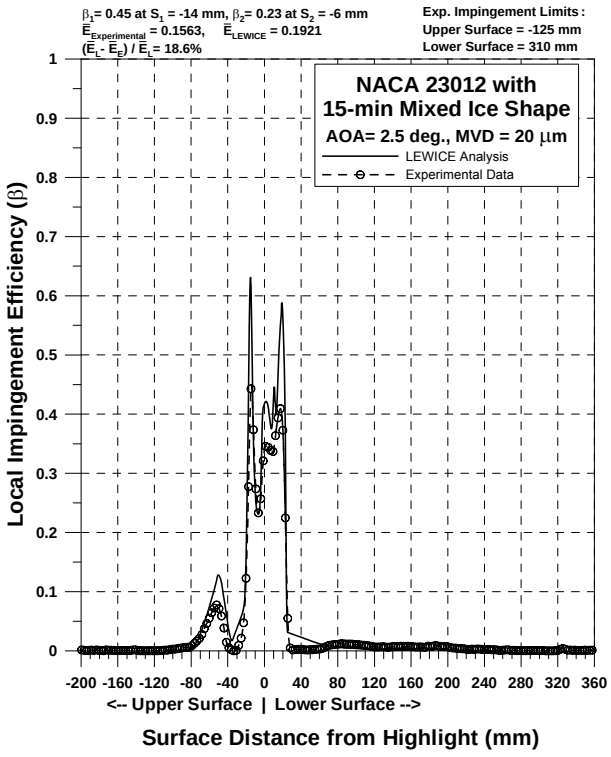

Figure 91a. Impingement Efficiency Distribution for NACA 23012 Airfoil With 15-min Mixed Ice Shape (c = 36 in., V_∞ = 175 mph, AOA = 2.5°, MVD = 20 μm)

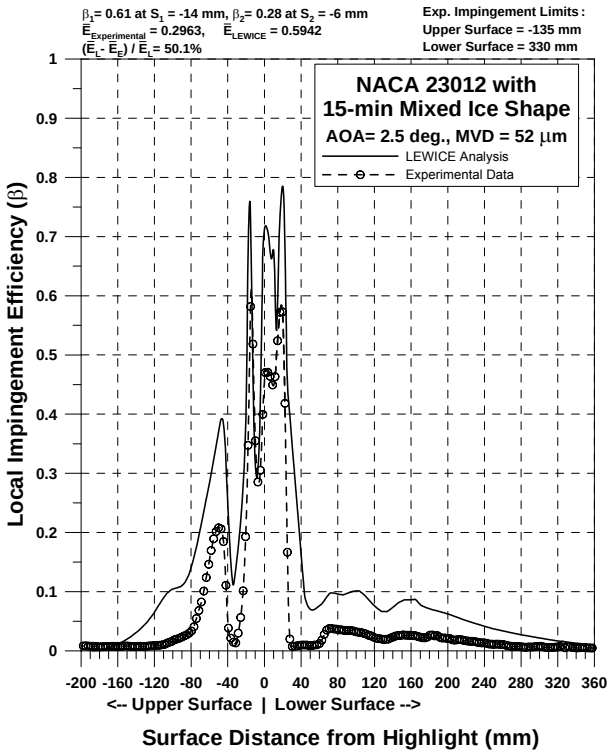

Figure 91b. Impingement Efficiency Distribution for NACA 23012 Airfoil With 15-min Mixed Ice Shape (c = 36 in., V_∞ = 175 mph, AOA = 2.5°, MVD = 52 μm)

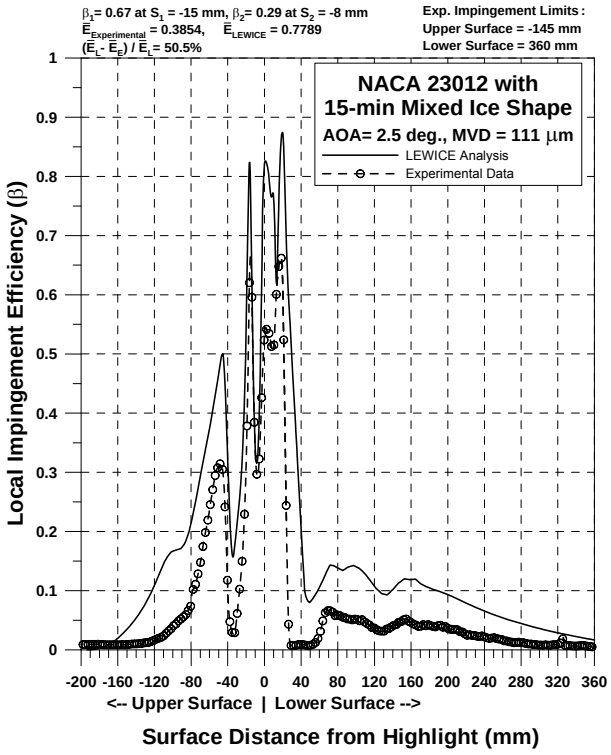

Figure 91c. Impingement Efficiency Distribution for NACA 23012 Airfoil With 15-min Mixed Ice Shape (c = 36 in., V_∞ = 175 mph, AOA = 2.5°, MVD = 111 μm)

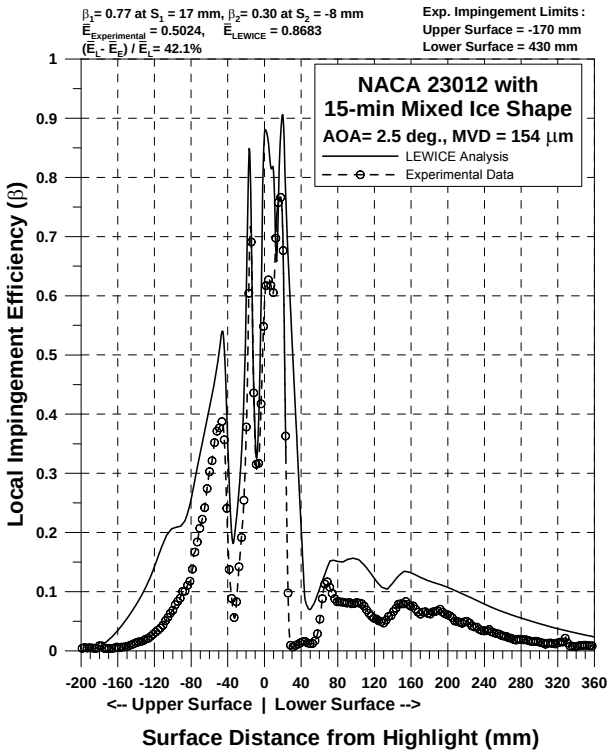

Figure 91d. Impingement Efficiency Distribution for NACA 23012 Airfoil With 15-min Mixed Ice Shape (c = 36 in., V_∞ = 175 mph, AOA = 2.5°, MVD = 154 μm)

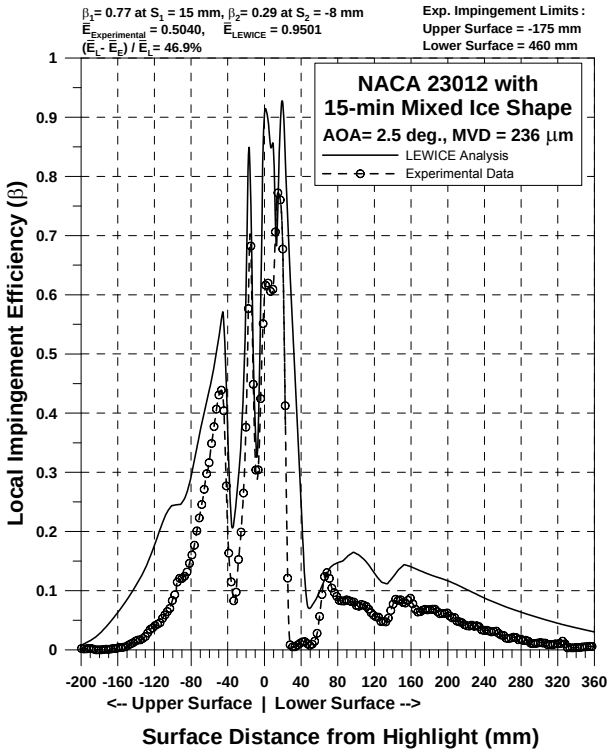

Figure 91e. Impingement Efficiency Distribution for NACA 23012 Airfoil With 15-min Mixed Ice Shape (c = 36 in., V_∞ = 175 mph, AOA = 2.5°, MVD = 236 μm)

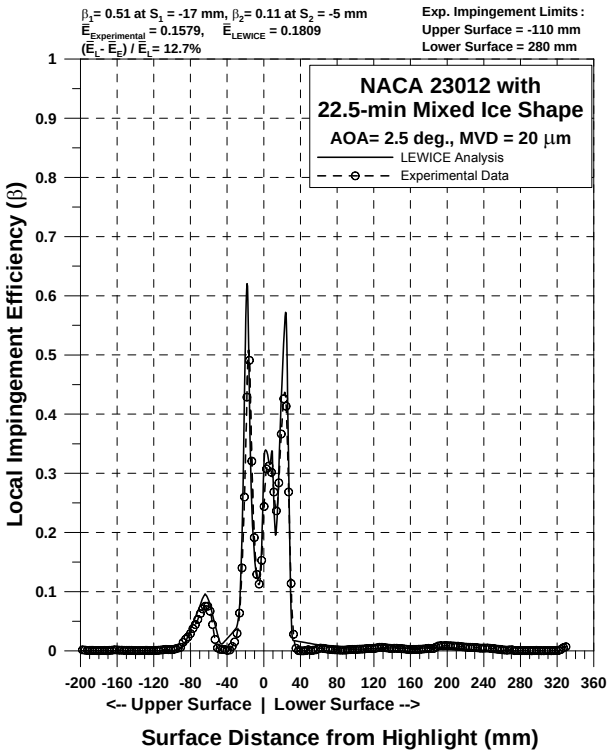

Figure 92a. Impingement Efficiency Distribution for NACA 23012 Airfoil With 22.5-min Mixed Ice Shape (c = 36 in., V_∞ = 175 mph, AOA = 2.5°, MVD = 20 μm)

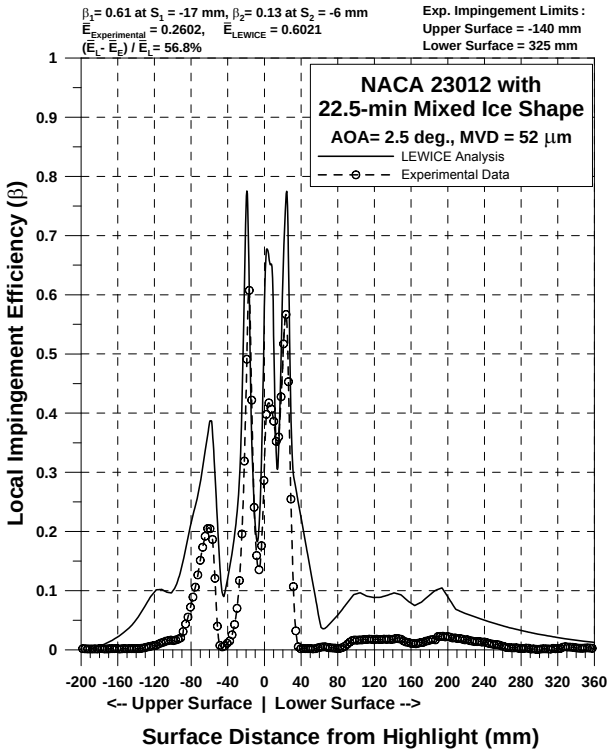

Figure 92b. Impingement Efficiency Distribution for NACA 23012 Airfoil With 22.5-min Mixed Ice Shape (c = 36 in., V_∞ = 175 mph, AOA = 2.5°, MVD = 52 μm)

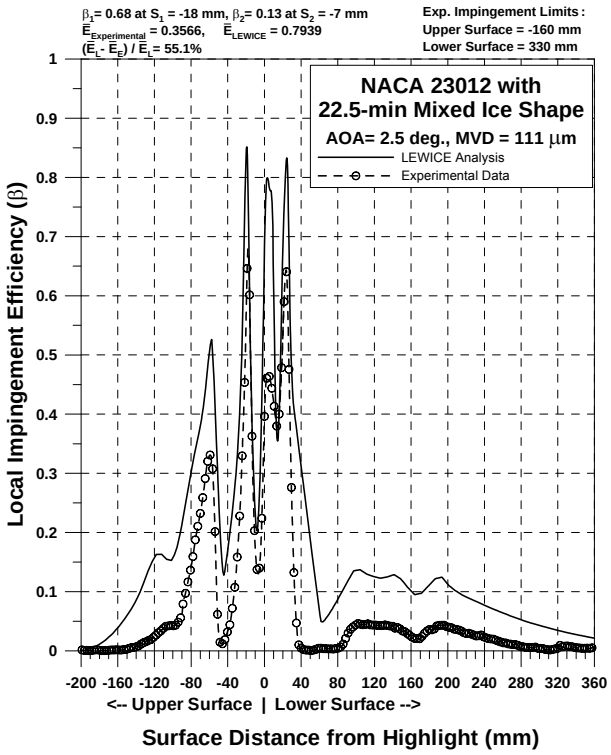

Figure 92c. Impingement Efficiency Distribution for NACA 23012 Airfoil With 22.5-min Mixed Ice Shape (c = 36 in., V_∞ = 175 mph, AOA = 2.5°, MVD = 111 μm)

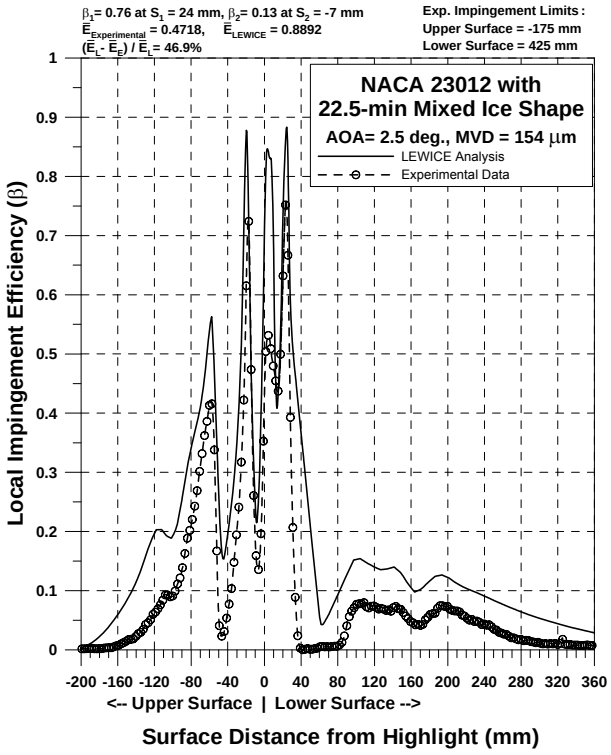

Figure 92d. Impingement Efficiency Distribution for NACA 23012 Airfoil With 22.5-min Mixed Ice Shape (c = 36 in., V_∞ = 175 mph, AOA = 2.5°, MVD = 154 μm)

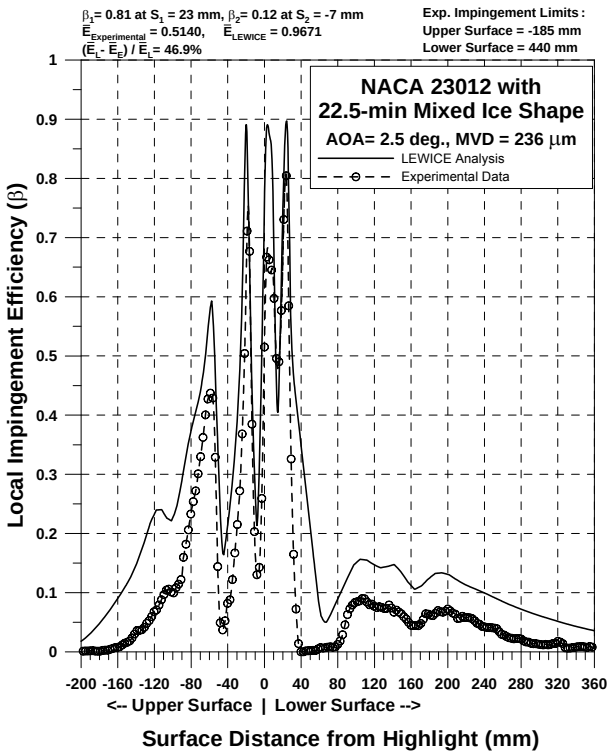

Figure 92e. Impingement Efficiency Distribution for NACA 23012 Airfoil With 22.5-min Mixed Ice Shape (c = 36 in., V_∞ = 175 mph, AOA = 2.5°, MVD = 236 μm)

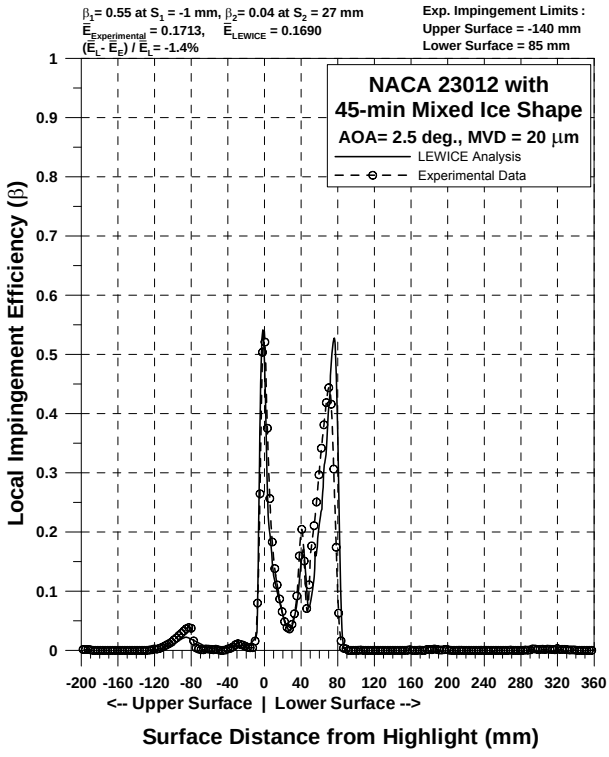

Figure 93a. Impingement Efficiency Distribution for NACA 23012 Airfoil With 45-min Mixed Ice Shape (c = 36 in., V_∞ = 175 mph, AOA = 2.5°, MVD = 20 μm)

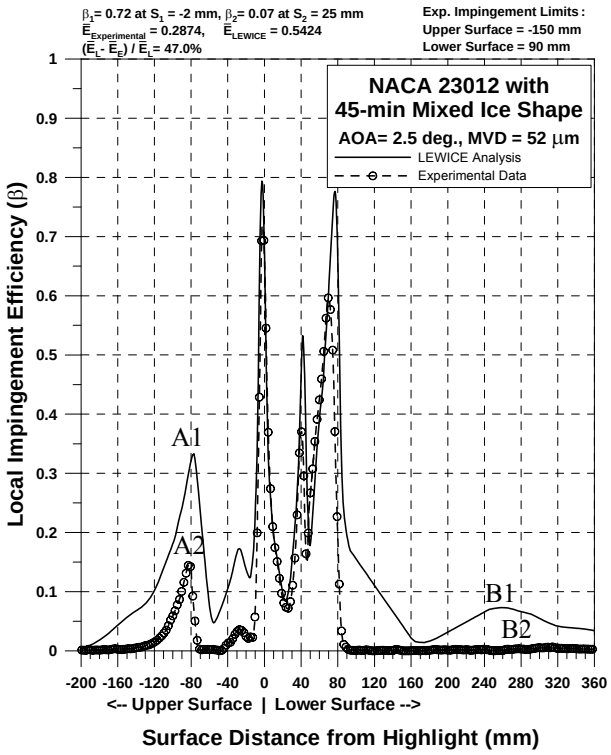

Figure 93b. Impingement Efficiency Distribution for NACA 23012 Airfoil With 45-min Mixed Ice Shape (c = 36 in., V_∞ = 175 mph, AOA = 2.5°, MVD = 52 μm)

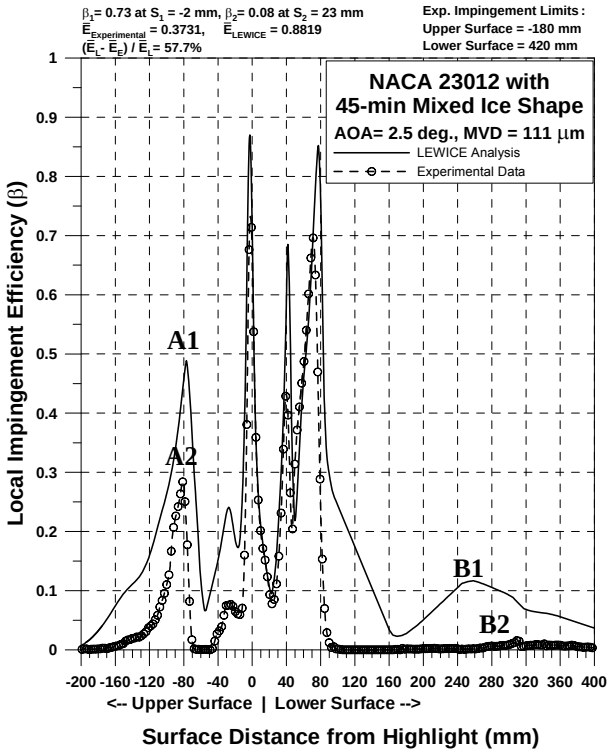

Figure 93c. Impingement Efficiency Distribution for NACA 23012 Airfoil With 45-min Mixed Ice Shape (c = 36 in., V_∞ = 175 mph, AOA = 2.5°, MVD = 111 μm)

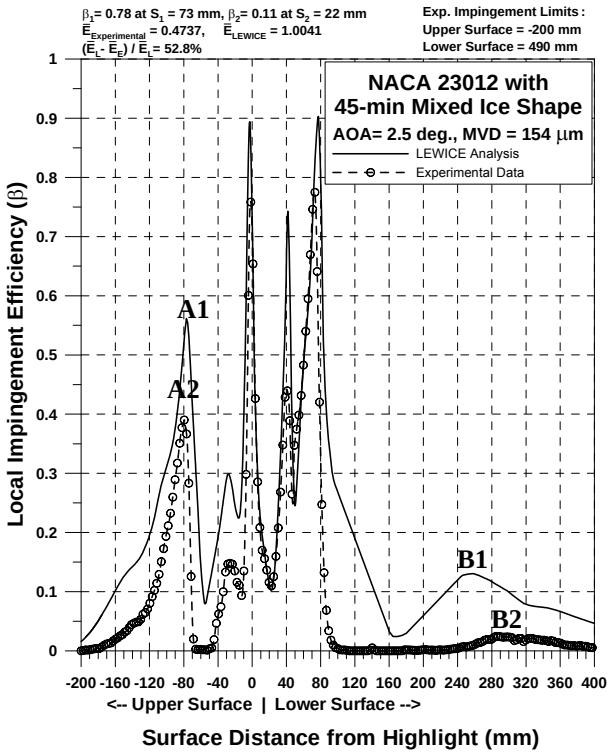

Figure 93d. Impingement Efficiency Distribution for NACA 23012 Airfoil With 45-min Mixed Ice Shape (c = 36 in., V_∞ = 175 mph, AOA = 2.5°, MVD = 154 μm)

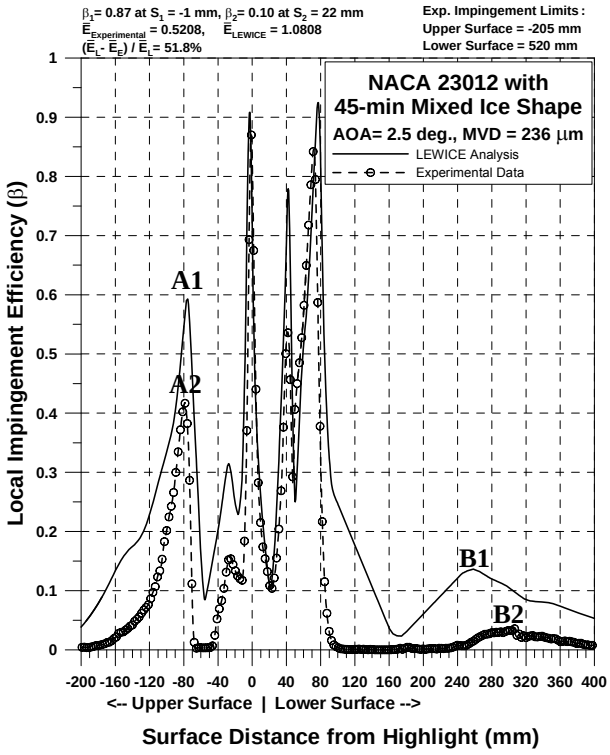

Figure 93e. Impingement Efficiency Distribution for NACA 23012 Airfoil With 45-min Mixed Ice Shape (c = 36 in., V_∞ = 175 mph, AOA = 2.5°, MVD = 236 μm)

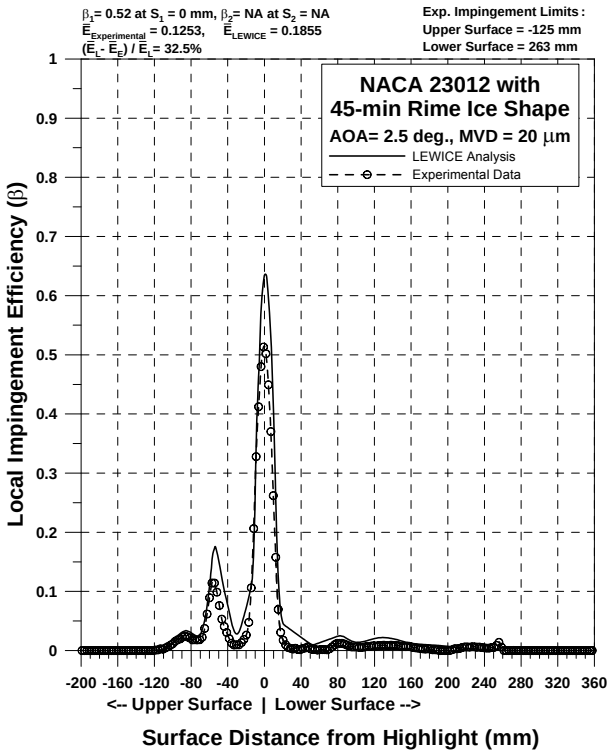

Figure 94a. Impingement Efficiency Distribution for NACA 23012 Airfoil With 45-min Rime Ice Shape (c = 36 in., V_∞ = 175 mph, AOA = 2.5°, MVD = 20 μm)

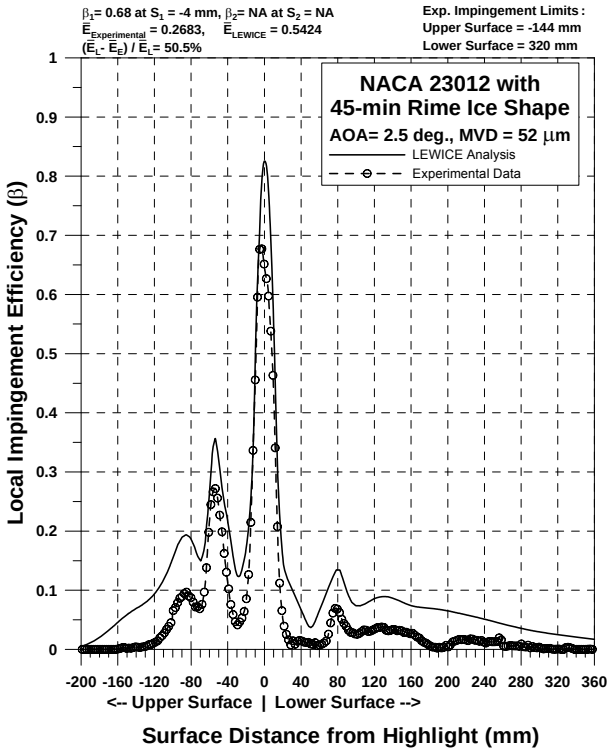

Figure 94b. Impingement Efficiency Distribution for NACA 23012 Airfoil With 45-min Rime Ice Shape (c = 36 in., V_∞ = 175 mph, AOA = 2.5°, MVD = 52 μm)

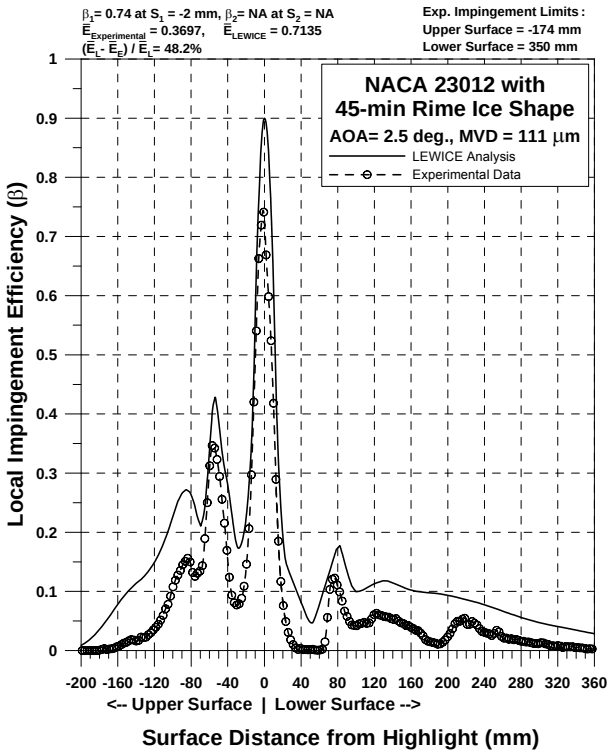

Figure 94c. Impingement Efficiency Distribution for NACA 23012 Airfoil With 45-min Rime Ice Shape (c = 36 in., V_∞ = 175 mph, AOA = 2.5°, MVD = 111 μm)

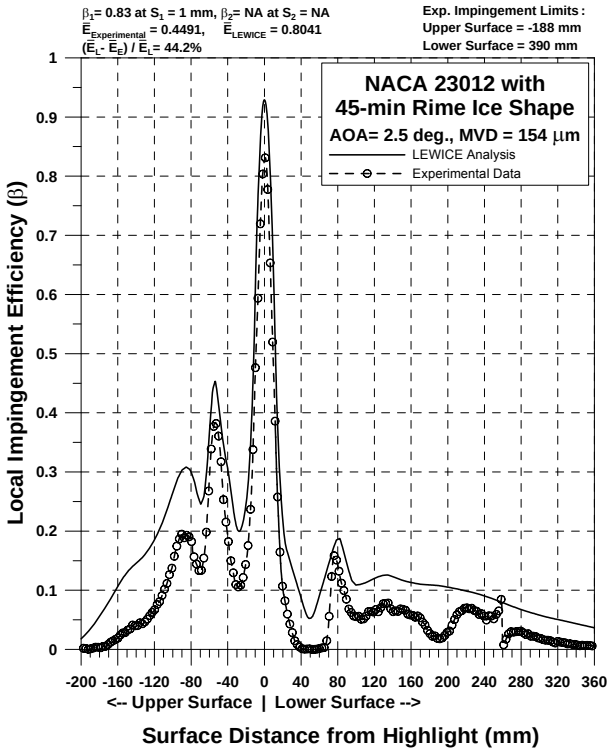

Figure 94d. Impingement Efficiency Distribution for NACA 23012 Airfoil With 45-min Rime Ice Shape (c = 36 in., V_∞ = 175 mph, AOA = 2.5°, MVD = 154 μm)

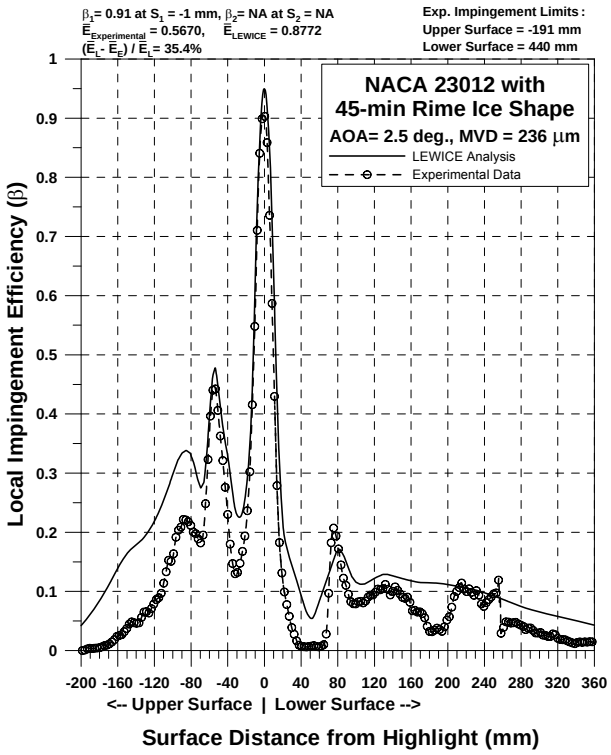

Figure 94e. Impingement Efficiency Distribution for NACA 23012 Airfoil With 45-min Rime Ice Shape (c = 36 in., V_∞ = 175 mph, AOA = 2.5°, MVD = 236 μm)

7.3.2.1 NACA 23012 Airfoil.

On the clean NACA 23012 airfoil, good agreement between experiment and analysis was observed for the 20-μm case. For the larger MVDs, however, LEWICE predicted higher total water impingement and greater impingement limits compared to the experimental data. Total impingement efficiency based on the experimental data, ranged from 18.7% to 56.2% as the MVD was increased from 20 to 236 μm compared to 17.4% to 84% for LEWICE.

7.3.2.2 NACA 23012 Airfoil With Simulated Glaze Ice Shapes.

Overall, the trends in the computed and experimental impingement curves were in good agreement for most of the ice shapes tests. However, for the large MVDs of 52, 111, 154, and 236 μm, the efficiency and extent of water impingement predicted by LEWICE were considerably greater than those obtained from the experiment. Even for the 20-μm case, the LEWICE impingement efficiencies near the leading edge (the region between ice horns) were higher than the experimental values by approximately 0.1 to 0.25, depending on surface location. Although the exact reason for the observed differences is not known, potential contributors include the difference in the experimental and computed flowfields, as shown in figures 62 through 66, and small variations in cloud uniformity within the region of measurement.

Experimental, $\overline{E}_E$, and LEWICE, $\overline{E}_L$, total impingement efficiencies for the five glaze ice shapes are provided in table 10. Note that in all cases, $\overline{E}_E$ and $\overline{E}_L$ increased as MVD increased,

albeit at different rates. For the five MVDs tested, the maximum $\overline{E}_E$ was obtained with the 45-min ice shape, and the minimum was obtained with the 10-min glaze ice shape. The results also demonstrate the differences between LEWICE and experimental total impingement efficiencies, $\Delta\overline{E} = \overline{E}_L - \overline{E}_E$. For the 20-μm case, $\Delta\overline{E}$ ranged from -0.002 to 0.05, depending on the test configuration. For the large drop cases (52, 111, 154, and 236 μm), $\Delta\overline{E}$ ranged from 0.24 to 0.69 and increased as the ice shape size increased from 5-min to 22.5-min glaze ice shape. The observed difference between LEWICE and the experimental impingement efficiencies was mainly due to the impingement region downstream of the ice horns, which was considerably overpredicted by LEWICE. For the 45-min ice shape, $\Delta\overline{E}$ was smaller than the remaining four glaze ice shapes because the horns of this ice shape shielded the airfoil surface downstream of the horns from direct drop impingement. LEWICE and experimental impingement data downstream of the horns were in good agreement. For the large MVDs (greater than 20 μm), the maximum total impingement efficiency computed with LEWICE corresponded to the 22.5-min glaze ice shape, whereas the experimental data showed that maximum total impingement was obtained with the 45-min glaze. The main reason for the difference between the experiment and the analysis is due to an interpolation method used in LEWICE to compute impingement efficiency between adjacent surface points, as discussed in section 7.3.2.5.

7.3.2.3 NACA 23012 Airfoil With Simulated Mixed Ice Shapes.

The trends and other notable features exhibited by the computational and experimental impingement are as follows:

- The total impingement efficiency and the extent of impingement limits increased as the MVD increased. For the 52-, 111-, 154-, and 236-μm MVD cases, LEWICE significantly overpredicted both the impingement limits and the local impingement efficiencies. For the 20-μm case, LEWICE predicted higher local impingement efficiency over the ice shape region by up to 0.2, depending on surface location.

- Total impingement efficiencies based on $\overline{E}_E$ and $\overline{E}_L$ increased as MVD increased, albeit at different rates.

- For MVD of 20 μm, $\Delta\overline{E}$ ranged from -0.002 to 0.05, while for the larger MVDs $\Delta\overline{E}$ ranged from 0.27 to 0.56. For most of the large MVDs, $\Delta\overline{E}$ increased as the ice shape size increased.

- Referring to figures 93b through 93e, the secondary impingement peaks on the upper and lower surfaces (indicated by the symbols A and B, respectively) were due to direct impingement by the large drops. Note that the peaks predicted by LEWICE (A1 and B1) were considerably higher than the experimental peaks (A2 and B2). The main reason for the difference is drop splashing, which is not simulated in LEWICE. Another interesting observation is that the experimental impingement peak (B2) on the lower surface occurred downstream of the peak predicted by LEWICE. A possible reason for this difference is drop breakup downstream of the lower horn, which is not simulated in

LEWICE. Studies performed at WSU (not presented in this report) with simulated ice shapes featuring large horns have shown that large drops could breakup downstream of the horns. The trajectories of the drop fragments (smaller drops) are affected by the shear flow behind the ice horn and, as a result, impinge further downstream compared to the impingement location without drop breakup. In addition, because the airfoil surface slope is lower at the point where the drop fragments impinge, the incoming water mass is spread over a larger surface area resulting in lower local impingement efficiency.

7.3.2.4 NACA 23012 Airfoil With Simulated Rime Ice Shape.

For the 45-min rime ice shape, the total impingement efficiency increased as the MVD size increased. LEWICE predictions of the local impingement efficiency and extent of water impingement, however, were considerably greater than the experiment, especially for the larger MVDs. For all MVDs tested, LEWICE overpredicted the total impingement efficiency by 0.06 to 0.36.

7.3.2.5 Comments on the Difference Between Experimental and LEWICE Results.

For the large MVD cases (52, 111, 154, and 236 μm) involving the 10-min glaze, 15-min glaze, 22.5-min glaze, 15-min mixed, 22.5-min mixed, and 45-min mixed ice shapes, the LEWICE data corresponding to the region immediately downstream of the horns (region A, figure 86b) exhibited a gradual decrease in $\overline{\beta}$ compared to the sharp drop seen in the experimental data. The reason for this difference is attributed to a numerical artifact in LEWICE. A detailed explanation is provided below.

The interpolation scheme used to calculate collection efficiency at a surface point in LEWICE can have difficulties for geometries with multiple impingement regions. Multiple impingement regions can occur on complex ice shapes, highly cambered wings, and multi-element wings. The method predicts water impingement in some of these cases where, in fact, there is no water impingement. The problem is due to the way the method calculates collection efficiency and assigns it to a surface point.

Collection efficiency is calculated as the distance between two adjacent impacting particles divided by the distance between these trajectories at the freestream release point. The collection efficiency at any surface point located between the impact points is calculated using the collection efficiency generated from these two particles.

The interpolation problem occurs when the two adjacent impacting particles are not part of the same impact region, but of two different impingement regions. In these cases, the trajectories are actually the limiting, or tangent, trajectories of two distinct impingement regions. For example, one trajectory represents the aft impingement limit of a forward impingement region and one trajectory represents the forward limit of the aft impingement region. In these cases, the collection efficiency between the two regions should be zero, but LEWICE interpolates values linearly between the two regions from the value at the limits of both regions. Solutions to this problem are complicated because it is difficult to differentiate between two distinct smaller impingement regions and one larger one. One approach for solving the impingement efficiency

interpolation issue in LEWICE is the use of the Monte-Carlo method for computing drop impingement efficiency. This method is presented in appendix E along with computed impingement curves obtained with a Monte-Carlo trajectory code developed at NASA Glenn. The computed impingement curves show the same sharp drop-off behind the ice horns as those from the experimental results. Note that Monte-Carlo computations are very intensive due to the large number of drops that are needed to accurately compute the impingement characteristics, as discussed in appendix E.

One crucial point to note is that although these errors appear large for some cases, they probably do not greatly affect the ice shape generation in LEWICE. This is because the observed errors occur mostly when there is a mismatch between the drop size used to generate the ice shape and the one used for the comparison to the experimental data. When the collection efficiencies are compared using the same drop size for the experimental data and to generate the ice shape, the agreement is good. For larger drop sizes, the error increases mostly in the region aft of the ice shape due to the larger drops hitting further back on the wing and forming a secondary impingement region.

The falloff in agreement between the experimental and LEWICE collection efficiencies for the case of drops larger than those used to accrete the ice shape is due to a close coupling between the icing and impingement limits for ice shapes. In general, as the ice shape generation progresses, the impingement limits, which are directly related to drop size, and the icing limits converge. This implies that the drops used to generate the ice shape do not impact aft of the icing limit. For this drop size, generally, there is only a single impingement region with no associated interpolation errors. When the drop size is increased from this value, the drops begin to hit aft of the ice shape, which results in secondary impingement regions. The formation of these secondary impingement regions causes interpolation errors between the two impingement regions, as described above. Therefore, there is an observed discrepancy in the comparison to the experimental data.

Other potential reasons for the discrepancies between the analysis and the experimental impingement data include the following:

- There are differences between the actual and the computed flowfield, particularly in the region between the horns. Also, flow separation downstream of the horns is not well modeled by potential flow models such as the one used in LEWICE. For the large ice shapes, the pressure data presented indicate considerable differences between the LEWICE and the experimental flowfields.

- Drop splashing was observed during large drop impingement experiments in references 6 and 7. The effect of splashing reduced water mass deposited on the surface of the airfoil. LEWICE does not model the effects of large drop splashing.

- Errors associated with the experimental investigation

7.3.3 The Effect of Geometry.

In this section, the change in the impingement characteristics as a function of ice shape size is discussed. The ice accretions considered are the five progressively larger (5 to 45 min) glaze ice shapes and the four mixed condition cases ranging from the 7.5- to the 45-min ice shapes. In addition, the differences between the impingement efficiencies of the three types of ice shapes tested are compared.

7.3.3.1 NACA 23012 Airfoil With Simulated Glaze Ice Shapes.

Figure 95 shows the change in water impingement efficiency as the glaze ice shapes become progressively larger in size, while the MVD is kept constant. The main observations from the experimental results presented are as follows:

- The extent of the water impingement in the vicinity of the leading edge increased monotonically as the size of the glaze ice shape was increased. For the 5-min glaze ice, the extent of water impingement over the leading edge ranged from approximately -25 (upper surface) to +25 mm (lower surface). For the 45-min ice shape the impingement extent was from -80 to +60 mm.

- Multiple local impingement peaks were observed between the ice horns. The magnitude of the peaks decreased near the center of the ice shape (s = 0 mm) and increased near the horn tips as the ice shapes became progressively larger.

- For all MVD cases, the maximum local impingement efficiency of the clean airfoil was greater than the maximum impingement efficiency of the ice shapes tested.

- Secondary impingement peaks were observed over the lower and upper surfaces of the airfoil downstream of the ice horns. These secondary peaks occurred between -30 and -90 mm (upper surface) and +30 and +60 mm (lower surface). The secondary impingement peaks decreased in magnitude and extent as the ice shapes increased in size from 5 to 15 min. For the 22.5- and 45-min ice shapes, no secondary peaks were observed immediately downstream of the horns due to the large horn size.

- For all MVDs tested, the maximum local impingement efficiency of the 45-min ice shape was less than the other four ice shapes.

- For all MVD cases, the total water impingement efficiency decreased in the following sequence: clean airfoil, 5-min glaze ice shape, and 10-min glaze ice shape. For the 15-, 22.5-, and 45-min ice accretions, the total impingement efficiency increased as the ice shape size was increased, except for the 236-μm case. For all MVD cases, the maximum total impingement efficiency was obtained with the 45-min ice shape, while the minimum total impingement efficiency was obtained with the 10-min glaze ice shape.

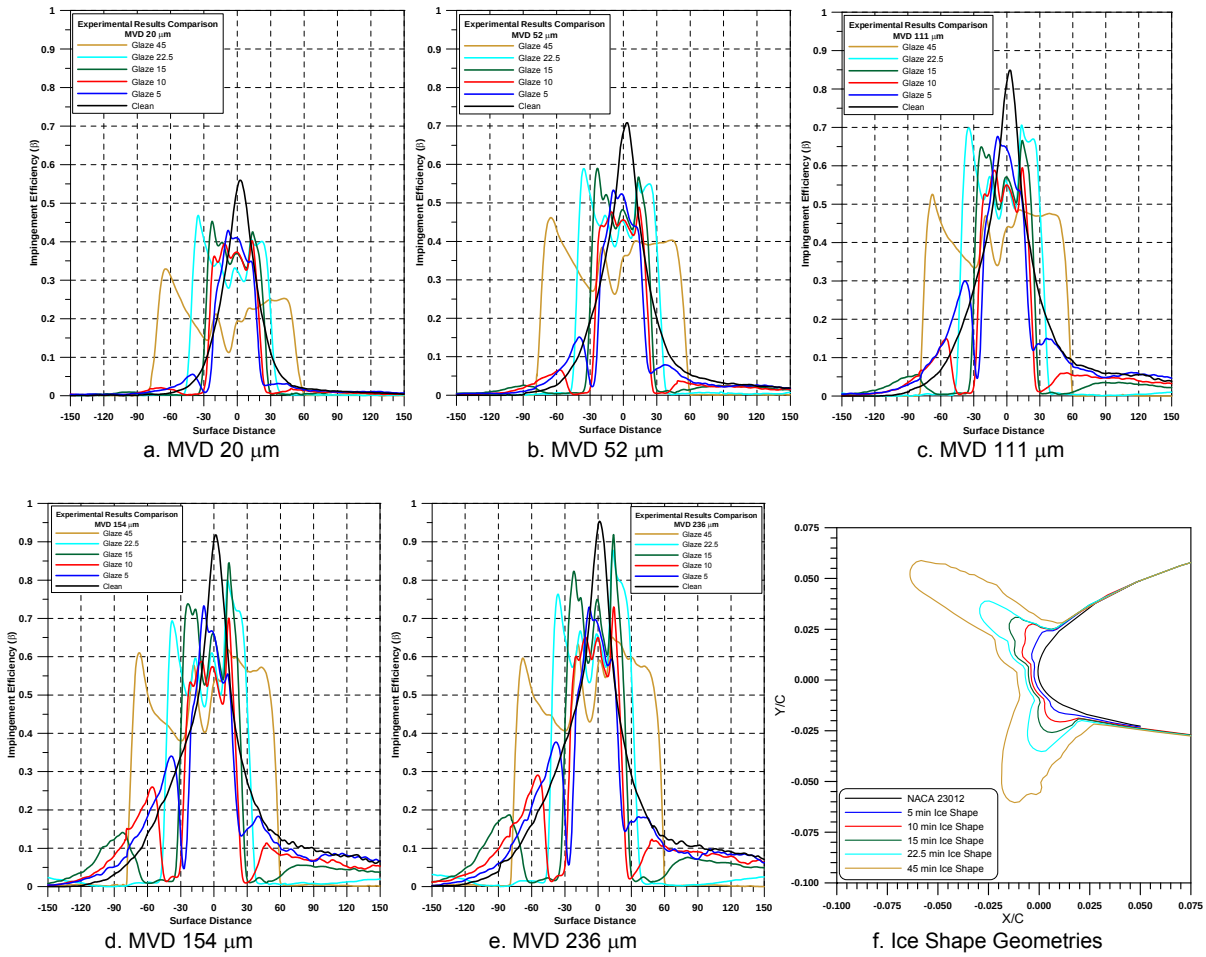

Figure 95. Impingement Efficiency Variation With Glaze Ice Test Geometry: Experimental Data, All MVDs

7.3.3.2 NACA 23012 Airfoil With Simulated Mixed Ice Shapes.

Figure 96 shows the change in impingement efficiency as the mixed ice shapes become progressively larger in size, while the MVD is kept constant. The key observations from the experimental results presented are as follows:

- The coverage of water impingement in the airfoil leading-edge vicinity increased monotonically as the size of the mixed ice shape increased from 7.5- to 22.5-min. For the 7.5-min mixed ice shape, the extent of water impingement over the leading edge ranged from approximately -20 (upper surface) to +20 mm (lower surface). For the 22.5-min ice shape, the impingement extent was from -45 to +35 mm. For the 45-min mixed ice shape, the impingement extent increased substantially, from -10 mm to +90 mm. These limits on both surfaces shifted toward the upper surface, a trend not observed with the smaller ice shapes (7.5 to 22.5 min).

- Multiple local impingement peaks were observed between the ice horns. The magnitude of the peaks decreased near the center of the ice shape (s = 0 mm) and increased near the horn tips as the ice shapes became progressively larger.

- For most MVDs tested, the maximum local impingement efficiency increased as the ice shape size increased.

- Maximum local impingement efficiency for the clean airfoil was greater than all mixed ice shape cases and for all MVDs tested (except for the 45-min 52-μm case).

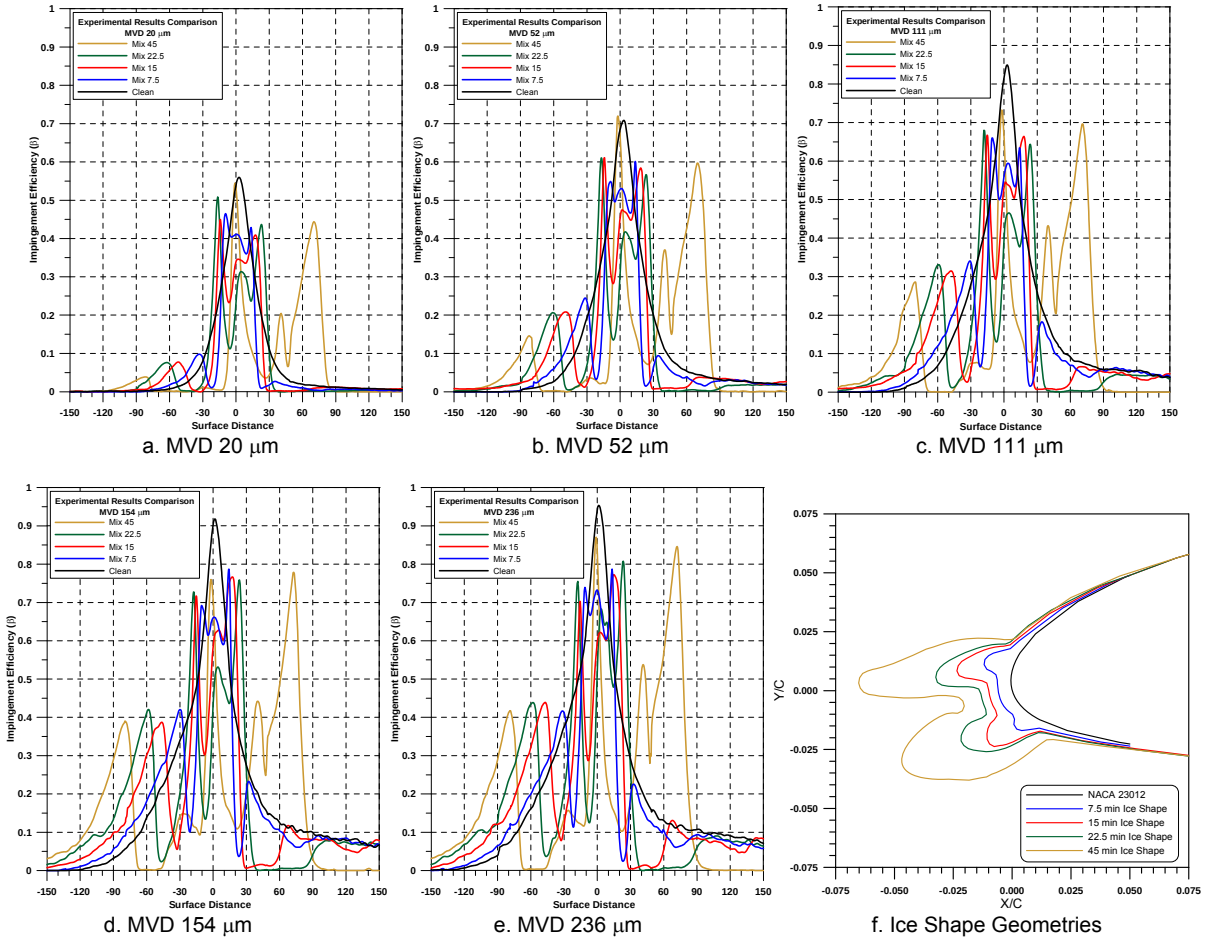

Figure 96. Impingement Efficiency Variation With Mixed Ice Test Geometry: Experimental Data, All MVDs

- Secondary impingement peaks were found downstream of the ice shapes between -30 and -80 mm along the airfoil upper surface and from +30 to +300 mm over the lower surface of the airfoil. The extent of the impingement peaks shifted downstream along both upper and lower surfaces as the ice shape size was increased.

- For most of the mixed ice shapes tested, the total impingement efficiency increased as the size of the ice accretion increased from 7.5 to 45 min. The 15-min mixed ice shape with

MVDs of 52, 111, and 154 μm had higher total impingement efficiency than its larger counterparts.

7.3.3.3 Comparison Between Glaze, Mixed, and Rime Ice Shape.

Figure 97 summarizes the impingement efficiency obtained with the 45-min rime ice shape for all MVDs tested. From table 10, the trends observed among the three types of ice shapes are as follows:

- Among the three 45-min ice accretions, the glaze ice shape had the largest total impingement efficiency. Total impingement efficiency for the 20-, 52-, 111-, and 154-μm MVDs decreased in the following sequence: glaze, mixed, and rime. For the 236-μm case, however, the rime ice shape exhibited higher total collection efficiency than the mixed ice shape.

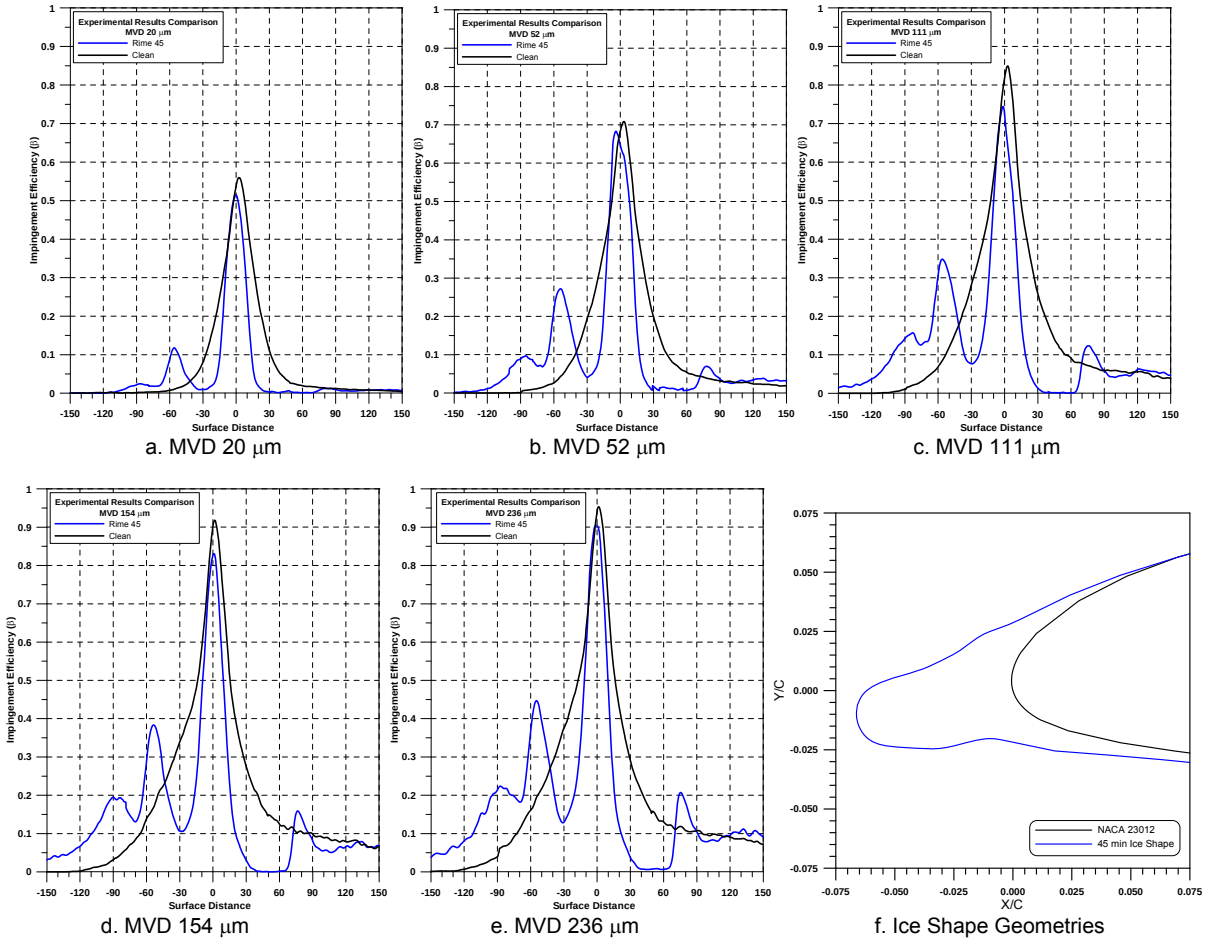

Figure 97. Impingement Efficiency Variation With Rime Ice Test Geometry: Experimental Data, All MVDs

- For all MVDs tested with the 45-min ice shapes, the glaze ice shape had the lowest maximum local impingement efficiency.

- Multiple peaks within the ice horns were observed in the glaze and mixed ice shape cases, while the rime ice shape had a single impingement peak.

- The secondary impingement peaks (downstream of the horns) on the glaze ice shapes shifted downstream from the highlight (s = 0 mm) by similar amounts as the ice shape size increased, while for the mixed ice shape the peak on the lower surface shifted significantly more than on the upper surface.

- The secondary impingement peaks in the glaze ice shapes tended to flatten out as the ice shape increased in size from 5 to 45 min. On the contrary, the secondary peaks in the mixed ice shape impingement curves remained distinctive as the ice shape increased in size from 7.5 to 45 min.

7.3.4 The Effect of MVD.

The effect of MVD on impingement efficiency for all tested ice shapes is shown in figures 98 through 110 and in table 10. In figures 98 and 99, local impingement efficiency ($\bar{\beta}$) is plotted versus surface distance from the highlight. In figures 100 through 110, impingement efficiency (horizontal axis) is plotted versus y/c and is related to model geometry to better illustrate the relation between impingement efficiency and body location.

The experimental results demonstrate the following trends.

- In general, local impingement efficiency and extent for the tested configurations increased as the cloud MVD was increased from 20 to 236 μm. Note that for the 45-min glaze ice shape, the impingement limits did not change with MVD, because the large horns of this ice shape prevented impingement downstream of the horns for the AOA. The incremental growth in $\bar{\beta}$ (difference in $\bar{\beta}$ between adjacent MVD cases) decreased as the MVD was increased. The most growth in $\bar{\beta}$ was observed between 20 and 52 μm and between 52 and 111 μm. For most of the larger MVDs, however, the growth in $\bar{\beta}$ decreased.

- For all glaze geometries, the change in total impingement efficiency between the 20- and 52-μm MVD cases, defined as $\Delta\overline{E} = \overline{E}_{52} - \overline{E}_{20}$, ranged from 0.065 to 0.166, depending on the glaze ice shape. The incremental growth in total impingement efficiency as the MVD was increased from 52 to 111 μm ranged from 0.057 to 0.114. Further increases in MVD from 111 to 154 μm, and then from 154 to 236 μm, resulted in total impingement efficiency increments of 0.042 to 0.100 and 0.027 to 0.093, respectively.

- For all mixed ice shape geometries, the change in total impingement efficiency between the 20- and 52-μm MVD cases ranged from 0.102 to 0.140, depending on the ice shape. The incremental growth in total impingement efficiency as the MVD was increased from 52 to 111 μm ranged from 0.086 to 0.109. Further increases in MVD from 111 to 154 μm, and then from 154 to 236 μm, resulted in total impingement efficiency increments of 0.101 to 0.117 and 0.002 to 0.047, respectively.

- For the 45-min rime ice shape, the increments in total impingement efficiency as the MVD was increased from 20 to 236 μm were 0.143, 0.101, 0.079, and 0.118.

- The results shown in figures 98 and 99 indicate multiple impingement peaks between the ice shape horns in the glaze and mixed ice shape cases. In general, these peaks became more prominent as the MVD and the size of the ice were increased.

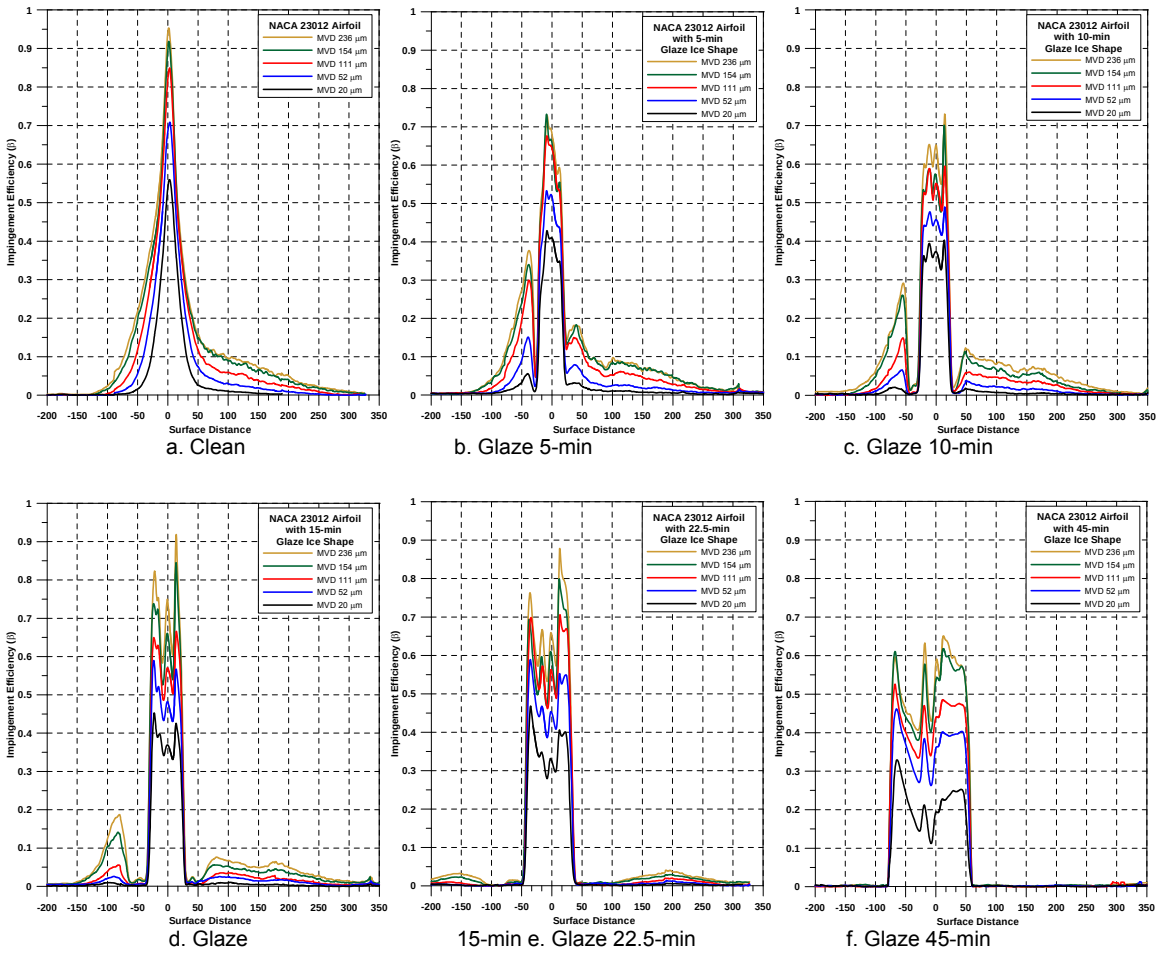

Figure 98. Impingement Efficiency Variation With MVD: Experimental Data, Clean, and Glaze Ice Geometries

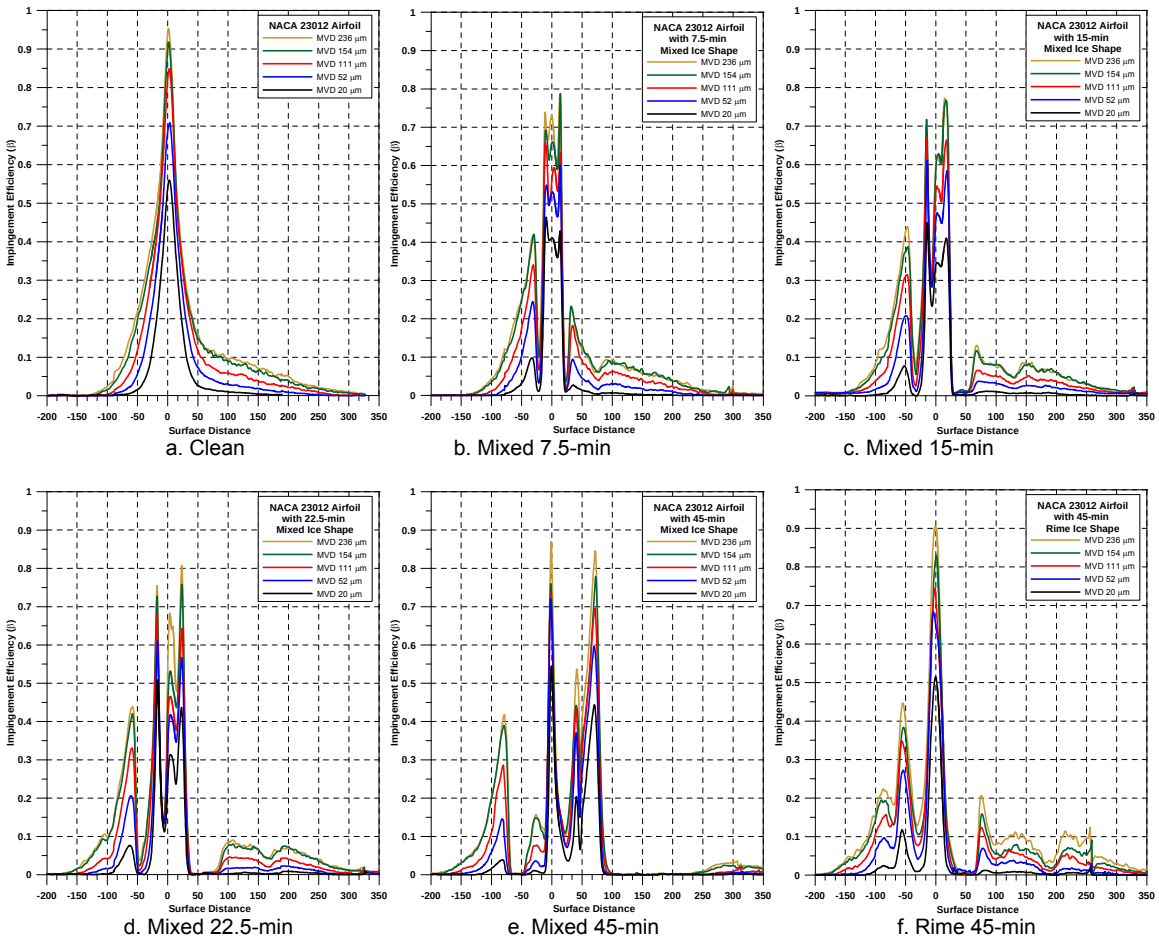

Figure 99. Impingement Efficiency Variation With MVD: Experimental Data, Clean, Mixed, and Rime Ice Geometries

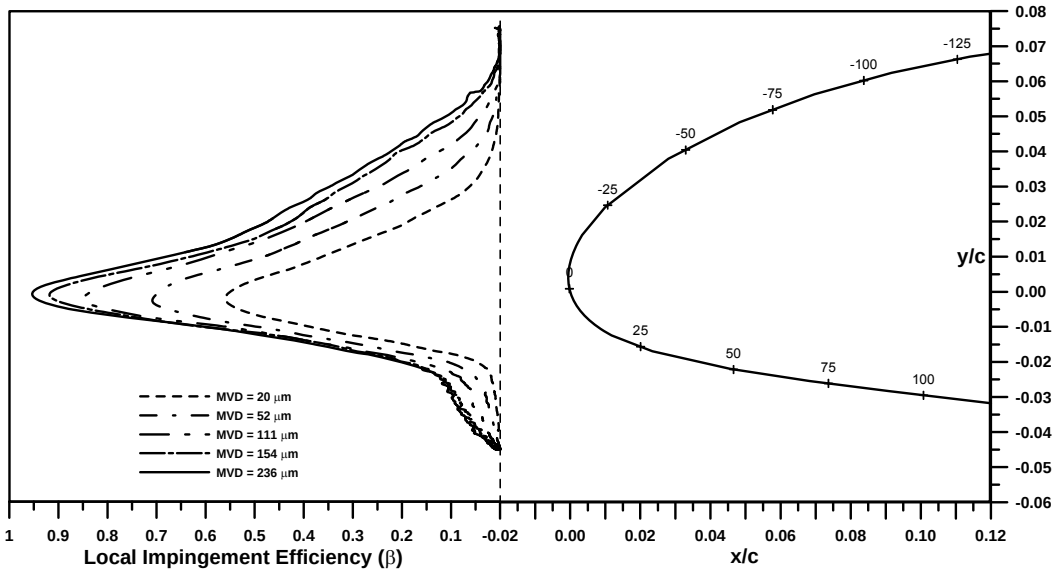

Figure 100. Experimental y/c vs Beta, NACA 23012

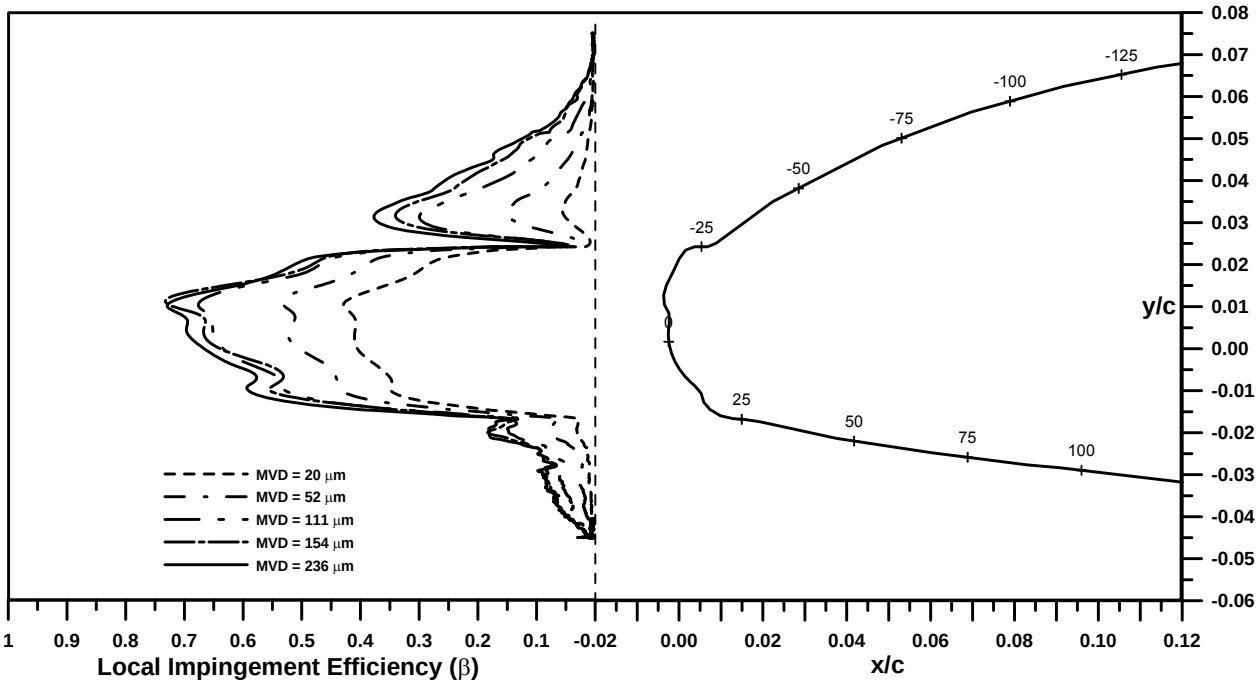

Figure 101. Experimental y/c vs Beta, NACA 23012 With 5-min Glaze Ice Shape

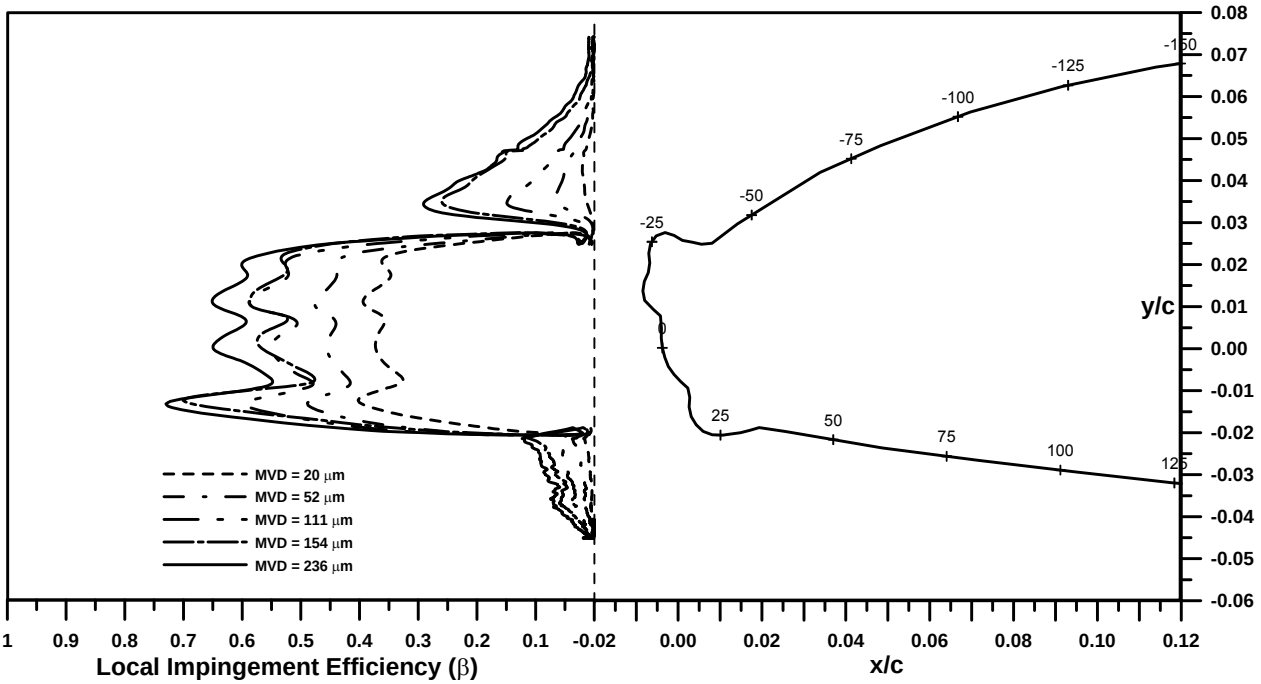

Figure 102. Experimental y/c vs Beta, NACA 23012 With 10-min Glaze Ice Shape

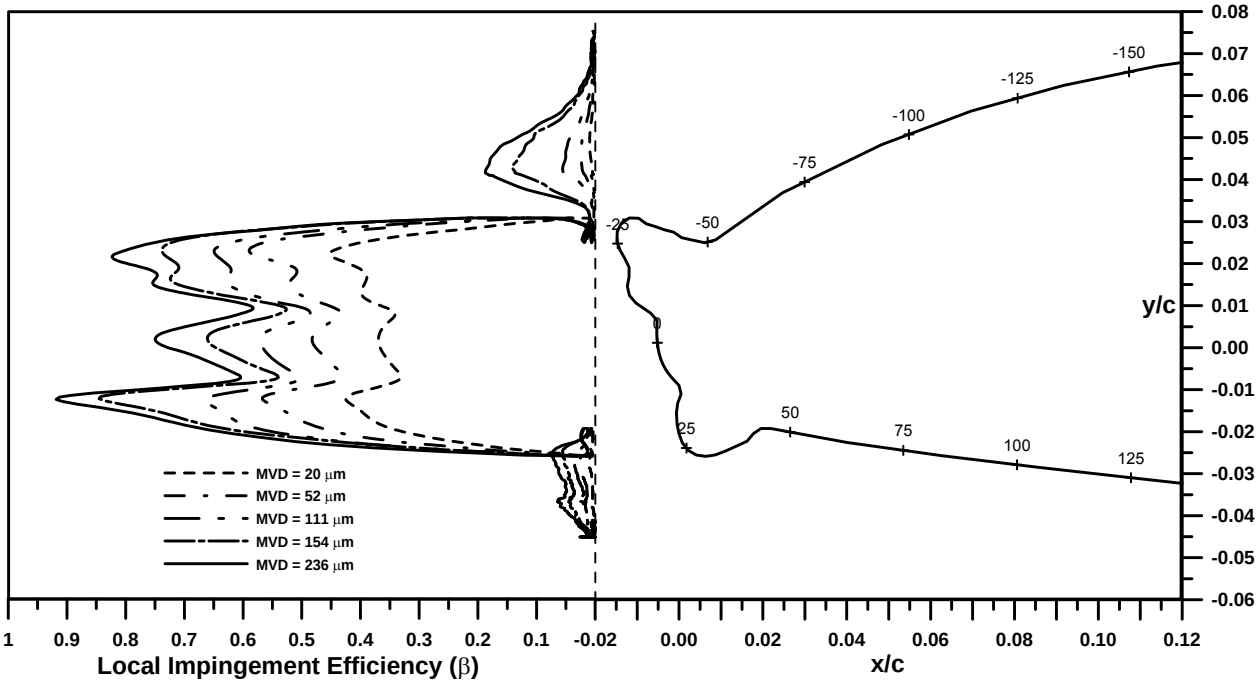

Figure 103. Experimental y/c vs Beta, NACA 23012 With 15-min Glaze Ice Shape

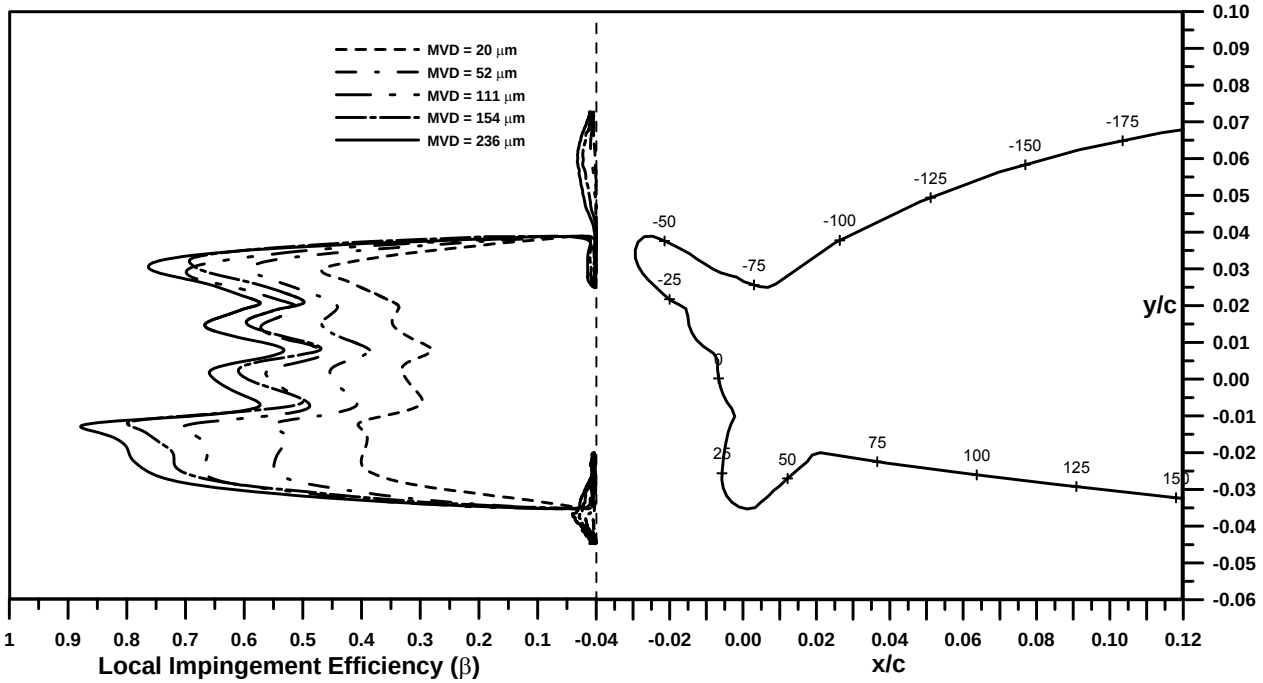

Figure 104. Experimental y/c vs Beta, NACA 23012 With 22.5-min Glaze Ice Shape

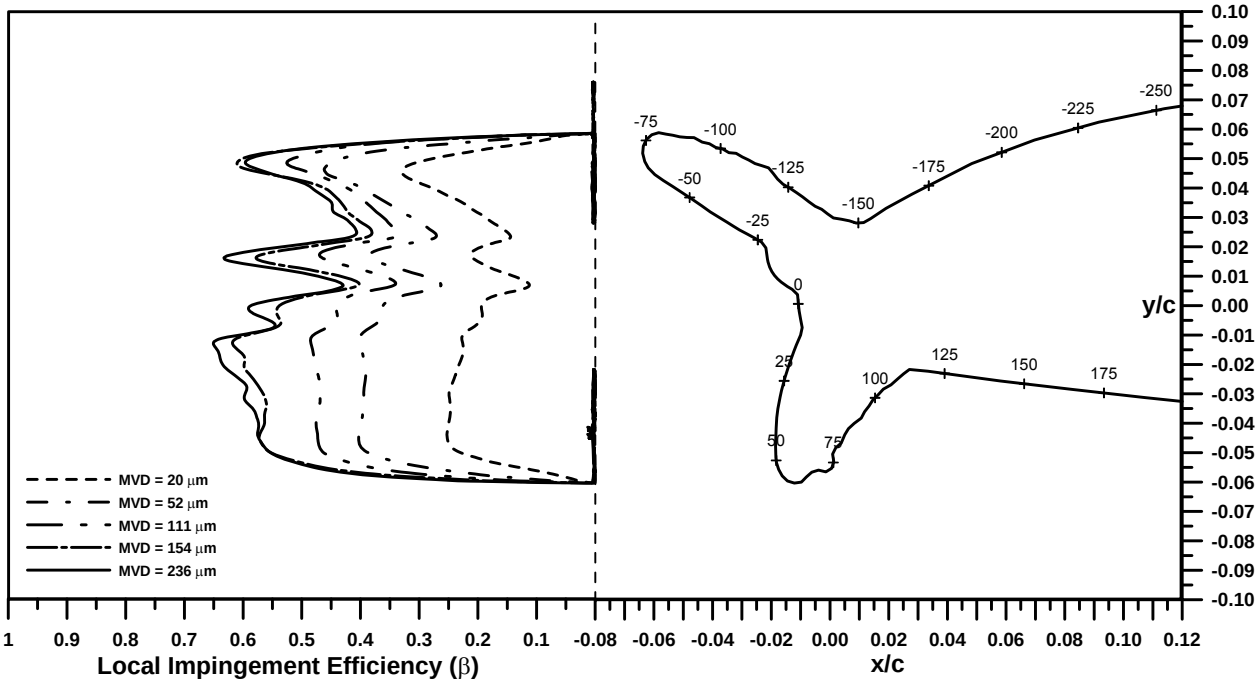

Figure 105. Experimental y/c vs Beta, NACA 23012 With 45-min Glaze Ice Shape

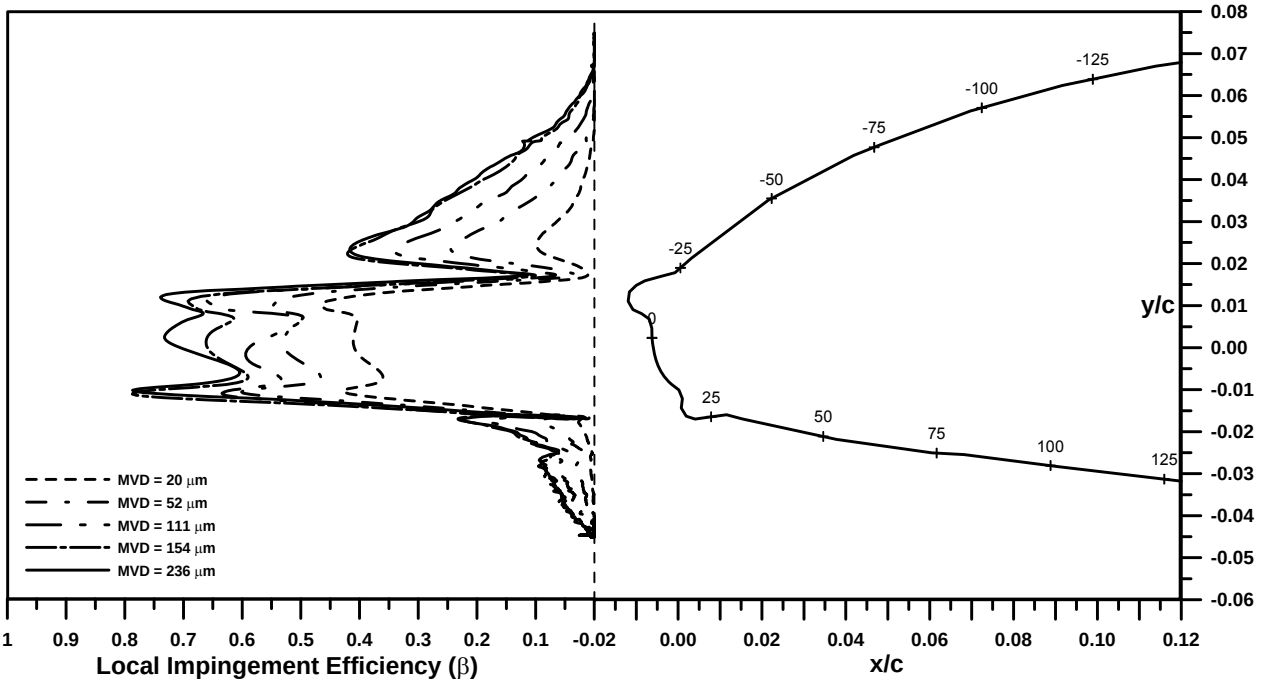

Figure 106. Experimental y/c vs Beta, NACA 23012 With 7.5-min Mixed Ice Shape

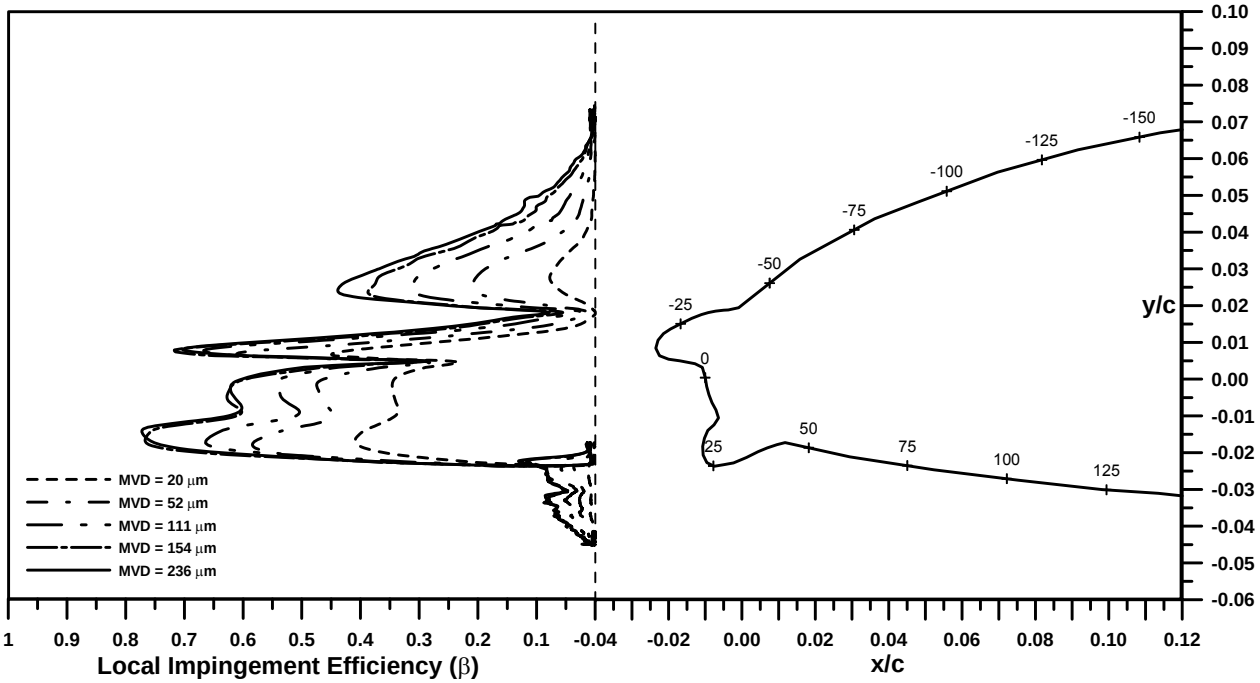

Figure 107. Experimental y/c vs Beta, NACA 23012 With 15-min Mixed Ice Shape

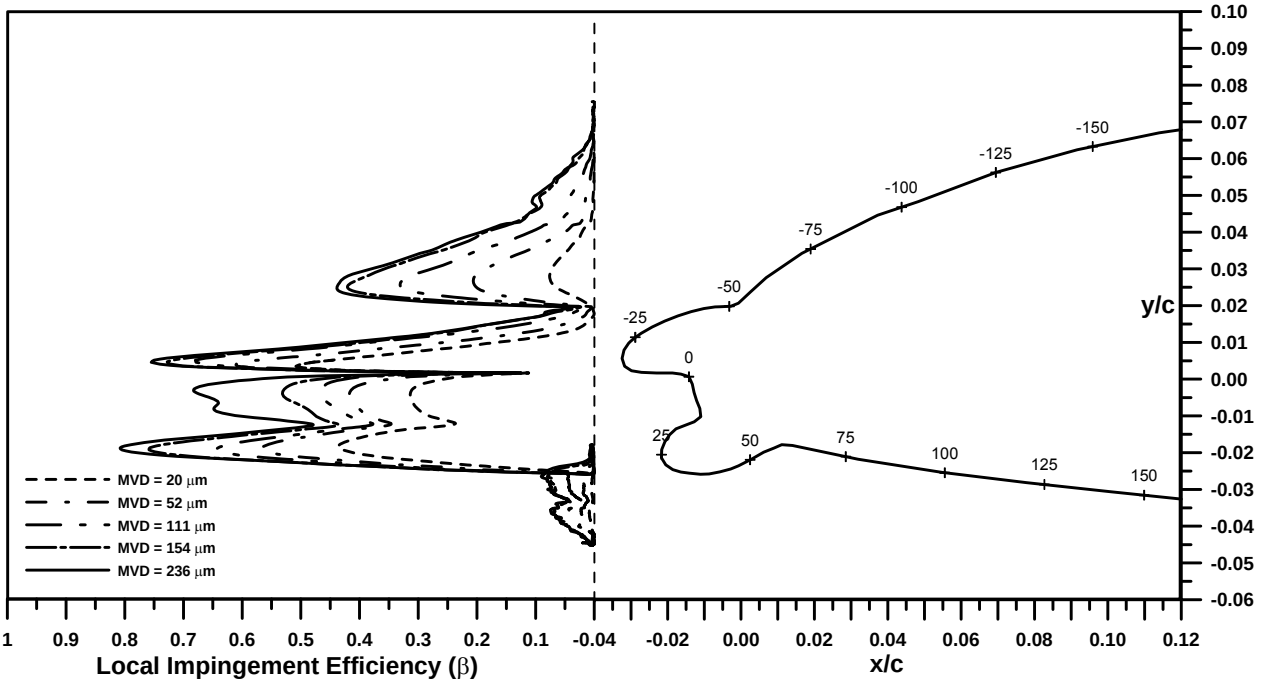

Figure 108. Experimental y/c vs Beta, NACA 23012 With 22.5-min Mixed Ice Shape

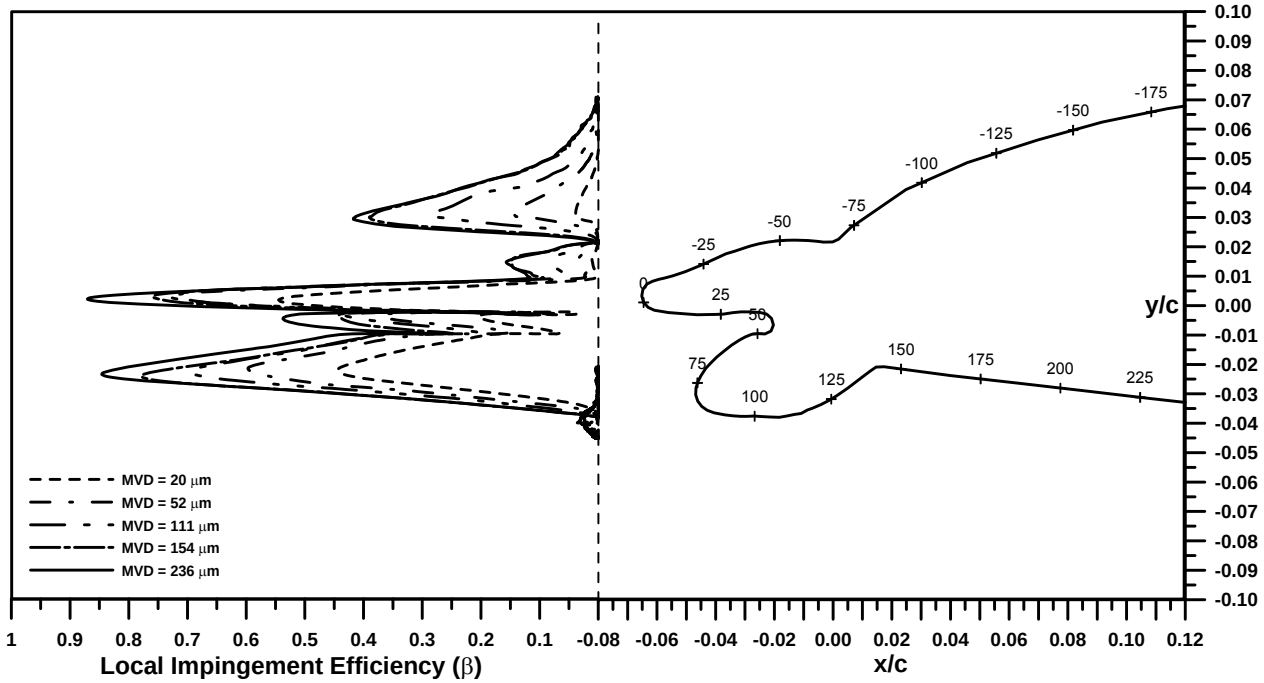

Figure 109. Experimental y/c vs Beta, NACA 23012 With 45-min Mixed Ice Shape

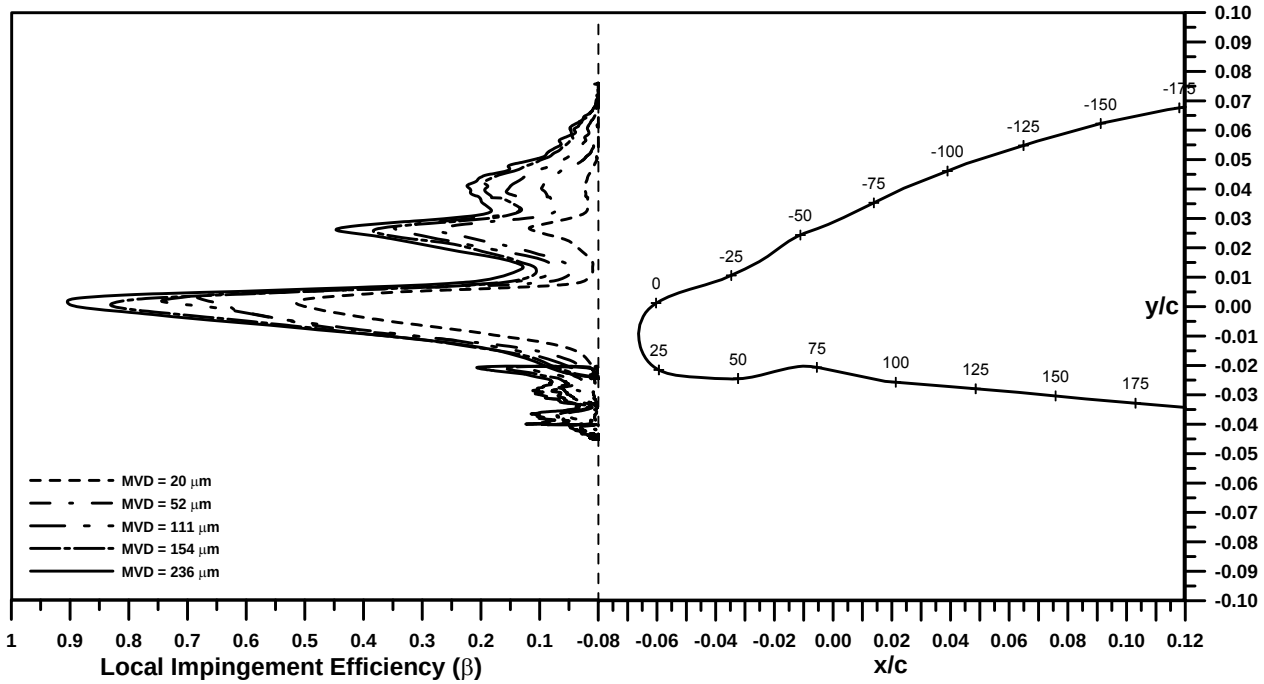

Figure 110. Experimental y/c vs Beta, NACA 23012 With 45-min Rime Ice Shape

7.4 DROP TRAJECTORIES.

Drop trajectories for selected test cases are shown in figures 111 through 114 to elucidate the impingement distribution trends observed with the iced configuration. The drop trajectories presented are for the clean NACA 23012 airfoil, the three 45-min ice shapes, and all five MVDs. All trajectories were computed with the LEWICE 1.7 code using a single drop-size set equal to the MVD of the experimental drop distribution.

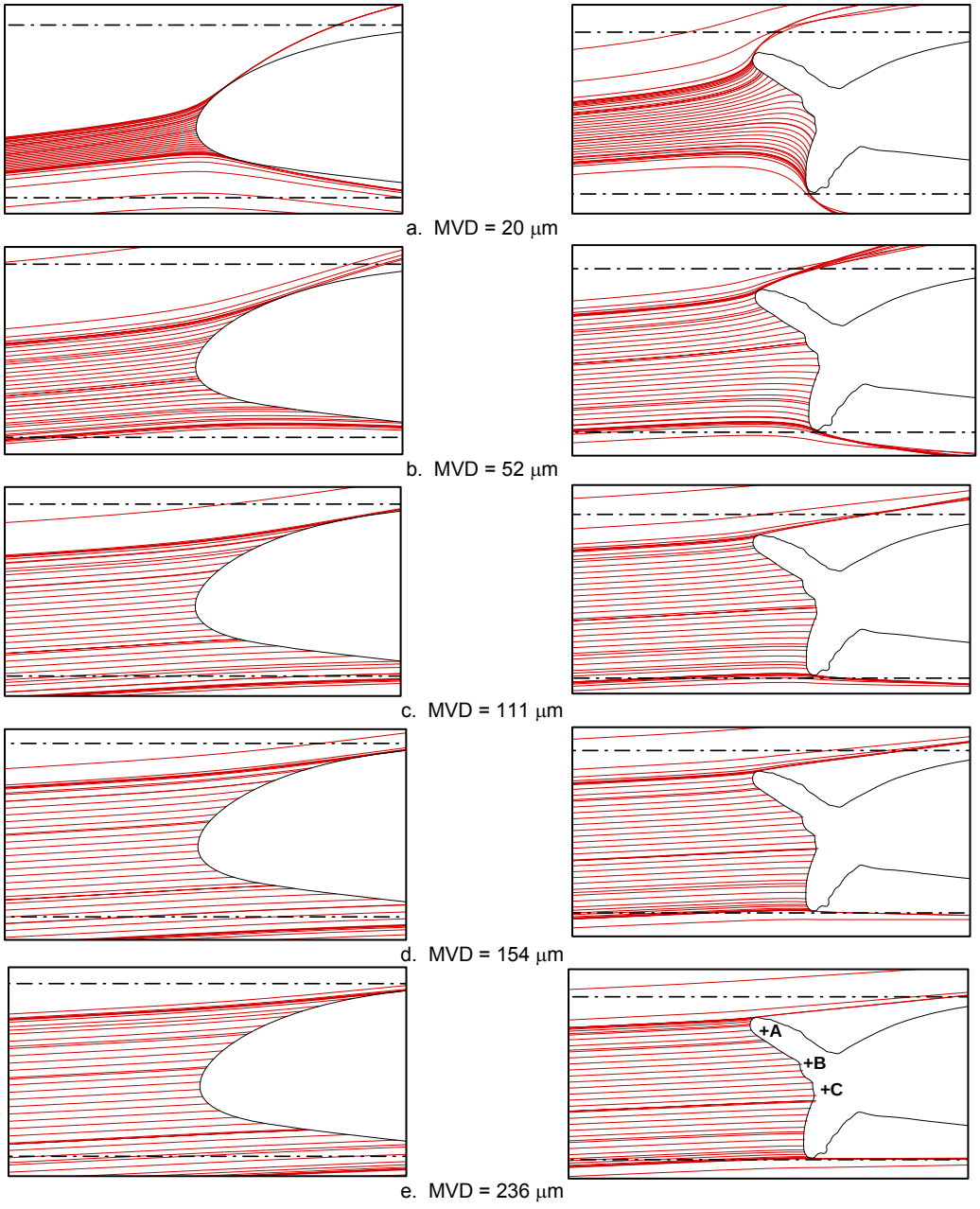

Figure 111. Particles Trajectories: NACA 23012 Airfoil

Figure 112. Particles Trajectories: NACA 23012 With 45-min Glaze Ice

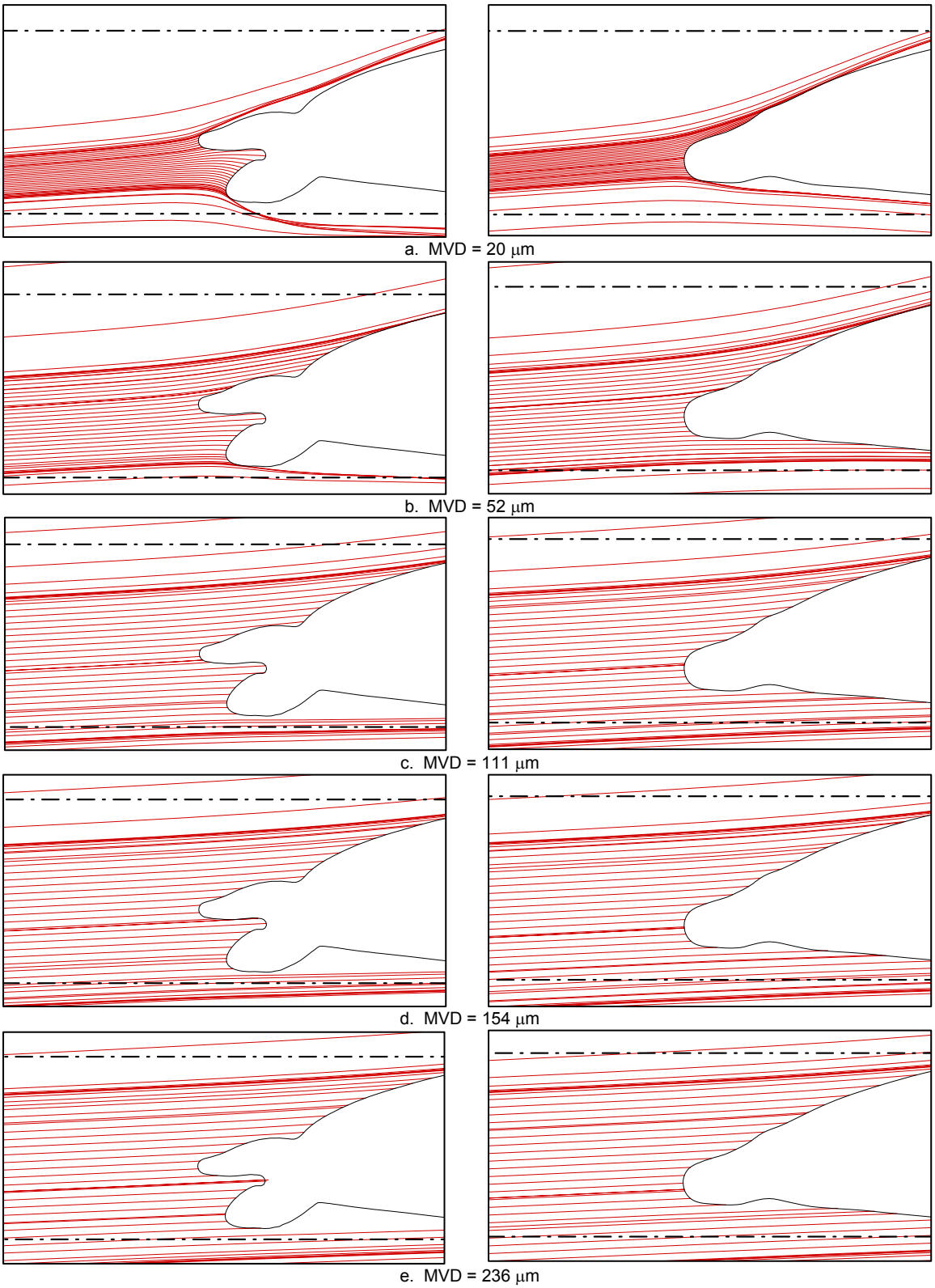

Figure 113. Particles Trajectories: NACA 23012 With 45-min Mixed Ice

Figure 114. Particles Trajectories: NACA 23012 With 45-min Rime Ice

The drop trajectories shown in figures 111 through 114 for the 20-μm case demonstrate considerable deflection in the vicinity to the ice shapes. The deflection of the trajectories became progressively smaller as the MVD size increased. At a drop size of 236 μm, the trajectories calculated for the 45-min mixed case were practically straight.

The experimental and computed impingement distributions shown exhibit several peaks in the region between the ice horns in the glaze and mixed ice shape cases. The trajectory simulations can be used to explain how these peaks form. For example, from the trajectory results shown in figure 112e, it is evident that near point A on the upper ice horn the impingement efficiency will be relatively high since the surface is nearly normal to the incoming drops. However, as the drops hit between locations A and B the impingement efficiency decreases due to the local slope of the surface. In the region between locations B and C the impingement efficiency increases or decreases depending on local slope.

The formation of the peaks in the experimental results was due to direct drop impingement as in the LEWICE case, but also due to potential water reimpingement due to drop splashing. The version of LEWICE used for the analysis did not have a splashing model so the deposition due to reimpingement was not included. Additional drop trajectories are provided in appendix D.

8. SUMMARY AND CONCLUSIONS.

Extensive wind tunnel tests were conducted at the National Aeronautics and Space Administration (NASA) Glenn Icing Research Tunnel (IRT) to expand the water drop impingement database for simulated ice shape configurations and for supercooled large drop (SLD) conditions. Tests were conducted with an MS(1)-0317 airfoil, and with a clean and iced National Advisory Committee for Aeronautics (NACA) 23012 airfoil. The iced configurations included ten simulated ice shapes that were defined with the NASA Glenn LEWICE 2.2 ice accretion code (LEWICE). The ice accretions tested with the NACA 23012 airfoil included 5-, 10-, 15-, 22.5-, and 45-min glaze ice shapes, 7.5-, 15-, 22.5-, and 45-min mixed ice shapes, and a 45-min rime ice shape. Test conditions included freestream velocity of approximately 175 mph, 2.5 degrees AOA, and cloud MVD of 20, 52, 111, 154, and 236 μm. Each experimental condition was repeated 3 to 4 times to establish a measure of test repeatability. Comparisons of experimental with impingement analysis data obtained with the NASA Glenn LEWICE (modified 27-bin, version 1.6) ice accretion code were performed. Below is a summary of key findings based on the work performed.

8.1 TEST REPEATABILITY.

- Repeated drop distribution measurements showed that the variation in MVD was ±0.5 μm from the average for the 20-μm cloud, ±2 μm for the 52-μm cloud, ±5 μm for the 111- and 154-μm clouds, and ±10 μm for the 236-μm cloud.

- For 55 of the 56 cases presented, the variation in total impingement efficiency of repeated impingement tests (3 to 4 tests) from the average was less than 10%. The number of repeated tests performed per test condition was not sufficient to establish a statistical average. However, the variations recorded were consistent for the 389 impingement tests

conducted with the two airfoils, ten ice shapes, and the collector device. In addition, impingement data for the MS(1)-0317 airfoil obtained during the 2003 IRT entry were in very good agreement with the data obtained for similar test conditions during five previous IRT entries. Thus, it would be reasonable to conclude that the experimental method used was repeatable.

8.2 PRESSURE DATA.

Comparison of experimental and LEWICE pressure distributions for the clean NACA 23012 airfoil and for most of the ice shapes tested were in good agreement. The main differences in the LEWICE and the experimental pressure distributions were observed with the large glaze ice shapes. In the 15- and 22.5-min glaze ice shape cases, LEWICE did not match the experimental pressure data over the forward 10% to 20% chord. For the 45-min ice shape, considerable disagreement between the experimental and the LEWICE pressure distributions were observed for the entire upper and lower surfaces. The observed discrepancy between experiment and analysis was due to the limitations of the potential method used in LEWICE in simulating viscous flowfields with extensive flow separation.

8.3 EXPERIMENTAL IMPINGEMENT DATA.

The impingement data for the clean NACA 23012 airfoil exhibited the following trends:

- Maximum impingement efficiency of 56%, 71%, 85%, 92%, and 95% for MVDs of 20, 52, 111, 154, and 236 μm, respectively. The corresponding values of total impingement efficiency were 19%, 30%, 42%, 51%, and 56%.

- The upper and lower impingement limits increased considerably as the MVD was increased. For the 236-μm case, the upper impingement limit extended to 11.6% chord and the lower impingement limit to 40.7% chord. Impingement limits locations for the clean NACA 23012 airfoil are shown in figure 115.

- For the large MVDs of 111, 154, and 236 μm, the growth in maximum and total impingement efficiencies and in the extent of impingement was reduced as the MVD was increased from 111 to 236 μm.

8.3.1 Glaze Ice Shapes.

The impingement data for the NACA 23012 airfoil with the five glaze ice shapes exhibited the following trends:

- Considerable impingement, characterized by multiple peaks, was observed in the leading-edge region between the ice horns. The impingement efficiency was, in general, greater near the horn tips than in the cavity between the horns, particularly for the larger ice shapes.

- Impingement efficiency and extent increased while MVD increased. Summary of chordwise locations of the impingement limits are provided in figures 116 through 120.

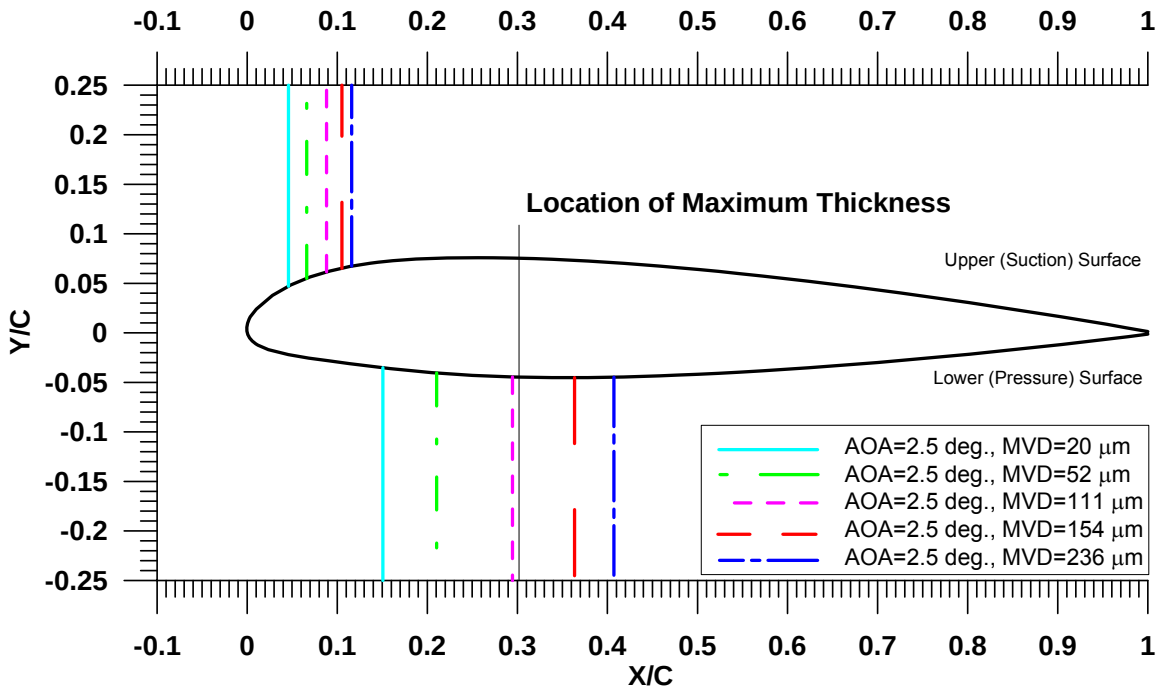

Figure 115. Experimental Impingement Limits for NACA 23012 Airfoil at AOA = 2.5°

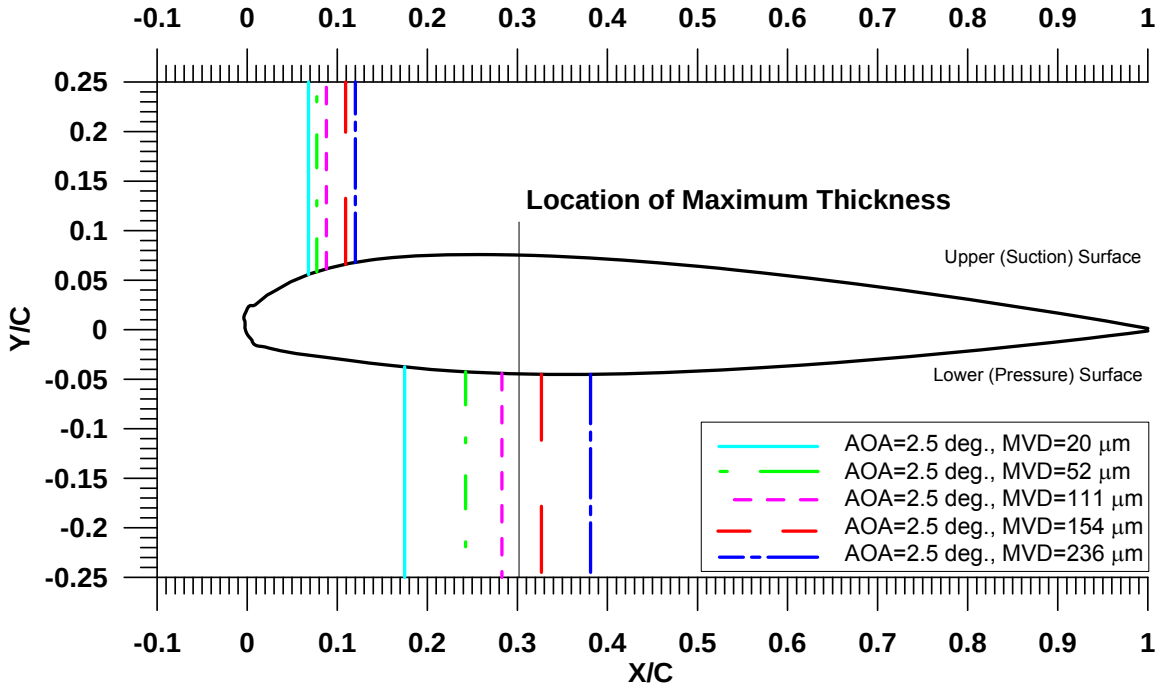

Figure 116. Experimental Impingement Limits for NACA 23012 Airfoil With 5-min Glaze Ice Shape at AOA = 2.5°

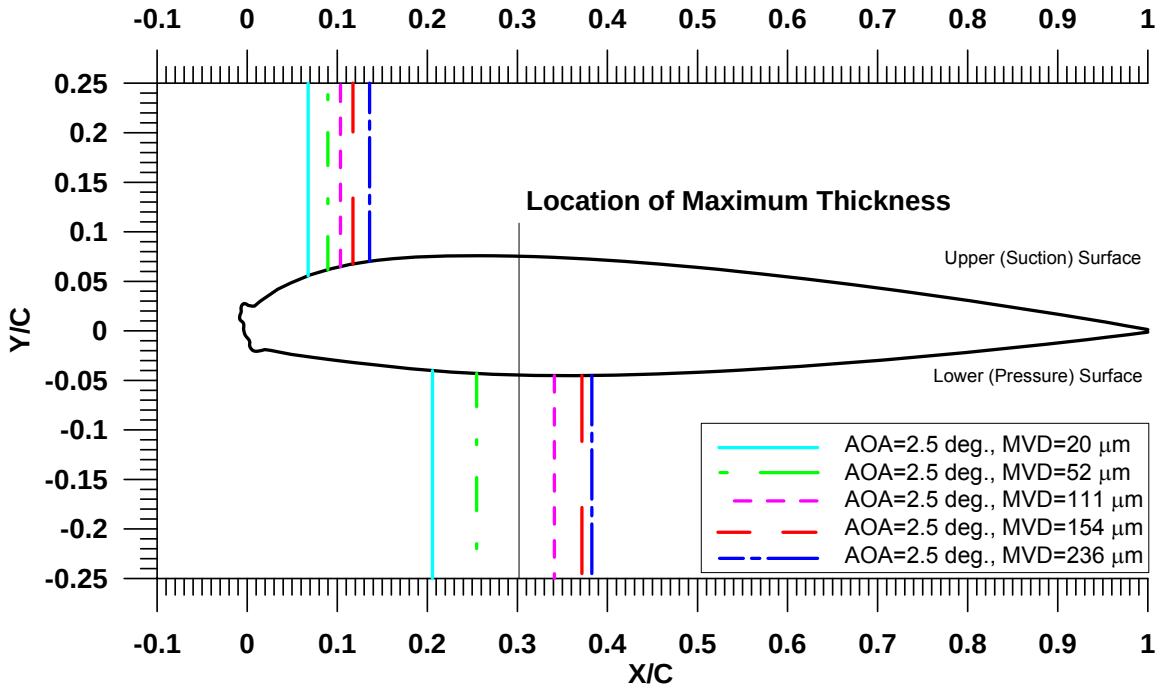

Figure 117. Experimental Impingement Limits for NACA 23012 Airfoil With 10-min Glaze Ice Shape at AOA = 2.5°

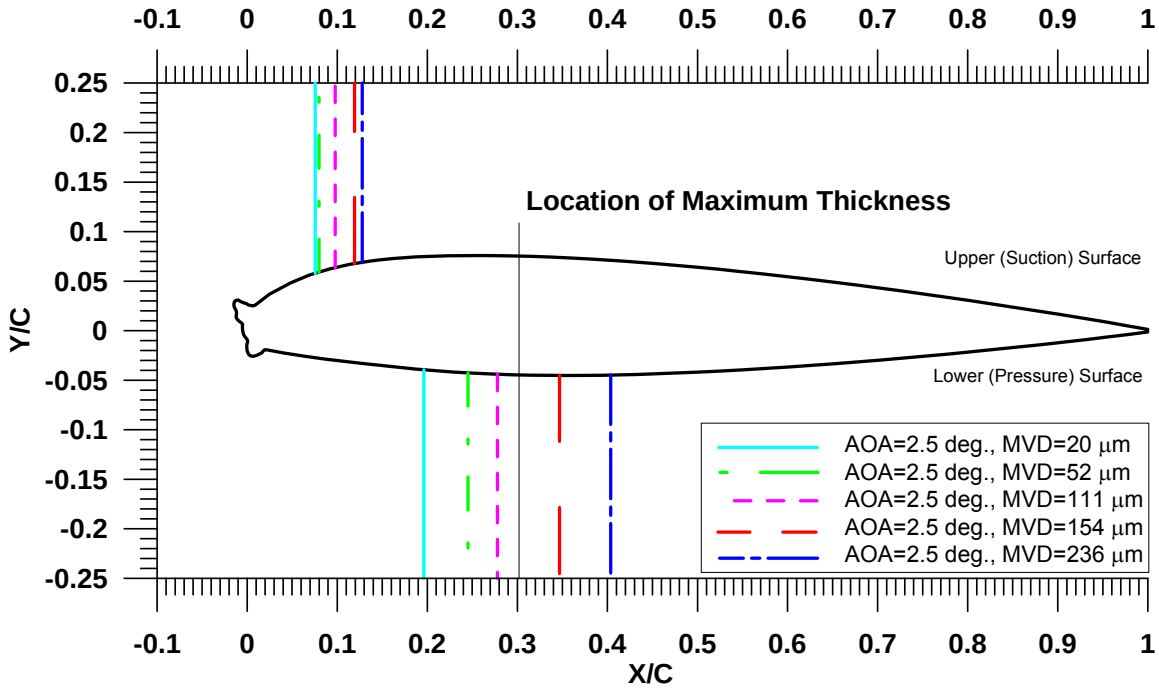

Figure 118. Experimental Impingement Limits for NACA 23012 Airfoil With 15-min Glaze Ice Shape at AOA = 2.5°

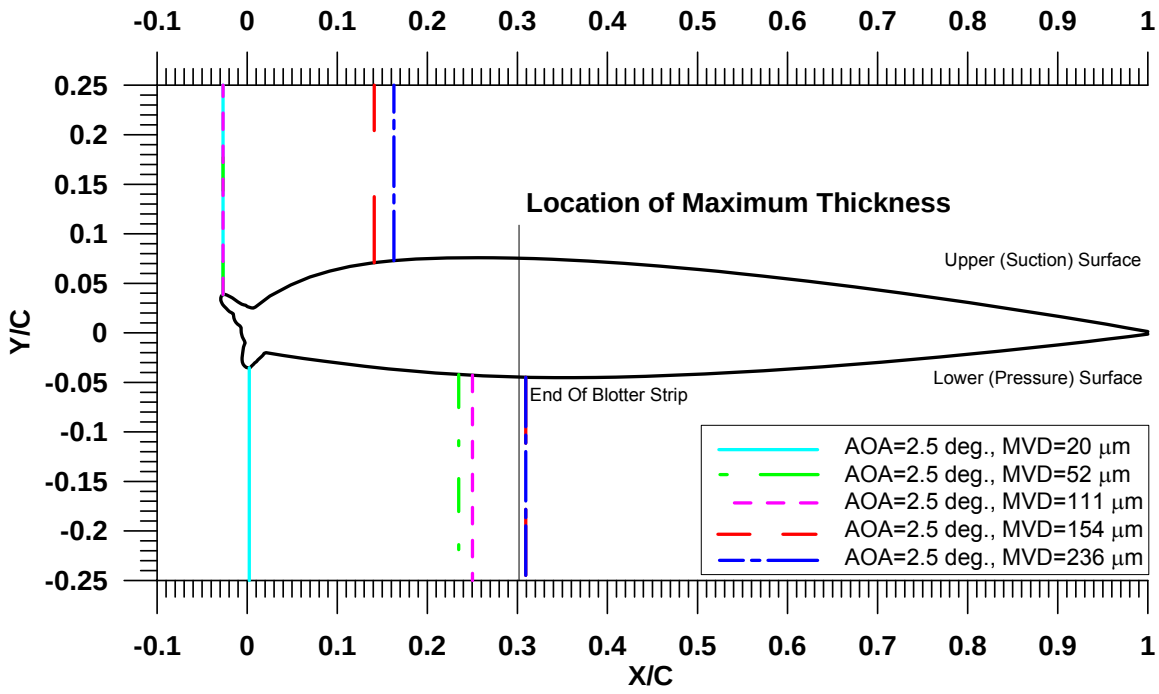

Figure 119. Experimental Impingement Limits for NACA 23012 Airfoil With 22.5-min Glaze Ice Shape at AOA = 2.5°

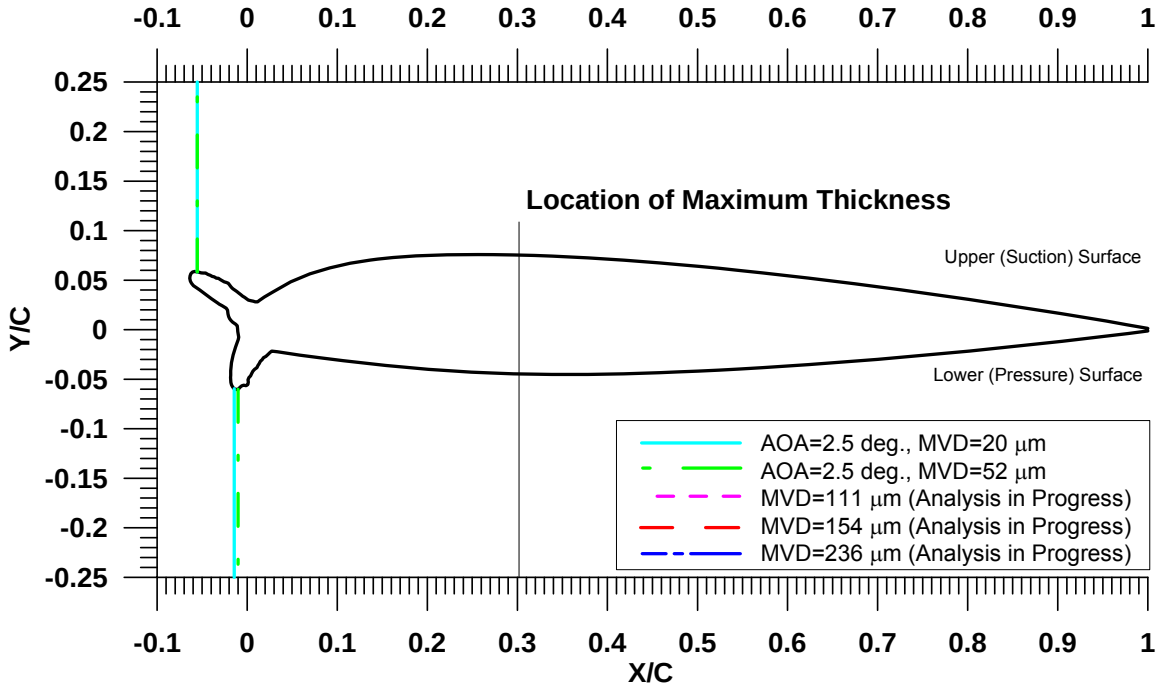

Figure 120. Experimental Impingement Limits for NACA 23012 Airfoil With 45-min Glaze Ice Shape at AOA = 2.5°

- In general, for all MVD, cases the total impingement efficiency decreased in the following sequence: clean, 5-min glaze ice shape, 10-min glaze ice shape. For the 15-, 22.5-, and 45-min glaze ice shapes, however, the total impingement efficiency increased as the size of the ice shape was increased. For all MVD cases, the maximum total impingement efficiency was obtained with the 45-min ice shape while the minimum total impingement efficiency was obtained with the 10-min glaze ice shape.

- For the 5-, 10-, and 15-min ice shapes, considerable impingement was observed on the upper and lower airfoil surfaces, downstream of the horns for MVDs, in the range of 52 to 236 μm. The efficiency and extent of the impingement decreased as the horn size was increased. For the 22.5- and 45-min ice shapes a sharp drop in impingement downstream of the horns was observed due to the horn shielding effect.

8.3.2 Mixed Ice Shapes.

The impingement data for the NACA 23012 airfoil with the four mixed ice shapes exhibited the following trends:

- Multiple impingement peaks were observed in the leading-edge region between the ice horns. The peak within the cavity area of the larger ice shapes was smaller than the impingement peaks obtained near the tip of the ice horns.

- In general, total impingement efficiency for all tested mixed ice shapes was lower than for the clean airfoil.

- Impingement efficiency and extent increased as the MVD was increased. For each MVD, the minimum total impingement efficiency was obtained with the 7.5-min mixed ice shape.

- The upper and lower impingement limits increased as the MVD was increased for all mixed ice shape cases. The upper impingement limits for each MVD were very similar for all ice shapes. The upper impingement limit was in the range of 5% to 8%, 7% to 9%, 10% to 11%, 12% to 13%, and 13% to 14% of chord for MVDs of 20, 52, 111, 154, and 236 μm, respectively. The lower impingement limit was found to be in the range of -4% to 30%, -3% to 32%, 31% to 36%, 39% to 43%, and 40% to 47% of chord as the MVD was increased from 20 to 236 μm. The negative sign indicates that the impingement limit was on the ice shape upstream of the airfoil leading edge. Impingement limits locations for the NACA 23012 airfoil with the mixed ice shapes are shown in figures 121-124.

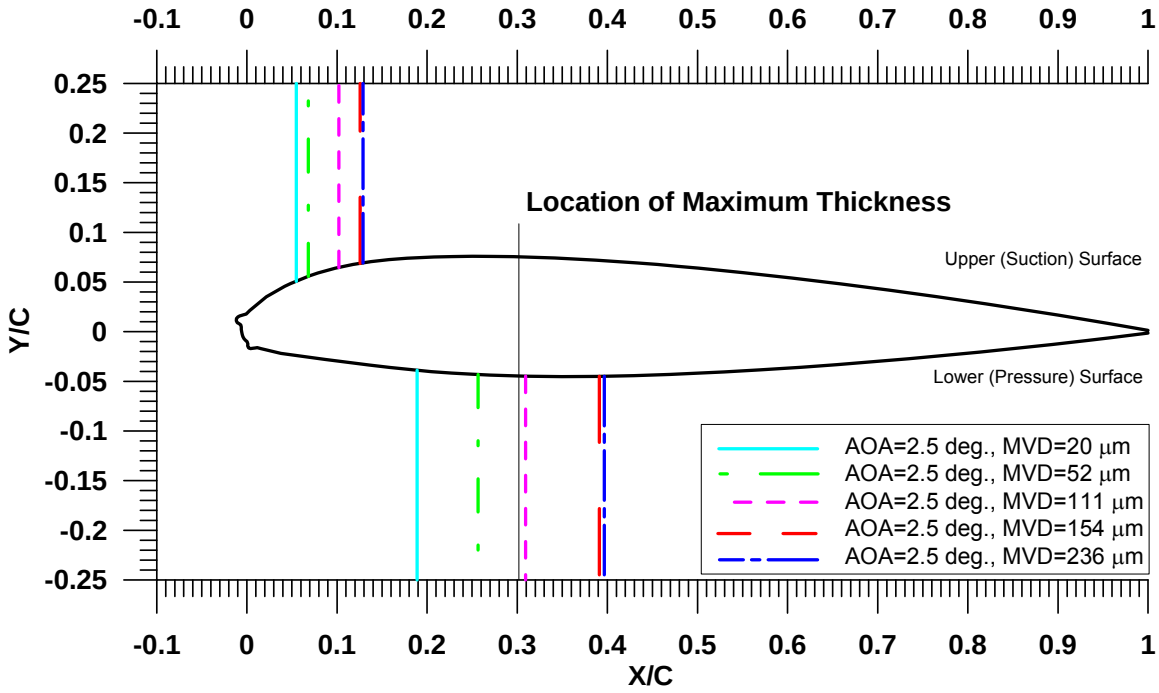

Figure 121. Experimental Impingement Limits for NACA 23012 Airfoil With 7.5-min Mixed Ice Shape at AOA = 2.5°

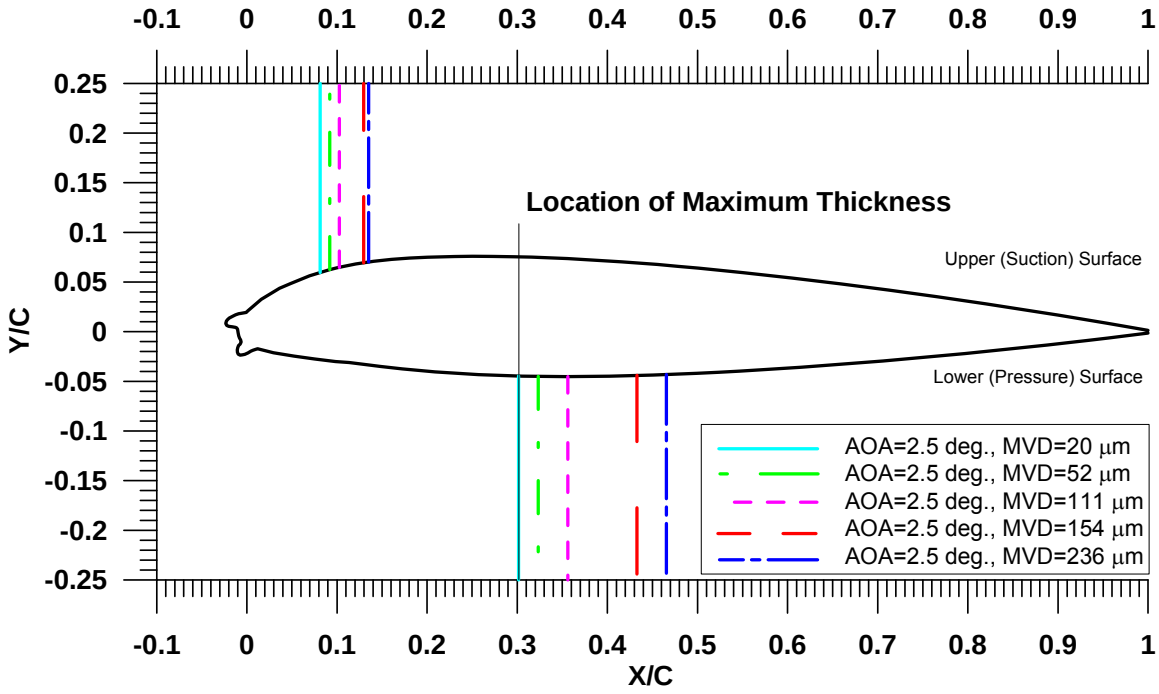

Figure 122. Experimental Impingement Limits for NACA 23012 Airfoil With 15-min Mixed Ice Shape at AOA = 2.5°

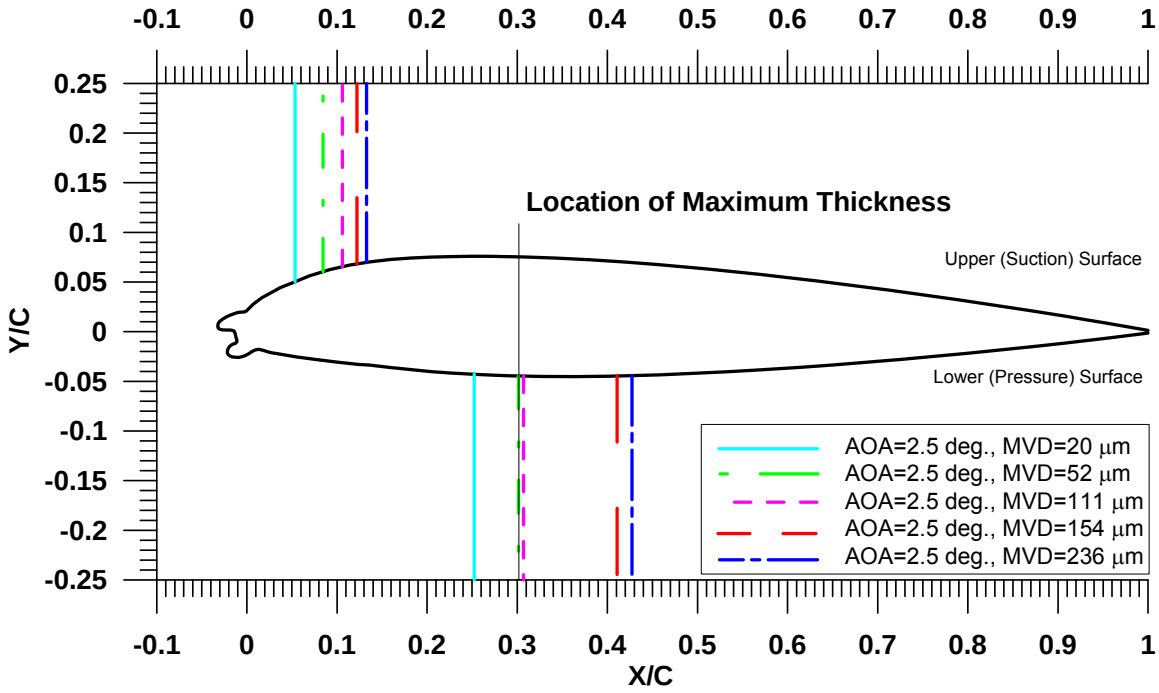

Figure 123. Experimental Impingement Limits for NACA 23012 Airfoil With 22.5-min Mixed Ice Shape at AOA = 2.5°

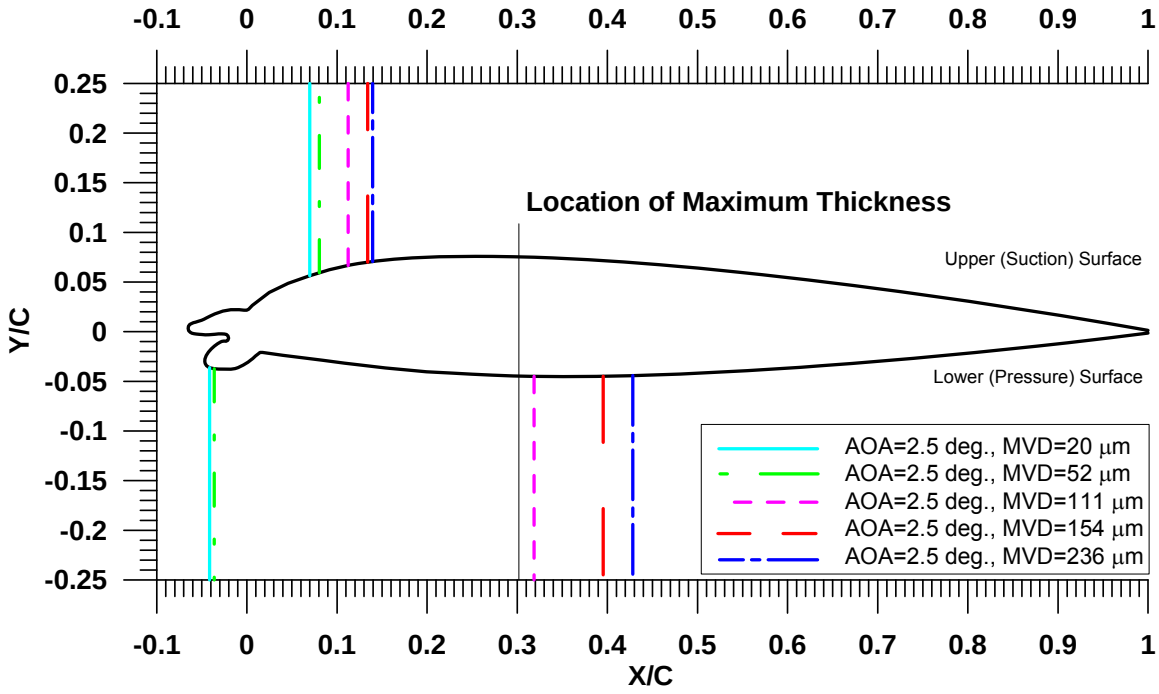

Figure 124. Experimental Impingement Limits for NACA 23012 Airfoil With 45-min Mixed Ice Shape at AOA = 2.5°

8.3.3 Rime Ice Shape.

The impingement data for the NACA 23012 airfoil with the rime ice shape exhibited the following trends:

- Total impingement efficiency for the 45-min rime ice shape was less than the clean NACA 23012 airfoil for all MVDs, except for the 236-μm case.

- Only a single peak was observed in the vicinity of the airfoil leading edge. The maximum local impingement efficiency for each tested MVD was also lower than the clean NACA 23012 airfoil.

- Maximum impingement efficiency of the 45-min rime ice shape was 52%, 68%, 74%, 83%, and 91%, while total impingement efficiency was 13%, 27%, 37%, 45%, and 57% for MVDs of 20, 52, 111, 154, and 236 μm, respectively.

- As the MVD increased from 20 to 236 μm, for the 45-min rime ice shape, the upper limit ranged from 6% to 13% chord, while the lower impingement limit ranged from 20% to 40% chord. Impingement limits locations for the NACA 23012 airfoil with 45-min rime ice shape are shown in figure 125.

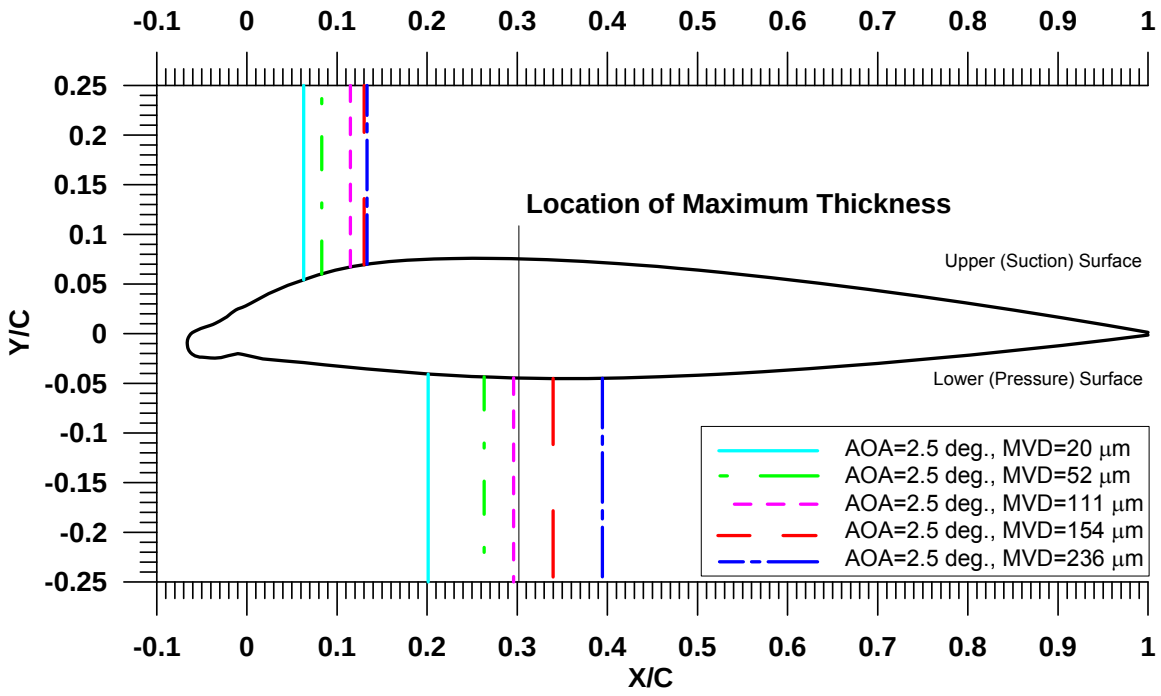

Figure 125. Experimental Impingement Limits for NACA 23012 Airfoil With 45-min Rime Ice Shape at AOA = 2.5°

8.4 LEWICE VS EXPERIMENTAL IMPINGEMENT DATA.

For the 20-μm MVD and the clean airfoil, the LEWICE and the experimental data were in good agreement. For the iced configurations, however, the predicted impingement efficiency for the 20-μm MVD was higher than that obtained experimentally. For the large MVD cases of 52, 111, 154, and 236 μm, the LEWICE impingement data exhibited considerably higher local and total impingement efficiencies and greater impingement limits compared to the experimental results. A possible reason for the observed differences between LEWICE and experiment for the large-MVD cases is drop splashing, which is not simulated in the LEWICE code. Another potential reason is the difference between the computed and the experimental flowfields, particularly for the large 22.5- and 45-min glaze ice shapes. Finally, a numerical interpolation scheme used in LEWICE to compute impingement efficiency, resulted in unrealistic impingement tails immediately downstream of the large glaze ice shape horns. This further exacerbated the difference between experimental and computed total impingement efficiencies. It was demonstrated that the use of the Monte-Carlo method to compute impingement efficiency in these cases improved the correlation between the experimental and computed results.

8.5 RECOMMENDATIONS FOR FURTHER WORK.

Experiments using advanced imaging methods should be conducted to investigate and document large drop splashing on large glaze ice shapes to determine the effects of splashed drops on the impingement characteristics of ice accretions. Of interest is the deposition of splashed drops in the region between the horns and the trajectories of drops splashing of the horn tips.

Based on the pressure data presented, the LEWICE did not match the experimental results particularly for the cases of the 22.5- and 45-min ice shapes. A Navier-Stokes analysis should be performed for the large ice shapes and the computed flowfield should be used in place of the LEWICE potential flow solution to perform a new impingement analysis.

A drop splash and breakup model should be incorporated in a trajectory code and the model should be used to compute impingement characteristics for the tested ice shapes. The calibration of this model may require additional impingement data at lower and higher tunnel speeds than those available in the 1985-2003 impingement data base.

9. REFERENCES.

1. Wolfe, H.E. and Andersen, W.H., "Kinetics, Mechanism, and Resultant Drop Sizes of the Aerodynamic Breakup of Liquid Drops," Aerojet-General Corporation Research and Engineering Division, Report No. 0395-04 (18) SP, 1964.

2. Hinze, J.O., "Fundamentals of the Hydrodynamic Mechanism of Splitting in Dispersion Processes," *A.I.Ch.E. Journal*, Vol. 1, No. 3, pp. 289-295, 1955.

3. Mundo, Chr., Sommerfeld, M., and Tropea, C., "Drop-Wall Collisions: Experimental Studies of the Deformation and Breakup Process," *International Journal of Multiphase Flow*, Vol. 21, No. 2, pp. 151-173, 1995.

4. Tan, S.C. and Papadakis, M., "General Effects of Large Droplet Dynamics on Ice Accretion Modeling," AIAA Paper 2003-0392, January 2003.

5. Tan, S.C., Papadakis, M., and Sampath, M.K., "Computational Study of Large Droplet Breakup in the Vicinity of an Airfoil," FAA report DOT/FAA/AR-05/42, October 2005.

6. Papadakis, M., Rachman, A., Wong, S.C., Hung, K.E., Vu, G.T., and Bidwell, C.S., "Experimental Study of Supercooled Large Droplet Impingement Effects," FAA report DOT/FAA/AR-03/59, September 2003.

7. Papadakis, M. and Bidwell, C.S., "An Experimental Investigation of SLD Impingement on Airfoils and Simulated Ice Shapes," *Proceeding of the FAA In-Flight Icing/Ground De-Icing International Conference*, Chicago, Illinois, June 2003.

8. Von Glahn, U., Gelder, T.F., and Smyers, W.H. Jr., "A Dye Tracer Technique for Experimentally Obtaining Impingement Characteristics of Arbitrary Bodies and a Method for Determining Droplet Size Distribution," NACA TN 3338, March 1955.

9. Gelder, T.F., Smyers, W.H. Jr., and Von Glahn, U., "Experimental Droplet Impingement on Several Two-Dimensional Airfoils With Thickness Ratios of 6 to 16 Percent," NACA TN 3839, December 1956.

10. Lewis, J.O. and Ruggeri, R.S., "Experimental Droplet Impingement on Four Bodies of Revolution," NACA TN 3587, 1957.

11. Lewis, James O. and Ruggeri, Robert S., "Experimental Droplet Impingement on Four Bodies of Revolution," NACA TN 4092, December 1955.

12. Gelder, T.F., "Droplet Impingement and Ingestion by Supersonic Nose Inlet in Subsonic Tunnel Conditions," NACA TN 4268, May 1958.

13. Papadakis, M., Elangovan, R., Freund, G.A., Jr., Breer, M., Zumwalt, G.W., and Whitmer, L., "An Experimental Method for Measuring Water Droplet Impingement Efficiency on Two- and Three-Dimensional Bodies," NASA CR 4257, FAA report DOT/FAA/CT-87/22, November 1989.

14. Papadakis, M., Breer, M.D., Craig, N., and Liu, X., "Experimental Water Droplet Impingement Data on Airfoils, Simulated Ice Shapes, an Engine Inlet, and a Finite Wing," NASA CR 4636, FAA report DOT/FAA/CT-TN93/18, December 1994.

15. Phillips, E.H., "ATR42/72 Review Focuses on Icing," *Aviation Week and Space Technology*, November 14, 1994.

16. Phillips, E.H., "FAA Lifts Icing Ban on ATR Flights," *Aviation Week and Space Technology*, June 5, 1995.

17. Papadakis, M., Hung, K.E., Vu, G.T., Yeong, H.W., Bidwell, C., Breer, M.D., and Bencic, T., "Experimental Investigation of Water Droplet Impingement on Airfoils, Finite Wings, and an S-Duct Engine Inlet," NASA/TM 2002-211700, September 2001.

18. "Airworthiness Standards: Transport Category Airplanes," Title 14 CFR Part 25, including Amendment 25-101, as published in the Federal Register on December 19, 2000.

19. Langmuir, I. and Blodgett, K.B., "A Mathematical Investigation of Water Droplet Trajectories," Army Air Forces Technical Report No. 5418, 1946.

20. Wright, W.B. and Potapczuk, M.G., "Semi-Empirical Modeling of SLD Physics," AIAA 2004-0412, *42nd AIAA Aerospace Sciences Meeting and Exhibit*, 2004.

21. Beard, K.V. and Pruppacher, H.R., "A Determination of the Terminal Velocity and Drag of Small Water Drops by Means of a Wind Tunnel," *Journal of Atmospheric Science*, Vol. 26, No. 26, pp. 1066-1072, 1969.

22. Pilch, M. and Erdman, C.A., "Use of Breakup Time Data and Velocity History Data to Predict the Maximum Size of Stable Fragments for Acceleration-Induced Breakup of a Liquid Drop," *International Journal of Multiphase Flow*, Vol. 13, No. 6, pp. 741-757, 1987.

23. Rutkowsky, A., Wright, W.B., and Potapczuk, M., "Numerical Study of Droplet Splashing and Re-Impingement," AIAA 2003-388, *41st AIAA Aerospace Sciences Meeting and Exhibit*, 2003.

24. Soeder, R.H., Sheldon, D.W., Ide., R.F., Spera, D.A., and Andracchio, C.R., "NASA Glenn Icing Research Tunnel User Manual," NASA TM-2003-212004, September 2003.

25. McGhee, R.J. and Beasley, W.D., "Low-Speed Aerodynamic Characteristics of a 17-Percent-Thick Medium-Speed Airfoil Designed for General Application," NASA TP 1786, 1980.

26. Wright, W.B., "User Manual for the NASA Glenn Ice Accretion Code LEWICE, 2.2.2 Final Report," NASA/CR-2002-211793, August 2002.

27. Oldenburg, J.R. and Ide, R.F., "Comparison of Drop Size Distributions From Two Droplet Sizing Systems," NASA TM 102520, March 1990.

28. "CSIRO-KING Liquid Water Content Probe PMS Model KLWC-5—Operating and Servicing Manual," Particle Measuring Systems, Inc., Boulder, Colorado.

29. Papadakis, M., Vu, G.T., Hung, E.K., Bidwell, C.S., Bencic, T., and Breer, M.D., "Progress in Measuring Water Impingement Characteristics on Aircraft Surfaces," AIAA Paper 98-0488, January 1988.

30. Wright, W.B., "Users Manual for the Improved NASA Lewis Ice Accretion Code LEWICE 1.6," NASA CR 198355, June 1995.

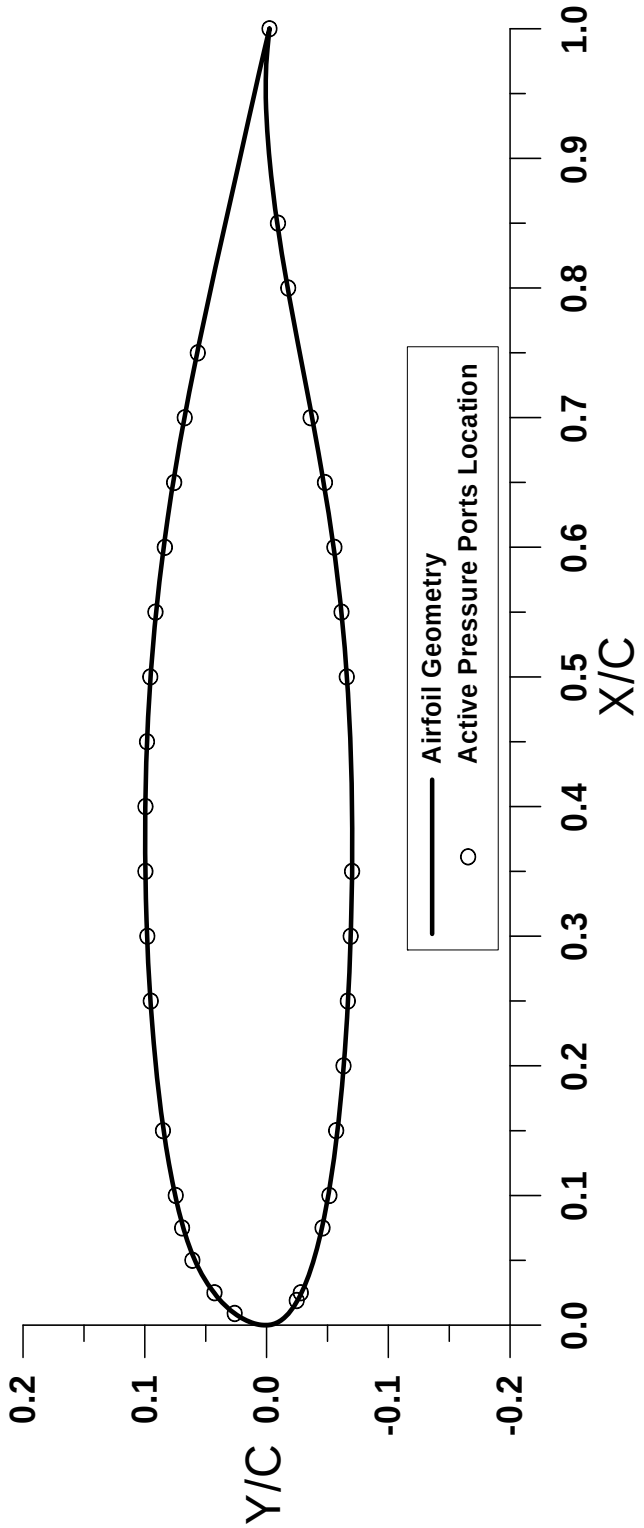

Figure A-1. MS(1)-0317 Airfoil

Table A-1. Coordinates of MS(1)-0317 Airfoil

Lower Surface						Upper Surface					
x/c	y/c	x/c	y/c	x/c	y/c	x/c	y/c	x/c	y/c	x/c	y/c
1	-0.0024	0.3147	-0.0695			0.0000	0.0022	0.2795	0.0972	1	-0.0024
0.9848	-0.0007	0.2977	-0.0690			0.0001	0.0042	0.2959	0.0980		
0.9725	0.0002	0.2811	-0.0684			0.0004	0.0062	0.3118	0.0986		
0.9603	0.0007	0.2643	-0.0676			0.0008	0.0081	0.3251	0.0990		
0.9469	0.0007	0.2473	-0.0667			0.0013	0.0101	0.3375	0.0993		
0.9332	0.0002	0.2306	-0.0657			0.0018	0.0120	0.3527	0.0996		
0.9193	-0.0006	0.2145	-0.0645			0.0025	0.0139	0.3690	0.0997		
0.9051	-0.0017	0.1982	-0.0631			0.0032	0.0157	0.3854	0.0997		
0.8907	-0.0032	0.1814	-0.0616			0.0040	0.0176	0.4020	0.0995		
0.8760	-0.0050	0.1657	-0.0600			0.0049	0.0193	0.4183	0.0992		
0.8612	-0.0070	0.1502	-0.0582			0.0059	0.0211	0.4341	0.0988		
0.8460	-0.0093	0.1348	-0.0562			0.0068	0.0229	0.4498	0.0983		
0.8304	-0.0119	0.1199	-0.0540			0.0079	0.0246	0.4658	0.0975		
0.8145	-0.0147	0.1055	-0.0516			0.0090	0.0262	0.4818	0.0966		
0.7981	-0.0177	0.0911	-0.0489			0.0101	0.0279	0.4971	0.0956		
0.7812	-0.0210	0.0772	-0.0459			0.0113	0.0295	0.5129	0.0943		
0.7640	-0.0244	0.0640	-0.0427			0.0126	0.0311	0.5290	0.0929		
0.7443	-0.0283	0.0496	-0.0385			0.0138	0.0326	0.5446	0.0913		
0.7249	-0.0323	0.0394	-0.0350			0.0152	0.0341	0.5601	0.0896		
0.7061	-0.0361	0.0323	-0.0321			0.0165	0.0355	0.5755	0.0877		
0.6903	-0.0392	0.0273	-0.0298			0.0180	0.0370	0.5908	0.0857		
0.6732	-0.0425	0.0238	-0.0280			0.0194	0.0383	0.6063	0.0836		
0.6576	-0.0454	0.0213	-0.0267			0.0209	0.0397	0.6223	0.0812		
0.6433	-0.0479	0.0196	-0.0257			0.0224	0.0410	0.6383	0.0787		
0.6273	-0.0507	0.0179	-0.0247			0.0245	0.0428	0.6545	0.0760		
0.6112	-0.0533	0.0162	-0.0236			0.0276	0.0453	0.6713	0.0730		
0.5956	-0.0557	0.0145	-0.0225			0.0320	0.0485	0.6871	0.0701		
0.5802	-0.0578	0.0129	-0.0213			0.0384	0.0527	0.7018	0.0673		
0.5648	-0.0597	0.0113	-0.0201			0.0479	0.0579	0.7178	0.0639		
0.5488	-0.0615	0.0098	-0.0188			0.0588	0.0628	0.7353	0.0602		
0.5328	-0.0632	0.0083	-0.0175			0.0708	0.0671	0.7518	0.0565		
0.5172	-0.0646	0.0070	-0.0160			0.0835	0.0709	0.7687	0.0528		
0.5014	-0.0658	0.0056	-0.0145			0.0967	0.0743	0.7858	0.0489		
0.4851	-0.0669	0.0044	-0.0129			0.1103	0.0774	0.8025	0.0451		
0.4690	-0.0679	0.0034	-0.0112			0.1245	0.0802	0.8211	0.0407		
0.4529	-0.0687	0.0024	-0.0095			0.1391	0.0828	0.8389	0.0365		
0.4367	-0.0693	0.0016	-0.0076			0.1541	0.0852	0.8565	0.0324		
0.4202	-0.0698	0.0010	-0.0057			0.1690	0.0873	0.8758	0.0278		
0.4061	-0.0701	0.0005	-0.0038			0.1843	0.0892	0.8946	0.0233		
0.3966	-0.0702	0.0002	-0.0018			0.2001	0.0910	0.9130	0.0189		
0.3824	-0.0703	0.0000	0.0002			0.2156	0.0925	0.9312	0.0145		
0.3655	-0.0703					0.2313	0.0939	0.9486	0.0103		
0.3487	-0.0702					0.2473	0.0952	0.9658	0.0062		
0.3317	-0.0699					0.2633	0.0962	0.9827	0.0020		

Table A-2. Coordinates of Active Pressure Ports of MS(1)-0317 Airfoil

Lower Surface		Upper Surface	
x/c	y/c	x/c	y/c
1.0000	-0.00236	0.0090	0.02624
0.8500	-0.00932	0.0250	0.04282
0.8000	-0.01772	0.0500	0.06098
0.7000	-0.03612	0.0750	0.06941
0.6500	-0.04792	0.1000	0.07465
0.6000	-0.05566	0.1500	0.08515
0.5500	-0.06151	0.2500	0.09516
0.5000	-0.06581	0.3000	0.09797
0.3500	-0.07019	0.3500	0.09956
0.3000	-0.06901	0.4000	0.09953
0.2500	-0.06670	0.4500	0.09827
0.2000	-0.06314	0.5000	0.09557
0.1500	-0.05714	0.5500	0.09131
0.1000	-0.05157	0.6000	0.08358
0.0750	-0.04592	0.6500	0.07596
0.0250	-0.02804	0.7000	0.06726
0.0190	-0.02472	0.7500	0.05654

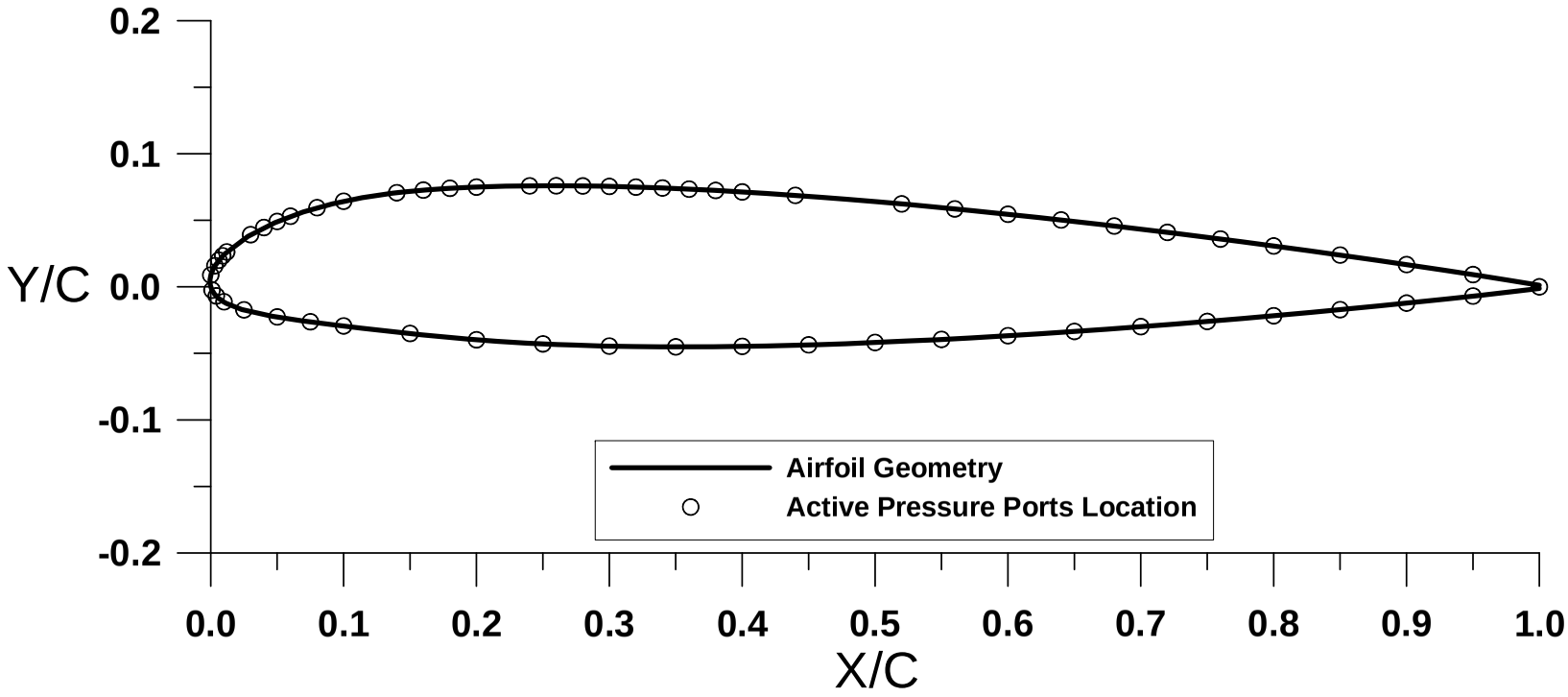

Figure A-2. NACA 23012 Airfoil

Table A-3. Coordinates of NACA 23012 Airfoil

Lower Surface						Upper Surface					
x/c	y/c	x/c	y/c	x/c	y/c	x/c	y/c	x/c	y/c	x/c	y/c
1.0000	-0.0013	0.0234	-0.0170			-0.0002	0.0008	0.7958	0.0313		
0.9783	-0.0038	0.0118	-0.0124			-0.0005	0.0031	0.8185	0.0282		
0.9556	-0.0063	0.0096	-0.0112			-0.0005	0.0054	0.8411	0.0251		
0.9330	-0.0088	0.0077	-0.0099			-0.0001	0.0076	0.8637	0.0220		
0.9103	-0.0112	0.0059	-0.0085			0.0004	0.0099	0.8863	0.0187		
0.8876	-0.0135	0.0043	-0.0070			0.0012	0.0120	0.9088	0.0154		
0.8649	-0.0157	0.0028	-0.0053			0.0022	0.0141	0.9314	0.0120		
0.8421	-0.0179	0.0015	-0.0034			0.0034	0.0161	0.9540	0.0086		
0.8194	-0.0200	0.0005	-0.0013			0.0099	0.0241	0.9765	0.0050		
0.7967	-0.0220					0.0280	0.0379	1.0000	0.0013		
0.7740	-0.0240					0.0483	0.0483				
0.7512	-0.0259					0.0696	0.0563				
0.7285	-0.0277					0.0916	0.0624				
0.7057	-0.0295					0.1140	0.0670				
0.6830	-0.0312					0.1365	0.0703				
0.6602	-0.0328					0.1592	0.0727				
0.6375	-0.0344					0.1820	0.0742				
0.6147	-0.0358					0.2048	0.0752				
0.5919	-0.0372					0.2276	0.0757				
0.5691	-0.0385					0.2504	0.0760				
0.5463	-0.0397					0.2732	0.0759				
0.5236	-0.0408					0.2961	0.0756				
0.5008	-0.0418					0.3189	0.0750				
0.4780	-0.0427					0.3417	0.0742				
0.4552	-0.0435					0.3645	0.0732				
0.4323	-0.0441					0.3873	0.0721				
0.4095	-0.0446					0.4100	0.0707				
0.3867	-0.0449					0.4328	0.0692				
0.3639	-0.0451					0.4556	0.0676				
0.3411	-0.0451					0.4783	0.0659				
0.3183	-0.0449					0.5011	0.0640				
0.2954	-0.0445					0.5238	0.0620				
0.2726	-0.0438					0.5465	0.0599				
0.2498	-0.0429					0.5692	0.0577				
0.2271	-0.0417					0.5919	0.0554				
0.2043	-0.0401					0.6146	0.0530				
0.1816	-0.0382					0.6373	0.0506				
0.1588	-0.0360					0.6600	0.0480				
0.1362	-0.0336					0.6826	0.0454				
0.1135	-0.0310					0.7053	0.0427				
0.0908	-0.0283					0.7280	0.0400				
0.0682	-0.0255					0.7506	0.0371				
0.0456	-0.0220					0.7732	0.0342				

Table A-4. Coordinates of Active Pressure Ports of NACA 23012 Airfoil

Lower Surface		Upper Surface	
x/c	y/c	x/c	y/c
1.0000	0.00000	0.0000	0.00886
0.9500	-0.00693	0.0031	0.01589
0.9000	-0.01223	0.0061	0.02001
0.8500	-0.01716	0.0090	0.02329
0.8000	-0.02175	0.0120	0.02623
0.7500	-0.02601	0.0300	0.03921
0.7000	-0.02994	0.0400	0.04456
0.6500	-0.03352	0.0500	0.04915
0.6000	-0.03673	0.0600	0.05306
0.5500	-0.03951	0.0800	0.05949
0.5000	-0.04183	0.1000	0.06435
0.4500	-0.04360	0.1400	0.07075
0.4000	-0.04474	0.1600	0.07272
0.3500	-0.04512	0.1800	0.07408
0.3000	-0.04456	0.2000	0.07497
0.2500	-0.04289	0.2400	0.07589
0.2000	-0.03979	0.2600	0.07596
0.1500	-0.03506	0.2800	0.07583
0.1000	-0.02938	0.3000	0.07548
0.0750	-0.02626	0.3200	0.07496
0.0500	-0.02261	0.3400	0.07428
0.0250	-0.01728	0.3600	0.07343
0.0100	-0.01121	0.3800	0.07245
0.0042	-0.00681	0.4000	0.07134
0.0010	-0.00245	0.4400	0.06874
		0.5200	0.06232
		0.5600	0.05859
		0.6000	0.05456
		0.6400	0.05026
		0.6800	0.04571
		0.7200	0.04093
		0.7600	0.03593
		0.8000	0.03071
		0.8500	0.02389
		0.9000	0.01673
		0.9500	0.00919

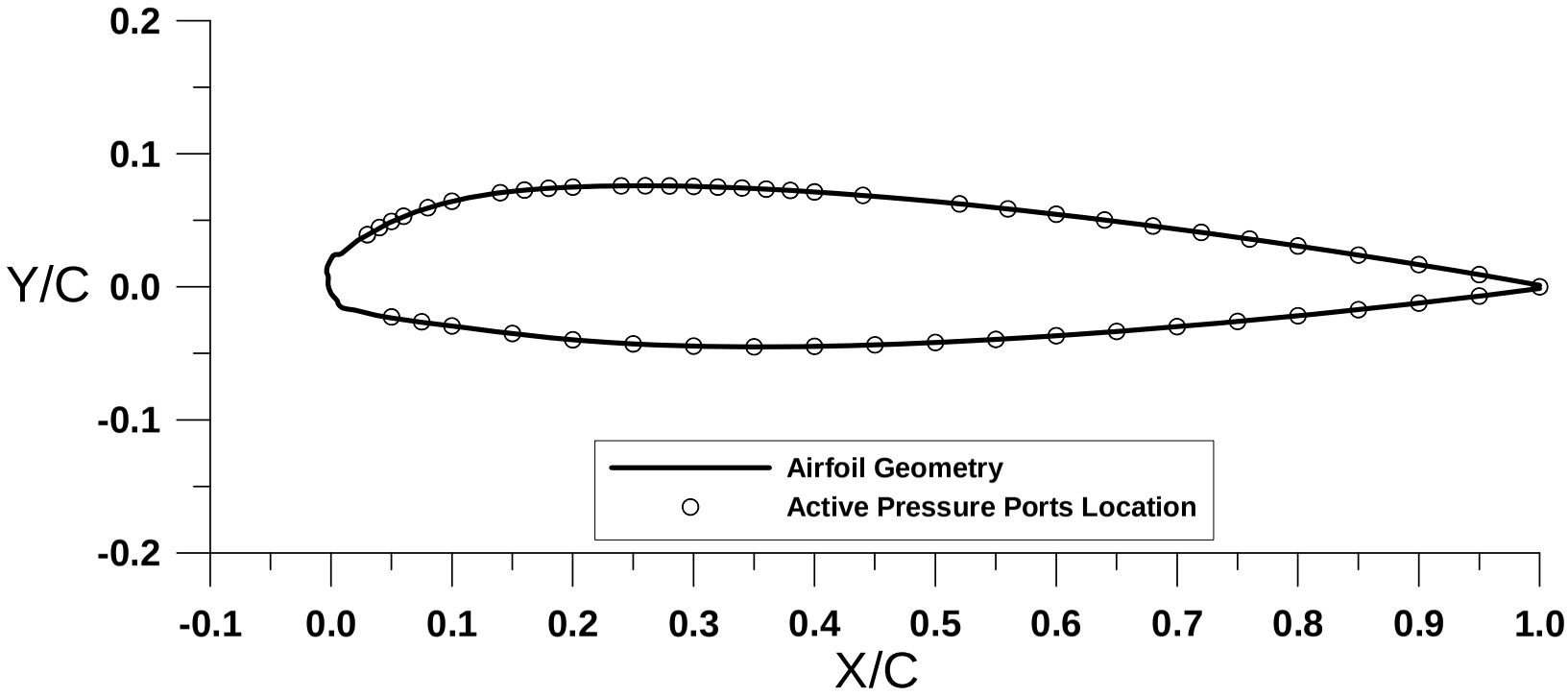

Figure A-3. NACA 23012 With 5-min Glaze Ice Shape

Table A-5. Coordinates of NACA 23012 With 5-min Glaze Ice Shape

Lower Surface						Upper Surface					
x/c	y/c	x/c	y/c	x/c	y/c	x/c	y/c	x/c	y/c	x/c	y/c
1.0000	-0.0013	0.0375	-0.0213			-0.0025	0.0016	0.6826	0.0454		
0.9783	-0.0038	0.0197	-0.0175			-0.0026	0.0039	0.7053	0.0427		
0.9556	-0.0063	0.0174	-0.0171			-0.0023	0.0062	0.7280	0.0400		
0.9330	-0.0088	0.0152	-0.0168			-0.0024	0.0084	0.7506	0.0371		
0.9103	-0.0112	0.0129	-0.0167			-0.0035	0.0104	0.7732	0.0342		
0.8876	-0.0135	0.0099	-0.0160			-0.0037	0.0127	0.7958	0.0313		
0.8649	-0.0157	0.0074	-0.0145			-0.0030	0.0151	0.8185	0.0282		
0.8421	-0.0179	0.0059	-0.0128			-0.0016	0.0180	0.8411	0.0251		
0.8194	-0.0200	0.0052	-0.0106			0.0001	0.0214	0.8637	0.0220		
0.7967	-0.0220	0.0037	-0.0088			0.0016	0.0234	0.8863	0.0187		
0.7740	-0.0240	0.0019	-0.0071			0.0037	0.0243	0.9088	0.0154		
0.7512	-0.0259	0.0004	-0.0053			0.0068	0.0242	0.9314	0.0120		
0.7285	-0.0277	-0.0008	-0.0034			0.0088	0.0251	0.9540	0.0086		
0.7057	-0.0295	-0.0020	-0.0006			0.0223	0.0350	0.9765	0.0050		
0.6830	-0.0312					0.0280	0.0379				
0.6602	-0.0328					0.0483	0.0483				
0.6375	-0.0344					0.0696	0.0563				
0.6147	-0.0358					0.0916	0.0624				
0.5919	-0.0372					0.1140	0.0670				
0.5691	-0.0385					0.1365	0.0703				
0.5463	-0.0397					0.1592	0.0727				
0.5236	-0.0408					0.1820	0.0742				
0.5008	-0.0418					0.2048	0.0752				
0.4780	-0.0427					0.2276	0.0757				
0.4552	-0.0435					0.2504	0.0760				
0.4323	-0.0441					0.2732	0.0759				
0.4095	-0.0446					0.2961	0.0756				
0.3867	-0.0449					0.3189	0.0750				
0.3639	-0.0451					0.3417	0.0742				
0.3411	-0.0451					0.3645	0.0732				
0.3183	-0.0449					0.3873	0.0721				
0.2954	-0.0445					0.4100	0.0707				
0.2726	-0.0438					0.4328	0.0692				
0.2498	-0.0429					0.4556	0.0676				
0.2271	-0.0417					0.4783	0.0659				
0.2043	-0.0401					0.5011	0.0640				
0.1816	-0.0382					0.5238	0.0620				
0.1588	-0.0360					0.5465	0.0599				
0.1362	-0.0336					0.5692	0.0577				
0.1135	-0.0310					0.5919	0.0554				
0.0908	-0.0283					0.6146	0.0530				
0.0830	-0.0277					0.6373	0.0506				
0.0602	-0.0248					0.6600	0.0480				

Table A-6. Coordinates of Active Pressure Ports of NACA 23012 With 5-min Glaze Ice Shape

Lower Surface		Upper Surface	
x/c	y/c	x/c	y/c
1.0000	0.00000	0.0300	0.03921
0.9500	-0.00693	0.0400	0.04456
0.9000	-0.01223	0.0500	0.04915
0.8500	-0.01716	0.0600	0.05306
0.8000	-0.02175	0.0800	0.05949
0.7500	-0.02601	0.1000	0.06435
0.7000	-0.02994	0.1400	0.07075
0.6500	-0.03352	0.1600	0.07272
0.6000	-0.03673	0.1800	0.07408
0.5500	-0.03951	0.2000	0.07497
0.5000	-0.04183	0.2400	0.07589
0.4500	-0.04360	0.2600	0.07596
0.4000	-0.04474	0.2800	0.07583
0.3500	-0.04512	0.3000	0.07548
0.3000	-0.04456	0.3200	0.07496
0.2500	-0.04289	0.3400	0.07428
0.2000	-0.03979	0.3600	0.07343
0.1500	-0.03506	0.3800	0.07245
0.1000	-0.02938	0.4000	0.07134
0.0750	-0.02626	0.4400	0.06874
0.0500	-0.02261	0.5200	0.06232
		0.5600	0.05859
		0.6000	0.05456
		0.6400	0.05026
		0.6800	0.04571
		0.7200	0.04093
		0.7600	0.03593
		0.8000	0.03071
		0.8500	0.02389
		0.9000	0.01673
		0.9500	0.00919

The following is the LEWICE 2.2 input file for the NACA 23012 with 5-min glaze ice shape.

```
Glaze 5-min Case
&LEW20
ITIMFL = 0
TSTOP  =  300.
IBOD   =    1
IFLO   =    4
DSMN   =    4.0D-4
NPL    =   24
&END
&DIST
FLWC   = 0.05, 0.1, 0.2, 0.3, 0.2, 0.1, 0.03, 0.01, 0.005, 0.005
DPD    = 4., 9.7, 14.2, 20.9, 28.2, 45.2, 70.1, 88.9, 103.4, 164.
&END
&ICE1
CHORD  = 0.9144
AOA    = 2.5
VINF   =  78.2
LWC    = 0.50
TINF   = 267.87
PINF   = 94806.00
RH     = 100.0
&END
&LPRNT
FPRT   = 1
HPRT   = 1
BPRT   = 1
TPRT   = 0
&END
&RDATA
&END
```

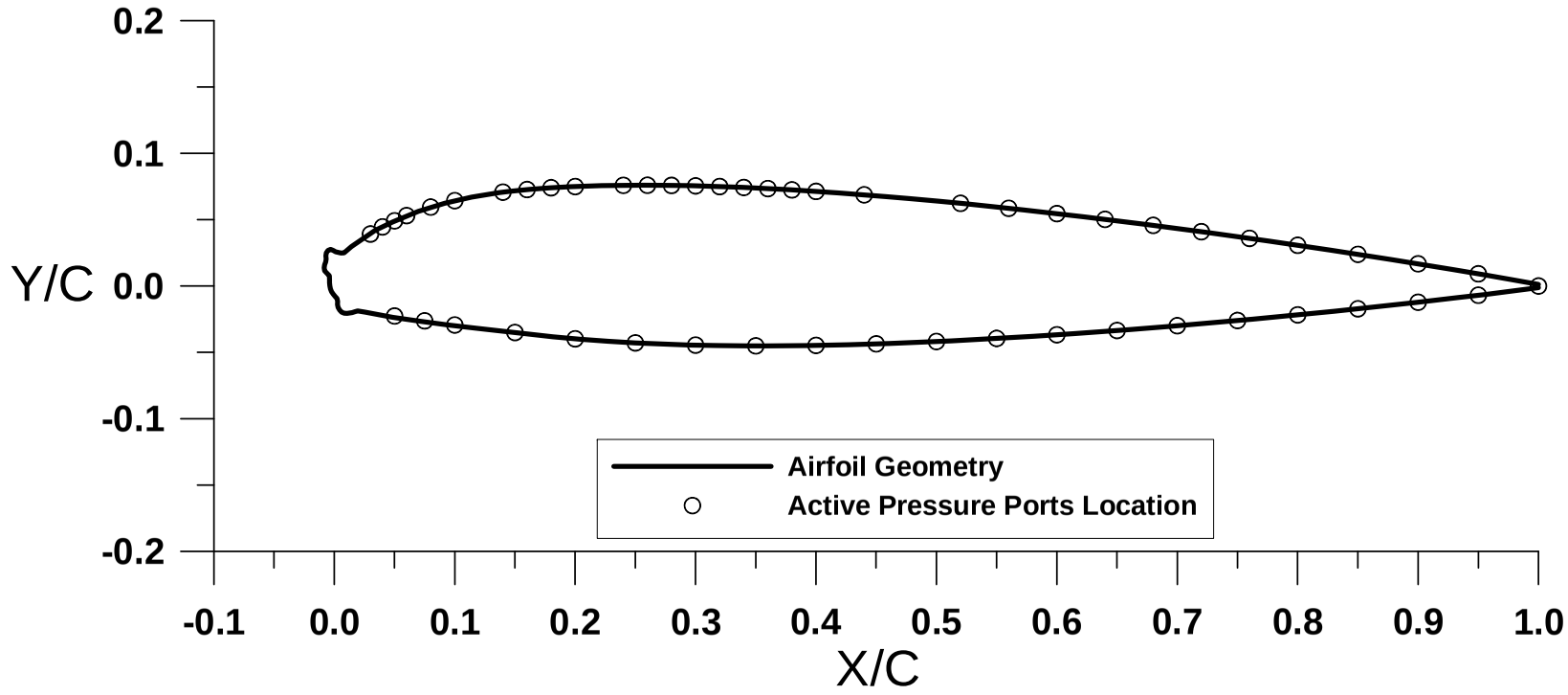

Figure A-4. NACA 23012 With 10-min Glaze Ice Shape

Table A-7. Coordinates of NACA 23012 With 10-min Glaze Ice Shape

Lower Surface						Upper Surface					
x/c	y/c	x/c	y/c	x/c	y/c	x/c	y/c	x/c	y/c	x/c	y/c
1.0000	-0.0013	0.0171	-0.0194			-0.0038	0.0002	0.5919	0.0554		
0.9783	-0.0038	0.0149	-0.0200			-0.0040	0.0025	0.6146	0.0530		
0.9556	-0.0063	0.0106	-0.0206			-0.0040	0.0048	0.6373	0.0506		
0.9330	-0.0088	0.0081	-0.0205			-0.0042	0.0078	0.6600	0.0480		
0.9103	-0.0112	0.0060	-0.0197			-0.0060	0.0094	0.6826	0.0454		
0.8876	-0.0135	0.0043	-0.0181			-0.0080	0.0115	0.7053	0.0427		
0.8649	-0.0157	0.0031	-0.0161			-0.0084	0.0137	0.7280	0.0400		
0.8421	-0.0179	0.0026	-0.0139			-0.0081	0.0160	0.7506	0.0371		
0.8194	-0.0200	0.0028	-0.0116			-0.0071	0.0181	0.7732	0.0342		
0.7967	-0.0220	0.0023	-0.0094			-0.0068	0.0204	0.7958	0.0313		
0.7740	-0.0240	0.0006	-0.0078			-0.0070	0.0227	0.8185	0.0282		
0.7512	-0.0259	-0.0010	-0.0061			-0.0066	0.0250	0.8411	0.0251		
0.7285	-0.0277	-0.0023	-0.0042			-0.0053	0.0268	0.8637	0.0220		
0.7057	-0.0295	-0.0032	-0.0021			-0.0031	0.0276	0.8863	0.0187		
0.6830	-0.0312					-0.0010	0.0269	0.9088	0.0154		
0.6602	-0.0328					0.0010	0.0257	0.9314	0.0120		
0.6375	-0.0344					0.0033	0.0253	0.9540	0.0086		
0.6147	-0.0358					0.0056	0.0249	0.9765	0.0050		
0.5919	-0.0372					0.0081	0.0251	1.0000	0.0013		
0.5691	-0.0385					0.0141	0.0297				
0.5463	-0.0397					0.0339	0.0420				
0.5236	-0.0408					0.0483	0.0483				
0.5008	-0.0418					0.0696	0.0563				
0.4780	-0.0427					0.0916	0.0624				
0.4552	-0.0435					0.1140	0.0670				
0.4323	-0.0441					0.1365	0.0703				
0.4095	-0.0446					0.1592	0.0727				
0.3867	-0.0449					0.1820	0.0742				
0.3639	-0.0451					0.2048	0.0752				
0.3411	-0.0451					0.2276	0.0757				
0.3183	-0.0449					0.2504	0.0760				
0.2954	-0.0445					0.2732	0.0759				
0.2726	-0.0438					0.2961	0.0756				
0.2498	-0.0429					0.3189	0.0750				
0.2271	-0.0417					0.3417	0.0742				
0.2043	-0.0401					0.3645	0.0732				
0.1816	-0.0382					0.3873	0.0721				
0.1588	-0.0360					0.4100	0.0707				
0.1362	-0.0336					0.4328	0.0692				
0.1179	-0.0319					0.4556	0.0676				
0.0948	-0.0294					0.4783	0.0659				
0.0717	-0.0266					0.5011	0.0640				
0.0486	-0.0236					0.5238	0.0620				
0.0257	-0.0198					0.5465	0.0599				
0.0193	-0.0188					0.5692	0.0577				

Table A-8. Coordinates of Active Pressure Ports of NACA 23012 With 10-min Glaze Ice Shape

Lower Surface		Upper Surface	
x/c	y/c	x/c	y/c
1.0000	0.00000	0.0300	0.03921
0.9500	-0.00693	0.0400	0.04456
0.9000	-0.01223	0.0500	0.04915
0.8500	-0.01716	0.0600	0.05306
0.8000	-0.02175	0.0800	0.05949
0.7500	-0.02601	0.1000	0.06435
0.7000	-0.02994	0.1400	0.07075
0.6500	-0.03352	0.1600	0.07272
0.6000	-0.03673	0.1800	0.07408
0.5500	-0.03951	0.2000	0.07497
0.5000	-0.04183	0.2400	0.07589
0.4500	-0.04360	0.2600	0.07596
0.4000	-0.04474	0.2800	0.07583
0.3500	-0.04512	0.3000	0.07548
0.3000	-0.04456	0.3200	0.07496
0.2500	-0.04289	0.3400	0.07428
0.2000	-0.03979	0.3600	0.07343
0.1500	-0.03506	0.3800	0.07245
0.1000	-0.02938	0.4000	0.07134
0.0750	-0.02626	0.4400	0.06874
0.0500	-0.02261	0.5200	0.06232
		0.5600	0.05859
		0.6000	0.05456
		0.6400	0.05026
		0.6800	0.04571
		0.7200	0.04093
		0.7600	0.03593
		0.8000	0.03071
		0.8500	0.02389
		0.9000	0.01673
		0.9500	0.00919

The following is the LEWICE 2.2. Input file for the NACA 23012 with 10-min glaze ice shape.

```
Glaze 10-min Case
&LEW20
ITIMFL = 0
TSTOP  =  600.
IBOD   =    1
IFLO   =    8
DSMN   =    4.0D-4
NPL    =   24
&END
&DIST
FLWC   = 0.05, 0.1, 0.2, 0.3, 0.2, 0.1, 0.03, 0.01, 0.005, 0.005
DPD    = 4., 9.7, 14.2, 20.9, 28.2, 45.2, 70.1, 88.9, 103.4, 164.
&END
&ICE1
CHORD  = 0.9144
AOA    = 2.5
VINF   =  78.2
LWC    = 0.50
TINF   = 267.87
PINF   = 94806.00
RH     = 100.0
&END
&LPRNT
FPRT   = 1
HPRT   = 1
BPRT   = 1
TPRT   = 0
&END
&RDATA
&END
```

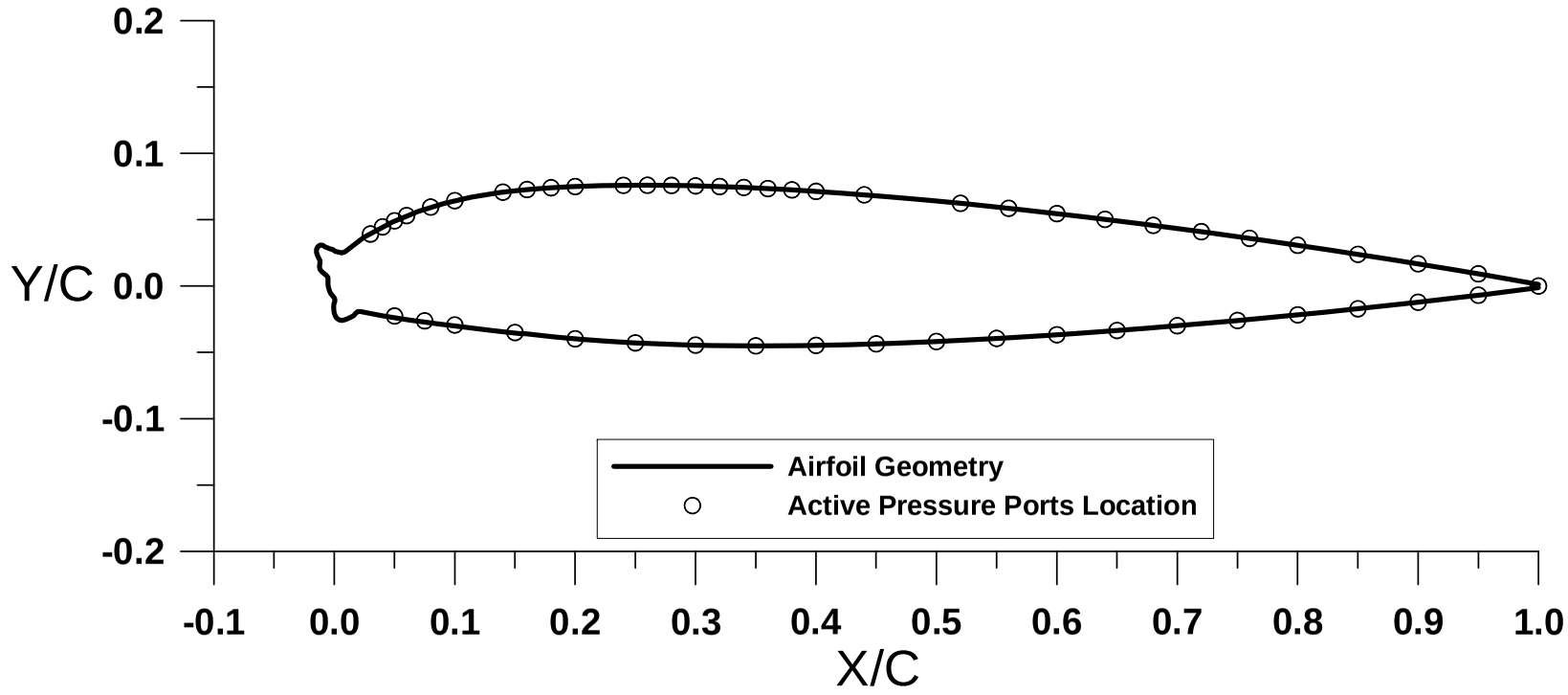

Figure A-5. NACA 23012 With 15-min Glaze Ice Shape

Table A-9. Coordinates of NACA 23012 With 15-min Glaze Ice Shape

Lower Surface						Upper Surface					
x/c	y/c	x/c	y/c	x/c	y/c	x/c	y/c	x/c	y/c	x/c	y/c
1.0000	-0.0013	0.0195	-0.0192			-0.0052	0.0012	0.5011	0.0640		
0.9783	-0.0038	0.0177	-0.0205			-0.0053	0.0035	0.5238	0.0620		
0.9556	-0.0063	0.0162	-0.0223			-0.0053	0.0065	0.5465	0.0599		
0.9330	-0.0088	0.0142	-0.0232			-0.0067	0.0081	0.5692	0.0577		
0.9103	-0.0112	0.0110	-0.0247			-0.0103	0.0106	0.5919	0.0554		
0.8876	-0.0135	0.0086	-0.0255			-0.0118	0.0124	0.6146	0.0530		
0.8649	-0.0157	0.0064	-0.0259			-0.0124	0.0146	0.6373	0.0506		
0.8421	-0.0179	0.0041	-0.0256			-0.0119	0.0169	0.6600	0.0480		
0.8194	-0.0200	0.0022	-0.0244			-0.0119	0.0191	0.6826	0.0454		
0.7967	-0.0220	0.0008	-0.0226			-0.0129	0.0212	0.7053	0.0427		
0.7740	-0.0240	0.0000	-0.0205			-0.0141	0.0232	0.7280	0.0400		
0.7512	-0.0259	-0.0005	-0.0182			-0.0148	0.0253	0.7506	0.0371		
0.7285	-0.0277	-0.0006	-0.0155			-0.0147	0.0276	0.7732	0.0342		
0.7057	-0.0295	-0.0003	-0.0132			-0.0137	0.0296	0.7958	0.0313		
0.6830	-0.0312	0.0005	-0.0111			-0.0119	0.0309	0.8185	0.0282		
0.6602	-0.0328	0.0000	-0.0090			-0.0096	0.0308	0.8411	0.0251		
0.6375	-0.0344	-0.0017	-0.0072			-0.0078	0.0295	0.8637	0.0220		
0.6147	-0.0358	-0.0031	-0.0053			-0.0056	0.0288	0.8863	0.0187		
0.5919	-0.0372	-0.0041	-0.0033			-0.0035	0.0280	0.9088	0.0154		
0.5691	-0.0385	-0.0048	-0.0011			-0.0013	0.0275	0.9314	0.0120		
0.5463	-0.0397					0.0006	0.0262	0.9540	0.0086		
0.5236	-0.0408					0.0029	0.0256	0.9765	0.0050		
0.5008	-0.0418					0.0061	0.0250	1.0000	0.0013		
0.4780	-0.0427					0.0087	0.0257				
0.4552	-0.0435					0.0246	0.0368				
0.4323	-0.0441					0.0483	0.0483				
0.4095	-0.0446					0.0696	0.0563				
0.3867	-0.0449					0.0916	0.0624				
0.3639	-0.0451					0.1140	0.0670				
0.3411	-0.0451					0.1365	0.0703				
0.3183	-0.0449					0.1592	0.0727				
0.2954	-0.0445					0.1820	0.0742				
0.2726	-0.0438					0.2048	0.0752				
0.2498	-0.0429					0.2276	0.0757				
0.2271	-0.0417					0.2504	0.0760				
0.2043	-0.0401					0.2732	0.0759				
0.1816	-0.0382					0.2961	0.0756				
0.1588	-0.0360					0.3189	0.0750				
0.1539	-0.0358					0.3417	0.0742				
0.1310	-0.0335					0.3645	0.0732				
0.1083	-0.0310					0.3873	0.0721				
0.0855	-0.0285					0.4100	0.0707				
0.0627	-0.0257					0.4328	0.0692				
0.0400	-0.0225					0.4556	0.0676				
0.0219	-0.0193					0.4783	0.0659				

Table A-10. Coordinates of Active Pressure Ports of NACA 23012 With 15-min Glaze Ice Shape

Lower Surface		Upper Surface	
x/c	y/c	x/c	y/c
1.0000	0.00000	0.0300	0.03921
0.9500	-0.00693	0.0400	0.04456
0.9000	-0.01223	0.0500	0.04915
0.8500	-0.01716	0.0600	0.05306
0.8000	-0.02175	0.0800	0.05949
0.7500	-0.02601	0.1000	0.06435
0.7000	-0.02994	0.1400	0.07075
0.6500	-0.03352	0.1600	0.07272
0.6000	-0.03673	0.1800	0.07408
0.5500	-0.03951	0.2000	0.07497
0.5000	-0.04183	0.2400	0.07589
0.4500	-0.04360	0.2600	0.07596
0.4000	-0.04474	0.2800	0.07583
0.3500	-0.04512	0.3000	0.07548
0.3000	-0.04456	0.3200	0.07496
0.2500	-0.04289	0.3400	0.07428
0.2000	-0.03979	0.3600	0.07343
0.1500	-0.03506	0.3800	0.07245
0.1000	-0.02938	0.4000	0.07134
0.0750	-0.02626	0.4400	0.06874
0.0500	-0.02261	0.5200	0.06232
		0.5600	0.05859
		0.6000	0.05456
		0.6400	0.05026
		0.6800	0.04571
		0.7200	0.04093
		0.7600	0.03593
		0.8000	0.03071
		0.8500	0.02389
		0.9000	0.01673
		0.9500	0.00919

The following is the LEWICE 2.2 input file for the NACA 23012 with 15-min glaze ice shape.

```
Glaze 15-min Case
&LEW20
ITIMFL = 0
TSTOP  =  900.
IBOD   =    1
IFLO   =   12
DSMN   =    4.0D-4
NPL    =   24
&END
&DIST
FLWC   = 0.05, 0.1, 0.2, 0.3, 0.2, 0.1, 0.03, 0.01, 0.005, 0.005
DPD    = 4., 9.7, 14.2, 20.9, 28.2, 45.2, 70.1, 88.9, 103.4, 164.
&END
&ICE1
CHORD  = 0.9144
AOA    = 2.5
VINF   =  78.2
LWC    = 0.50
TINF   = 267.87
PINF   = 94806.00
RH     = 100.0
&END
&LPRNT
FPRT   = 1
HPRT   = 1
BPRT   = 1
TPRT   = 0
&END
&RDATA
&END
```

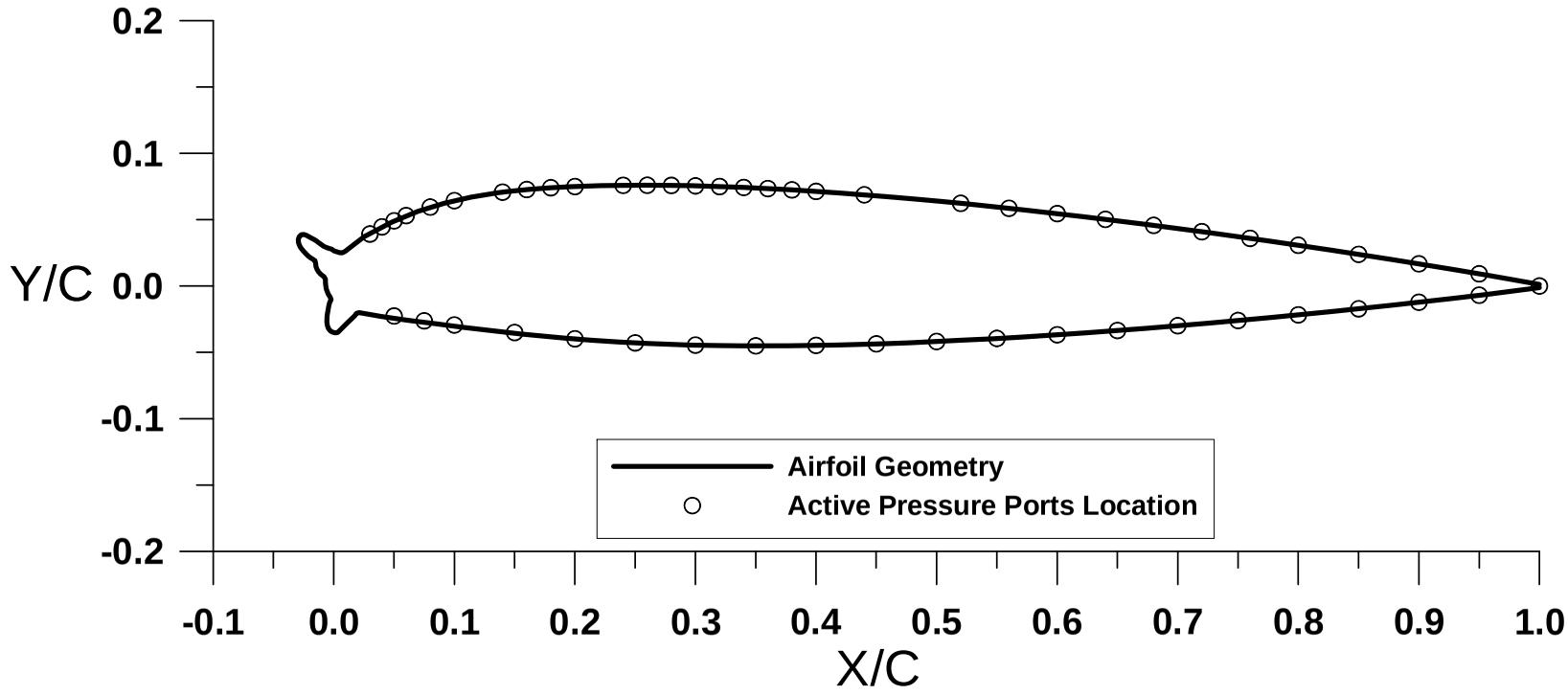

Figure A-6. NACA 23012 With 22.5-min Ice Shape

Table A-11. Coordinates of NACA 23012 With 22.5-min Glaze Ice Shape

Lower Surface						Upper Surface					
x/c	y/c	x/c	y/c	x/c	y/c	x/c	y/c	x/c	y/c	x/c	y/c
1.0000	-0.0013	0.0175	-0.0225			-0.0067	0.0002	0.1820	0.0742		
0.9783	-0.0038	0.0155	-0.0242			-0.0069	0.0027	0.2048	0.0752		
0.9556	-0.0063	0.0118	-0.0273			-0.0069	0.0051	0.2276	0.0757		
0.9330	-0.0088	0.0102	-0.0289			-0.0080	0.0070	0.2504	0.0760		
0.9103	-0.0112	0.0083	-0.0303			-0.0108	0.0089	0.2732	0.0759		
0.8876	-0.0135	0.0067	-0.0320			-0.0127	0.0107	0.2961	0.0756		
0.8649	-0.0157	0.0050	-0.0334			-0.0139	0.0126	0.3189	0.0750		
0.8421	-0.0179	0.0033	-0.0349			-0.0148	0.0148	0.3417	0.0742		
0.8194	-0.0200	0.0011	-0.0353			-0.0150	0.0170	0.3645	0.0732		
0.7967	-0.0220	-0.0011	-0.0348			-0.0156	0.0192	0.3873	0.0721		
0.7740	-0.0240	-0.0031	-0.0335			-0.0175	0.0203	0.4100	0.0707		
0.7512	-0.0259	-0.0045	-0.0318			-0.0195	0.0214	0.4328	0.0692		
0.7285	-0.0277	-0.0054	-0.0297			-0.0214	0.0228	0.4556	0.0676		
0.7057	-0.0295	-0.0058	-0.0274			-0.0232	0.0245	0.4783	0.0659		
0.6830	-0.0312	-0.0057	-0.0251			-0.0258	0.0270	0.5011	0.0640		
0.6602	-0.0328	-0.0053	-0.0211			-0.0274	0.0288	0.5238	0.0620		
0.6375	-0.0344	-0.0047	-0.0176			-0.0286	0.0307	0.5465	0.0599		
0.6147	-0.0358	-0.0041	-0.0144			-0.0293	0.0329	0.5692	0.0577		
0.5919	-0.0372	-0.0033	-0.0122			-0.0294	0.0351	0.5919	0.0554		
0.5691	-0.0385	-0.0023	-0.0102			-0.0286	0.0373	0.6146	0.0530		
0.5463	-0.0397	-0.0030	-0.0081			-0.0269	0.0387	0.6373	0.0506		
0.5236	-0.0408	-0.0044	-0.0062			-0.0247	0.0389	0.6600	0.0480		
0.5008	-0.0418	-0.0054	-0.0042			-0.0226	0.0381	0.6826	0.0454		
0.4780	-0.0427	-0.0062	-0.0020			-0.0205	0.0372	0.7053	0.0427		
0.4552	-0.0435					-0.0185	0.0362	0.7280	0.0400		
0.4323	-0.0441					-0.0165	0.0351	0.7506	0.0371		
0.4095	-0.0446					-0.0145	0.0340	0.7732	0.0342		
0.3867	-0.0449					-0.0126	0.0327	0.7958	0.0313		
0.3639	-0.0451					-0.0105	0.0314	0.8185	0.0282		
0.3411	-0.0451					-0.0081	0.0299	0.8411	0.0251		
0.3183	-0.0449					-0.0061	0.0290	0.8637	0.0220		
0.2954	-0.0445					-0.0039	0.0283	0.8863	0.0187		
0.2726	-0.0438					-0.0017	0.0278	0.9088	0.0154		
0.2498	-0.0429					0.0002	0.0265	0.9314	0.0120		
0.2271	-0.0417					0.0023	0.0258	0.9540	0.0086		
0.2043	-0.0401					0.0045	0.0252	0.9765	0.0050		
0.1760	-0.0381					0.0068	0.0249	1.0000	0.0013		
0.1532	-0.0359					0.0090	0.0259				
0.1304	-0.0336					0.0252	0.0372				
0.1076	-0.0311					0.0483	0.0483				
0.0848	-0.0286					0.0696	0.0563				
0.0621	-0.0258					0.0916	0.0624				
0.0393	-0.0229					0.1140	0.0670				
0.0210	-0.0200					0.1365	0.0703				
0.0188	-0.0207					0.1592	0.0727				

Table A-12. Coordinates of Active Pressure Ports of NACA 23012 With 22.5-min Glaze Ice Shape

Lower Surface		Upper Surface	
x/c	y/c	x/c	y/c
1.0000	0.00000	0.0300	0.03921
0.9500	-0.00693	0.0400	0.04456
0.9000	-0.01223	0.0500	0.04915
0.8500	-0.01716	0.0600	0.05306
0.8000	-0.02175	0.0800	0.05949
0.7500	-0.02601	0.1000	0.06435
0.7000	-0.02994	0.1400	0.07075
0.6500	-0.03352	0.1600	0.07272
0.6000	-0.03673	0.1800	0.07408
0.5500	-0.03951	0.2000	0.07497
0.5000	-0.04183	0.2400	0.07589
0.4500	-0.04360	0.2600	0.07596
0.4000	-0.04474	0.2800	0.07583
0.3500	-0.04512	0.3000	0.07548
0.3000	-0.04456	0.3200	0.07496
0.2500	-0.04289	0.3400	0.07428
0.2000	-0.03979	0.3600	0.07343
0.1500	-0.03506	0.3800	0.07245
0.1000	-0.02938	0.4000	0.07134
0.0750	-0.02626	0.4400	0.06874
0.0500	-0.02261	0.5200	0.06232
		0.5600	0.05859
		0.6000	0.05456
		0.6400	0.05026
		0.6800	0.04571
		0.7200	0.04093
		0.7600	0.03593
		0.8000	0.03071
		0.8500	0.02389
		0.9000	0.01673
		0.9500	0.00919

The following is the LEWICE 2.2 input file for the NACA 23012 with 22.5-min glaze ice shape.

```
Glaze 22.5-min Case
&LEW20
ITIMFL = 0
TSTOP  =  1350.
IBOD   =    1
IFLO   =    18
DSMN   =    4.0D-4
NPL    =   24
&END
&DIST
FLWC   = 0.05, 0.1, 0.2, 0.3, 0.2, 0.1, 0.03, 0.01, 0.005, 0.005
DPD    = 4., 9.7, 14.2, 20.9, 28.2, 45.2, 70.1, 88.9, 103.4, 164.
&END
&ICE1
CHORD  = 0.9144
AOA    = 2.5
VINF   =  78.2
LWC    = 0.50
TINF   = 267.87
PINF   = 94806.00
RH     = 100.0
&END
&LPRNT
FPRT   = 1
HPRT   = 1
BPRT   = 1
TPRT   = 0
&END
&RDATA
&END
```

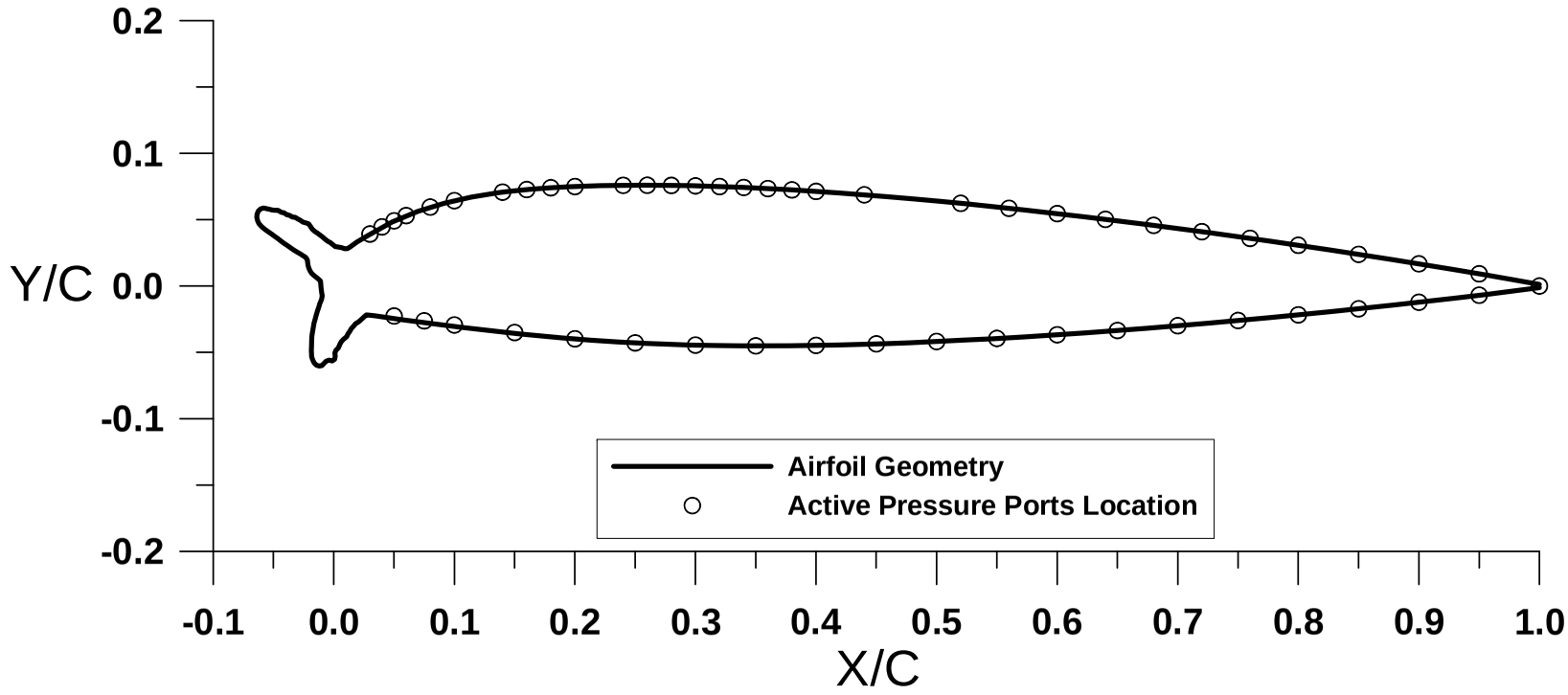

Figure A-7. NACA 23012 With 45-min Glaze Ice Shape

Table A-13. Coordinates of NACA 23012 With 45-min Glaze Ice Shape

Lower Surface						Upper Surface					
x/c	y/c	x/c	y/c	x/c	y/c	x/c	y/c	x/c	y/c	x/c	y/c
1.0000	-0.0013	0.0232	-0.0248			-0.0108	0.0006	-0.0233	0.0476	0.6146	0.0530
0.9783	-0.0038	0.0208	-0.0269			-0.0111	0.0038	-0.0210	0.0468	0.6373	0.0506
0.9556	-0.0063	0.0181	-0.0284			-0.0130	0.0055	-0.0194	0.0450	0.6600	0.0480
0.9330	-0.0088	0.0164	-0.0303			-0.0161	0.0076	-0.0179	0.0430	0.6826	0.0454
0.9103	-0.0112	0.0146	-0.0320			-0.0180	0.0092	-0.0160	0.0413	0.7053	0.0427
0.8876	-0.0135	0.0133	-0.0341			-0.0196	0.0112	-0.0134	0.0397	0.7280	0.0400
0.8649	-0.0157	0.0118	-0.0361			-0.0207	0.0134	-0.0114	0.0384	0.7506	0.0371
0.8421	-0.0179	0.0106	-0.0383			-0.0213	0.0158	-0.0094	0.0370	0.7732	0.0342
0.8194	-0.0200	0.0082	-0.0401			-0.0219	0.0197	-0.0072	0.0353	0.7958	0.0313
0.7967	-0.0220	0.0063	-0.0418			-0.0233	0.0216	-0.0050	0.0338	0.8185	0.0282
0.7740	-0.0240	0.0050	-0.0439			-0.0256	0.0229	-0.0028	0.0327	0.8411	0.0251
0.7512	-0.0259	0.0038	-0.0467			-0.0279	0.0242	-0.0009	0.0312	0.8637	0.0220
0.7285	-0.0277	0.0019	-0.0483			-0.0309	0.0257	0.0012	0.0298	0.8863	0.0187
0.7057	-0.0295	0.0009	-0.0505			-0.0330	0.0271	0.0039	0.0294	0.9088	0.0154
0.6830	-0.0312	0.0013	-0.0529			-0.0351	0.0283	0.0066	0.0288	0.9314	0.0120
0.6602	-0.0328	0.0006	-0.0553			-0.0383	0.0303	0.0090	0.0281	0.9540	0.0086
0.6375	-0.0344	-0.0014	-0.0565			-0.0408	0.0319	0.0114	0.0282	0.9765	0.0050
0.6147	-0.0358	-0.0039	-0.0559			-0.0437	0.0339	0.0139	0.0296	1.0000	0.0013
0.5919	-0.0372	-0.0062	-0.0566			-0.0464	0.0358	0.0191	0.0331		
0.5691	-0.0385	-0.0081	-0.0583			-0.0484	0.0371	0.0280	0.0379		
0.5463	-0.0397	-0.0098	-0.0600			-0.0517	0.0393	0.0483	0.0483		
0.5236	-0.0408	-0.0122	-0.0604			-0.0538	0.0406	0.0696	0.0563		
0.5008	-0.0418	-0.0145	-0.0596			-0.0568	0.0425	0.0916	0.0624		
0.4780	-0.0427	-0.0163	-0.0579			-0.0597	0.0446	0.1140	0.0670		
0.4552	-0.0435	-0.0175	-0.0557			-0.0619	0.0468	0.1365	0.0703		
0.4323	-0.0441	-0.0183	-0.0534			-0.0631	0.0490	0.1592	0.0727		
0.4095	-0.0446	-0.0185	-0.0509			-0.0638	0.0518	0.1820	0.0742		
0.3867	-0.0449	-0.0185	-0.0484			-0.0636	0.0543	0.2048	0.0752		
0.3639	-0.0451	-0.0185	-0.0459			-0.0626	0.0565	0.2276	0.0757		
0.3411	-0.0451	-0.0184	-0.0414			-0.0607	0.0581	0.2504	0.0760		
0.3183	-0.0449	-0.0181	-0.0381			-0.0584	0.0588	0.2732	0.0759		
0.2954	-0.0445	-0.0178	-0.0350			-0.0560	0.0583	0.2961	0.0756		
0.2726	-0.0438	-0.0170	-0.0311			-0.0536	0.0579	0.3189	0.0750		
0.2498	-0.0429	-0.0163	-0.0281			-0.0512	0.0574	0.3417	0.0742		
0.2271	-0.0417	-0.0154	-0.0248			-0.0488	0.0572	0.3645	0.0732		
0.2043	-0.0401	-0.0146	-0.0223			-0.0463	0.0571	0.3873	0.0721		
0.1816	-0.0386	-0.0133	-0.0184			-0.0435	0.0556	0.4100	0.0707		
0.1569	-0.0364	-0.0124	-0.0157			-0.0411	0.0551	0.4328	0.0692		
0.1322	-0.0339	-0.0115	-0.0134			-0.0390	0.0538	0.4556	0.0676		
0.1074	-0.0313	-0.0100	-0.0100			-0.0366	0.0533	0.4783	0.0659		
0.0827	-0.0285	-0.0095	-0.0074			-0.0344	0.0520	0.5011	0.0640		
0.0581	-0.0256	-0.0100	-0.0046			-0.0320	0.0518	0.5238	0.0620		
0.0334	-0.0223	-0.0106	-0.0019			-0.0299	0.0506	0.5465	0.0599		
0.0270	-0.0217					-0.0277	0.0495	0.5692	0.0577		
0.0251	-0.0232					-0.0256	0.0483	0.5919	0.0554		

Table A-14. Coordinates of Active Pressure Ports of NACA 23012 With 45-min Glaze Ice Shape

Lower Surface		Upper Surface	
x/c	y/c	x/c	y/c
1.0000	0.00000	0.0300	0.03921
0.9500	-0.00693	0.0400	0.04456
0.9000	-0.01223	0.0500	0.04915
0.8500	-0.01716	0.0600	0.05306
0.8000	-0.02175	0.0800	0.05949
0.7500	-0.02601	0.1000	0.06435
0.7000	-0.02994	0.1400	0.07075
0.6500	-0.03352	0.1600	0.07272
0.6000	-0.03673	0.1800	0.07408
0.5500	-0.03951	0.2000	0.07497
0.5000	-0.04183	0.2400	0.07589
0.4500	-0.04360	0.2600	0.07596
0.4000	-0.04474	0.2800	0.07583
0.3500	-0.04512	0.3000	0.07548
0.3000	-0.04456	0.3200	0.07496
0.2500	-0.04289	0.3400	0.07428
0.2000	-0.03979	0.3600	0.07343
0.1500	-0.03506	0.3800	0.07245
0.1000	-0.02938	0.4000	0.07134
0.0750	-0.02626	0.4400	0.06874
0.0500	-0.02261	0.5200	0.06232
		0.5600	0.05859
		0.6000	0.05456
		0.6400	0.05026
		0.6800	0.04571
		0.7200	0.04093
		0.7600	0.03593
		0.8000	0.03071
		0.8500	0.02389
		0.9000	0.01673
		0.9500	0.00919

The following is the LEWICE 2.2 input file for the NACA 23012 with 45-min glaze ice shape.

```
Glaze 45-min Case
&LEW20
ITIMFL = 1
TSTOP  =  2700.
IBOD   =    1
IFLO   =    18
DSMN   =    4.0D-4
NPL    =   24
&END
&DIST
FLWC   = 0.05, 0.1, 0.2, 0.3, 0.2, 0.1, 0.03, 0.01, 0.005, 0.005
DPD    = 4., 9.7, 14.2, 20.9, 28.2, 45.2, 70.1, 88.9, 103.4, 164.
&END
&ICE1
CHORD  = 0.9144
AOA    = 2.5
VINF   =  78.2
LWC    = 0.50
TINF   = 267.87
PINF   = 94806.00
RH     = 100.0
&END
&LPRNT
FPRT   = 1
HPRT   = 1
BPRT   = 1
TPRT   = 0
&END
&RDATA
&END
```

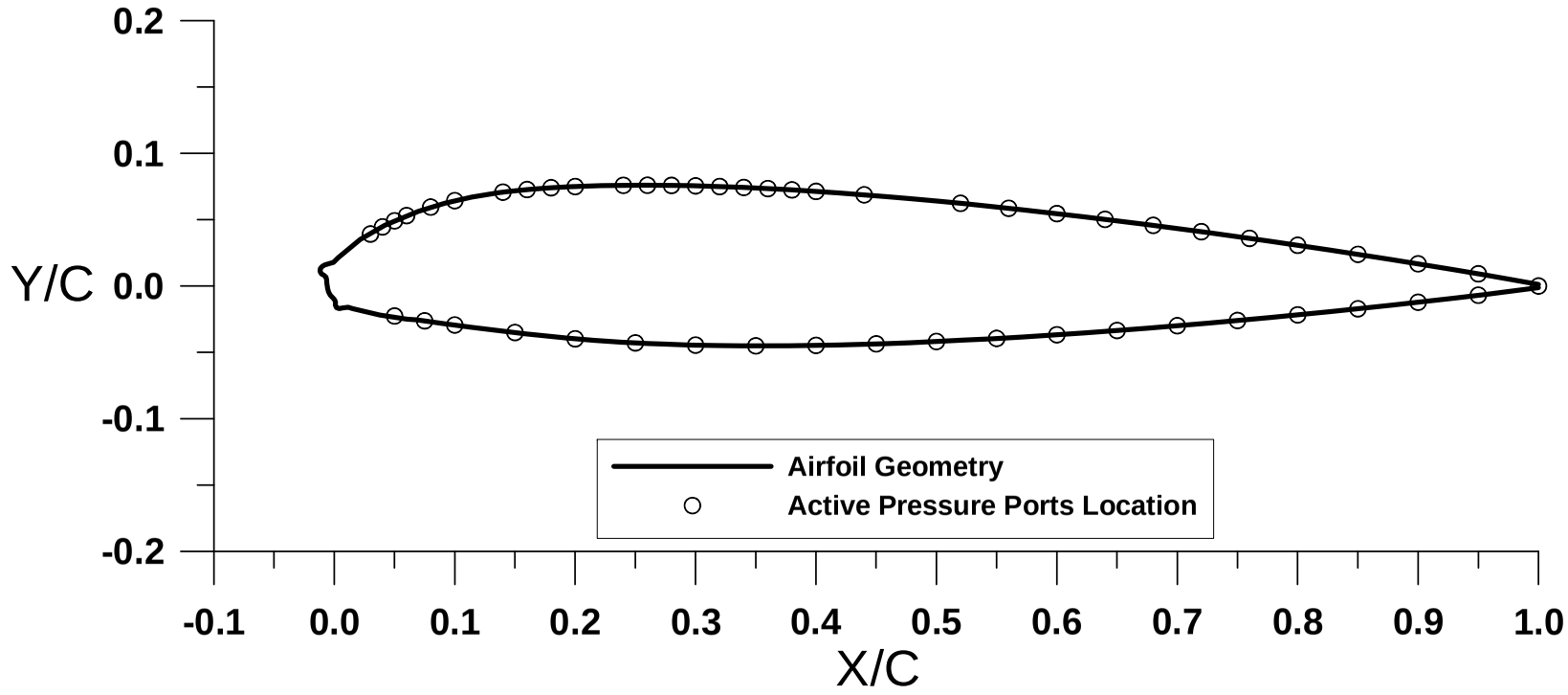

Figure A-8. NACA 23012 With 7.5-min Mixed Ice Shape

Table A-15. Coordinates of NACA 23012 With 7.5-min Mixed Ice Shape

Lower Surface						Upper Surface					
x/c	y/c	x/c	y/c	x/c	y/c	x/c	y/c	x/c	y/c	x/c	y/c
1.0000	-0.0013	0.0115	-0.0160			-0.0062	0.0023	0.7506	0.0371		
0.9783	-0.0038	0.0093	-0.0163			-0.0063	0.0046	0.7732	0.0342		
0.9556	-0.0063	0.0065	-0.0167			-0.0069	0.0068	0.7958	0.0313		
0.9330	-0.0088	0.0040	-0.0170			-0.0087	0.0081	0.8185	0.0282		
0.9103	-0.0112	0.0019	-0.0163			-0.0108	0.0091	0.8411	0.0251		
0.8876	-0.0135	0.0008	-0.0144			-0.0119	0.0110	0.8637	0.0220		
0.8649	-0.0157	0.0010	-0.0121			-0.0116	0.0133	0.8863	0.0187		
0.8421	-0.0179	0.0002	-0.0101			-0.0100	0.0148	0.9088	0.0154		
0.8194	-0.0200	-0.0017	-0.0087			-0.0080	0.0159	0.9314	0.0120		
0.7967	-0.0220	-0.0032	-0.0070			-0.0039	0.0170	0.9540	0.0086		
0.7740	-0.0240	-0.0045	-0.0050			-0.0008	0.0178	0.9765	0.0050		
0.7512	-0.0259	-0.0053	-0.0029			0.0032	0.0213	1.0000	0.0013		
0.7285	-0.0277	-0.0058	-0.0007			0.0215	0.0351				
0.7057	-0.0295					0.0419	0.0457				
0.6830	-0.0312					0.0483	0.0483				
0.6602	-0.0328					0.0696	0.0563				
0.6375	-0.0344					0.0916	0.0624				
0.6147	-0.0358					0.1140	0.0670				
0.5919	-0.0372					0.1365	0.0703				
0.5691	-0.0385					0.1592	0.0727				
0.5463	-0.0397					0.1820	0.0742				
0.5236	-0.0408					0.2048	0.0752				
0.5008	-0.0418					0.2276	0.0757				
0.4780	-0.0427					0.2504	0.0760				
0.4552	-0.0435					0.2732	0.0759				
0.4323	-0.0441					0.2961	0.0756				
0.4095	-0.0446					0.3189	0.0750				
0.3867	-0.0449					0.3417	0.0742				
0.3639	-0.0451					0.3645	0.0732				
0.3411	-0.0451					0.3873	0.0721				
0.3183	-0.0449					0.4100	0.0707				
0.2954	-0.0445					0.4328	0.0692				
0.2726	-0.0438					0.4556	0.0676				
0.2498	-0.0429					0.4783	0.0659				
0.2271	-0.0417					0.5011	0.0640				
0.2043	-0.0401					0.5238	0.0620				
0.1816	-0.0382					0.5465	0.0599				
0.1588	-0.0360					0.5692	0.0577				
0.1362	-0.0336					0.5919	0.0554				
0.1135	-0.0310					0.6146	0.0530				
0.0908	-0.0283					0.6373	0.0506				
0.0682	-0.0255					0.6600	0.0480				
0.0605	-0.0250					0.6826	0.0454				
0.0377	-0.0218					0.7053	0.0427				
0.0153	-0.0170					0.7280	0.0400				

Table A-16. Coordinates of Active Pressure Ports of NACA 23012 With 7.5-min Mixed Ice Shape

Lower Surface		Upper Surface	
x/c	y/c	x/c	y/c
1.0000	0.00000	0.0300	0.03921
0.9500	-0.00693	0.0400	0.04456
0.9000	-0.01223	0.0500	0.04915
0.8500	-0.01716	0.0600	0.05306
0.8000	-0.02175	0.0800	0.05949
0.7500	-0.02601	0.1000	0.06435
0.7000	-0.02994	0.1400	0.07075
0.6500	-0.03352	0.1600	0.07272
0.6000	-0.03673	0.1800	0.07408
0.5500	-0.03951	0.2000	0.07497
0.5000	-0.04183	0.2400	0.07589
0.4500	-0.04360	0.2600	0.07596
0.4000	-0.04474	0.2800	0.07583
0.3500	-0.04512	0.3000	0.07548
0.3000	-0.04456	0.3200	0.07496
0.2500	-0.04289	0.3400	0.07428
0.2000	-0.03979	0.3600	0.07343
0.1500	-0.03506	0.3800	0.07245
0.1000	-0.02938	0.4000	0.07134
0.0750	-0.02626	0.4400	0.06874
0.0500	-0.02261	0.5200	0.06232
		0.5600	0.05859
		0.6000	0.05456
		0.6400	0.05026
		0.6800	0.04571
		0.7200	0.04093
		0.7600	0.03593
		0.8000	0.03071
		0.8500	0.02389
		0.9000	0.01673
		0.9500	0.00919

The following is the LEWICE 2.2 input file for the NACA 23012 with 7.5-min mixed ice shape.

```
Mixed 7.5-min Case
&LEW20
ITIMFL = 0
TSTOP  =  450.
IBOD   =    1
IFLO   =    6
DSMN   =    4.0D-4
NPL    =   24
&END
&DIST
FLWC   = 0.05, 0.1, 0.2, 0.3, 0.2, 0.1, 0.03, 0.01, 0.005, 0.005
DPD    = 4., 9.7, 14.2, 20.9, 28.2, 45.2, 70.1, 88.9, 103.4, 164.
&END
&ICE1
CHORD  = 0.9144
AOA    = 2.5
VINF   =  78.2
LWC    = 0.50
TINF   = 264.
PINF   = 94806.00
RH     = 100.0
&END
&LPRNT
FPRT   = 1
HPRT   = 1
BPRT   = 1
TPRT   = 0
&END
&RDATA
&END
```

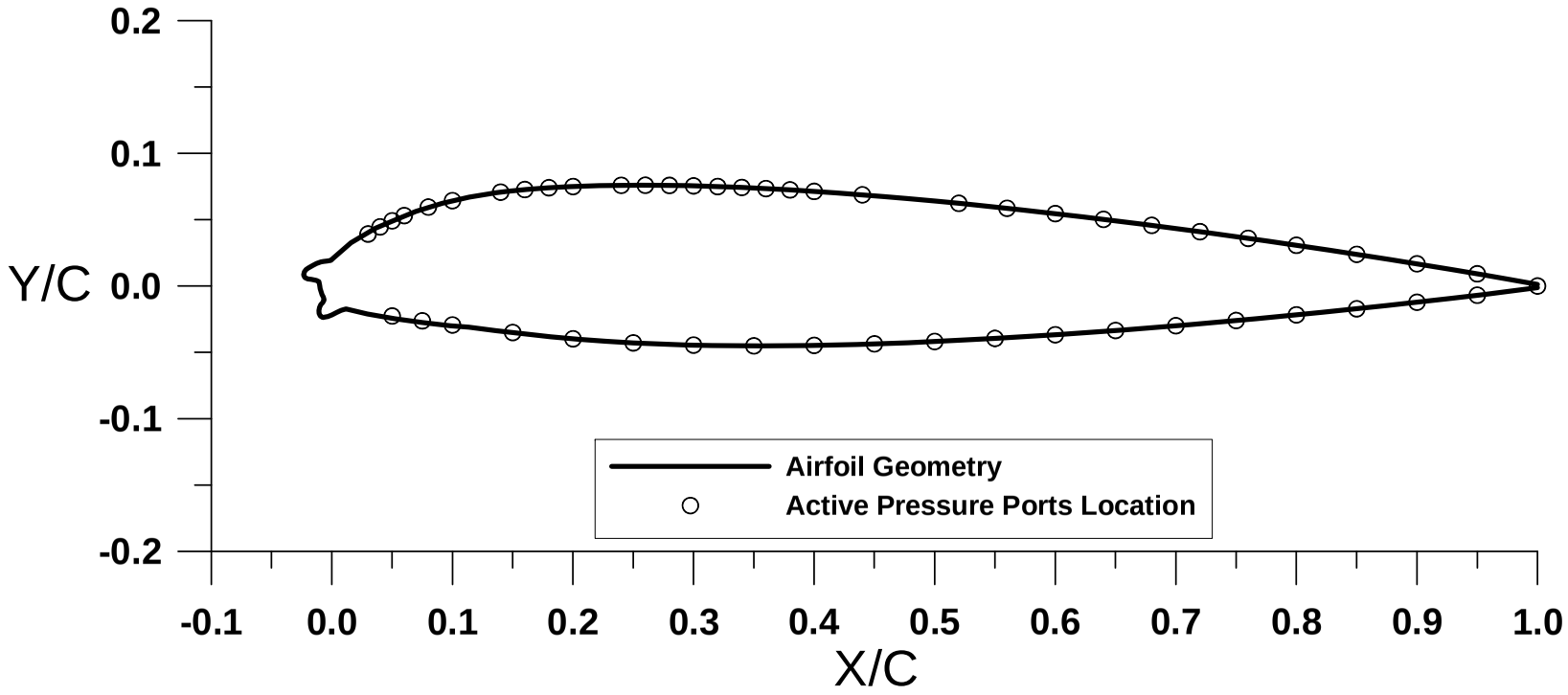

Figure A-9. NACA 23012 With 15-min Mixed Ice Shape

Table A-17. Coordinates of NACA 23012 With 15-min Mixed Ice Shape

Lower Surface						Upper Surface					
x/c	y/c	x/c	y/c	x/c	y/c	x/c	y/c	x/c	y/c	x/c	y/c
1.0000	-0.0013	0.0095	-0.0178			-0.0100	0.0004	0.6373	0.0506		
0.9783	-0.0038	0.0069	-0.0187			-0.0108	0.0032	0.6600	0.0480		
0.9556	-0.0063	0.0044	-0.0197			-0.0128	0.0042	0.6826	0.0454		
0.9330	-0.0088	0.0012	-0.0213			-0.0169	0.0050	0.7053	0.0427		
0.9103	-0.0112	-0.0023	-0.0228			-0.0200	0.0054	0.7280	0.0400		
0.8876	-0.0135	-0.0050	-0.0233			-0.0225	0.0064	0.7506	0.0371		
0.8649	-0.0157	-0.0076	-0.0237			-0.0235	0.0084	0.7732	0.0342		
0.8421	-0.0179	-0.0096	-0.0227			-0.0229	0.0106	0.7958	0.0313		
0.8194	-0.0200	-0.0106	-0.0206			-0.0214	0.0124	0.8185	0.0282		
0.7967	-0.0220	-0.0107	-0.0183			-0.0195	0.0137	0.8411	0.0251		
0.7740	-0.0240	-0.0102	-0.0161			-0.0155	0.0157	0.8637	0.0220		
0.7512	-0.0259	-0.0093	-0.0140			-0.0127	0.0169	0.8863	0.0187		
0.7285	-0.0277	-0.0076	-0.0124			-0.0091	0.0181	0.9088	0.0154		
0.7057	-0.0295	-0.0064	-0.0106			-0.0069	0.0185	0.9314	0.0120		
0.6830	-0.0312	-0.0071	-0.0084			-0.0037	0.0188	0.9540	0.0086		
0.6602	-0.0328	-0.0082	-0.0064			-0.0009	0.0194	0.9765	0.0050		
0.6375	-0.0344	-0.0090	-0.0042			0.0010	0.0210	1.0000	0.0013		
0.6147	-0.0358	-0.0096	-0.0020			0.0158	0.0326				
0.5919	-0.0372					0.0362	0.0436				
0.5691	-0.0385					0.0483	0.0483				
0.5463	-0.0397					0.0696	0.0563				
0.5236	-0.0408					0.0916	0.0624				
0.5008	-0.0418					0.1140	0.0670				
0.4780	-0.0427					0.1365	0.0703				
0.4552	-0.0435					0.1592	0.0727				
0.4323	-0.0441					0.1820	0.0742				
0.4095	-0.0446					0.2048	0.0752				
0.3867	-0.0449					0.2276	0.0757				
0.3639	-0.0451					0.2504	0.0760				
0.3411	-0.0451					0.2732	0.0759				
0.3183	-0.0449					0.2961	0.0756				
0.2954	-0.0445					0.3189	0.0750				
0.2726	-0.0438					0.3417	0.0742				
0.2498	-0.0429					0.3645	0.0732				
0.2271	-0.0417					0.3873	0.0721				
0.2043	-0.0401					0.4100	0.0707				
0.1816	-0.0382					0.4328	0.0692				
0.1588	-0.0360					0.4556	0.0676				
0.1362	-0.0336					0.4783	0.0659				
0.1135	-0.0310					0.5011	0.0640				
0.0983	-0.0300					0.5238	0.0620				
0.0753	-0.0275					0.5465	0.0599				
0.0523	-0.0246					0.5692	0.0577				
0.0294	-0.0211					0.5919	0.0554				
0.0118	-0.0172					0.6146	0.0530				

Table A-18. Coordinates of Active Pressure Ports of NACA 23012 With 15-min Mixed Ice Shape

Lower Surface		Upper Surface	
x/c	y/c	x/c	y/c
1.0000	0.00000	0.0300	0.03921
0.9500	-0.00693	0.0400	0.04456
0.9000	-0.01223	0.0500	0.04915
0.8500	-0.01716	0.0600	0.05306
0.8000	-0.02175	0.0800	0.05949
0.7500	-0.02601	0.1000	0.06435
0.7000	-0.02994	0.1400	0.07075
0.6500	-0.03352	0.1600	0.07272
0.6000	-0.03673	0.1800	0.07408
0.5500	-0.03951	0.2000	0.07497
0.5000	-0.04183	0.2400	0.07589
0.4500	-0.04360	0.2600	0.07596
0.4000	-0.04474	0.2800	0.07583
0.3500	-0.04512	0.3000	0.07548
0.3000	-0.04456	0.3200	0.07496
0.2500	-0.04289	0.3400	0.07428
0.2000	-0.03979	0.3600	0.07343
0.1500	-0.03506	0.3800	0.07245
0.1000	-0.02938	0.4000	0.07134
0.0750	-0.02626	0.4400	0.06874
0.0500	-0.02261	0.5200	0.06232
		0.5600	0.05859
		0.6000	0.05456
		0.6400	0.05026
		0.6800	0.04571
		0.7200	0.04093
		0.7600	0.03593
		0.8000	0.03071
		0.8500	0.02389
		0.9000	0.01673
		0.9500	0.00919

The following is the LEWICE 2.2 input file for the NACA 23012 with 15-min mixed ice shape.

```
Mixed 15-min Case
&LEW20
ITIMFL = 0
TSTOP  =  900.
IBOD   =    1
IFLO   =    12
DSMN   =    4.0D-4
NPL    =   24
&END
&DIST
FLWC   = 0.05, 0.1, 0.2, 0.3, 0.2, 0.1, 0.03, 0.01, 0.005, 0.005
DPD    = 4., 9.7, 14.2, 20.9, 28.2, 45.2, 70.1, 88.9, 103.4, 164.
&END
&ICE1
CHORD  = 0.9144
AOA    = 2.5
VINF   =  78.2
LWC    = 0.50
TINF   = 264.
PINF   = 94806.00
RH     = 100.0
&END
&LPRNT
FPRT   = 1
HPRT   = 1
BPRT   = 1
TPRT   = 0
&END
&RDATA
&END
```

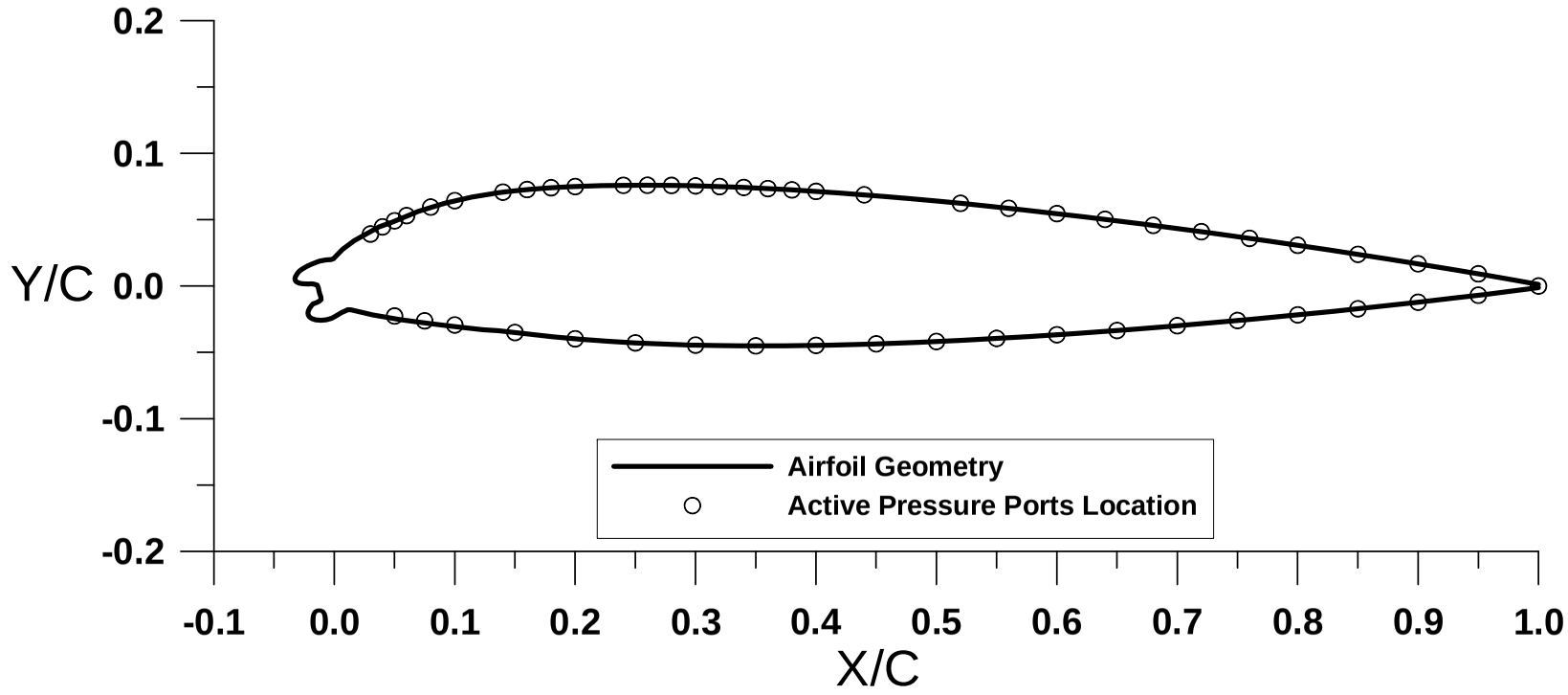

Figure A-10. NACA 23012 With 22.5-min Mixed Ice Shape

Table A-19. Coordinates of NACA 23012 With 22.5-min Mixed Ice Shape

Lower Surface						Upper Surface					
x/c	y/c	x/c	y/c	x/c	y/c	x/c	y/c	x/c	y/c	x/c	y/c
1.0000	-0.0013	0.0111	-0.0178			-0.0142	0.0007	0.5238	0.0620		
0.9783	-0.0038	0.0090	-0.0187			-0.0164	0.0014	0.5465	0.0599		
0.9556	-0.0063	0.0062	-0.0199			-0.0187	0.0017	0.5692	0.0577		
0.9330	-0.0088	0.0030	-0.0217			-0.0230	0.0016	0.5919	0.0554		
0.9103	-0.0112	-0.0007	-0.0236			-0.0272	0.0018	0.6146	0.0530		
0.8876	-0.0135	-0.0028	-0.0244			-0.0298	0.0023	0.6373	0.0506		
0.8649	-0.0157	-0.0058	-0.0252			-0.0317	0.0035	0.6600	0.0480		
0.8421	-0.0179	-0.0087	-0.0258			-0.0324	0.0056	0.6826	0.0454		
0.8194	-0.0200	-0.0110	-0.0259			-0.0319	0.0079	0.7053	0.0427		
0.7967	-0.0220	-0.0141	-0.0256			-0.0306	0.0098	0.7280	0.0400		
0.7740	-0.0240	-0.0164	-0.0253			-0.0289	0.0113	0.7506	0.0371		
0.7512	-0.0259	-0.0186	-0.0246			-0.0267	0.0128	0.7732	0.0342		
0.7285	-0.0277	-0.0205	-0.0233			-0.0228	0.0148	0.7958	0.0313		
0.7057	-0.0295	-0.0217	-0.0214			-0.0198	0.0162	0.8185	0.0282		
0.6830	-0.0312	-0.0216	-0.0191			-0.0151	0.0179	0.8411	0.0251		
0.6602	-0.0328	-0.0207	-0.0170			-0.0124	0.0187	0.8637	0.0220		
0.6375	-0.0344	-0.0194	-0.0151			-0.0084	0.0195	0.8863	0.0187		
0.6147	-0.0358	-0.0177	-0.0135			-0.0058	0.0197	0.9088	0.0154		
0.5919	-0.0372	-0.0156	-0.0127			-0.0028	0.0198	0.9314	0.0120		
0.5691	-0.0385	-0.0128	-0.0116			-0.0007	0.0207	0.9540	0.0086		
0.5463	-0.0397	-0.0110	-0.0102			0.0026	0.0237	0.9765	0.0050		
0.5236	-0.0408	-0.0112	-0.0080			0.0069	0.0276	1.0000	0.0013		
0.5008	-0.0418	-0.0121	-0.0059			0.0166	0.0342				
0.4780	-0.0427	-0.0128	-0.0036			0.0372	0.0446				
0.4552	-0.0435	-0.0133	-0.0014			0.0483	0.0483				
0.4323	-0.0441					0.0696	0.0563				
0.4095	-0.0446					0.0916	0.0624				
0.3867	-0.0449					0.1140	0.0670				
0.3639	-0.0451					0.1365	0.0703				
0.3411	-0.0451					0.1592	0.0727				
0.3183	-0.0449					0.1820	0.0742				
0.2954	-0.0445					0.2048	0.0752				
0.2726	-0.0438					0.2276	0.0757				
0.2498	-0.0429					0.2504	0.0760				
0.2271	-0.0417					0.2732	0.0759				
0.2043	-0.0401					0.2961	0.0756				
0.1816	-0.0382					0.3189	0.0750				
0.1588	-0.0360					0.3417	0.0742				
0.1362	-0.0336					0.3645	0.0732				
0.1237	-0.0330					0.3873	0.0721				
0.1007	-0.0306					0.4100	0.0707				
0.0777	-0.0281					0.4328	0.0692				
0.0547	-0.0254					0.4556	0.0676				
0.0319	-0.0218					0.4783	0.0659				
0.0140	-0.0180					0.5011	0.0640				

Table A-20. Coordinates of Active Pressure Ports of NACA 23012 With 22.5-min Mixed Ice Shape

Lower Surface		Upper Surface	
x/c	y/c	x/c	y/c
1.0000	0.00000	0.0300	0.03921
0.9500	-0.00693	0.0400	0.04456
0.9000	-0.01223	0.0500	0.04915
0.8500	-0.01716	0.0600	0.05306
0.8000	-0.02175	0.0800	0.05949
0.7500	-0.02601	0.1000	0.06435
0.7000	-0.02994	0.1400	0.07075
0.6500	-0.03352	0.1600	0.07272
0.6000	-0.03673	0.1800	0.07408
0.5500	-0.03951	0.2000	0.07497
0.5000	-0.04183	0.2400	0.07589
0.4500	-0.04360	0.2600	0.07596
0.4000	-0.04474	0.2800	0.07583
0.3500	-0.04512	0.3000	0.07548
0.3000	-0.04456	0.3200	0.07496
0.2500	-0.04289	0.3400	0.07428
0.2000	-0.03979	0.3600	0.07343
0.1500	-0.03506	0.3800	0.07245
0.1000	-0.02938	0.4000	0.07134
0.0750	-0.02626	0.4400	0.06874
0.0500	-0.02261	0.5200	0.06232
		0.5600	0.05859
		0.6000	0.05456
		0.6400	0.05026
		0.6800	0.04571
		0.7200	0.04093
		0.7600	0.03593
		0.8000	0.03071
		0.8500	0.02389
		0.9000	0.01673
		0.9500	0.00919

The following is the LEWICE 2.2 input file for the NACA 23012 with 22.5-min mixed ice shape.

```
Mixed 22.5-min Case
&LEW20
ITIMFL = 0
TSTOP  =  1350.
IBOD   =    1
IFLO   =    18
DSMN   =    4.0D-4
NPL    =   24
&END
&DIST
FLWC   = 0.05, 0.1, 0.2, 0.3, 0.2, 0.1, 0.03, 0.01, 0.005, 0.005
DPD    = 4., 9.7, 14.2, 20.9, 28.2, 45.2, 70.1, 88.9, 103.4, 164.
&END
&ICE1
CHORD  = 0.9144
AOA    = 2.5
VINF   =  78.2
LWC    = 0.50
TINF   = 264.
PINF   = 94806.00
RH     = 100.0
&END
&LPRNT
FPRT   = 1
HPRT   = 1
BPRT   = 1
TPRT   = 0
&END
&RDATA
&END
```

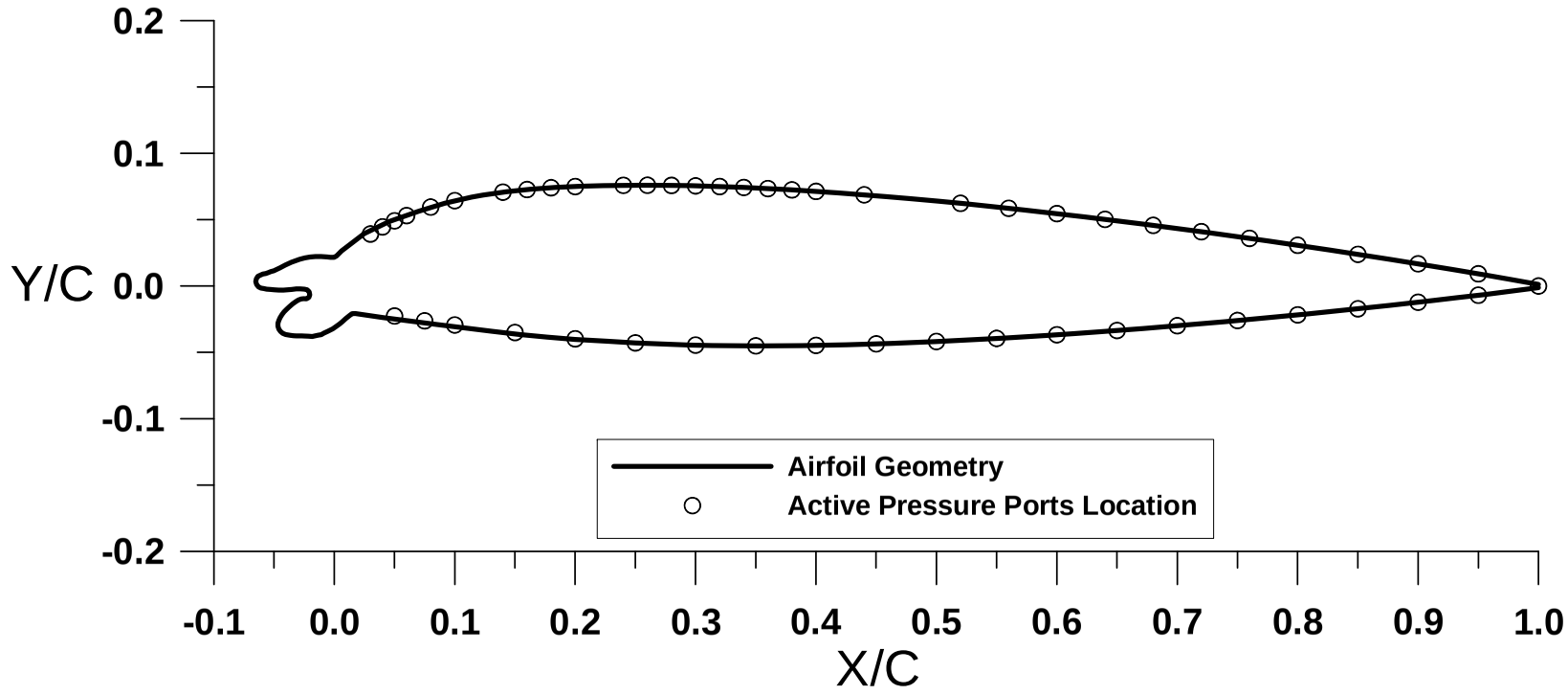

Figure A-11. NACA 23012 With 45-min Mixed Ice Shape

Table A-21. Coordinates of NACA 23012 With 45-min Mixed Ice Shape

Lower Surface						Upper Surface					
x/c	y/c	x/c	y/c	x/c	y/c	x/c	y/c	x/c	y/c	x/c	y/c
1.0000	-0.0013	0.0126	-0.0223	-0.0342	-0.0024	-0.0646	0.0011	0.3873	0.0721		
0.9783	-0.0038	0.0095	-0.0245	-0.0374	-0.0029	-0.0652	0.0033	0.4100	0.0707		
0.9556	-0.0063	0.0065	-0.0269	-0.0402	-0.0030	-0.0648	0.0055	0.4328	0.0692		
0.9330	-0.0088	0.0043	-0.0286	-0.0435	-0.0031	-0.0635	0.0073	0.4556	0.0676		
0.9103	-0.0112	0.0011	-0.0306	-0.0462	-0.0031	-0.0614	0.0083	0.4783	0.0659		
0.8876	-0.0135	-0.0013	-0.0322	-0.0500	-0.0028	-0.0592	0.0090	0.5011	0.0640		
0.8649	-0.0157	-0.0033	-0.0333	-0.0527	-0.0026	-0.0570	0.0094	0.5238	0.0620		
0.8421	-0.0179	-0.0057	-0.0343	-0.0562	-0.0023	-0.0548	0.0101	0.5465	0.0599		
0.8194	-0.0200	-0.0087	-0.0355	-0.0585	-0.0019	-0.0527	0.0108	0.5692	0.0577		
0.7967	-0.0220	-0.0109	-0.0367	-0.0609	-0.0016	-0.0502	0.0116	0.5919	0.0554		
0.7740	-0.0240	-0.0132	-0.0370	-0.0630	-0.0006	-0.0474	0.0127	0.6146	0.0530		
0.7512	-0.0259	-0.0155	-0.0375			-0.0452	0.0137	0.6373	0.0506		
0.7285	-0.0277	-0.0183	-0.0380			-0.0405	0.0158	0.6600	0.0480		
0.7057	-0.0295	-0.0215	-0.0379			-0.0365	0.0176	0.6826	0.0454		
0.6830	-0.0312	-0.0246	-0.0377			-0.0337	0.0184	0.7053	0.0427		
0.6602	-0.0328	-0.0269	-0.0376			-0.0295	0.0199	0.7280	0.0400		
0.6375	-0.0344	-0.0292	-0.0377			-0.0258	0.0210	0.7506	0.0371		
0.6147	-0.0358	-0.0315	-0.0377			-0.0228	0.0215	0.7732	0.0342		
0.5919	-0.0372	-0.0339	-0.0375			-0.0196	0.0219	0.7958	0.0313		
0.5691	-0.0385	-0.0368	-0.0372			-0.0169	0.0223	0.8185	0.0282		
0.5463	-0.0397	-0.0405	-0.0365			-0.0146	0.0223	0.8411	0.0251		
0.5236	-0.0408	-0.0429	-0.0356			-0.0123	0.0223	0.8637	0.0220		
0.5008	-0.0418	-0.0447	-0.0343			-0.0100	0.0222	0.8863	0.0187		
0.4780	-0.0427	-0.0461	-0.0325			-0.0078	0.0220	0.9088	0.0154		
0.4552	-0.0435	-0.0468	-0.0303			-0.0055	0.0219	0.9314	0.0120		
0.4323	-0.0441	-0.0467	-0.0280			-0.0032	0.0216	0.9540	0.0086		
0.4095	-0.0446	-0.0461	-0.0259			-0.0002	0.0217	0.9765	0.0050		
0.3867	-0.0449	-0.0451	-0.0238			0.0019	0.0226	1.0000	0.0013		
0.3639	-0.0451	-0.0434	-0.0213			0.0060	0.0265				
0.3411	-0.0451	-0.0417	-0.0195			0.0248	0.0394				
0.3183	-0.0449	-0.0397	-0.0175			0.0457	0.0487				
0.2954	-0.0445	-0.0376	-0.0158			0.0696	0.0563				
0.2726	-0.0438	-0.0347	-0.0135			0.0916	0.0624				
0.2498	-0.0429	-0.0319	-0.0117			0.1140	0.0670				
0.2271	-0.0417	-0.0299	-0.0106			0.1365	0.0703				
0.1995	-0.0403	-0.0277	-0.0098			0.1592	0.0727				
0.1766	-0.0385	-0.0255	-0.0095			0.1820	0.0742				
0.1538	-0.0365	-0.0232	-0.0096			0.2048	0.0752				
0.1310	-0.0342	-0.0212	-0.0086			0.2276	0.0757				
0.1083	-0.0316	-0.0203	-0.0066			0.2504	0.0760				
0.0855	-0.0290	-0.0210	-0.0044			0.2732	0.0759				
0.0627	-0.0263	-0.0226	-0.0029			0.2961	0.0756				
0.0400	-0.0238	-0.0249	-0.0024			0.3189	0.0750				
0.0174	-0.0208	-0.0282	-0.0021			0.3417	0.0742				
0.0146	-0.0209	-0.0315	-0.0021			0.3645	0.0732				

Table A-22. Coordinates of Active Pressure Ports of NACA 23012 With 45-min Mixed Ice Shape

Lower Surface		Upper Surface	
x/c	y/c	x/c	y/c
1.0000	0.00000	0.0300	0.03921
0.9500	-0.00693	0.0400	0.04456
0.9000	-0.01223	0.0500	0.04915
0.8500	-0.01716	0.0600	0.05306
0.8000	-0.02175	0.0800	0.05949
0.7500	-0.02601	0.1000	0.06435
0.7000	-0.02994	0.1400	0.07075
0.6500	-0.03352	0.1600	0.07272
0.6000	-0.03673	0.1800	0.07408
0.5500	-0.03951	0.2000	0.07497
0.5000	-0.04183	0.2400	0.07589
0.4500	-0.04360	0.2600	0.07596
0.4000	-0.04474	0.2800	0.07583
0.3500	-0.04512	0.3000	0.07548
0.3000	-0.04456	0.3200	0.07496
0.2500	-0.04289	0.3400	0.07428
0.2000	-0.03979	0.3600	0.07343
0.1500	-0.03506	0.3800	0.07245
0.1000	-0.02938	0.4000	0.07134
0.0750	-0.02626	0.4400	0.06874
0.0500	-0.02261	0.5200	0.06232
		0.5600	0.05859
		0.6000	0.05456
		0.6400	0.05026
		0.6800	0.04571
		0.7200	0.04093
		0.7600	0.03593
		0.8000	0.03071
		0.8500	0.02389
		0.9000	0.01673
		0.9500	0.00919

The following is the LEWICE 2.2 input file for the NACA 23012 with 45-min mixed ice shape.

```
Mixed 45-min Case
&LEW20
ITIMFL = 1
TSTOP  =  2700.
IBOD   =    1
IFLO   =    18
DSMN   =    4.0D-4
NPL    =   24
&END
&DIST
FLWC   = 0.05, 0.1, 0.2, 0.3, 0.2, 0.1, 0.03, 0.01, 0.005, 0.005
DPD    = 4., 9.7, 14.2, 20.9, 28.2, 45.2, 70.1, 88.9, 103.4, 164.
&END
&ICE1
CHORD  = 0.9144
AOA    = 2.5
VINF   =  78.2
LWC    = 0.50
TINF   = 264.
PINF   = 94806.00
RH     = 100.0
&END
&LPRNT
FPRT   = 1
HPRT   = 1
BPRT   = 1
TPRT   = 0
&END
&RDATA
&END
```

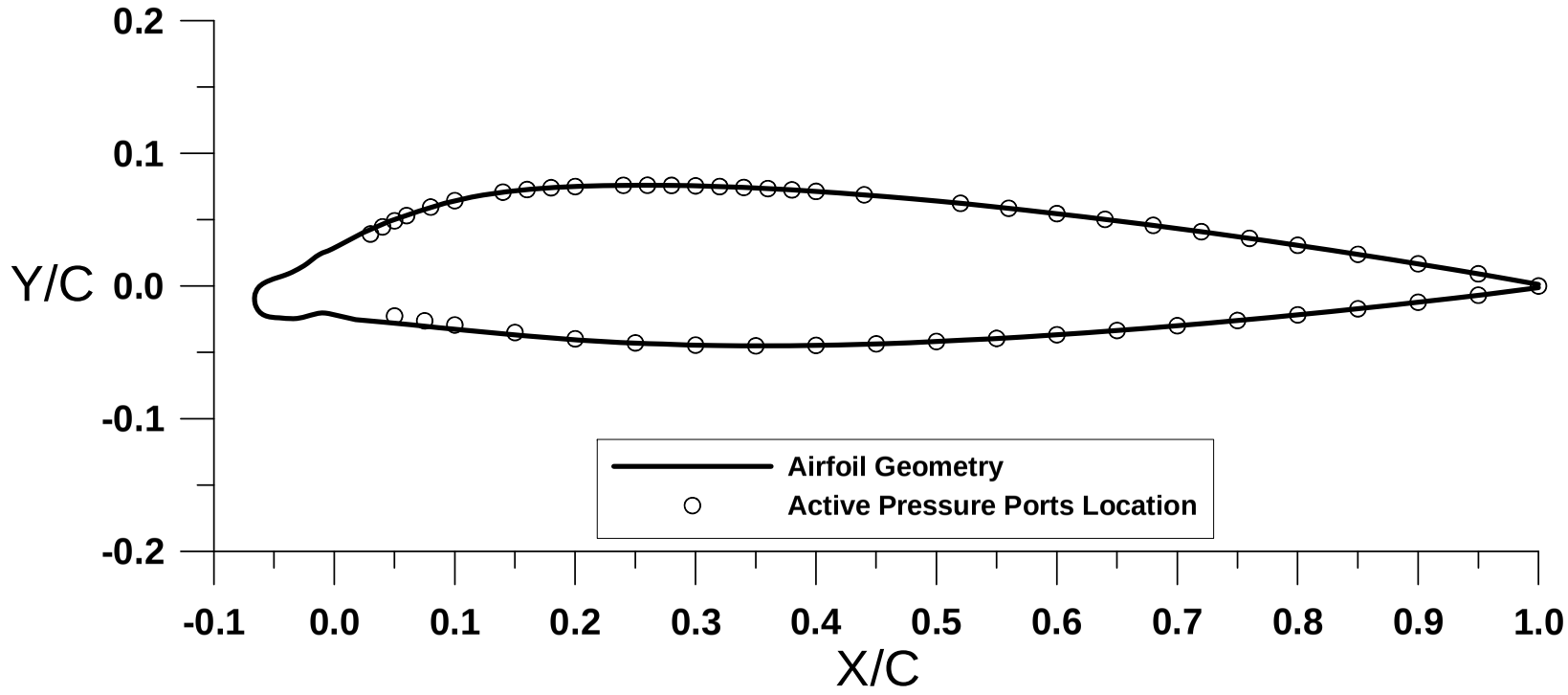

Figure A-12. NACA 23012 With 45-min Rime Ice Shape

Table A-23. Coordinates of NACA 23012 With 45-min Rime Ice Shape

Lower Surface						Upper Surface					
x/c	y/c	x/c	y/c	x/c	y/c	x/c	y/c	x/c	y/c	x/c	y/c
1.0000	-0.0013	-0.0076	-0.0203			-0.0603	0.0012	0.6373	0.0506		
0.9783	-0.0038	-0.0102	-0.0202			-0.0576	0.0027	0.6600	0.0480		
0.9556	-0.0063	-0.0125	-0.0205			-0.0550	0.0037	0.6826	0.0454		
0.9330	-0.0088	-0.0164	-0.0212			-0.0511	0.0051	0.7053	0.0427		
0.9103	-0.0112	-0.0206	-0.0222			-0.0464	0.0067	0.7280	0.0400		
0.8876	-0.0135	-0.0260	-0.0237			-0.0409	0.0083	0.7506	0.0371		
0.8649	-0.0157	-0.0286	-0.0241			-0.0379	0.0092	0.7732	0.0342		
0.8421	-0.0179	-0.0310	-0.0244			-0.0352	0.0104	0.7958	0.0313		
0.8194	-0.0200	-0.0359	-0.0245			-0.0301	0.0128	0.8185	0.0282		
0.7967	-0.0220	-0.0402	-0.0244			-0.0252	0.0153	0.8411	0.0251		
0.7740	-0.0240	-0.0457	-0.0240			-0.0223	0.0171	0.8637	0.0220		
0.7512	-0.0259	-0.0498	-0.0237			-0.0177	0.0204	0.8863	0.0187		
0.7285	-0.0277	-0.0531	-0.0234			-0.0151	0.0222	0.9088	0.0154		
0.7057	-0.0295	-0.0567	-0.0226			-0.0123	0.0238	0.9314	0.0120		
0.6830	-0.0312	-0.0598	-0.0214			-0.0098	0.0250	0.9540	0.0086		
0.6602	-0.0328	-0.0617	-0.0199			-0.0053	0.0266	0.9765	0.0050		
0.6375	-0.0344	-0.0637	-0.0177			-0.0016	0.0280	1.0000	0.0013		
0.6147	-0.0358	-0.0649	-0.0158			0.0036	0.0303				
0.5919	-0.0372	-0.0657	-0.0136			0.0241	0.0403				
0.5691	-0.0385	-0.0661	-0.0114			0.0454	0.0487				
0.5463	-0.0397	-0.0663	-0.0091			0.0696	0.0563				
0.5236	-0.0408	-0.0658	-0.0062			0.0916	0.0624				
0.5008	-0.0418	-0.0650	-0.0040			0.1140	0.0670				
0.4780	-0.0427	-0.0638	-0.0021			0.1365	0.0703				
0.4552	-0.0435	-0.0624	-0.0003			0.1592	0.0727				
0.4323	-0.0441					0.1820	0.0742				
0.4095	-0.0446					0.2048	0.0752				
0.3867	-0.0449					0.2276	0.0757				
0.3639	-0.0451					0.2504	0.0760				
0.3411	-0.0451					0.2732	0.0759				
0.3183	-0.0449					0.2961	0.0756				
0.2954	-0.0445					0.3189	0.0750				
0.2726	-0.0438					0.3417	0.0742				
0.2460	-0.0429					0.3645	0.0732				
0.2232	-0.0419					0.3873	0.0721				
0.2003	-0.0406					0.4100	0.0707				
0.1775	-0.0390					0.4328	0.0692				
0.1546	-0.0372					0.4556	0.0676				
0.1318	-0.0353					0.4783	0.0659				
0.1090	-0.0334					0.5011	0.0640				
0.0862	-0.0314					0.5238	0.0620				
0.0634	-0.0292					0.5465	0.0599				
0.0405	-0.0273					0.5692	0.0577				
0.0177	-0.0254					0.5919	0.0554				
-0.0047	-0.0208					0.6146	0.0530				

Table A-24. Coordinates of Active Pressure Ports of NACA 23012 With 45-min Rime Ice Shape

Lower Surface		Upper Surface	
x/c	y/c	x/c	y/c
1.0000	0.00000	0.0300	0.03921
0.9500	-0.00693	0.0400	0.04456
0.9000	-0.01223	0.0500	0.04915
0.8500	-0.01716	0.0600	0.05306
0.8000	-0.02175	0.0800	0.05949
0.7500	-0.02601	0.1000	0.06435
0.7000	-0.02994	0.1400	0.07075
0.6500	-0.03352	0.1600	0.07272
0.6000	-0.03673	0.1800	0.07408
0.5500	-0.03951	0.2000	0.07497
0.5000	-0.04183	0.2400	0.07589
0.4500	-0.04360	0.2600	0.07596
0.4000	-0.04474	0.2800	0.07583
0.3500	-0.04512	0.3000	0.07548
0.3000	-0.04456	0.3200	0.07496
0.2500	-0.04289	0.3400	0.07428
0.2000	-0.03979	0.3600	0.07343
0.1500	-0.03506	0.3800	0.07245
0.1000	-0.02938	0.4000	0.07134
0.0750	-0.02626	0.4400	0.06874
0.0500	-0.02261	0.5200	0.06232
		0.5600	0.05859
		0.6000	0.05456
		0.6400	0.05026
		0.6800	0.04571
		0.7200	0.04093
		0.7600	0.03593
		0.8000	0.03071
		0.8500	0.02389
		0.9000	0.01673
		0.9500	0.00919

The following is the LEWICE 2.2 input file for the NACA 23012 with 45-min rime ice shape.

```
Rime 45-min Case
&LEW20
ITIMFL = 1
TSTOP  =  2700.
IBOD   =    1
IFLO   =    18
DSMN   =    4.0D-4
NPL    =   24
&END
&DIST
FLWC   = 0.05, 0.1, 0.2, 0.3, 0.2, 0.1, 0.03, 0.01, 0.005, 0.005
DPD    = 4., 9.7, 14.2, 20.9, 28.2, 45.2, 70.1, 88.9, 103.4, 164.
&END
&ICE1
CHORD  = 0.9144
AOA    = 2.5
VINF   =  78.2
LWC    = 0.50
TINF   = 252.32
PINF   = 94806.00
RH     = 100.0
&END
&LPRNT
FPRT   = 1
HPRT   = 1
BPRT   = 1
TPRT   = 0
&END
&RDATA
&END
```

Date: 04/07/2003 Monday
Concentration: 0.0003 grams/cc
Average P_{static} = 13.821 psi, Average P_{total} = 14.364 psi
Geometry: MS-317 airfoil

Run I.D.	TAS (mph)	AOA (deg.)	TOTAL TEMP. (°F)	STATIC TEMP. (°F)	R.H. (%)	P_{air} (psi)	P_{water} (psi)	MVD (μm)	Spray Time (sec)	Clock Time (EST)	IRT Air (psi)	Remark
325	175	0	40.4	34.9	69.8	6	37	111	1.5	19:57	40	ALL minus N1, N6 and N7, steam on, doors
326	175	0	40.4	35.0	70.0	6	37	111	1.5	20:12	40	ALL minus N1, N6 and N7, steam on, doors
327	175	0	40.6	35.1	69.0	6	37	111	4	20:21	40	ALL minus N1, N6 and N7, steam on, doors
328	175	0	40.8	35.2	69.9	6	37	111	1.5	20:44	60	ALL minus N1, N6 and N7, steam on, doors
329	175	0	39.3	33.9	71.3	22	70	20	1.5	21:22	40	ALL, steam on, doors
330	175	0	39.6	34.1	70.4	22	70	20	1.5	21:27	40	ALL, steam on, doors
331	175	0	40.9	35.4	70.0	22	70	20	1.5	21:34	40	ALL, steam on, doors
332	175	0	39.9	34.4	68.1	22	70	20	4	21:45	40	ALL, steam on, doors
333	175	0	39.5	34.1	67.4	5	70	236	0.75	21:55	40	ALL minus N1, N6 and N7, steam on, doors
334	175	0	39.3	33.9	68.7	5	70	236	0.75	22:07	40	ALL minus N1, N6 and N7, steam on, doors
335	175	0	40.3	34.8	74.5	5	70	236	4	22:24	40	ALL minus N1, N6 and N7, steam on, doors
336	175	0	41.0	35.5	70.7	5	70	236	0.75	22:30	40	ALL minus N1, N6 and N7, steam on, doors
337	175	0	40.4	34.9	70.8	5	55	154	1	22:39	40	ALL minus N1, N6 and N7, steam on, doors
338	175	0	41.5	36.0	70.8	10	45	52	1.5	22:44	40	ALL, steam on, doors
339	175	0	39.6	34.1	68.5	10	45	52	1.5	22:52	40	ALL minus N1, N6 and N7, steam on, doors

$(AOA)_{IRT} = (AOA)_{MS\text{-}317}$
The bottom edge of the blotter strip is placed 37″ above the floor.

Date: 04/10/2003 Thursday
Concentration: 0.0003 grams/cc
Average P_{static} = 13.807 psi, Average P_{total} = 14.321 psi
Geometry: NACA 23012 airfoil

Run I.D.	TAS (mph)	AOA (deg.)	TOTAL TEMP. (°F)	STATIC TEMP. (°F)	R.H. (%)	P_{air} (psi)	P_{water} (psi)	MVD (μm)	Spray Time (sec)	Clock Time (EST)	IRT Air (psi)	Remark
406	175	2.5	69.7	64.2	71.1	6	37	111	1.5	19:30	40	ALL minus N1, N6 and N7, steam on
407	175	2.5	68.9	63.4	70.9	6	37	111	1.5	19:42	40	ALL minus N1, N6 and N7, steam on
408	175	2.5	68.4	62.9	71.8	6	37	111	1.5	19:54	40	ALL minus N1, N6 and N7, steam on
409	175	2.5	68.2	62.6	71.7	6	37	111	4	20:06	40	ALL minus N1, N6 and N7, steam on
410	175	2.5	67.9	62.4	71.8	10	45	52	1.5	20:18	40	ALL, steam on
411	175	2.5	67.6	62.1	71.8	10	45	52	1.5	20:30	40	ALL, steam on
412	175	2.5	67.6	62.2	71.8	10	45	52	1.5	20:41	40	ALL, steam on
413	175	2.5	67.6	62.1	71.7	10	45	52	4	20:53	40	ALL, steam on
414	175	2.5	67.5	61.9	71.7	5	55	154	1	21:02	40	ALL minus N1, N6 and N7, steam on
415	175	2.5	67.5	62.0	71.6	5	55	154	1	21:13	40	ALL minus N1, N6 and N7, steam on
416	175	2.5	67.4	61.9	72.0	5	55	154	1	21:23	40	ALL minus N1, N6 and N7, steam on
417	175	2.5	67.4	61.9	71.7	5	55	154	4	21:33	40	ALL minus N1, N6 and N7, steam on
418	175	2.5	67.4	62.2	71.2	22	70	20	1.5	21:44	40	ALL, steam on
419	175	2.5	67.3	61.9	71.7	22	70	20	1.5	21:53	40	ALL, steam on
420	175	2.5	67.2	71.5	71.5	22	70	20	1.5	22:02	40	ALL, steam on
421	175	2.5	67.1	61.7	72.0	22	70	20	4	22:13	40	ALL, steam on
422	175	2.5	67.1	61.7	71.8	5	70	236	0.75	22:20	40	ALL minus N1, N6 and N7, steam on
423	175	2.5	66.9	61.4	71.8	5	70	236	0.75	22:33	40	ALL minus N1, N6 and N7, steam on
424	175	2.5	67.0	61.5	71.9	5	70	236	0.75	22:41	40	ALL minus N1, N6 and N7, steam on
425	175	2.5	66.8	61.3	71.9	5	70	236	4	22:53	40	ALL minus N1, N6 and N7, steam on

AOA's tabulated are with respect to geometry. They are negative to IRT turnable AOA's. (i.e., $(AOA)_{NACA} = -(AOA)_{IRT}$)

Date: 04/11/2003 Friday
Concentration: 0.0003 grams/cc
Average P_{static} = 13.731 psi, Average P_{total} = 14.240 psi
Geometry: NACA 23012 airfoil + 22.5-min glaze ice

Run I.D.	TAS (mph)	AOA (deg.)	TOTAL TEMP. (°F)	STATIC TEMP. (°F)	R.H. (%)	P_{air} (psi)	P_{water} (psi)	MVD (μm)	Spray Time (sec)	Clock Time (EST)	IRT Air (psi)	Remark
427	175	2.5	69.6	64.2	68.5	6	37	111	1.5	19:00	40	ALL minus N1, N6 and N7, steam on
428	175	2.5	69.0	63.6	69.0	6	37	111	1.5	19:27	40	ALL minus N1, N6 and N7, steam on
429	175	2.5	68.6	63.1	71.7	6	37	111	1.5	19:51	40	ALL minus N1, N6 and N7, steam on
430	175	2.5	68.5	63.0	71.4	6	37	111	4	20:13	40	ALL minus N1, N6 and N7, steam on
431	175	2.5	68.2	62.8	72.0	10	45	52	1.5	20:33	40	ALL, steam on
432	175	2.5	67.7	62.4	71.1	10	45	52	1.5	20:56	40	ALL, steam on
433	175	2.5	67.3	61.8	71.8	10	45	52	1.5	21:21	40	ALL, steam on
434	175	2.5	67.4	61.9	71.3	10	45	52	4	21:43	40	ALL, steam on
435	175	2.5	67.3	61.9	72.0	5	55	154	1	22:03	40	ALL minus N1, N6 and N7, steam on
436	175	2.5	67.0	61.5	71.9	5	55	154	1	22:26	40	ALL minus N1, N6 and N7, steam on
437	175	2.5	66.9	61.5	71.6	5	55	154	1	22:45	40	ALL minus N1, N6 and N7, steam on

Date: 04/12/2003 Saturday
Concentration: 0.0003 grams/cc
Average P_{static} = 13.780 psi, Average P_{total} = 14.290 psi
Geometry: NACA 23012 airfoil + 22.5-min glaze ice (R438-R447) / 45-min glaze ice (R448-R449)

Run I.D.	TAS (mph)	AOA (deg.)	TOTAL TEMP. (°F)	STATIC TEMP. (°F)	R.H. (%)	P_{air} (psi)	P_{water} (psi)	MVD (μm)	Spray Time (sec)	Clock Time (EST)	IRT Air (psi)	Remark
438	175	2.5	72.2	66.6	71.7	5	55	154	4	09:24	40	ALL minus N1, N6 and N7, steam on
439	175	2.5	71.3	65.9	72.1	22	70	20	1.5	09:47	40	ALL, steam on
440	175	2.5	71.0	65.5	71.7	22	70	20	1.5	10:11	40	ALL, steam on
441	175	2.5	70.6	65.2	71.7	22	70	20	1.5	10:32	40	ALL, steam on
442	175	2.5	70.3	64.8	72.1	22	70	20	4	10:51	40	ALL, steam on
443	175	2.5	70.0	64.6	71.5	5	70	236	0.75	11:14	40	ALL minus N1, N6 and N7, steam on
444	175	2.5	70.0	64.6	71.9	5	70	236	0.75	11:33	40	ALL minus N1, N6 and N7, steam on
445	175	2.5	69.8	64.3	71.6	5	70	236	0.75	11:53	40	ALL minus N1, N6 and N7, steam on
446	175	2.5	69.6	64.2	72.2	5	70	236	4	12:13	40	ALL minus N1, N6 and N7, steam on
447	175	2.5	69.3	63.9	71.9	5	55	154	1	12:34	40	ALL minus N1, N6 and N7, **Repeat**
448	175	2.5	68.0	62.6	71.8	6	37	111	4	14:26	40	ALL minus N1, N6 and N7, steam on
449	175	2.5	67.7	62.3	71.5	10	45	52	4	15:03	40	ALL, steam on

Date: 04/14/2003 Monday
Concentration: 0.0003 grams/cc
Average P_{static} = 13.867 psi, Average P_{total} = 14.379 psi
Geometry: NACA 23012 airfoil + 45-min glaze ice

Run I.D.	TAS (mph)	AOA (deg.)	TOTAL TEMP. (°F)	STATIC TEMP. (°F)	R.H. (%)	P_{air} (psi)	P_{water} (psi)	MVD (μm)	Spray Time (sec)	Clock Time (EST)	IRT Air (psi)	Remark
450	175	2.5	68.7	63.4	71.4	5	55	154	4	15:17	40	ALL minus N1, N6 and N7, steam on
451	175	2.5	68.2	62.7	71.6	22	70	20	4	15:35	40	ALL, steam on
452	175	2.5	67.6	62.2	71.8	5	70	236	4	15:57	40	ALL minus N1, N6 and N7, steam on
452A	175	2.5	67.7	62.3	70.1	5	70	236	30	15:19	40	ALL minus N1, N6 and N7, steam on
453	175	2.5	69.0	63.5	71.9	6	37	111	1.5	16:41	40	ALL minus N1, N6 and N7, steam on
454	175	2.5	70.0	64.5	71.5	6	37	111	1.5	17:04	40	ALL minus N1, N6 and N7, steam on
455	175	2.5	70.7	65.3	71.6	6	37	111	1.5	17:21	40	ALL minus N1, N6 and N7, steam on
456	175	2.5	71.1	65.6	71.7	10	45	52	1.5	17:39	40	ALL, steam on
457	175	2.5	71.3	65.9	71.7	10	45	52	1.5	17:57	40	ALL, steam on
458	175	2.5	71.5	66.0	71.7	10	45	52	1.5	18:17	40	ALL, steam on
459	175	2.5	71.7	66.3	71.9	5	55	154	1	18:35	40	ALL minus N1, N6 and N7, steam on
460	175	2.5	71.9	66.5	71.7	5	55	154	1	18:53	40	ALL minus N1, N6 and N7, steam on
461	175	2.5	72.1	66.7	71.6	5	55	154	1	19:11	40	ALL minus N1, N6 and N7, steam on
462	175	2.5	72.4	66.9	71.4	22	70	20	1.5	19:32	40	ALL, steam on
463	175	2.5	72.8	67.3	71.9	22	70	20	1.5	19:48	40	ALL, steam on
464	175	2.5	72.7	67.3	71.9	22	70	20	1.5	20:06	40	ALL, steam on
465	175	2.5	73.1	67.6	72.1	5	70	236	0.75	20:24	40	ALL minus N1, N6 and N7, steam on
466	175	2.5	73.1	67.7	71.3	5	70	236	0.75	20:40	40	ALL minus N1, N6 and N7, steam on
467	175	2.5	73.2	67.7	71.9	5	70	236	0.75	20:55	40	ALL minus N1, N6 and N7, steam on

Date: 04/15/2003 Tuesday
Concentration: 0.0003 grams/cc
Average P_{static} = 13.756 psi, Average P_{total} = 14.260 psi
Geometry: NACA 23012 airfoil + 22.5-min mixed ice

Run I.D.	TAS (mph)	AOA (deg.)	TOTAL TEMP. (°F)	STATIC TEMP. (°F)	R.H. (%)	P_{air} (psi)	P_{water} (psi)	MVD (μm)	Spray Time (sec)	Clock Time (EST)	IRT Air (psi)	Remark
470	175	2.5	76.1	70.7	66.7	6	37	111	4	15:15	40	ALL minus N1, N6 and N7, steam on
471	175	2.5	75.2	69.7	72.1	10	45	52	4	15:41	40	ALL, steam on
472	175	2.5	75.4	70.0	71.4	5	55	154	4	16:04	40	ALL minus N1, N6 and N7, steam on
473	175	2.5	75.6	70.2	71.6	22	70	20	4	16:26	40	ALL, steam on
474	175	2.5	75.8	70.3	71.7	5	70	236	4	16:47	40	ALL minus N1, N6 and N7, steam on
475	175	2.5	76.1	70.6	71.8	6	37	111	1.5	17:07	40	ALL minus N1, N6 and N7, steam on
476	175	2.5	76.4	70.9	71.4	6	37	111	1.5	17:27	40	ALL minus N1, N6 and N7, steam on
477	175	2.5	76.6	71.1	71.4	6	37	111	1.5	17:47	40	ALL minus N1, N6 and N7, steam on
478	175	2.5	76.6	71.1	71.9	10	45	52	1.5	18:06	40	ALL, steam on
479	175	2.5	76.8	71.3	71.7	10	45	52	1.5	18:26	40	ALL, steam on
480	175	2.5	76.9	71.4	71.9	10	45	52	1.5	18:46	40	ALL, steam on
481	175	2.5	77.1	71.6	70.3	5	55	154	1	19:04	40	ALL minus N1, N6 and N7, steam on
482	175	2.5	77.5	71.9	72.0	5	55	154	1	19:24	40	ALL minus N1, N6 and N7, steam on
483	175	2.5	77.6	72.2	71.8	5	55	154	1	19:40	40	ALL minus N1, N6 and N7, steam on
484	175	2.5	77.4	72.0	71.8	22	70	20	1.5	19:58	40	ALL, steam on
485	175	2.5	77.4	71.9	71.9	22	70	20	1.5	20:17	40	ALL, steam on
486	175	2.5	77.4	71.9	71.9	22	70	20	1.5	20:35	40	ALL, steam on
487	175	2.5	77.2	71.8	72.0	5	70	236	0.75	20:53	40	ALL minus N1, N6 and N7, steam on
488	175	2.5	77.1	71.6	71.7	5	70	236	0.75	21:12	40	ALL minus N1, N6 and N7, steam on
489	175	2.5	77.0	71.5	71.9	5	70	236	0.75	21:30	40	ALL minus N1, N6 and N7, steam on

Date: 04/16/2003 Wednesday
Concentration: 0.0003 grams/cc
Average P_{static} = 13.772 psi, Average P_{total} = 14.277 psi
Geometry: NACA 23012 airfoil + 45-min mixed ice

Run I.D.	TAS (mph)	AOA (deg.)	TOTAL TEMP. (°F)	STATIC TEMP. (°F)	R.H. (%)	P_{air} (psi)	P_{water} (psi)	MVD (μm)	Spray Time (sec)	Clock Time (EST)	IRT Air (psi)	Remark
492	175	2.5	77.3	71.8	71.8	6	37	111	4	15:07	40	ALL minus N1, N6 and N7, steam on
493	175	2.5	76.8	71.3	71.9	10	45	52	4	15:27	40	ALL, steam on
494	175	2.5	76.7	71.2	71.9	5	55	154	4	15:45	40	ALL minus N1, N6 and N7, steam on
495	175	2.5	76.6	71.1	72.0	22	70	20	4	16:04	40	ALL, steam on
496	175	2.5	76.6	71.2	71.7	5	70	236	4	16:23	40	ALL minus N1, N6 and N7, steam on
497	175	2.5	76.7	71.2	71.7	6	37	111	1.5	16:41	40	ALL minus N1, N6 and N7, steam on
498	175	2.5	76.7	71.3	71.5	6	37	111	1.5	16:59	40	ALL minus N1, N6 and N7, steam on
499	175	2.5	76.5	71.0	72.2	6	37	111	1.5	17:16	40	ALL minus N1, N6 and N7, steam on
500	175	2.5	76.3	70.9	71.8	10	45	52	1.5	17:33	40	ALL, steam on
501	175	2.5	76.1	70.7	72.0	10	45	52	1.5	17:50	40	ALL, steam on
502	175	2.5	75.8	70.4	71.9	10	45	52	1.5	18:09	40	ALL, steam on
503	175	2.5	75.4	69.9	72.1	5	55	154	1	18:28	40	ALL minus N1, N6 and N7, steam on
504	175	2.5	74.4	68.9	71.5	5	55	154	1	18:54	40	ALL minus N1, N6 and N7, steam on
505	175	2.5	74.6	69.2	72.2	5	55	154	1	19:11	40	ALL minus N1, N6 and N7, steam on
506	175	2.5	74.5	69.0	72.0	22	70	20	1.5	19:28	40	ALL, steam on
507	175	2.5	74.3	68.9	71.8	22	70	20	1.5	19:44	40	ALL, steam on
508	175	2.5	74.1	68.6	71.8	22	70	20	1.5	20:02	40	ALL, steam on
509	175	2.5	73.9	68.4	71.5	5	70	236	0.75	20:20	40	ALL minus N1, N6 and N7, steam on
510	175	2.5	73.7	68.3	71.6	5	70	236	0.75	20:37	40	ALL minus N1, N6 and N7, steam on
511	175	2.5	73.6	68.1	71.9	5	70	236	0.75	20:53	40	ALL minus N1, N6 and N7, steam on

Date: 04/17/2003 Thursday
Concentration: 0.0003 grams/cc
Average P_{static} = 13.770 psi, Average P_{total} = 14.280 psi
Geometry: NACA 23012 airfoil + 15-min mixed ice (R514-535) / 15-min glaze ice (R537-541)

Run I.D.	TAS (mph)	AOA (deg.)	TOTAL TEMP. (°F)	STATIC TEMP. (°F)	R.H. (%)	P_{air} (psi)	P_{water} (psi)	MVD (μm)	Spray Time (sec)	Clock Time (EST)	IRT Air (psi)	Remark
514	175	2.5	69.2	63.7	72.2	6	37	111	4	15:03	40	ALL minus N1, N6 and N7, steam on
515	175	2.5	69.8	64.4	72.1	10	45	52	4	15:20	40	ALL, steam on
516	175	2.5	70.3	64.8	71.9	5	55	154	4	15:38	40	ALL minus N1, N6 and N7, steam on
517	175	2.5	70.6	65.1	72.0	22	70	20	4	15:56	40	ALL, steam on
518	175	2.5	70.8	65.3	71.8	5	70	236	4	16:12	40	ALL minus N1, N6 and N7, steam on
519	175	2.5	70.7	65.2	72.0	6	37	111	1.5	16:27	40	ALL minus N1, N6 and N7, steam on
520	175	2.5	70.8	65.3	71.7	6	37	111	1.5	16:42	40	ALL minus N1, N6 and N7, steam on
521	175	2.5	70.9	65.4	71.9	6	37	111	1.5	16:55	40	ALL minus N1, N6 and N7, steam on
522	175	2.5	71.0	65.5	71.9	10	45	52	1.5	17:08	40	ALL, steam on
523	175	2.5	71.1	65.7	71.7	10	45	52	1.5	17:21	40	ALL, steam on
524	175	2.5	71.3	65.7	71.9	10	45	52	1.5	17:34	40	ALL, steam on
525	175	2.5	71.4	65.9	71.1	5	55	154	1	17:48	40	ALL minus N1, N6 and N7, steam on
526	175	2.5	71.4	66.0	71.9	5	55	154	1	18:03	40	ALL minus N1, N6 and N7, steam on
527	175	2.5	71.5	66.0	71.8	5	55	154	1	18:16	40	ALL minus N1, N6 and N7, steam on
528	175	2.5	72.3	66.8	69.0	22	70	20	1.5	18:31	40	ALL, steam on
529	175	2.5	72.2	66.8	71.9	22	70	20	1.5	18:46	40	ALL, steam on
530	175	2.5	72.2	66.7	71.9	22	70	20	1.5	18:59	40	ALL, steam on
531	175	2.5	72.3	66.9	71.8	5	70	236	0.75	19:13	40	ALL minus N1, N6 and N7, steam on
532	175	2.5	72.7	67.2	71.9	5	70	236	0.75	19:26	40	ALL minus N1, N6 and N7, steam on
533	175	2.5	72.8	67.3	71.8	5	70	236	0.75	19:40	40	ALL minus N1, N6 and N7, steam on
534	175	2.5	72.9	67.4	71.9	22	70	20	1.5	19:53	40	ALL, steam on, REPEAT
535	175	2.5	73.0	67.5	72.0	5	70	236	0.75	20:09	40	ALL minus N1, N6 and N7, REPEAT
537	175	2.5	73.6	68.2	71.7	6	37	111	4	21:36	40	ALL minus N1, N6 and N7, steam on
538	175	2.5	73.6	68.1	71.8	10	45	52	4	21:51	40	ALL, steam on
539	175	2.5	73.4	67.9	71.9	5	55	154	4	22:05	40	ALL minus N1, N6 and N7, steam on
540	175	2.5	73.2	67.7	71.9	22	70	20	4	22:20	40	ALL, steam on
541	175	2.5	73.2	67.8	71.4	5	70	236	4	22:33	40	ALL minus N1, N6 and N7, steam on

Date: 04/18/2003 Friday
Concentration: 0.0003 grams/cc
Average P_{static} = 13.866 psi, Average P_{total} = 14.376 psi
Geometry: NACA 23012 airfoil + 15-min glaze ice (R542-557) / 10-min glaze ice (R560-567)

Run I.D.	TAS (mph)	AOA (deg.)	TOTAL TEMP. (°F)	STATIC TEMP. (°F)	R.H. (%)	P_{air} (psi)	P_{water} (psi)	MVD (μm)	Spray Time (sec)	Clock Time (EST)	IRT Air (psi)	Remark
542	175	2.5	72.4	67.1	72.1	6	37	111	1.5	15:08	40	ALL minus N1, N6 and N7, steam on
543	175	2.5	72.5	67.0	72.1	6	37	111	1.5	15:23	40	ALL minus N1, N6 and N7, steam on
544	175	2.5	72.6	67.2	72.1	6	37	111	1.5	15:38	40	ALL minus N1, N6 and N7, steam on
545	175	2.5	72.9	67.4	72.0	10	45	52	1.5	15:50	40	ALL, steam on
546	175	2.5	72.9	67.4	72.0	10	45	52	1.5	16:05	40	ALL, steam on
547	175	2.5	73.3	67.8	71.9	10	45	52	1.5	16:23	40	ALL, steam on
548	175	2.5	73.7	68.2	71.9	5	55	154	1	16:36	40	ALL minus N1, N6 and N7, steam on
549	175	2.5	74.0	68.5	72.0	5	55	154	1	16:46	40	ALL minus N1, N6 and N7, steam on
550	175	2.5	73.9	68.4	72.0	5	55	154	1	16:58	40	ALL minus N1, N6 and N7, steam on
551	175	2.5	73.9	68.5	71.7	22	70	20	1.5	17:11	40	ALL, steam on
552	175	2.5	74.1	68.6	71.7	22	70	20	1.5	17:23	40	ALL, steam on
553	175	2.5	74.3	68.8	71.9	22	70	20	1.5	17:34	40	ALL, steam on
554	175	2.5	74.2	68.8	71.8	5	70	236	0.75	17:47	40	ALL minus N1, N6 and N7, steam on
555	175	2.5	74.4	68.9	71.9	5	70	236	0.75	17:59	40	ALL minus N1, N6 and N7, steam on
556	175	2.5	74.5	69.0	72.1	5	70	236	0.75	18:12	40	ALL minus N1, N6 and N7, steam on
557	175	2.5	74.6	69.1	71.9	5	55	154	1	18:24	40	ALL minus N1, N6 and N7, steam on
560	175	2.5	75.8	70.4	71.9	6	37	111	4	21:14	40	ALL minus N1, N6 and N7, steam on
561	175	2.5	76.2	70.6	71.7	10	45	52	4	21:27	40	ALL, steam on
562	175	2.5	75.9	70.4	71.9	5	55	154	4	21:38	40	ALL minus N1, N6 and N7, steam on
563	175	2.5	75.8	70.3	71.8	22	70	20	4	21:52	40	ALL, steam on
564	175	2.5	75.7	70.2	72.1	5	70	236	4	22:04	40	ALL minus N1, N6 and N7, steam on
565	175	2.5	75.6	70.1	72.0	6	37	111	1.5	22:17	40	ALL minus N1, N6 and N7, steam on
566	175	2.5	75.4	69.9	71.6	6	37	111	1.5	22:29	40	ALL minus N1, N6 and N7, steam on
567	175	2.5	75.5	70.0	71.8	6	37	111	1.5	22:40	40	ALL minus N1, N6 and N7, steam on

Date: 04/22/2003 Tuesday
Concentration: 0.0003 grams/cc
Average P_{static} = 13.794 psi, Average P_{total} = 14.315 psi
Geometry: NACA 23012 airfoil + 10-min glaze ice

Run I.D.	TAS (mph)	AOA (deg.)	TOTAL TEMP. (°F)	STATIC TEMP. (°F)	R.H. (%)	P_{air} (psi)	P_{water} (psi)	MVD (μm)	Spray Time (sec)	Clock Time (EST)	IRT Air (psi)	Remark
611	175	2.5	66.9	61.4	72.1	6	37	111	1.5	19:19	40	ALL minus N1, N6 and N7, steam on
612A	175	2.5	67.2	61.7	71.2	10	45	52	1.5	19:33	40	ALL, steam on
612B	175	2.5	65.4	59.9	71.9	10	45	52	1.5	20:07	40	ALL, steam on
613	175	2.5	66.1	60.5	71.9	10	45	52	1.5	20:19	40	ALL, steam on
614	175	2.5	66.7	61.1	71.8	10	45	52	1.5	20:33	40	ALL, steam on
615	175	2.5	67.1	61.1	72.1	5	55	154	1	20:45	40	ALL minus N1, N6 and N7, steam on
616	175	2.5	67.4	61.9	72.1	5	55	154	1	20:58	40	ALL minus N1, N6 and N7, steam on
617	175	2.5	67.2	62.1	72.5	5	55	154	1	20:10	40	ALL minus N1, N6 and N7, steam on
618	175	2.5	67.9	62.4	72.1	22	70	20	1.5	20:24	40	ALL, steam on
619	175	2.5	68.1	62.5	72.2	22	70	20	1.5	20:35	40	ALL, steam on
620	175	2.5	68.1	62.6	72.2	22	70	20	1.5	20:46	40	ALL, steam on
621	175	2.5	68.2	62.7	72.1	5	70	236	0.75	20:58	40	ALL minus N1, N6 and N7, steam on
622	175	2.5	68.3	62.7	72.2	5	70	236	0.75	21:09	40	ALL minus N1, N6 and N7, steam on
623	175	2.5	68.3	62.8	72.1	5	70	236	0.75	21:21	40	ALL minus N1, N6 and N7, steam on

Date: 04/23/2003 Wednesday
Concentration: 0.0003 grams/cc
Average P_{static} = 13.868 psi, Average P_{total} = 14.387 psi
Geometry: NACA 23012 airfoil + 5-min glaze ice

Run I.D.	TAS (mph)	AOA (deg.)	TOTAL TEMP. (°F)	STATIC TEMP. (°F)	R.H. (%)	P_{air} (psi)	P_{water} (psi)	MVD (μm)	Spray Time (sec)	Clock Time (EST)	IRT Air (psi)	Remark
625A	175	2.5	64.3	58.9	71.5	6	37	111	1.5	17:00	40	ALL minus N1, N6 and N7, steam on
626A	175	2.5	64.2	58.7	70.3	6	37	111	1.5	17:20	40	ALL minus N1, N6 and N7, steam on
625B	175	2.5	69.0	63.4	68.2	6	37	111	1.5	19:35	40	ALL minus N1, N6 and N7, steam on
626B	175	2.5	68.4	62.8	71.6	6	37	111	1.5	19:50	40	ALL minus N1, N6 and N7, steam on
627	175	2.5	68.0	62.5	71.2	10	45	52	1.5	20:04	40	ALL, steam on
628	175	2.5	67.8	62.3	72.1	10	45	52	1.5	20:17	40	ALL, steam on
629	175	2.5	67.6	62.1	72.1	5	55	154	1	20:32	40	ALL minus N1, N6 and N7, steam on
630	175	2.5	67.6	62.1	72.1	5	55	154	1	20:44	40	ALL minus N1, N6 and N7, steam on
631	175	2.5	67.4	61.9	72.1	22	70	20	1.5	20:57	40	ALL, steam on
632	175	2.5	67.5	61.9	72.0	22	70	20	1.5	21:08	40	ALL, steam on
633	175	2.5	67.3	61.8	72.2	5	70	236	0.75	21:22	40	ALL minus N1, N6 and N7, steam on
634	175	2.5	67.2	61.6	71.9	5	70	236	0.75	21:34	40	ALL minus N1, N6 and N7, steam on
635	175	2.5	67.0	61.5	72.3	5	55	154	1	21:47	40	ALL minus N1, N6 and N7, steam on
636	175	2.5	66.8	61.3	72.0	6	37	111	4	22:00	40	ALL minus N1, N6 and N7, steam on
637	175	2.5	66.5	61.1	72.1	5	55	154	4	22:15	40	ALL minus N1, N6 and N7, steam on
638	175	2.5	66.5	61.0	71.9	5	70	236	4	22:28	40	ALL minus N1, N6 and N7, steam on

Date: 04/24/2003 Thursday
Concentration: 0.0003 grams/cc
Average P_{static} = 13.794 psi, Average P_{total} = 14.306 psi
Geometry: NACA 23012 airfoil + 7.5-min mixed ice (R641-R654) / 45-min rime ice (R655-R666)

Run I.D.	TAS (mph)	AOA (deg.)	TOTAL TEMP. (°F)	STATIC TEMP. (°F)	R.H. (%)	P_{air} (psi)	P_{water} (psi)	MVD (μm)	Spray Time (sec)	Clock Time (EST)	IRT Air (psi)	Remark
641	175	2.5	71.4	65.9	71.8	6	37	111	1.5	16:21	40	ALL minus N1, N6 and N7, steam on
642	175	2.5	71.4	66.0	72.1	6	37	111	1.5	16:36	40	ALL minus N1, N6 and N7, steam on
643	175	2.5	71.3	65.8	72.1	10	45	52	1.5	16:49	40	ALL, steam on
644	175	2.5	71.2	65.8	72.1	10	45	52	1.5	17:03	40	ALL, steam on
645	175	2.5	71.2	65.7	71.9	5	55	154	1	17:16	40	ALL minus N1, N6 and N7, steam on
646	175	2.5	70.9	65.5	72.0	5	55	154	1	17:30	40	ALL minus N1, N6 and N7, steam on
647	175	2.5	70.9	65.4	72.0	22	70	20	1.5	17:44	40	ALL, steam on
648	175	2.5	71.0	65.4	72.0	22	70	20	1.5	17:57	40	ALL, steam on
649	175	2.5	70.8	65.3	71.7	5	70	236	0.75	18:12	40	ALL minus N1, N6 and N7, steam on
650	175	2.5	70.8	65.3	72.0	5	70	236	0.75	18:25	40	ALL minus N1, N6 and N7, steam on
651	175	2.5	70.6	65.1	72.0	6	37	111	1.5	18:39	40	ALL minus N1, N6 and N7, REPEAT
652	175	2.5	70.4	65.0	71.6	6	37	111	4	18:54	40	ALL minus N1, N6 and N7, steam on
653	175	2.5	70.3	64.8	72.1	5	55	154	4	19:08	40	ALL minus N1, N6 and N7, steam on
654	175	2.5	70.1	64.7	72.8	5	70	236	4	19:23	40	ALL minus N1, N6 and N7, steam on
655	175	2.5	69.2	63.9	71.9	6	37	111	1.5	20:18	40	ALL minus N1, N6 and N7, steam on
656	175	2.5	69.4	63.9	71.2	6	37	111	1.5	20:30	40	ALL minus N1, N6 and N7, steam on
657	175	2.5	69.5	64.0	72.0	10	45	52	1.5	20:42	40	ALL, steam on
658	175	2.5	69.5	64.0	72.1	10	45	52	1.5	20:55	40	ALL, steam on
659	175	2.5	69.7	64.2	71.4	5	55	154	1	21:07	40	ALL minus N1, N6 and N7, steam on
660	175	2.5	69.7	64.2	71.0	5	55	154	1	21:22	40	ALL minus N1, N6 and N7, steam on
661	175	2.5	69.6	64.2	72.0	22	70	20	1.5	21:35	40	ALL, steam on
662	175	2.5	69.8	64.3	71.9	22	70	20	1.5	21:47	40	ALL, steam on
663	175	2.5	69.6	64.2	72.1	5	70	236	0.75	22:01	40	ALL minus N1, N6 and N7, steam on
664	175	2.5	69.7	64.2	72.0	5	70	236	0.75	22:14	40	ALL minus N1, N6 and N7, steam on
665	175	2.5	69.7	64.2	72.0	10	45	52	1.5	22:25	40	ALL, steam on, REPEAT
666	175	2.5	69.6	64.1	72.0	5	70	236	0.75	22:40	40	ALL minus N1, N6 and N7, REPEAT

APPENDIX C—SUMMARY OF EXPERIMENTAL AND LEWICE IMPINGEMENT DATA—ALL TEST GEOMETRIES AND MEDIAN VOLUMETRIC DIAMETERS

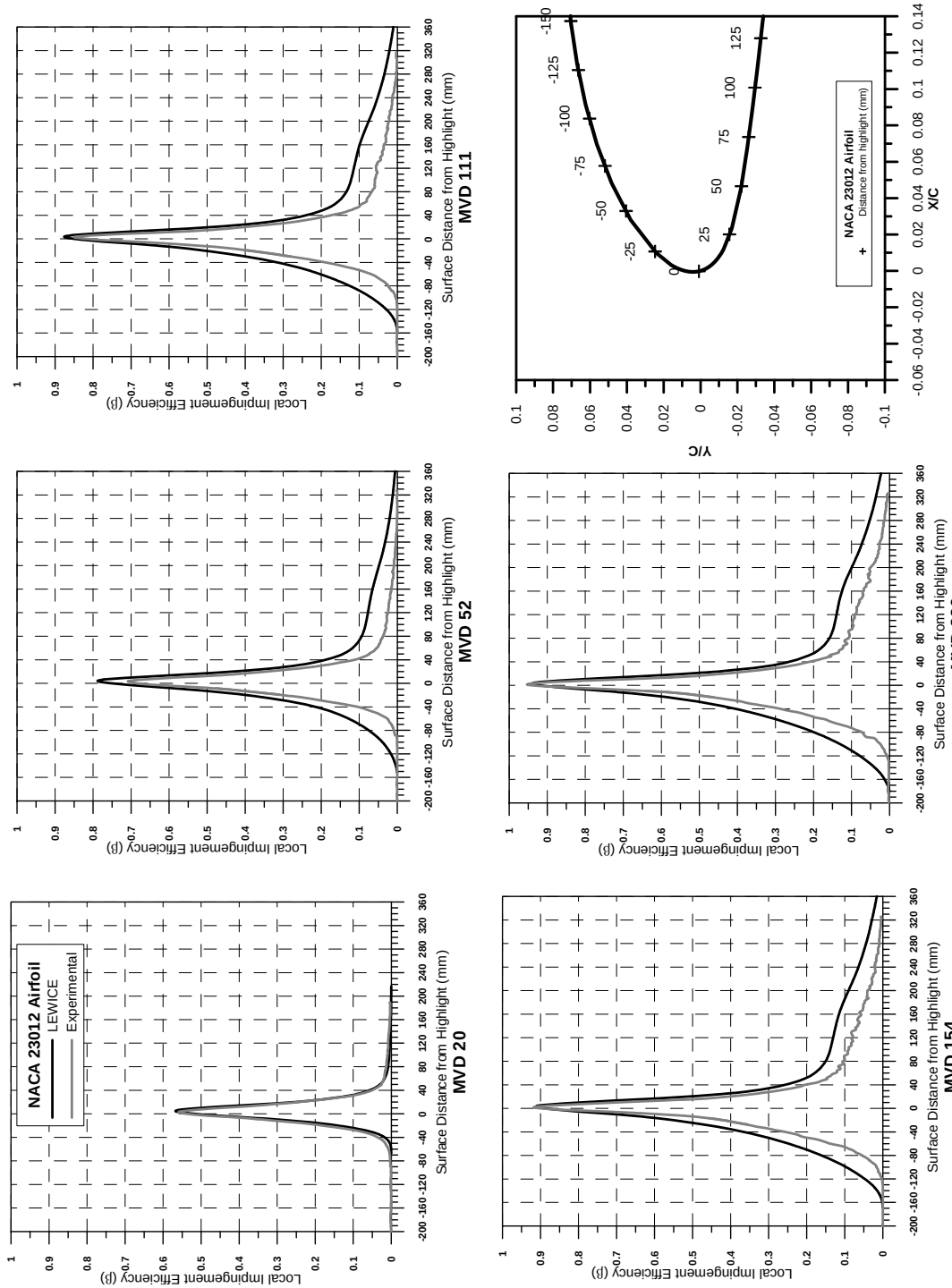

Figure C-1. Comparison of LEWICE and Experimental Impingement Data (CCD Reflectometer); NACA 23012 Airfoil

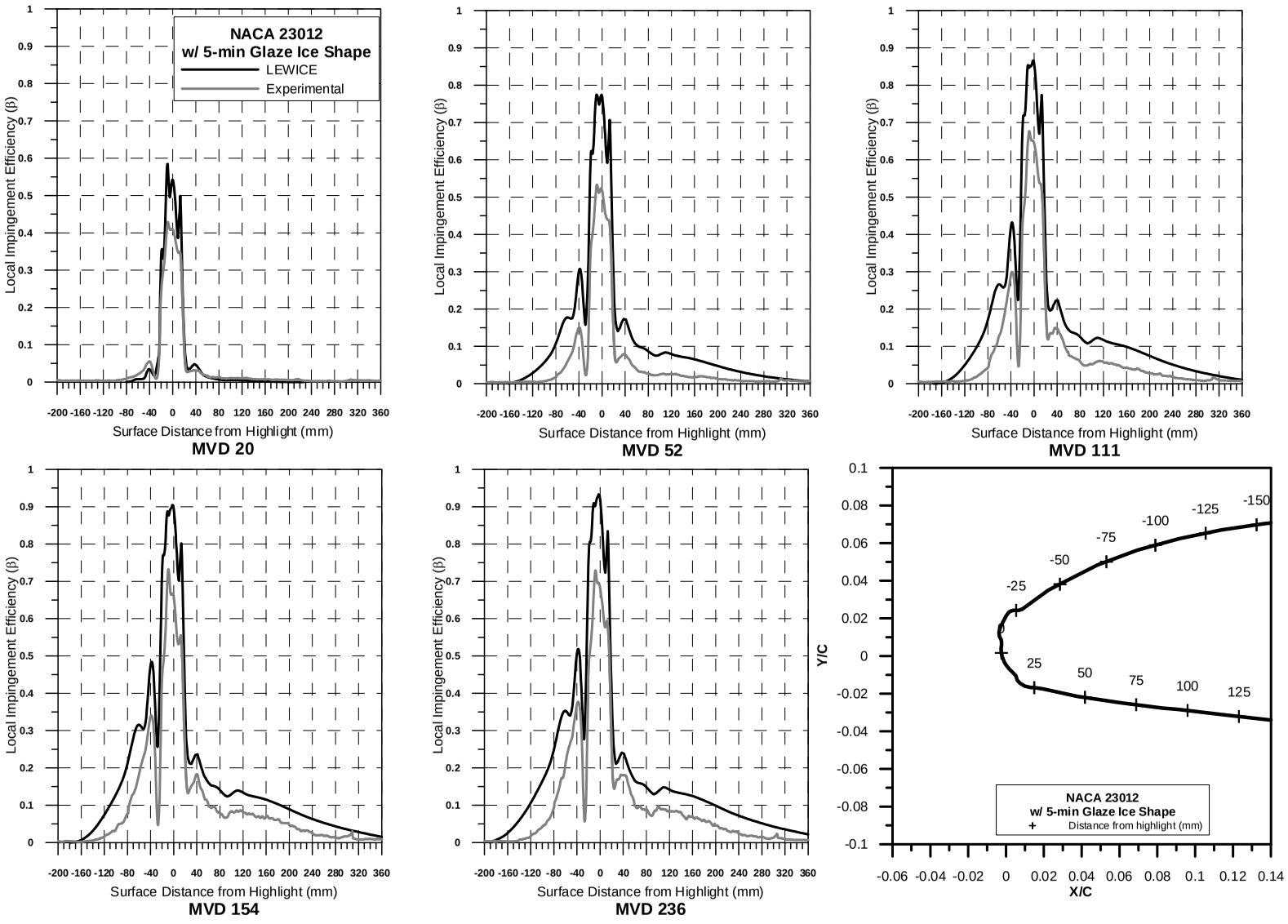

Figure C-2. Comparison of LEWICE and Experimental Impingement Data (CCD Reflectometer); NACA 23012 Airfoil With 5-min Glaze Ice Shape

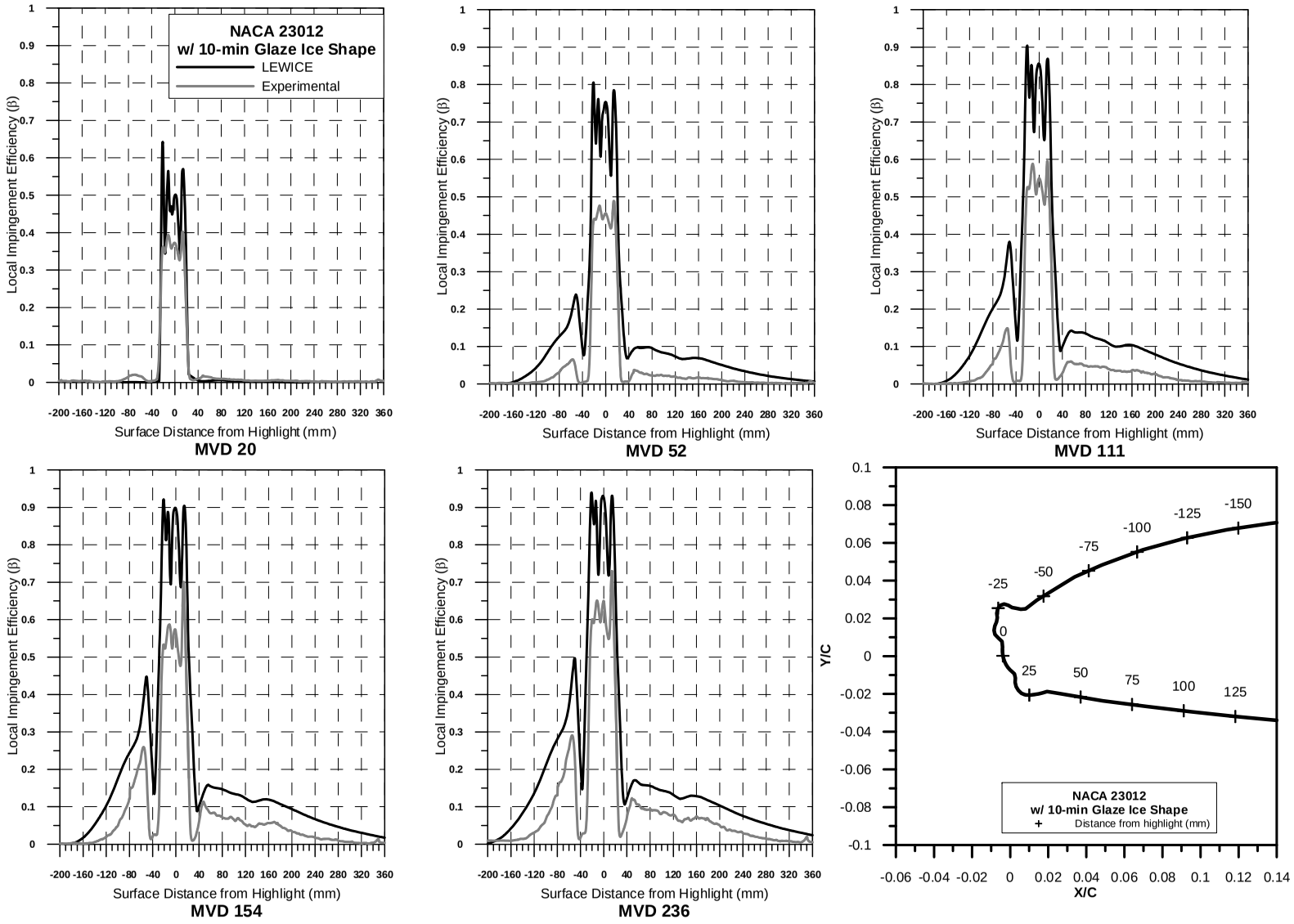

Figure C-3. Comparison of LEWICE and Experimental Impingement Data (CCD Reflectometer); NACA 23012 Airfoil With 10-min Glaze Ice Shape

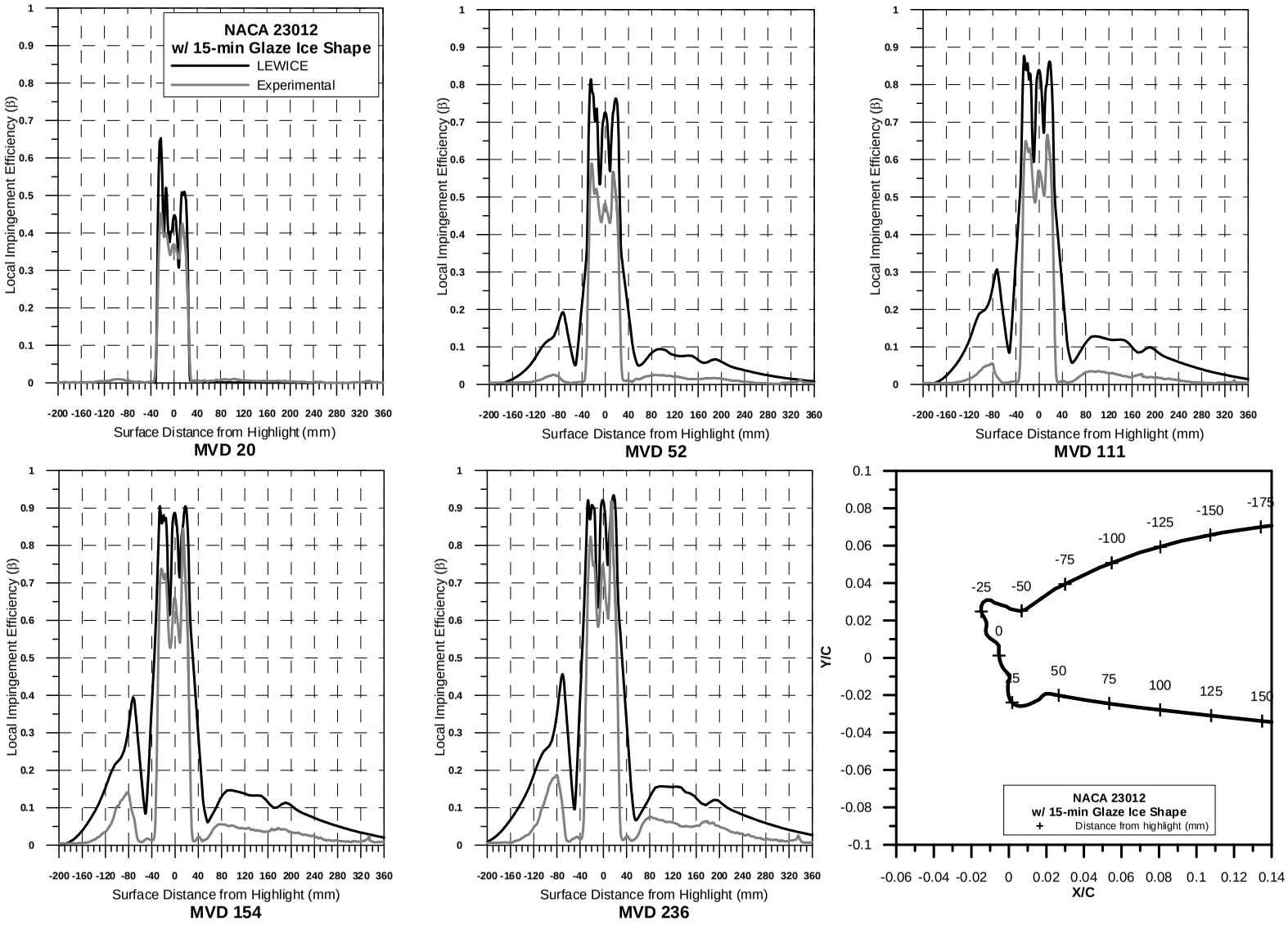

Figure C-4. Comparison of LEWICE and Experimental Impingement Data (CCD Reflectometer); NACA 23012 Airfoil With 15-min Glaze Ice Shape

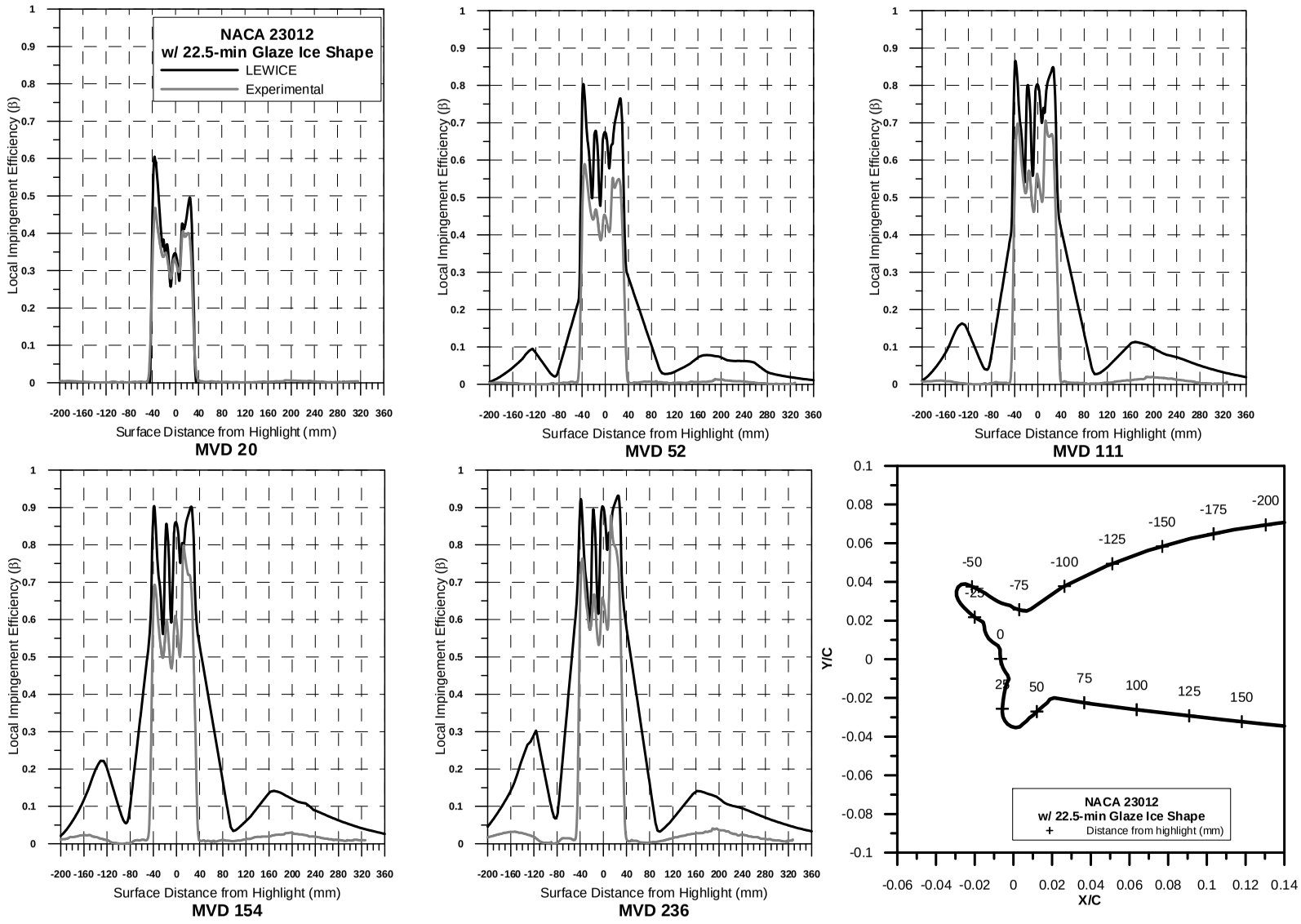

Figure C-5. Comparison of LEWICE and Experimental Impingement Data (CCD Reflectometer); NACA 23012 Airfoil With 22.5-min Glaze Ice Shape

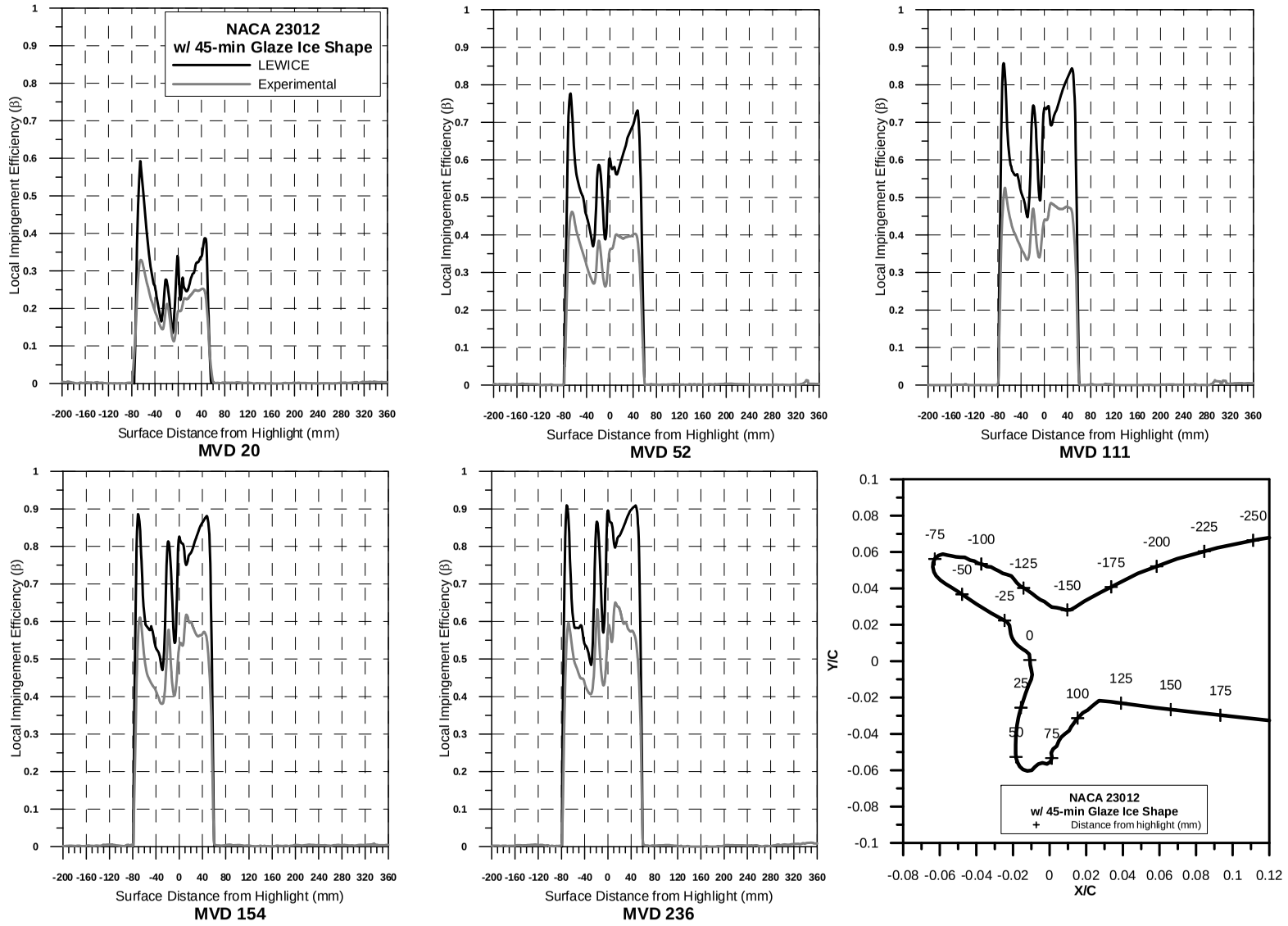

Figure C-6. Comparison of LEWICE and Experimental Impingement Data (CCD Reflectometer); NACA 23012 Airfoil With 45-min Glaze Ice Shape

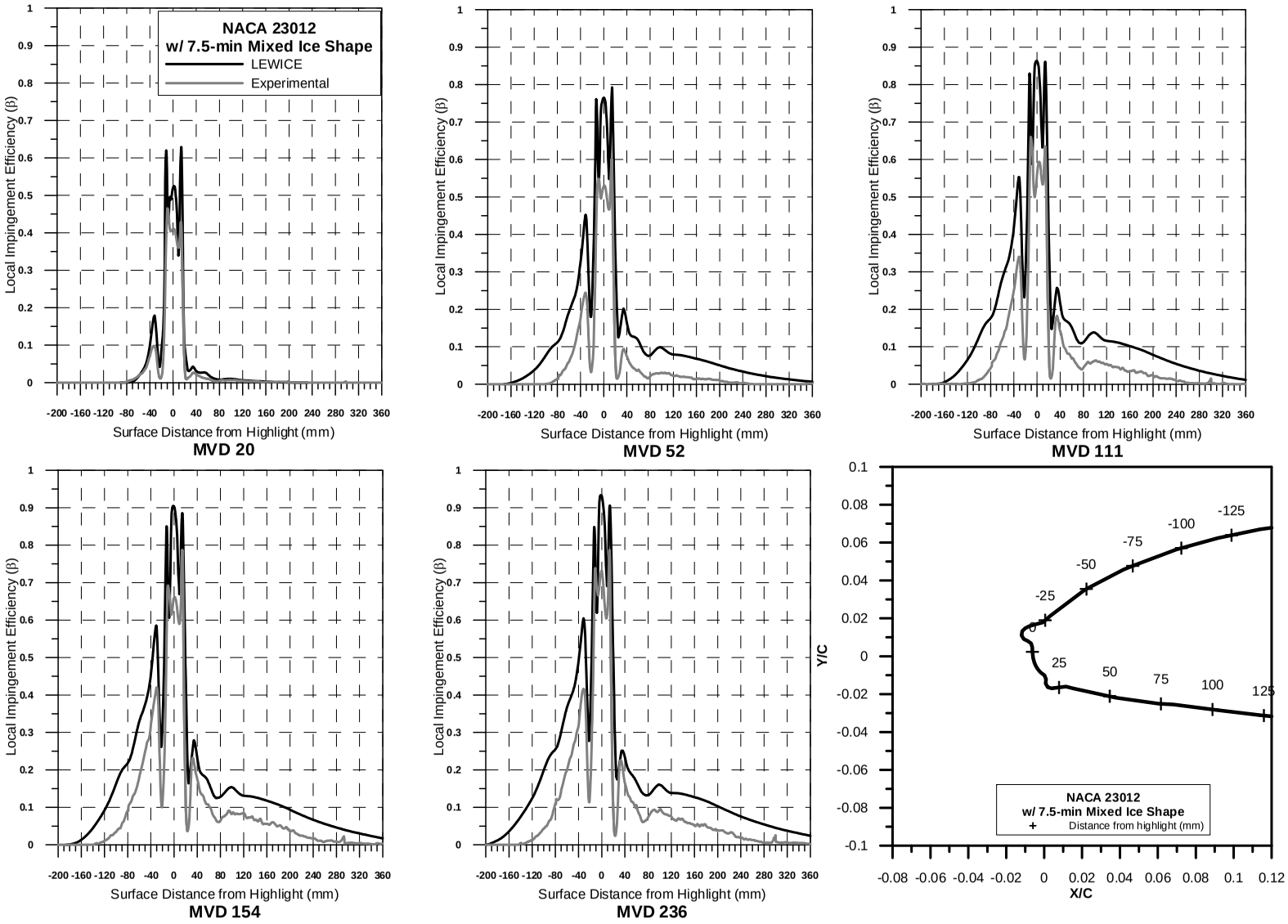

Figure C-7. Comparison of LEWICE and Experimental Impingement Data (CCD Reflectometer); NACA 23012 Airfoil With 7.5-min Mixed Ice Shape

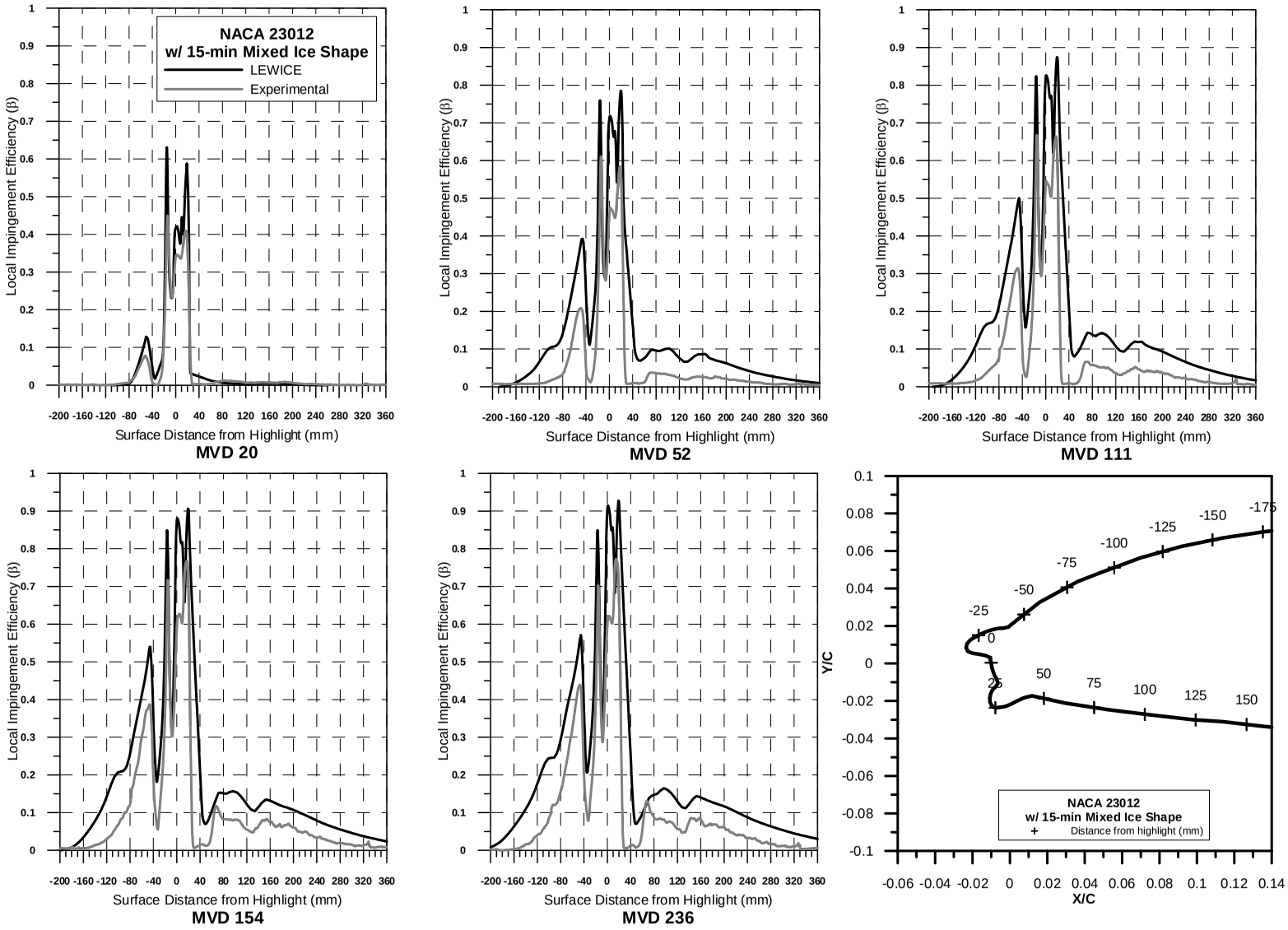

Figure C-8. Comparison of LEWICE and Experimental Impingement Data (CCD Reflectometer); NACA 23012 Airfoil With 15-min Mixed Ice Shape

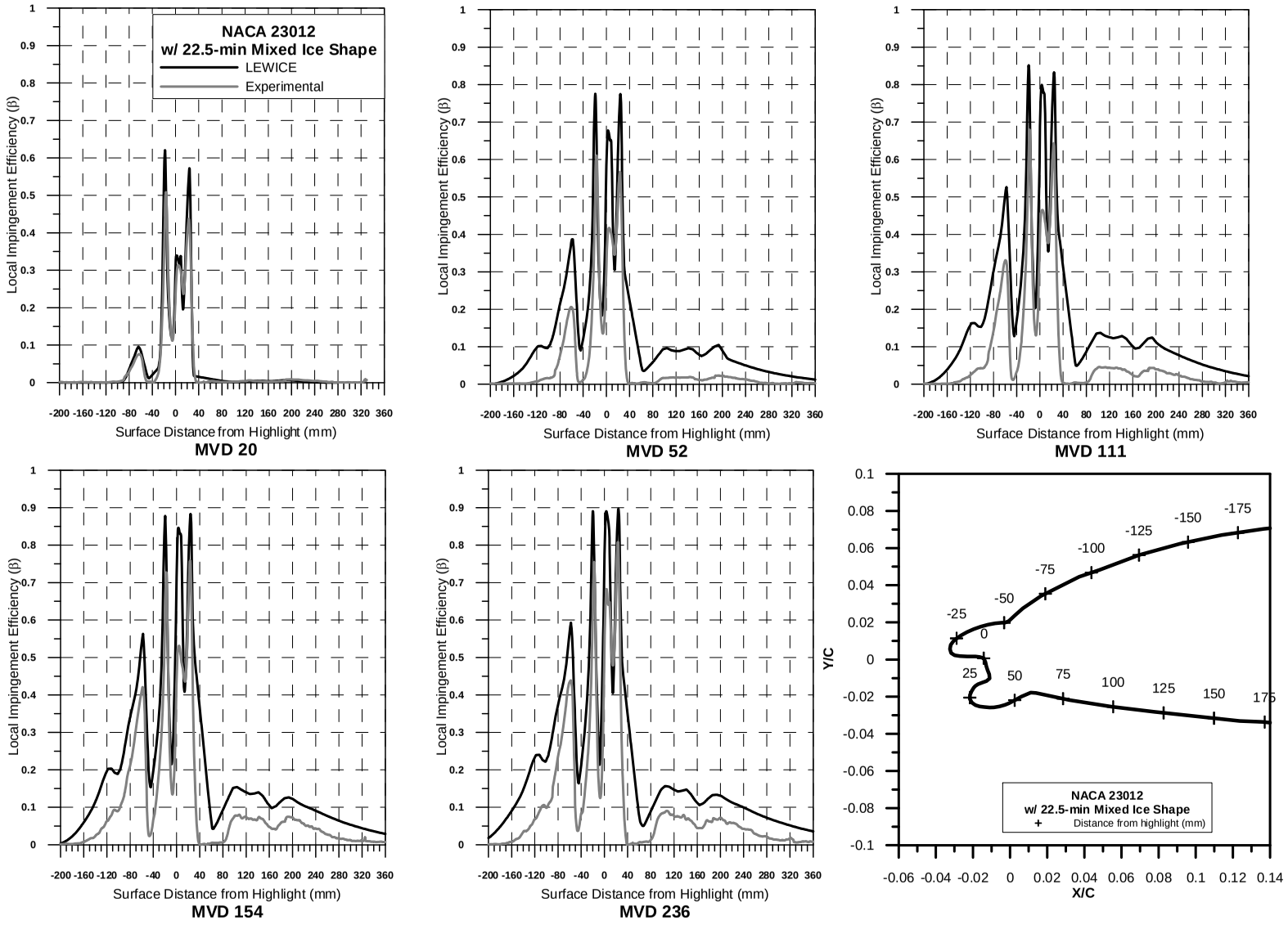

Figure C-9. Comparison of LEWICE and Experimental Impingement Data (CCD Reflectometer); NACA 23012 Airfoil With 22.5-min Mixed Ice Shape

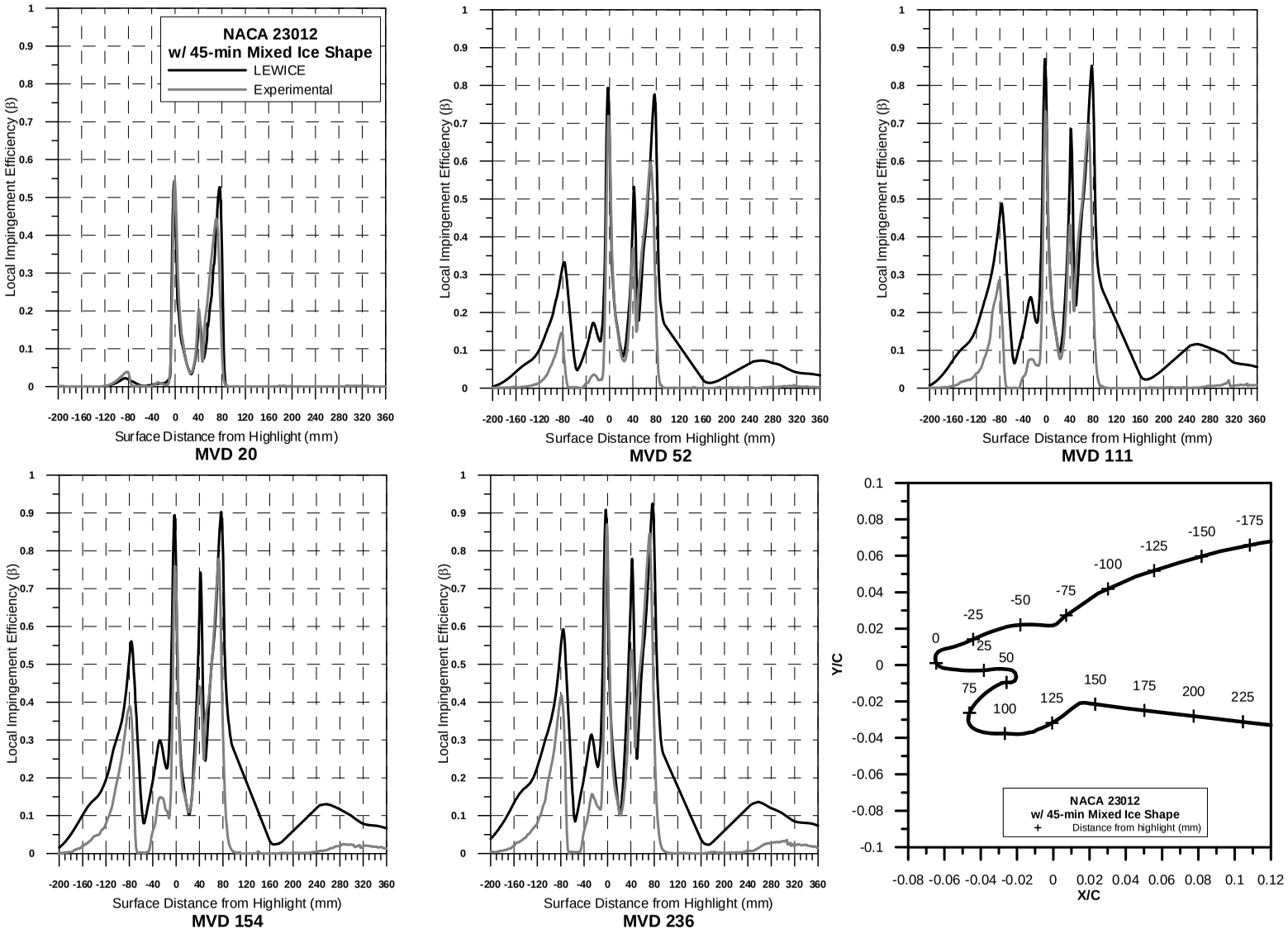

Figure C-10. Comparison of LEWICE and Experimental Impingement Data (CCD Reflectometer); NACA 23012 Airfoil With 45-min Mixed Ice Shape

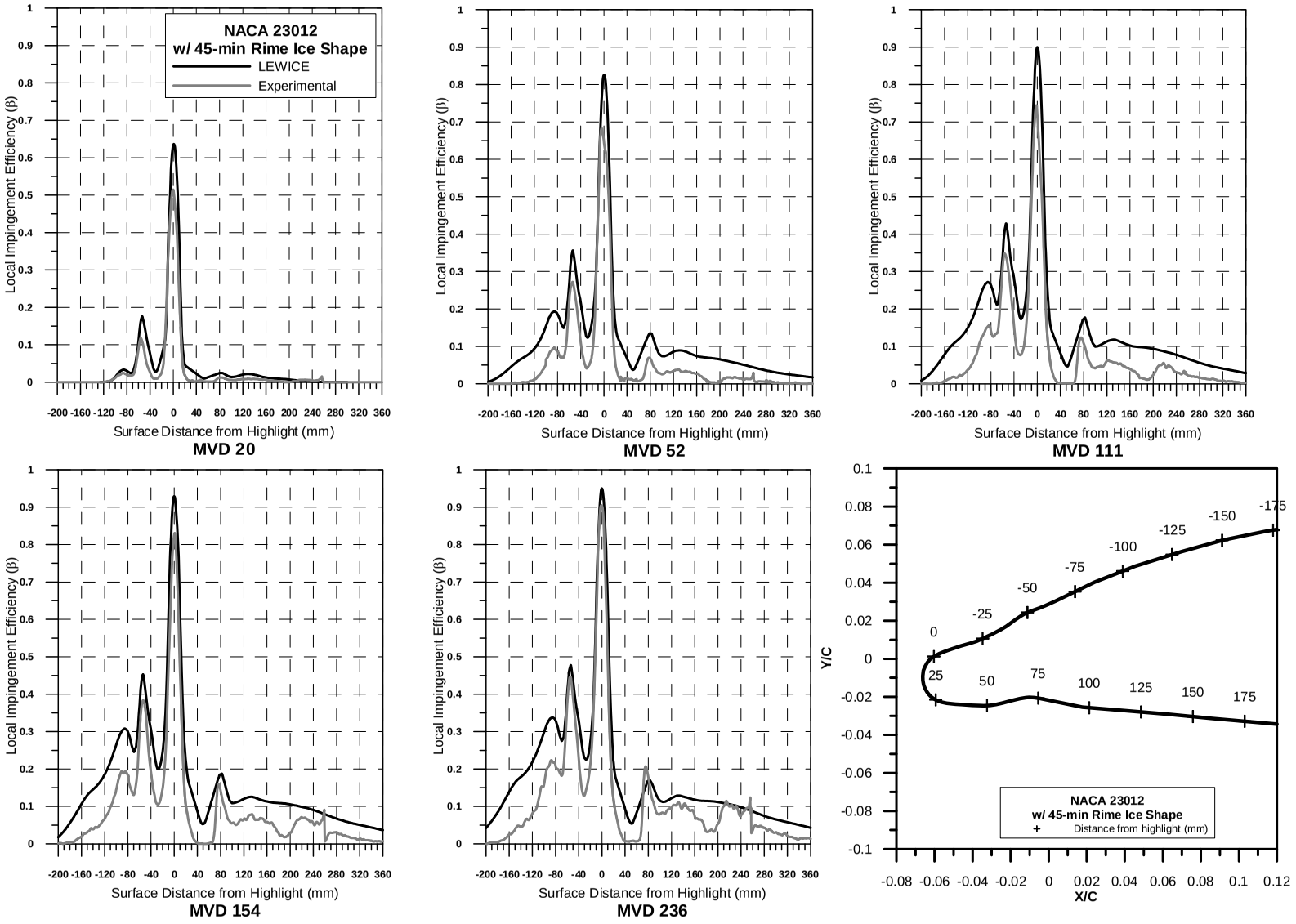

Figure C-11. Comparison of LEWICE and Experimental Impingement Data (CCD Reflectometer); NACA 23012 Airfoil With 45-Min Rime Ice Shape

APPENDIX D—DROP TRAJECTORIES

The trajectories presented in this appendix were computed using the LEWICE 1.7 code and the 10-point discrete approximations (table 5) of the measured drop distributions. Figures D-1 through D-8 consist of ten trajectory plots each, one plot for each drop size in the measured drop distributions. Each of the ten plots in the figures was obtained with the LEWICE code using a single drop size. Note that the LEWICE code does not simulate large drop splashing, thus, the trajectory simulations for the large-median volumetric diameter (MVD) cases do not include drop splashing effects. Furthermore, for some cases, such as the 45-min glaze ice shape, the flowfield predicted by LEWICE was not in good agreement with the experimental pressure data, as shown in figure 66. This was due to the inability of the potential flow method used in LEWICE to simulate flow separation and viscous effects such as the ones associated with large glaze ice accretions. Despite these limitations, however, the computed trajectories provide insight into the contributions made by the individual drop sizes in the spray clouds used in the experiments. Consider, for example, the computed trajectories for the 45-min glaze ice shape shown in figure D-4. For the large MVD of 236 μm, the smallest drop in the 10-point distribution was 16.3 μm. For this drop size, the trajectories experienced considerable deflection near the 45-min ice shapes. The remaining nine drop sizes in the distribution ranged from 63.7 to 1046.8 μm. For these drop sizes the deflection of the trajectories became progressively smaller until about 508.5 μm. For drops larger than 508.5 μm, the trajectories were practically straight. Thus, for the 2.5-degree angle of attack used in the experiments, the small drops in the distribution contributed more to the impingement in the upper horn area, while the impingement, due to the large drops in the distribution, was more even across the region between the two horns.

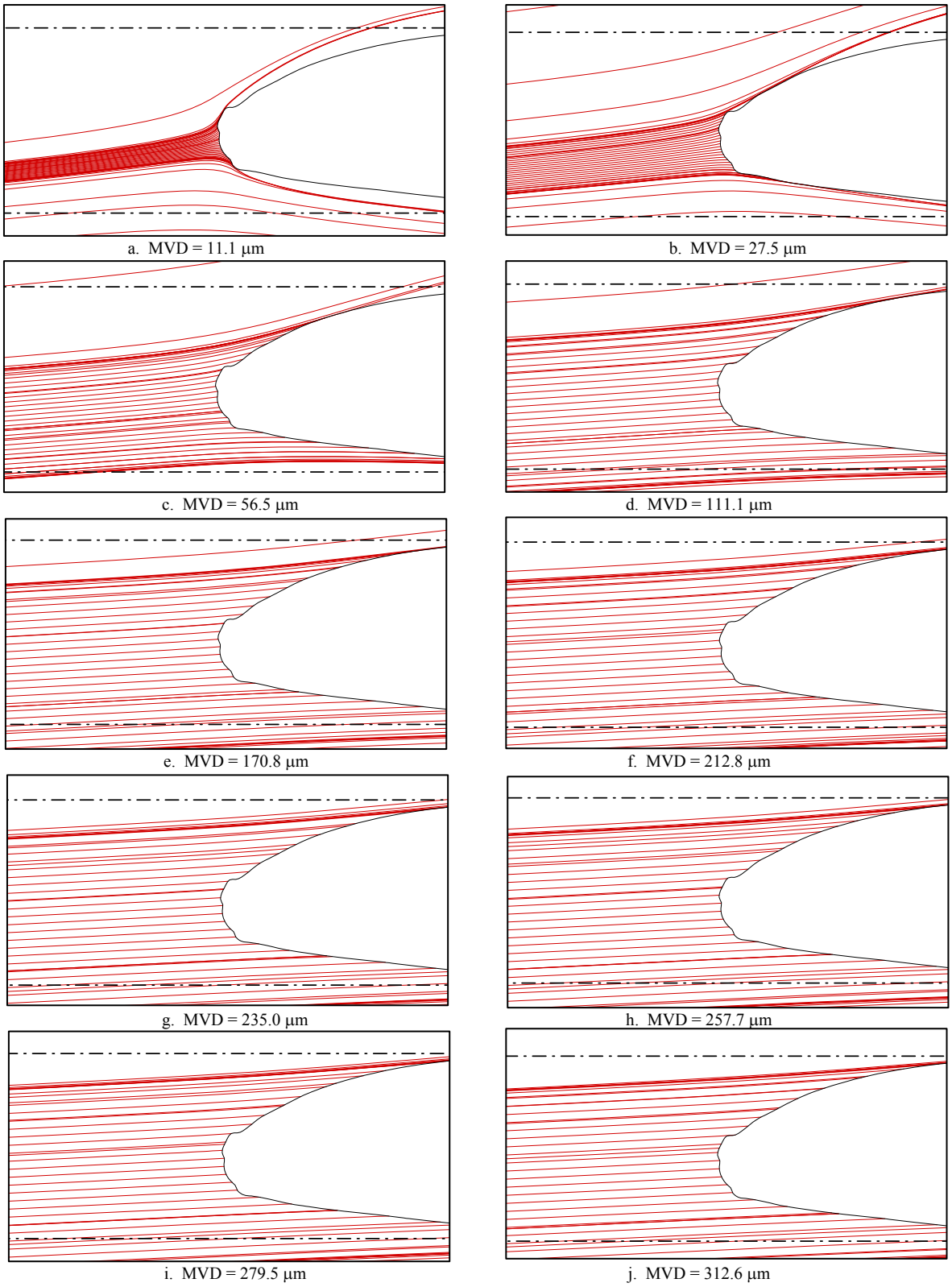

Figure D-1. Computed Drop Trajectories With LEWICE Code; NACA 23012 With 5-min Glaze Ice, 111-μm Spray Cloud

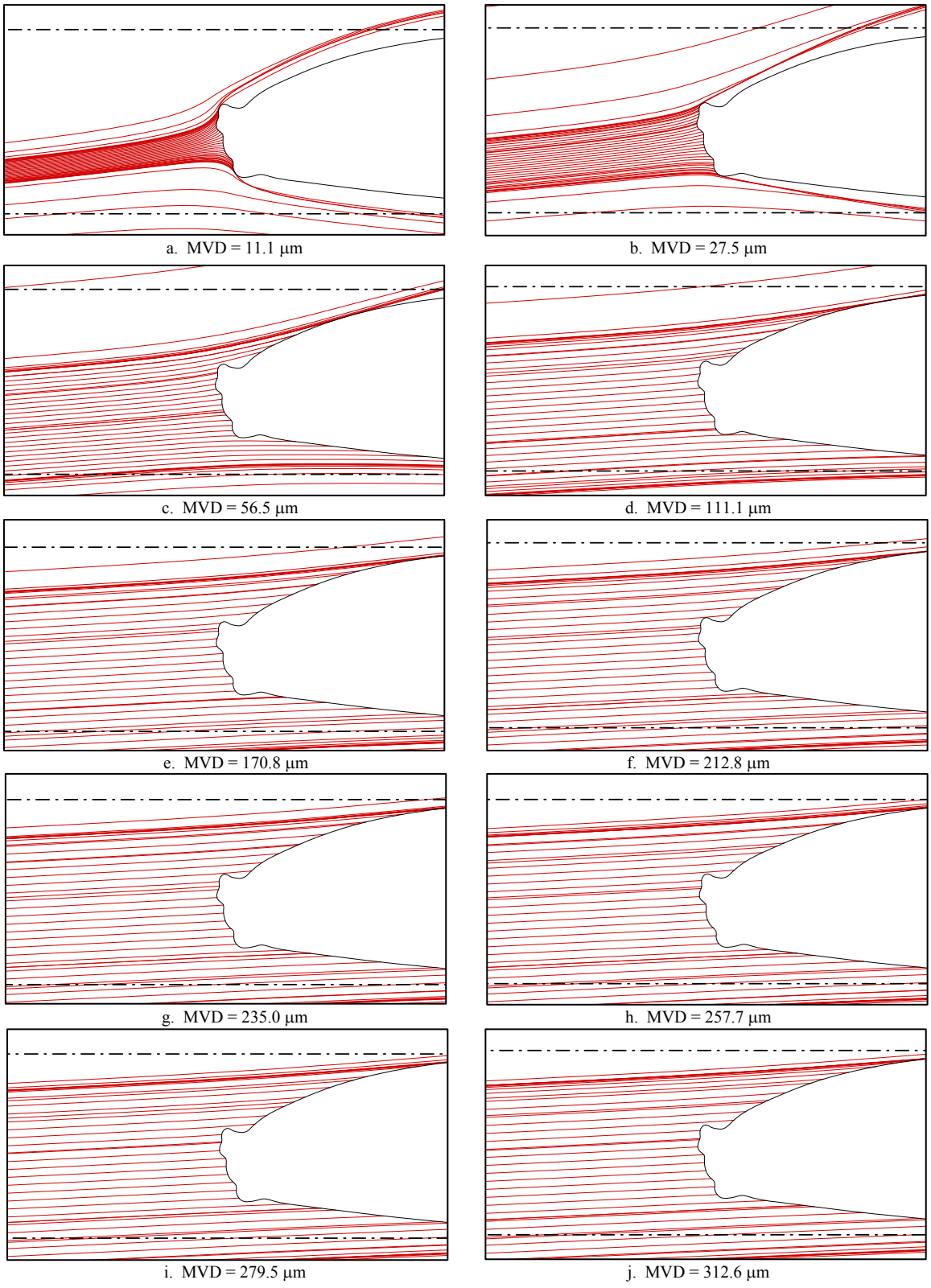

Figure D-2. Computed Drop Trajectories With LEWICE Code; NACA 23012 With 10-min Glaze Ice, 111-μm Spray Cloud

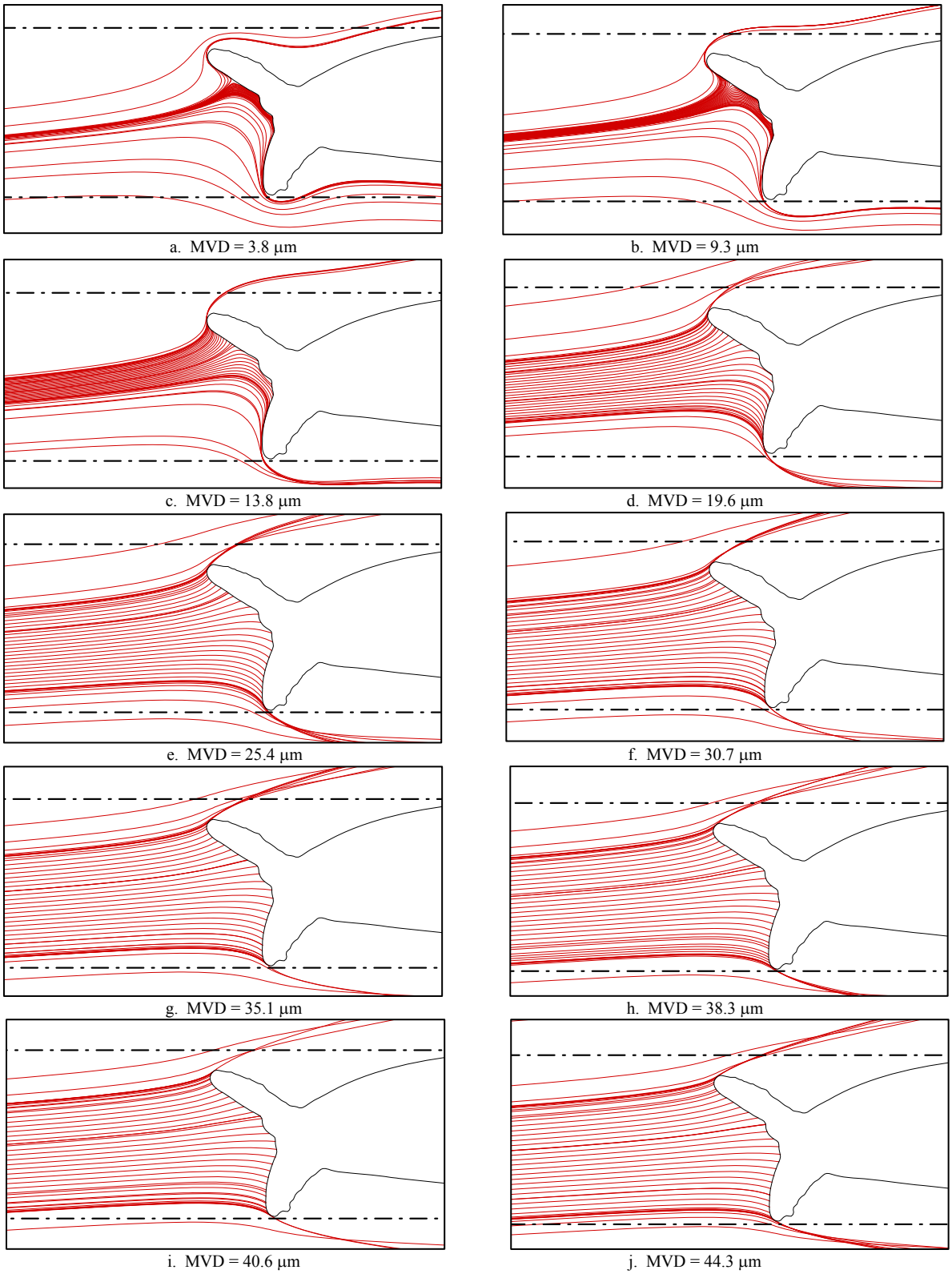

Figure D-3. Computed Drop Trajectories With LEWICE Code; NACA 23012 With 45-min Glaze Ice, 20-μm Spray Cloud

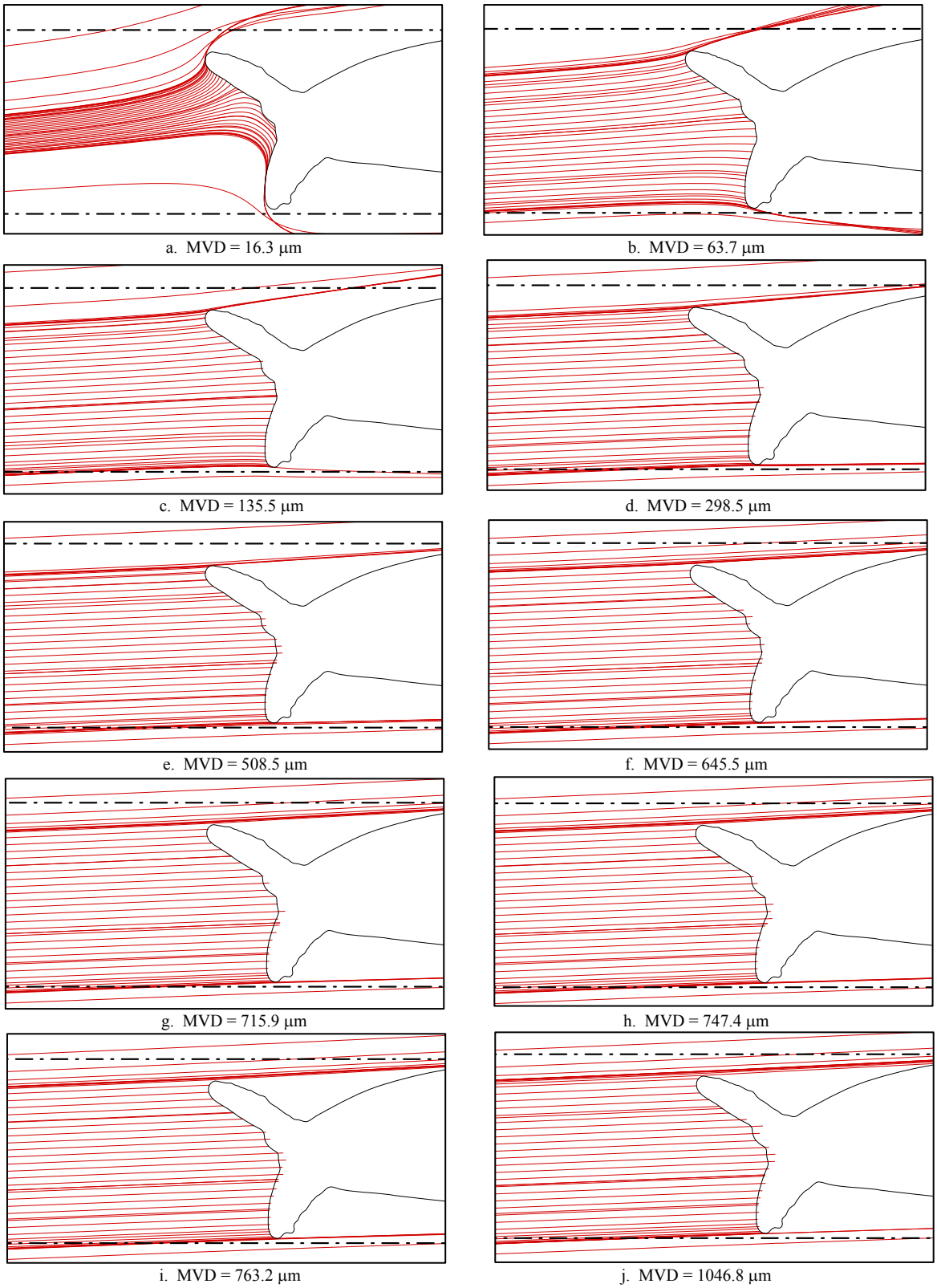

Figure D-4. Computed Drop Trajectories With LEWICE Code; NACA 23012 With 45-min Glaze Ice, 236-µm Spray Cloud

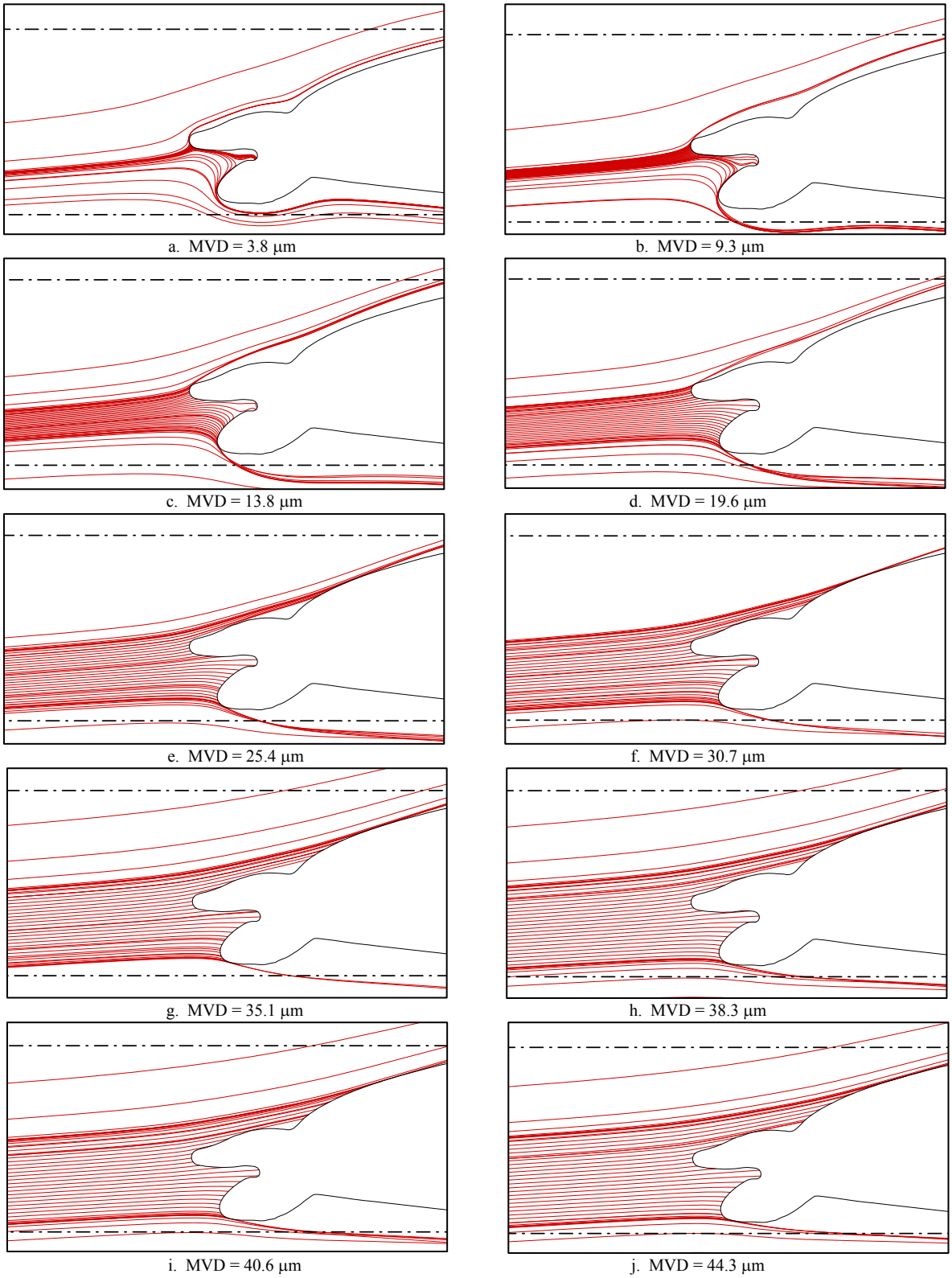

Figure D-5. Computed Drop Trajectories With LEWICE Code; NACA 23012 With 45-min Mixed Ice, 20-µm Spray Cloud

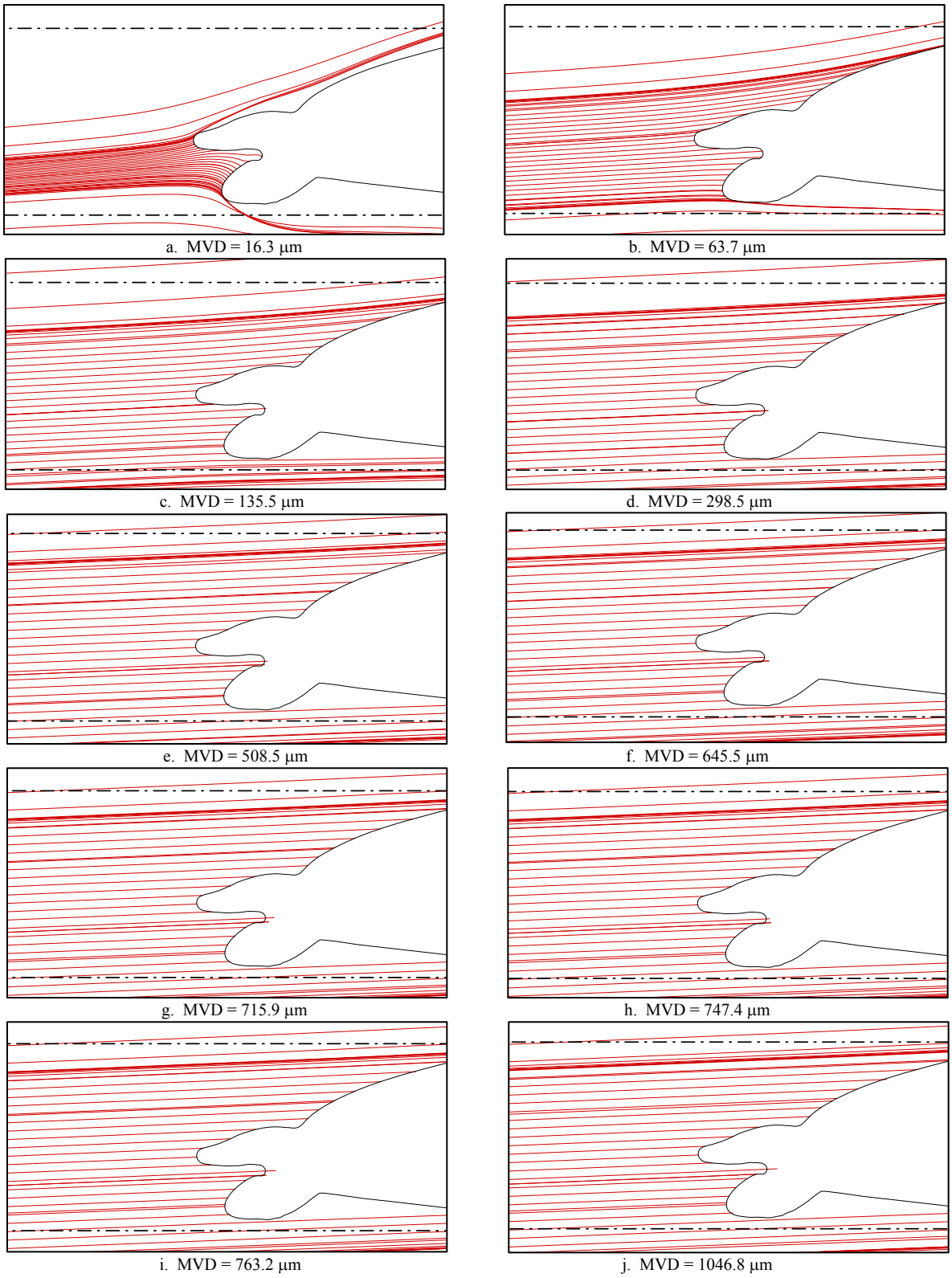

Figure D-6. Computed Drop Trajectories With LEWICE Code; NACA 23012 With 45-min Mixed Ice, 236-µm Spray Cloud

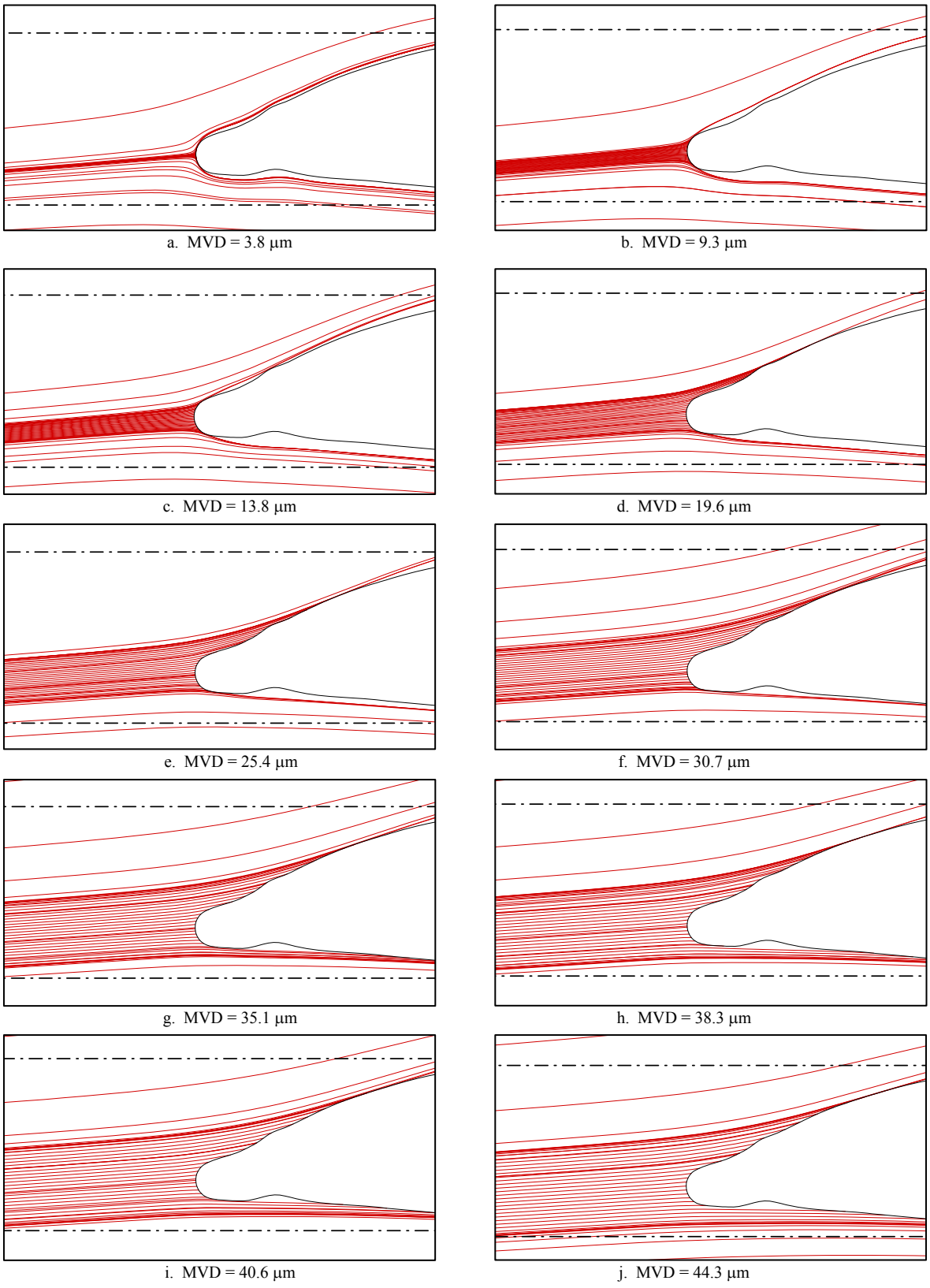

Figure D-7. Computed Drop Trajectories With LEWICE Code; NACA 23012 With 45-min Rime Ice, 20-μm Spray Cloud

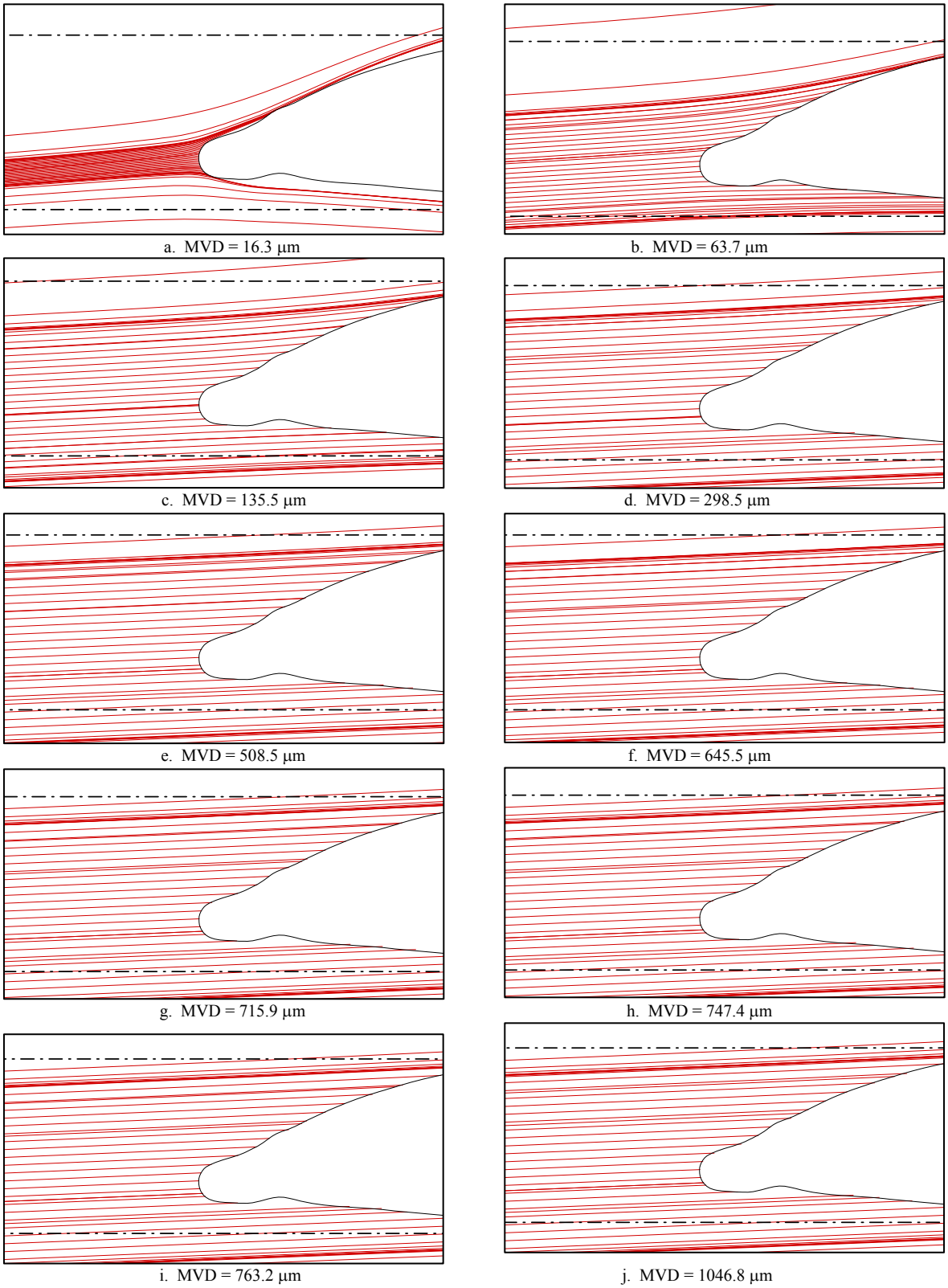

Figure D-8. Computed Drop Trajectories With LEWICE Code; NACA 23012 With 45-min Rime Ice, 236-μm Spray Cloud

APPENDIX E— IMPINGEMENT ANALYSIS DATA COMPUTED WITH A MODIFIED LEWICE CODE USING THE MONTE-CARLO METHOD

Computations of collection efficiency were conducted with a modified LEWICE program capable of performing drop trajectory analysis using the Monte-Carlo method. The Monte-Carlo method was developed to allow the incorporation of more sophisticated drop-splashing and drop-breakup models. The method also overcomes some of interpolation difficulties found in the public version of the LEWICE code, which effect the computation of collection efficiency in shadow impingement regions downstream of ice shapes with large horns.

The Monte-Carlo collection efficiency method involves the tracking of individual particles to and about a body. The method has the capability to recursively track the resulting particles from a drop breakup (due to excessive acceleration or deceleration) or splash (due to impact with the surface). The method stores the amount of mass collected from the impacting drops at each surface panel. From this mass, the local collection efficiency is calculated. The following equations are used to calculate the collection efficiency at each panel due to a drop distribution that can breakup due to splashing or excessive acceleration.

$$\tilde{\beta}_m = 1/\omega_\tau \sum_{i=1}^{ndis} \beta_{im} \Delta\omega_i \tag{E-1}$$

$$\beta_{im} = D_i^3 A_i / (N_i A_m) \sum_{j=1}^{nimp_{im}} d_{imj}^{\ 3} \tag{E-2}$$

where

$\tilde{\beta}_m$ = collection efficiency at panel m
ω_τ = total normalized liquid water content
$\Delta\omega_i$ = fraction of total liquid contained in drop i in distribution
β_{im} = collection efficiency at panel m due to drop i in distribution
A_i = freestream release area of impacting particles of drop i in distribution
A_m = area of panel m
D_i = diameter of drop i in distribution
d_{imj} = diameter of drop j impacting panel m from drop i in distribution
ndis = number of drops defining distribution
$nimp_{im}$ = number of particles impacting panel m from drop i in distribution
N_i = number of particles released from free-stream for particle size i

In the Monte-Carlo collection efficiency method, the impact drops are totaled to compute the correct collection efficiency at the surface. The term Monte-Carlo does not necessarily suggest randomization employed in release of particles from a distribution. For the computations presented in this appendix, an evenly distributed set of particles for each of the 27 bins (about 1000) were released from the freestream position. The number of particles that hit each surface panel and panel area were used to calculate the collection efficiency. Figures E-1 through E-50

compare experimental impingement data for the ten ice shapes and the five tested MVDs with LEWICE data obtained with the standard version of the LEWICE 1.6 code (in-house 27-bin) and the LEWICE Monte-Carlo version. Consider, for example, as shown in figures E-7, E-12, E-17, E-18, and E-43, the artificial impingement tails produced by the interpolation method in the standard LEWICE version are absent in the results obtained with the Monte-Carlo version of LEWICE. Note that no attempt was made to model drop-splashing and breakup with the LEWICE Monte-Carlo version. In figures E-53 through E-60, the total impingement efficiency distributions obtained with the two LEWICE methods for a given geometry are compared to the experimental data as a function of MVD size. Figures E-61 and E-62 summarize the total impingement efficiency distributions as function of geometry and MVD size from the experimental and LEWICE Monte-Carlo results, respectively. The percentage differences in total impingement efficiency between LEWICE 1.6 and the experimental data for all geometries and MVDs are presented in figure E-63. The percentage differences in total impingement efficiency between LEWICE Monte-Carlo and experimental data are shown in figure E-64.

Table E-1. Summary of Impingement Efficiency Data for 2003 IRT Tests

Model	Test Conditions		$\overline{E}_L$	$\overline{E}_E$	$\overline{E}_{LMC}$	$(\overline{E}_L - \overline{E}_E)/\overline{E}_E$ (%)	$(\overline{E}_{LMC} - \overline{E}_E)/\overline{E}_E$ (%)	$(\overline{E}_L - \overline{E}_E)/\overline{E}_{LMC}$ (%)	$(\overline{E}_{LMC} - \overline{E}_E)/\overline{E}_{LMC}$ (%)
	AOA	MVD							
NACA 23012 with 5-min glaze ice shape	2.5	20	0.1788	0.1805	0.1714	-0.9	-5.0	-1.0	-5.3
		52	0.5236	0.2823	0.5061	85.5	79.3	47.7	44.2
		111	0.6928	0.3961	0.6719	74.9	69.6	44.2	41.0
		154	0.7830	0.4963	0.7619	57.8	53.5	37.6	34.9
		236	0.8590	0.5228	0.8369	64.3	60.1	40.2	37.5
NACA 23012 with 10-min glaze ice shape	2.5	20	0.1902	0.1713	0.1859	11.0	8.5	10.2	7.9
		52	0.5539	0.2366	0.5066	134.1	114.1	62.6	53.3
		111	0.7400	0.3251	0.6708	127.6	106.3	61.9	51.5
		154	0.8320	0.4103	0.7597	102.8	85.2	55.5	46.0
		236	0.9168	0.4942	0.8372	85.5	69.4	50.5	41.0
NACA 23012 with 15-min glaze ice shape	2.5	20	0.2124	0.1862	0.2104	14.1	13.0	12.5	11.5
		52	0.6223	0.2857	0.5146	117.8	80.1	65.4	44.5
		111	0.8198	0.3423	0.6713	139.5	96.1	71.1	49.0
		154	0.9269	0.4351	0.7607	113.0	74.8	64.7	42.8
		236	1.0177	0.5277	0.8372	92.9	58.7	58.5	37.0
NACA 23012 with 22.5-min glaze ice shape	2.5	20	0.2515	0.2319	0.2501	8.5	7.9	7.8	7.3
		52	0.7069	0.3236	0.4977	118.4	53.8	77.0	35.0
		111	0.9212	0.4015	0.6615	129.4	64.8	78.6	39.3
		154	1.0874	0.4436	0.7493	145.1	68.9	85.9	40.8
		236	1.1840	0.4988	0.8291	137.4	66.2	82.6	39.8
NACA 23012 with 45-min glaze ice shape	2.5	20	0.3227	0.2705	0.3077	19.3	13.7	17.0	12.1
		52	0.6360	0.4360	0.6356	45.9	45.8	31.5	31.4
		111	0.7586	0.5239	0.7605	44.8	45.2	30.9	31.1
		154	0.8097	0.6072	0.8122	33.3	33.8	24.9	25.2
		236	0.8455	0.6362	0.8469	32.9	33.1	24.7	24.9

Table E-1. Summary of Impingement Efficiency Data for 2003 IRT Tests (Continued)

Model	Test Conditions		$\overline{E}_L$	$\overline{E}_E$	$\overline{E}_{LMC}$	$(\overline{E}_L - \overline{E}_E)/\overline{E}_E$ (%)	$(\overline{E}_{LMC} - \overline{E}_E)/\overline{E}_E$ (%)	$(\overline{E}_L - \overline{E}_E)/\overline{E}_{LMC}$ (%)	$(\overline{E}_{LMC} - \overline{E}_E)/\overline{E}_{LMC}$ (%)
	AOA	MVD							
NACA 23012 with 7.5-min mixed ice shape	2.5	20	0.1896	0.1377	0.1688	37.7	22.6	30.7	18.4
		52	0.5434	0.2411	0.5063	125.4	110.0	59.7	52.4
		111	0.7108	0.3496	0.6737	103.3	92.7	53.6	48.1
		154	0.8006	0.4600	0.7627	74.0	65.8	44.7	39.7
		236	0.8751	0.4754	0.8368	84.1	76.0	47.8	43.2
NACA 23012 with 15-min mixed ice shape	2.5	20	0.1921	0.1563	0.1700	22.9	8.8	21.1	8.1
		52	0.5942	0.2963	0.5059	100.5	70.7	58.9	41.4
		111	0.7789	0.3854	0.6738	102.1	74.8	58.4	42.8
		154	0.8683	0.5024	0.7619	72.8	51.7	48.0	34.1
		236	0.9501	0.5040	0.8379	88.5	66.2	53.2	39.8
NACA 23012 with 22.5-min mixed ice shape	2.5	20	0.1809	0.1579	0.1603	14.6	1.5	14.3	1.5
		52	0.6021	0.2602	0.5021	131.4	93.0	68.1	48.2
		111	0.7939	0.3566	0.6701	122.6	87.9	65.3	46.8
		154	0.8892	0.4718	0.7612	88.5	61.3	54.8	38.0
		236	0.9671	0.5140	0.8374	88.2	62.9	54.1	38.6
NACA 23012 with 45-min mixed ice shape	2.5	20	0.1690	0.1713	0.1564	-1.3	-8.7	-1.5	-9.5
		52	0.5424	0.2874	0.4903	88.7	70.6	52.0	41.4
		111	0.8819	0.3731	0.6548	136.4	75.5	77.7	43.0
		154	1.0041	0.4737	0.7494	112.0	58.2	70.8	36.8
		236	1.0808	0.5208	0.8299	107.5	59.3	67.5	37.2
NACA 23012 with 45-min rime ice shape	2.5	20	0.1855	0.1253	0.1541	48.0	23.0	39.1	18.7
		52	0.5424	0.2683	0.5013	102.2	86.9	54.7	46.5
		111	0.7135	0.3697	0.6726	93.0	81.9	51.1	45.0
		154	0.8041	0.4491	0.7616	79.0	69.6	46.6	41.1
		236	0.8772	0.5670	0.8355	54.7	47.4	37.1	32.1

$\overline{E}$ represents the total impingement efficiency, which is defined as $\overline{E} = \frac{A_{\overline{\beta}}}{A_f}$, where A_f represents the projected frontal area of the airfoil. $\overline{E}_E$ is the experimental total impingement efficiency. $\overline{E}_L$ is the computational total impingement efficiency using LEWICE 1.6. Note that few $\overline{E}_L$ exceeded 1.0 due to the presence of artificial impingement tails. $\overline{E}_{LMC}$ is the computational total impingement efficiency using LEWICE Monte-Carlo.

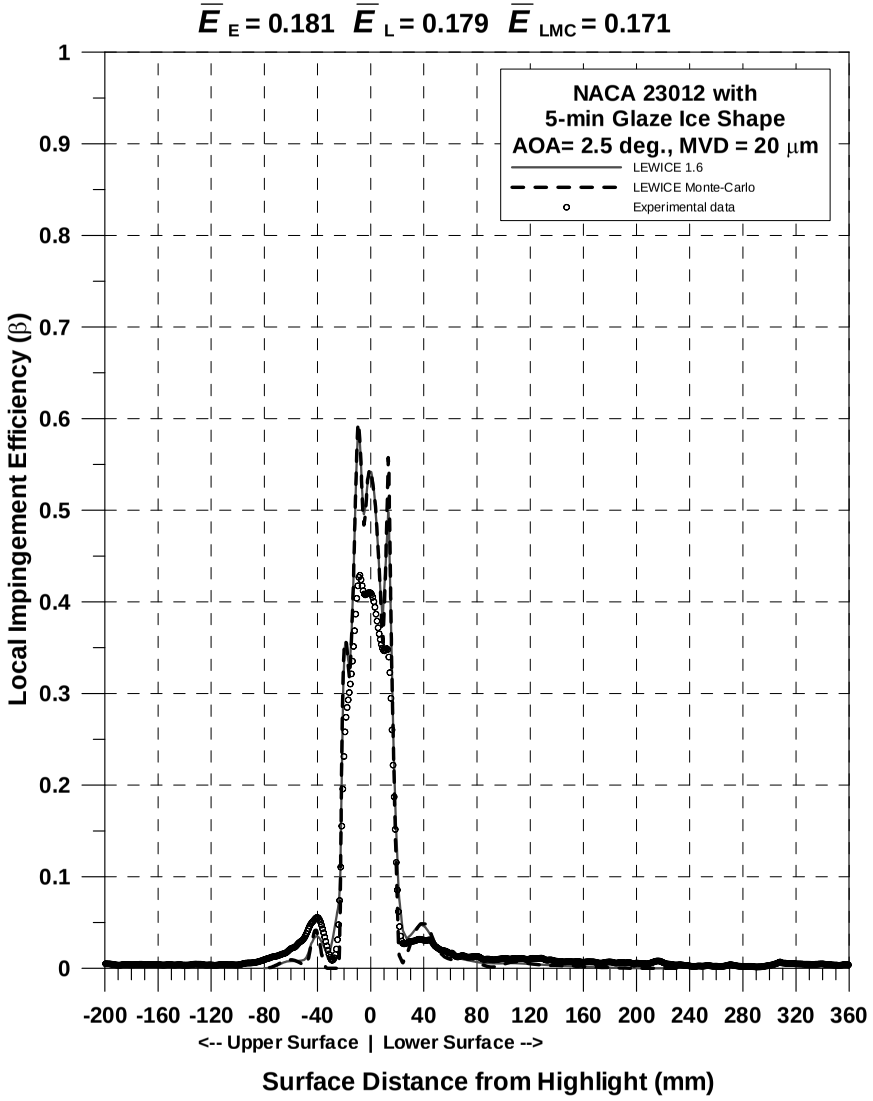

Figure E-1. Impingement Efficiency Distribution for NACA 23012 Airfoil With 5-min Glaze Ice Shape (c = 36 in., V_∞ = 175 mph, AOA = 2.5°, MVD = 20 μm)

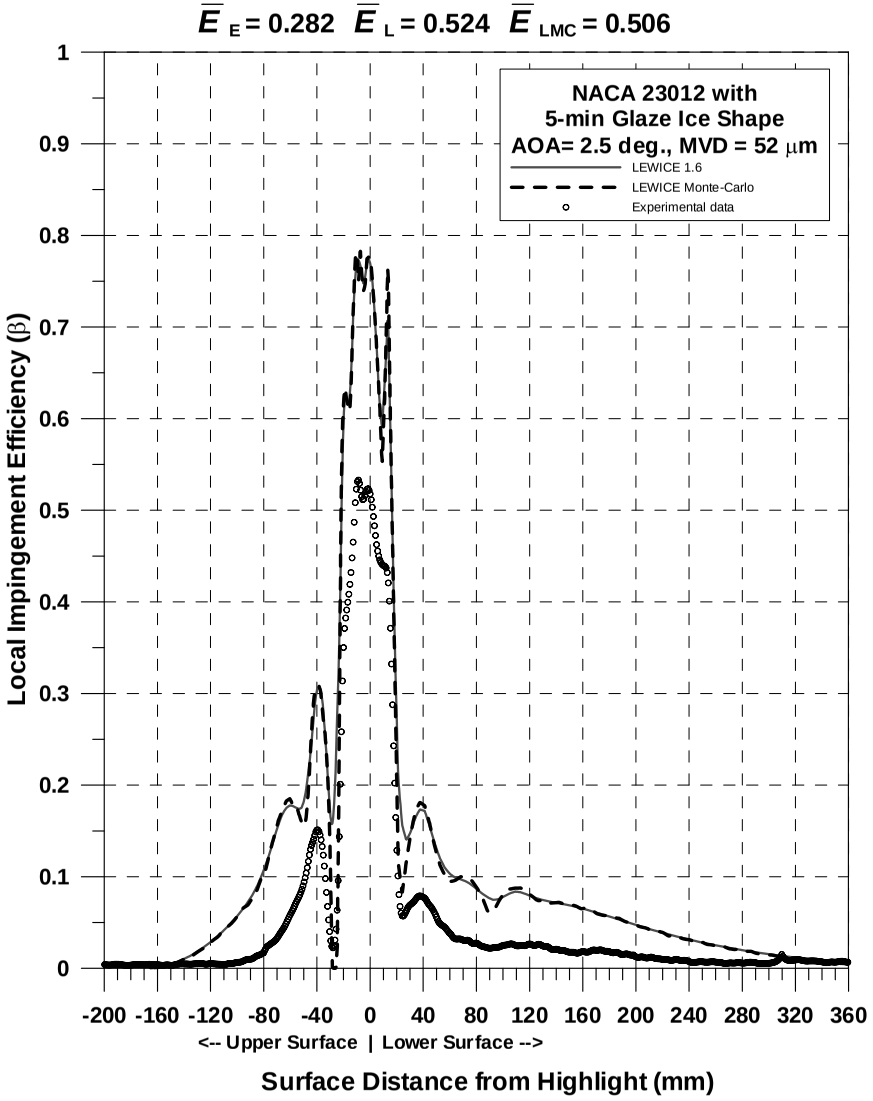

Figure E-2. Impingement Efficiency Distribution for NACA 23012 Airfoil With 5-min Glaze Ice Shape (c = 36 in., V_∞ = 175 mph, AOA = 2.5°, MVD = 52 μm)

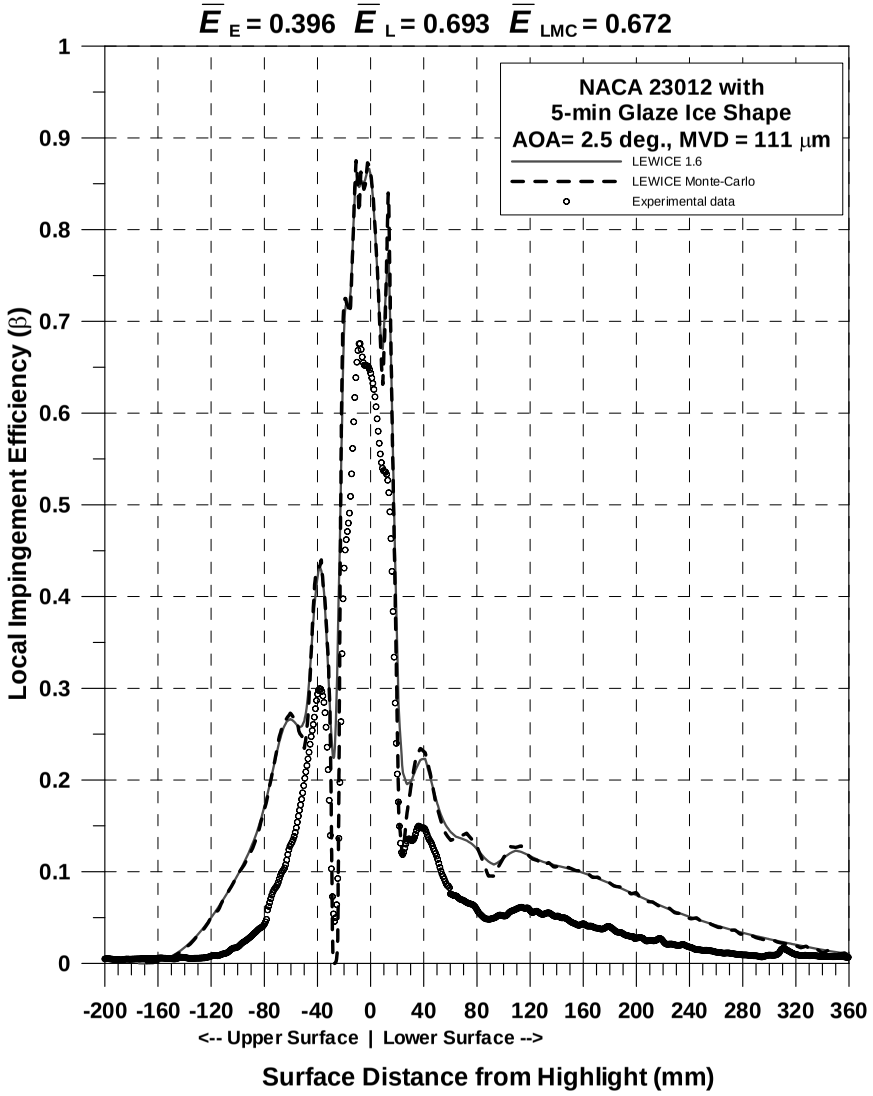

Figure E-3. Impingement Efficiency Distribution for NACA 23012 Airfoil With 5-min Glaze Ice Shape (c = 36 in., V_∞ = 175 mph, AOA = 2.5°, MVD = 111 μm)

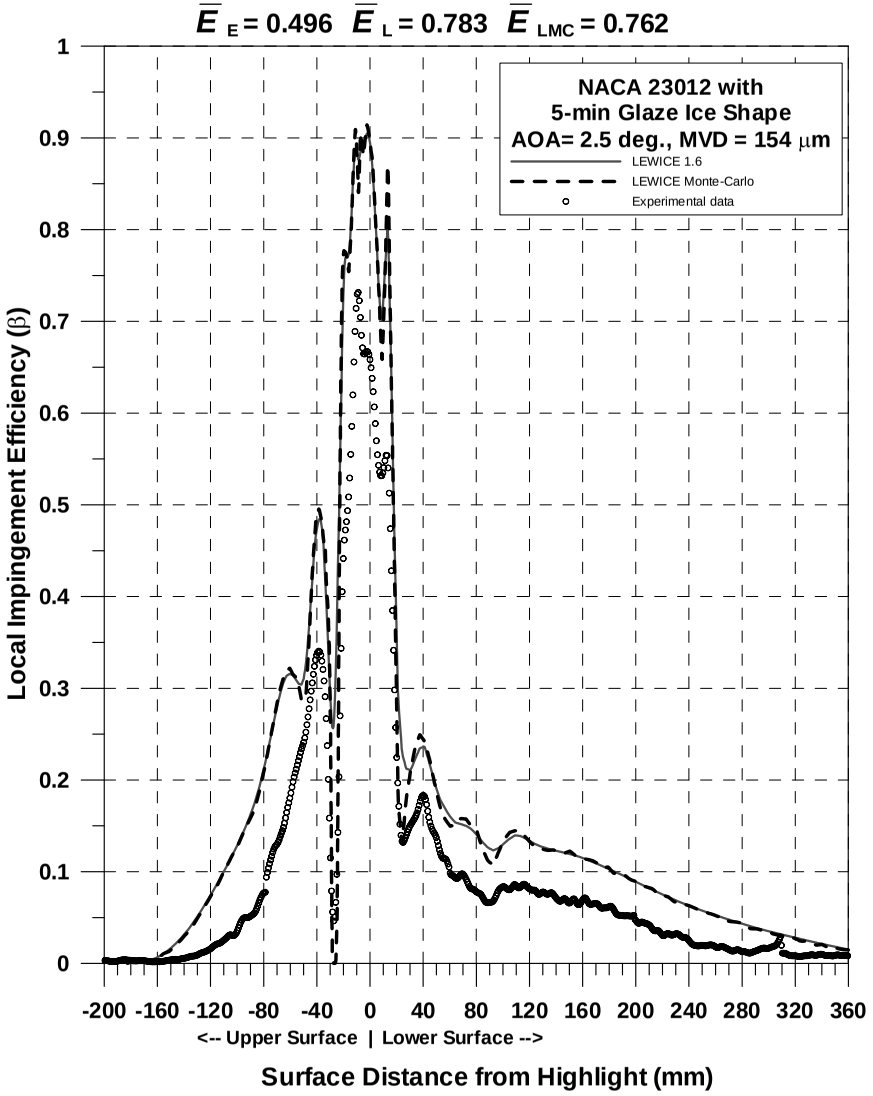

Figure E-4. Impingement Efficiency Distribution for NACA 23012 Airfoil With 5-min Glaze Ice Shape (c = 36 in., V_∞ = 175 mph, AOA = 2.5°, MVD = 154 μm)

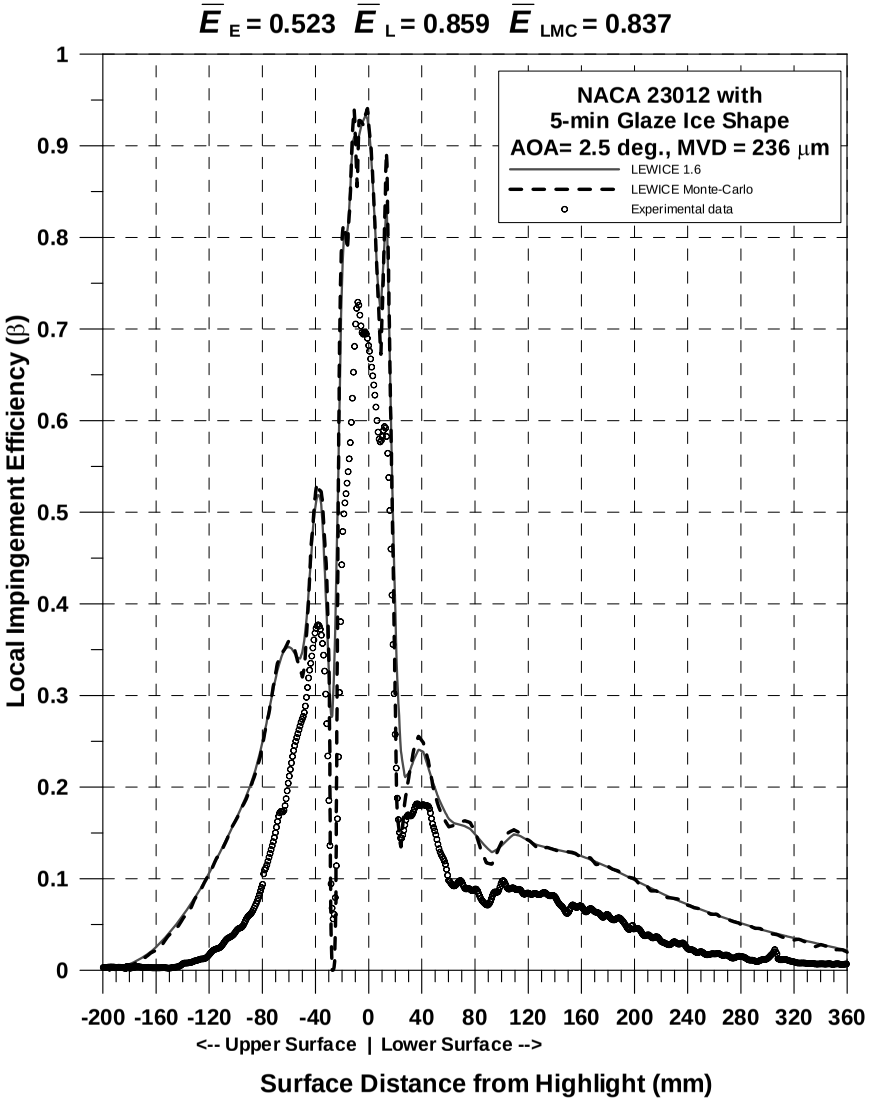

Figure E-5. Impingement Efficiency Distribution for NACA 23012 Airfoil With 5-min Glaze Ice Shape (c = 36 in., V_∞ = 175 mph, AOA = 2.5°, MVD = 236 μm)

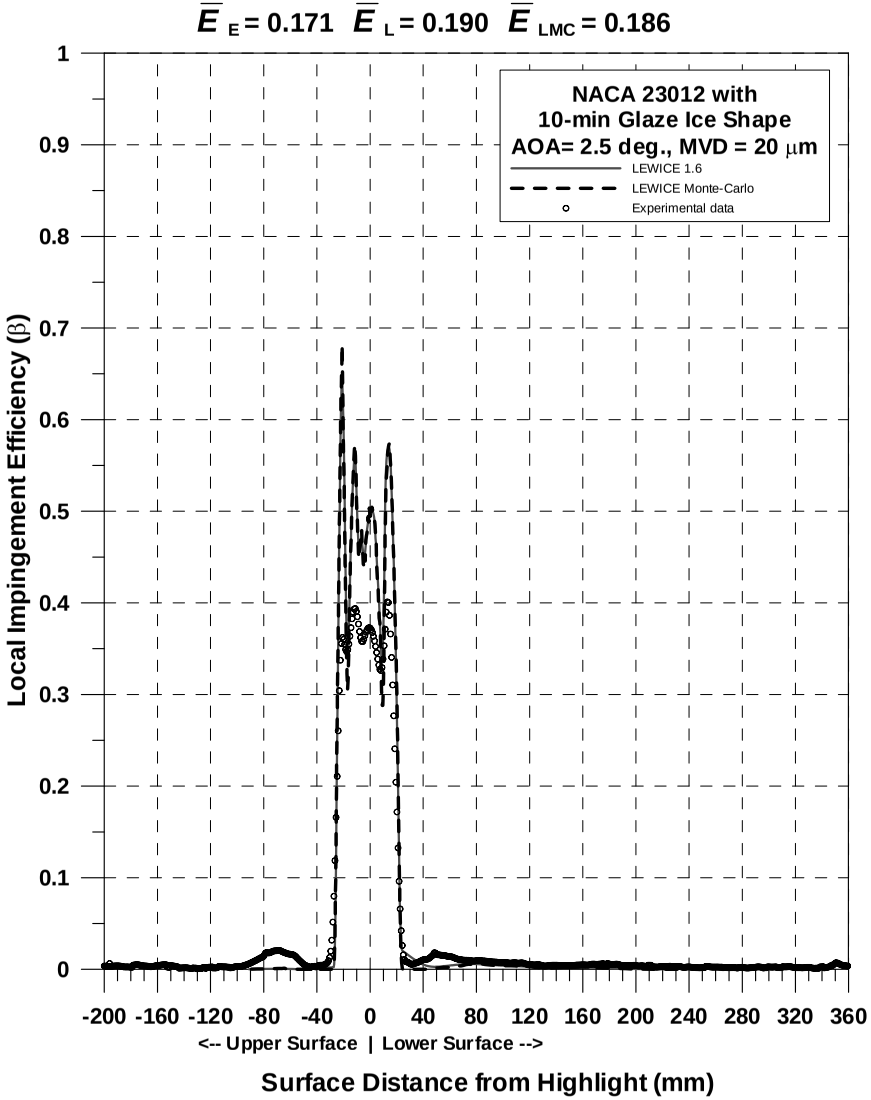

Figure E-6. Impingement Efficiency Distribution for NACA 23012 Airfoil With 10-min Glaze Ice Shape (c = 36 in., V_∞ = 175 mph, AOA = 2.5°, MVD = 20 μm)

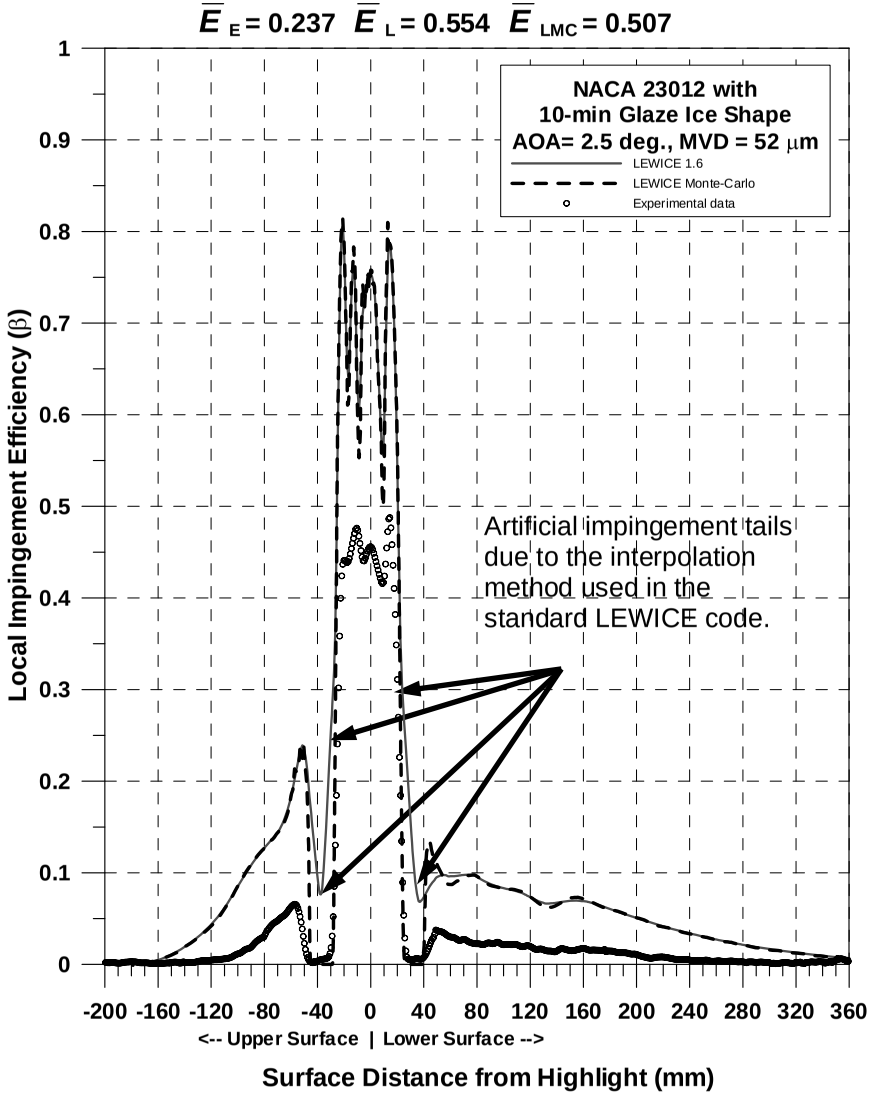

Figure E-7. Impingement Efficiency Distribution for NACA 23012 Airfoil With 10-min Glaze Ice Shape (c = 36 in., V_∞ = 175 mph, AOA = 2.5°, MVD = 52 μm)

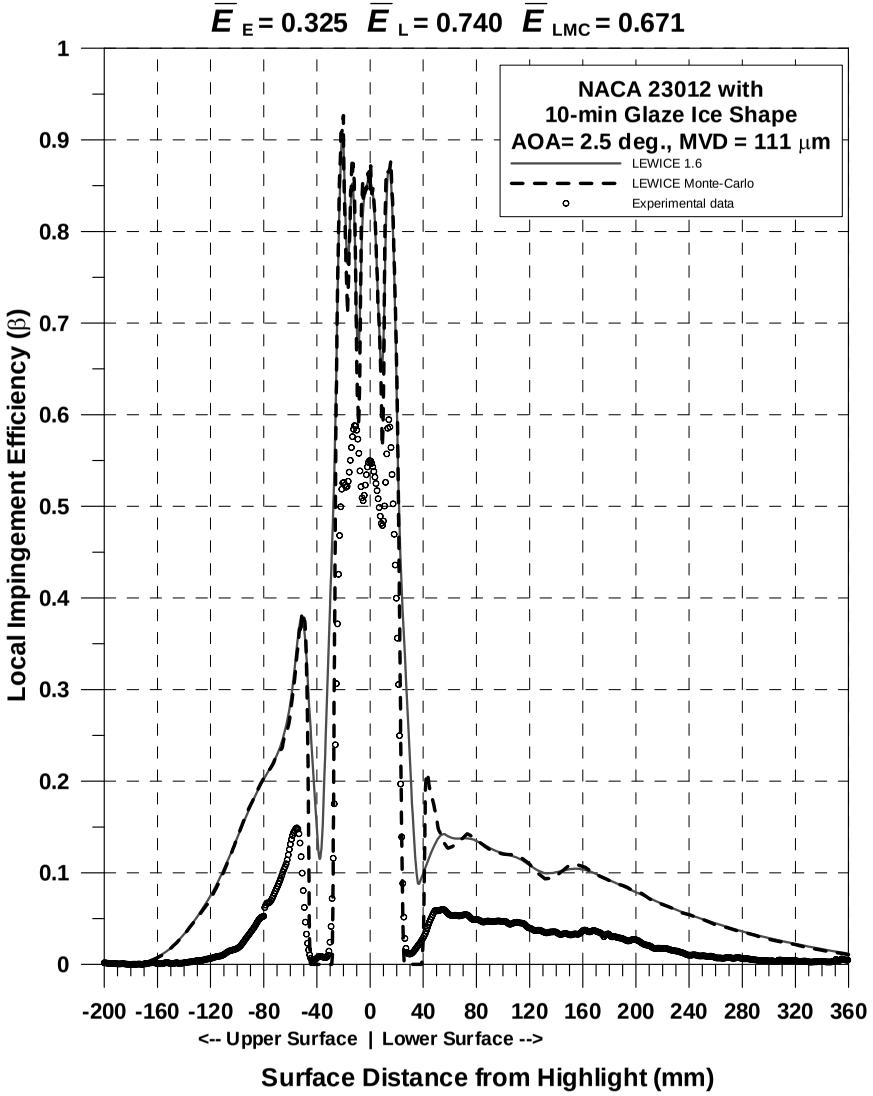

Figure E-8. Impingement Efficiency Distribution for NACA 23012 Airfoil With 10-min Glaze Ice Shape (c = 36 in., V_∞ = 175 mph, AOA = 2.5°, MVD = 111 μm)

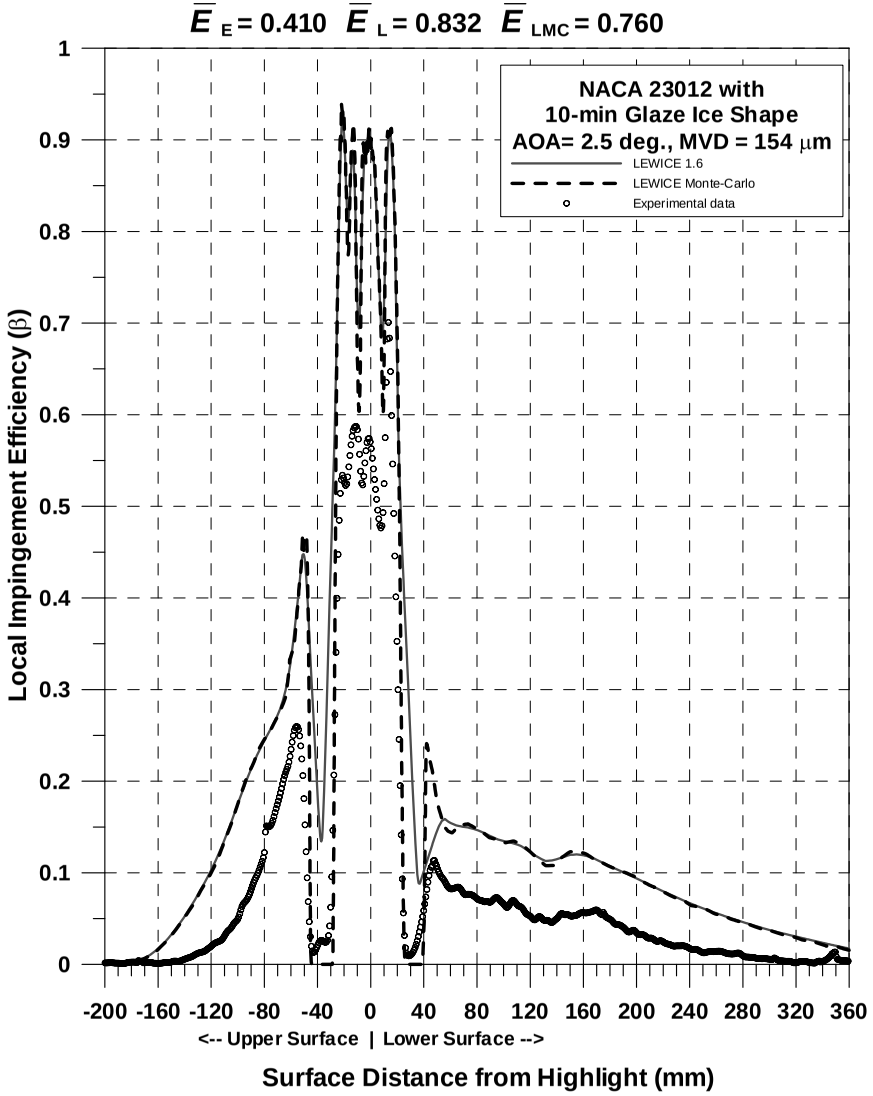

Figure E-9. Impingement Efficiency Distribution for NACA 23012 Airfoil With 10-min Glaze Ice Shape (c = 36 in., V_∞ = 175 mph, AOA = 2.5°, MVD = 154 μm)

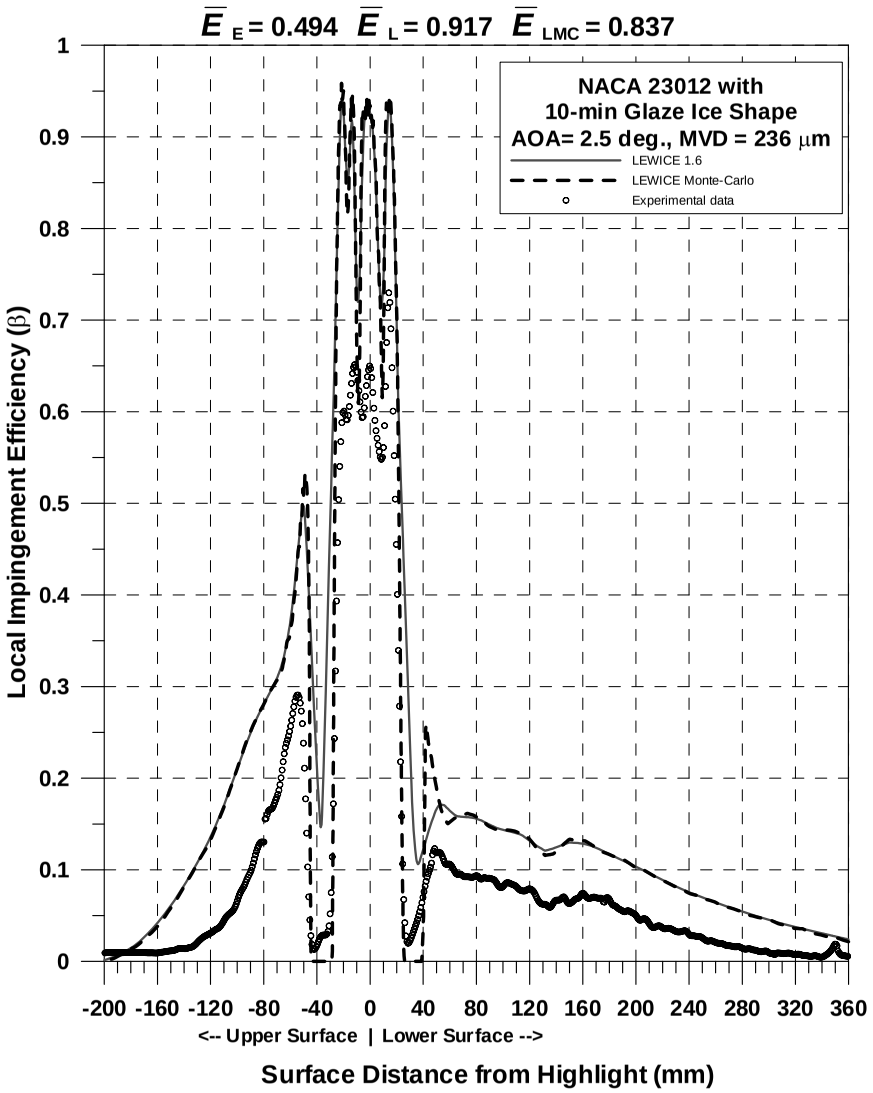

Figure E-10. Impingement Efficiency Distribution for NACA 23012 Airfoil With 10-min Glaze Ice Shape (c = 36 in., V_∞ = 175 mph, AOA = 2.5°, MVD = 236 μm)

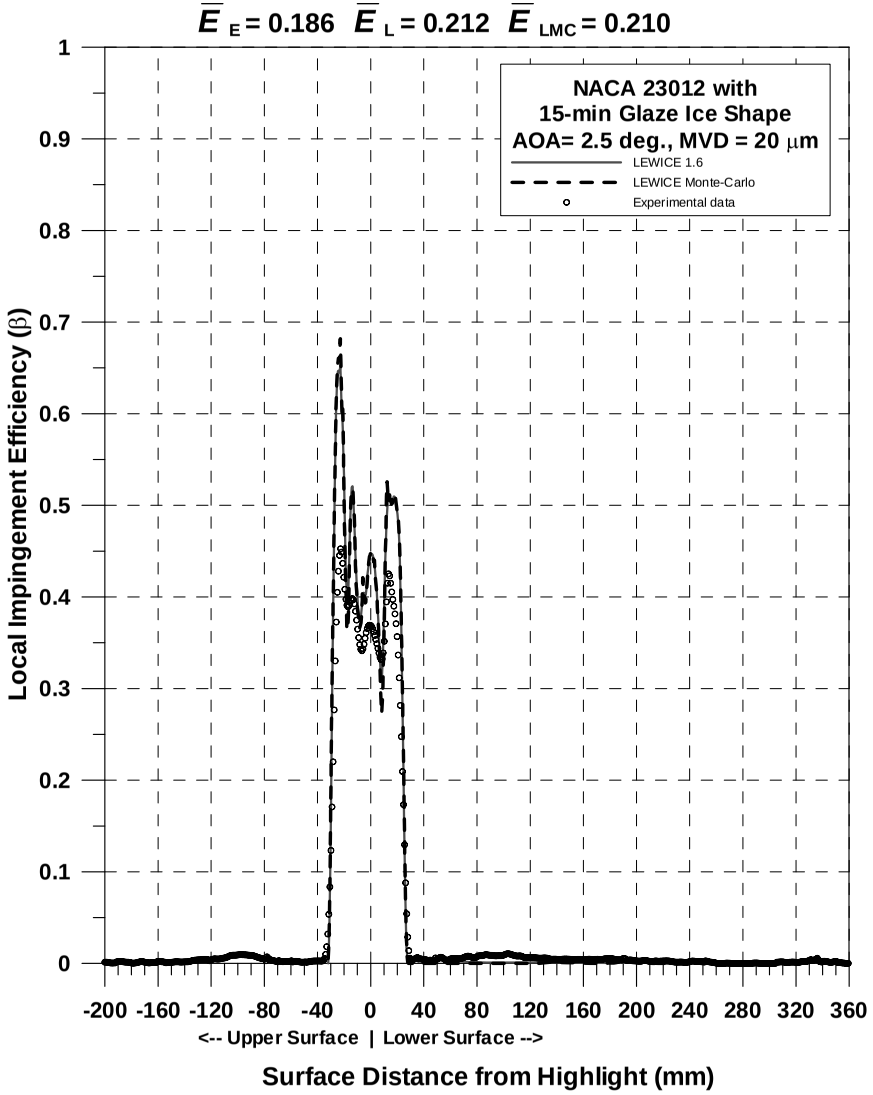

Figure E-11. Impingement Efficiency Distribution for NACA 23012 Airfoil With 15-min Glaze Ice Shape (c = 36 in., V_∞ = 175 mph, AOA = 2.5°, MVD = 20 μm)

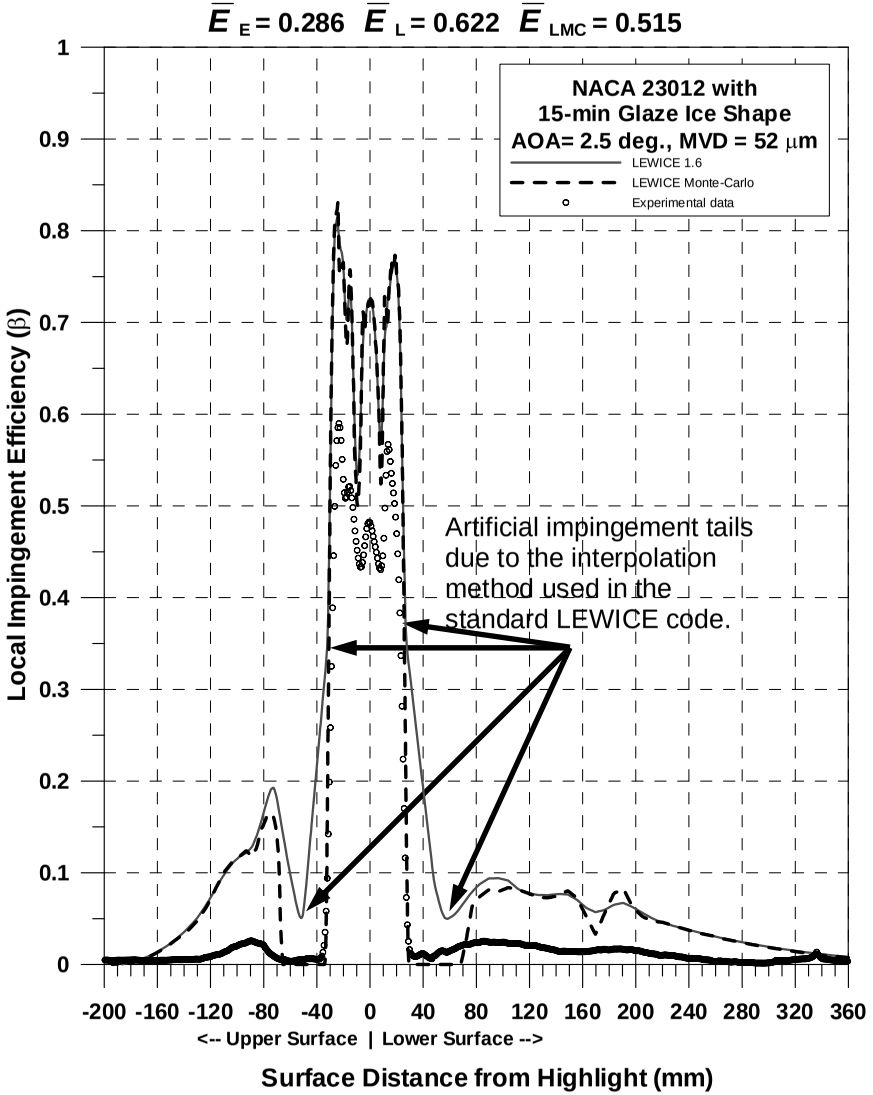

Figure E-12. Impingement Efficiency Distribution for NACA 23012 Airfoil With 15-min Glaze Ice Shape (c = 36 in., V_∞ = 175 mph, AOA = 2.5°, MVD = 52 μm)

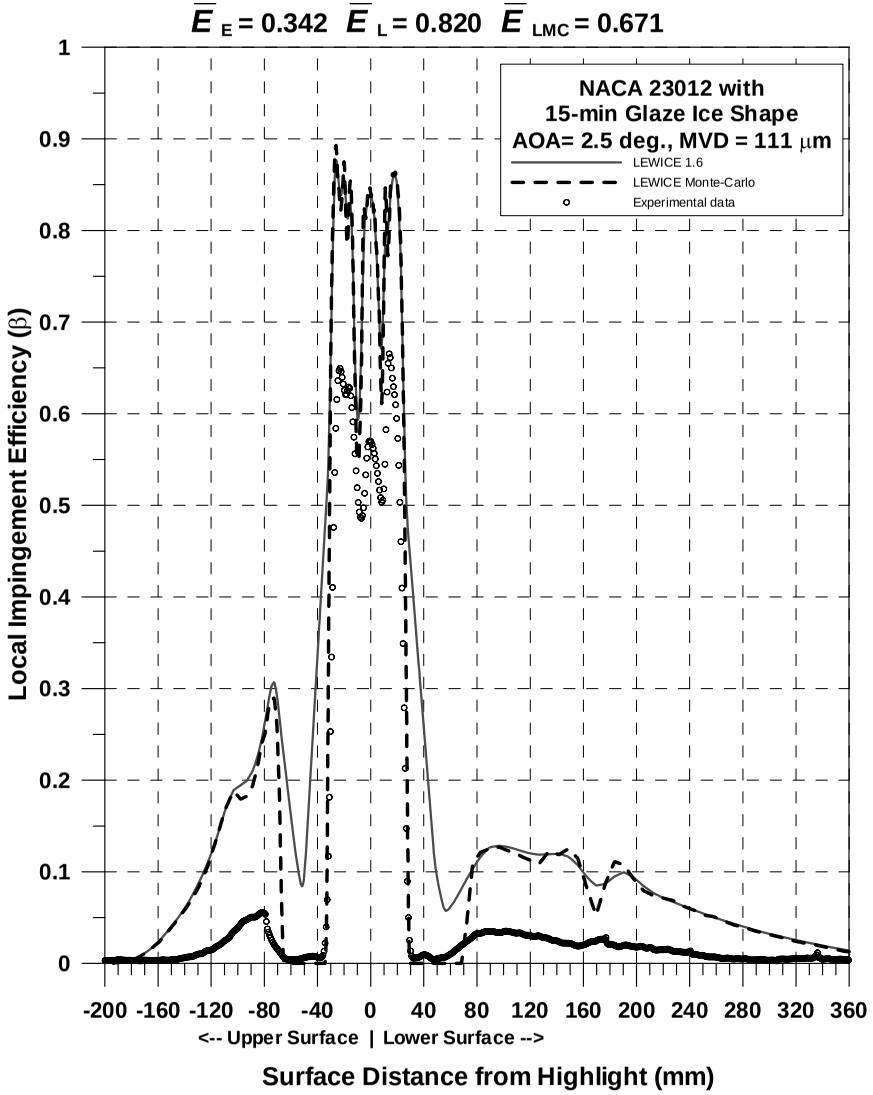

Figure E-13. Impingement Efficiency Distribution for NACA 23012 Airfoil With 15-min Glaze Ice Shape (c = 36 in., V_∞ = 175 mph, AOA = 2.5°, MVD = 111 μm)

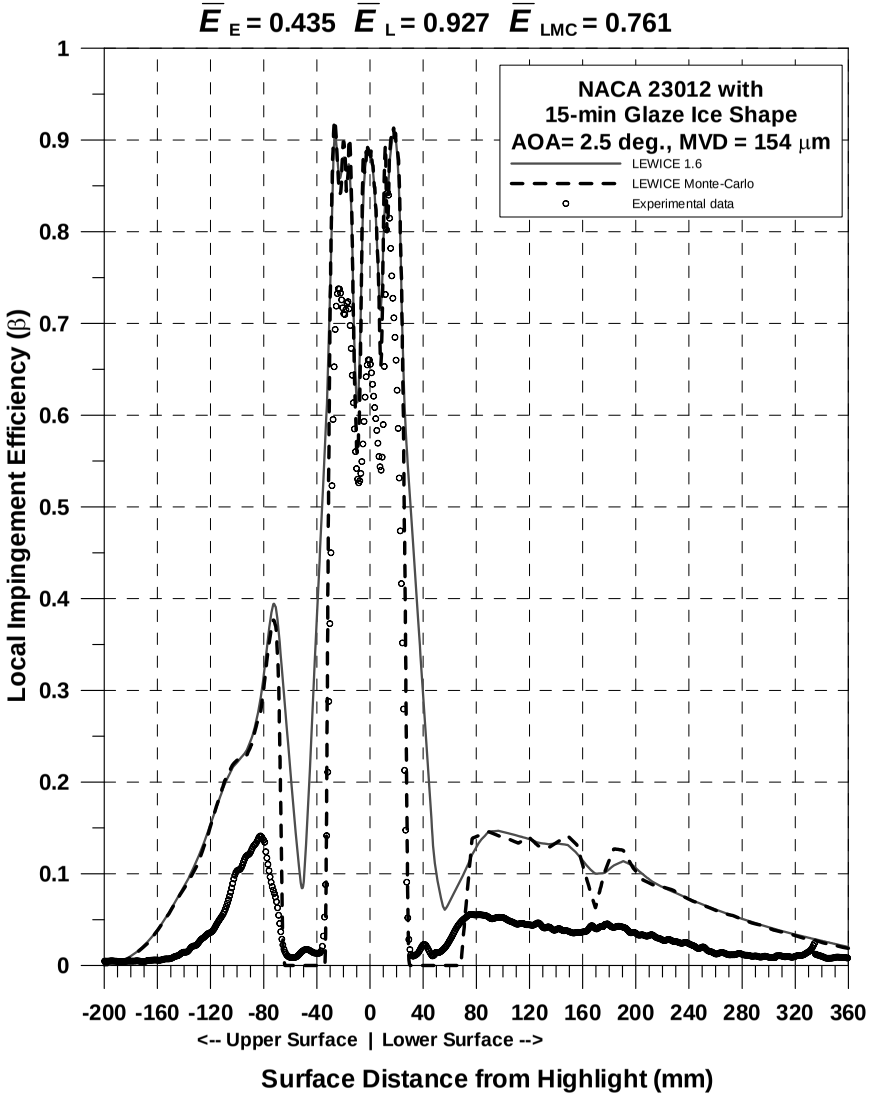

Figure E-14. Impingement Efficiency Distribution for NACA 23012 Airfoil With 15-min Glaze Ice Shape (c = 36 in., V_∞ = 175 mph, AOA = 2.5°, MVD = 154 μm)

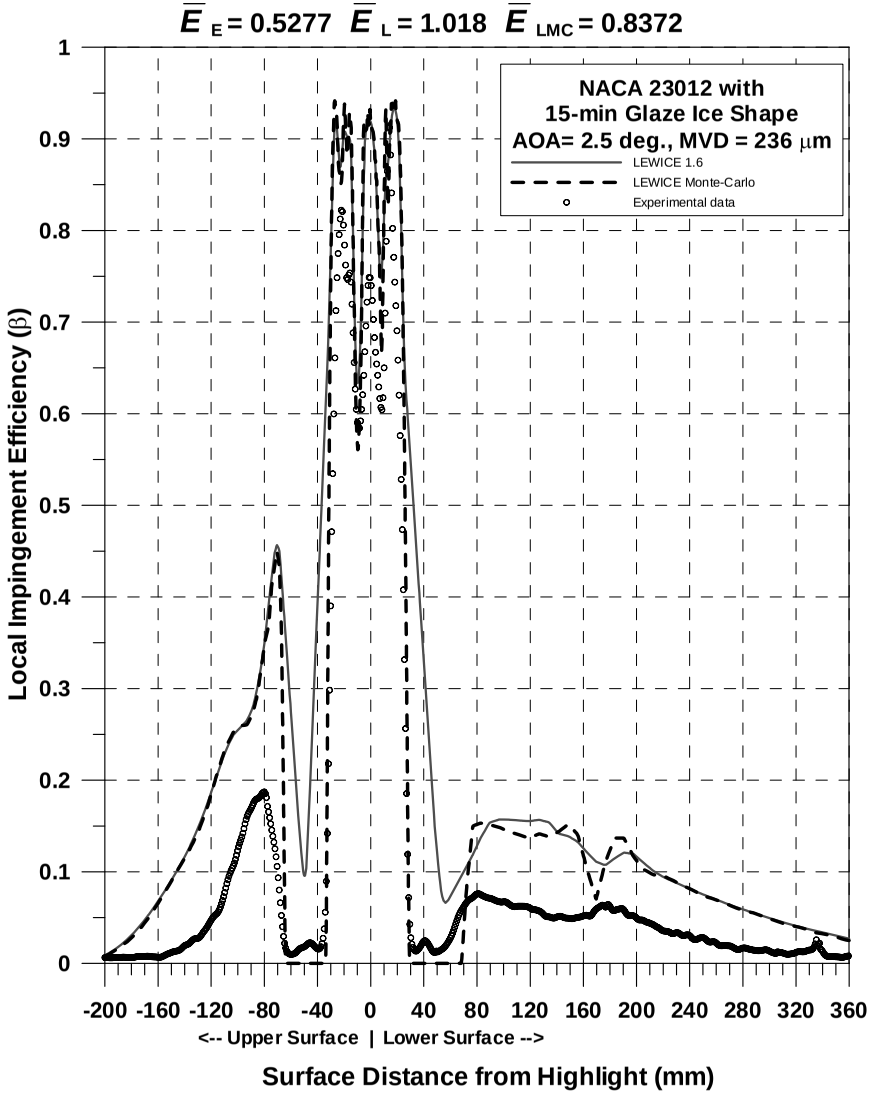

Figure E-15. Impingement Efficiency Distribution for NACA 23012 Airfoil With 15-min Glaze Ice Shape (c = 36 in., V_∞ = 175 mph, AOA = 2.5°, MVD = 236 μm)

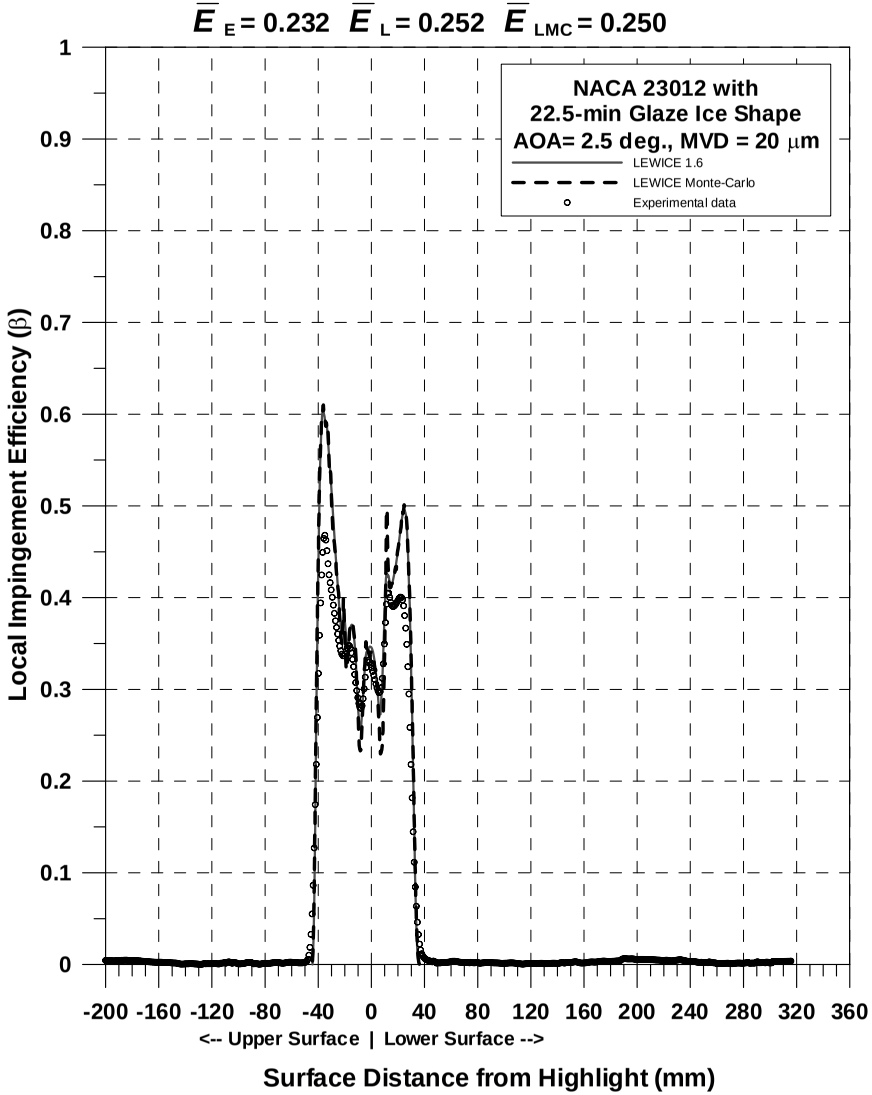

Figure E-16. Impingement Efficiency Distribution for NACA 23012 Airfoil With 22.5-min Glaze Ice Shape (c = 36 in., V_∞ = 175 mph, AOA = 2.5°, MVD = 20 μm)

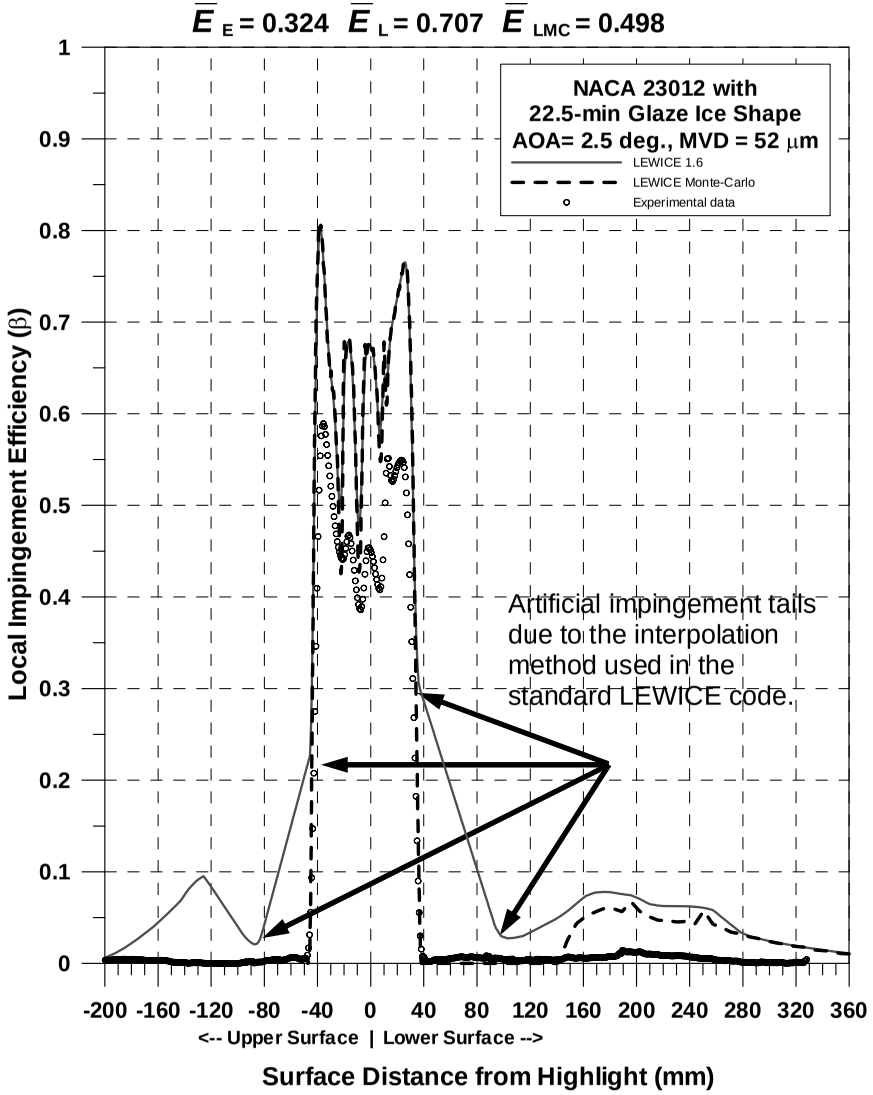

Figure E-17. Impingement Efficiency Distribution for NACA 23012 Airfoil With 22.5-min Glaze Ice Shape (c = 36 in., V_∞ = 175 mph, AOA = 2.5°, MVD = 52 μm)

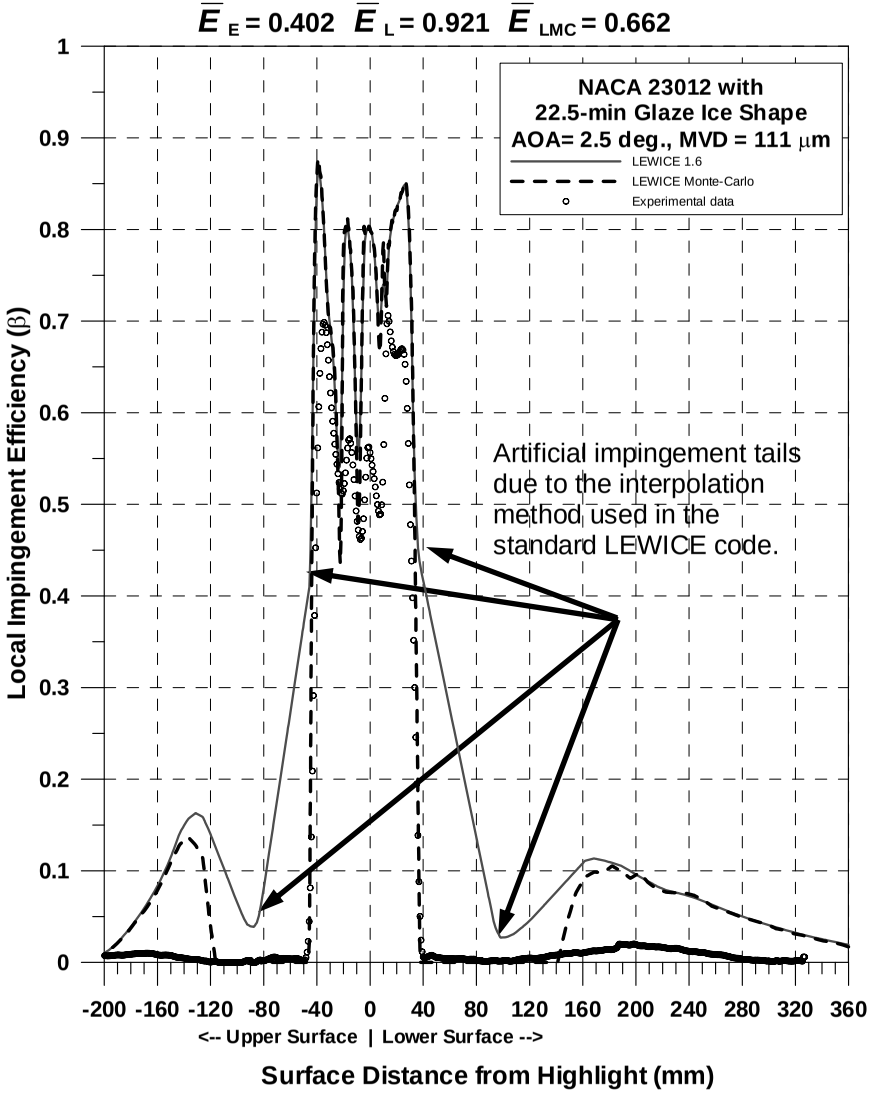

Figure E-18. Impingement Efficiency Distribution for NACA 23012 Airfoil With 22.5-min Glaze Ice Shape (c = 36 in., V_∞ = 175 mph, AOA = 2.5°, MVD = 111 μm)

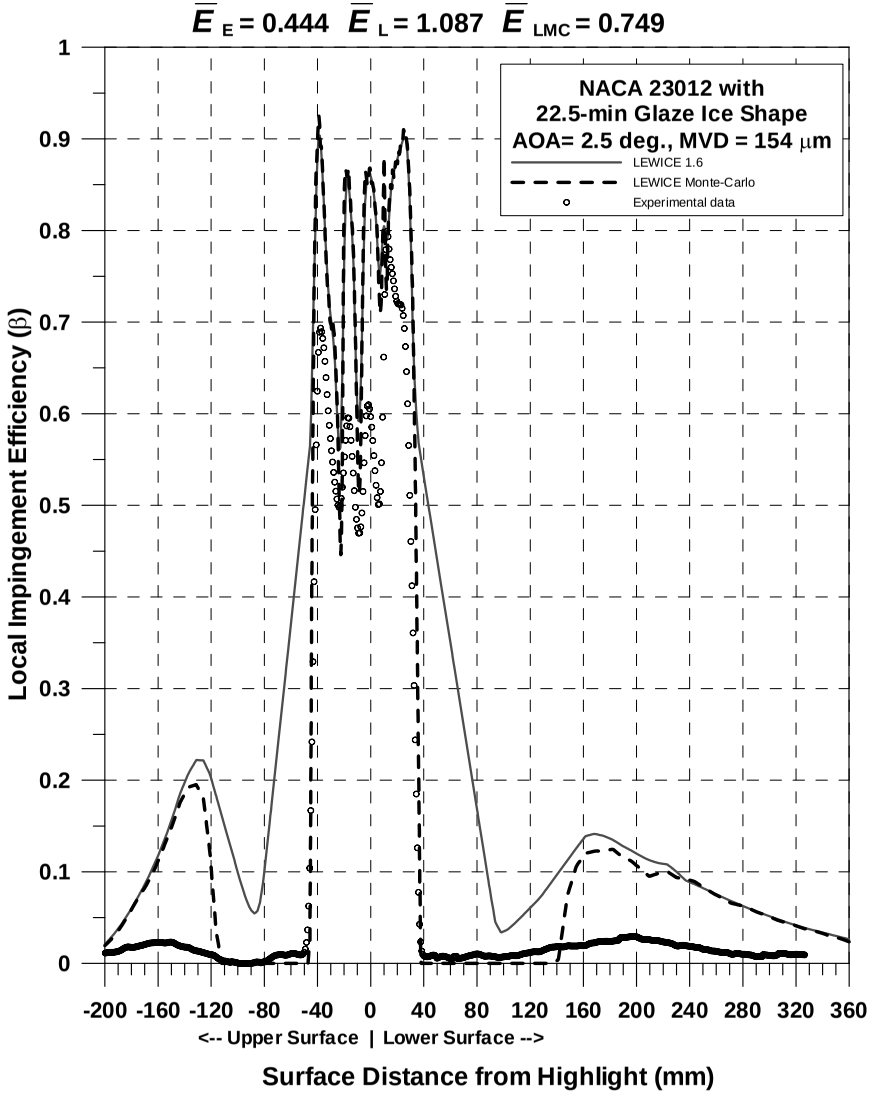

Figure E-19. Impingement Efficiency Distribution for NACA 23012 Airfoil With 22.5-min Glaze Ice Shape (c = 36 in., V_∞ = 175 mph, AOA = 2.5°, MVD = 154 μm)

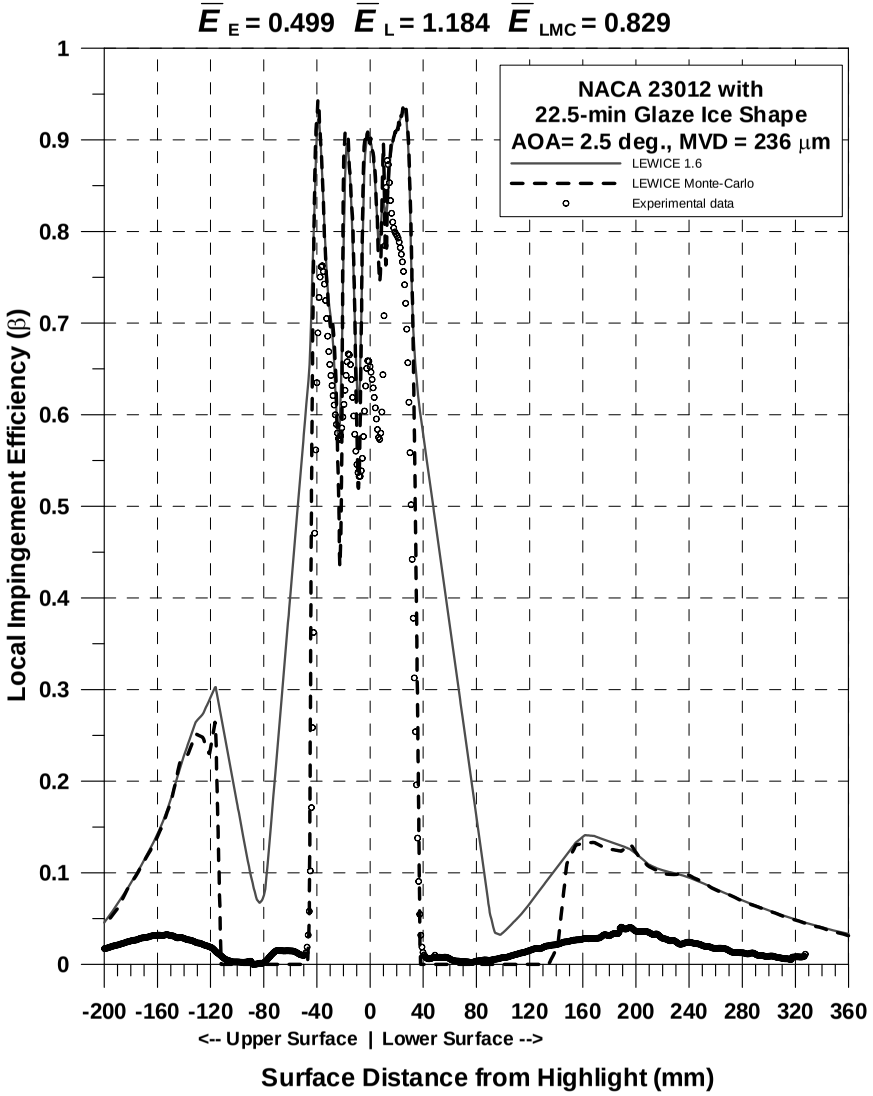

Figure E-20. Impingement Efficiency Distribution for NACA 23012 Airfoil With 22.5-min Glaze Ice Shape (c = 36 in., V_∞ = 175 mph, AOA = 2.5°, MVD = 236 μm)

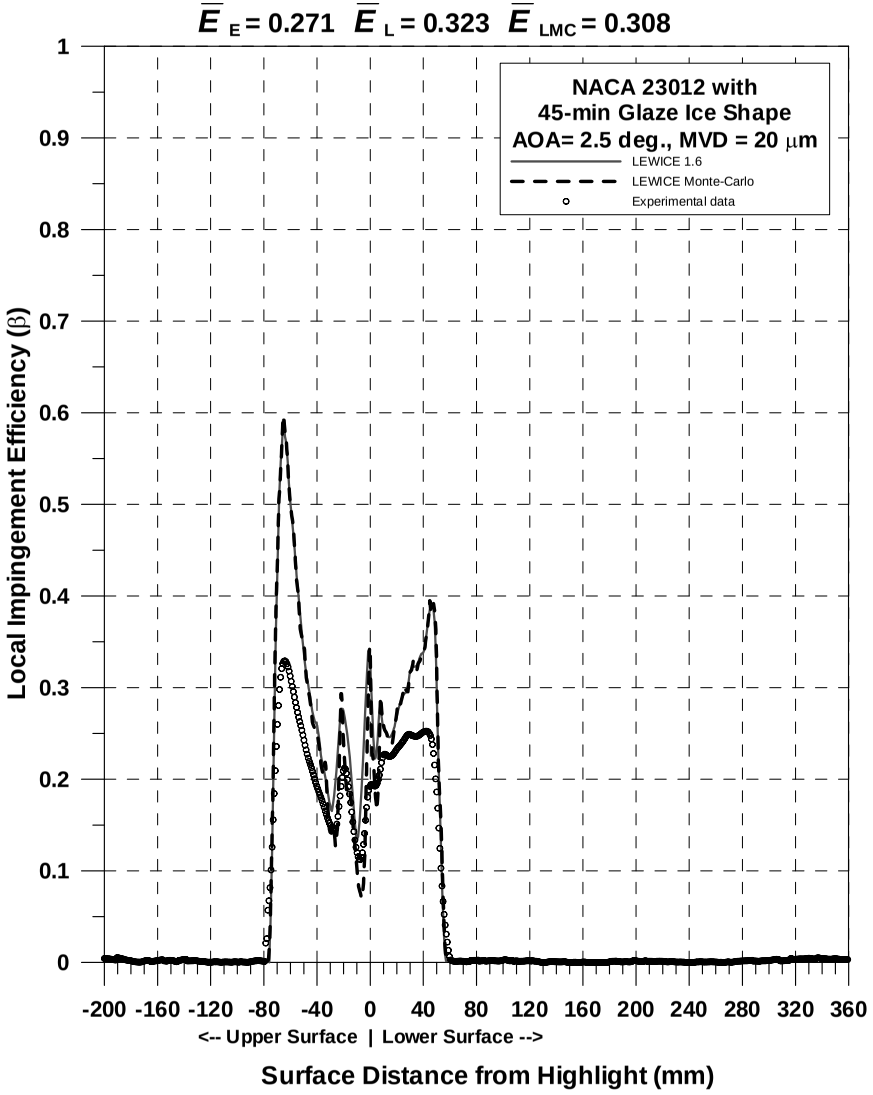

Figure E-21. Impingement Efficiency Distribution for NACA 23012 Airfoil With 45-min Glaze Ice Shape (c = 36 in., V_∞ = 175 mph, AOA = 2.5°, MVD = 20 μm)

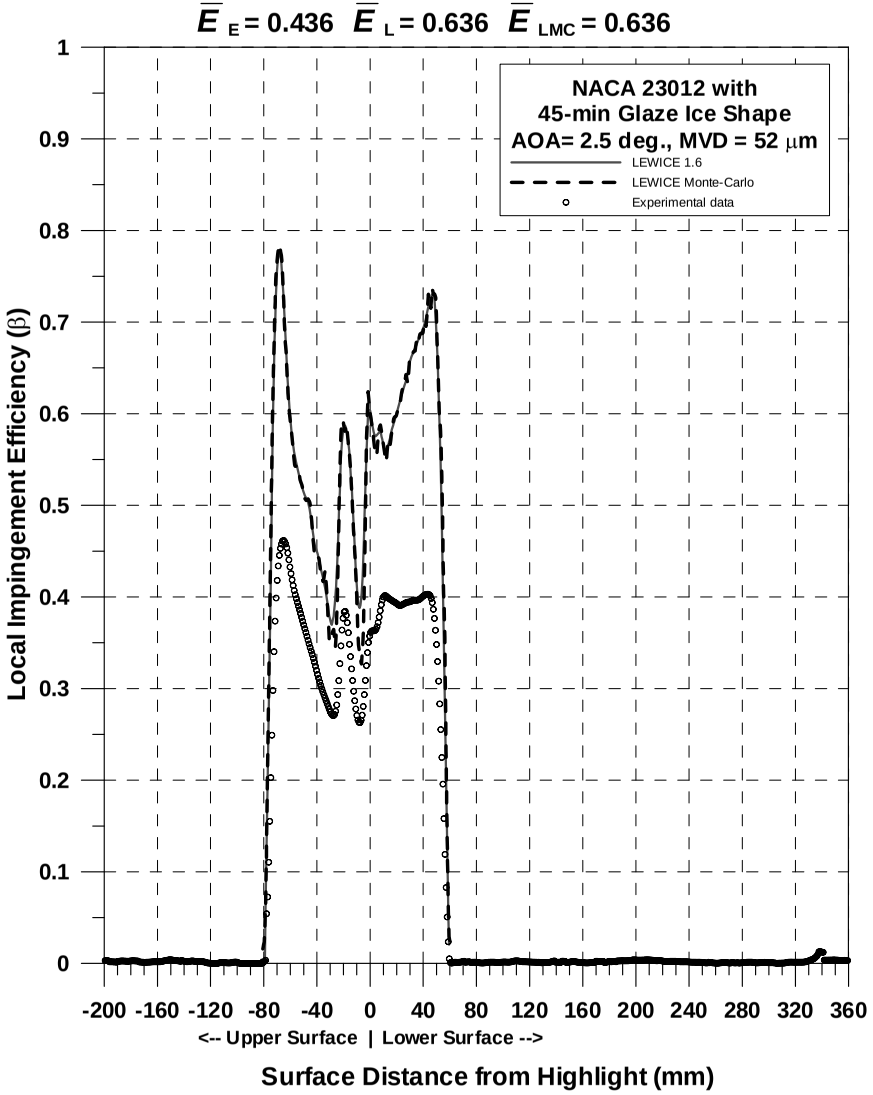

Figure E-22. Impingement Efficiency Distribution for NACA 23012 Airfoil With 45-min Glaze Ice Shape (c = 36 in., V_∞ = 175 mph, AOA = 2.5°, MVD = 52 μm)

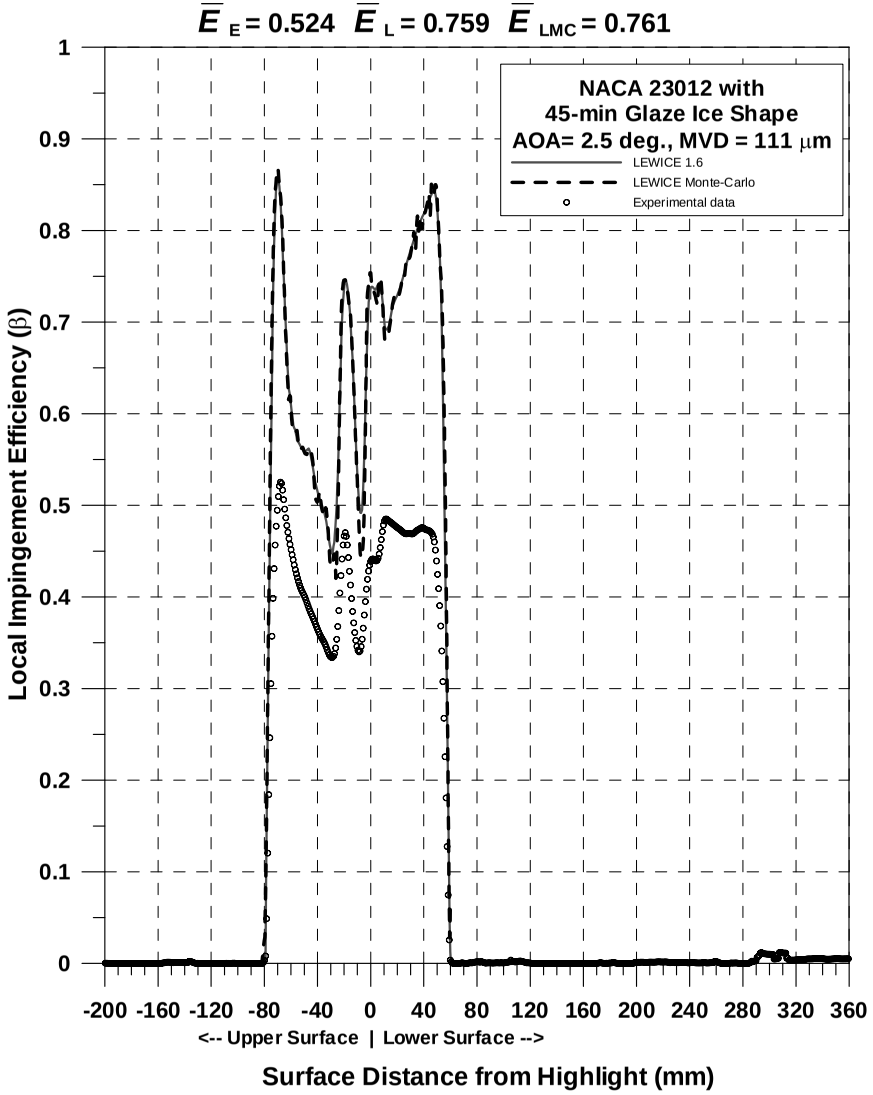

Figure E-23. Impingement Efficiency Distribution for NACA 23012 Airfoil With 45-min Glaze Ice Shape (c = 36 in., V_∞ = 175 mph, AOA = 2.5°, MVD = 111 μm)

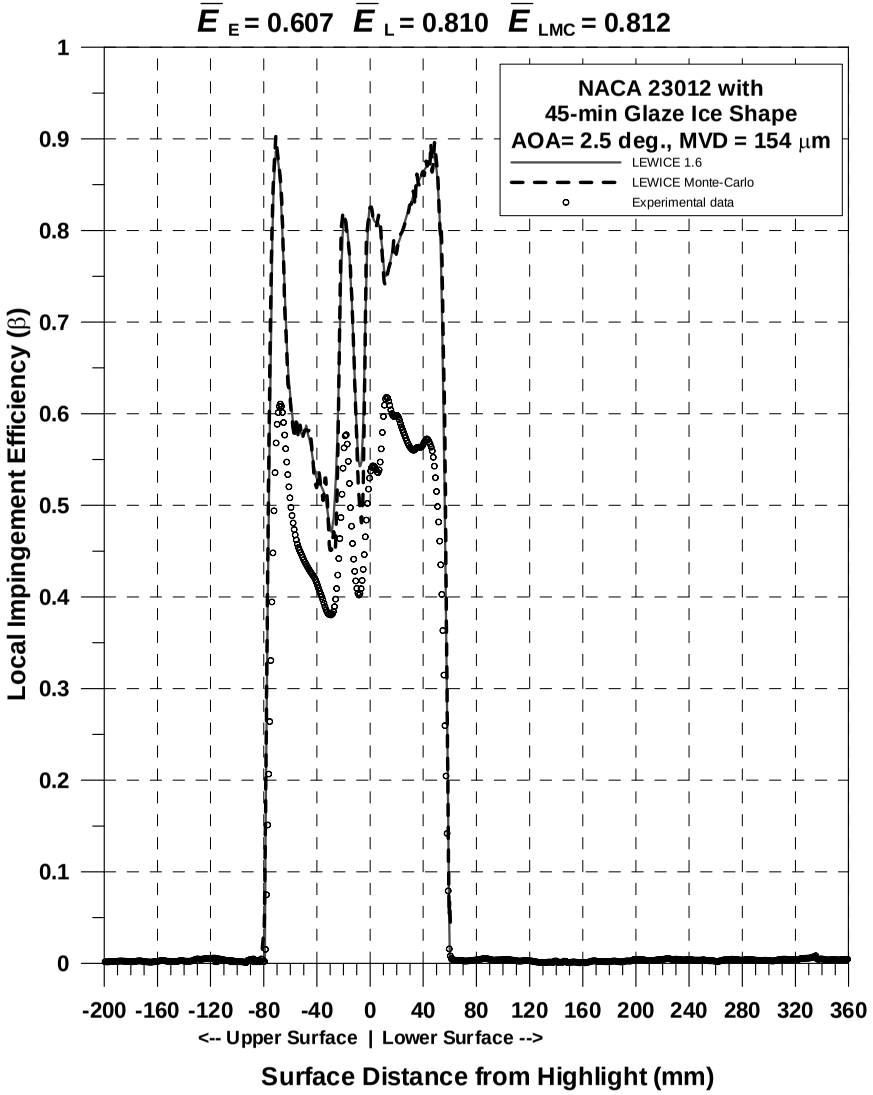

Figure E-24. Impingement Efficiency Distribution for NACA 23012 Airfoil With 45-min Glaze Ice Shape (c = 36 in., V_∞ = 175 mph, AOA = 2.5°, MVD = 154 μm)

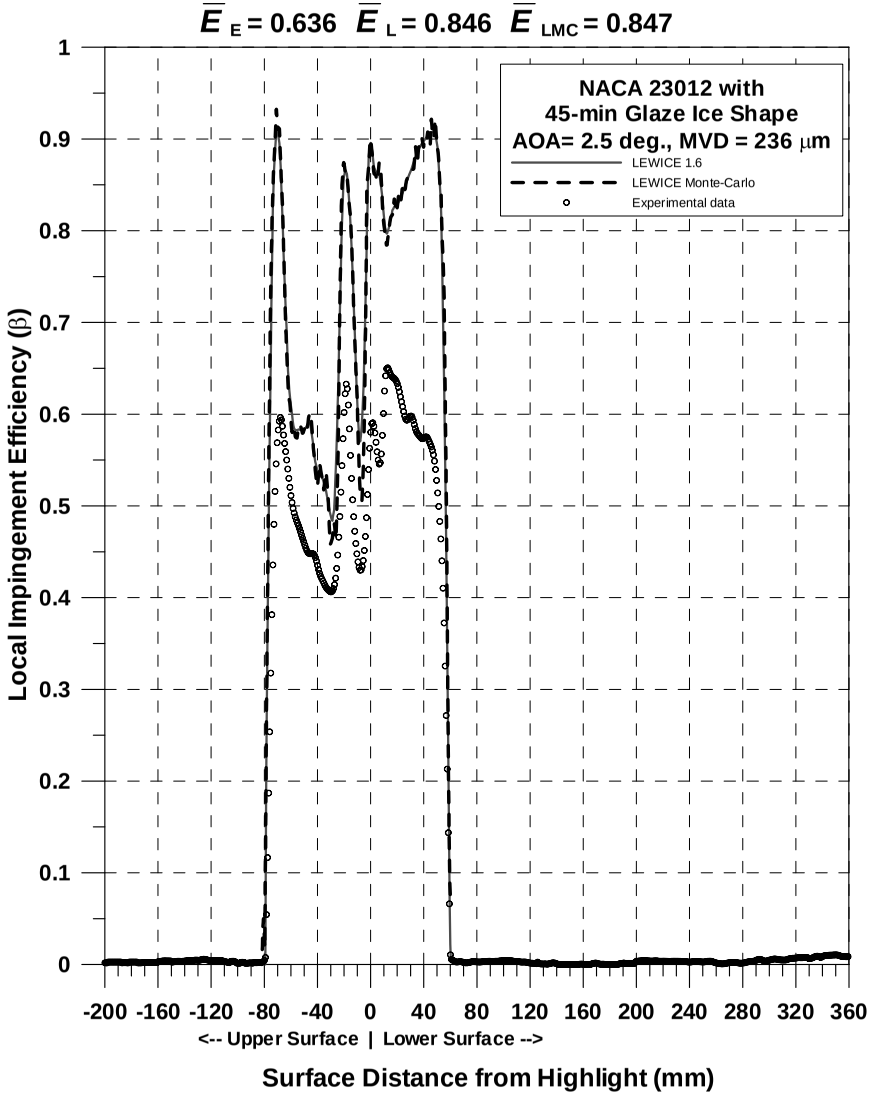

Figure E-25. Impingement Efficiency Distribution for NACA 23012 Airfoil With 45-min Glaze Ice Shape (c = 36 in., V_∞ = 175 mph, AOA = 2.5°, MVD = 236 μm)

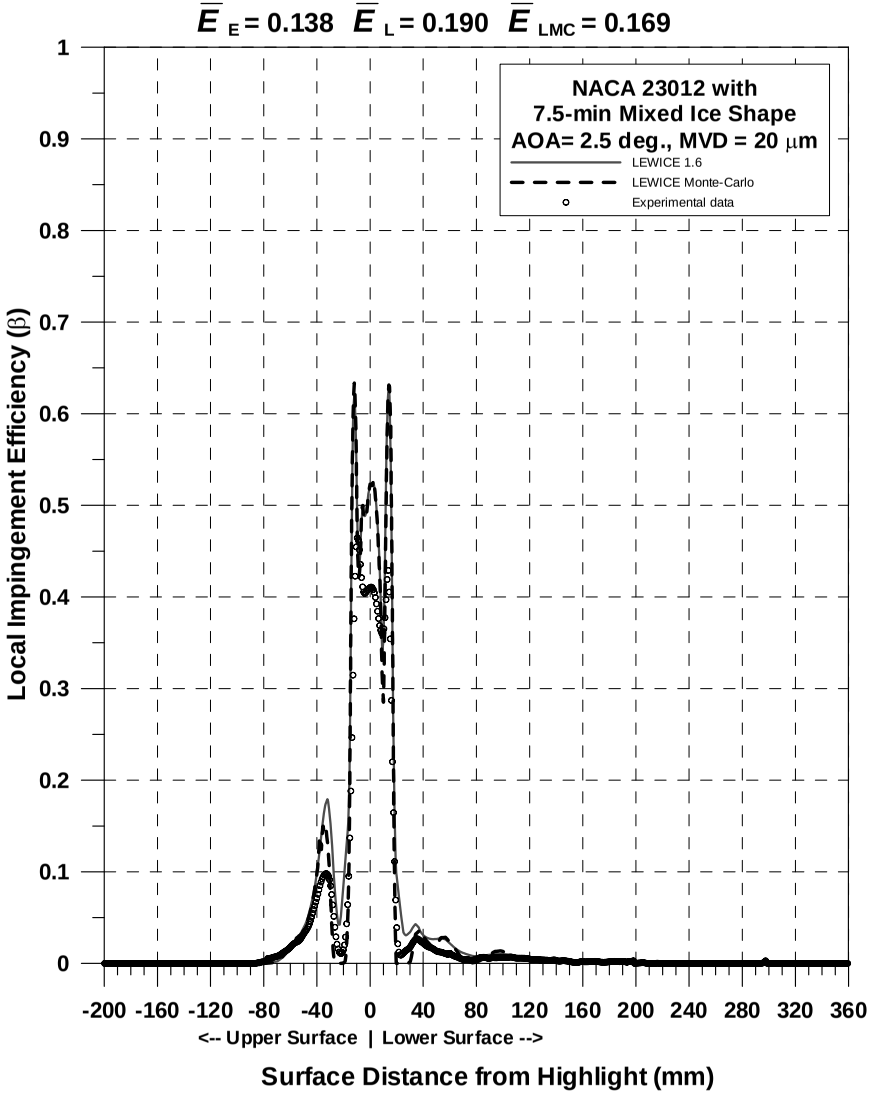

Figure E-26. Impingement Efficiency Distribution for NACA 23012 Airfoil With 7.5-min Mixed Ice Shape (c = 36 in., V_∞ = 175 mph, AOA = 2.5°, MVD = 20 μm)

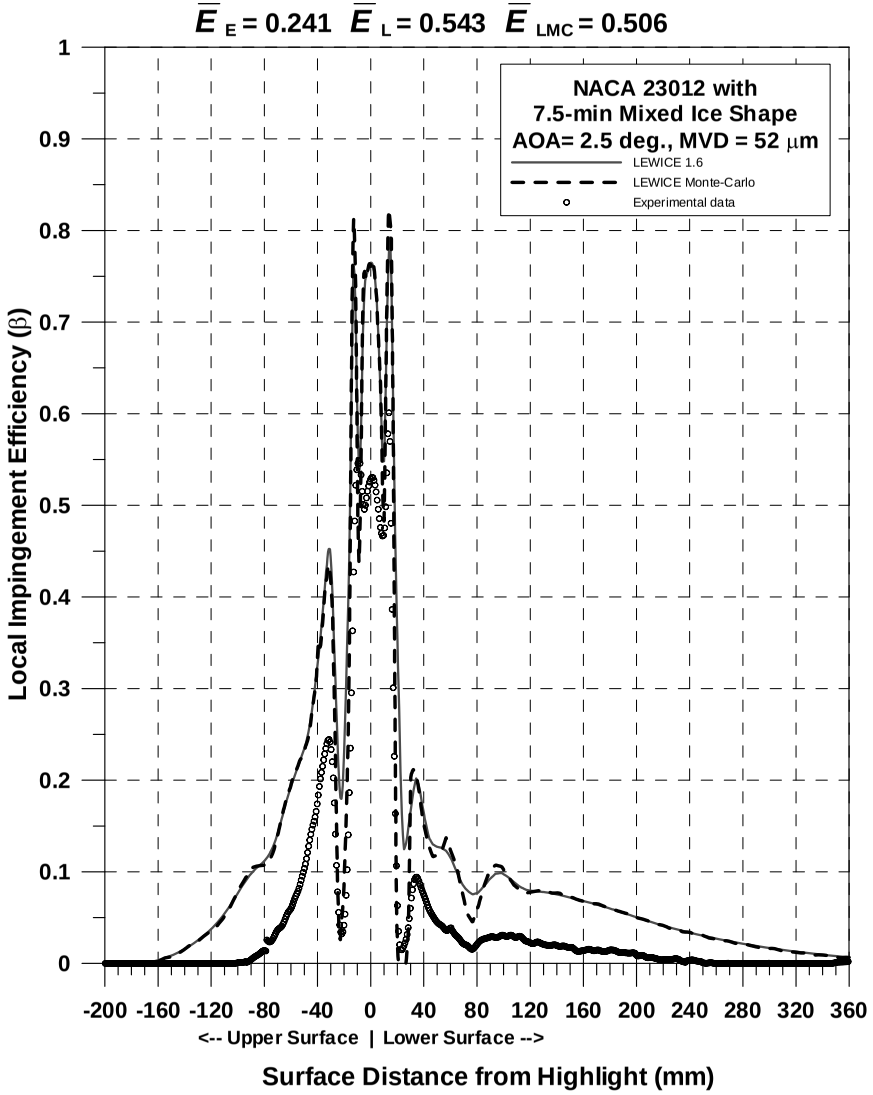

Figure E-27. Impingement Efficiency Distribution for NACA 23012 Airfoil With 7.5-min Mixed Ice Shape (c = 36 in., V_∞ = 175 mph, AOA = 2.5°, MVD = 52 μm)

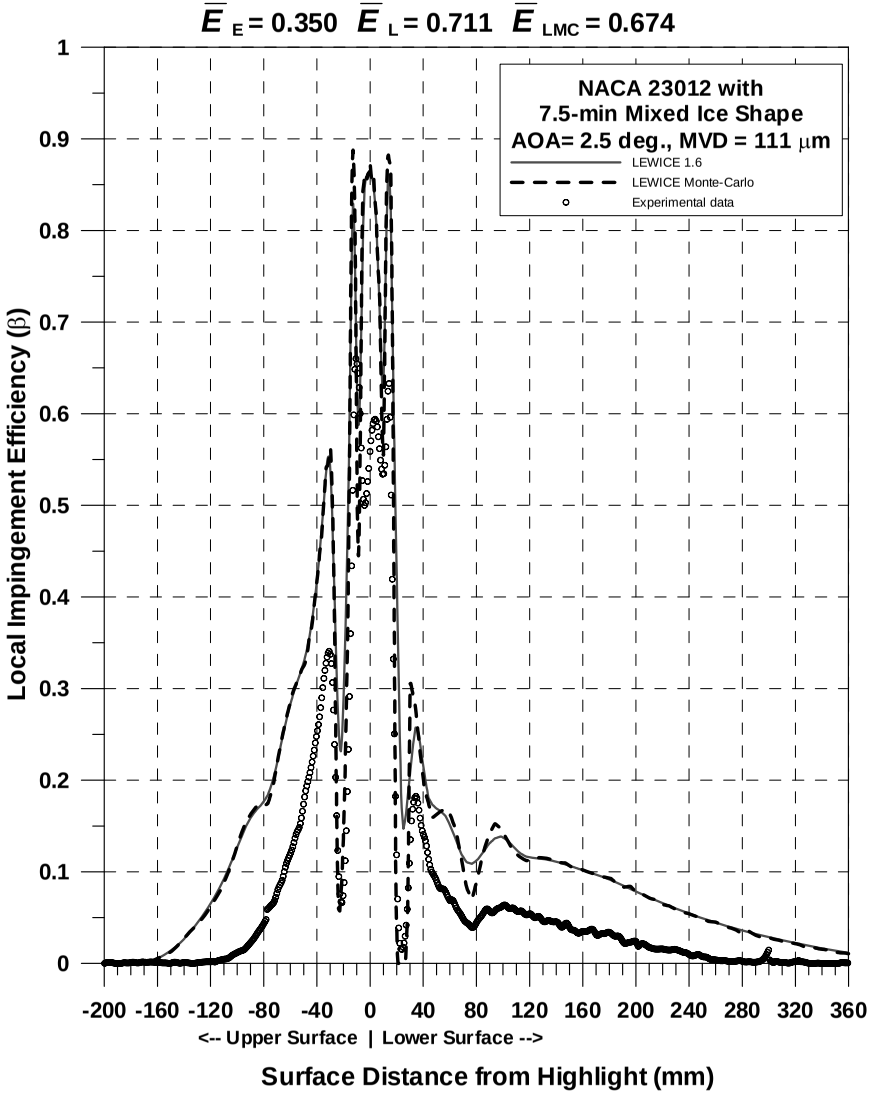

Figure E-28. Impingement Efficiency Distribution for NACA 23012 Airfoil With 7.5-min Mixed Ice Shape (c = 36 in., V_∞ = 175 mph, AOA = 2.5°, MVD = 111 μm)

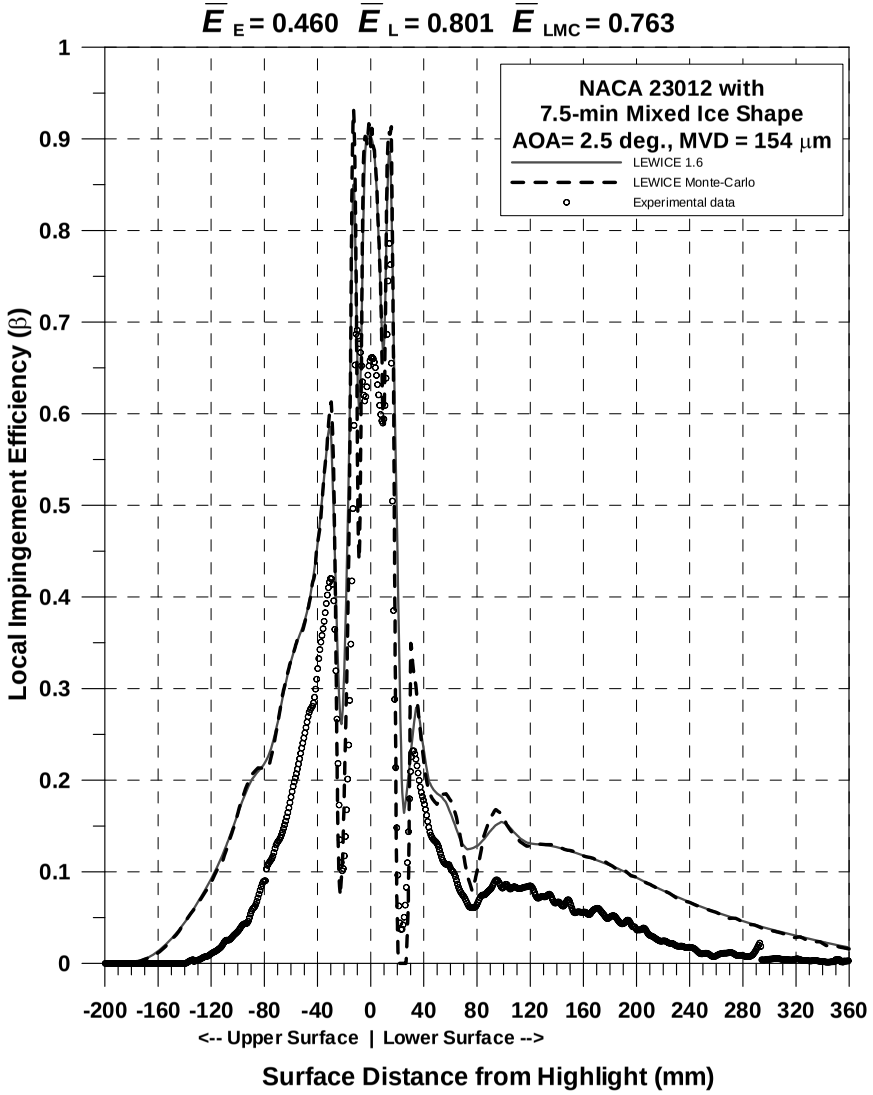

Figure E-29. Impingement Efficiency Distribution for NACA 23012 Airfoil With 7.5-min Mixed Ice Shape (c = 36 in., V_∞ = 175 mph, AOA = 2.5°, MVD = 154 μm)

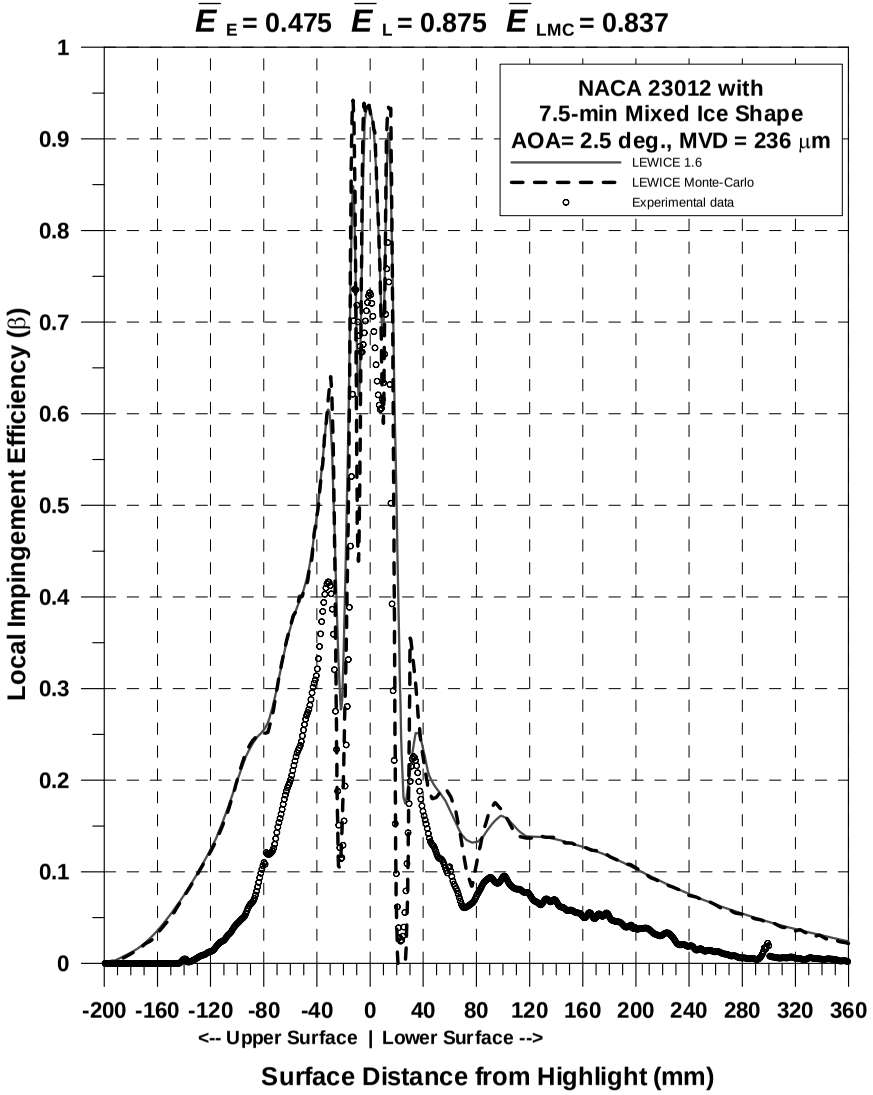

Figure E-30. Impingement Efficiency Distribution for NACA 23012 Airfoil With 7.5-min Mixed Ice Shape (c = 36 in., V_∞ = 175 mph, AOA = 2.5°, MVD = 236 μm)

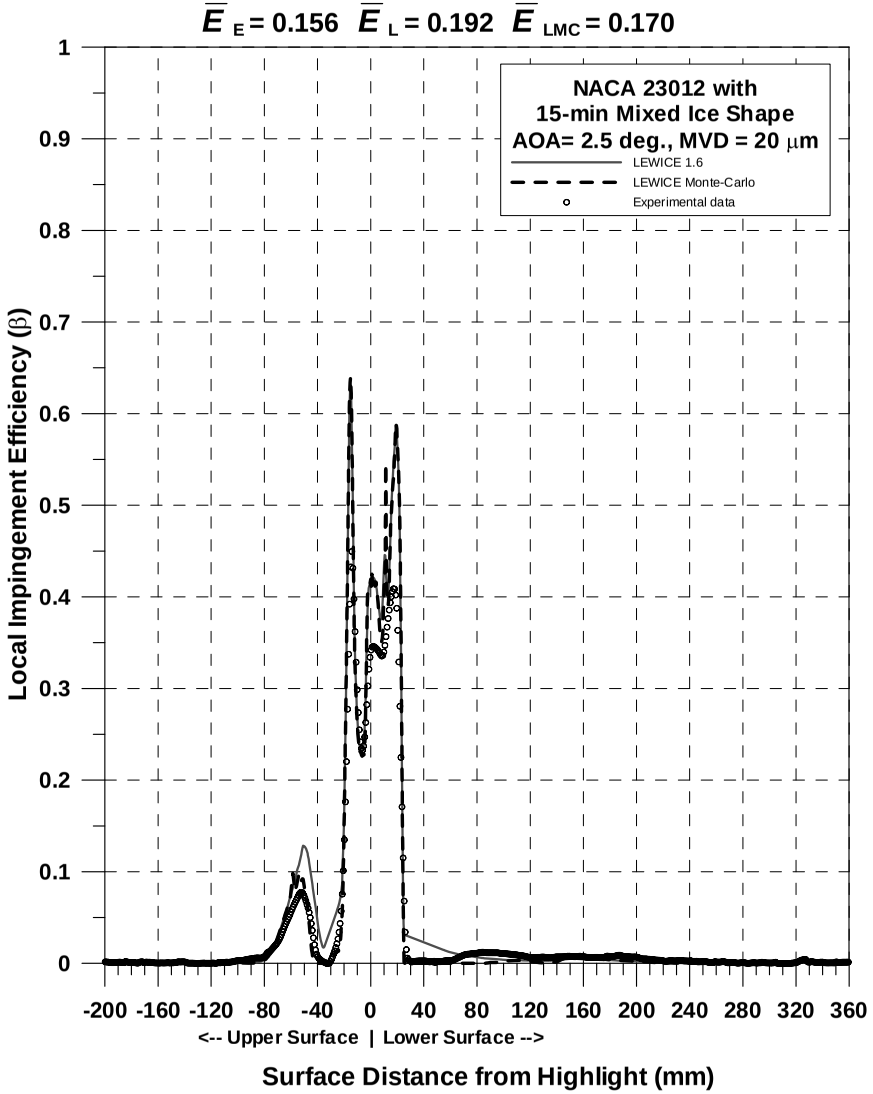

Figure E-31. Impingement Efficiency Distribution for NACA 23012 Airfoil With 15-min Mixed Ice Shape (c = 36 in., V_∞ = 175 mph, AOA = 2.5°, MVD = 20 μm)

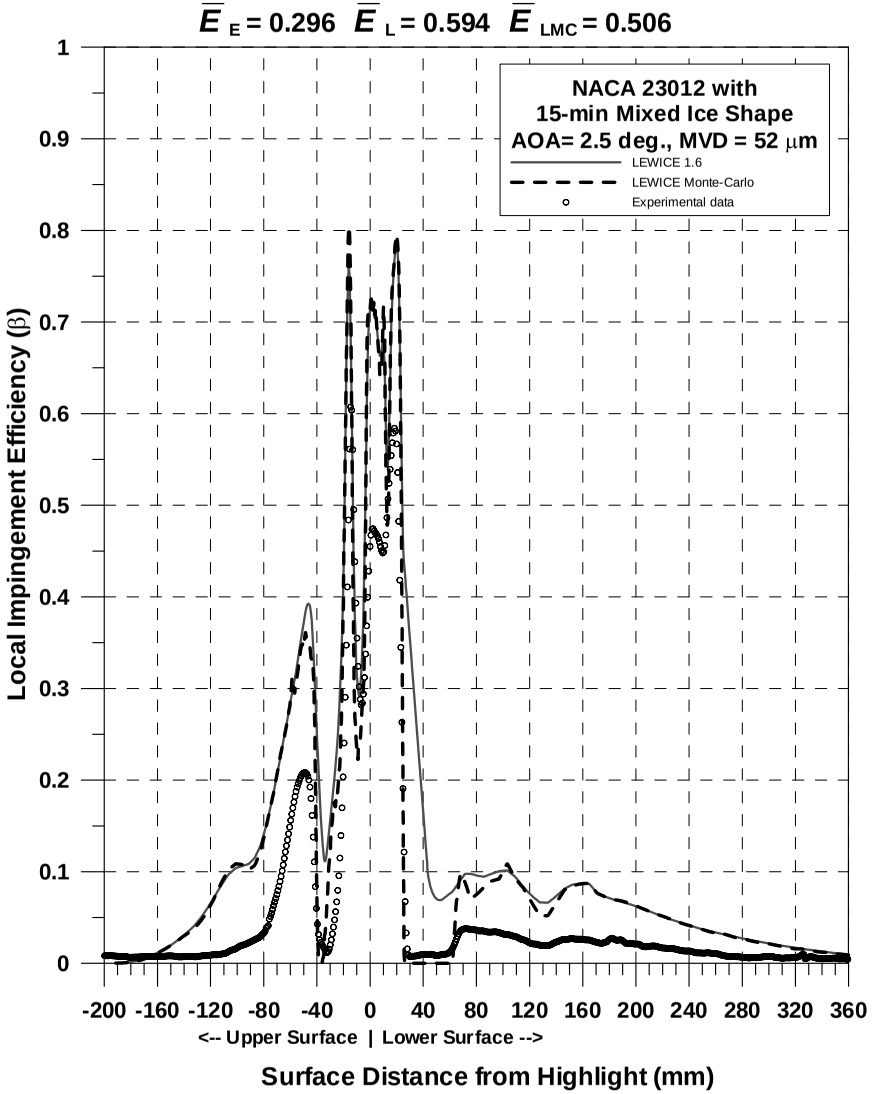

Figure E-32. Impingement Efficiency Distribution for NACA 23012 Airfoil With 15-min Mixed Ice Shape (c = 36 in., V_∞ = 175 mph, AOA = 2.5°, MVD = 52 μm)

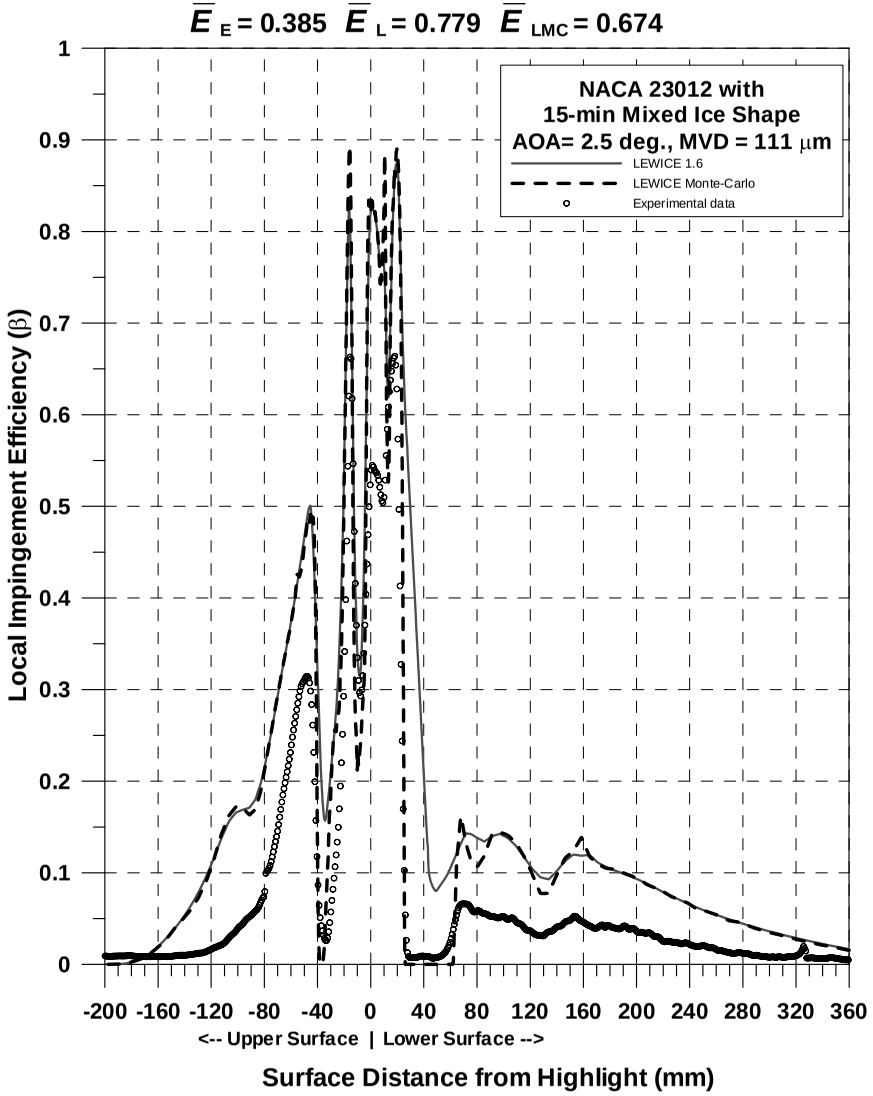

Figure E-33. Impingement Efficiency Distribution for NACA 23012 Airfoil With 15-min Mixed Ice Shape (c = 36 in., V_∞ = 175 mph, AOA = 2.5°, MVD = 111 μm)

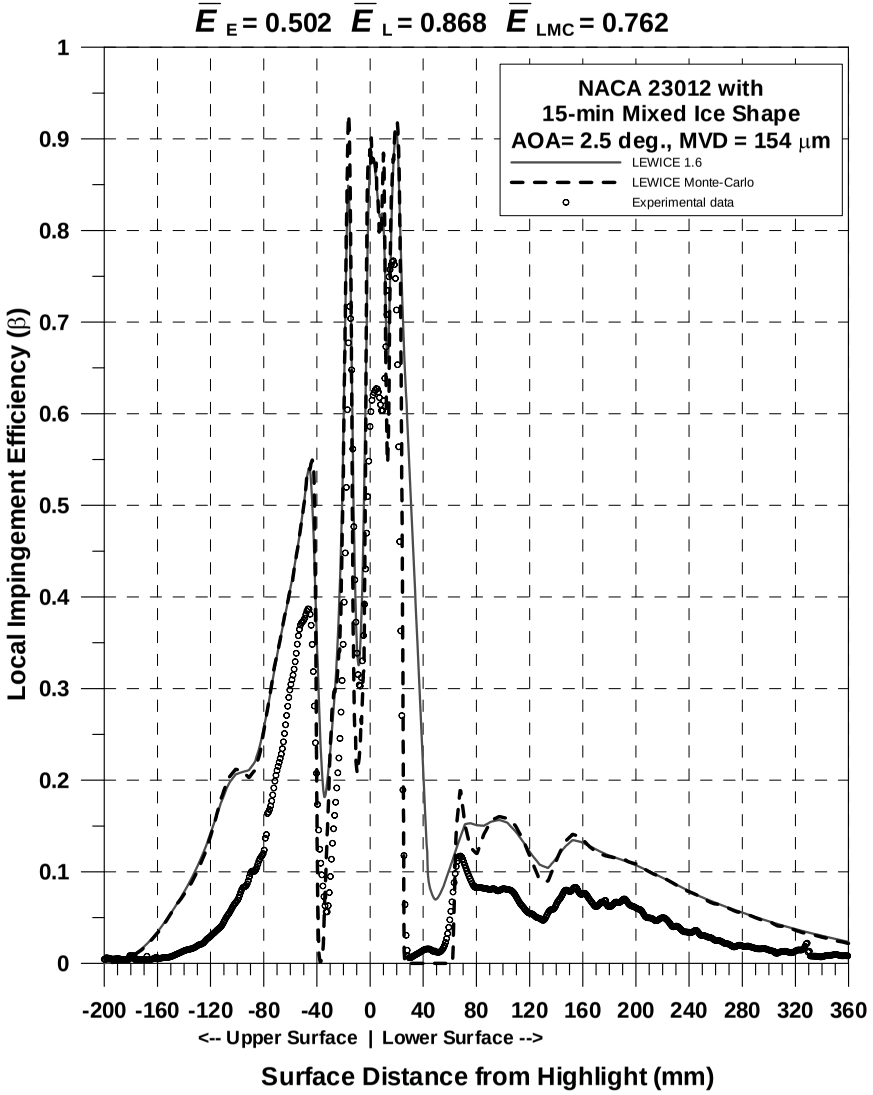

Figure E-34. Impingement Efficiency Distribution for NACA 23012 Airfoil With 15-min Mixed Ice Shape (c = 36 in., V_∞ = 175 mph, AOA = 2.5°, MVD = 154 μm)

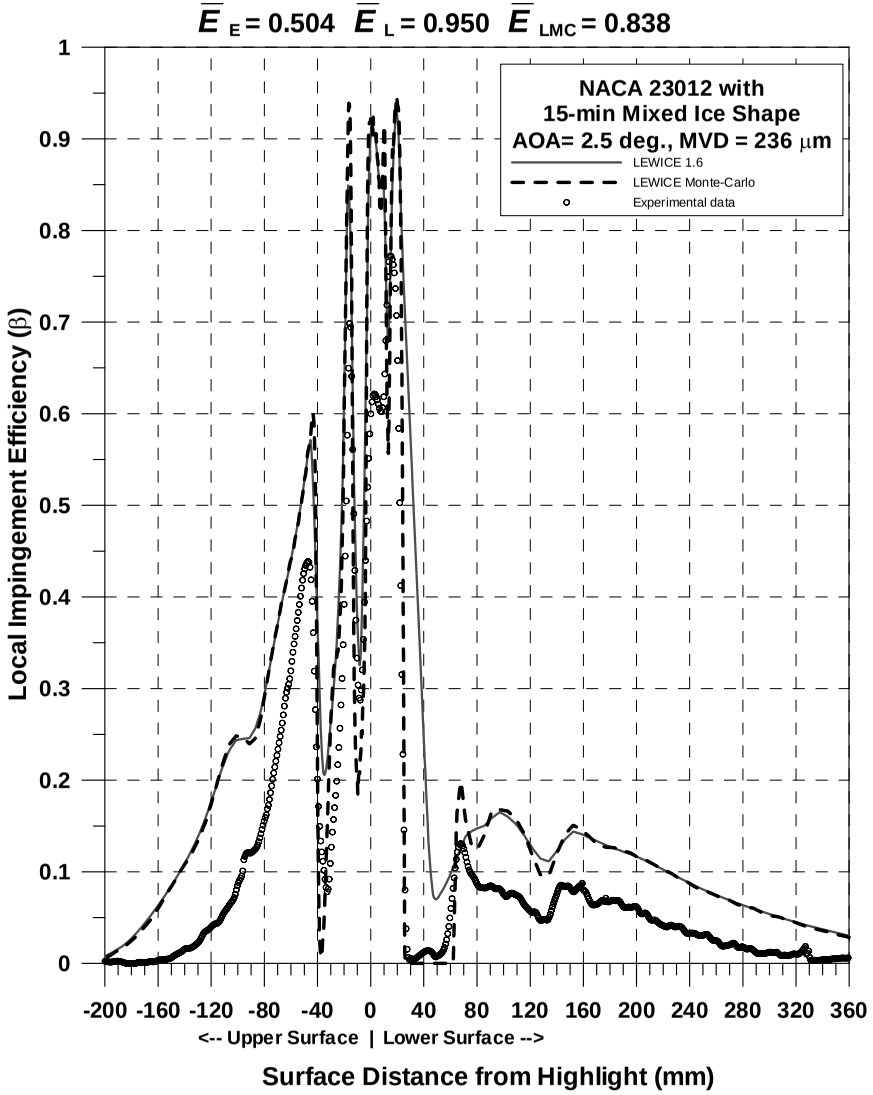

Figure E-35. Impingement Efficiency Distribution for NACA 23012 Airfoil With 15-min Mixed Ice Shape (c = 36 in., V_∞ = 175 mph, AOA = 2.5°, MVD = 236 μm)

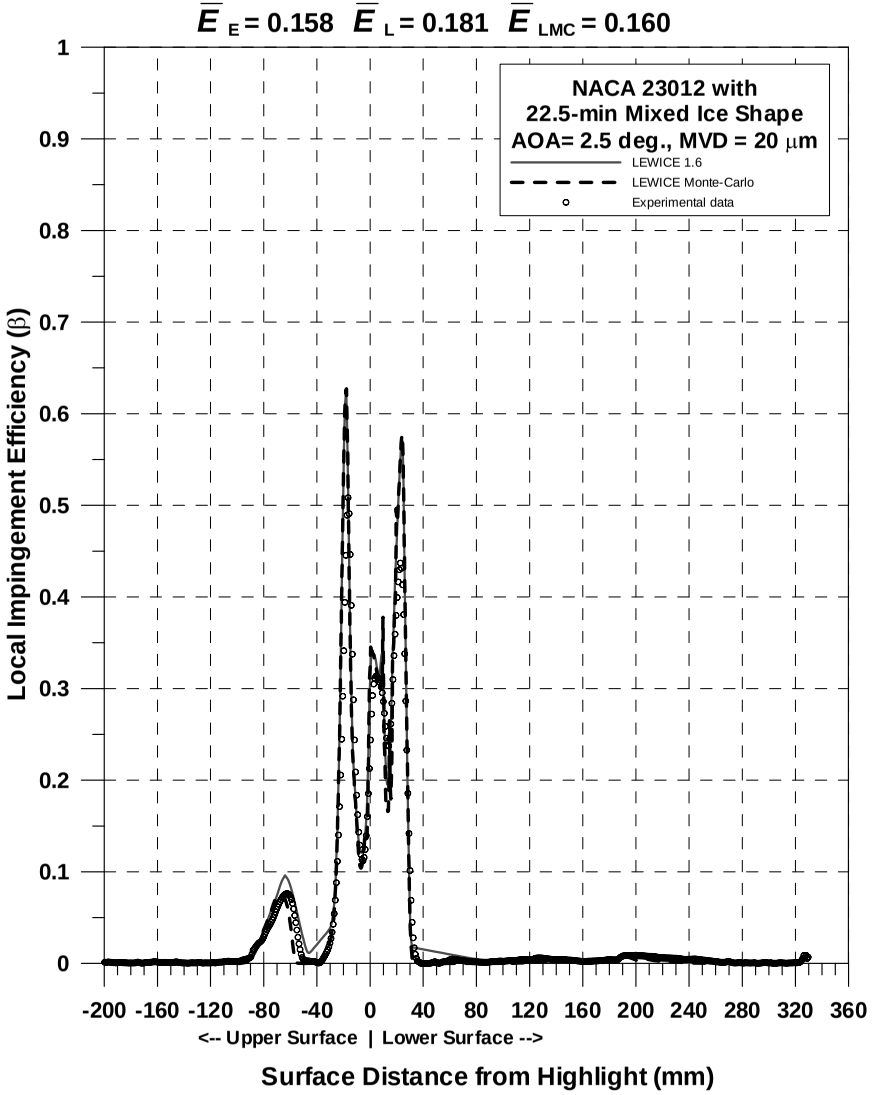

Figure E-36. Impingement Efficiency Distribution for NACA 23012 Airfoil With 22.5-min Mixed Ice Shape (c = 36 in., V_∞ = 175 mph, AOA = 2.5°, MVD = 20 μm)

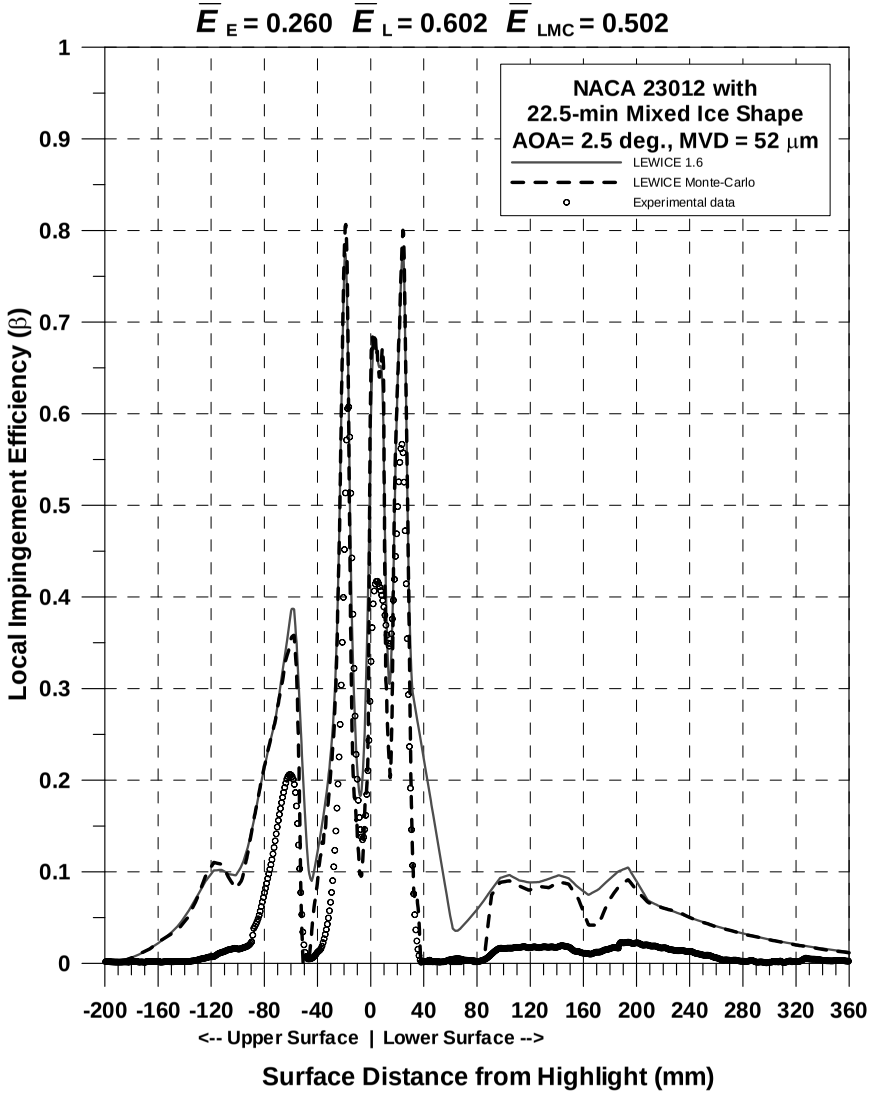

Figure E-37. Impingement Efficiency Distribution for NACA 23012 Airfoil With 22.5-min Mixed Ice Shape (c = 36 in., V_∞ = 175 mph, AOA = 2.5°, MVD = 52 μm)

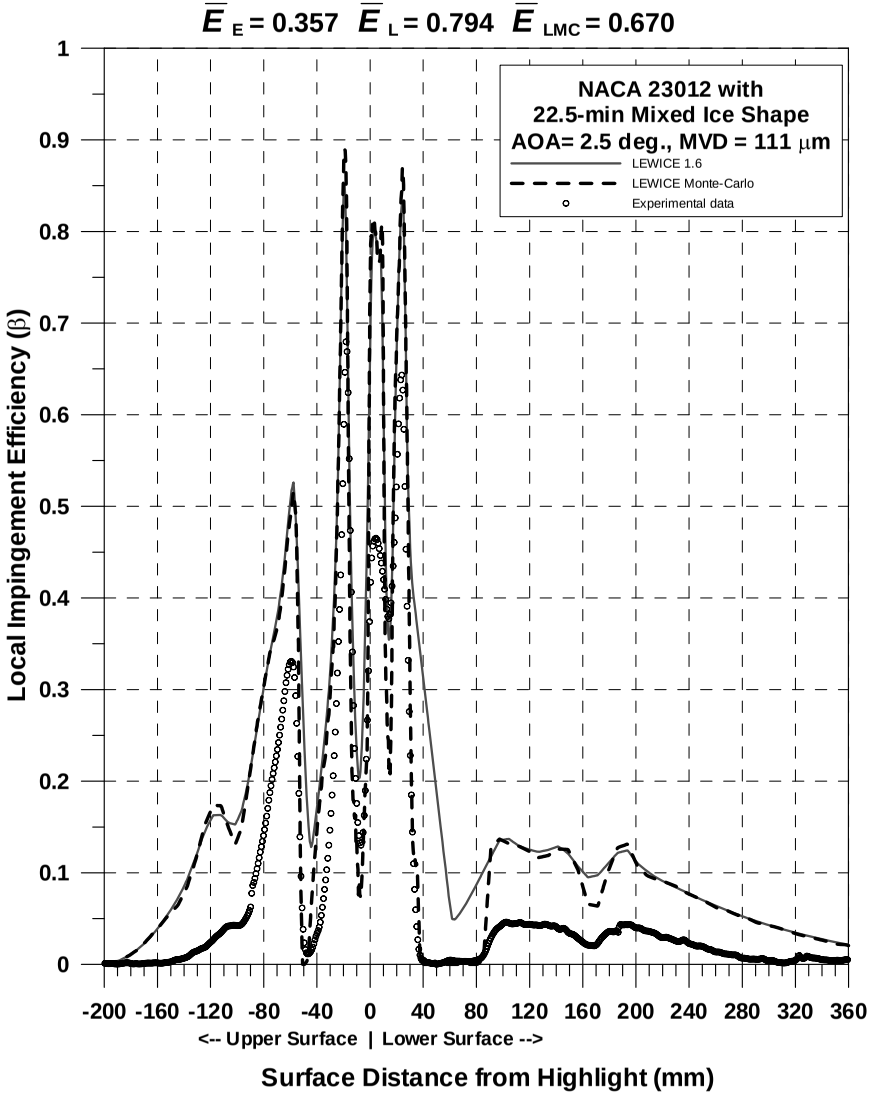

Figure E-38. Impingement Efficiency Distribution for NACA 23012 Airfoil With 22.5-min Mixed Ice Shape (c = 36 in., V_∞ = 175 mph, AOA = 2.5°, MVD = 111 μm)

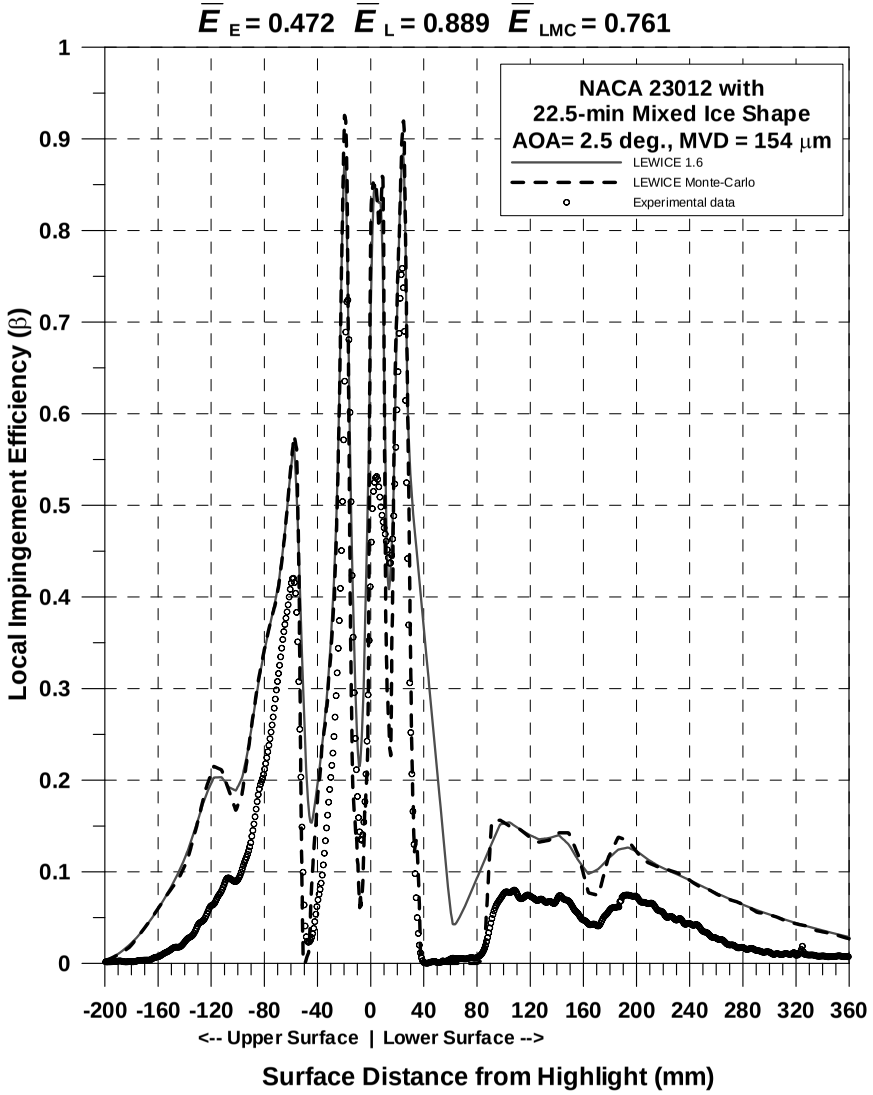

Figure E-39. Impingement Efficiency Distribution for NACA 23012 Airfoil With 22.5-min Mixed Ice Shape (c = 36 in., V_∞ = 175 mph, AOA = 2.5°, MVD = 154 μm)

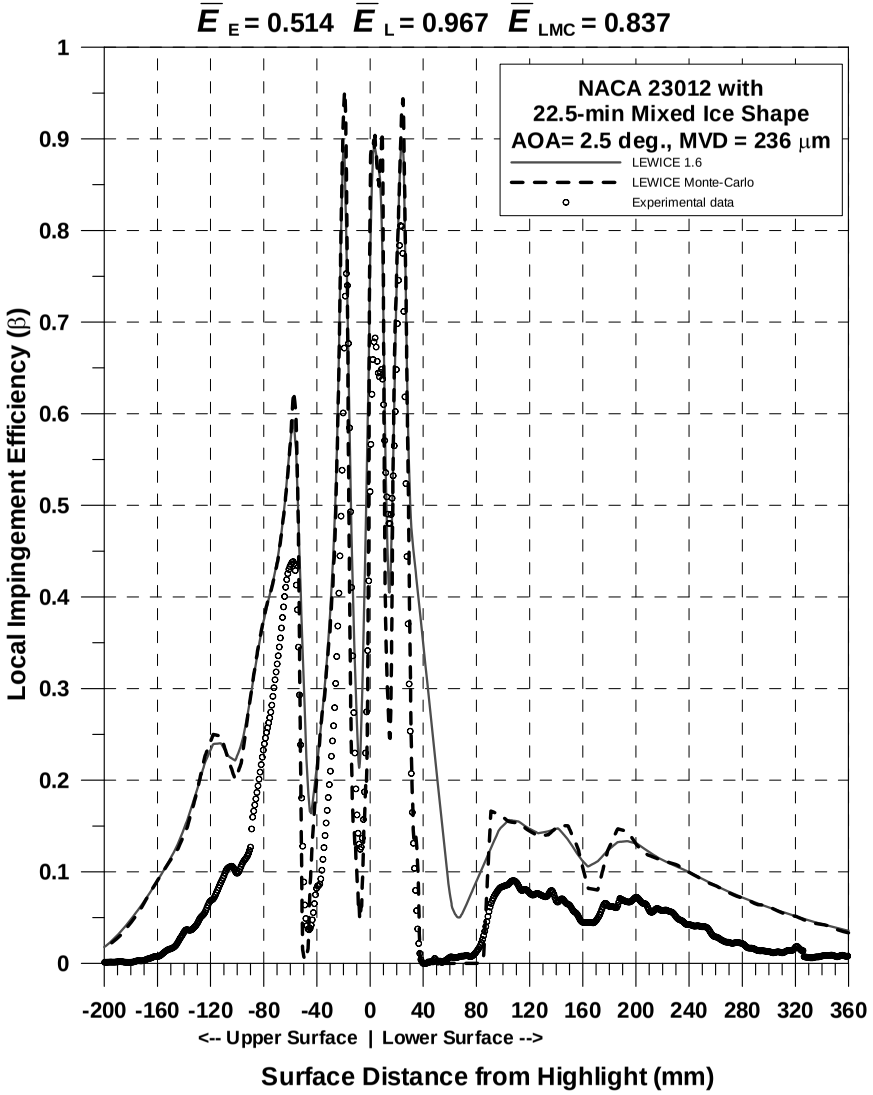

Figure E-40. Impingement Efficiency Distribution for NACA 23012 Airfoil With 22.5-min Mixed Ice Shape (c = 36 in., V_∞ = 175 mph, AOA = 2.5°, MVD = 236 μm)

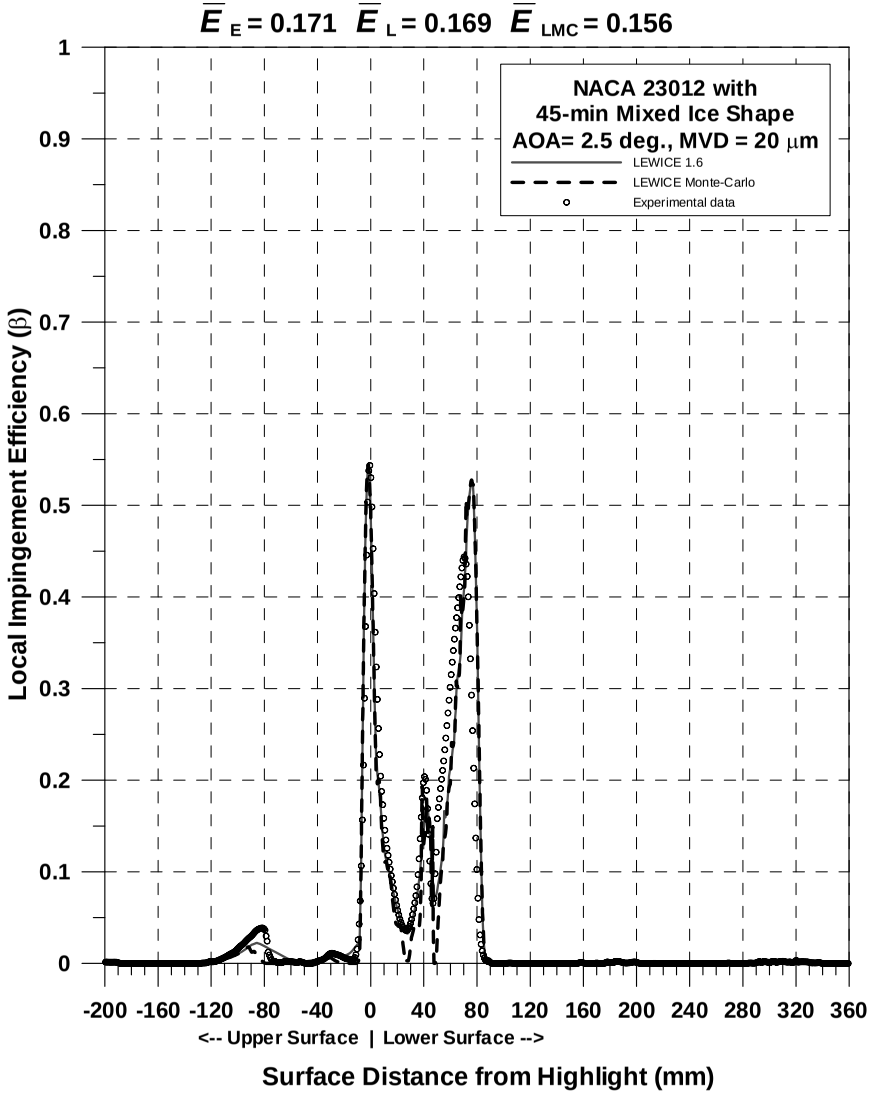

Figure E-41. Impingement Efficiency Distribution for NACA 23012 Airfoil With 45-min Mixed Ice Shape (c = 36 in., V_∞ = 175 mph, AOA = 2.5°, MVD = 20 μm)

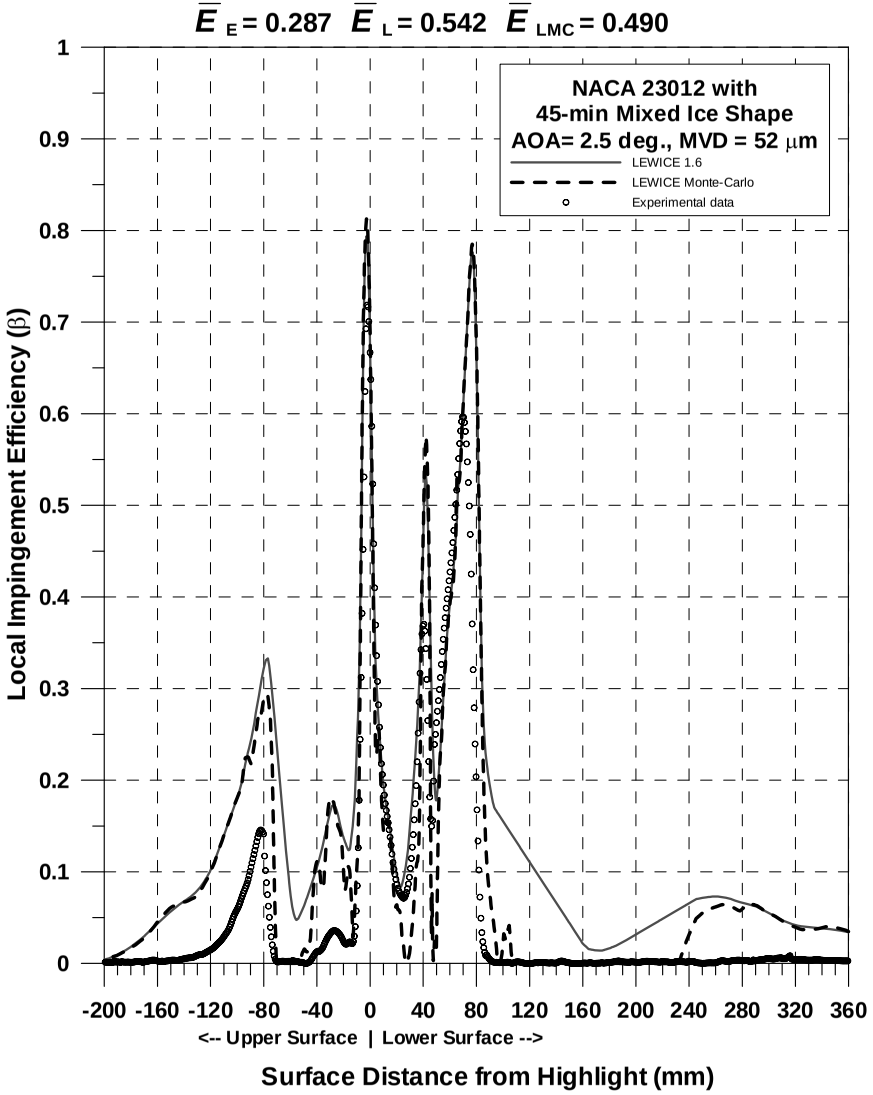

Figure E-42. Impingement Efficiency Distribution for NACA 23012 Airfoil With 45-min Mixed Ice Shape (c = 36 in., V_∞ = 175 mph, AOA = 2.5°, MVD = 52 μm)

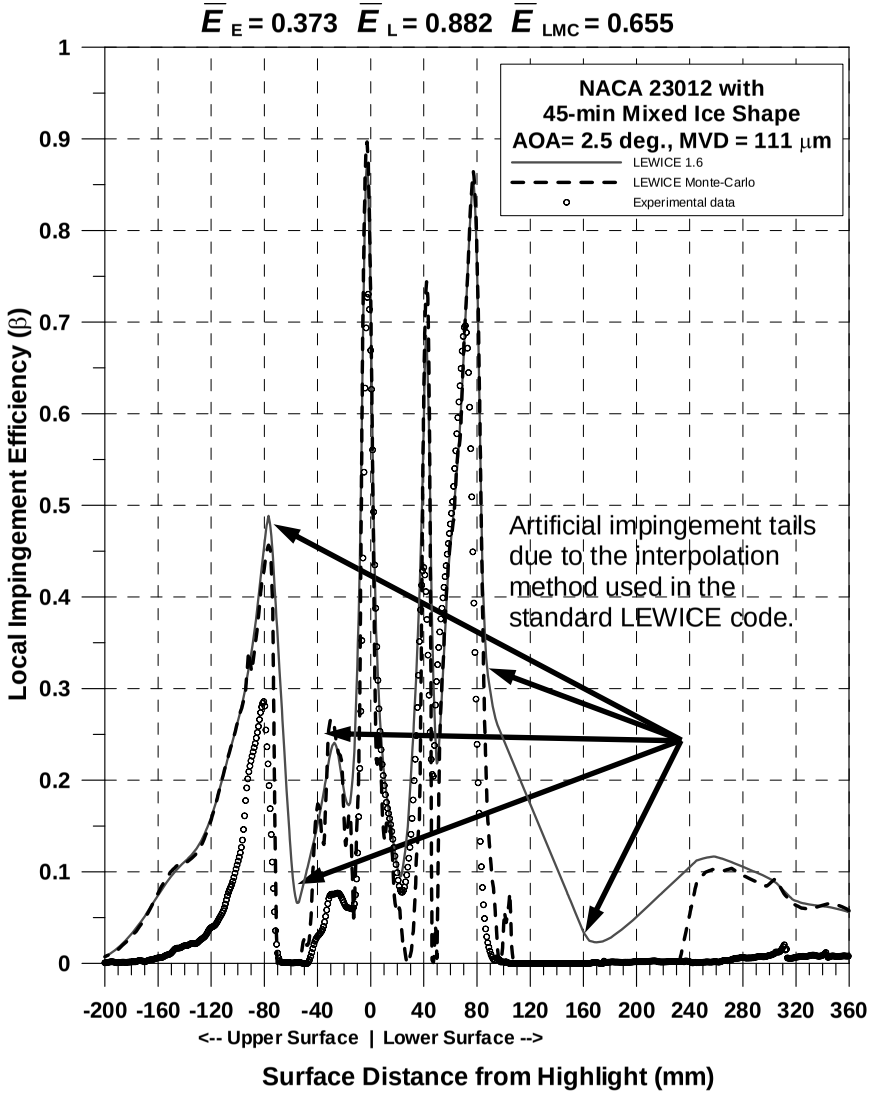

Figure E-43. Impingement Efficiency Distribution for NACA 23012 Airfoil With 45-min Mixed Ice Shape (c = 36 in., V_∞ = 175 mph, AOA = 2.5°, MVD = 111 μm)

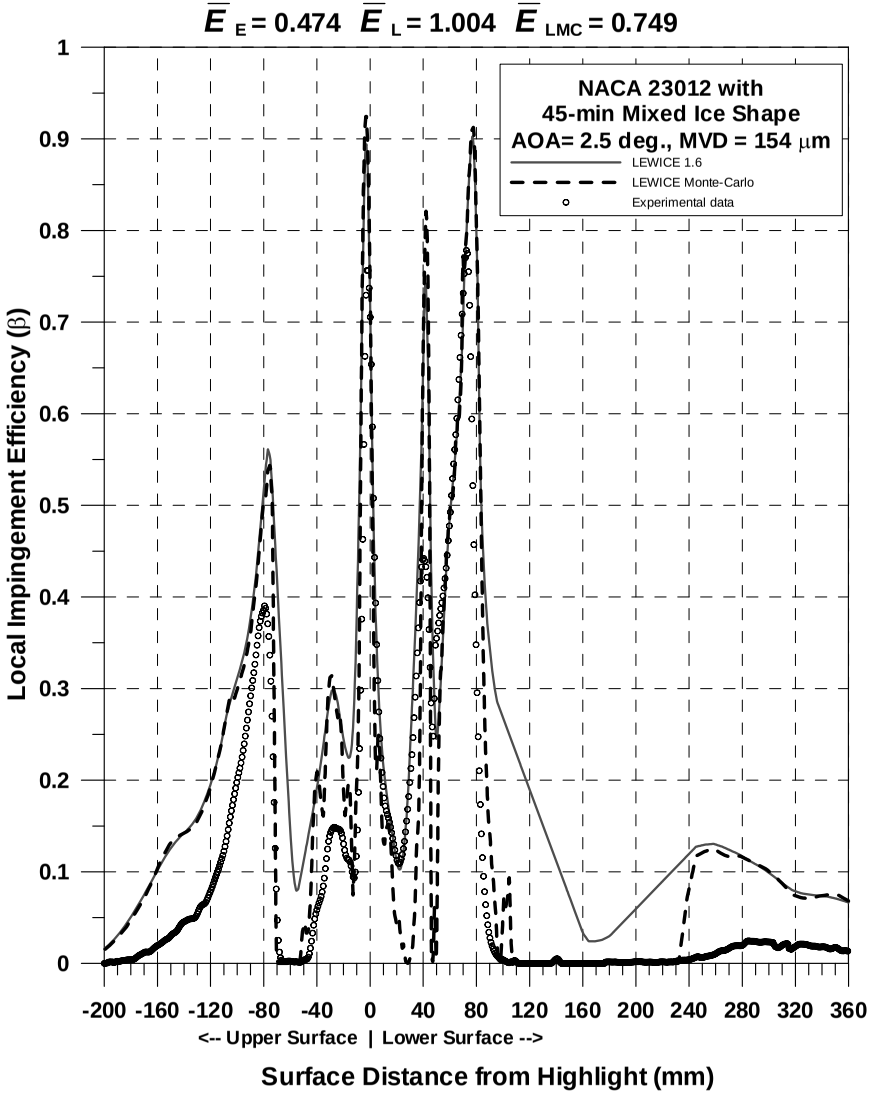

Figure E-44. Impingement Efficiency Distribution for NACA 23012 Airfoil With 45-min Mixed Ice Shape (c = 36 in., V_∞ = 175 mph, AOA = 2.5°, MVD = 154 μm)

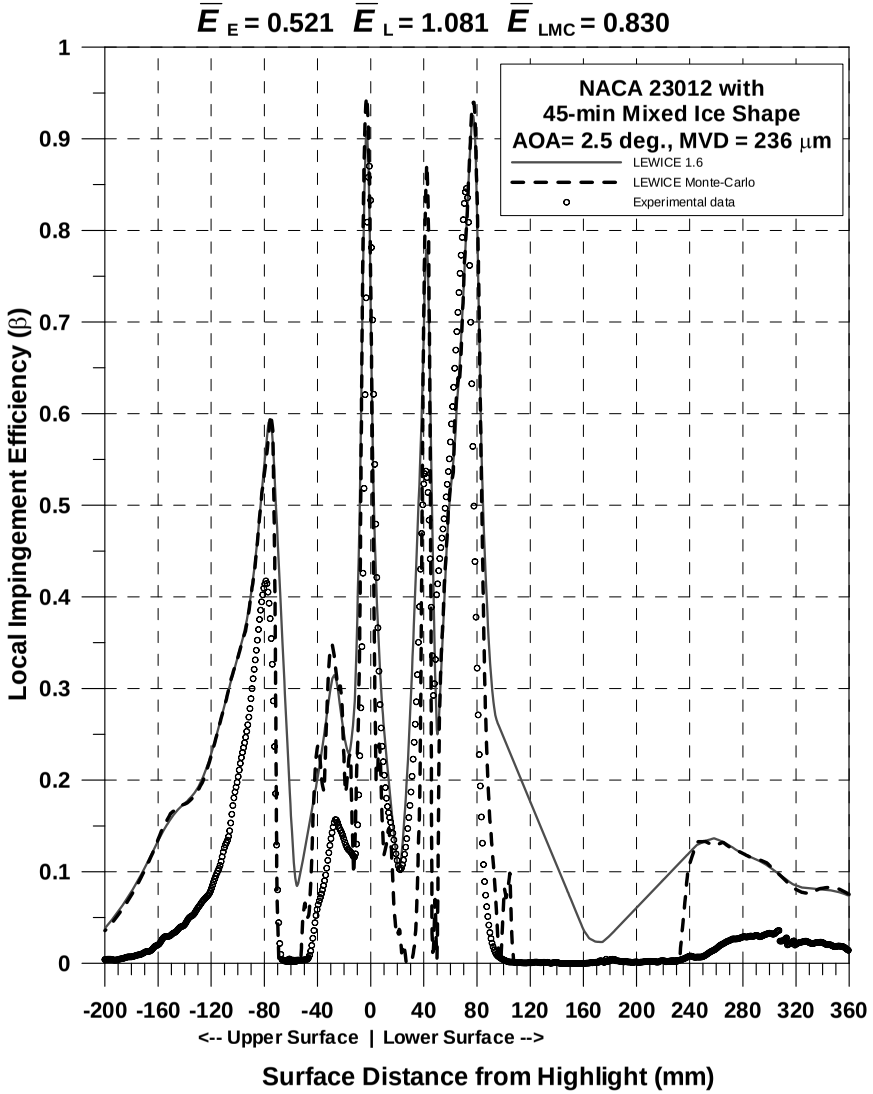

Figure E-45. Impingement Efficiency Distribution for NACA 23012 Airfoil With 45-min Mixed Ice Shape (c = 36 in., V_∞ = 175 mph, AOA = 2.5°, MVD = 236 μm)

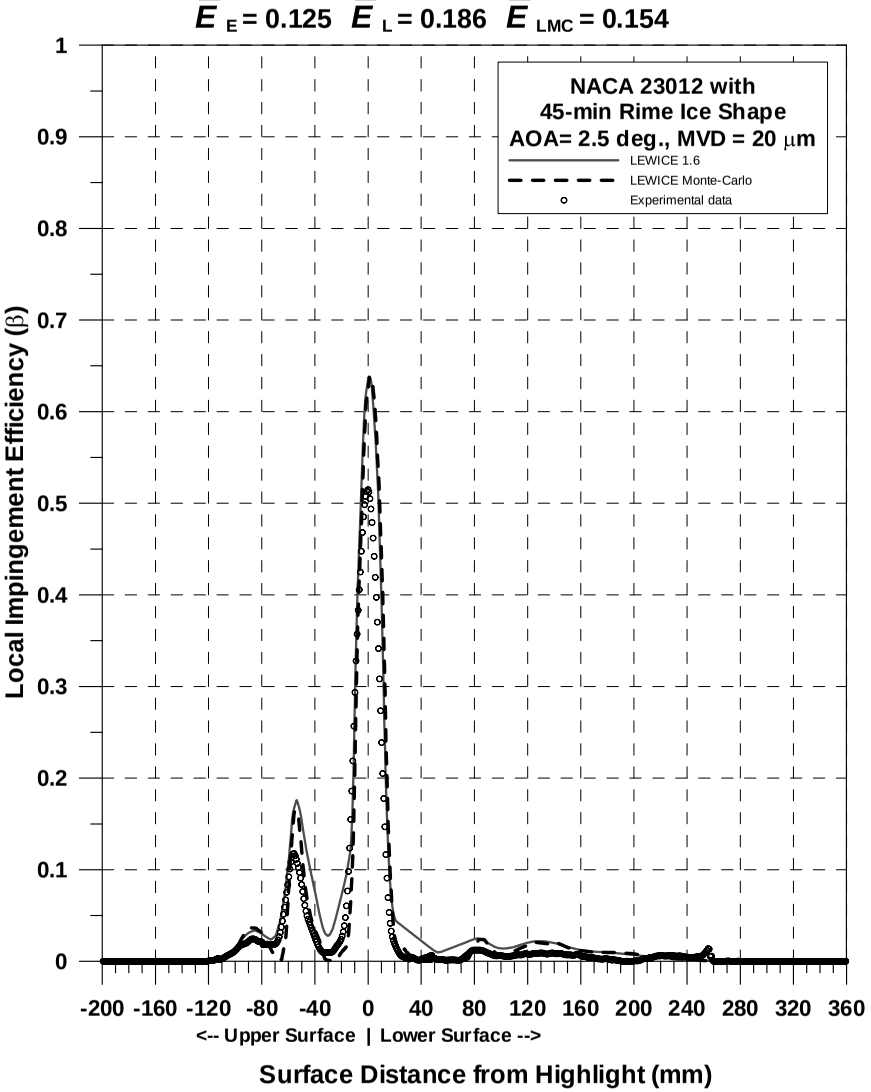

Figure E-46. Impingement Efficiency Distribution for NACA 23012 Airfoil With 45-min Mixed Ice Shape (c = 36 in., V_∞ = 175 mph, AOA = 2.5°, MVD = 20 μm)

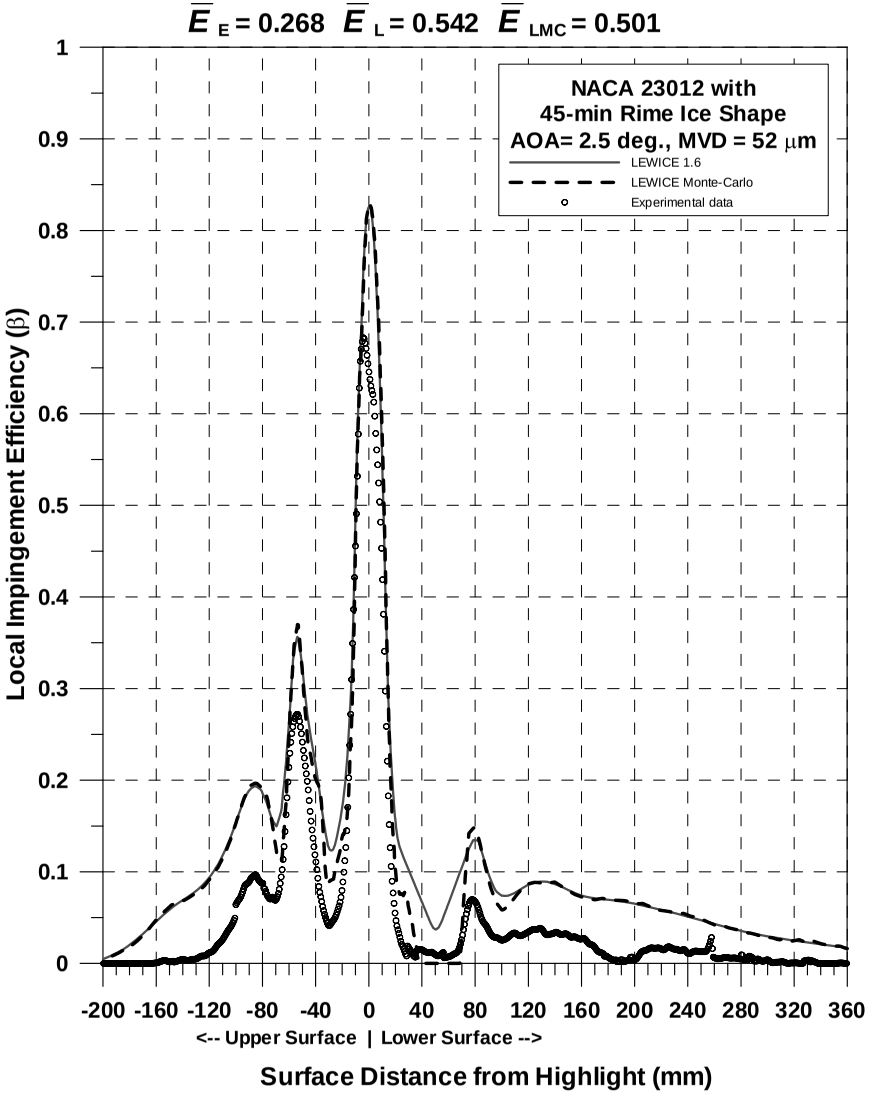

Figure E-47. Impingement Efficiency Distribution for NACA 23012 Airfoil With 45-min Rime Ice Shape (c = 36 in., V_∞ = 175 mph, AOA = 2.5°, MVD = 52 μm)

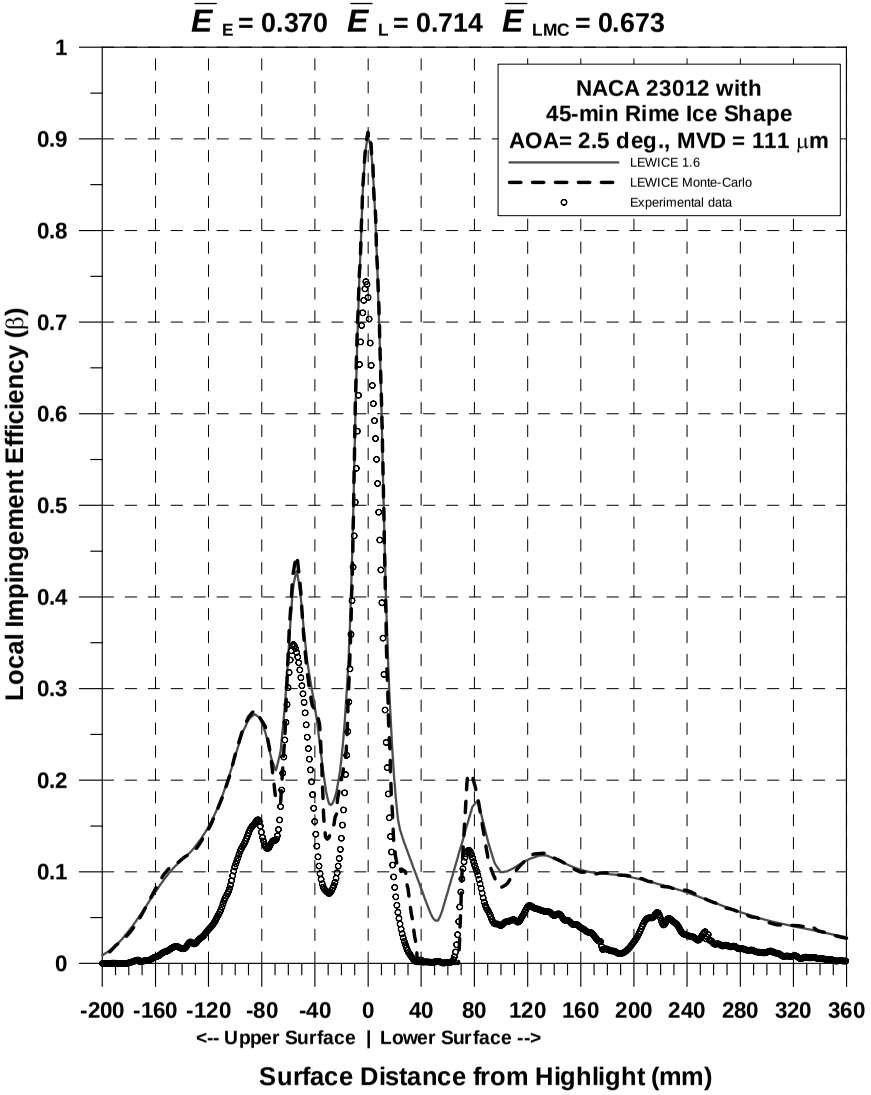

Figure E-48. Impingement Efficiency Distribution for NACA 23012 Airfoil With 45-min Rime Ice Shape (c = 36 in., V_∞ = 175 mph, AOA = 2.5°, MVD = 111 μm

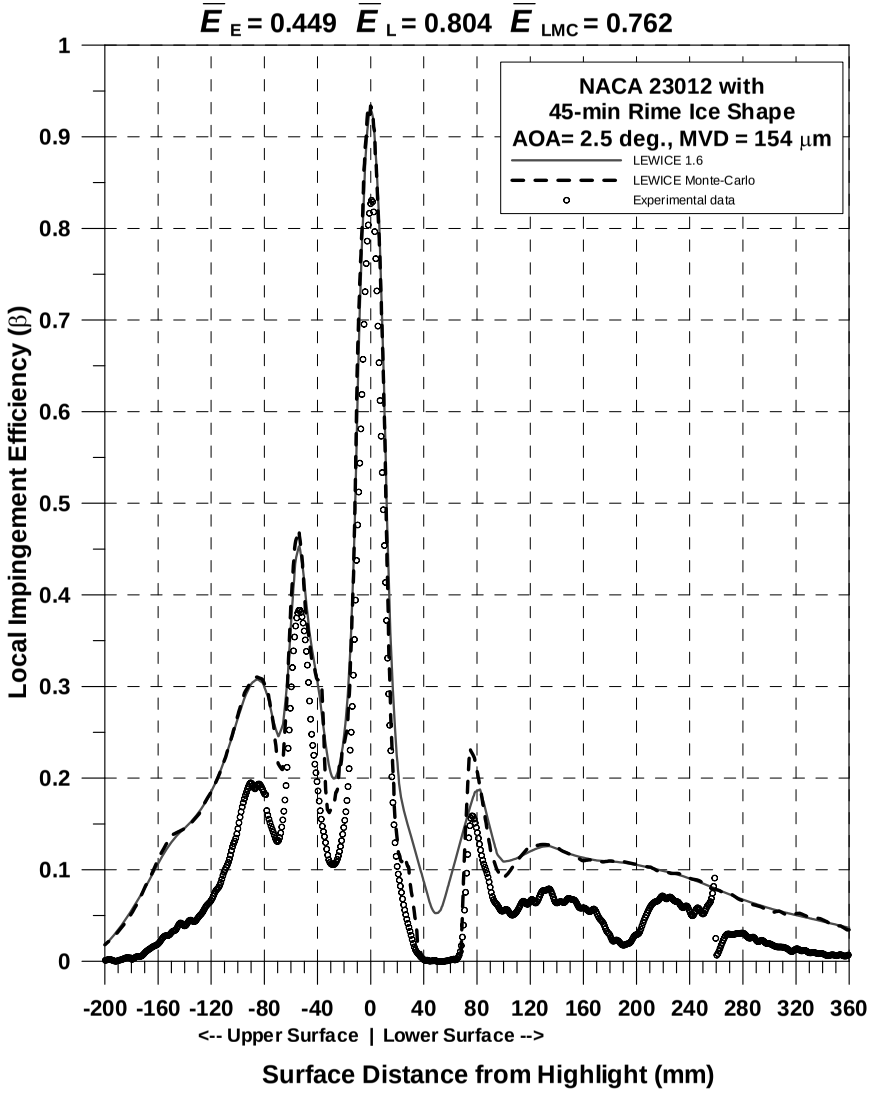

Figure E-49. Impingement Efficiency Distribution for NACA 23012 Airfoil With 45-min Rime Ice Shape (c = 36 in., V_∞ = 175 mph, AOA = 2.5°, MVD = 154 μm)

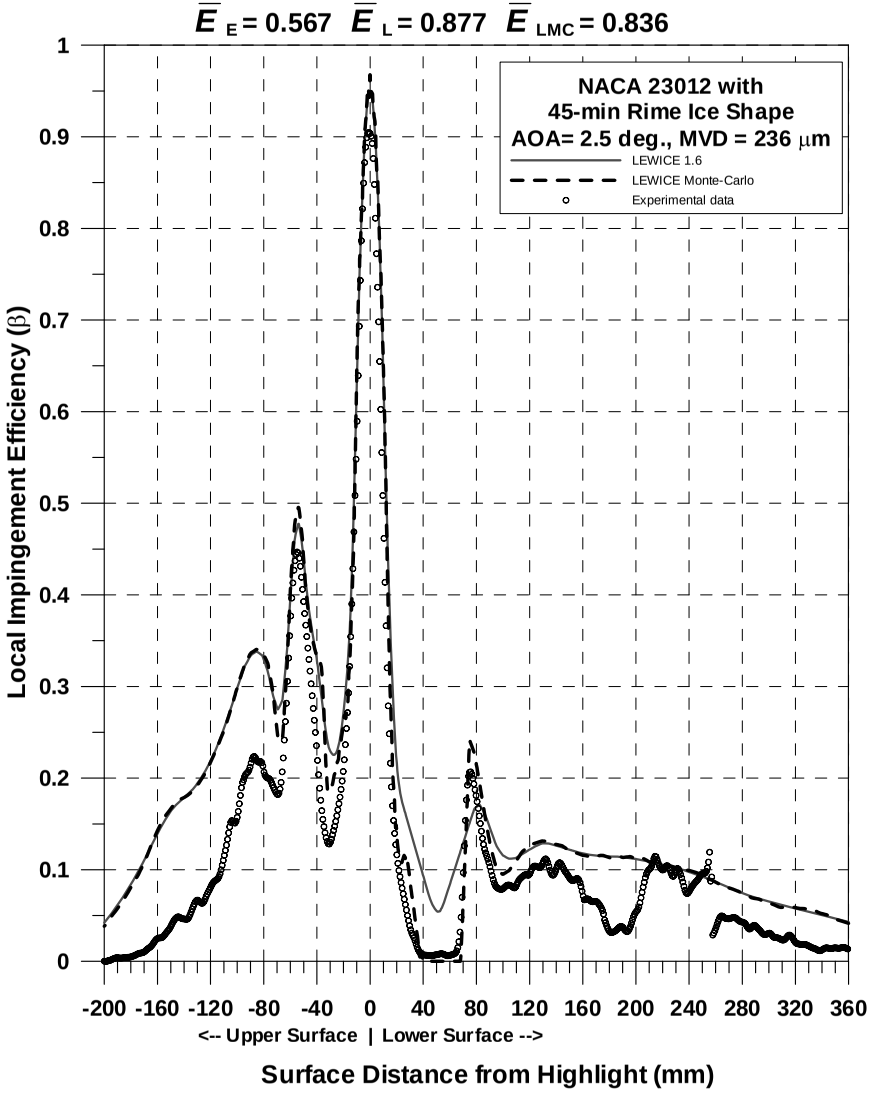

Figure E-50. Impingement Efficiency Distribution for NACA 23012 Airfoil With 45-min Rime Ice Shape (c = 36 in., V_∞ = 175 mph, AOA = 2.5°, MVD = 236 μm)

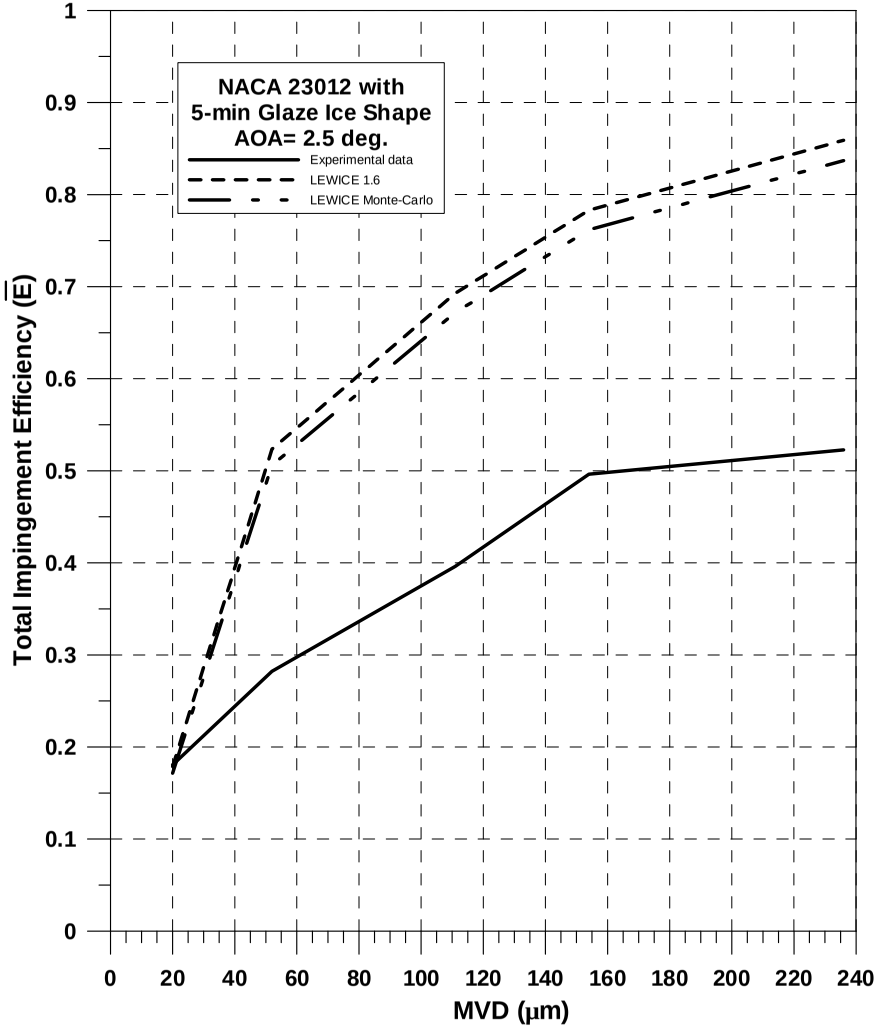

Figure E-51. Total Impingement Efficiency Distribution for NACA 23012 Airfoil With 5-min Glaze Ice Shape (c = 36 in., V_∞ = 175 mph, AOA = 2.5°)

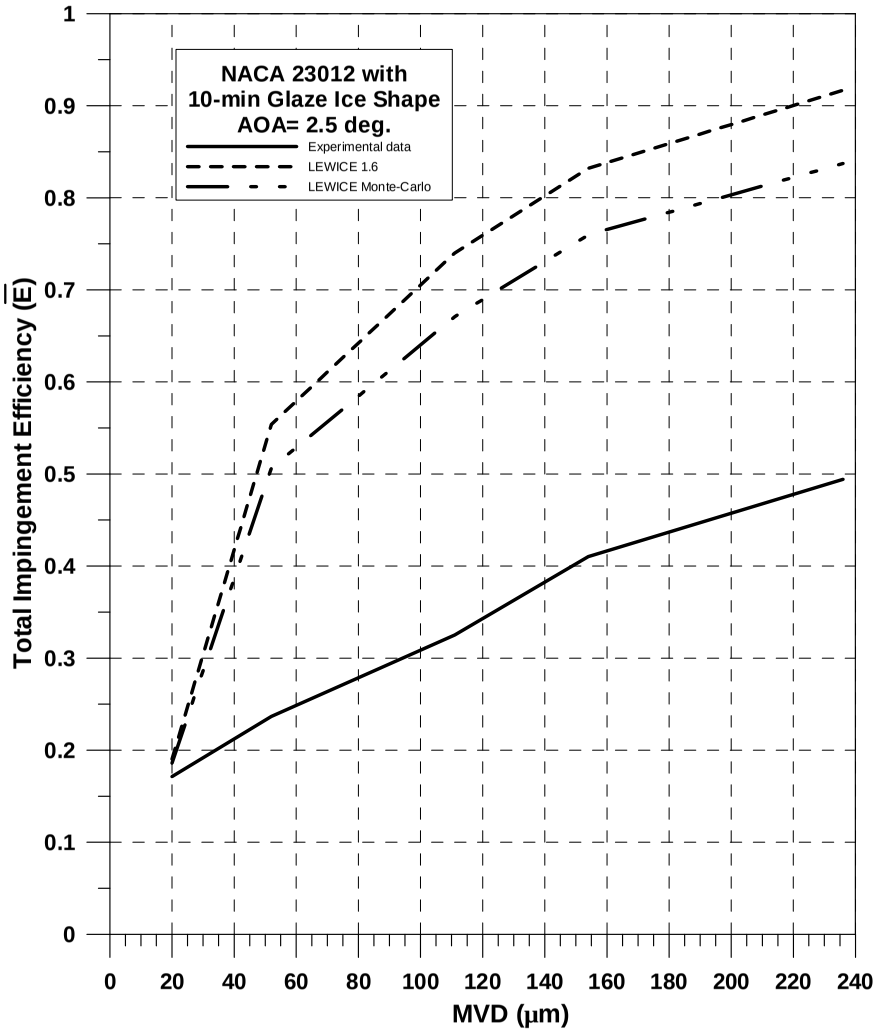

Figure E-52. Total Impingement Efficiency Distribution for NACA 23012 Airfoil With 10-min Glaze Ice Shape (c = 36 in., V_∞ = 175 mph, AOA = 2.5°)

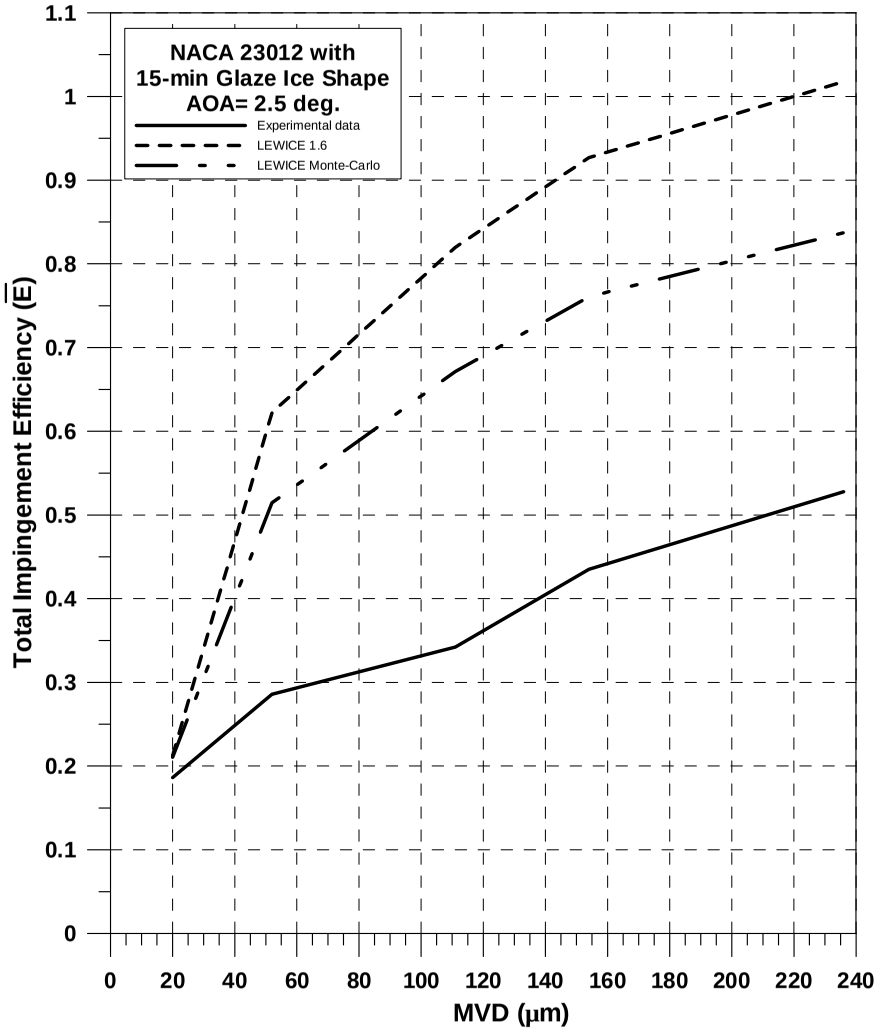

Figure E-53. Total Impingement Efficiency Distribution for NACA 23012 Airfoil With 15-min Glaze Ice Shape (c = 36 in., V_∞ = 175 mph, AOA = 2.5°)

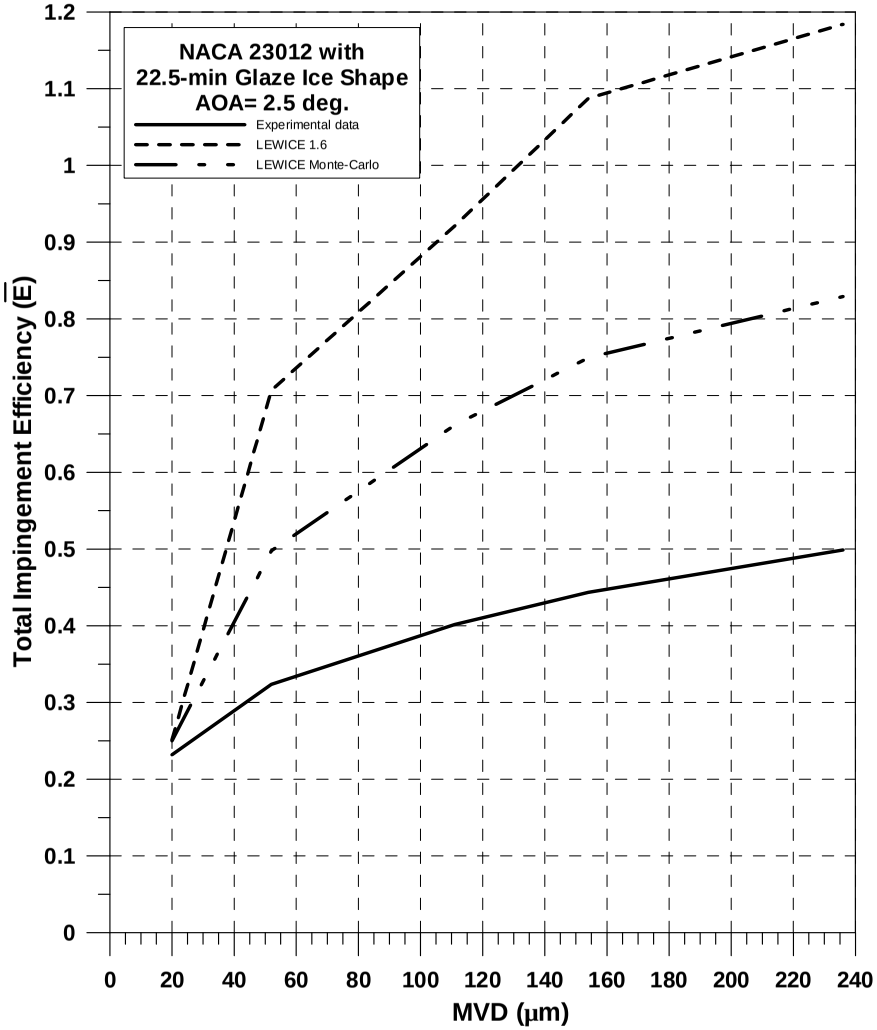

Figure E-54. Total Impingement Efficiency Distribution for NACA 23012 Airfoil With 22.5-min Glaze Ice Shape (c = 36 in., V_∞ = 175 mph, AOA = 2.5°)

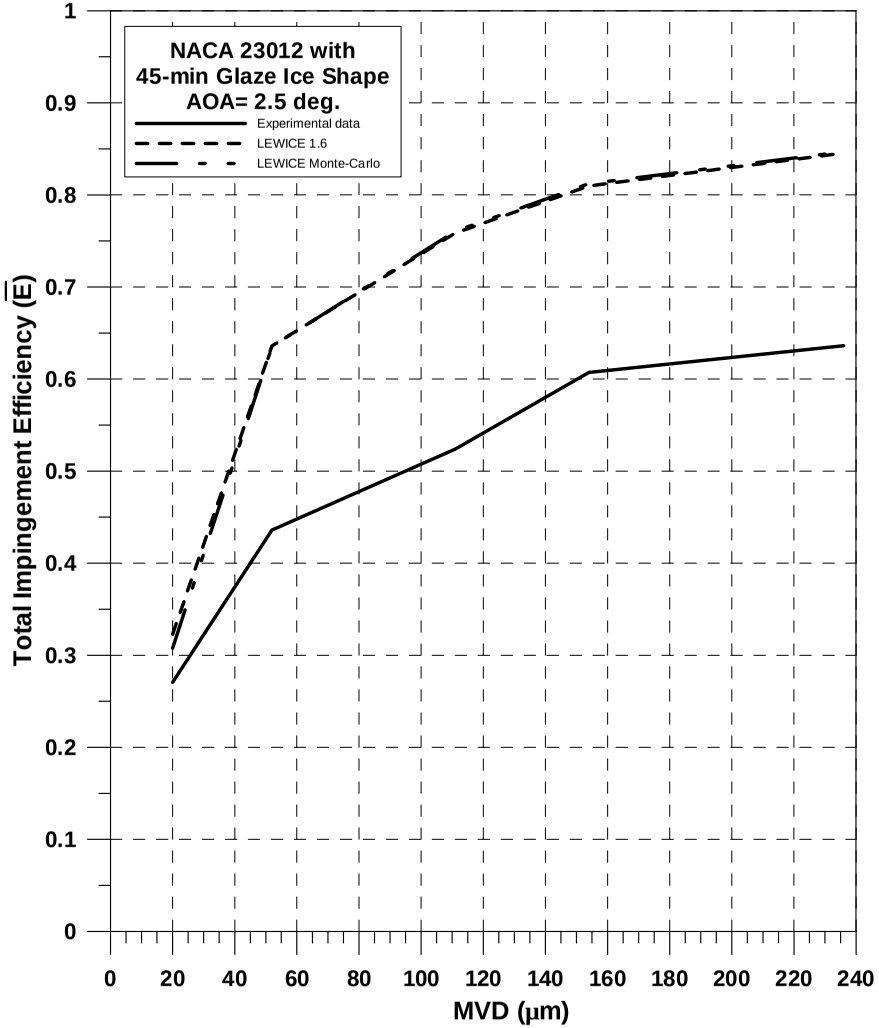

Figure E-55. Total Impingement Efficiency Distribution for NACA 23012 Airfoil With 45-min Glaze Ice Shape (c = 36 in., V_∞ = 175 mph, AOA = 2.5°)

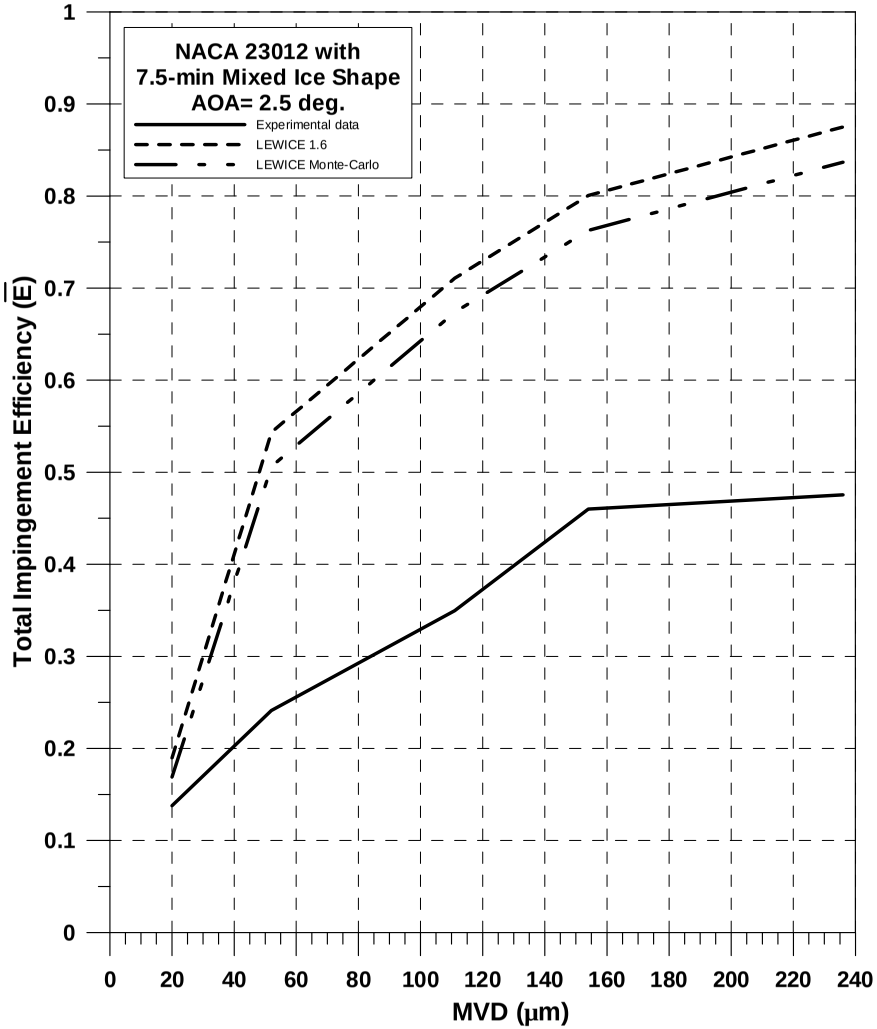

Figure E-56. Total Impingement Efficiency Distribution for NACA 23012 Airfoil With 7.5-min Mixed Ice Shape (c = 36 in., V_∞ = 175 mph, AOA = 2.5°)

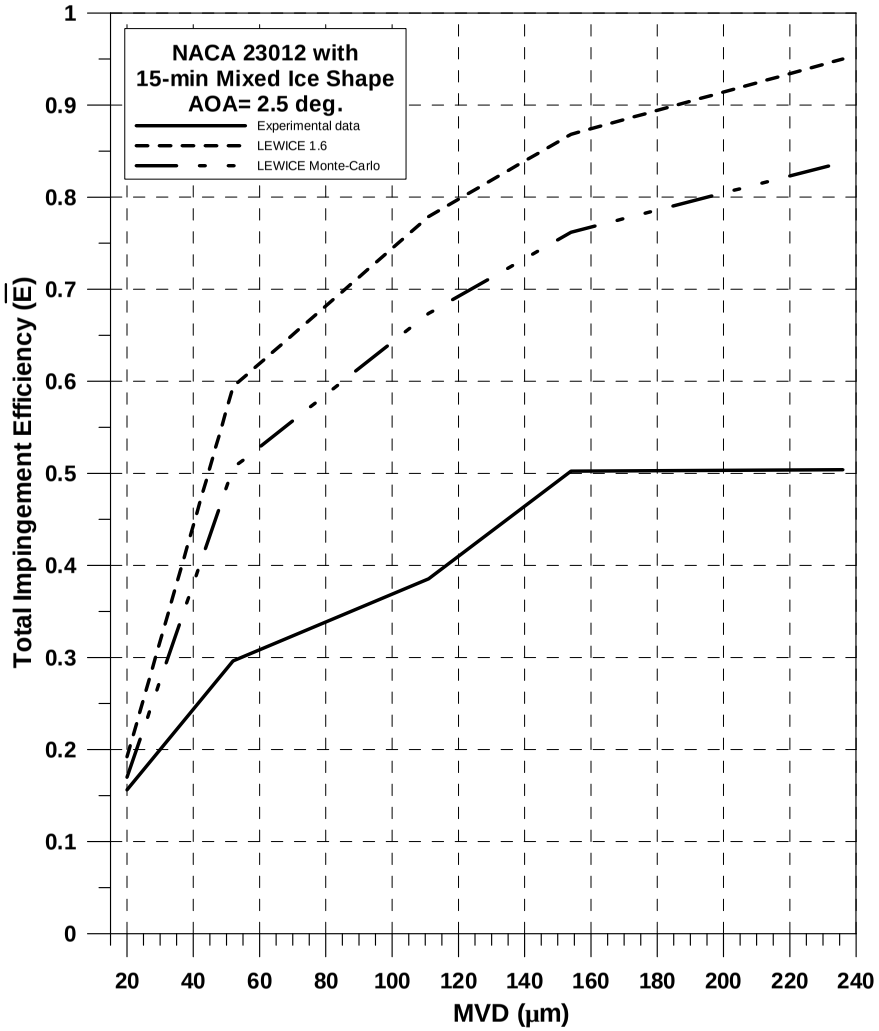

Figure E-57. Total Impingement Efficiency Distribution for NACA 23012 Airfoil With 15-min Mixed Ice Shape (c = 36 in., V_∞ = 175 mph, AOA = 2.5°)

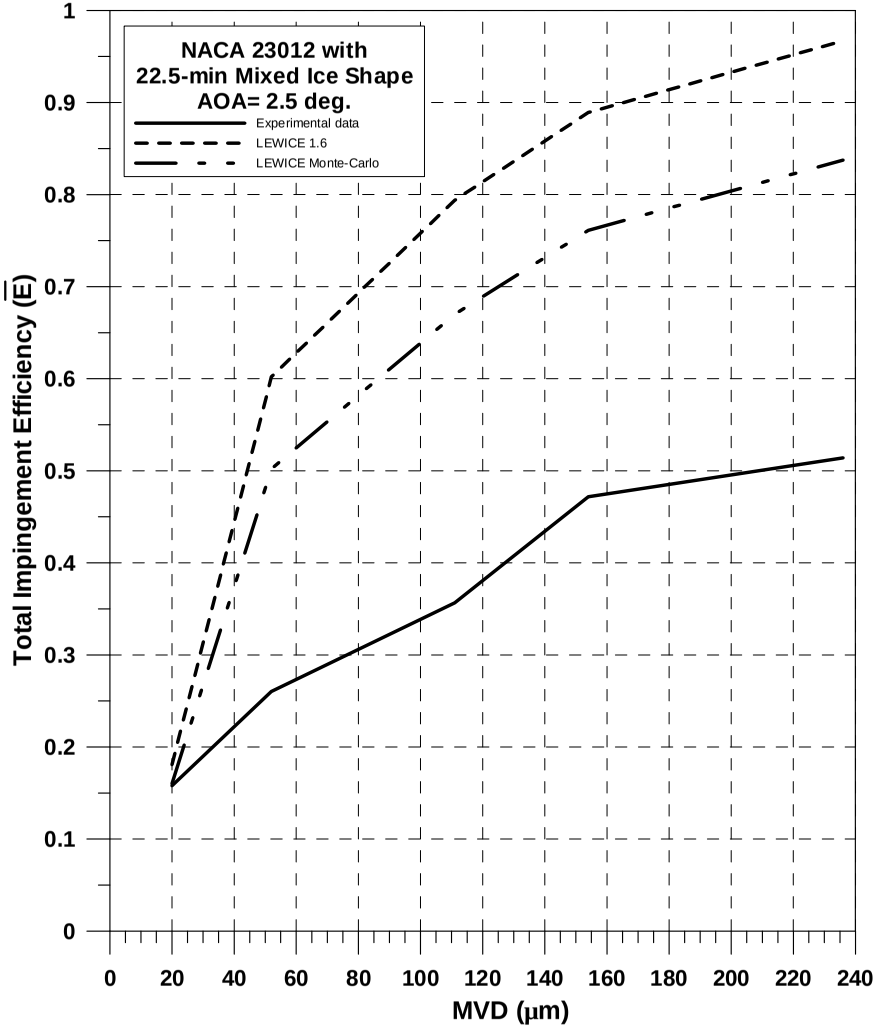

Figure E-58. Total Impingement Efficiency Distribution for NACA 23012 Airfoil With 22.5-min Mixed Ice Shape (c = 36 in., V_∞ = 175 mph, AOA = 2.5°)

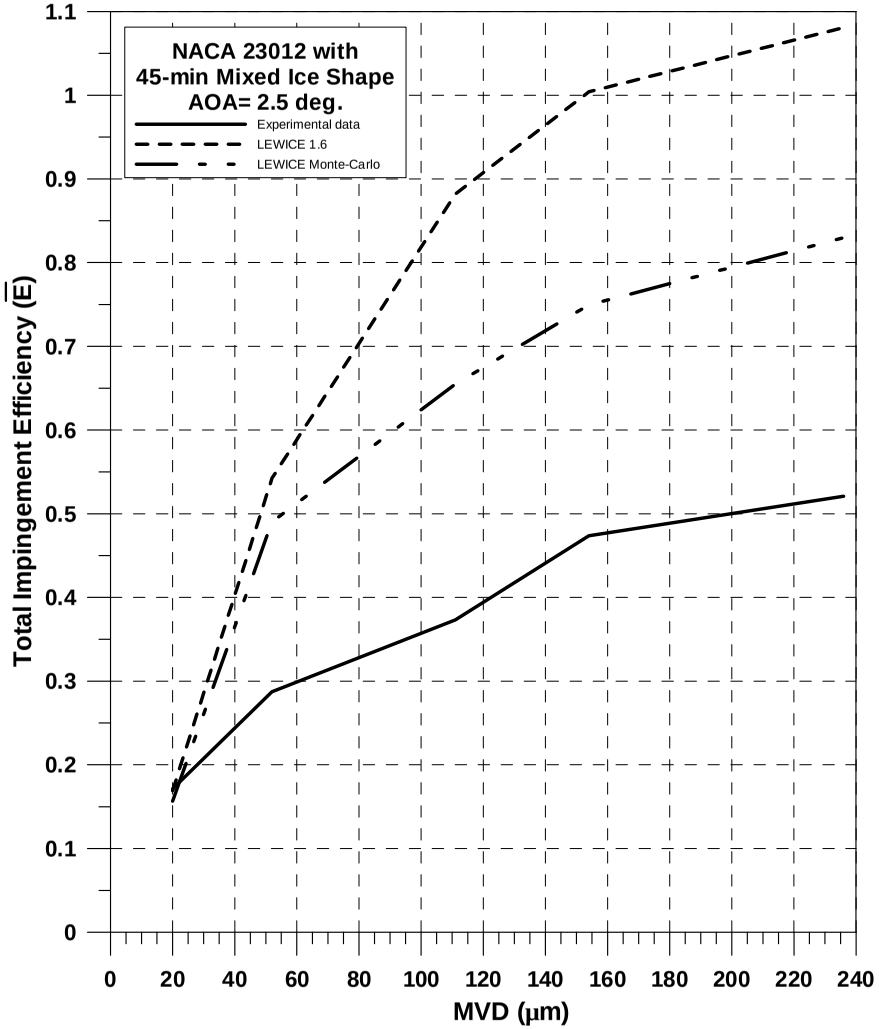

Figure E-59. Total Impingement Efficiency Distribution for NACA 23012 Airfoil With 45-min Mixed Ice Shape (c = 36 in., V_∞ = 175 mph, AOA = 2.5°)

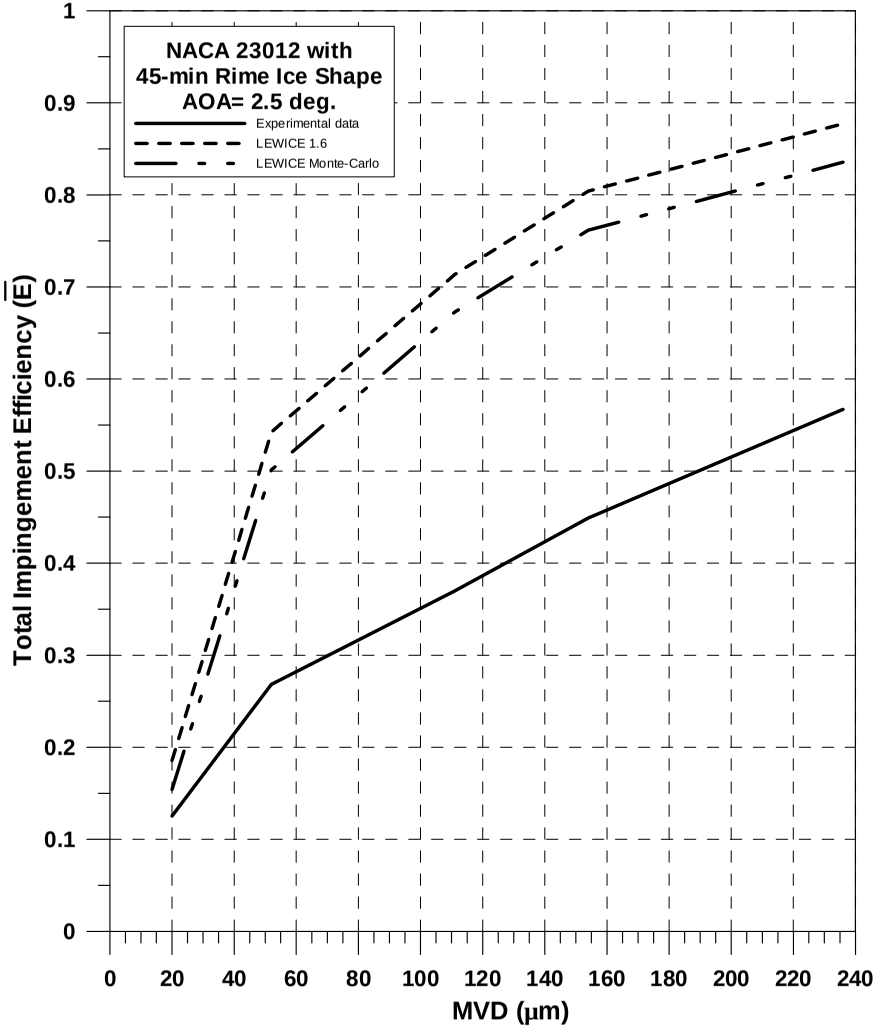

Figure E-60. Total Impingement Efficiency Distribution for NACA 23012 Airfoil With 45-min Rime Ice Shape (c = 36 in., V_∞ = 175 mph, AOA = 2.5°

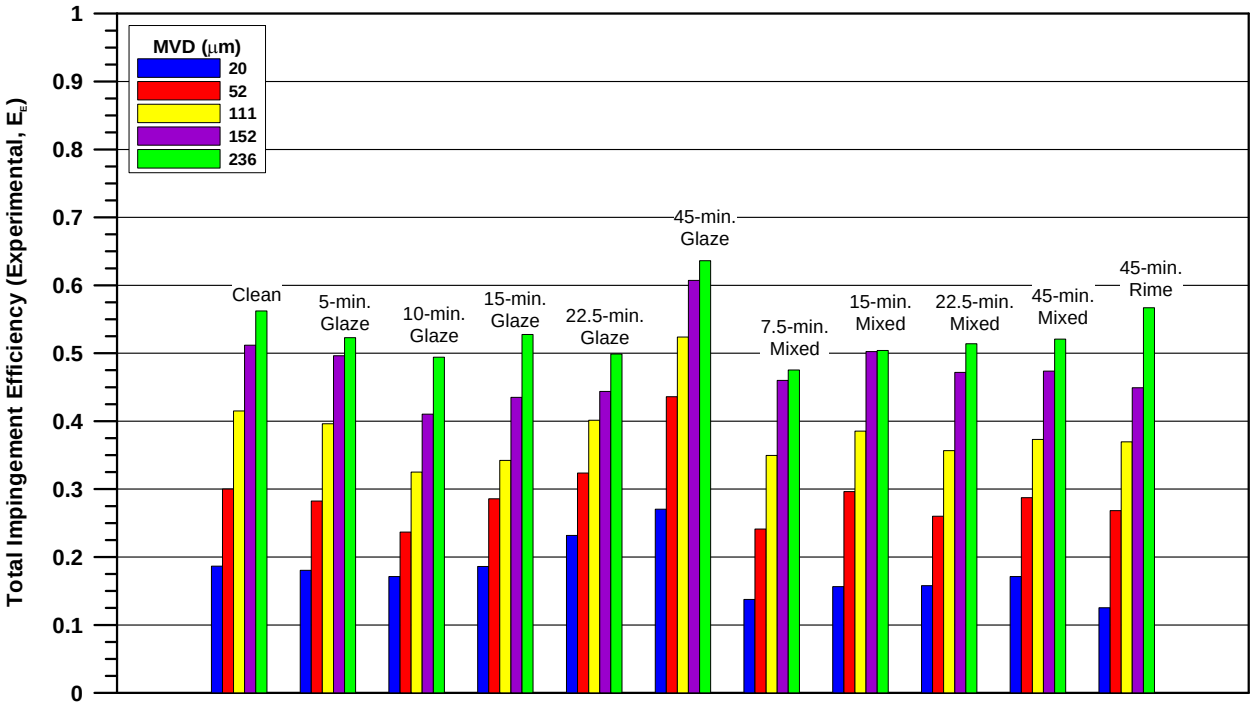

Figure E-61. Summary of Experimental Total Impingement Efficiency Distributions

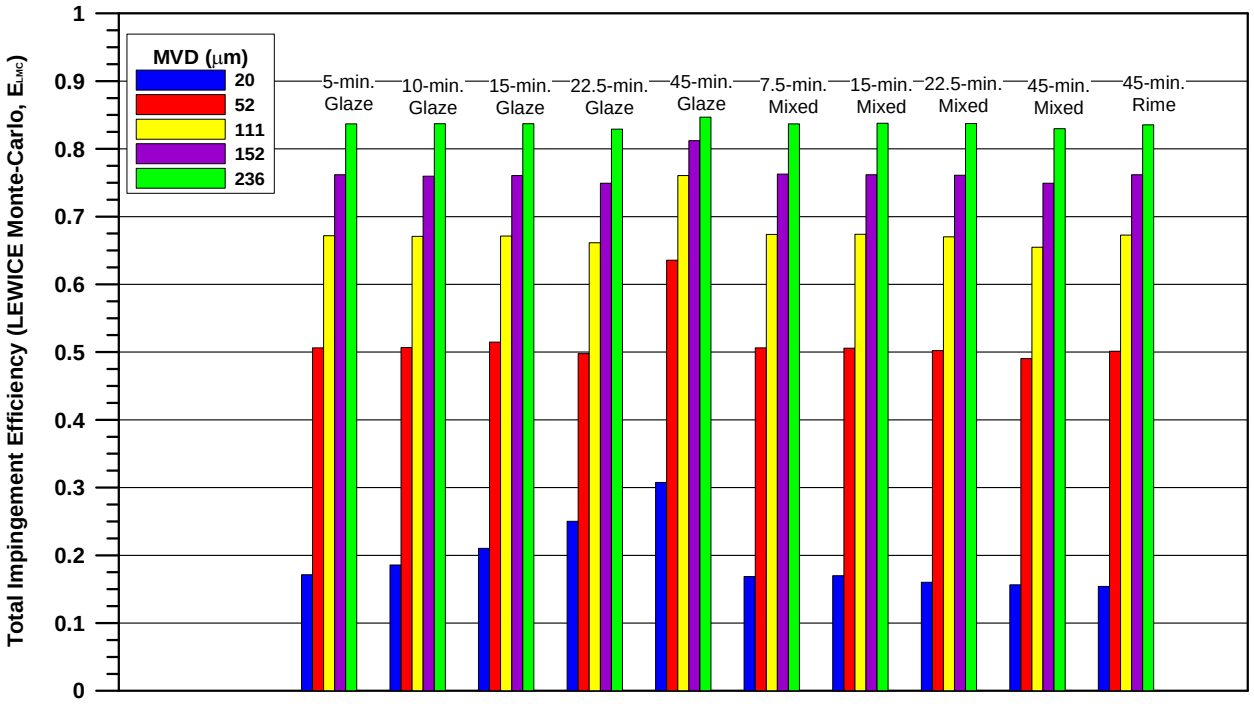

Figure E-62. Summary of LEWICE Monte-Carlo Total Impingement Efficiency Distributions

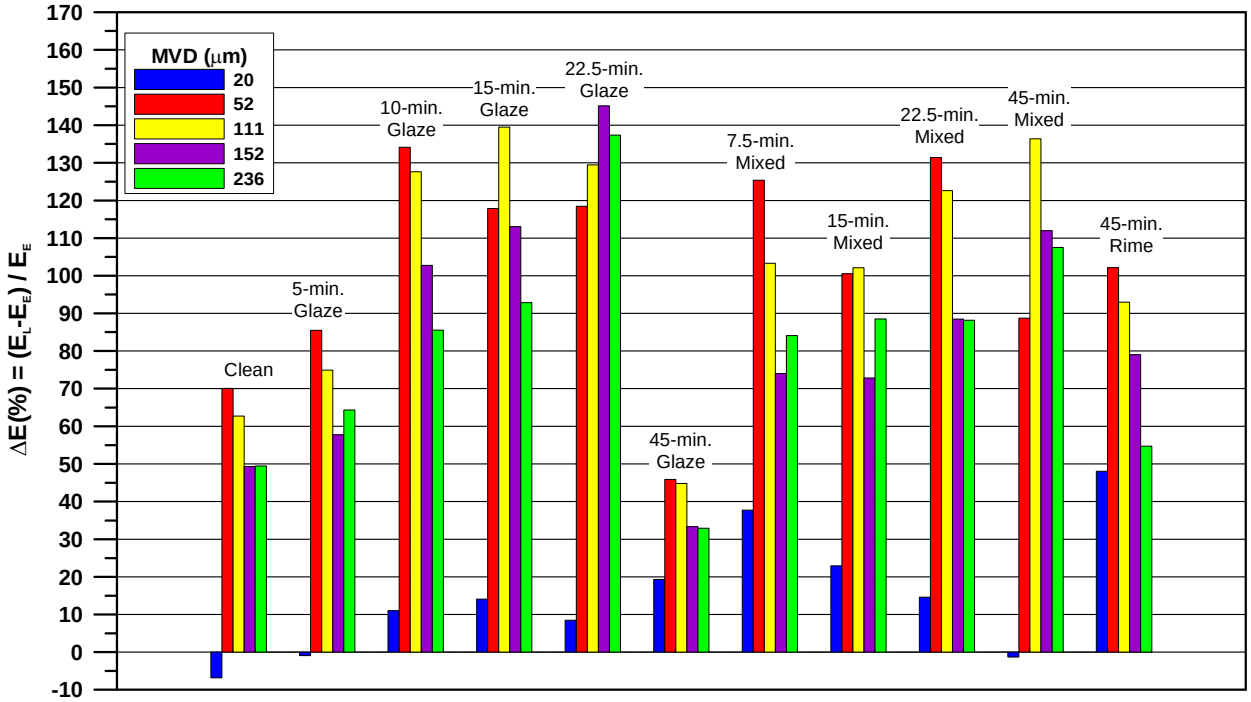

Figure E-63. Percentage Difference in Total Impingement Efficiency Between LEWICE 1.6 and Experimental Data

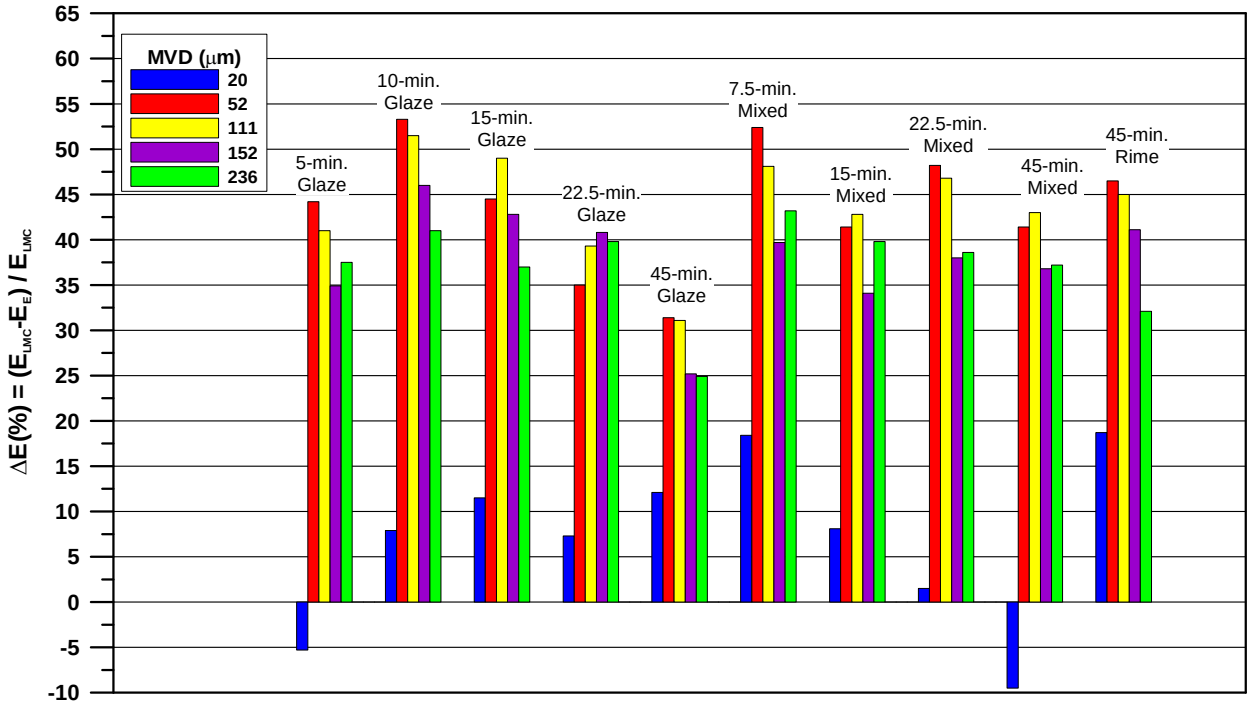

Figure E-64. Percentage Difference in Total Impingement Efficiency Between LEWICE Monte-Carlo and Experimental Data